

UC San Diego

UC San Diego Electronic Theses and Dissertations

Title

Organoferrous Antitumor Agents

Permalink

<https://escholarship.org/uc/item/1dk4s4vc>

Author

Aubrey, Marissa Caroline

Publication Date

2015

Peer reviewed|Thesis/dissertation

UNIVERSITY OF CALIFORNIA, SAN DIEGO

Organoferrous Antitumor Agents

A dissertation submitted in partial satisfaction of the requirements for the degree
Doctor of Philosophy

in

Chemistry

by

Marissa Caroline Aubrey

Committee in charge:

Professor Joseph M. O'Connor, Chair
Professor Seth M. Cohen
Professor William Fenical
Professor Charles L. Perrin
Professor Jerry Yang

2015

Copyright

Marissa Caroline Aubrey, 2015

All rights reserved.

The Dissertation of Marissa Caroline Aubrey is approved, and it is acceptable in quality and form for publication on microfilm and electronically:

Chair

University of California, San Diego

2015

TABLE OF CONTENTS

Signature Page	iii
Table of Contents	iv
List of Figures	vii
List of Tables	xvi
List of Schemes	xviii
List of Abbreviations.....	xxii
Acknowledgements	xxiii
Curriculum Vita	xxiv
Abstract of the Dissertation	xxv
 Chapter I. Introduction to Ferrous Antitumor Agents and Naturally Occurring and	
Synthetic Eneidyne	1
A. Biological Activity of Ferrocene and Ferrocenium.....	2
B. Transportation and Storage of Cellular Iron.....	4
C. Iron and Reactive Oxygen Species (ROS).....	7
D. Other Ferrocene-based Antitumor Agents.....	12
E. The Bergman Cycloaromatization.....	20
F. The Eneidyne Natural Products.....	22
G. Mechanism of Action for Calicheamicin- γ_1^1	24
H. Eneidyne Distance Theory.....	27
I. Metal Mediated Cycloaromatization: Select Examples.....	28
J. Photochemical Properties of Ferrocene.....	33

K. Photochemical Properties of Benzoyl and 1,1'-Dibenzoyl Ferrocene.....	35
L. Proposal.....	40
M. References.....	44
Chapter II. Photosensitive Ferrocene-Based Antitumor Agents.....	49
A. Introduction.....	50
B. Results.....	54
C. Discussion.....	93
D. Conclusions	118
E. Experimental.....	121
F. Appendix 1.....	149
G. Appendix 2.....	199
H. Appendix 3.....	208
I. References.....	212
J. Acknowledgments.....	215
Chapter III. Photosensitive Ferrocene-Based Eneidyne	216
A. Introduction.....	217
B. Results.....	220
C. Discussion.....	253
D. Conclusions.....	275
E. Experimental.....	277

F. Appendix 1.....	299
G. Appendix 2.....	339
H. References.....	345

LIST OF FIGURES

Figure 1.1. Organometallic antitumor agents.....	3
Figure 1.2. Iron transportation and storage in mammalian cells.....	5
Figure 1.3. Inner coordination sphere for one of the ferric ions in $Tf(Fe^{3+})_2$	6
Figure 1.4. Selected antitumor ferrocene complexes	12
Figure 1.5. Ferrocene complexes that target DNA.	14
Figure 1.6. Ferrocene substituted testosterone mimics for treatment of prostate cancer.....	15
Figure 1.7. SERM raloxifen 19 and its ferrocene derivative 20	16
Figure 1.8. Clinical breast cancer drug tamoxifen and its ferrocene analog hydroxyferrocifen.....	17
Figure 1.9. Eneidyne natural products.....	23
Figure 1.10. Mylotarg [®] a synthetic enediyne for cancer.....	24
Figure 1.11. Shorter <i>cd</i> distances have been shown to lower the barrier to cycloaromatization.....	27
Figure 1.12. Ring strain effects on the barrier to cycloaromatization.....	28
Figure 1.13. Benzoyl and 1,1'-dibenzoylferrocene.....	36
Figure 1.14. Generation of toxic hydroxyl radicals from benzoylferrocene using visible light irradiation.....	41
Figure 1.15. Synthetic enediynes that become activated upon exposure to visible light.....	43
Figure 2.1. Selected metal compounds displaying biological activity.....	51
Figure 2.2. Resonance structure depicting the MLCT character for the low-energy excited state of benzoylferrocene.....	52
Figure 2.3. Photochemical generation of solvated iron (II) and catalytic formation of reactive oxygen species.	54

Figure 2.4. Photochemical decomposition of 15 at 490 nm.....	58
Figure 2.5. Photochemical decomposition of 21 at 490 nm.....	58
Figure 2.6. Photochemical decomposition of 24 at 490 nm.	59
Figure 2.7. Pipetting scheme for the 96-well microtiter plate in the two concentrations assay.....	61
Figure 2.8. Modified pipetting scheme for the 96-well microtiter plate in the two concentrations assay.	62
Figure 2.9. 1-Benzoylferrocenes and 1,1'-dibenzoylferrocenes screened for cytotoxicity in the dark and under irradiation conditions.	64
Figure 2.10. ORTEP view of 7	68
Figure 2.11. ORTEP view of 15	69
Figure 2.12. ORTEP view of 29	69
Figure 2.13. ORTEP view of 30	70
Figure 2.14. ORTEP view of 31	70
Figure 2.15. Cytotoxicity dose responses for 30 (right panel) and 31 (left panel) and their photoproducts in HeLa and A549 cells.....	75
Figure 2.16. Linear calibration relating $\log P$ and $\log k$	79
Figure 2.17. Iron concentration in the HeLa cell lysate as a function of extracellular 31 concentration.....	82
Figure 2.18. UV-Vis profile of 31 photolysis in 50:50 H ₂ O:DMF in the presence of 2,2'-bipyridyl	85
Figure 2.19. ¹ H NMR spectra of photoreaction for complex 31 in DMF- <i>d</i> ₇ and D ₂ O. Bottom: t = 0; Middle: t = 30 min; top: following filtration.....	88
Figure 2.20. Potential isomers formed upon protonation of anion 38	90
Figure 2.21. TEM of dialyzed micelles	93

Figure 2.22. Equations for Type I and Type II processes in photodynamic therapy.....	96
Figure 2.23. Cytotoxicity dose response of 30 in HeLa cells when exposed to > 450 nm light for various amounts of time.	100
Figure 2.24. HeLa cells before and after being subjected to standard photolysis conditions with complex 30 at 10x magnification. Top row: before photolysis, middle row: immediately following photolysis, bottom row: 12 h post photolysis.....	101
Figure 2.25. Cytotoxicity dose responses for 30 (left panel) and 31 (right panel) in A549 and MRC-5 cells in the dark and under irradiation conditions.....	104
Figure 2.26. Relationship of log <i>P</i> to IC ₅₀ of selected benzoylferrocene complexes (black = absence of light; yellow = under irradiation conditions.....)	109
Figure 2.27. Typical Bradford Assay standard curve.	112
Figure 2.28. Proposed mechanism for photochemical decomposition of 31	118
Figure 2.29. Ansa ferrocene derivative 46	120
Figure 2.30. ¹ H NMR spectrum of 7	149
Figure 2.31. ¹³ C NMR spectrum of 7	150
Figure 2.32. ¹ H NMR spectrum of 13	151
Figure 2.33. ¹³ C NMR spectrum of 13	152
Figure 2.34. ¹ H NMR spectrum of 14	153
Figure 2.35. ¹³ C NMR spectrum of 14	154
Figure 2.36. ¹ H NMR spectrum of 15	155
Figure 2.37. ¹ H NMR spectrum of 15	156
Figure 2.38. ¹³ C NMR spectrum of 15	157
Figure 2.39. ¹ H NMR spectrum of 18	158

Figure 2.40. ^{13}C NMR spectrum of 18	159
Figure 2.41. ^{13}C NMR spectrum of 19	160
Figure 2.42. ^{13}C NMR spectrum of 19	161
Figure 2.43. ^1H NMR spectrum of 20	162
Figure 2.44. ^{13}C NMR spectrum of 20	163
Figure 2.45. ^1H NMR spectrum of 21	164
Figure 2.46. ^{13}C NMR spectrum of 21	165
Figure 2.47. ^1H NMR spectrum of 22	166
Figure 2.48. ^{13}C NMR spectrum of 22	167
Figure 2.49. ^1H NMR spectrum of 24	168
Figure 2.50. ^{13}C NMR spectrum of 24	169
Figure 2.51. ^1H NMR spectrum of 25	170
Figure 2.52. ^{13}C NMR spectrum of 25	171
Figure 2.53. ^1H NMR spectrum of 26	172
Figure 2.54. ^{13}C NMR spectrum of 26	173
Figure 2.55. ^1H NMR spectrum of 27	174
Figure 2.56. ^{13}C NMR spectrum of 27	175
Figure 2.57. ^1H NMR spectrum of 28	176
Figure 2.58. ^{13}C NMR spectrum of 28	177
Figure 2.59. ^1H NMR spectrum of 29	178
Figure 2.60. ^{13}C NMR spectrum of 29	179
Figure 2.61. ^1H NMR spectrum of 30	180

Figure 2.62. ^{13}C NMR spectrum of 30	181
Figure 2.63. ^{13}C NMR spectrum of 30	182
Figure 2.64. ^1H NMR spectrum of 31	183
Figure 2.65. ^{13}C NMR spectrum of 31	184
Figure 2.66. ^1H NMR spectrum of 32	185
Figure 2.67. ^{13}C NMR spectrum of 32	186
Figure 2.68. ^1H NMR spectrum of 35	187
Figure 2.69. ^{13}C NMR spectrum of 35	188
Figure 2.70. ^1H NMR spectrum of 36	189
Figure 2.71. ^{13}C NMR spectrum of 36	190
Figure 2.72. ^1H NMR spectrum of 37	191
Figure 2.73. ^{13}C NMR spectrum of 37	192
Figure 2.74. ^1H NMR spectrum of 39	193
Figure 2.75. ^{13}C NMR spectrum of 39	194
Figure 2.76. ^1H NMR spectrum of 40(phen)	195
Figure 2.77. ^{13}C NMR spectrum of 40(phen)	196
Figure 2.78. ^{13}C NMR spectrum of 31 in DMF- d_7 , H ₂ O (0.6 mL, 0.1 mL).....	197
Figure 2.79. ^{13}C NMR spectrum of 31 photoproducts in DMF- d_7 , H ₂ O (0.6 mL, 0.1 mL).....	198
Figure 2.80. Numbered ORTEP of 7	204
Figure 2.81. Numbered ORTEP of 15	205
Figure 2.82. Numbered ORTEP of 29	206
Figure 2.83. Numbered ORTEP of 30	206

Figure 2.84. Numbered ORTEP of 31	207
Figure 2.85. HeLa cells before after being treated with complex 30 in the dark at 10x magnification. Top row: before photolysis, middle row: immediately following photolysis, bottom row: 12 h post photolysis.....	208
Figure 2.86. HeLa cells before and after being treated with complex 30 in the dark at 10x magnification. Images taken in parallel with corresponding photolyzed samples.	209
Figure 2.87. Cells after being subjected to 30 and standard photolysis conditions (top row) or ferrocene complex without irradiation in the dark (bottom row) at 10x magnification (images of both plates taken in parallel).....	209
Figure 2.88. HeLa cells before and after being subjected to standard photolysis conditions at 20x magnification with 30 . Top row: before photolysis, middle row: immediately following photolysis, bottom row: 12 h post photolysis	210
Figure 2.89. HeLa cells before after being treated with ferrocene complex 30 in the dark at 20x magnification. Images taken in parallel with the corresponding photolyzed samples.	211
Figure 2.90. HeLa Cells before after being subjected to ferrocene complex 30 and standard photolysis conditions (top row) or ferrocene complex in the dark (bottom row) at 20x magnification (images of both plates taken in parallel).....	211
Figure 3.1. Resonance structure representative of the MLCT character in the low-energy excited state of 6	219
Figure 3.2. Proposed ferrocenyl enediynes.....	220
Figure 3.3. ORTEP drawing for 24	230
Figure 3.4. ORTEP drawing for 26	231
Figure 3.5. ORTEP drawing for 32	232
Figure 3.6. ORTEP Drawing of 59	245

Figure 3.7. Ferrocenyl enediyne 1	254
Figure 3.8. Excitation and conversion of 6 to 66	255
Figure 3.9. Previous work on metal-assisted cyclization reactions.....	256
Figure 3.10. Proposed method to generate reactive enediynes from ferrocene.....	263
Figure 3.11. Thermal parameters for some characterized enediynes.....	264
Figure 3.12. Ring strain effects in organic and ferrocene-based enediynes.....	266
Figure 3.13. Proposed organic photoproducts of 45 , 59 , 61 , and 62	271
Figure 3.14. ¹ H NMR spectrum of 20	299
Figure 3.15. ¹³ C NMR spectrum of 20	300
Figure 3.16. ¹ H NMR spectrum of 21	301
Figure 3.17. ¹³ C NMR spectrum of 21	302
Figure 3.18. ¹ H NMR spectrum of 13	303
Figure 3.19. ¹ H NMR spectrum of 6⁻/6⁺	304
Figure 3.20. ¹³ C NMR spectrum of 6⁻/6⁺	305
Figure 3.21. ¹ H NMR spectrum of 31	306
Figure 3.22. ¹³ C NMR spectrum of 31	307
Figure 3.23. ¹ H NMR spectrum of 26	308
Figure 3.24. ¹³ C NMR spectrum of 26	309
Figure 3.25. ¹ H NMR spectrum of 48	310
Figure 3.26. ¹³ C NMR spectrum of 48	311
Figure 3.27. ¹ H NMR spectrum of 53	312
Figure 3.28. ¹³ C NMR spectrum of 53	313

Figure 3.29. ^1H NMR spectrum of 54	314
Figure 3.30. ^{13}C NMR spectrum of 54	315
Figure 3.31. ^1H NMR spectrum of 55	316
Figure 3.32. ^{13}C NMR spectrum of 55	317
Figure 3.33. ^1H NMR spectrum of 56	318
Figure 3.34. ^{13}C NMR spectrum of 56	319
Figure 3.35. ^1H NMR spectrum of 57	320
Figure 3.36. ^{13}C NMR spectrum of 57	321
Figure 3.37. ^1H NMR spectrum of 58	322
Figure 3.38. ^{13}C NMR spectrum of 58	323
Figure 3.39. ^1H NMR spectrum of 45	324
Figure 3.40. ^{13}C NMR spectrum of 45	325
Figure 3.41. ^1H NMR spectrum of 60	326
Figure 3.42. ^{13}C NMR spectrum of 60	327
Figure 3.43. ^1H NMR spectrum of 59	328
Figure 3.44. ^{13}C NMR spectrum of 59	329
Figure 3.45. ^1H NMR spectrum of 61	330
Figure 3.46. ^{13}C NMR spectrum of 61	331
Figure 3.47. ^1H NMR spectrum of 63	332
Figure 3.48. ^1H NMR spectrum of 64	333
Figure 3.49. ^{13}C NMR spectrum of 64	334
Figure 3.50. ^1H NMR spectrum of 65	335

Figure 3.51. ^{13}C NMR spectrum of 65	336
Figure 3.52. ^1H NMR spectrum of 62	337
Figure 3.53. ^{13}C NMR spectrum of 62	338
Figure 3.54. Numbered ORTEP of 24	343
Figure 3.55. Numbered ORTEP of 26	344
Figure 3.54. Numbered ORTEP of 32	345

LIST OF TABLES

Table 2.1. Selected bond metrics for X-ray structures of 7 , 15 , and 29-31	71
Table 2.2. IC _{50-light} values (μM) for 30 and 31 with increasing irradiation time.....	74
Table 2.3. IC ₅₀ values (μM) for active benzoylferrocene complexes.....	74
Table 2.4. Effect of washing on IC ₅₀ values (μM) in A549 cells for complex 31	76
Table 2.5. IC ₅₀ values (μM) in healthy cell lines.....	77
Table 2.6. HPLC retention times and partition coefficients for selected standards.....	79
Table 2.7. Benzoylferrocene complexes and their estimated log <i>P</i> values.....	80
Table 2.8. Iron concentration in HeLa cell lysates (ng Fe/mg protein) following treatment with various iron containing drugs.....	81
Table 2.9. Cyclic voltammetry data (vs Fc/Fc ⁺) for the tested benzoylferrocene complexes.....	83
Table 2.10. UV-Vis data for benzoylferrocene complexes (50:50 DMF/H ₂ O).....	84
Table 2.11. Relative energies of cyclopentadiene isomers calculated using Density Functional Theory (BLYP/6-31++G**).....	90
Table 2.12. Photobiological Activity of benzoylferrocene complexes.....	103
Table 2.13. Comparison of lipophilicity and PI ratios for active complexes.....	108
Table 2.14. Concentration of iron in cell lysates following treatment with various iron containing complexes (60 μM).....	113
Table 2.15. Crystal data and structure refinement for 7	199
Table 2.16. Crystal data and structure refinement for 15	200
Table 2.17. Crystal data and structure refinement for 29	201
Table 2.18. Crystal data and structure refinement for 30	202

Table 2.19. Crystal data and structure refinement for 31	203
Table 3.1. Key angles for complexes 6, 24, 26 and 32	232
Table 3.2. Iron Cp-carbon bond distances for complexes 6, 24, 26 and 32	232
Table 3.3. Key bond distances and angles for complexes 6, 24, 26 and 32	233
Table 3.4. Key bond distances for complexes 26 and 32	233
Table 3.5. Key bond angles for complexes 26 and 32	233
Table 3.6. Key bond lengths and angles for complex 59	245
Table 3.7. Iron Cp-carbon bond distances for complex 59	245
Table 3.8. Key bond lengths and angles for complex 59	246
Table 3.9. IC ₅₀ values (μM) for ferrous enediyne complexes.....	248
Table 3.10. IC ₅₀ values (μM) for ferrous enediyne complexes.....	251
Table 3.11. Log <i>P</i> values for synthesized ferrocenyl enediynes.....	252
Table 3.12. Calculated Bond lengths (\AA), angles, and energies for free enediynes 89^a-89^e using DFT BLYP/6-31++G**	274
Table 3.13. IC ₅₀ (μM), phototoxicity index (P.I.) and log <i>P</i> for tested ferrocene enediynes.....	275
Table 3.14. Crystal data and structure refinement for 24	339
Table 3.15. Crystal data and structure refinement for 26	340
Table 3.16. Crystal data and structure refinement for 32	341
Table 3.17. Crystal data and structure refinement for 59	342

LIST OF SCHEMES

Scheme 1.1. Generation of hydroxyl radical via the Haber-Weiss Cycle.....	8
Scheme 1.2. Mechanism for phospholipid peroxidation initiated by ferrous iron.....	9
Scheme 1.3. Mechanism for DNA base peroxidation initiated by ferrous iron.....	10
Scheme 1.4. Generation of reactive oxygen species in cells.....	11
Scheme 1.5. A proposed mechanism of action for 23	19
Scheme 1.6. Robert Bergman's 1972 classic enediyne scrambling experiment.....	21
Scheme 1.7. Trapping of <i>para</i> -benzyne by various solvents.....	22
Scheme 1.8. Enediyne activation mechanism for calicheamicin- γ_1^I	25
Scheme 1.9. Mechanism of double-stranded DNA cleavage initiated by calicheamicin- γ_1^I	26
Scheme 1.10. Coordination of mercury drastically lowers temperature for 39 to cyclize.....	29
Scheme 1.11. Coordination to enediyne 41 drastically lowers to barrier to cyclization.....	30
Scheme 1.12. Coordination of magnesium to 43 drastically lowers to barrier to cyclization.....	30
Scheme 1.13. Ruthenium and iron-mediated cyclization of acyclic enediynes.....	31
Scheme 1.14. Chromium mediated cycloaromatization of enediyne 50 and structure of possible intermediate 56	32
Scheme 1.15. Photochemical decomposition of ferrocene.....	34
Scheme 1.16. Decomposition of 1 as reported by Traverso <i>et al</i>	34
Scheme 1.17. Decomposition of 1 to give ester 59	35
Scheme 1.18. Proposed mechanism for decomposition of 60 by Tarr and Wiles.....	37

Scheme 1.19. Photodecomposition of 60 as reported by Ali <i>et al</i>	38
Scheme 1.20. Photodecomposition of 60 as reported by Bozak <i>et al</i>	39
Scheme 1.21. Kutal's mechanism for photodissociation of benzoylferrocene.....	40
Scheme 2.1. A proposed mechanism for the photochemical dissociation of the ligands in 7	53
Scheme 2.2. Synthesis of water-soluble benzoylferrocene 15	55
Scheme 2.3. Synthesis of anionic water-soluble derivative 21	56
Scheme 2.4. Synthesis of ROMP monomer 24	57
Scheme 2.5. Experimental procedure for the crystal violet assay.....	60
Scheme 2.6. Synthesis of derivatives 14 , 25-28	65
Scheme 2.7. Friedel-Crafts acylation to form 7 and 29-31	66
Scheme 2.8. Friedel-Crafts acylation to form 1,1'-dibenzoylferrocenes.....	67
Scheme 2.9. Photoactivity of 31 in DMF- <i>d</i> ₇ and D ₂ O.....	88
Scheme 2.10. ¹ H NMR and ¹³ C NMR spectral data for the photoreaction of complex 31 in DMF- <i>d</i> ₇ and D ₂ O.	89
Scheme 2.11. Photochemical synthesis of 40	91
Scheme 2.12. Synthesis of benzoylferrocene-containing polymers.....	92
Scheme 3.1. Proposed dissociation and aromatization of ferrocenyl-enediynes....	218
Scheme 3.2. Proposed synthesis of tethered enediyne 13	220
Scheme 3.3. Synthesis of enediyne 12	221
Scheme 3.4. Synthesis of primary alkyl halide 19	222
Scheme 3.5. Friedel Crafts acylation to generate benzoylferrocene 20	222
Scheme 3.6. Synthesis of acetal 21 by azeotropic water removal.....	223

Scheme 3.7. Synthesis of tethered enediyne 13 from 21	224
Scheme 3.8. Synthesis of 6 and 24	225
Scheme 3.9. Photolysis of benzoylferrocenes 6 and 24 with 25 or triphos.....	227
Scheme 3.10. Synthesis of complex 30	228
Scheme 3.11. Synthesis of pyrrolidine 26	229
Scheme 3.12. Synthesis and photochemical activity of 32	230
Scheme 3.13. Literature procedure for synthesis of diethynylferrocene.....	234
Scheme 3.14. Synthesis of Ohira-Taber reagent 41	235
Scheme 3.15. Synthesis of ferrous enediyne 35	235
Scheme 3.16. Photolysis of 35 to generate 44	236
Scheme 3.17. Attempted cycloaromatization of 44	237
Scheme 3.18. Synthesis of 47	238
Scheme 3.19. Sodium borohydride reduction of 47 to yield 48	238
Scheme 3.20. Deprotection of acetal 48	239
Scheme 3.21. Attempted acetal deprotection to synthesize 52	240
Scheme 3.22. Protection of alcohol 49 to form 53	240
Scheme 3.23. Alkynylation of protected dialdehyde 53 with 41 and subsequent methylation to give enediyne 55	241
Scheme 3.24. Deprotection of 55 and oxidation of 56 to form aldehyde 57	242
Scheme 3.25. Two step conversion of aldehyde 57 to benzoyl ketone 45	243
Scheme 3.26. Synthesis of enediyne 59	244
Scheme 3.27. Adol Condensation to form ketone 61	246
Scheme 3.28. Synthesis of 10-membered ring ferrocenyl enediyne 65	250

Scheme 3.29. Synthesis of α,β -unsaturated benzoyl ferrocene enediyne 62	251
Scheme 3.30. Proposed mechanism for metal-assisted intramolecular enediyne cyclization.....	257
Scheme 3.31. Synthesis of 13	258
Scheme 3.32. Attempted photochemical reactions of 24	260
Scheme 3.33. Synthesis of pyrrolidine 26	261
Scheme 3.34. Possible mechanism for photochemical decomposition of 35	267
Scheme 3.35. Synthesis of key intermediate 57 and enediynes 45 , 59 , and 61	269
Scheme 3.36. Synthesis of strained-ring enediyne 62	270
Scheme 3.37. Photochemical metal-mediated cycloaromatization of enediynes 45 , 59 , and 61	272
Scheme 3.38. Photolysis of 62 and proposed cycloaromatization of 87 and 88^b	273

LIST OF ABBREVIATIONS

Alphabetical within Category

Chemical Abbreviations

(- indicates covalent substituent)

B: general base

1,4-CHD: 1,4-cyclohexadiene

ⁿBu: *n*-butyl, -CH₂(CH₂)₂CH₃

^tBu: *t*-butyl, -C(CH₃)₃

Cp: cyclopentadienyl

Cp*: pentamethylcyclopentadienyl

Cp[‡]: 1,2,3,4-tetramethyl-5-trifluoromethylcyclopentadienyl

D/ -d: deuterium

DCM: dichloromethane

DMF: N,N-dimethylformamide

-Et: ethyl, -CH₂CH₃

Fc: ferrocene

Fc⁺: ferrocenium

L: metal ligand (e.g. AuL)

-Me: methyl, -CH₃

MeCN: acetonitrile

-OAc: acetate, -OC(O)CH₃

-Ph: phenyl, -C₆H₅

ⁿPr: *n*-propyl, -CH₂CH₂CH₃

THF: tetrahydrofuran

-TBS: *tert*-Butyldimethylsilyl ether

-TMS: trimethylsilyl

Experimental/ Spectroscopic

δ: chemical shift

η^x: x atoms π bound to metal

λ: wavelength

d: doublet

ESI: electrospray ionization

FT-IR: fourier transform infrared spectroscopy

hν: light

HRMS: high resolution mass spectrometry

J: coupling constant

KIE: kinetic isotope effect

m: multiplet

NMR: nuclear magnetic resonance spectroscopy

p: pentet

q: quartet

rt: room temperature

s: singlet

t: triplet

TLC: thin layer chromatography

TOF: time of flight

uv: ultraviolet radiation

Parameter Units

(Conventional SI prefixes were used)

Å: Angstrom

°C: degree Celsius

h: hour

Hz: Hertz

cm⁻¹: wavenumber

eV: electron volt

K: Kelvin

L: liter

M: molar

m: meter

min: minute

mol: mole

ppm: parts per million

s: seco

ACKNOWLEDGEMENTS

Tremendous thanks to Professor Joseph O'Connor, my advisor. His door has always been open to me as I navigated the many difficulties of my project. Thanks also to my thesis committee: Professors Jerry Yang, Seth Cohen, Bill Fenical, and especially Dr. Perrin, whose advice was invaluable during my time here. I am particularly grateful to Dr. María Proetto in the Gianneschi Group for her persistence and teaching me everything I know about tissue culture and sterile technique. I would also like to thank Dr. Yongxuan Su (UCSD MS Facility) for his assistance with mass spectrometry measurements, Dr. Anthony Mrse (UCSD NMR Facility), and Dr. Mohand Melaimi for his help with cyclic voltammetry experiments. Thanks to Paterno Castillo and Chris MacIsaac (Scripps Institution of Oceanography) for their assistance with ICP-OES measurements. Thanks also to past and present members of the O'Connor Lab, Ryan Holland, David Hitt, Carmen Velez, Stephen Cope, Christina Hoong, and Kate Veccharelli for their scientific insight and more importantly, keeping graduate school fun. Finally, I am grateful for the presence of my friends and family members, thank you for making this possible.

The material in Chapter II, in part, will be included in the submission for publication. Aubrey, Marissa; Proetto, María; Hoong, Christina; Melaimi, Mohand; O'Connor, Joseph. "Photoactivated Organoferrous Antitumor Agents". The dissertation author was the primary investigator and author of this material.

CURRICULUM VITA

- 2008 Bachelors of Science, University of North Carolina at Asheville
Chemistry
- 2010 Masters of Science, University of California, San Diego
Chemistry
- 2015 Doctor of Philosophy, University of California, San Diego
Chemistry
Dissertation title: Organoferrous Antitumor Agents

PUBLICATIONS

M.C. Aubrey, M. Proetto, C. Hoong, S. Fox, M. Melaimi, N. Gianneschi, G. Bertrand, J.M. O'Connor, "Photoactivated Organoferrous Antitumor Agents" 2015, manuscript in preparation.

M.C. Aubrey, J.M. O'Connor, "Radical Implications: Iron Antitumor Agents and Reactive Oxygen Species" 2015, manuscript in preparation.

J.M. O'Connor, M.C. Aubrey, M. Proetto, N. Gianneschi, "Photoactivated Organoferrous Antitumor Agents," 2015, patent in preparation.

J. M. O'Connor, K. K. Baldrige, B. L. Rodgers, M. Aubrey, R. L. Holland, S. W. Kassel, A. L. Rheingold, "A Photochemical Metallocene Route to Anionic Eneidyne: Synthesis, Solid-State Structures, and ab Initio Computations on Cyclopentadienoidenyne" *J. Am. Chem. Soc.*, 2010, 132, 11030-11032.

K.D. Bunker, A.L. Rheingold, C.E. Moore, M. Aubrey, J.M. O'Connor, "Synthesis of the cobalt-alkyne complex $(\eta^5\text{-C}_5\text{H}_5)(\text{PPh}_3)\text{Co}\{\eta^2\text{-(Me}_3\text{Si)C}\equiv\text{C(CO}_2\text{Et)}\}$ and structural characterization of trimethylsilyl substituted cobaltacyclopentadiene complexes derived therefrom" *J. Organomet. Chem.*, 2014, 749, 100-105.

ABSTRACT OF THE DISSERTATION

Organoferrous Antitumor Agents

by

Marissa Caroline Aubrey

Doctor of Philosophy in Chemistry

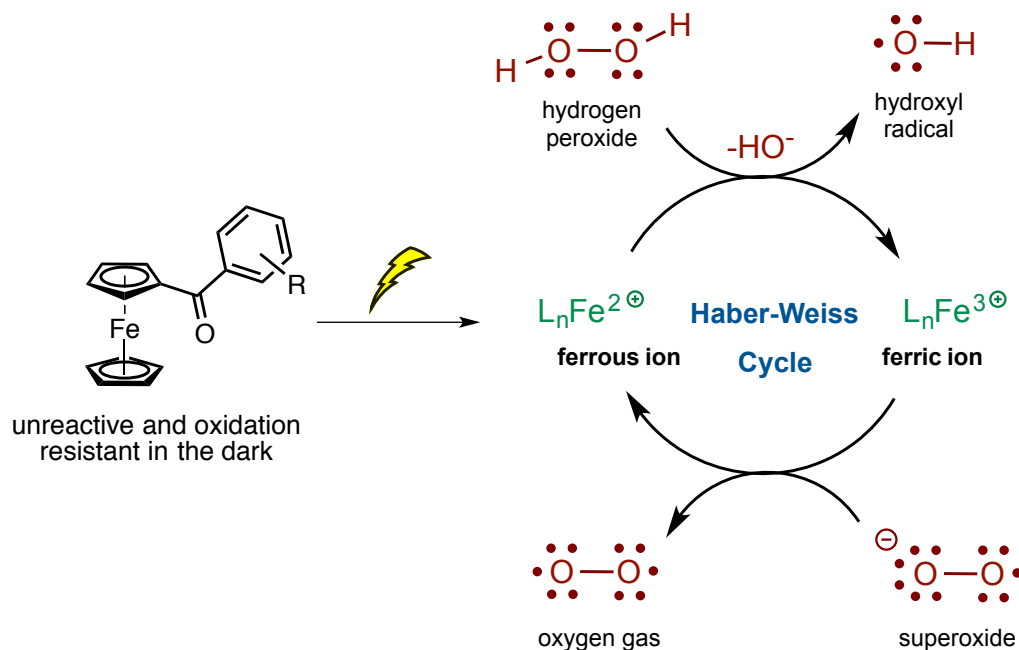
University of California, San Diego, 2015

Professor Joseph M. O'Connor, Chair

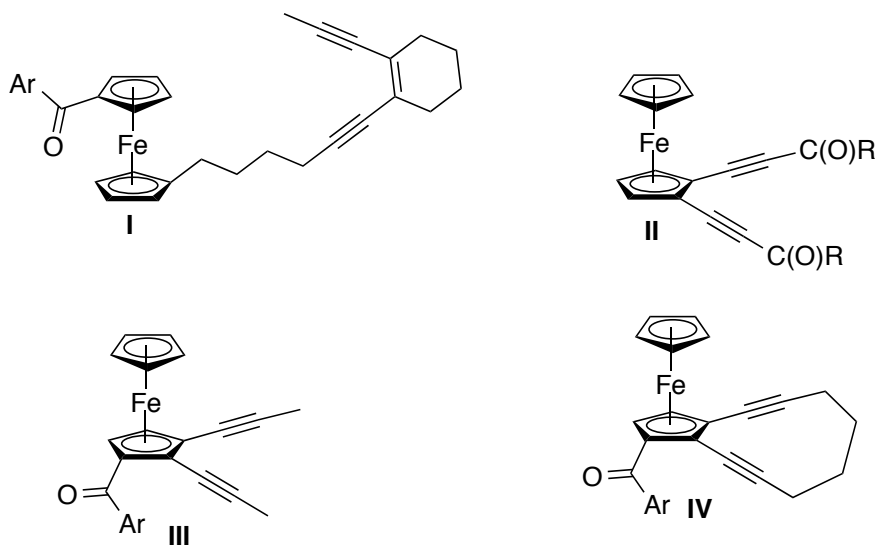
The discovery of ferrocene in 1951 and subsequent structure elucidation essentially founded the field of modern organometallic chemistry. The remarkable stability of the sandwich complex's iron-carbon bonds and ease of derivatization have made the archetypal metallocene ubiquitous across an array of scientific disciplines. Due to the wealth of literature available on ferrocene functionalization and the complex's stability in aqueous and aerobic media, it is no

wonder ferrocene has gained widespread popularity among anti-cancer researchers in particular.

Our research has explored two avenues of cytotoxicity for ferrocene-based antitumor agents. First, we wished to investigate selective generation of cytotoxic *metals* in tumor cells. To this end, we describe the preparation of a series of benzoylferrocene derivatives that are photosensitive and undergo successive ring-slips to form cyclopentadienes and inorganic iron(II) when exposed to visible light. We proposed the photochemically generated iron(II) would form reactive oxygen species *in situ* by reaction with endogenous hydrogen peroxide and form the highly toxic hydroxyl radical via the Haber Weiss Cycle. The synthesis, characterization, photochemical properties, and biological activity of the synthesized antitumor agents were examined in detail.



Second we wished to take advantage of the unique photochemical properties of benzoylferrocene to selectively deliver cytotoxic enediyne *ligands* to tumor cells. We proposed that once the organoferrous enediynes were localized within the cell, irradiation with visible light would trigger enediyne cycloaromatization. The reactive *para*-benzyne diradical could abstract hydrogen atoms from DNA in a similar manner to that of the enediyne antibiotics. To this end we describe the preparation of **I**, which was expected to cyclize intramolecularly to form *para*-benzyne. Then we describe the synthesis and characterization of ferrous enediynes **II-IV**, which are extremely light sensitive upon irradiation. The biological activity of selected ferrous enediynes in both the light and dark is provided and discussed.



Chapter I.
Introduction to Ferrous Antitumor Agents and
Naturally Occurring and Synthetic Eneidyne

Introduction

The discovery of ferrocene (**1**) in 1951 by Kealy and Pauson, and subsequent structure elucidation by Wilkinson, Rosenblum, Whiting, and Woodward, led to a revolution in how chemists perceived metal-carbon bonding.^[1,2] The quintessential organometallic complex's remarkably stable iron-carbon bonds and facile ease of derivatization led to a series of rapid advancements in regards to how metals interact with hydrocarbons, essentially founding the field of modern organometallic chemistry.³ Since that time, due to its low cost and high availability, ferrocene has become ubiquitous in building blocks for a wealth of applications including catalysis, sensors, materials, and biomolecules.⁴ Given the wealth of literature available on ferrocene functionalization and the sandwich complex's stability in aqueous and aerobic media, it is no wonder ferrocene has also gained widespread popularity among anti-cancer researchers in particular.^[5,6,7,8] Here, we discuss the biological activity of iron antitumor complexes, the reactivity of iron in biological systems, and potential strategies for the delivery for novel, ferrocene-based, therapeutic compounds.

A. Biological Activity of Ferrocene (**1**) and Ferrocenium (**2**).

Köpf-Maier first described the antitumor activity of a series of ferrocenium salts against Ehrlich ascites tumor (EAT) cell lines in 1984.⁹ While ferrocene (FeCp_2 , **1**) and ferrocenium (FeCp_2^+ , **2**) are also members of the classic organometallic sandwich complex family, the authors speculated the reactivity of **3** in biological

systems would differ drastically from previously discovered medicinal metallocenes **4-6** (Figure 1.1).^[10,11,12,13] While the early-metal metallocenes **4-6** have labile chloride and tilted cyclopentadienyl ligands, FeCp_2 and FeCp_2^+ have a parallel arrangement of the two cyclopentadienyl rings, lack labile ligands, and are thus less likely to participate in ligand substitution reactions *in vitro*.

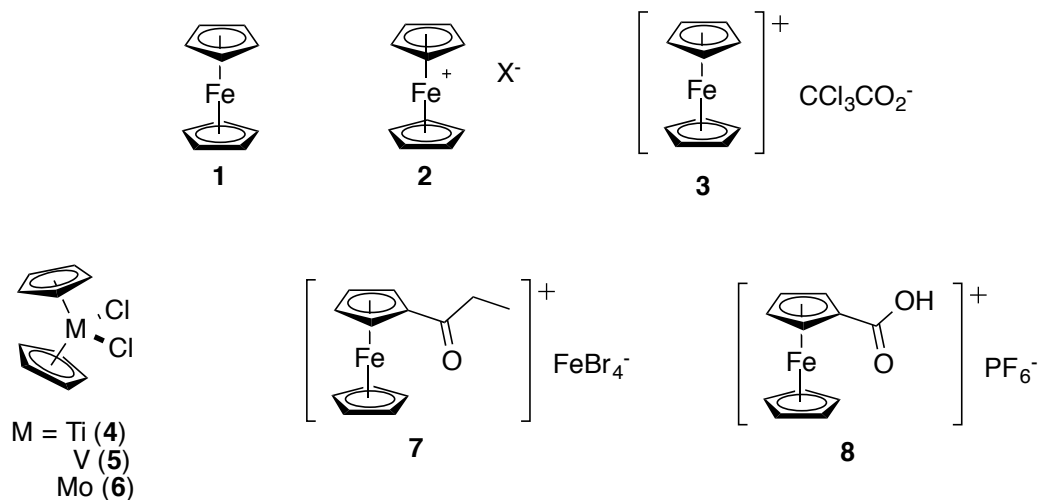


Figure 1.1. Organometallic antitumor agents.

Given the known ability of iron(II) ions to generate reactive oxygen species, which oxidize lipids, proteins, and DNA, it seemed reasonable to suspect the anti-tumor activity of the ferrocenium sandwich complex **2** was simply related to its ability to act as low molecular weight iron carrier.¹⁴ In 1997 Tamura elegantly demonstrated the relationship between ferrocenium-mediated reactive oxygen species generation, DNA cleavage, and cytotoxicity.¹⁵ Using gel electrophoresis studies, the authors were able to show the cytotoxic acyl-substituted ferrocenium cation **7** induced DNA strand cleavage. Addition of a hydroxyl radical spin trap

(thiourea) to the experiment resulted in complete inhibition of DNA scission, but addition of a reductant, dithiothreitol (DDT), gave the opposite result. The enhancement of DNA cleaving activity was attributed by the authors to DDT mediated formation of iron(II) species *in situ*. While these experiments clearly linked DNA strand cleavage, and thus cytotoxicity, to iron-mediated hydroxyl radical production, the mechanism by which iron(II) is produced from ferrocenium was not speculated on.¹⁵ Later work by Osella and coworkers demonstrated DNA from cells treated with ferrocenium derivative **8** was also fragmented, suggestive of iron-mediated DNA strand breakage.¹⁶ Electron spin resonance (ESR) experiments with **8** in the presence of spin trap 5,5-dimethyl-1-pyrroline-N-oxide (DMPO) positively identified the hydroxyl radical spin trap adduct in aqueous solutions. Addition of a suspension of EAT cells to **8** and DMPO resulted in a gradual attenuation and disappearance of the ESR signal with increasing concentrations of biomass, implying that the EAT cells were capable of reacting with the hydroxyl radicals generated in aqueous media.¹⁶

B. Transportation and Storage of Cellular Iron

To prevent free iron from participating in damaging redox chemistry, nature has developed elegant strategies to sequester iron for transportation, storage, and utilization. The human body requires 25 mg of iron daily for various biological functions, and while 12-18 mg are typically consumed within a day, only 1-2 mg of dietary iron is absorbed by the intestine. In order to make up for this deficiency,

cells have developed intricate methods to recycle, store, and release iron depending on the biological demand.^[17,18]

Due to the high toxicity levels of solvated, redox-active iron,^[14,19] the transportation of iron from the intestines (enterocytes), where it is absorbed, to other areas of the body is highly controlled (Figure 1.2). The expression of ferroportin (Fpn), the only known iron exporter to date, is regulated by the master iron regulatory hormone hepcidin, which acts as a negative regulator of plasma iron. When iron levels are too high, hepcidin binds to Fpn and the exporter protein is engulfed into the cell and degraded in the lysosome, resulting in lower iron serum levels. When iron needs to be transported out of the enterocyte to other areas, iron(II) is transported out of the enterocytes by Fpn and oxidized to its ferric state by hephaestin, a multicopper oxidase protein. Once oxidized and exported, the iron is then transferred to the iron transport protein transferrin (Tf).¹⁸

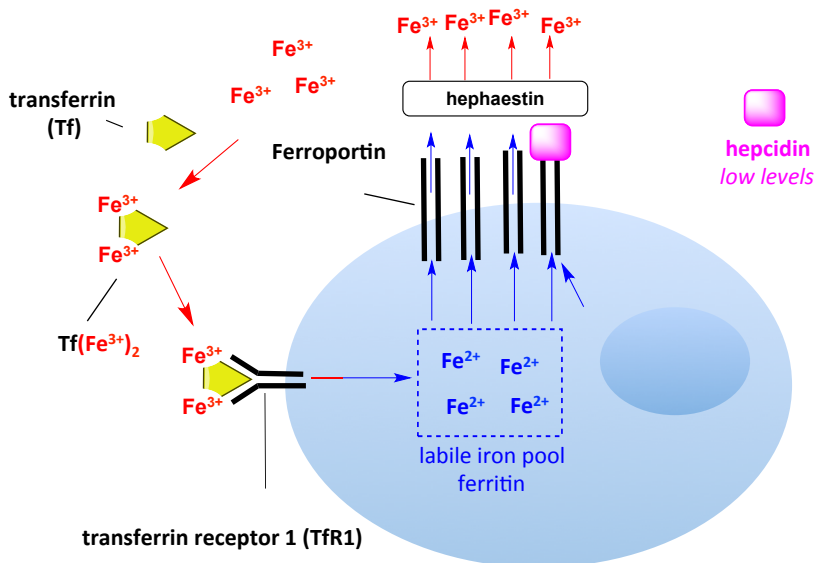


Figure 1.2. Iron transportation and storage in mammalian cells.¹⁷

Iron in the serum is present in low concentrations (3-5 μg) and is bound to transferrin, which sequesters the labile iron pool during delivery to cells. Tf is capable of binding two iron ions, readily forming a $\text{Tf}(\text{Fe}^{3+})_2$ complex, where each iron is coordinated to four amino acid residues (histidine, aspartate, and two tyrosines) and a labile bidentate carbonate ligand (Figure 1.3.). Once Tf has arrived at its destination, it binds to the transferrin receptor (TfR) and is engulfed into the cell.^{17,18} After being endocytosed, the low pH of the endosome (pH = 5.5) induces release of ferric iron by protonation of the labile carbonate ligand.²⁰ Iron(III) is then reduced to the ferrous state by ferric reductase and is exported into the cytosol by divalent metal transporter 1 (DMT1). Transferrin is then released from the cell, free to bind and deliver two more iron(III) ions.^[17,18]

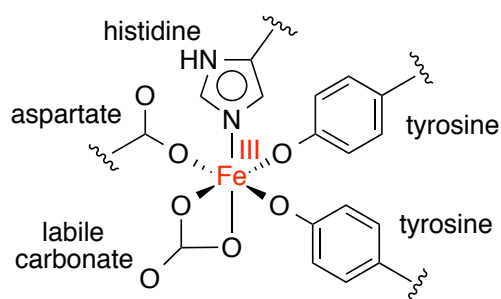


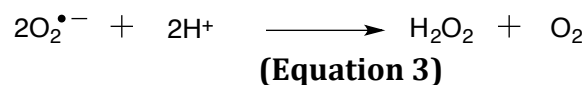
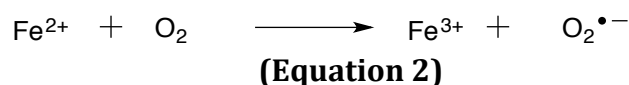
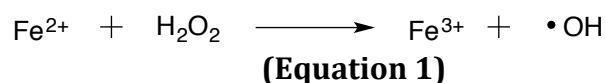
Figure 1.3. Inner coordination sphere for one of the ferric ions in $\text{Tf}(\text{Fe}^{3+})_2$.¹⁷

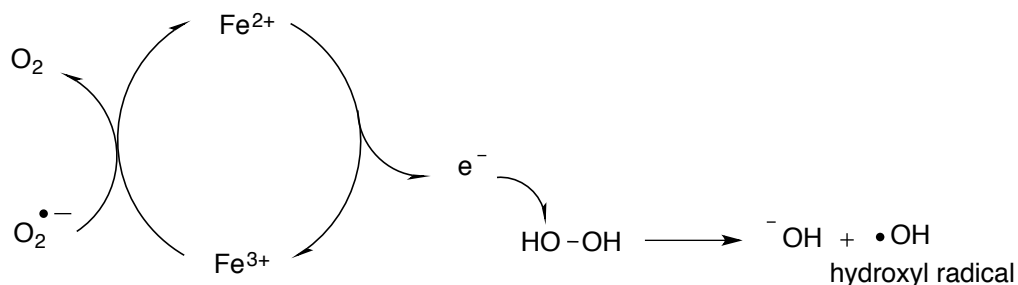
Once in the cell, Fe(II) has entered the 'labile iron pool', where it is used for incorporation into proteins or sequestered in order to avoid detrimental redox chemistry. The major iron storage protein, ferritin, stores up to 4,500 iron atoms/protein and is found in the cytoplasm, nucleus, and mitochondria. The most common, cytoplasmic ferritin, is expressed in nearly all tissues and contains most of

the iron in cells. Under conditions of iron depletion, ferritin degradation is mediated by lysosomes, resulting in an increase in the labile iron pool.^[17,18]

C. Iron And Reactive Oxygen Species (ROS).

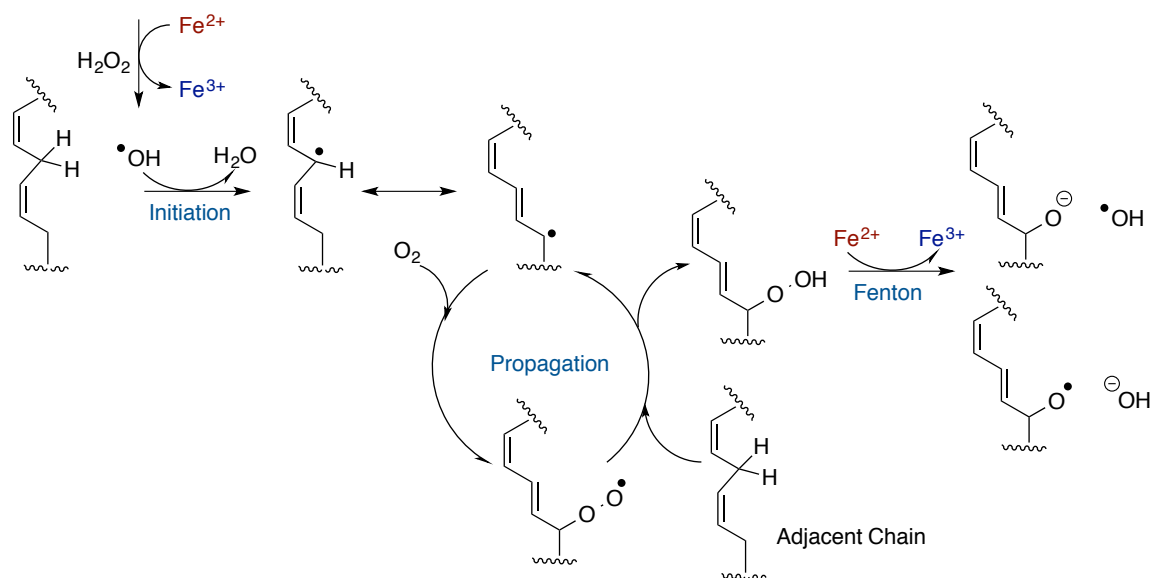
The primary mechanism by which iron causes cellular damage is via Fenton chemistry, a reaction in which Fe(II) converts hydrogen peroxide to hydroxide and hydroxyl radical (Equation 1). In biological systems, ferrous ion can then be regenerated by superoxide-mediated one-electron reduction of Fe(III), creating a catalytic cycle known as the Haber-Weiss Cycle (Scheme 1.1). Via this cycle, at biologically relevant pH, more than 50 hydroxyl radicals can be generated from a single molecule of chelated iron (Fe-EDTA).¹⁴ Additionally, it has been demonstrated that iron(II) can react directly with oxygen in an electron-transfer reaction to give iron(III) and superoxide. Once formed, superoxide can dismutate to hydrogen peroxide and molecular oxygen, providing the necessary reagents for the Fenton reaction even in the absence of endogenous hydrogen peroxide.¹⁹





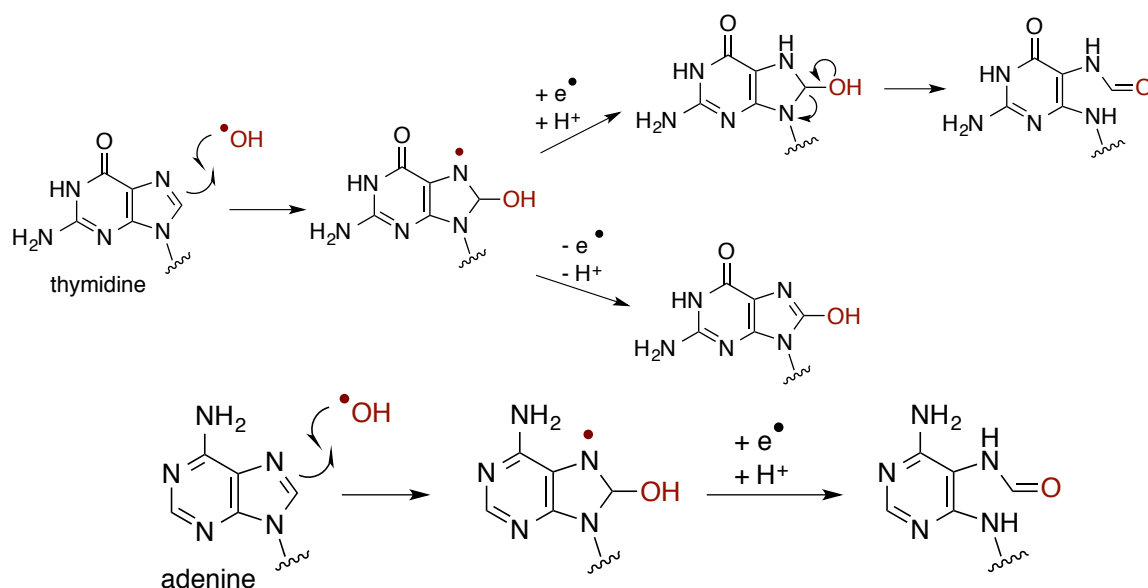
Scheme 1.1. Generation of hydroxyl radical via the Haber-Weiss Cycle.²¹

Once generated, the highly reactive hydroxyl radical cannot diffuse significantly from its site of formation and as a result, participates in detrimental free radical reactions with the nearest biomolecule, such as the cell membrane or DNA. Phospholipid peroxidation is initiated by formation of a hydroxyl radical from Fe(II) and endogenous hydrogen peroxide via the Fenton reaction (Scheme 1.2). Alternately, it has also been demonstrated that lipid peroxidation can be initiated in the absence of endogenous hydrogen peroxide by initial reaction of iron(II) with dioxygen (Equation 2) and formation of hydrogen peroxide by dismutation of superoxide (Equation 3).¹⁹ Following initiation, hydrogen atom abstraction from a bis-allylic carbon atom located on the fatty acid chain generates a carbon-centered radical, which reacts with molecular oxygen to generate a peroxy radical. The peroxy radical can subsequently react with another nearby fatty acid chain, creating a free radical chain reaction that rapidly expands across the cell membrane.²²



Scheme 1.2. Mechanism for phospholipid peroxidation initiated by ferrous iron.²²

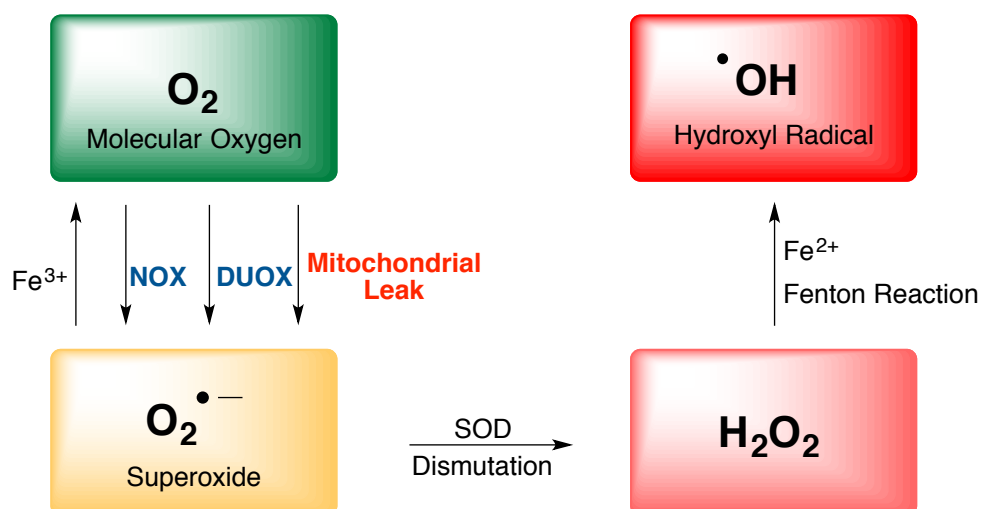
Oxidative DNA damage has also been linked to hydroxyl radical formation via the Fenton reaction (Scheme 1.3). The negatively charged phosphate backbone of DNA serves as a good ligand for labile Fe(II) ions, allowing for localization of the redox-active metal close to oxidation-prone nucleotides. Once bound to DNA, iron(II)-mediated generation of hydroxyl radical results in oxidation of the nearby pyrimidine DNA bases, causing DNA strand breakage.²² Even in the absence of added hydrogen peroxide, iron(II) salts have been demonstrated to induce calf thymus DNA cleavage in the presence of molecular oxygen, indicating that hydrogen peroxide, and thus hydroxyl radical, may be formed *in situ* via Equations 2 and 3.^[19,23]



Scheme 1.3. Mechanism for DNA base peroxidation initiated by ferrous iron.²²

The hydrogen peroxide needed for the Fenton reaction is necessary for several vital cell functions including immune response, apoptosis, cell signaling, and gene expression and is produced by cells in both regulated and unregulated processes (Scheme 1.4).^[24,25] ROS producing enzymes NADPH oxidase (NOX) and DUOX (dual oxidase) are ubiquitous and expressed by a wide range of human cell types including phagocytes, colon, kidney, thyroid, vascular smooth muscle, and lung cells. While originally believed to be confined to the cell membrane, more recent work has indicated NOX enzymes are also found in the endoplasmic reticulum, nucleus and mitochondria. The enzymatic generation of hydrogen peroxide by NOX is initiated by electron transfer from NADPH to flavin adenine dinucleotide (FAD). Subsequent shuttling through a series of heme centers in the liquid bilayer and reaction with molecular oxygen generates superoxide. Once

generated, superoxide can be converted to hydrogen peroxide thermally (slow) or enzymatically by SOD (superoxide dismutase). The DUOX family is structurally similar to the NOX enzymes, but contains a peroxidase-like domain located to the N-terminus of the enzyme to convert superoxide directly to hydrogen peroxide. This enzymatic generation of superoxide and H_2O_2 allows for control of both the type and concentration ROS being produced, allowing cells to carefully manipulate the oxidation of biomolecules.²⁶



Scheme 1.4. Generation of reactive oxygen species in cells.^{25,26}

ROS are also commonly produced via a non-enzymatic process known as mitochondrial leak during cellular respiration. ATP synthesis during cellular respiration is primarily driven by a proton gradient that is formed between the mitochondrial matrix and the intermembrane space in the mitochondria. Formation of this gradient is in turn driven by the electron transport chain (ETC), where electrons are shuttled through successive redox centers with increasing oxidation

potentials.²⁷ Under ideal conditions, the final step of the ETC is coordinated, two-electron reduction of molecular oxygen to water by Complex IV cytochrome oxidase. Escape of an electron from one of the intermediate redox centers prior to reduction at Complex IV leads to premature reaction with oxygen, and generation of the superoxide anion. An estimated 1-3% of electrons are believed to leak out of the electron transport chain and, given the highly reducing environment of the intramitochondrial space and the known reduction potential of molecular oxygen (-0.160 V), superoxide formation is unavoidable.^[27,28] In light of this fact, mitochondria have developed antioxidant defense mechanisms such as the enzymes superoxide dismutase (SOD), glutathione peroxidase, and catalase, that allow for precise control of hydrogen peroxide levels in the cell (10^{-8} - 10^{-7} M).^[19,28,29]

D. Other Ferrocene-based Antitumor Agents.

The anticancer activity of ferrocene derivatives were first explored by Brynes and co-workers, who demonstrated **9** was active against leukemia P-388 tumors (Figure 1.4). While the antitumor activity of the sandwich complex was low, the result was significant, as it demonstrated for this first time that the neutral biscyclopentadienyl iron moiety could be used to induce antitumor activity.³⁰

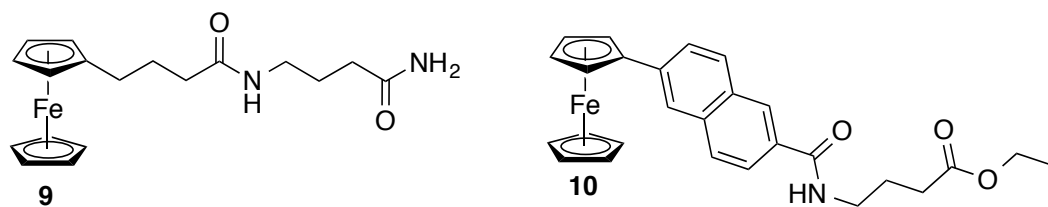


Figure 1.4. Selected antitumor ferrocene complexes.

Since that time, a common strategy for the development of ferrous antitumor agents has been conjugation of the ferrocene scaffold to biomolecules in the hopes of making a more selective drug. Complex **10**, synthesized by Kenny and co-workers, was designed to contain three key moieties: (1) a peptide to deliver the cytotoxic ferrocene to biomolecules, taking advantage of secondary interactions such as hydrogen bonding, (2) the redox active iron core, and (3) a conjugated aromatic linker to lower the oxidation potential (58 mV relative to Fc/Fc⁺) of the complex, making it easier to form ferrocenium species and generate hydroxyl radicals *in vitro*. The viability of such a strategy was reflected in the remarkably low IC₅₀ of **10** in H1299 human lung carcinoma cells (IC₅₀ = 0.62 μM).^[31,32]

Given the known ability of iron to interact with the phosphate backbone of DNA and generate highly damaging hydroxyl radicals (see section **B**), much effort has been expended on creating ferrocene derivatives that target DNA. Ong and coworkers prepared **11** to covalently link a known DNA intercalator, acridine, to the redox active ferrocene moiety (Figure 1.5). Control complex **12** lacking the ability to intercalate was synthesized as a control. While **11** was shown to be highly cytotoxic to each of the cancer cell lines tested, control complex **12** was inactive.³³ A second strategy in the development of ferrocene complexes that target DNA are derivatives that inhibit topoisomerase, the enzyme responsible for unwinding and winding DNA in preparation for replication. An added benefit to this strategy is that rapidly dividing cancer cells express elevated levels of topoisomerase IIβ, making the drug more selective for tumor cells. With this strategy in mind, Kondapi and co-workers

synthesized **13** and **14**, which were demonstrated to significantly inhibit topoisomerase II β .^[34,35]

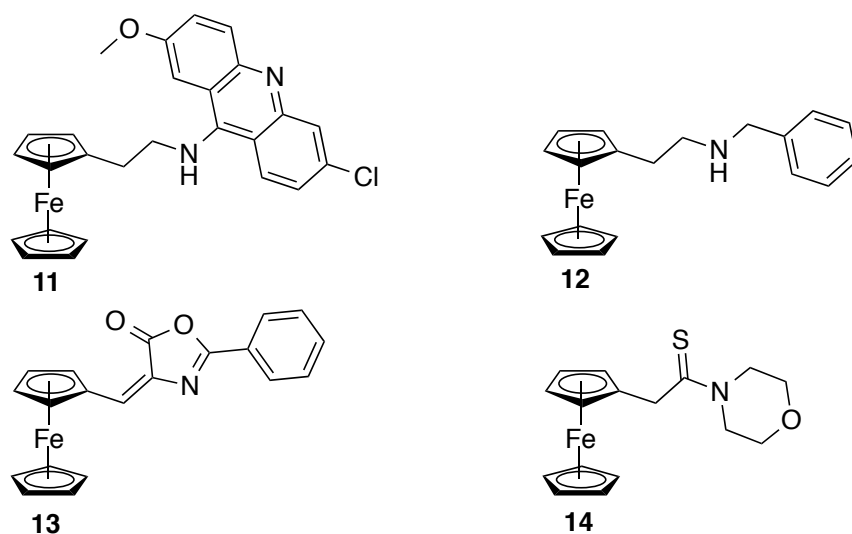


Figure 1.5. Ferrocene complexes that target DNA.^[33,34,35]

The progression of prostate cancer is promoted by testosterone (**15**) and its metabolite dihydrotestosterone (**16**), which bind to the cell surface and stimulate malignant cell growth (Figure 1.6). Therefore, the development of anti-androgens that competitively bind to cell receptors and prevent binding of **15** and **16** is a potential strategy for cancer therapeutics. Jaouen *et al.* synthesized ferrocenyl analogs **17** and **18** by joining the hormone and ferrocene regions with an ethyne linker. While the synthesized derivatives showed low affinity for receptor binding, a strong cytotoxic effect was found on hormone-independent PC-3 prostate cancer cell line ($IC_{50} = 4.7$ and $8.3 \mu\text{M}$ respectively).³⁶

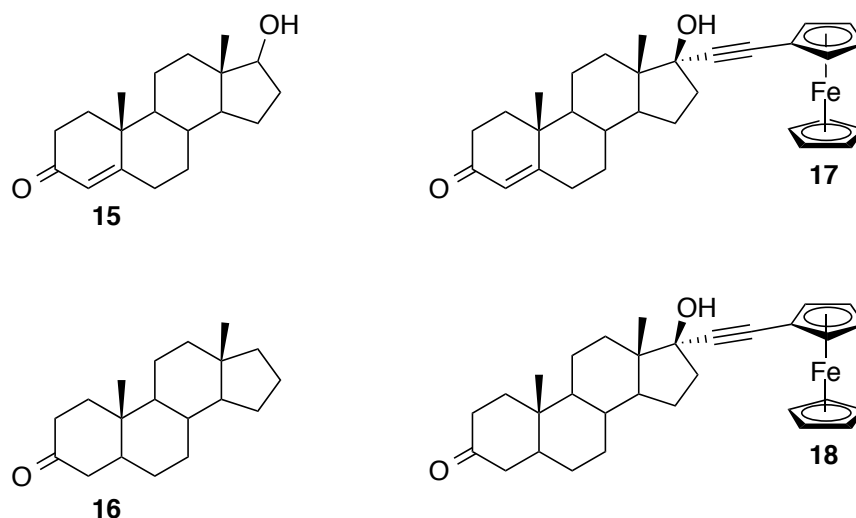


Figure 1.6. Ferrocene substituted testosterone mimics for treatment of prostate cancer.³⁶

A similar strategy in treatment of breast cancer is the targeting of cancer cells using selective estrogen receptor modulators (SERMs). Breast tumors are divided into two subclasses, those that express the estrogen receptor (ER(+)) and those that lack the estrogen receptor (ER(-)). The majority of patients belong to the ER(+) type which is highly treatable by hormone therapy using SERMS.

Marques and coworkers prepared ferrocenyl SERM **19** by replacing a phenyl ring on the known SERM raloxifen (**20**) with the ferrocene moiety (Figure 1.7). The development of new pharmaceuticals by substitution of a phenyl ring in an established drug for the lipophilic and ball-shaped ferrocene is a concept known as bioisosterism, and has led to a large number of new iron antitumor agents with varying degrees of success. Complex **19** is a successful example of this concept, with IC_{50} values in the low micromolar range (mean $IC_{50} = 1.64 \mu M$ across eight cell lines). While any mechanism of action was deemed highly speculative, the authors

proposed the biological activity may be linked to facile oxidation of the iron center ($E_{1/2} = 0.07$ V) and generation of reactive oxygen species via the Fenton reaction, allowing for DNA damage.³⁷

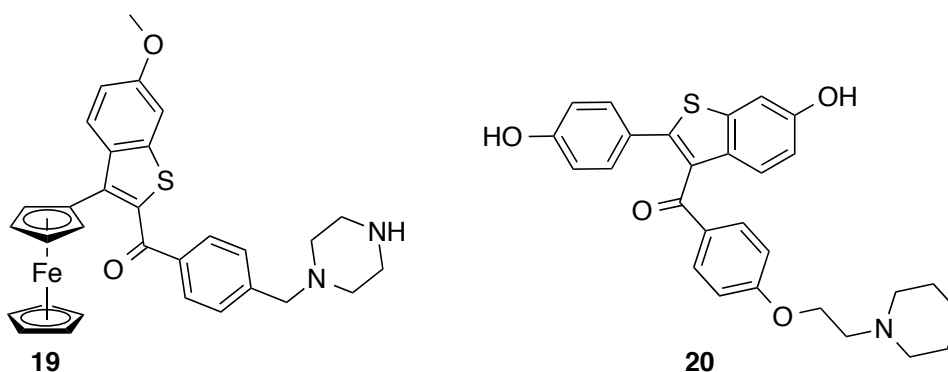


Figure 1.7. SERM raloxifen **19** and its ferrocene derivative **20**.³⁷

Tamoxifen (**21**) (Figure 1.8) is a commonly prescribed SERM that acts by binding to the estrogen receptor, $ER\alpha$, on the surface of the tumor cell, repressing estradiol-mediated DNA transcription. Patients with $ER(-)$ breast cancer are not treatable by this type of hormone therapy and even for patients that do respond to hormone therapy, additional problems arise when $ER\alpha$ becomes down-regulated due to prolonged tamoxifen exposure.³⁸ Hydroxyferrocifen (**22**), the ferrocene analog of the active metabolite of tamoxifen, was developed by Jaouen as a bioisostere of **21** to overcome the drug resistance that occurs with extended tamoxifen treatment. A series of derivatives were synthesized where double bond geometry, chain length of the amino substituent, and substituents on the phenyl ring were systematically varied. The structure activity relationship revealed that as the side chain was lengthened, the binding affinity for the receptor decreased.³⁸ Also key

to biological activity was the presence of phenol groups in the *para* position and the ethylene linker between the phenol and ferrocene moieties.^{39,40,41} Substitution of the iron center for other transition metals including titanium, rhenium, ruthenium, and manganese failed to replicate the cytotoxicity of ferrocene complex **22**, indicating the cytotoxic affect was related to the iron center.^[39,42,43]

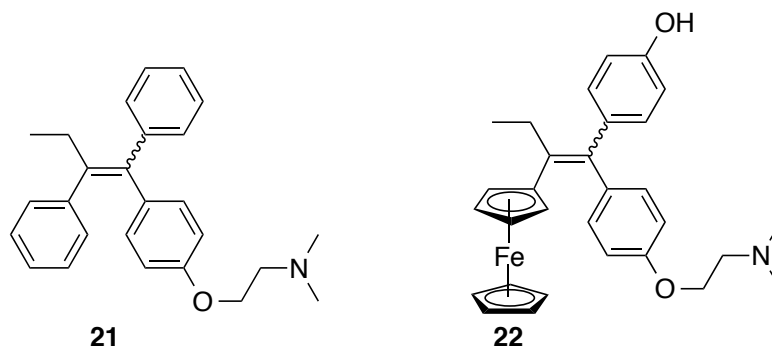
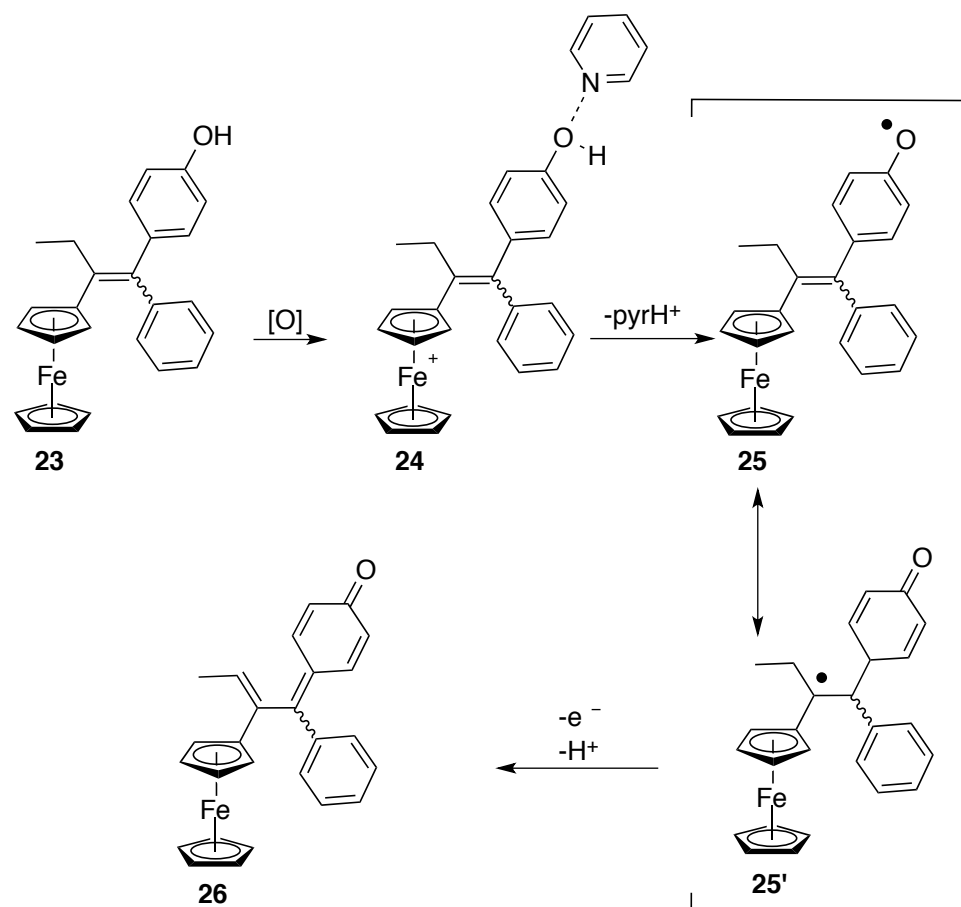


Figure 1.8. Clinical breast cancer drug tamoxifen and its ferrocene analog hydroxyferrocifen.³⁸

As predicted, hydroxyferrocifen was found to be cytotoxic in MCF-7 ER(+) cell lines. More exciting however was the discovery that **22** was also cytotoxic ($IC_{50} = 0.5 \mu\text{M}$) against ER(-) cell lines, such as MDA-MB231 cells which lack the estrogen receptor, suggestive of an estrogen-independent mechanism of action. By a series of elegant cyclic voltammetry studies, Hillard and co-workers demonstrated that ferrocifen derivative **23** is easily oxidized to the cytotoxic quinone methide **26** (Scheme 1.5). Once formed, **26** is susceptible to nucleophilic attack by cellular nucleophiles including glutathione and nucleobases in a similar fashion to that of tamoxifen.⁴⁴ The enhanced bioactivity of the ferrocene analog relative to the organic drug was demonstrated to be related to the redox activity of the iron center. Under

biological conditions, the iron center serves as a stable electron 'hole' (**24**) until the sandwich complex reaches the target in the cell where it becomes activated. In this manner, the ferrocene moiety acts as an oxidation 'antenna' that allows for facile, intramolecular oxidation to the biologically active organic quinone ligand (**25**, **25'**).⁴¹ Later studies also detected the presence of reactive oxygen species that were associated with cell cycle arrest and senescence in ER (+) and ER (-) cell lines.⁴⁵ The unexpected biological activity of hydroxyferrocifen is one particularly elegant example in which the organic ligands and redox activity of the metal center work synergistically, inducing unique modes of reactivity that would not be possible with a simple organic drug.



Scheme 1.5. A proposed mechanism of action for **23**.⁴¹

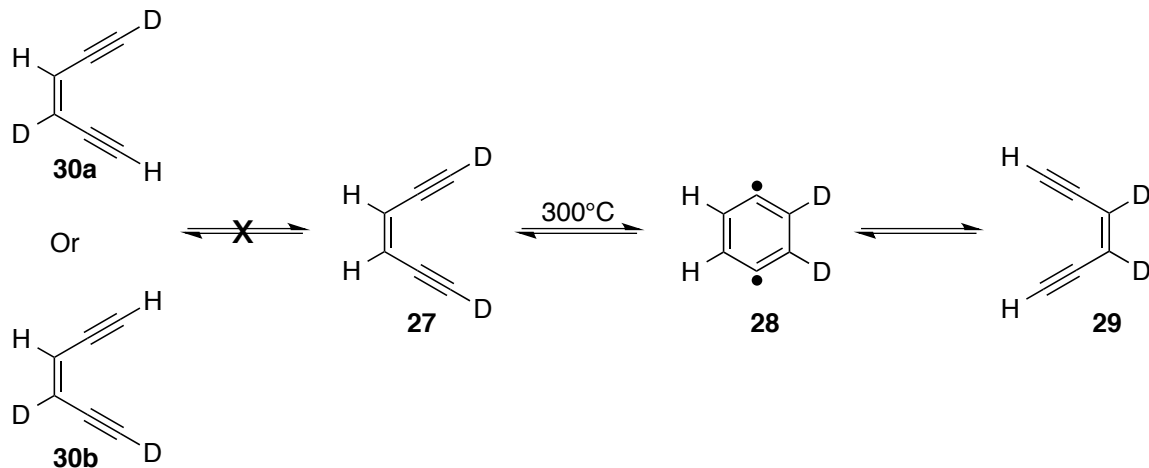
In summary, the discovery that ferrocenium salts induce cytotoxic effects by the generation of reactive oxygen species set the stage for the development of ferrocene-based antitumor drugs.⁹ Oftentimes, new ferrocene-based antitumor agents are developed by substitution of a phenyl ring for the lipophilic and ball-shaped ferrocene, with the hope that a change in shape or biological distribution will improve the drug's anticancer properties.^[37,38] Another popular strategy involves conjugating the ferrocene moiety to biomolecules in order to target a specific location within the cell.^[33,34,36] These methods have led to a large number of

new iron antitumor agents with varying degrees of success.^[5,6] Use of the organometallic scaffold allows for many new and exciting opportunities for anticancer researchers. The fact that ferrocene derivatives may induce antiproliferative effects stemming from the organic cyclopentadienyl ligands, or by formation of reactive oxygen species generated from the iron(II) center, allows for the exploitation of novel cytotoxicity pathways that are not possible for purely organic drugs.

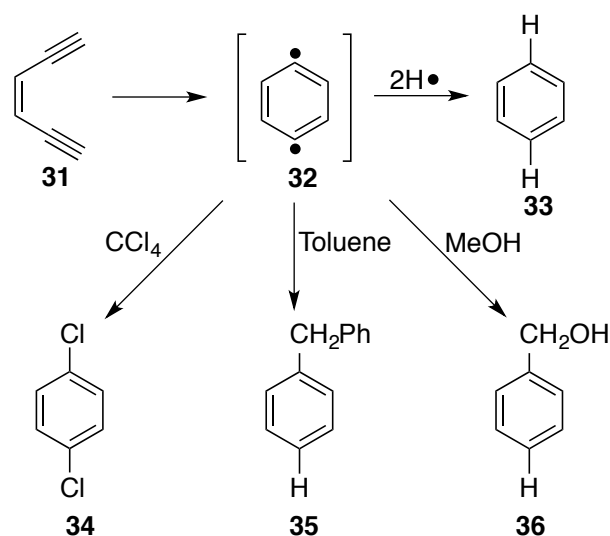
E. The Bergman Cycloaromatization

Given the remarkable stability of ferrocene in aqueous media and the demonstrated success of ferrocene-based antitumor agents, the O'Connor lab became interested in delivery of toxic enediyne ligands using stable organometallic precursors. The now classic cycloaromatization mechanism of (*Z*)-1,5-diyne-3-enes was elucidated in 1972 by Robert Bergman. Bergman demonstrated that when pyrolyzed in the gas phase at 300 °C for 30 seconds, the deuterium-labeled enediyne [1,6-D₂]-(*Z*)-1,5-hexadiyn-3-ene (**27**) underwent rapid isotopic scrambling between the acetylenic and vinylic positions (Scheme 1.6). The small amount of (*E*)-enediyne present in the starting materials remained unreacted and none of the mixed acetylenic and vinylic deuterium labeled isomers **30a** and **30b** were observed.⁴⁶ When **31** was heated in 2,6,10,14-tetramethylpentadecane, benzene was formed as the starting enediyne was consumed (Scheme 1.7). In CCl₄, 1,4-dichlorobenzene was recovered as the major organic product, and in toluene diphenylmethane was

formed, demonstrating the free radical reactivity of the intermediate. Even when **31** was heated in a polar solvent such as methanol, benzene and benzyl alcohol were formed, but no anisole. The observed scrambling of **27** to only **29** and the observed free radical reactivity led Bergman to propose *para*-benzyne as the intermediate (**28**).⁴⁶ While the reaction was fundamentally intriguing, the high temperatures needed to afford the cyclization products severely hampered its application in synthesis, and the Bergman Cyclization was largely forgotten until a fortuitous discovery of a new class of molecules in 1987, the enediyne antibiotics.



Scheme 1.6. Robert Bergman's 1972 classic enediyne scrambling experiment.⁴⁶



Scheme 1.7. Trapping of *para*-benzyne by various solvents.⁴⁶

F. The Eneidyne Natural Products.

While the discovery of the Bergman Cycloaromatization was exciting in its own right, the scientific community largely regarded the cyclization as an academic curiosity until the discovery of the enediyne natural products. Calicheamicin- γ_1^I , esperamicin A₁, dynemicin A, kedarcidin, and the C-1027 chromophore (Figure 1.9) each possess a highly reactive (*Z*)-hex-3-ene-1,5-diyne moiety that is inactive until reaching the minor groove of DNA, where chemical transformation places the enediyne under conditions of higher strain, prompting the enediyne to cycloaromatize. The highly reactive *para*-benzyne diradical then abstracts one hydrogen atom from each strand of DNA, resulting in a double stranded cut and eventually cell death.^[47,48,49,50,51,52]

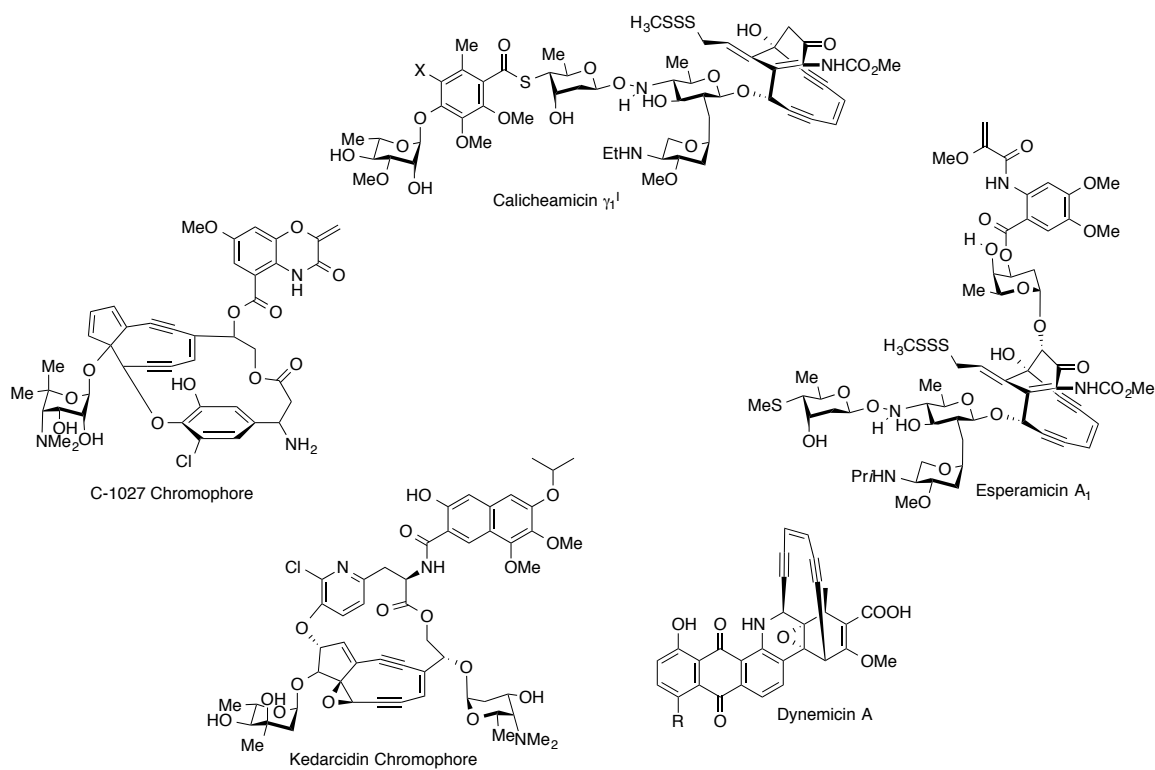


Figure 1.9. Enediyne natural products.⁵¹

The enediynes shown in Figure 1.9 are highly cytotoxic with active doses in the 0.1-5 $\mu\text{g}/\text{kg}$ range; however, animal studies found they are too toxic to be used in their isolated forms. The most promising antitumor candidate of the family, Calicheamicin- γ_1^1 , was initially approved for treatment of acute myeloid leukemia as an antibody conjugate under the brand name Mylotarg[®], but was recently withdrawn from the market (Figure 1.10). Thus, scientists are still searching for methods to control cycloaromatization in both the lab and *in vitro*.⁵¹

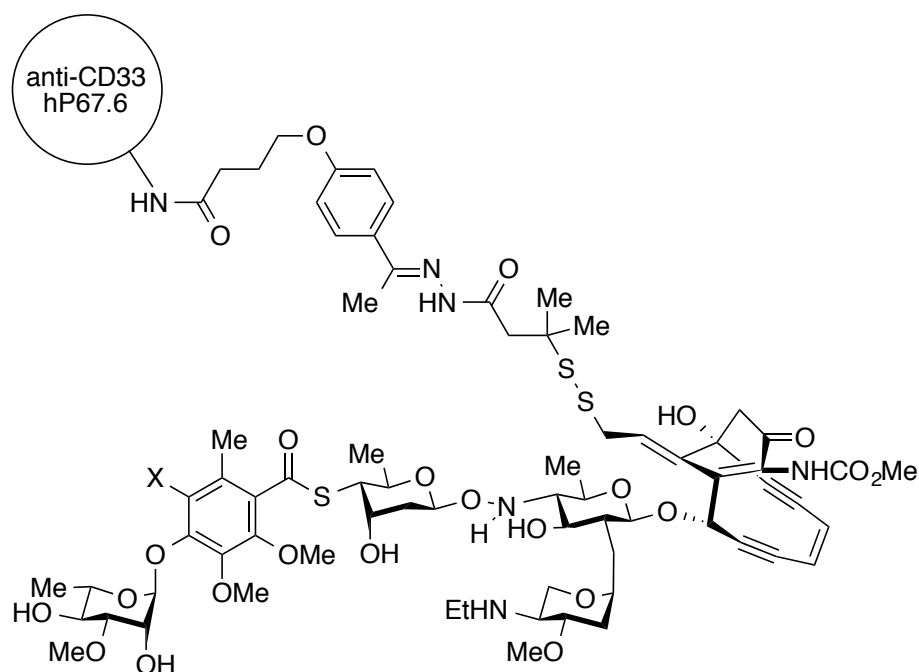
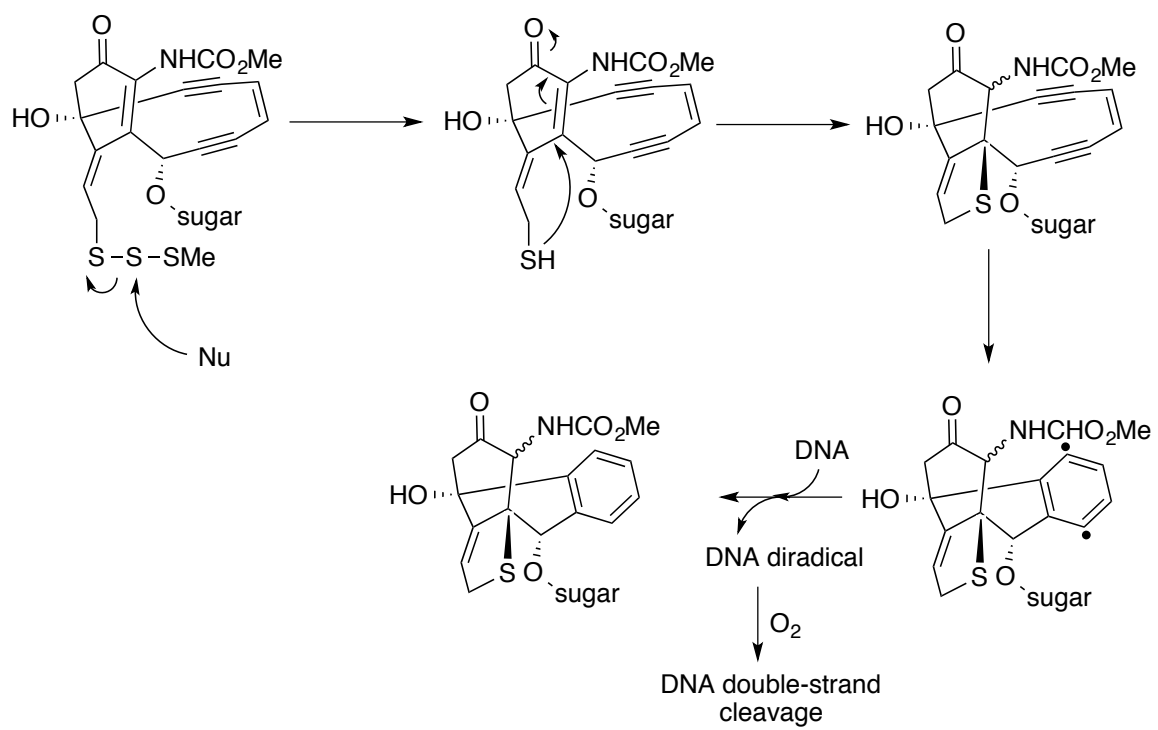


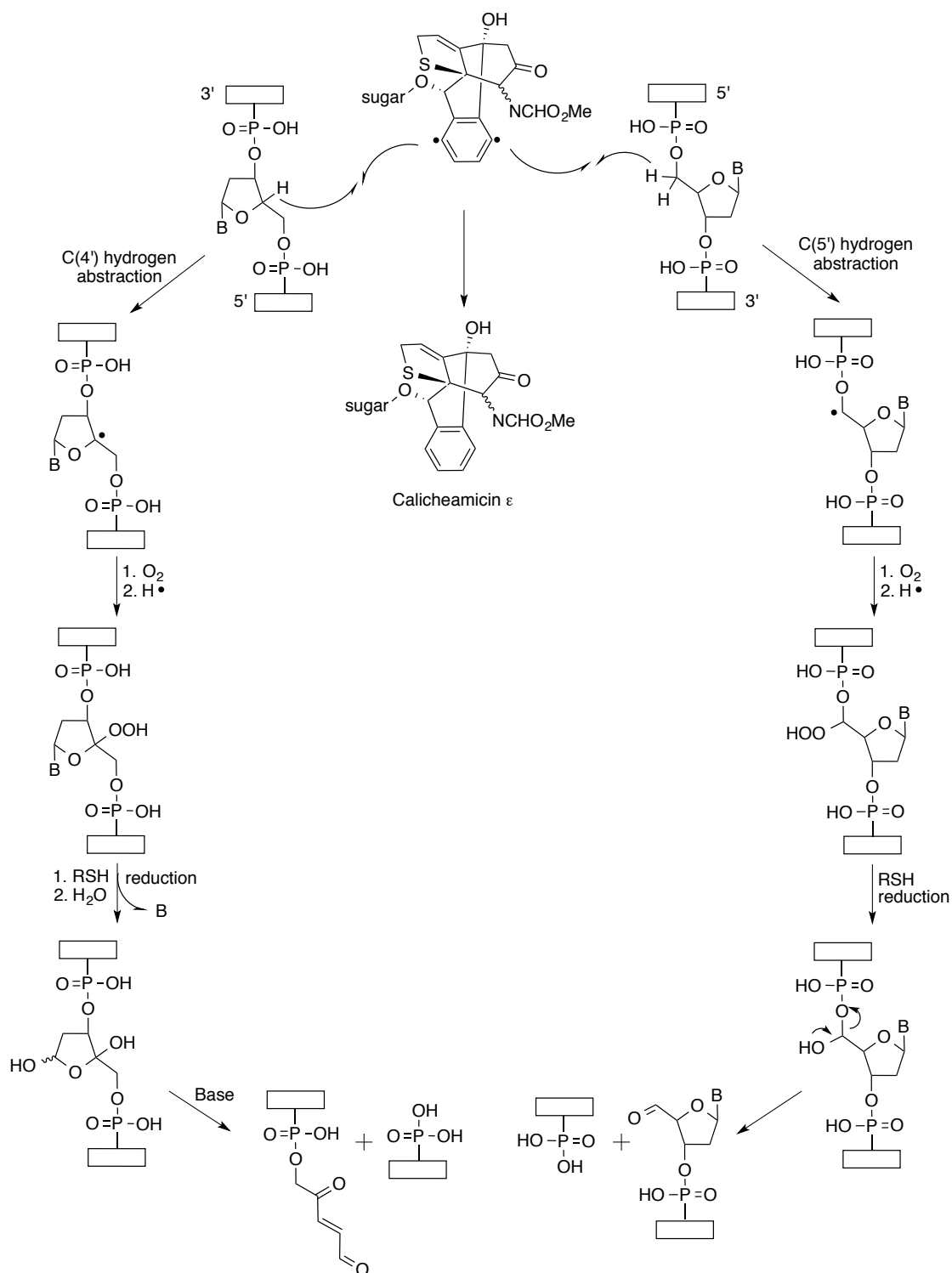
Figure 1.10. Mylotarg® a synthetic enediyne for cancer.

G. Mechanism of Action for Calicheamicin- γ_1^I

The structure of calicheamicin- γ_1^I consists of two distinct regions, each with its own function. The section containing four sugar residues selectively delivers the enediyne warhead to DNA, where it intercalates into the minor groove of the double helix. Once positioned, the enediyne portion of the molecule is activated by a nucleophilic attack on the α,β -unsaturated ketone, causing the sp^2 carbon atom to re-hybridize to an sp^3 center (Scheme 1.8). The resulting severe strain induced in the 10-membered ring enediyne prompts cycloaromatization to *para*-benzyne. The biradical, positioned within the double helix, then abstracts a hydrogen atom from each strand of DNA, inducing fatal damage (Scheme 1.9).^[50,53,54,55,56]



Scheme 1.8. Eneidyne activation mechanism for calicheamicin- γ_1 .^[50,53]



Scheme 1.9. Mechanism of double-stranded DNA cleavage initiated by calicheamicin- γ_1^I .^[54,56,55]

H. Eneidyne Distance Theory

The mechanism and cause for the unique and highly selective cycloaromatization reactions of the enediyne antibiotics have intrigued scientists since their discovery. Nicolaou first proposed enediyne 'distance theory' in 1988 after analysis of molecular mechanics calculations on **37** and **38** that revealed the distance between the alkyne termini must be within a 'critical distance' (cd) for spontaneous cyclization at ambient temperature (3.20 to 3.31 Å) (Figure 1.11). For calicheamicin- γ_1 ¹ the distance between the alkyne termini in stable enediyne **37** is 3.35 Å - much longer than in the activated 10-membered ring (**38**), 3.16 Å.⁵³

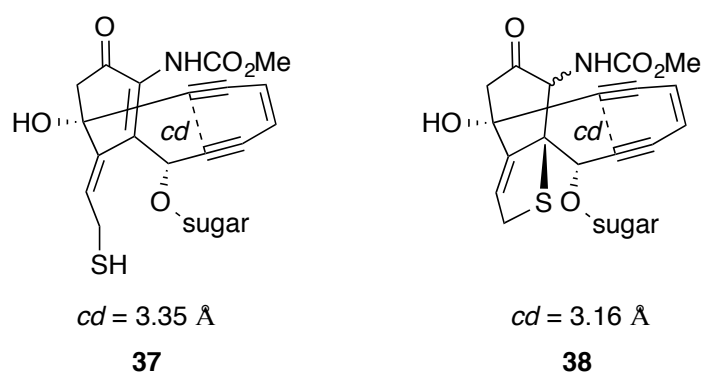


Figure 1.11. Shorter cd distances have been shown to lower the barrier to cycloaromatization.⁵³

Recent investigations have determined that the propensity of an enediyne to cyclize is closely related to the relative energies of the ground and transition state for cycloaromatization (Figure 1.12). While decreasing the cd distance certainly correlates to increasing likelihood to cyclize, calculations have shown the major driving force for cyclization are strain effects that raise the ground state energy of the enediyne relative to the transition state (Figure 1.12).⁵⁷ The effect of ring-strain

on enediyne cyclization is also demonstrated experimentally by the drastically lowered cyclization enthalpies for cyclodec-3-ene-1,5-diyne relative to (*Z*)-hexa-3-en-1,5-diyne.⁵⁸

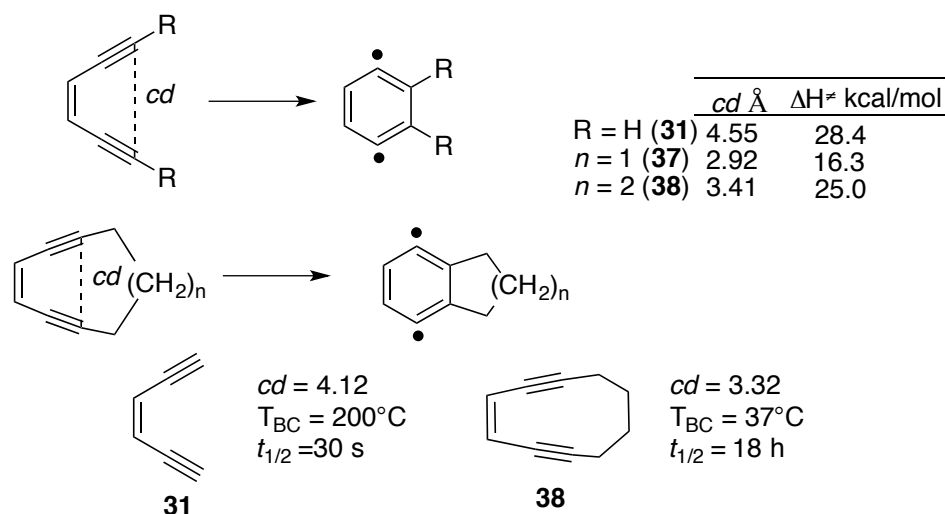


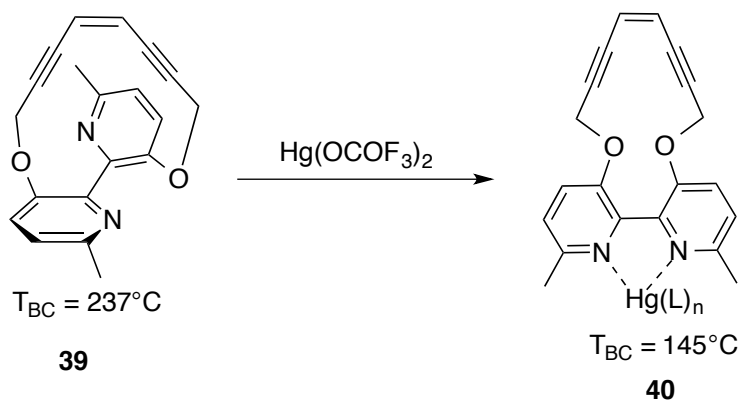
Figure 1.12. Ring strain effects on the barrier to cycloaromatization.^[46,57,58]

I. Metal-Mediated Cycloaromatizations: Select Examples

Ultimately for synthetic enediynes to be applicable in the clinic, two major obstacles must be overcome: (1) any potential drug must cyclize in a selective manner and (2), the cycloaromatization must occur at biologically relevant temperatures. Given the high temperatures necessary for cycloaromatization of acyclic enediynes, much time and effort has been expended by organometallic chemists to lower the barrier to cycloaromatization using transition metals.

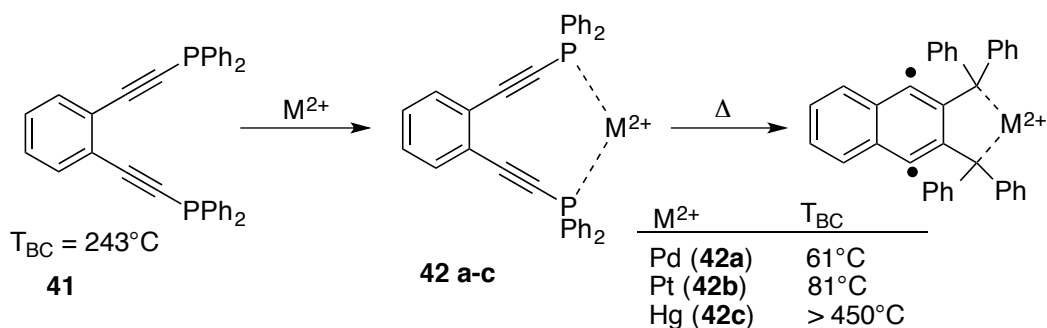
The first method to lower the cycloaromatization barrier involves metal coordination to heteroatoms contained within the enediyne framework. Köning and co-workers first demonstrated how transition metal coordination can alter the

conformation and reactivity of an unreactive enediyne (Scheme 1.10).⁵⁹ Bipyridyl-based enediyne **39** exists in a transoid conformation where the enediyne termini are far apart and the macrocycle is stable to cyclization. Addition of $\text{Hg}(\text{tfa})_2$ to a solution of **39** in methanol results in mercury coordination to each of the bipyridyl ligands, forcing the enediyne to adopt a cisoid conformation (**40**). In this more reactive conformation, differential scanning calorimetry (DSC) demonstrated the coordinated enediyne underwent cycloaromatization at 145 °C, almost 100 °C lower than the organic enediyne.



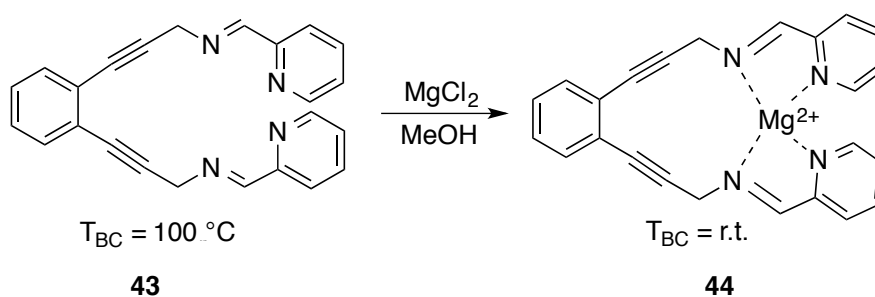
Scheme 1.10. Coordination of mercury drastically lowers temperature for **39** to cyclize.⁵⁹

The same year Buchwald *et al.* also observed the pronounced effect metal coordination can have on cycloaromatization of acyclic enediynes.⁶⁰ Enediyne **41** is stable to cycloaromatization up to 243 °C, however upon palladium(II) or platinum(II) coordination (**42a** and **42b**) the cyclization temperature drastically decreases (Scheme 1.11). When enediyne **41** complexes to mercury the opposite effect is observed; no cyclization occurs even upon heating at 450 °C.



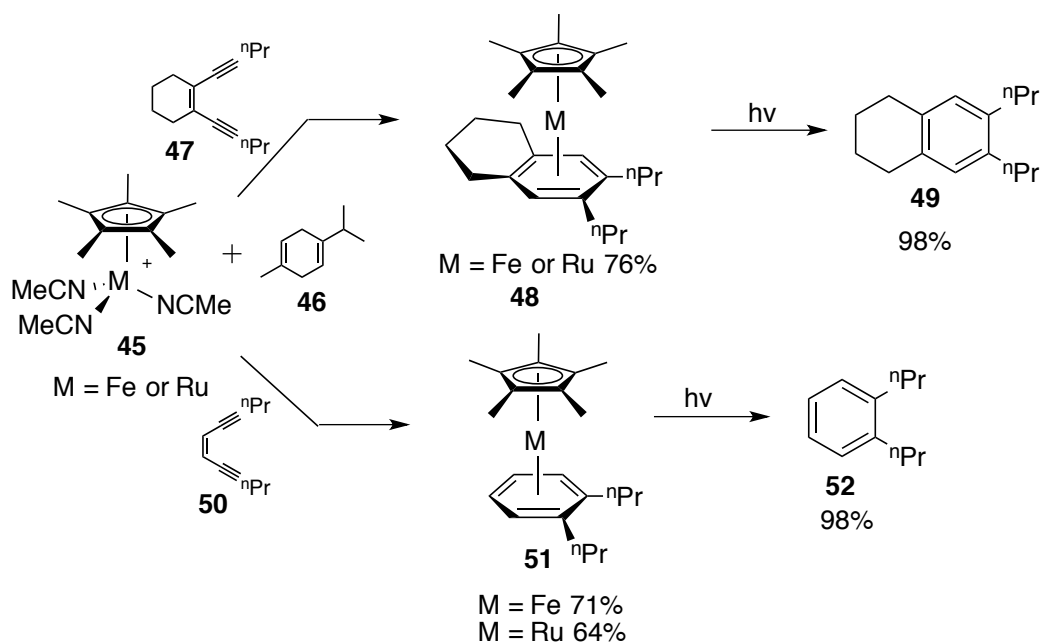
Scheme 1.11. Coordination to enediyne **41** drastically lowers the barrier to cyclization.⁶⁰

Perhaps the most exciting example of metal-chelation-assisted Bergman cycloaromatization was work reported by Zaleski, who demonstrated that pyridine based enediyne **43** undergoes facile cyclization at room temperature in the presence of a hydrogen atom donor (Scheme 1.12).⁶¹ The drastically lower temperature required to affect cyclization following magnesium coordination was certainly impressive, but more significantly, for the first time it was demonstrated that a biologically relevant metal could be used to achieve cyclization at ambient temperatures.



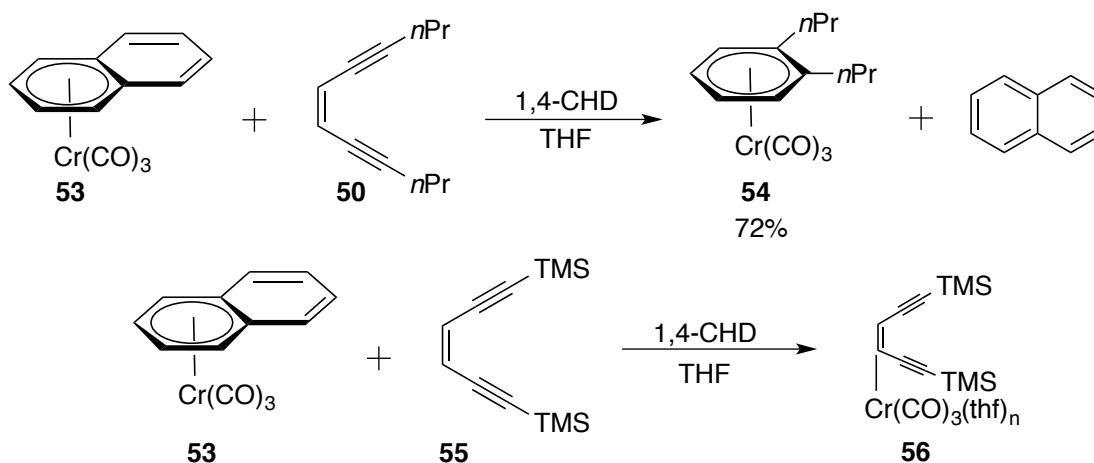
Scheme 1.12. Coordination of magnesium to **43** drastically lowers the barrier to cyclization.⁶¹

A second method to induce cycloaromatization at biologically relevant temperatures involves coordination of a metal directly to the π backbone of the enediyne. Pentamethylcyclopentadienyl ruthenium and iron have both been demonstrated to trigger cyclization of otherwise unreactive enediynes, giving good to excellent yields of Bergman cycloaromatization products (Scheme 1.13).^[62,63] While $\text{Cp}^*\text{Fe}(\text{MeCN})_3^+$ failed to cyclize enediynes where the *ene* was incorporated into a five membered ring, the iron half-sandwich complex binds arenes much more weakly than ruthenium, and as a result the product arene is easily photodissociated. As a result of this weaker metal-ligand bonding, **45**-Fe catalyzes enediyne cyclization; when **50** was irradiated at room temperature in the presence of sub-stoichiometric $[\text{Cp}^*\text{Fe}(\text{NCMe})_3]\text{PF}_6$ for 144 h, the arene product was generated in 91% yield with a turn over number of 3.9.⁶³



Scheme 1.13. Ruthenium and iron-mediated cyclization of acyclic enediynes.^[62,63]

In a much similar fashion, Peter Küdig later demonstrated [$\text{Cr}(\text{CO})_3(\eta^6\text{-naphthalene})$] (**53**) readily cyclizes acyclic enediynes in THF to give chromium-arene products in good yields (Scheme 1.14).⁶⁴ While substitution of a TMS group at the alkyne carbons made the enediyne unreactive to cyclization in THF-*d*₈, the authors were able to detect a potential intermediate by ¹H NMR and ¹³C NMR spectroscopy. Due to the large shifts observed for the alkene carbons (38 ppm) upon addition of **53** they assigned the intermediate as the THF stabilized chromium alkene complex **56**.



Scheme 1.14. Chromium-mediated cycloaromatization of enediyne **50** and structure of possible intermediate **56**.⁶⁴

In summary, the remarkable cytotoxicity of the naturally occurring enediyne antibiotics has been attributed to formation of *para*-benzyne *in vitro*. While nature accomplishes the cyclization of enediyne substrates in a seemingly simple and elegant fashion, chemists have struggled to control the reactivity of enediyne substrates in both the lab and *in vitro*.⁵⁰ Attempted strategies to induce

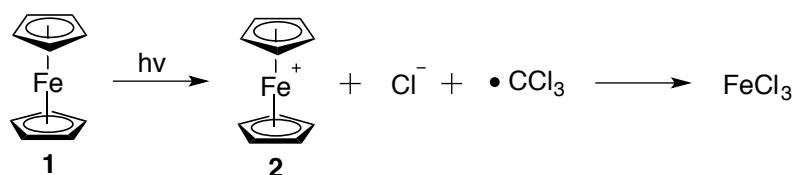
cycloaromatization at biologically relevant temperatures include metal chelation to heteroatoms located of the alkyne termini^[59,60,61] and transition-metal binding to the enediyne π backbone.^[62,63,64] Despite these advances, chemists are still searching for novel ways to selectively trigger formation of *para*-benzyne *in vitro* with the hopes of creating a selective enediyne anticancer drug.

J. Photochemical Properties of Ferrocene

Given the redox-active nature of successful iron antitumor agents, including ferrocenium, hydroxyferrocifen, **10**, and **20**, we wondered if inorganic iron(II) could be delivered to cancer cells in a selective manner by photochemical activation of ferrocene. Once released from the organic ligands, iron(II) would be free to participate in detrimental Fenton chemistry by reaction with endogenous hydrogen peroxide to form highly toxic hydroxyl radicals (section C).

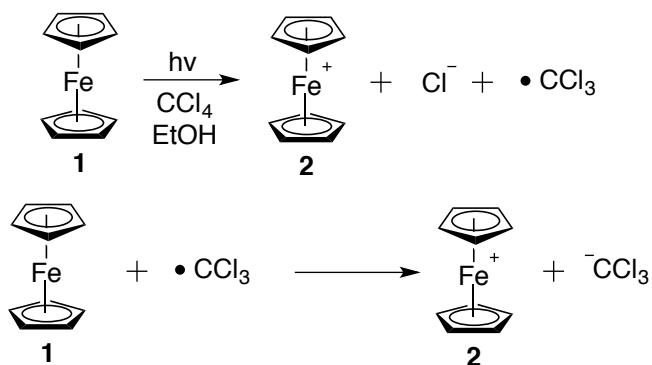
While ferrocene itself is exceptionally stable *thermally*, its photochemistry is rich and relatively unexplored. While **1** is photoinert in cyclohexane, decalin, acetone, methanol, propanol, and isopropanol, Brand and Snedden reported photolysis in either CCl₄ or CCl₃Br results in rapid (< 30s!) decomposition of the otherwise stable sandwich complex (Scheme 1.15). The remarkable reactivity under these conditions was attributed by the authors to an initial ferrocene-to-solvent charge transfer. Following excitation, **1** initially decomposes to ferrocenium (identified by a new absorption in the UV-Vis spectrum at 615 nm), chloride ion, and

trichloromethyl radical. Further decomposition then leads to the formation of the end product, ferric chloride.⁶⁵



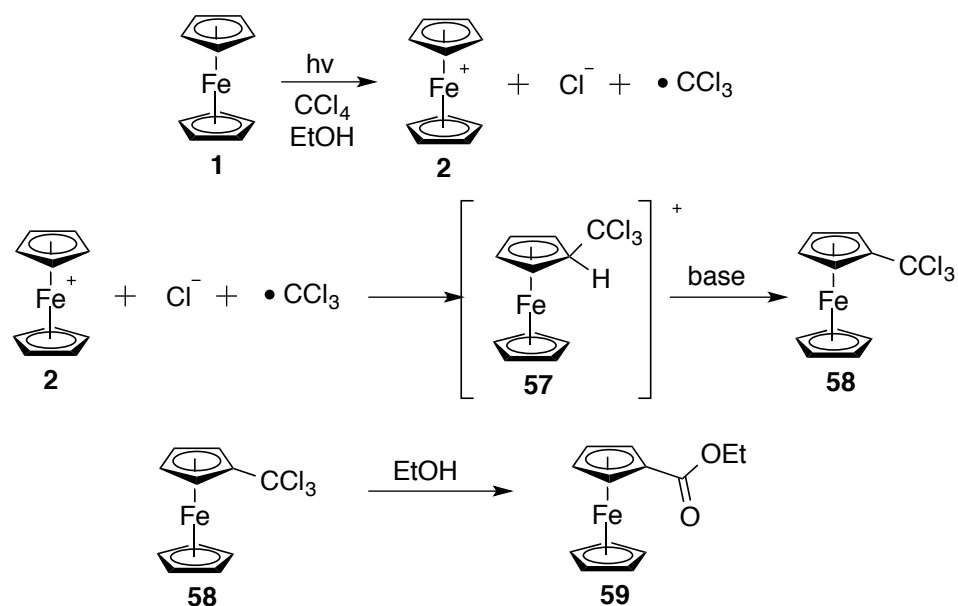
Scheme 1.15. Photochemical decomposition of ferrocene.⁶⁵

Later work by Traverso and Scandola confirmed the primary photochemical products were ferrocenium cation and the organic $\bullet\text{CCl}_3$ radical, which they trapped with acrylamide. In the absence of the radical trap, a second *thermal* ferrocene oxidation occurred to generate an additional equivalent of the oxidized metallocene (Scheme 1.16). While this result was intriguing, the authors were never able to isolate the iron-containing photoproducts, which were identified solely by their UV-Vis spectra.⁶⁶



Scheme 1.16. Decomposition of **1** as reported by Traverso.⁶⁶

Shortly thereafter, Sugimori was able to isolate and fully characterize not only the ferrocenium cation that was formed upon photolysis, but also additional products where one of the cyclopentadienyl rings was alkylated when irradiated in the presence of an alkyl chloride. The authors proposed a mechanism consistent with Brand and Snedden where a ferrocene-to-solvent charge transfer initially generated ferrocenium and the $\bullet\text{CCl}_3$ radical (Scheme 1.17). Attack of the radical on the cyclopentadienyl ring and deprotonation by advantageous base gave proposed intermediate **58**. Hydrolysis by ethanol gave the observed product **59**.^[67,68,69]



Scheme 1.17. Decomposition of **1** to give ester **59**.^[67,68,69]

K. Photochemical Properties of Benzoyl and 1,1'-Dibenzoyl Ferrocene

Concurrent with the discovery that ferrocene was photochemically active, was the observation that benzoylferrocene decomposes upon exposure to visible light. While benzophenone cleanly gives benzopinacol when irradiated in alcoholic

solvents, the photochemical decomposition of the ferrous analog has proven to be much more difficult to decipher. The first publication regarding the photoactivity of **60** reported that while benzoylferrocene and 1,1'-dibenzoylferrocene (**61**) are stable in the dark for weeks, they rapidly decompose in methanol upon exposure to wavelengths of light identical to either one of their absorption bands at 470 nm and 354 nm. These absorptions, which were noted to be drastically intensified relative to ferrocene, were attributed to the presence of the conjugated carbonyl group, and were tentatively assigned as a metal-to-ligand charge transfer bands.

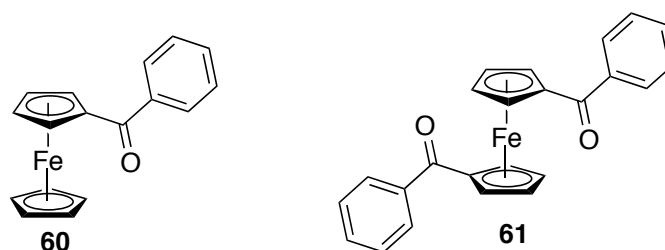
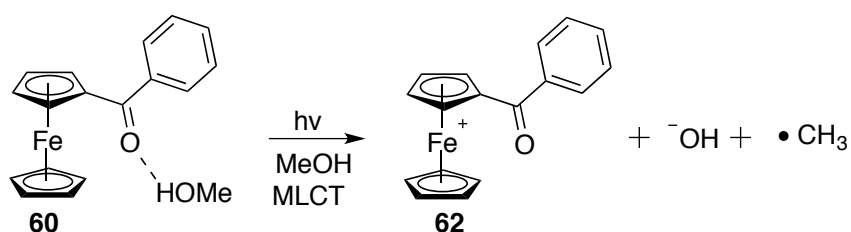


Figure 1.13. Benzoyl and 1,1'-dibenzoylferrocene.

Ferrocene derivatives where the carbonyl was not in conjugation with the cyclopentadienyl ring were photoinert, leading the authors to speculate a unique interaction between the iron atom and the neighboring carbonyl group was responsible for photoactivity. In contrast to ferrocene, the decomposition was slowest in CCl₄ and rapid in water and methanol mixtures. The only identifiable product from the reaction mixture was methyl benzoate and an intractable iron solid, which was suspected to be ferrous benzoate. While the authors remarked that any mechanism was highly speculative, they proposed initial activation of the

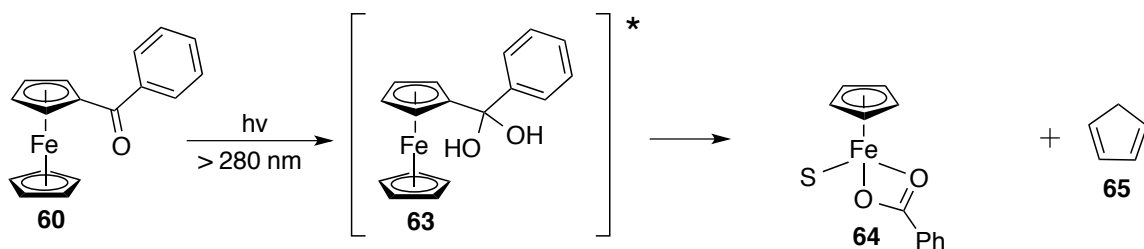
carbonyl by hydrogen-bonding with the alcoholic solvent followed by a low energy metal-to-ligand charge transfer generated ferrocenium cation **62** (Scheme 1.18). The resultant weakening of metal-ring bonding upon oxidation was speculated to lead to further decomposition, in a manner similar to that of ferrocene.⁷⁰



Scheme 1.18. Proposed mechanism for decomposition of **60** by Tarr and Wiles.⁷⁰

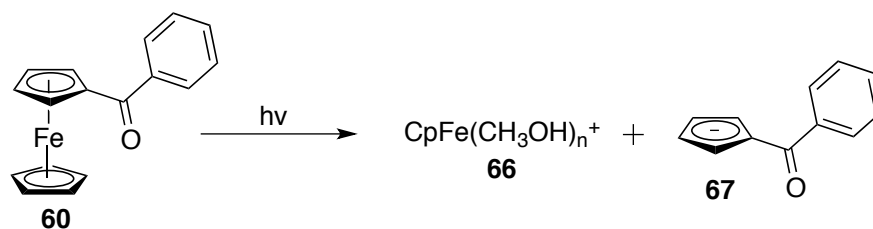
In 1973 Ali and coworkers demonstrated that the photochemical decomposition of benzoylferrocene also occurred in wet polar solvents such as DMSO, DMF, and pyridine.⁷¹ Monitoring of the reaction by IR spectroscopy in DMSO demonstrated that upon photolysis (> 280 nm) the absorption for the starting benzoylferrocene (1638 cm^{-1}) was supplanted by new carbonyl stretches at 1538 and 1364 cm^{-1} , assigned to a carboxylate group. Monitoring by ^1H NMR spectroscopy was frustrated by formation of solids in the NMR tube, but formation of free cyclopentadiene and a single iron-bound cyclopentadienyl ligand were evident. Treatment of the crude reaction mixture with HCl gave benzoic acid (50% yield), which was positively identified by mass spectroscopy, IR, and melting point. Based on the data the authors assigned the photoproduct as solvated Cp-iron benzoate complex **64** (Scheme 1.19). While any mechanism was again, highly

speculative, the authors proposed an initial aqutation of the carbonyl followed by cyclopentadienyl-iron ring cleavage.⁷²



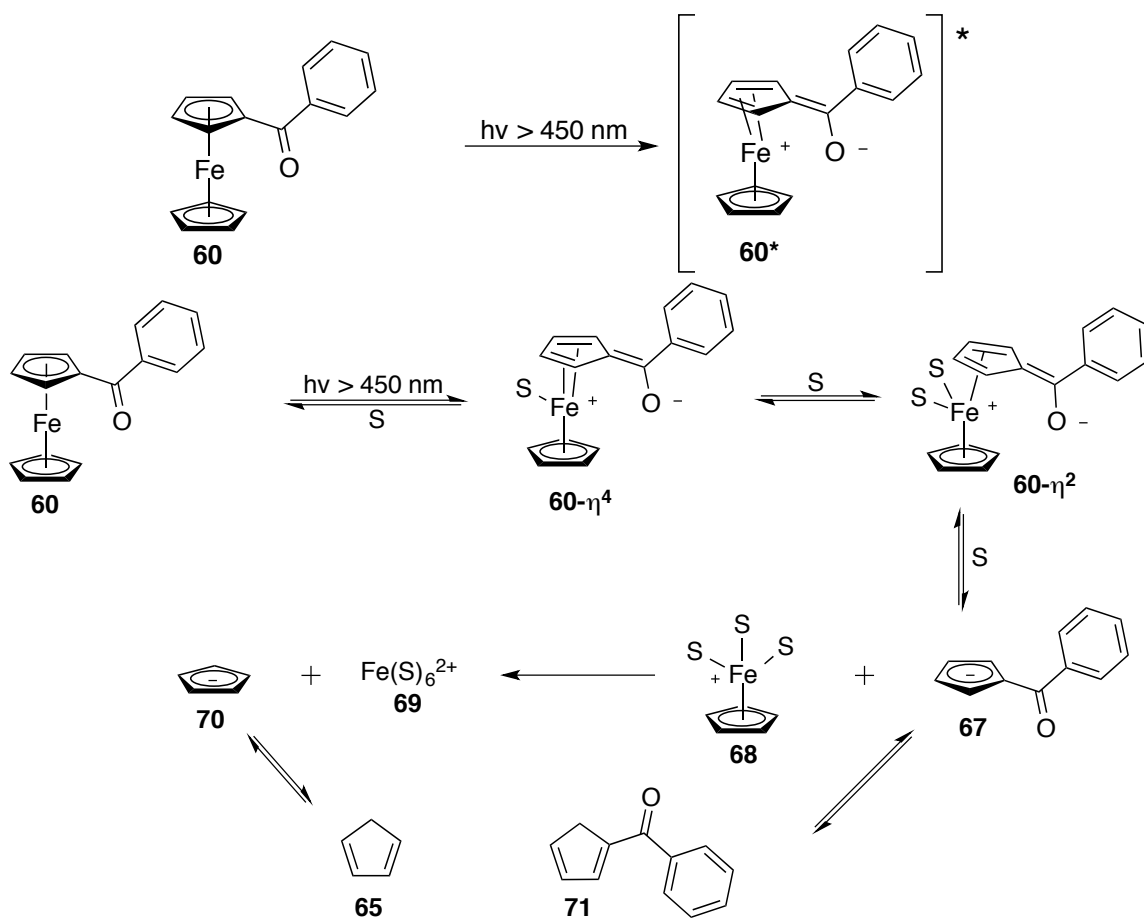
Scheme 1.19. Photodecomposition of **60** as reported by Ali *et al.*⁷²

Bozak and Javaheripour also reported photolysis of benzoylferrocene results in iron-cyclopentadienyl ring cleavage stemming from the dissociative charge-transfer bands at 370 and 480 nm.⁷³ After light exposure for 30 min in methanol, they observed the intact benzoylcyclopentadienyl anion, **67**, which was protonated under the reaction conditions to give the substituted cyclopentadiene (Scheme 1.20). In contrast to the reports of Kemp, no debenzoylated product was identified. Treatment of the crude reaction mixture with aqueous 1,10-phenanthroline indicated the presence of iron(II) by colorimetric analysis. Following isolation of the organics, mass spectrometry-gas chromatography detected benzoylcyclopentadiene, cyclopentadiene, and Diels-Alder adducts of each monomer.



Scheme 1.20. Photodecomposition of **60** as reported by Bozak *et al.*⁷³

Most recently, Kutal proposed the enhanced UV-Vis absorptions and photoactivity of benzoylferrocene were the result of mixing metal-to-ligand charge transfer character into the low energy excited states of the metallocene complex. This MLCT character in the excited state was described pictorially by Kutal as resonance structure **60***, where the conjugated carbonyl of the benzoyl group effectively draws electron density away from the iron and to the ligand, reminiscent of early observations of Tarr and Wiles (Scheme 1.21).^[74,75,76] As a consequence of this, upon exposure to visible light in methanol or acetonitrile, benzoylferrocene rapidly dissociates to form the cyclopentadienide anion **67** and solvent-stabilized half sandwich complex **68** via a series of ring-slipped intermediates. Photoproducts **65**, **67**, **68**, and **71** were each identified by gas chromatography-mass spectrometry from the photolysis mixture. Treatment of an irradiated solution with 2,2'-bipyridyl gave the characteristic red color of Fe(bipy)₂⁺, consistent with the observations of Bozak and Javaheripour.^{76,73}



Scheme 1.21. Katal's mechanism for the photodecomposition of benzoylferrocene.^[74,76]

L. Proposal

In light of the previously described literature precedents, we proposed two mechanisms by which benzoylferrocenes derivatives could photochemically generate cytotoxic agents in cells. We were especially enthusiastic about the extra requirement of photochemical activation, as it would allow for enhanced spatiotemporal control, resulting in toxicity only in cancerous cells.

First, we wished to investigate *iron redox-driven* cytotoxicity. While the literature regarding the photochemical decomposition of benzoylferrocene was

conflicting, both Kotal^{75,76} and Bozak⁷³ reported formation of $\text{Fe}(\text{bipy})_3^{2+}$ (or 1,10-phenanthroline) complexes from the photochemical decomposition of **60**. Based on their work, we proposed that photolysis of **60** in cell media would give inorganic iron(II) *in situ*. The solvated, labile iron(II) could then react with hydrogen peroxide, and generate highly toxic hydroxyl radicals - in a similar fashion to ferrocenium and established electron-rich medicinal ferrocene complexes (Figure 1.14). We also speculated since **60** is electron-deficient relative to ferrocene that the organometallic complex would be relatively stable to oxidation in aqueous media and therefore, may not induce cytotoxic Fenton chemistry in the absence of light.

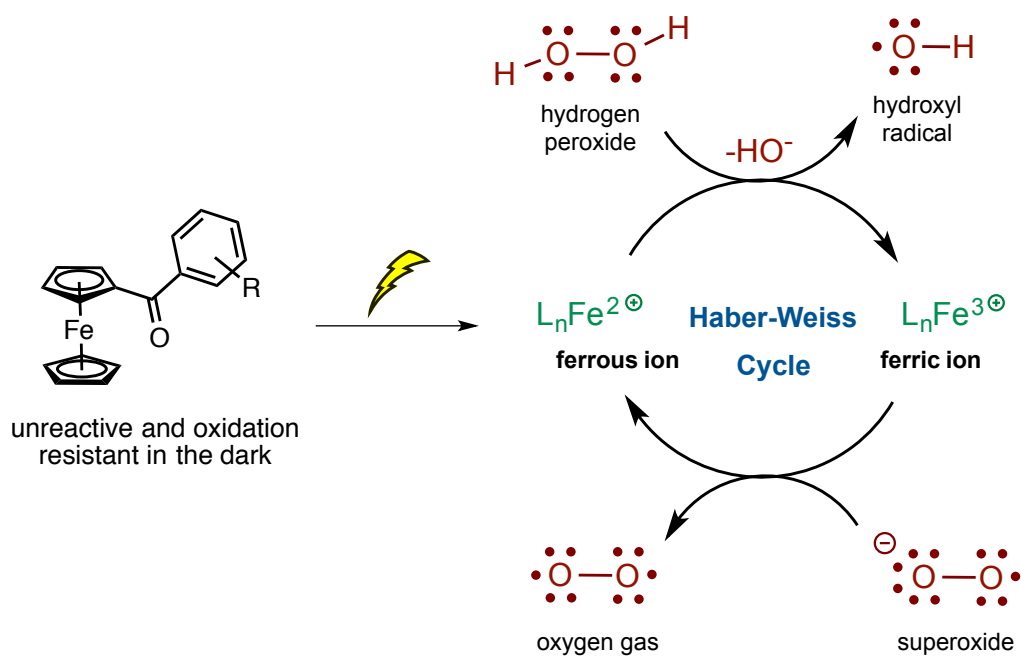


Figure 1.14. Generation of toxic hydroxyl radicals from benzoylferrocene using visible light irradiation.

Second, we wished to take advantage of the unique photochemical properties of benzoylferrocene to deliver reactive enediyne *ligands* to tumor cells. We proposed that once localized in the cell, irradiation with visible light could trigger the enediyne to cycloaromatize, forming the reactive *para*-benzyne diradical, which could abstract hydrogen atoms from DNA in a similar manner to that of the enediyne antibiotics. To this end, we first planned to prepare readily accessible complex **72** to confirm enediynes could be liberated photochemically from the organometallic precursor. Derivative **73** was expected to generate a CpFeL₃⁺ catalyst upon photochemical loss of the benzoylcyclopentadiene ligand, which would then cyclize the tethered enediyne intramolecularly to generate *para*-benzyne.⁶³ Lastly, derivatives **74** and **75** were prepared in hopes that the enediyne could be liberated and the anion, or its cyclopentadiene analogue, would undergo cycloaromatization. While we believed complex **74** would be less likely to cycloaromatize than **75** due to longer *cd* distances, we proposed the CpFe⁺ cation, generated following photo-induced ligand loss, could coordinate to the enediyne and prompt cyclization. Once we had the organoferrous prodrugs in hand we proposed to test each complex cancer cells, under both irradiation conditions and in the dark, with the hopes that cytotoxicity would be enhanced following visible light exposure. In the following chapter we describe the synthesis and phototoxicity of benzoylferrocene ferrocene derivatives. In Chapter III we discuss the synthesis, photochemistry, and biological activity of ferrous enediynes.

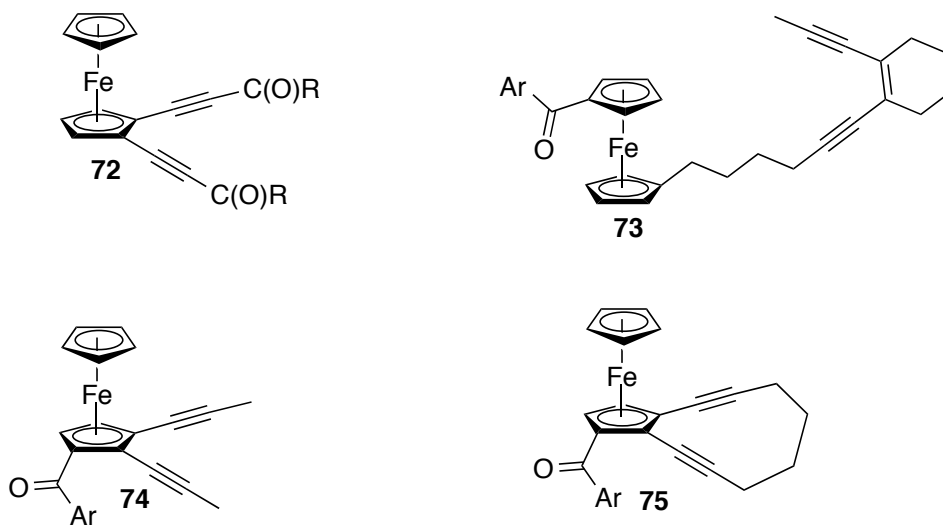


Figure 1.15. Synthetic enediynes that become activated upon exposure to visible light.

M. References

- (1) Kealy, T. J.; Pauson, P. L. *Nature* **1951**, *168*, 1039.
- (2) Wilkinson, G.; Rosenblum, M.; Whiting, M. C.; Woodward, R. B. *J. Am. Chem. Soc.* **1952**, *74*, 2125.
- (3) Dagani, R. O. N.; Washington, E. N. *C & E News*. 2002, pp. 23–29.
- (4) *Ferrocenes*; Stepnicka, P., Ed.; Wiley: West Sussex, England, 2008.
- (5) Braga, S. S.; Silva, A. M. S. *Organometallics* **2013**, *32*, 5626.
- (6) Ornelas, C. *New J. Chem.* **2011**, *35*, 1973.
- (7) Gasser, G.; Ott, I.; Metzler-Nolte, N. *J. Med. Chem.* **2011**, *54*, 3.
- (8) Gasser, G.; Metzler-Nolte, N. *Curr. Opin. Chem. Biol.* **2012**, *16*, 84.
- (9) Köpf-Maier, P.; Köpf, H.; Neuse, E. W. *J. Cancer Res. Clin. Oncol.* **1984**, *108*, 336.
- (10) Kroger, N.; Kleeberg, U.R.; Mross, K.; Edler, L.; Sab, G.; Hossfeld, D. K. *Onkologie* **2000**, *23*, 60.
- (11) Waern, J. B.; Harris, H. H.; Lai, B.; Cai, Z.; Harding, M. M.; Dillon, C. T. *J. Biol. Inorg. Chem.* **2005**, *10*, 443.
- (12) Christodoulou, C. V; Eliopoulos, a G.; Young, L. S.; Hodgkins, L.; Ferry, D. R.; Kerr, D. J. *Br. J. Cancer* **1998**, *77*, 2088.
- (13) Guo, M.; Sun, H.; McArdle, H.J.; Gambling, L.; Sadler, P. J. *Biochemistry* **2000**, *39*, 10023.
- (14) Sutton, H. C. *J. Free Radic. Biol. Med.* **1985**, *1*, 195.
- (15) Tamura, H.; Miwa, M. *Chem. Lett.* **1997**, 1177.
- (16) Osella, D.; Ferrali, M.; Zanello, P.; Laschi, F.; Fontani, M.; Nervi, C.; Cavigliolo, G. *Inorganica Chim. Acta* **2000**, *306*, 42.
- (17) Crichton, R. *Iron Metabolism*; 3rd ed.; Wiley: West Sussex U.K., 2009.
- (18) MacKenzie, E. L.; Iwasaki, K.; Tsuji, Y. *Antioxid. Redox Signal.* **2008**, *10*, 997.

- (19) Halliwell, B.; Gutteridge, J. M. *Free Radicals in Biology and Medicine*; 4th ed.; Oxford University Press: Oxford, 2007.
- (20) MacGillivray, R.T.A.; Moore, S.A.; Chen, J.; Anderson, B.F.; Baker, H.; Luo, Y.; Bewley, M.; Smith, C.A.; Murphy, M.E.P.; Wang, Y.; Mason, A.B.; Woodworth, R.C.; Brayer, G.D.; Baker, E. N. *Biochemistry* **1998**, *37*, 7919.
- (21) Haber, F.; Weiss, J. *Proc. R. Soc. London. Ser. A* **1934**, *147*, 332.
- (22) Avendano, C; Menendez, J. C. *Medicinal Chemistry of Anticancer Drugs*; 1st ed.; Wiley: Amsterdam, 2008.
- (23) Hertzberg, R. P.; Dervan, P. B. *Biochemistry* **1984**, *23*, 3934.
- (24) Groeger, G.; Quiney, C.; Cotter, T. G. *Antioxid. Redox Signal.* **2009**, *11*, 2655.
- (25) Gough, D. R.; Cotter, T. G. *Cell Death Dis.* **2011**, *2*, e213.
- (26) Lambeth, J. D. *Nat. Rev. Immunol.* **2004**, *4*, 181.
- (27) Jastroch, M.; Divakaruni, A.S.; Mookerjee, S.; Treberg, J.R.; Brand, M. D. *Essays Biochem* **2010**, *47*, 53.
- (28) Gao, X.; Campian, J. L.; Qian, M.; Sun, X.-F.; Eaton, J. W. *J. Biol. Chem.* **2009**, *284*, 4767.
- (29) Boveris, A.; Cadenas, E. *Life* **2000**, *50*, 245.
- (30) Fiorina, V.J.; Dubois, R.J.; Brynes, S. *J. Med. Chem.* **1978**, *21*, 393.
- (31) Mooney, Á.; Corry, A. J.; O'Sullivan, D.; Rai, D. K.; Kenny, P. T. M. *J. Organomet. Chem.* **2009**, *694*, 886.
- (32) Mooney, A.; Corry, A. J.; Ní Ruairc, C.; Mahgoub, T.; O'Sullivan, D.; O'Donovan, N.; Crown, J.; Varughese, S.; Draper, S. M.; Rai, D. K.; Kenny, P. T. M. *Dalton Trans.* **2010**, *39*, 8228.
- (33) Ong, C.; Jeng, J.; Juang, S.; Chen, C. *Bioorg. Med. Chem. Lett.* **1992**, *2*, 929.
- (34) Vashisht Gopal, Y. N.; Jayaraju, D.; Kondapi, a K. *Arch. Biochem. Biophys.* **2000**, *376*, 229.
- (35) Krishna, a. D. S.; Panda, G.; Kondapi, A. K. *Arch. Biochem. Biophys.* **2005**, *438*, 206.

- (36) Top, S.; Thibaudeau, C.; Vessières, A.; Brulé, E.; Le Bideau, F.; Joerger, J. M.; Plamont, M. A.; Samreth, S.; Edgar, A.; Marrot, J.; Herson, P.; Jaouen, G. *Organometallics* **2009**, *28*, 1414.
- (37) Ferreira, A. P.; da Silva, J. L. F.; Duarte, M. T.; da Piedade, M. F. M.; Robalo, M. P.; Harjivan, S. G.; Marzano, C.; Gandin, V.; Marques, M. M. *Organometallics* **2009**, *28*, 5412.
- (38) Nguyen, A.; Top, S.; Pigeon, P.; Vessières, A.; Hillard, E. a.; Plamont, M. A.; Huché, M.; Rigamonti, C.; Jaouen, G. *Chem. - A Eur. J.* **2009**, *15*, 684.
- (39) Hillard, E. a.; Vessières, A.; Top, S.; Pigeon, P.; Kowalski, K.; Huché, M.; Jaouen, G. *J. Organomet. Chem.* **2007**, *692*, 1315.
- (40) Heilmann, J. B.; Hillard, E. a.; Plamont, M. A.; Pigeon, P.; Bolte, M.; Jaouen, G.; Vessières, A. *J. Organomet. Chem.* **2008**, *693*, 1716.
- (41) Hillard, E.; Vessières, A.; Thouin, L.; Jaouen, G.; Amatore, C. *Angew. Chemie - Int. Ed.* **2005**, *45*, 285.
- (42) Jaouen, G.; Top, S.; Vessières, A.; Pigeon, P.; Leclercq, G.; Laios, I. *Chem. Commun.* **2001**, 383.
- (43) Pigeon, P.; Top, S.; Vessières, a; Huché, M.; Hillard, E. a; Salomon, E.; Jaouen, G. *J. Med. Chem.* **2005**, *48*, 2814.
- (44) Zhang, F.; Fan, P. W.; Liu, X.; Shen, L.; Van Breemen, R. B.; Bolton, J. L. *Chem. Res. Toxicol.* **2000**, *13*, 53.
- (45) Vessières, A.; Corbet, C.; Heldt, J. M.; Lories, N.; Jouy, N.; Laios, I.; Leclercq, G.; Jaouen, G.; Toillon, R. A. *J. Inorg. Biochem.* **2010**, *104*, 503.
- (46) Jones, R. R.; Bergman, R. G. *J. Am. Chem. Soc.* **1972**, *94*, 660.
- (47) Golik, J.; Clardy, J.; Dubay, G.; Groenewold, G.; Kawaguchi, H; Konishi, M; Krishan, B.; Ohkuma, H.; Saitoh, K.; Doyle, T. W. *J. Am. Chem. Soc.* **1987**, *109*, 3461.
- (48) Lee, M.D.; Dunne, T.S.; Chang, C.C.; Allestad, G.A.; Siegel, M.M; Morton, G.O.; McGahren, W.J.; Borders, D. B. *J. Am. Chem. Soc.* **1987**, *109*, 3466.
- (49) Golik, J.; Dubaj, G.; Groenewold, G.; Kawaguchi, H.; Konishi, M.; Krishan, B.; Ohkuma, H.; Saitoh, K.; Doyle, T. W. *J. Am. Chem. Soc.* **1987**, *109*, 3462.

- (50) Nicalaou, K.C.; Dai, W. *Angew. Chem. Int. Ed.* **1991**, *30*, 1387.
- (51) Galm, U.; Hager, M. H.; Van Lanen, S. G.; Ju, J.; Thorson, J. S.; Shen, B. *Chem. Rev.* **2005**, *105*, 739.
- (52) Magnus, P.; Carter, P.; Elliott, J.; Lewis, R.; Harling, J.; Pitterna, T.; Bauta, W. E.; Forttt, S. *J. Am. Chem. Soc.* **1992**, *114*, 2544.
- (53) Nicolaou, K.C.; Zuccarello, G.; Ogawa, Y.; Schweiger, E.J.; Kumazawa, T. *J. Am. Chem. Soc.* **1988**, *110*, 4868.
- (54) Zein, N.; McGahren, W.J.; Morton, G.O.; Ashcroft, J.; Ellestad, G. A. *J. Am. Chem. Soc.* **1989**, *111*, 6888.
- (55) Hangeland, J. J.; Voss, J. J. De; Heath, J. A.; Townsend, C. A. *J. Am. Chem. Soc.* **1992**, *114*, 9200.
- (56) Voss, J. J. De; Townsend, C. A.; Tabor, A. B.; Schreiber, S. L. *J. Am. Chem. Soc.* **1990**, *112*, 9669.
- (57) Schreiner, P. R. *J. Am. Chem. Soc.* **1998**, *120*, 4184.
- (58) Semmelhack, M.F.; Neu, T.; Foubelo, F. *J. Org. Chem* **1994**, *59*, 5038.
- (59) König, B.; Hollnagel, H.; Ahrens, B.; Jones, P. G. *Angew. Chemie Int. Ed. English* **1995**, *34*, 2538.
- (60) Warner, B.P.; Miller, S.P.; Broee, R.D.; Buchwald, S. L. *Science* **1995**, *269*, 814.
- (61) Rawat, D. S.; Zaleski, J. M. *J. Am. Chem. Soc.* **2001**, *123*, 9675.
- (62) O'Connor, J. M.; Friese, S. J.; Tichenor, M. *J. Am. Chem. Soc.* **2002**, *124*, 3506.
- (63) O'Connor, J. M.; Friese, S. J.; Rodgers, B. L. *J. Am. Chem. Soc.* **2005**, *127*, 16342.
- (64) Ylijoki, K. E. O.; Lavy, S.; Fretzen, A.; Kündig, E. P.; Berclaz, T.; Bernardinelli, G.; Besnard, C. *Organometallics* **2012**, *31*, 5396.
- (65) Brand, J. C. D.; Snedden, W. *Trans. Faraday Soc.* **1957**, *53*, 894.
- (66) Traverso, O.; Scandola, F. *Inorganica Chim. Acta* **1970**, *4*, 493.
- (67) Akiyama, T.; Sugimori, A.; Hermann, H. *Bull. Chem. Soc. Jpn.* **1973**, *46*, 1855.

- (68) Akiyama, T.; Hoshi, Y.; Goto, S.; Sugimori, A. *Bull. Chem. Soc. Jpn.* **1973**, *46*, 1851.
- (69) Akiyama, T.; Kitamura, T.; Kato, T.; Watanabe, H.; Serizawa, T.; Sugimori, A. *Bull. Chem. Soc. Jpn.* **1977**, *50*, 1137.
- (70) Tarr, A.M.; Wiles, D. M. *Can. J. Chem.* **1968**, *46*, 2725.
- (71) Ali, L. H.; Cox, a.; Kemp, T. J. *J. Chem. Soc. Chem. Commun.* **1972**, 265.
- (72) Ali, L.H.; Cox, A.; Kemp, T. J. *J.C.S. Dalt.* **1973**, 1468.
- (73) Bozak, R.E.; Javaheripour, H. *Chem. Ind.* **1973**, 696.
- (74) Yamaguchi, Y.; Ding, W.; Sanderson, C. T.; Borden, M. L.; Morgan, M. J.; Kutal, C. *Coord. Chem. Rev.* **2007**, *251*, 515.
- (75) Yamaguchi, Y.; Kutal, C. *Inorg. Chem.* **1999**, *38*, 4861.
- (76) Ding, W.; Sanderson, C.T.; Conover, R.C.; Johnson, M.K.; Amster, I.J.; Kutal, C. *Inorg. Chem.* **2003**, *42*, 1532.

Chapter II.
Photosensitive Ferrocene-Based Antitumor Agents

A. Introduction

Since the discovery and successful clinical application of cis-platin (**1**) as an antitumor agent, the interest in transition metal complexes as therapeutic compounds has rapidly increased.^[1,2,3,4,5,6,7,8] While the iron-based metallocene **2** does not induce antitumor activity, the more water-soluble ferrocenium cation (**3**) was shown by Kopf-Maier in 1984 to exhibit antitumor activity against Ehrlich ascites tumor (EAT) cell lines.⁹ While the mechanism of action for **3** was not well understood at the time, elegant follow-up studies by Tamura linked the cytotoxicity of **4** to the generation of hydroxyl radicals and DNA strand cleavage. Incubation of DNA with cytotoxic ferrocenium cation **4** resulted in DNA strand cleavage, as determined by gel electrophoresis; however, addition of a hydroxyl radical scavenger, thiourea, resulted in complete inhibition of DNA cleavage.¹⁰ Shortly following, Osella and coworkers confirmed the DNA-cleaving ability of ferrocenium cations. Electron spin resonance spectroscopy experiments with **5** and the spin trap 5,5-dimethyl-1-pyrroline-N-oxide (DMPO) demonstrated that hydroxyl radicals were readily formed in aqueous solutions. Addition of EAT cells to the aqueous solution of DMPO and **5** led to a complete disappearance of the ESR signal, suggesting that cells are capable of reacting with hydroxyl radicals generated by **5**.¹¹ Since that time, substituted ferrocene derivatives have also been investigated by many groups for antitumor activity. The mechanism of action for the ferrocene analog of prevalent breast cancer drug tamoxifen (**6**) was long thought to involve an iron-mediated oxidation of the organic ligand to give the cytotoxic agent;¹² however,

more recent studies using the fluorescent probe H₂DCFDA (dihydro-2',7'-dichlorofluorescein) have suggested a reactive oxygen species (ROS) pathway that results in cell cycle arrest and senescence.¹³

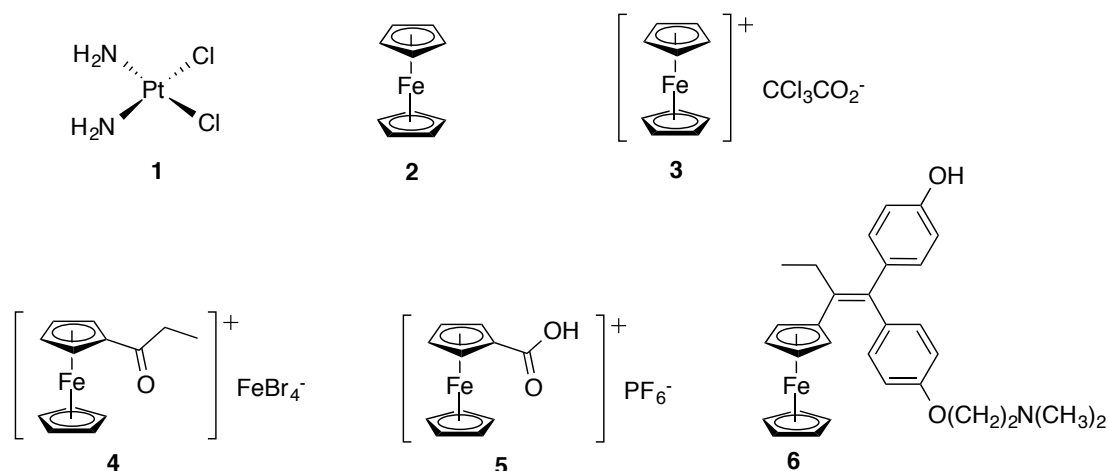


Figure 2.1. Selected metal compounds displaying biological activity.^[9,10,11,12,14,15]

Ferrocene-based antitumor agents are extremely attractive drug candidates for several reasons: (1) iron is inexpensive relative to other transition metals such as platinum; (2) ferrocene derivatives are air-stable and relatively easy to synthesize; (3) a wealth of synthetic literature on ferrocene functionalization is readily available; and (4) the oxidation potential and therefore redox behavior of ferrocenes are easily modified by variation of the cyclopentadienyl ligand substituents. Additionally, while ferrocene itself is not cytotoxic, its lipophilic nature ($\log P = 3.3$) suggests that derivatives of the parent complex should cross the cell membrane without difficulty.⁴ While iron overload is a concern for ferrous drugs, accumulation in the body is typically treatable by chelation therapy.¹⁶

In the O'Connor lab, we became interested in using light as a triggering device for selective delivery of redox-active iron to cancer cells. A fundamental precedent for our work was the observation by Kutal^[17,18,19] that benzoylferrocene (**7**) undergoes photochemical loss of the organic ligands to give solvated Fe(II) upon irradiation at 546 nm in acetonitrile or methanol. Kutal attributed the unique photochemical activity of benzoylferrocene to metal-to-ligand charge transfer (MLCT) character in the low energy excited states. Upon photolysis, the charge-separated excited state, represented by resonance structure **7a**, results in a shift of electron density away from the metal and to the ligands (Figure 2.2). Sequential solvent substitutions at the electron-deficient iron center then lead to the formation of solvated iron(II) via a series of cyclopentadienyl ligand ring-slips (Scheme 2.1). However, other groups have also reported on the photoreaction of benzoylferrocene upon exposure to visible light, and the proposed identities of the iron-containing and organic photoproducts varies widely.^[20,21,22,23]

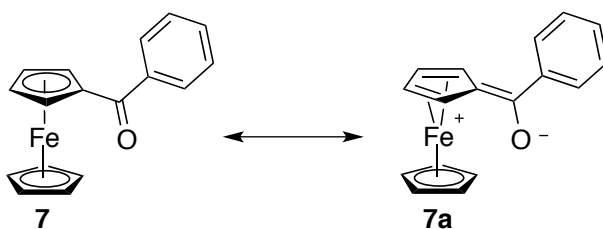
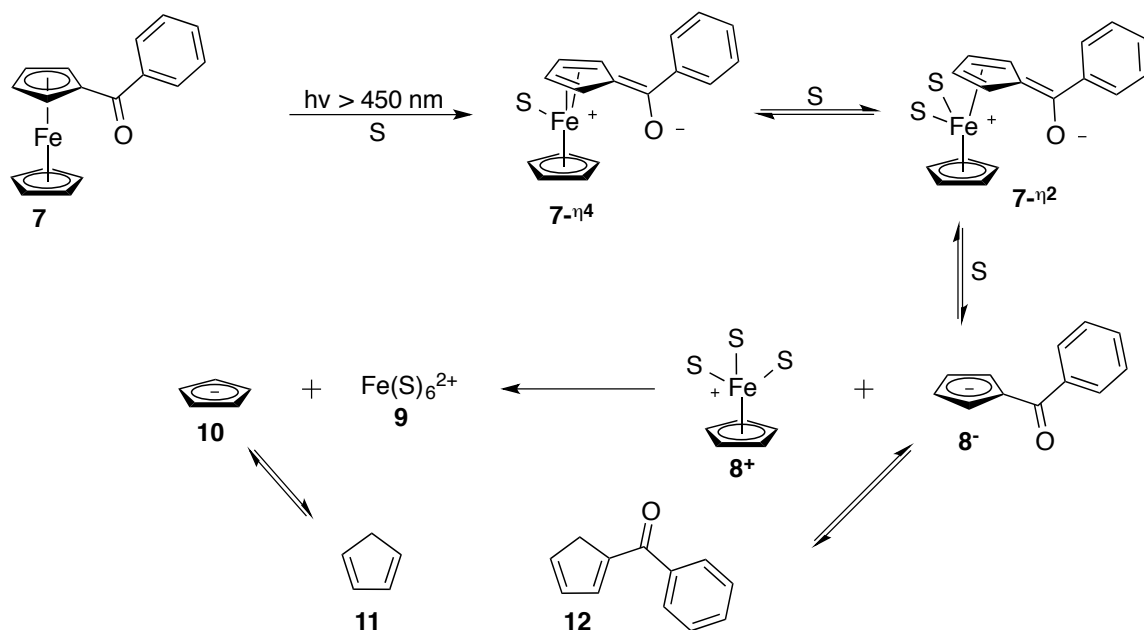


Figure 2.2. Resonance structure depicting the MLCT character for the low-energy excited state of benzoylferrocene.¹⁹



Scheme 2.1. A proposed mechanism for the photochemical dissociation of the ligands in 7.^[17,18,19]

The transportation and storage of iron in cells is a highly regulated and sophisticated process that evolved to prevent labile iron(II) from participating in toxic redox chemistry. In light of Kutal's observations, we predicted that a benzoylferrocene derivative could mask cytotoxic iron(II) as the organometallic complex until iron release is triggered photochemically. The photo-generated solvated iron(II) in biological media could then catalyze the conversion of endogenous hydrogen peroxide (H_2O_2) to hydroxyl radical ($\bullet\text{OH}$), fundamentally disrupting cellular homeostasis (Figure 2.3). We further postulated that the relatively electron-deficient and oxidation-resistant organometallic prodrug would not be inclined to participate in detrimental redox chemistry in the absence of light. Thus, an additional advantage of our proposal was the potential for enhanced

spatiotemporal control, as the cytotoxic agents would be generated *in situ* only upon exposure to visible light. Our initial goals were therefore to: (1) synthesize a series of benzoylferrocene derivatives; (2) determine if the benzoyl functional group would indeed promote the photodissociation of the organic ligands to generate solvated iron(II) in aqueous conditions; and (3) determine the cytotoxicity of the organoferrous prodrugs in both the dark and under irradiation conditions to determine if an enhancement of cytotoxicity occurs following light exposure.

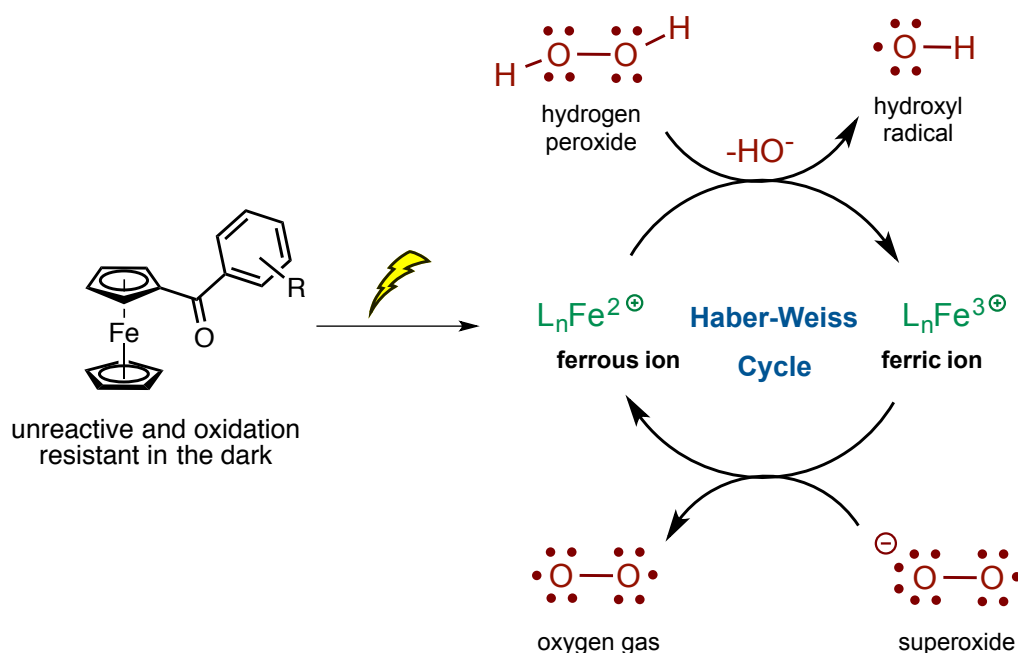


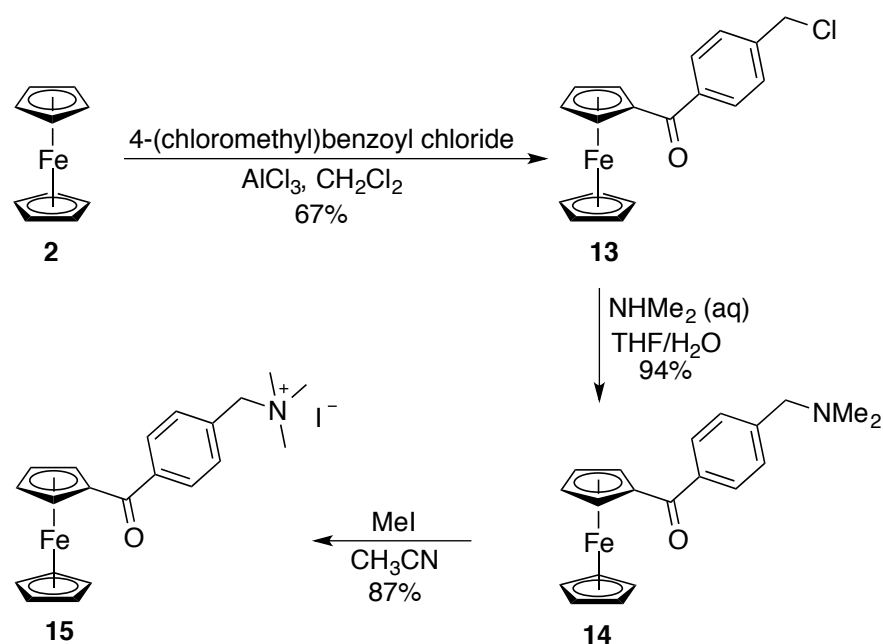
Figure 2.3. Photochemical generation of solvated iron(II) and catalytic formation of reactive oxygen species.

B. Results

1. Synthesis of water-soluble benzoylferrocenes 15 and 21

Cationic and anionic water-soluble benzoylferrocene derivatives were chosen as initial targets. Cation **15** was synthesized from ferrocene in three steps. Friedel-

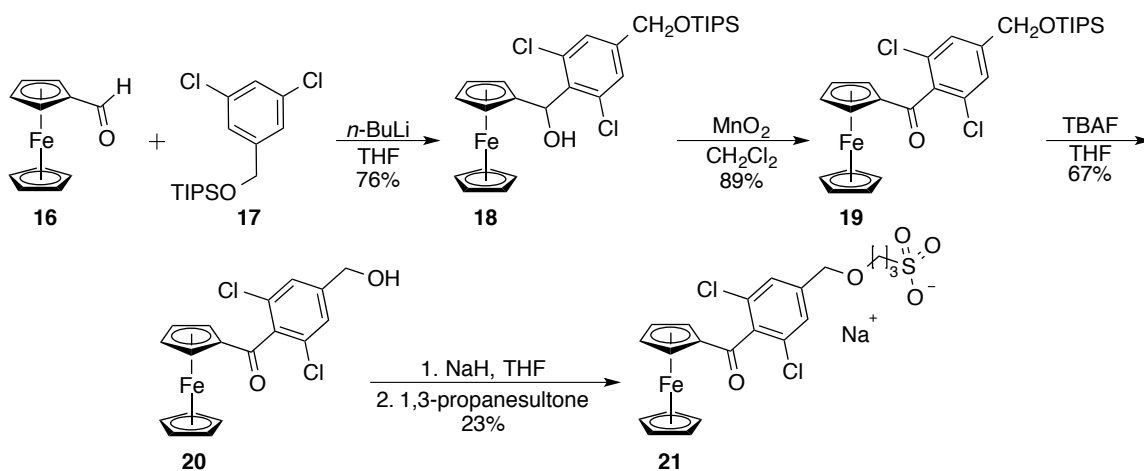
Crafts acylation with 4-(chloromethyl)benzoyl chloride yielded benzoylferrocene derivative **13**. Installation of the amine group was achieved by a substitution reaction with aqueous dimethylamine (**14**) and the water-soluble derivative **15** was subsequently synthesized by alkylation with methyl iodide in refluxing acetonitrile.



Scheme 2.2. Synthesis of water-soluble benzoylferrocene **15**.

A negatively charged analog, sulfonate **21**, was also prepared (Scheme 2.3). Synthesis of the anionic derivative proved to be much more difficult than synthesis of cation **15**. Lithiation of TIPS protected alcohol **17** with *n*-butyllithium and subsequent treatment with ferrocene carboxaldehyde gave benzylic alcohol **18** in 76% yield. Facile oxidation of the benzylic alcohol with freshly activated manganese dioxide (89%)²⁴ and deprotection of the TIPS group with tetrabutylammonium fluoride solution yielded benzoylferrocene derivative **19** in 67% yield.

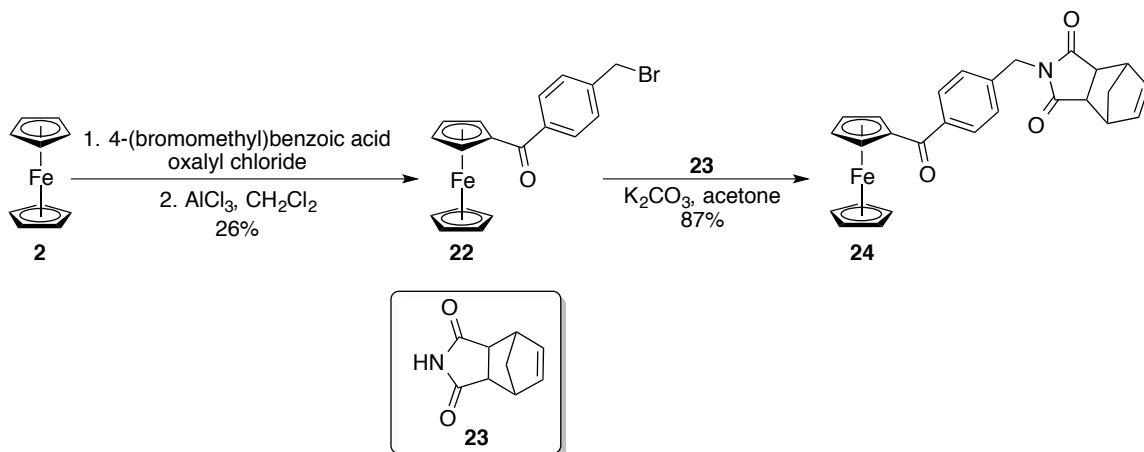
Deprotonation of the benzylic alcohol and subsequent nucleophilic ring-opening of 1,3-propanesultone proved to be non-trivial; 1,3-propanesultone is highly hydroscopic and undergoes rapid hydrolysis to the hydroxysulfonic acid. Deprotonation of **20** with *n*-BuLi and lithium bis(trimethylsilyl)amide led to isolation of only the starting materials. Under rigorous anhydrous conditions, treatment of **20** with dry sodium hydride in THF and subsequent addition of 1,3-propanesultone allowed for isolation complex **21**, albeit in low yield (Scheme 2.3).²⁵



Scheme 2.3. Synthesis of anionic water-soluble derivative **21**.

For the purpose of initial cell studies we also synthesized a neutral derivative. Ring-opening metathesis polymerization (ROMP) monomer **24** was chosen as a target as we thought that incorporation of the iron complex into a micelle could serve as a selective delivery mechanism to cancer cells (Scheme 2.4).²⁶ Benzylic bromide **22** was synthesized by first reacting 4-(bromomethyl)benzoic acid with oxalyl chloride to generate the acid chloride. Removal of the volatiles and reaction with ferrocene in the presence of aluminum chloride gave **22** in 26% yield

over the two steps. S_N2 reaction with 4,7,7a-tetrahydro-1H-4,7-methanoisindole-1,3(2H)-dione (**23**) in refluxing acetone with potassium carbonate afforded ROMP monomer **24** in 87% yield.



Scheme 2.4. Synthesis of ROMP monomer **24**.

2. UV-Vis photochemical profile and decomposition of **15**, **21**, and **24**.

To confirm the light sensitivity of compounds **15**, **21**, and **24**, the photodecomposition of each prodrug was monitored upon exposure to 490 nm light by UV-Vis spectroscopy.²⁷ Each derivative was prepared as a 0.5 mM solution and photolyzed in water (**15** and **21**) or methanol (**24**). The prepared solutions were placed in quartz cuvettes, photolyzed at 490 nm, and decomposition was monitored over time (Figure 2.4 – 2.6). Each spectrum initially displayed the characteristic metal-to-ligand charge transfer bands of benzoylferrocene in the near-ultraviolet and visible regions centered at 350 and 490 nm, which disappeared within a few minutes of light exposure.¹⁸

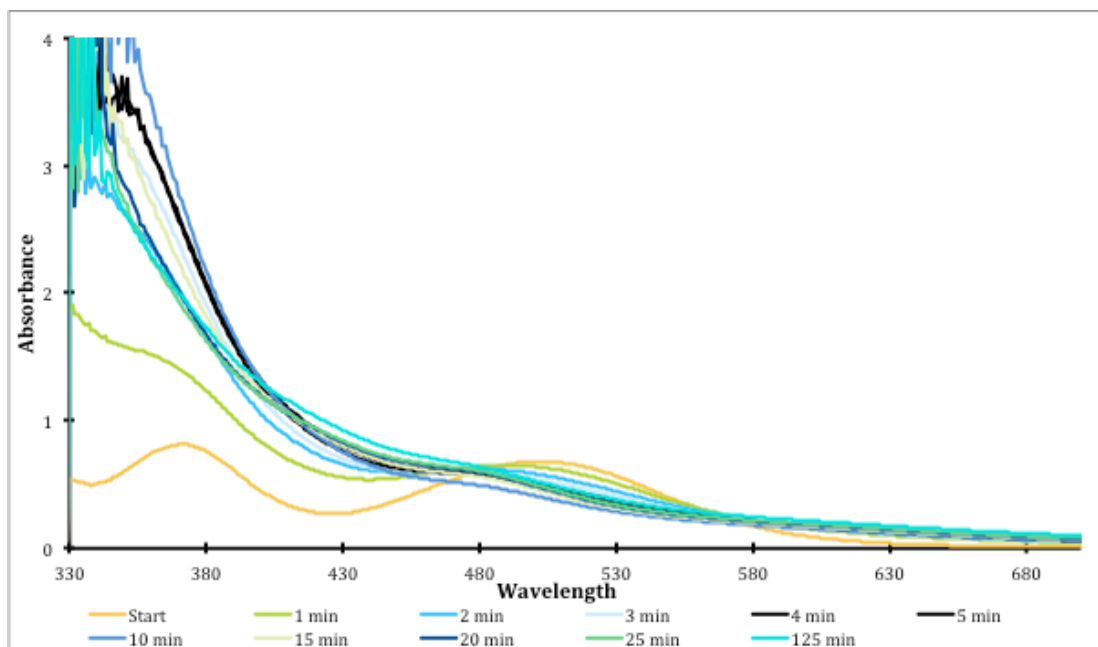


Figure 2.4. Photochemical decomposition of **15** at 490 nm.

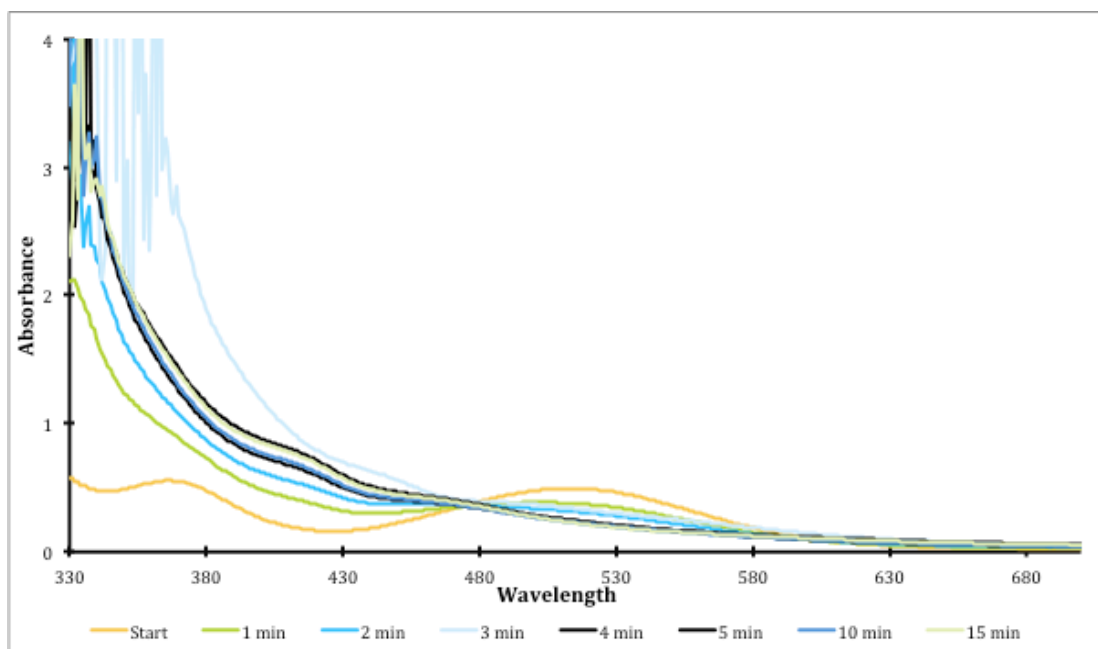


Figure 2.5. Photochemical decomposition of **21** at 490 nm.

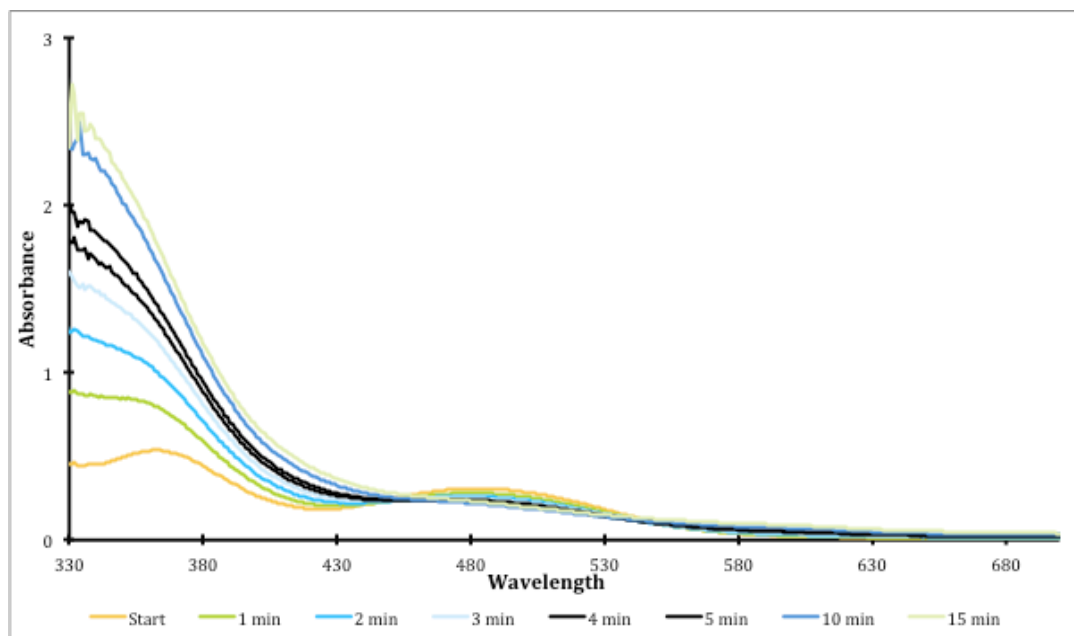
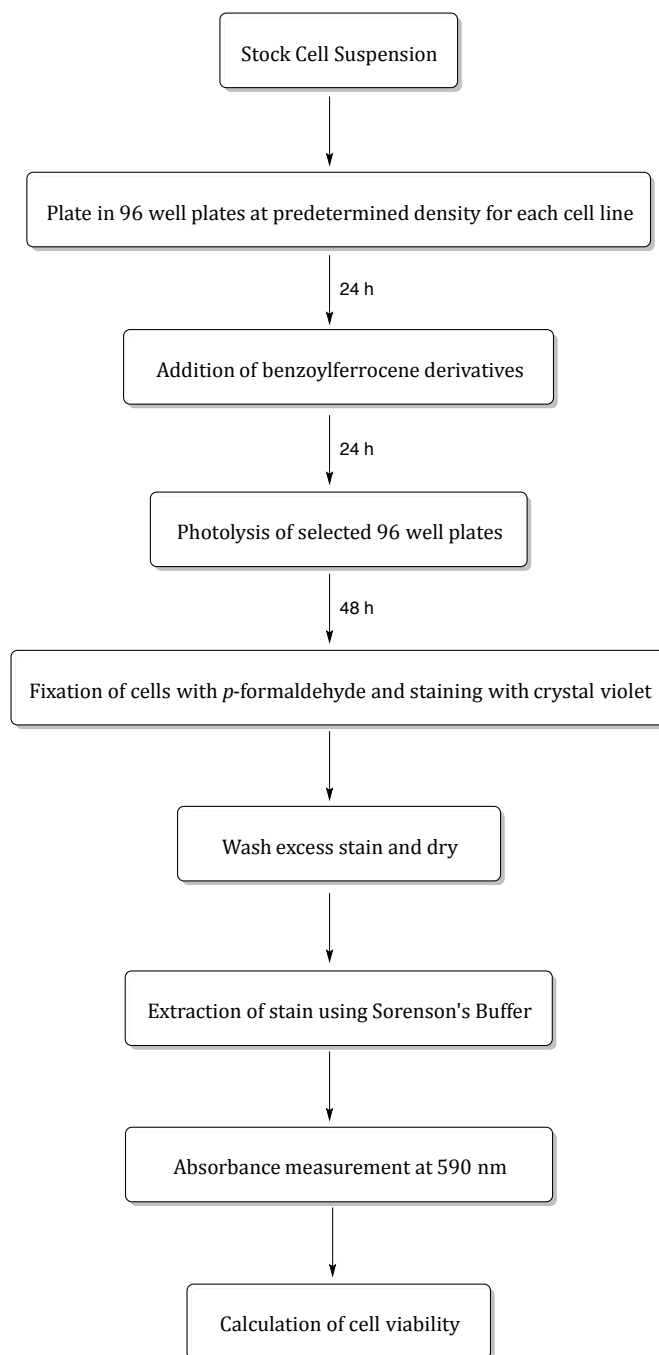


Figure 2.6. Photochemical decomposition of **24** at 490 nm.

3. Cytotoxicity studies of **15**, **21** and **24**

With the photochemical activity of **15**, **21**, and **24** confirmed, we set out to test the cytotoxicity of each complex in cervical cancer cells (HeLa) under irradiation conditions and in the absence of light. In order to ensure consistent results, a standard protocol was developed such that outcomes between separate assays would be comparable (Scheme 2.5).^[28,29] Two separate 96-well plates were prepared for each test, one to test toxicity under irradiation conditions and a second that remained in the dark inside the incubator as a control. The benzoylferrocene derivatives were diluted in dimethylformamide (DMF) and for the purpose of initial cell studies, a two-concentrations assay was performed where each complex was tested at 20 μM and 10 μM concentrations (Figure 2.7). Irradiation of one of the 96-

well plate 24 h later with a standard incandescent light bulb for 3 h resulted in death for the cells treated with the benzoylferrocene complexes, but also, disappointingly, the control cells.



Scheme 2.5. Experimental procedure for the crystal violet assay.

	1	2	3	4	5	6	7
A							
B							
C							
D	Control	15	15	21	21	24	24
E	(DMF)	20 μ M	10 μ M	20 μ M	10 μ M	20 μ M	10 μ M
F							
G							
H							

Figure 2.7. Pipetting scheme for the 96-well microtiter plate in the two-concentrations assay.

Finding a photolysis set-up for the tissue culture plates with adequate radiant fluence, consistent light exposure over the entire microtiter plate, and temperature control over the course of photolysis, turned out to be a non-trivial task. Several light sources and heating methods were screened in hopes that exposure of the cells to **15**, **21**, or **24** would induce cell death under favorable irradiation conditions while not affecting the viability of the control cells. To establish that cells in the center of the plate were dying due to drug exposure and not excessive heat or light, the control wells were placed across the center of the 96-well plates (Figure 2.8) to demonstrate that control cell viability was uniform across the entire plate. We next purchased an Illumatool Tunable Lighting System LT 9500, believing this was an attractive option as the system allowed for both irradiation at the desired wavelength (490 nm) and illumination intensity control; however, under our experimental conditions we found the light source did not illuminate the 96-well plate evenly. Irradiation of the tissue culture plate without the use of cut-off filters resulted in excessive heat generation and death of control

cells. Use of an Eco-Star LED recessed lighting fixture pleasingly generated little heat, irradiated the surface of the 96-well plate evenly, and did not affect the viability of the control cells; however, no decrease of cell viability in the wells treated with ferrous prodrugs was observed upon comparing the irradiated and dark plates. Suspecting that the light source was not powerful enough, we next employed a Richee 2014-SLT-CW/WW 50W flood light. Pleasingly, under these conditions, a *slight* increase in toxicity was noted for **24** under photoconditions.

	1	2	3	4	5	6
A	Control					
B	15	15	21	21	24	24
C	20 μ M	10 μ M	20 μ M	10 μ M	20 μ M	10 μ M
D	Control					
E	15	15	21	21	24	24
F	20 μ M	10 μ M	20 μ M	10 μ M	20 μ M	10 μ M
G						
H	Control					

Figure 2.8. Modified pipetting scheme for the 96-well microtiter plate in the two concentrations assay.

While this light source irradiated the plate evenly without affecting the viability of the control cells, measurement of the media temperature during photolysis (3 h) revealed a drop in temperature over the course of irradiation. A simple heated sand bath proved difficult to control, and resulted in inconsistent cell-viability results that were unable to be reproduced. A Denville Incuboc with two solid aluminum blocks proved to be a good alternative, and the temperature of the blocks was set such that the temperature of the media in the wells remained at 37 °C for the entirety of the light exposure. Finally, a 455 nm longpass filter was allowed

to rest on top of the 96-well plate, in hopes that irradiation of only the longer wavelength MLCT band would be enough to effect photoliberation of iron(II) *in vitro*. Disappointingly, even under these optimized conditions, water-soluble complexes **15** and **21** were inactive in both the absence of light and under irradiation conditions up to concentrations of 1000 μM . ROMP monomer **24**, while non-toxic in the dark up to the solubility limit (40 μM), exhibited a very *slight* increase in toxicity upon irradiation. While this result was certainly less than ideal, we were encouraged enough to synthesize and determine cytotoxicity for a second series of benzoylferrocene derivatives.

4. Synthesis of second-generation benzoylferrocene derivatives

To find a derivative that would exhibit enhanced cytotoxicity upon exposure to visible light, a second series of benzoylferrocene prodrugs were synthesized and characterized (Figure 2.9). With the observation that **24** was a much more promising lead than charged complexes **15** and **21**, complexes **25-27**, **14** and **28** were prepared with the expectation that they would display similar or improved toxicity upon exposure to light (Scheme 2.6). Reaction of benzylic chloride **13** with the appropriate nucleophile in refluxing acetone gave complexes **25** and **26** (74 and 72% yield, respectively). The identity of **25** was confirmed by the ^1H NMR spectrum (CD_2Cl_2), by the deshielded methylene proton signal in **25** relative to **13** (δ 4.90 and 4.69 respectively). The appearance of a new singlet in the ^1H NMR spectrum for the succinimide methylene protons at δ 2.72 (CD_2Cl_2) confirmed the formation of

complex **26**. Derivatives **14**, **27** and **28** were also prepared in good yield by simple substitution reactions in THF/water solvent mixtures.

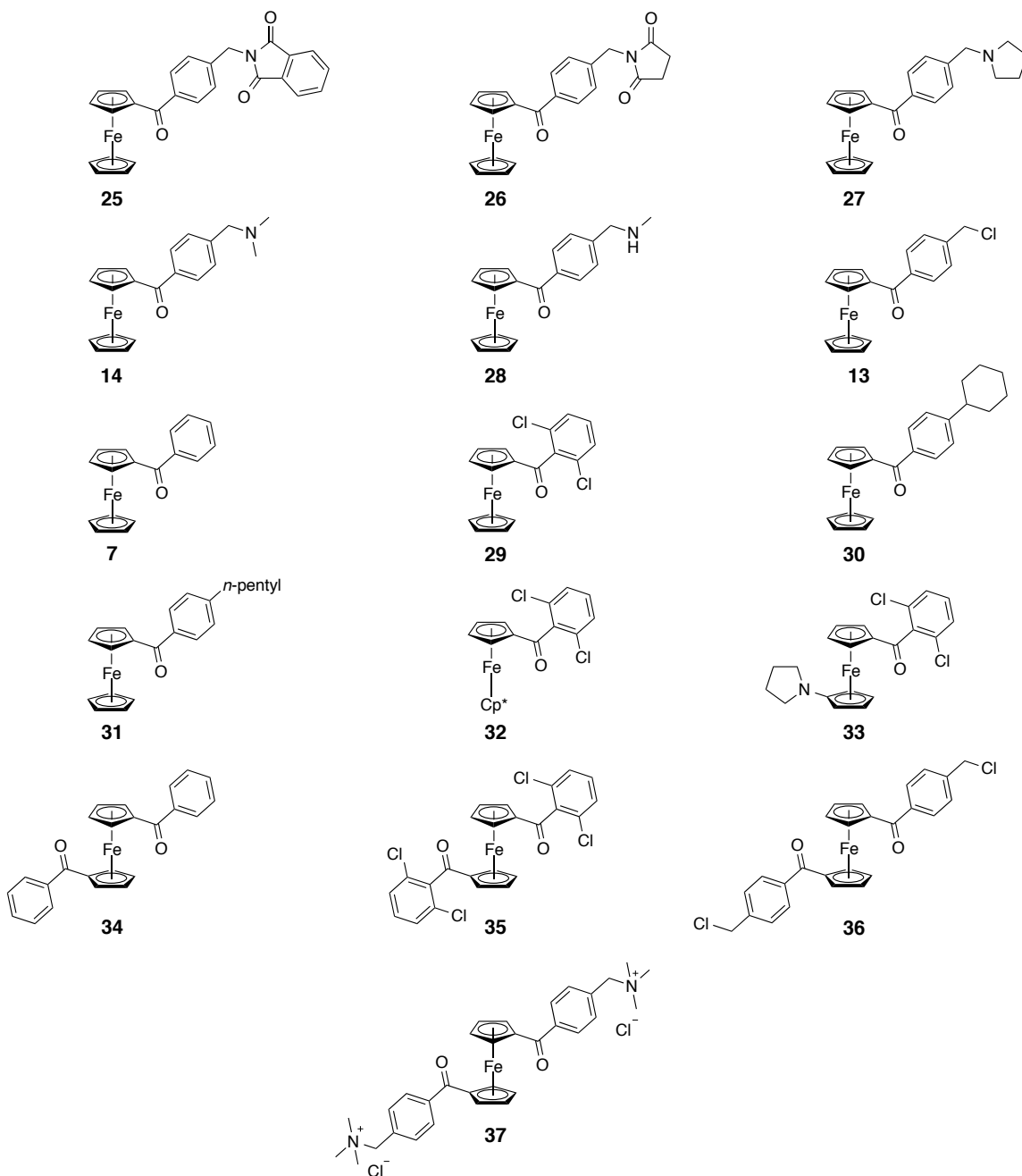
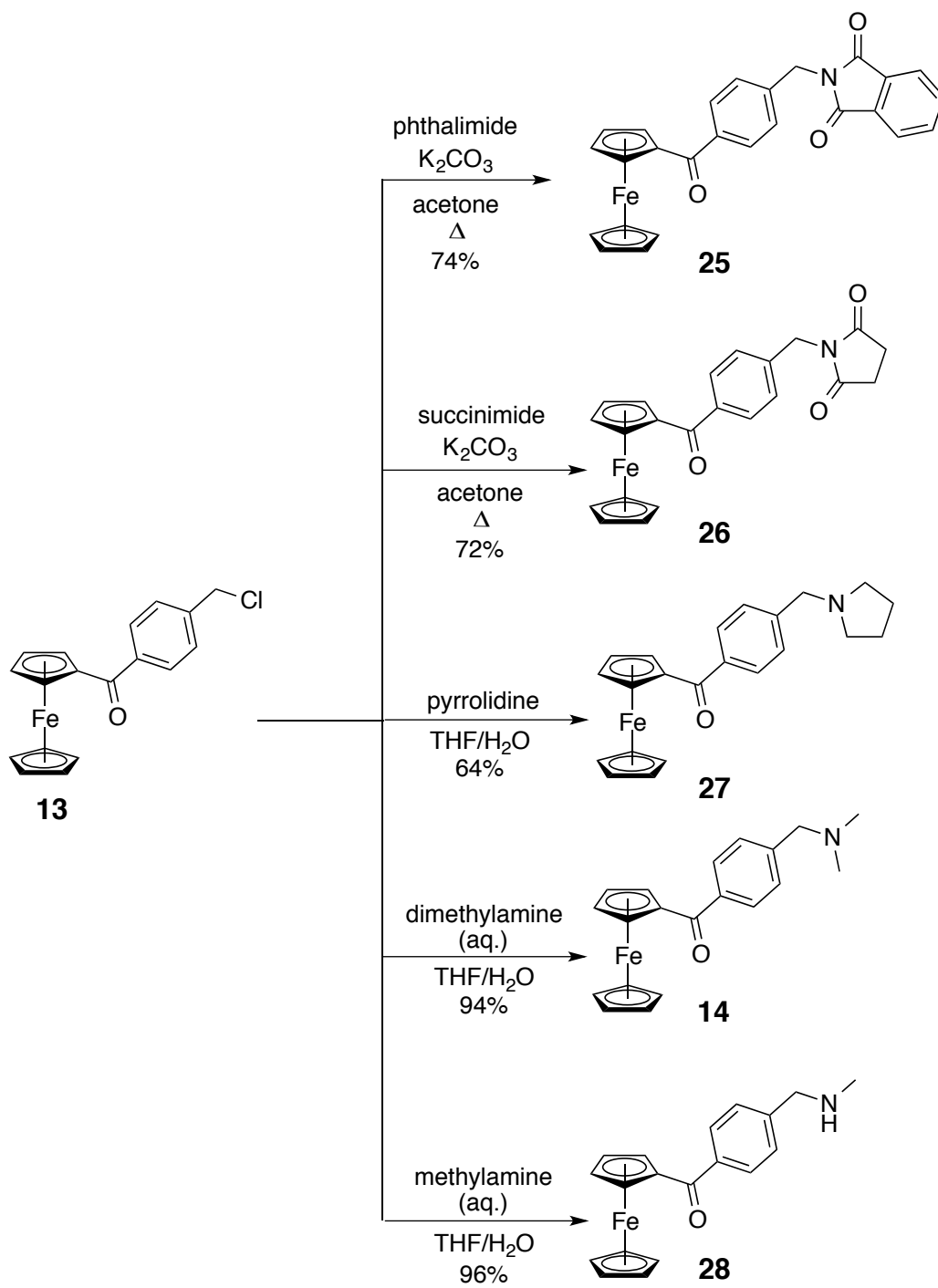
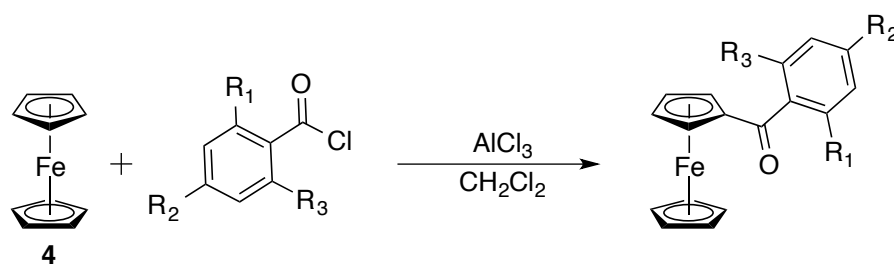


Figure 2.9. 1-Benzoylferrocenes and 1,1'-dibenzoylferrocenes screened for cytotoxicity in the dark and under irradiation conditions.



Scheme 2.6. Synthesis of derivatives **14**, **25-28**.

Benzoylferrocene (**7**) and analogs **29-31** were synthesized from ferrocene and the corresponding benzoyl chlorides by Friedel-Crafts acylation in good yields (Scheme 2.7).³⁰ All acid chlorides were commercially available, with the exception of 4-cyclohexylbenzoyl chloride, which was prepared by refluxing the carboxylic acid in neat thionyl chloride for 6 h prior to reaction with ferrocene and aluminum chloride. Product formation was evident in the ¹H NMR spectra (CD₂Cl₂) of the ketone products by the deshielded chemical shifts observed for the substituted-cyclopentadienyl-ring hydrogens (~ δ 4.5 - 4.8) relative to the chemical shift for the hydrogens in ferrocene (δ 4.17). In the ¹³C NMR spectra (CD₂Cl₂), the carbonyl carbon resonances for **7**, **29**, **30**, and **31** were observed at δ 198.9, 197.8, 198.4, and 198.9, respectively.

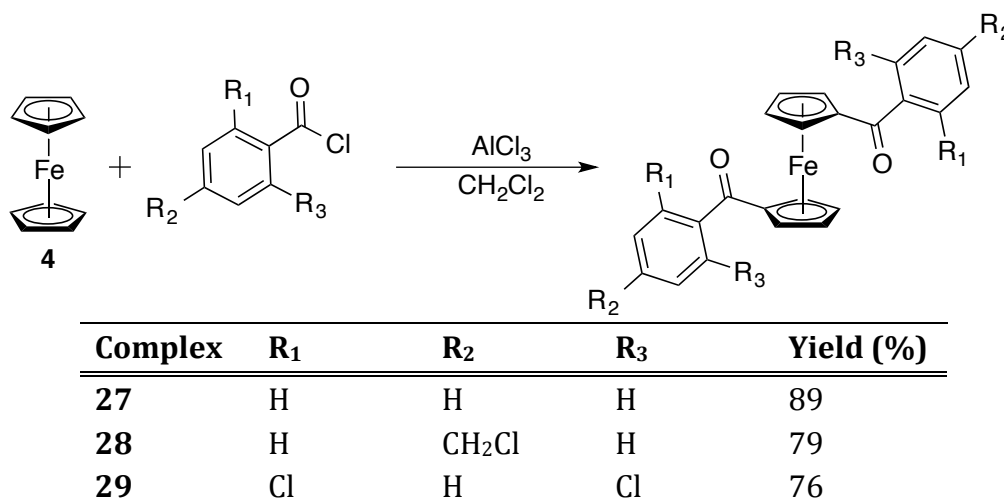


Complex	R ₁	R ₂	R ₃	Yield (%)
7	H	H	H	85
29	Cl	H	Cl	82
30	H	<i>n</i> -pentyl	H	76
31	H	cyclohexyl	H	54

Scheme 2.7. Friedel-Crafts acylation to form **7** and **29-31**

1,1'-Dibenzoylferrocene derivatives **34-36** were synthesized by a similar procedure to that employed for the preparation of the 1-benzoylferrocenes (Scheme 2.8);³¹ ferrocene was diacylated in good yields using two equivalents of both

aluminum chloride and the corresponding acid chloride. Product formation was evident by ^1H NMR spectroscopy (CD_2Cl_2); the hydrogen atoms on the symmetrically substituted cyclopentadienyl rings in each complex resonated between δ 4.6 and 4.9 ppm. Product formation was also evident from the ^{13}C NMR (CD_2Cl_2) spectroscopic data, with the *ipso*-cyclopentadienyl-carbon resonances being significantly deshielded relative to the unsubstituted cyclopentadienyl-ring-carbon resonances (δ 80 and 73-74 ppm respectively). In addition, the carbonyl-carbon resonances for this series of complexes were observed at $\sim \delta$ 196 ppm. Dication **37** was prepared in 89% yield by treatment of **36** with aqueous trimethylamine in water/THF. The synthesis of the electrons-rich analogs, **32** and **33**, is discussed in Chapter 3.



Scheme 2.8. Friedel-Crafts acylation to form 1,1'-dibenzoylferrocenes.

5. X-ray Crystal Structures of **7**, **15**, **29**, **30** and **31**

X-ray quality crystals of the benzoylferrocene analogs were grown by slow diffusion of either hexanes into ethyl acetate or of diethyl ether into ethanol. Refinement (full data for each structure tabulated in the Appendix Section) gave the

structures shown in Figures 2.10-2.14. There are two independent molecules within the unit cell of **31**, indicated here as **31** and **31'**. Selected bond distances and angles are in Table 2.1. The C(1)-C(5)-C(6)-O(1) torsion angles fall between -13 and 14 deg. In each complex, O(1) is displaced from the plane of the C(1-5) cyclopentadienyl ring significantly (0.028 to 0.340 Å), with the exception of complex **29** where the carbonyl oxygen is essentially located in the plane of the C1-C5 ring.

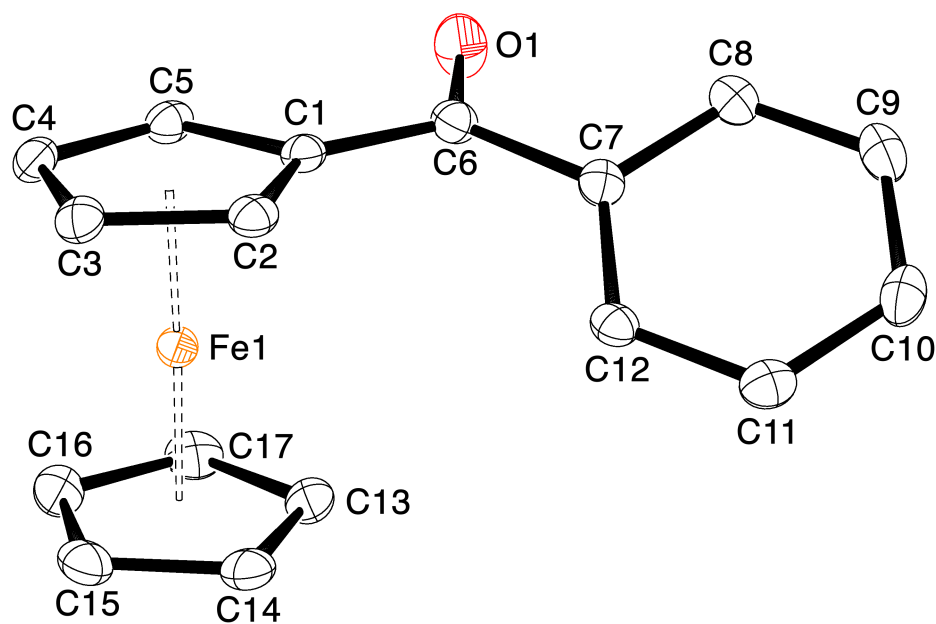


Figure 2.10. ORTEP view of **7**.

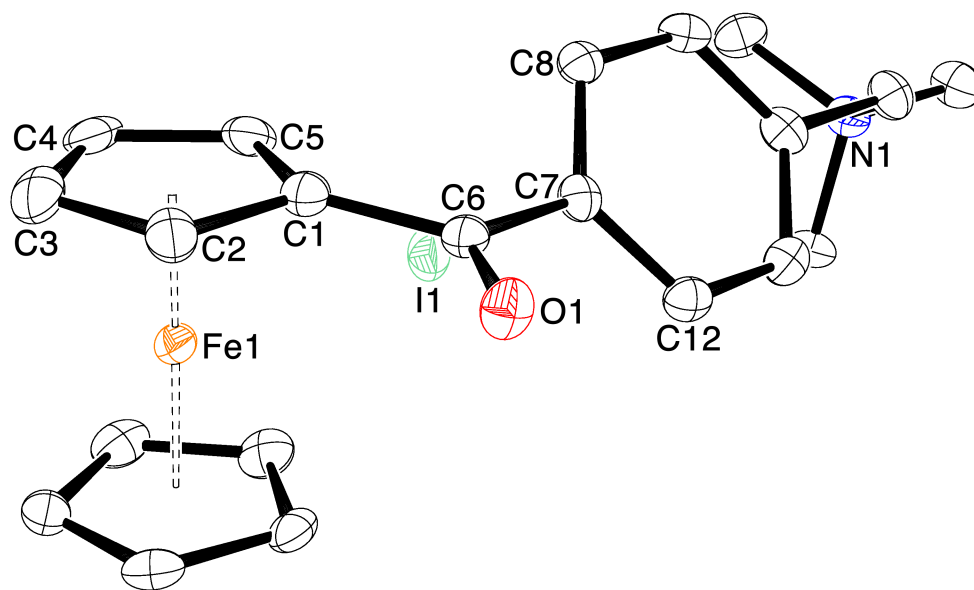


Figure 2.11. ORTEP view of 15

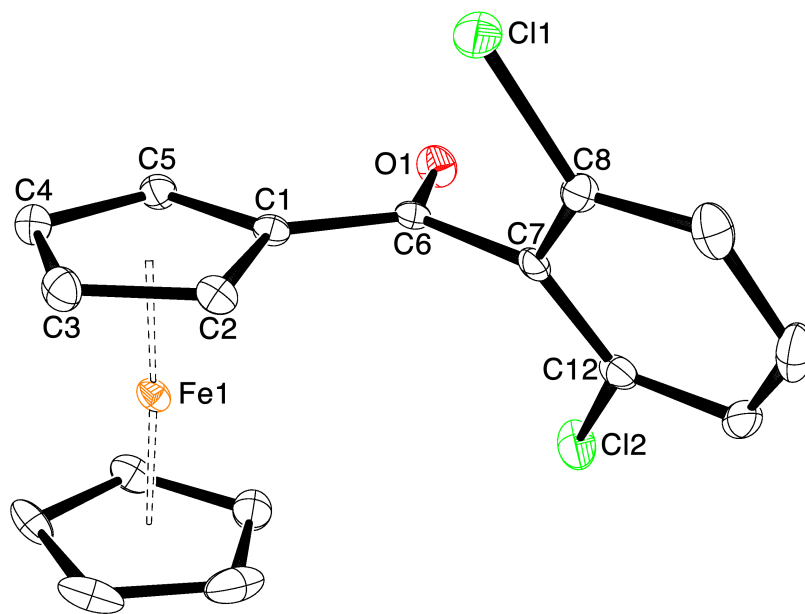


Figure 2.12. ORTEP view of 29.

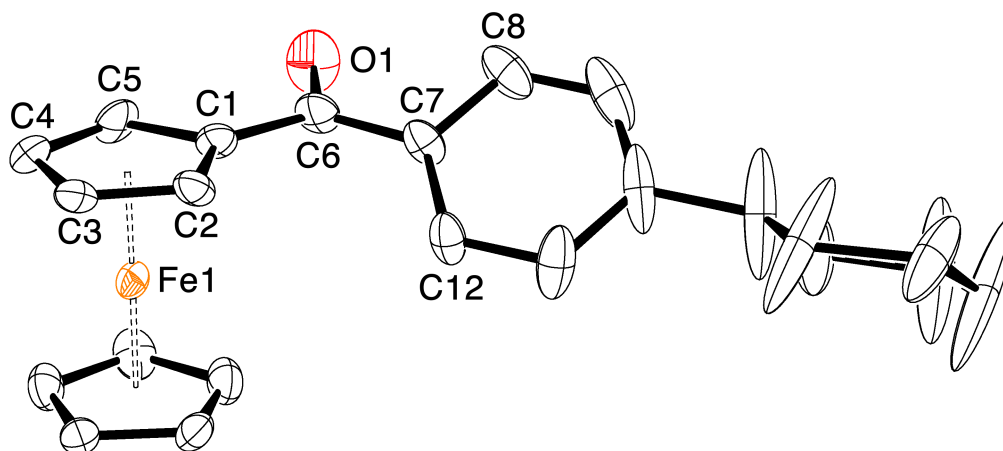


Figure 2.13. ORTEP view of **30**. The large thermal ellipsoids on the cyclohexane ring are due to disorder resulting from three or more low-occupation sites.

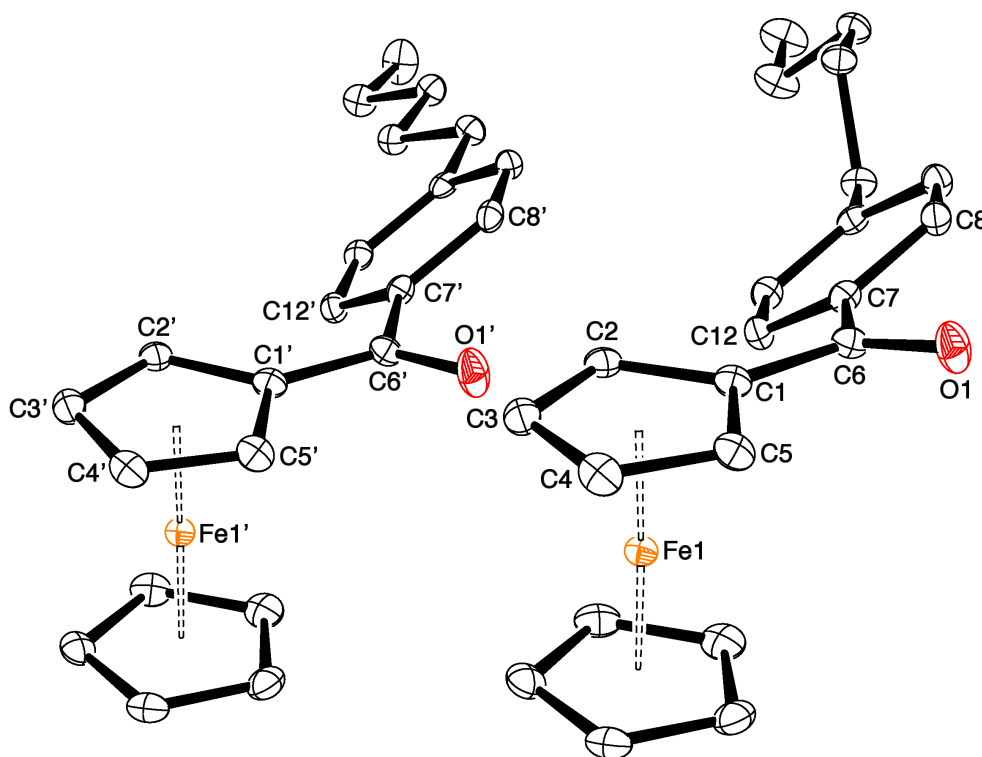


Figure 2.14. ORTEP view of **31** and **31'**. There are two independent molecules within the unit cell of **31**, indicated here as **31** and **31'**.

Table 2.1. Selected bond metrics for X-ray structures of **7**, **15**, and **29-31**.

Complex	C(1)-C(5)-C(6)- O(1) [°]	O(1)-C(1-5) [Å]*	Fe(1)-C(1-5) [Å]**	R(F)
7	14.0(3)	0.339	1.648	0.0336
15	-3.7(5)	0.281	1.638	0.0313
29	2.2(2)	0.028	1.65	0.0196
30	9.6(7)	0.257	1.649	0.0579
31	-7.3(3)	0.206	1.651	0.0301
31'	-12.5(3)	0.283	1.654	0.0301

Complex	C(1)-C(6) [Å]	C(6)-O(1) [Å]	C(6)-C(7) [Å]	C(1)-C(6)- O(1) [°]
7	1.472(3)	1.224(2)	1.505(3)	119.4(2)
15	1.465(4)	1.232(4)	1.500(4)	120.9(3)
29	1.464(2)	1.223(2)	1.517(2)	122.1(1)
30	1.482(7)	1.226(5)	1.483(8)	119.0(4)
31	1.479(3)	1.229(2)	1.492(3)	118.5(2)
31'	1.480(3)	1.228(2)	1.496(3)	119.0(2)

*O(1)-C(1-5) is the distance O(1) lies from the C(1)-C(2)-C(3)-C(4)-C(5) mean plane.
 **Fe(1)-C(1-5) is the distance of the iron atom from the C(1)-C(2)-C(3)-C(4)-C(5) mean plane.

6. Cytotoxicity of complexes **7**, **13**, **14**, and **25-37**.

With a variety of functionalized benzoylferrocene derivatives in hand, and a standard protocol developed to test the efficacy of the organoferrous drugs in both the light and the dark, the toxicity of the benzoylferrocene derivatives was determined in HeLa cells. Given the large number of compounds to test, initial screening was performed using a three-concentrations assay with up to four substances being tested together on one 96-well plate. One plate was irradiated for a period of 3 h, while an exact duplicate was allowed to remain in the absence of light inside the incubator. The complexes that displayed cytotoxicity in either the light or the dark were further investigated for biological activity.

For all half-maximal inhibitory concentration assays, cells were seeded at a density specific to the cell line, then incubated with varying concentrations of complexes in the dark for 24 h prior to irradiation with a > 450 nm longpass filter. Forty-eight hours post photolysis when the cells had reach confluency, the efficacy of the complexes in both the light and the dark was determined by the crystal violet staining method. The UV-Vis absorbance at 590 nm was then used to calculate cell-viability using Equation 1.²⁸ Each test was performed independently in at least triplicate.

$$\frac{(\text{Absorbance}_{\text{drug containing wells}} - \text{Absorbance}_{\text{control wells}})}{\text{Absorbance}_{\text{control wells}}}$$

(Equation 1)

Complexes **14** and **25-27** were tested first in HeLa cells due to the initial promising result with complex **24**; however, each of these derivatives was inactive in both the light and dark up to the solubility limit of the complex. Exposure of HeLa cells to benzoylferrocene (**7**) in the dark and under irradiation conditions (3 h) resulted in similar toxicity values ($IC_{50\text{-dark}} = 33.5$ (5.2), $IC_{50\text{-light}} = 30.8$ (3.8) μM). While this result was less than ideal, we were encouraged as it indicated benzoylferrocenes were capable of inducing cytotoxicity and could potentially deliver solvated iron(II) to cells by simple modification of the organic ligands. The 2,6-dichloro substituted benzoylferrocene **29** had similar cytotoxicity in the light and the dark. The electron-rich Cp* analog **32** displayed activity in the dark at its solubility limit, but no increase in activity was induced upon irradiation. Increasing electron density at the iron center by addition of a pyrrolidine substituent onto the

cyclopentadienyl ring (**33**) caused a drastic lowering of the IC_{50} value in the dark, but no appreciable increase in toxicity was observed upon exposure to light. 1,1'-Dibenzoylferrocenes, which are more photoactive and oxidation-resistant than their monosubstituted analogs, induced mild toxicity in the dark at the solubility limit ($40 \mu M$), but no increase in cytotoxicity was observed upon photolysis. Increasing the hydrophobicity of the phenyl-substituent by inclusion of a *para*-pentyl or *para*-cyclohexyl group led to a decrease in cytotoxicity in the dark for **31** ($IC_{50\text{-dark}} 57.9$ (5.0)), and **30** was determined to be non-toxic up to its solubility limit ($40 \mu M$). More significant however, was a pronounced increase in toxicity exhibited by both **30** and **31** upon exposure to visible light.

With long-sought lead-compounds **30** and **31** in hand we were able to determine optimal irradiation conditions in HeLa cells. The 96-well plates with drug containing media were photolyzed for 1, 2, 3, or 5 h (Table 2.2); then cell viability was quantified by the crystal violet staining method once the cells reached confluency. Each time test was performed in at least triplicate and an IC_{50} was then calculated. A significant increase in cytotoxicity was observed for up to three hours of light exposure, but prolonged photolysis (5 h) led to no increase in phototoxicity. Given the success with **30** and **31** in HeLa cells, cytotoxicity was also determined in human carcinoma alveolar basal epithelial (A549) cells with varying photolysis times. While prolonged photolysis time slightly decreased the $IC_{50\text{-light}}$ for both **30** and **31** the effect was not nearly as pronounced as in HeLa cells. With the irradiation time optimized, we obtained cytotoxicity data in A549 cells for **7** and **29**,

which again failed to induce additional toxicity upon exposure to light (3 h). The results of the photobiological studies are summarized in Table 2.3.

Table 2.2. IC_{50-light} values (μM) for **30** and **31** with increasing irradiation time.

Complex	HeLa			A549		
	1 h	2 h	3 h	1 h	2 h	3 h
30	> 40*	> 20*	8.7 (2.3)	10.1 (0.5)	8.7 (1.2)	6.8 (2.4)
31	21.2 (1.9)	18.5 (1.4)	12.8 (1.8)	14.9 (2.8)	11.2 (1.1)	9.5 (2.7)

* Due to solubility constraints not all IC₅₀ values could be determined.

Table 2.3. IC₅₀ values (μM) for active benzoylferrocene complexes.

Complex	HeLa _{dark}	HeLa _{light} ^a	A549 _{dark}	A549 _{light} ^a
7	33.5 (5.2)	30.8 (3.8)	41.3 (2.7)	43.5 (2.0)
29	47.1 (3.1)	40.5 (2.5)	36.1 (5.2)	33.2 (4.3)
30	> 40*	8.7 (2.3)	> 40*	6.8 (2.4)
31	57.9 (5.0)	12.8 (1.8)	49.0 (6.7)	9.5 (2.7)
33	10.7 (0.8)	6.8 (1.0)	n.d.	n.d.

n.d. not determined; ^aHeLa and A549 cells were irradiated for 3 h; *not all IC₅₀ values could be determined due to solubility constraints.

To demonstrate that the cytotoxic agent was being generated inside the cell from the organometallic prodrug, complexes **30** and **31** were pre-irradiated (3 h) in cell-growth media at the same concentrations previously used to dose the cells. To determine cell viability upon treatment with the photolysis products, the media was removed carefully by pipette from the 96 well plate, and the cells (HeLa or A549) were washed three times with 200 μL of dPBS. Then immediately post photolysis, 200 μL of the photolysis mixture was added to each well. Forty-eight hours post-addition when the cells had reached confluency, cell viability was determined by the

crystal violet staining assay. Under these conditions in HeLa and A549 cells, cytotoxicity was non-existent for **30** up to the solubility limit of the organoferrous complex, and the IC_{50} for **31** was determined to be $>150 \mu\text{M}$ (Figure 2.15).

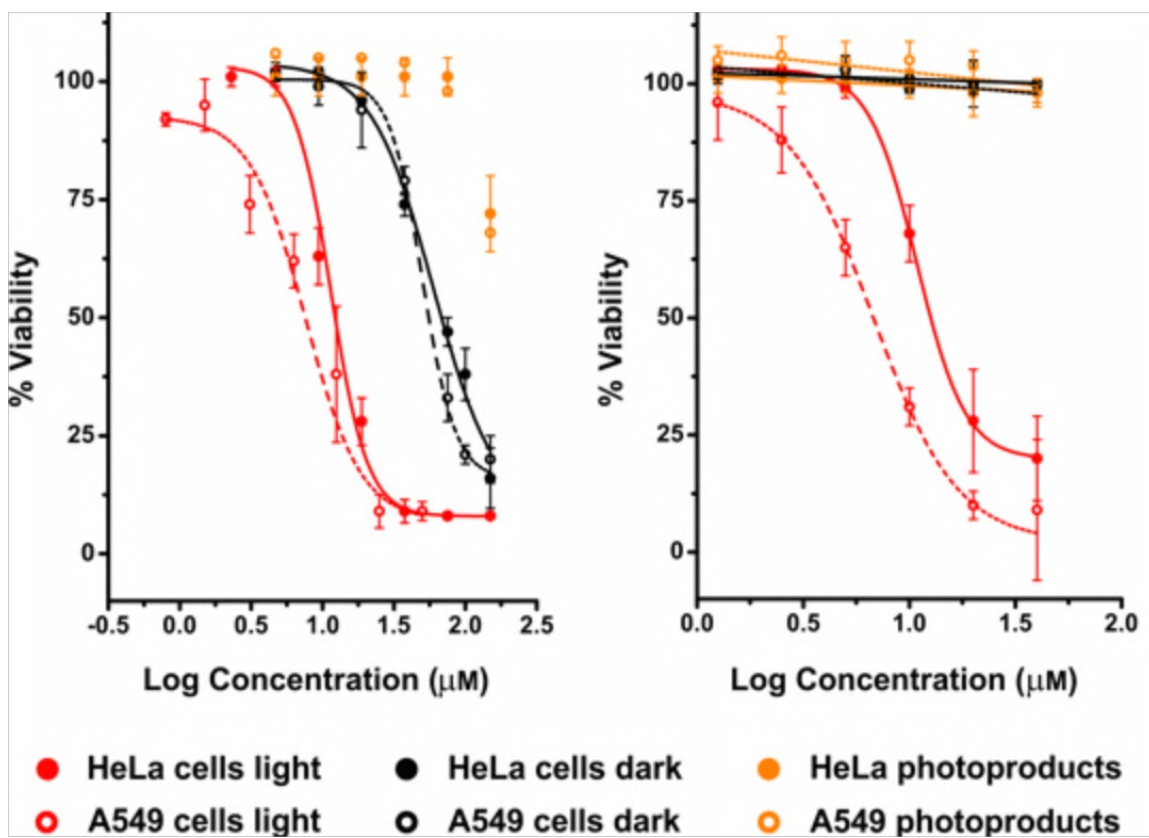


Figure 2.15. Cytotoxicity dose responses for **30** (right panel) and **31** (left panel) and their photoproducts in HeLa and A549 cells.

Additional studies in HeLa cells demonstrated that treatment of the HeLa cells with FeSO_4 resulted in no decrease of cell viability up to $1000 \mu\text{M}$ in both the dark and under irradiation conditions. Similarly, in A549 cells, treatment with FeSO_4 led to no cell death in the dark up to $150 \mu\text{M}$ (the solubility limit of **31**). Under irradiation conditions, iron(II) sulfate was demonstrated to be non-toxic only

until the solubility limit of the parent complex was reached (150 μM), where cell viability dropped to 67.9 (6.2%).

To further demonstrate that phototoxicity was due to organoferrous agents located inside the cells, A549 cells were exposed to media containing **31** for 24 h. The extracellular **31** was then gently removed by pipette, the cells were washed three times with 100 μL warm dPBS to remove any residual extracellular prodrug, and 200 μL of fresh drug-free media was added to each well. The 96-well plates were then irradiated for 3 h and cell-viability was determined 48 h post photolysis using the crystal violet staining assay (Table 2.4). The results demonstrated that removal of extracellular **31** prior to photolysis had no deleterious effect on cytotoxicity, thereby suggesting that the intact sandwich complex must be located inside the cell prior to photogeneration of the cytotoxic agent.

Table 2.4. Effect of washing on IC_{50} values (μM) in A549 cells for complex **31**.

Complex	A549 IC_{50}		
	Dark	Light	Light _{wash}
31	49.0 (6.7)	9.5 (2.7)	7.7 (1.7)

7. Studies on healthy cell lines

With the cytotoxicity of **30** and **31** demonstrated in cancer cell lines, their toxicity was next determined in three healthy cell lines: human embryonic kidney 293 cells (HEK-293), mouse subcutaneous connective tissue (L929), and healthy human fibroblast lung cells (MRC-5) (Table 2.5). The toxicities of **30** and **31** in L929 and HEK-293 cells were nearly identical to the cytotoxicity in the cancer cell

lines. The HEK-293 cells were found to adhere poorly to the 96-well plates, and therefore cell viability was determined by the CellTiter-Blue assay rather than the crystal violet staining assay. Most importantly, studies in MRC-5 cells were performed to compare toxicity in both healthy lung cells (MRC-5) and cancerous lung cells (A549). While the toxicity in MRC-5 cells is comparable for both **30** and **31** under irradiation conditions, in the absence of light **30** is not toxic up to the solubility limit, and the $IC_{50-dark}$ for **31** was determined to be greater than the solubility limit of the organoferrous complex (150 μ M).

Table 2.5. IC_{50} values (μ M) in healthy cell lines.

Complex	IC_{50}					
	MRC-5 _{dark}	MRC-5 _{light}	L929 _{dark}	L929 _{light}	HEK-293 _{dark}	HEK-293 _{light}
30	> 40*	> 5*	> 40*	4.6 (1.0)	> 40*	5.6 (1.9)
31	> 150*	6.9 (2.9)	36.1 (7.1)	8.3 (1.5)	> 75*	12.3 (3.6)

n.d. is not determined. * IC_{50} could not be calculated due to solubility constraints.

8. Lipophilicity Determinations

Veith demonstrated that high-performance liquid chromatography (HPLC) is a quick, facile way to determine the *n*-octanol/water partition coefficient (*P*) of a drug using the retention time on a reverse phase column.^[32,33] Specifically, the logarithm of the retention factor (*k*), calculated from the observed retention time (t_R) and column dead time (t_0) by equation 2, was found to be linearly correlated to the logarithm of *P* ($\log P$).

$$k = (t_R - t_0) / t_0$$

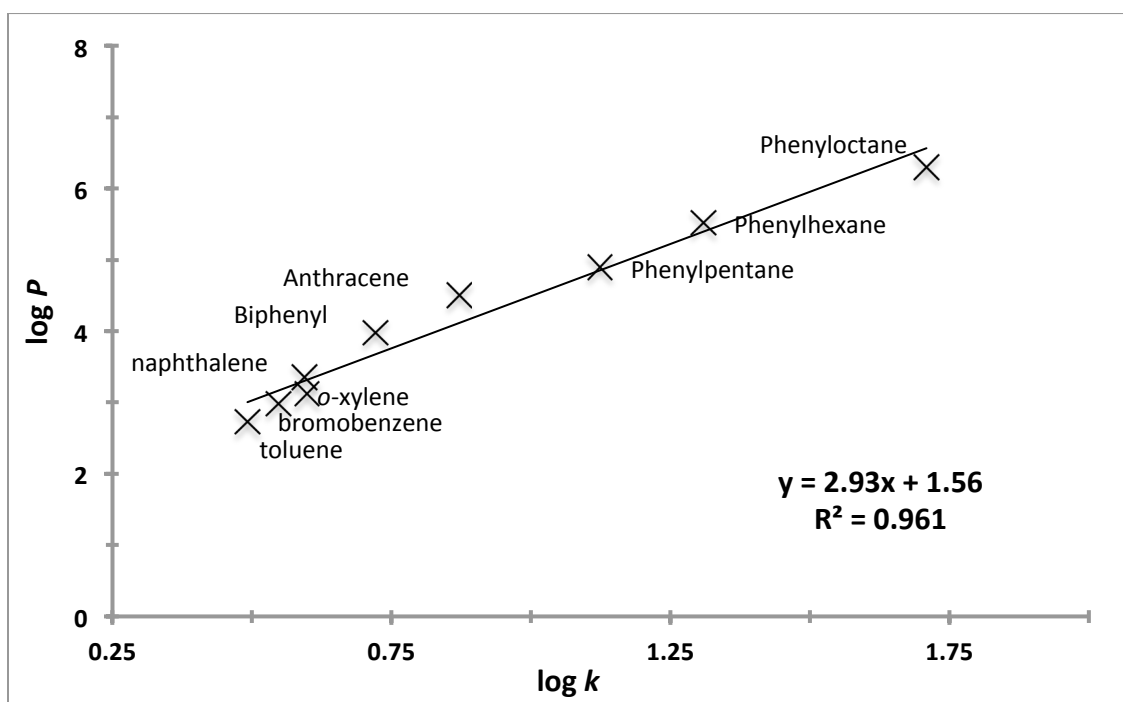
(Equation 2)

To determine lipophilicity of the benzoylferrocene drugs, a standard curve was constructed using a series of standards with known $\log P$ values ranging from 2.73 to 6.30 (Table 2.6).³⁴ A solvent system for the isocratic chromatography was chosen such that the unknown benzoylferrocenes were detected over a wide range of retention times (55:45 acetonitrile:water). The standards were then chromatographed individually and the observed retention time (t_r) was correlated to lipophilicity using average values of $\log P$ obtained from literature.³⁴ A calibration graph was then constructed by plotting $\log (k)$ against $\log (P)$ for each of the standards and fitting the points by use of a linear regression. Using this method we obtained equation 3 with a correlation coefficient $R^2 = 0.961$ (Figure 2.16). The benzoylferrocene complexes were then injected and chromatographed individually under conditions identical to that of the calibration mixture and $\log k$ was calculated using the observed retention time. $\log P$ values were then determined using equation 3.

Table 2.6. HPLC retention times and partition coefficients for selected standards.*

Compound	Retention time (minutes)	log k	log P
Toluene	5.13	0.492	2.73
Bromobenzene	5.66	0.548	2.99
<i>o</i> -Xylene	6.26	0.599	3.12
Naphthalene	6.15	0.593	3.35
Biphenyl	7.83	0.721	3.98
Anthracene	10.63	0.871	4.50
<i>n</i> -Pentylbenzene	17.88	1.124	4.90
<i>n</i> -Hexylbenzene	26.73	1.309	5.52
<i>n</i> -Octylbenzene	65.2	1.709	6.30

*Values are reported as an average of three independent experiments.

**Figure 2.16.** Linear calibration relating log *P* and log *k*.

$$y = 2.93x + 1.56$$

(Equation 3)

Table 2.7. Benzoylferrocene complexes and their estimated log *P* values

Complex	Retention Time	log <i>P</i>	log <i>P</i> Standard Deviation
7	6.01	3.3	0.02
13	6.99	3.5	0.03
14	1.81	0.56	0.02
24	6.01	3.28	0.01
25	6.89	3.46	0.04
26	3.55	2.34	0.02
27	1.95	0.82	0.02
29	8.89	3.86	0.04
30	29.78	5.54	0.04
31	30.12	5.62	0.01
32	41.27	5.89	0.02
33	2.97	1.79	0.02
34	6.34	3.35	0.03
35	16.02	4.71	0.01

9. Cell accumulation studies

The amount of iron accumulated in HeLa cells following treatment with selected benzoylferrocene complexes was determined by relating the cellular protein concentration to the concentration of iron in the cell lysates. As the control cells not treated with the benzoylferrocene complexes were also expected to contain iron, it was crucial that the method to detect iron accumulation be a technique with high sensitivity. For this reason, inductively coupled plasma optical emission spectrometry (ICP-OES) was chosen to determine iron concentration in the cellular extract due its sensitivity and low detection limit.³⁵

Cell accumulation data was obtained for four iron-containing compounds: water-soluble **21**, benzoylferrocene (**7**), lead-compound **31**, and ferrous sulfate.

Briefly, HeLa cells were grown in 75 cm² flasks until confluent and treated with a 60 μ M solution of each drug in FBS free media for 2 h. For each drug-containing flask, a separate control flask was prepared with an identical concentration of either DMF (for **7** and **31** controls) or water (for complexes **21** and FeSO₄ controls). The cells were then harvested for iron and protein analysis. Protein concentration of the cell lysates was determined by the Bradford method.³⁶ Following lyophilization and treatment with concentrated nitric acid, the iron concentration was quantified by ICP-OES. Each experiment was performed in at least triplicate.

HeLa cells treated with 60 μ M of the inactive complex **21** displayed iron accumulation values nearly identical with that of the control, as did cells treated with **7** (Table 2.8). As anticipated from the cytotoxicity studies, the iron content of the cells treated with a 60 μ M solution of **31** had significantly higher levels of iron accumulation. HeLa cells treated with a 60 μ M solution of FeSO₄ displayed a similar iron accumulation to those treated with **31**.

Table 2.8. Iron concentration in HeLa cell lysates (ng Fe/mg protein) following treatment with various iron containing drugs.

Complex	Average Fe	Standard Deviation
7	416	145
21	397.6	123
31	6,100	496
FeSO ₄	6,900	651
Control (H ₂ O)	346	82
Control (DMF)	326	89

Once it was established that treatment of cells with **31** resulted in a measureable increase in iron accumulation, accumulation was further investigated

as a function of drug concentration (Figure 2.17). As the concentration of **31** was increased in the extracellular media, the concentration of iron in the cell lysate also increased. The response was found to be linear and can be described by equation 4, with a R^2 of 0.8458.

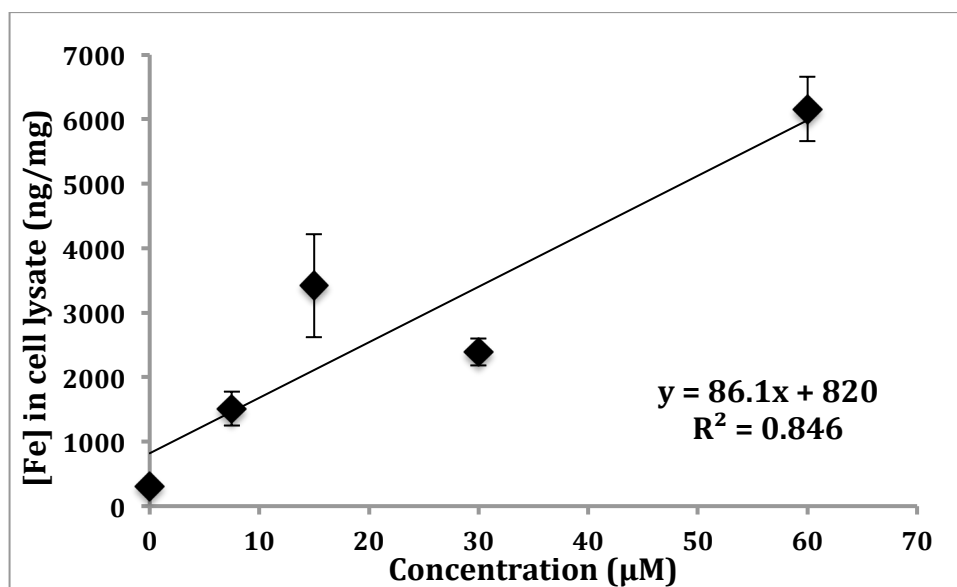


Figure 2.17. Iron concentration in the HeLa cell lysate as a function of extracellular **31** concentration.

$$y = 86.1x + 820$$

(Equation 4)

10. Cyclic voltammetry studies

In collaboration with Dr. Mohand Melaimi of the Bertrand lab at UC-San Diego, cyclic voltammetry (CV) data was obtained on each of the benzoylferrocene prodrugs (Table 2.9). The scans were done in acetonitrile with added tetrabutylammonium hexafluorophosphate (0.1 M) as electrolyte, with the scan initiated in the positive potential direction. Potentials were then calibrated against

the Fc/Fc⁺ couple as an internal standard. Only one chemically reversible wave was detected for each complex unless noted otherwise.

Table 2.9. Cyclic voltammetry data (vs Fc/Fc⁺) for tested benzoylferrocene complexes.

Compound Number	E _{1/2} (V)
7	0.250
14	0.254, 0.706*
15	0.272 ^a
21	0.302 ^b
24	0.250
25	0.255
26	0.251
27	0.262, 0.590*
29	0.319
30	0.251
31	0.251
32	0.010 ^c
33	-0.160
34	0.462
35	0.464
36	0.474
37	0.509, 0.242* ^d
39	0.441

*a wave corresponding to oxidation of the ligand was also detected. ^aC.V. data was collected on the BF₄ salt for solubility reasons. ^bData was collected by differential pulse voltammetry due to the low solubility of **21** in MeCN. ^creferenced relative to decamethylferrocene.³⁷ ^dC.V. data was collected on the BPh₄ salt for solubility reasons.

11. UV-Vis photochemical profiles

Electronic absorption spectra were obtained for each of the benzoylferrocene derivatives (Table 2.10).²⁷ Each complex was prepared as a 0.5 mM solution in 50:50 DMF:H₂O unless noted otherwise. The prodrugs all displayed bands of

significant intensity in the near-ultraviolet and visible regions, with λ_{\max} values approximately equal to 365 and 490 nm.

Table 2.10. UV-Vis data for benzoylferrocene complexes (50:50 DMF/H₂O).

Compound Number	λ_{\max}^a (ϵ^b)
7	368 (1512), 487 (1015)
14	364 (1108), 488 (690)
15	343 (1628), 482 (1360) (H ₂ O)
21	359 (1114), 491 (986) (H ₂ O)
24	363 (1072), 483 (614) (MeOH)
25	362 (2008), 488 (1096)
26	367 (1544), 490 (882)
27	360 (2734), 481 (1220)
29	361 (996), 485 (802) (CH ₂ Cl ₂)
30	350 (890), 460 (446)
31	360 (1458), 486 (948)
32	382 (3988), 509 (4210) (MeCN)
33	362 (2966), 498 (1270) (MeCN)
34	352 (1864), 481 (618)
35	488
37	478 (1118) (H ₂ O)

^a λ_{\max} is reported in nm. ^b ϵ is reported in M⁻¹cm⁻¹

12. UV-Vis spectroscopic monitoring of the photochemical decomposition of **31**

Given that previous reports were conflicting with regard to the identity of the benzoylferrocene photoproducts, we wished to identify both the iron-containing and organic photoproducts of prodrug **31**. When **31** (0.25 mM, 50:50 DMF:H₂O) was photolyzed (> 450 nm) in a quartz cuvette in the absence of oxygen, the solution quickly lost its characteristic orange color and an intractable grey-green

solid formed. Photolysis in the presence of 2,2'-bipyridyl (three equivalents) under identical conditions led to a slow color change from orange to deep red with no formation of precipitate. The presence of solvated iron(II), trapped as the $\text{Fe}(\text{bipy})_3^{2+}$ complex, was confirmed by the presence of the characteristic λ_{max} at 522 nm for the tris(bipy) complex (Figure 2.18).^[38,39] Monitoring an identically prepared sample by UV-Vis spectroscopy confirmed the inactivity of the sandwich complex in the dark.

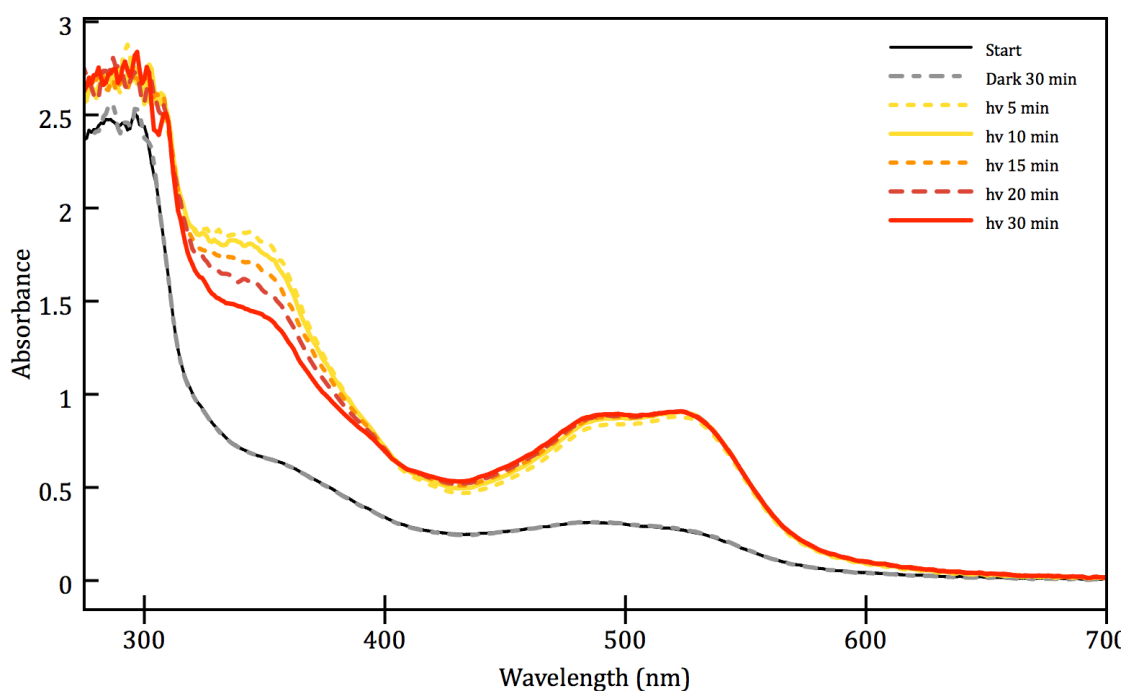


Figure 2.18. UV-Vis profile of **31** photolysis in 50:50 H_2O :DMF in the presence of 2,2'-bipyridyl.

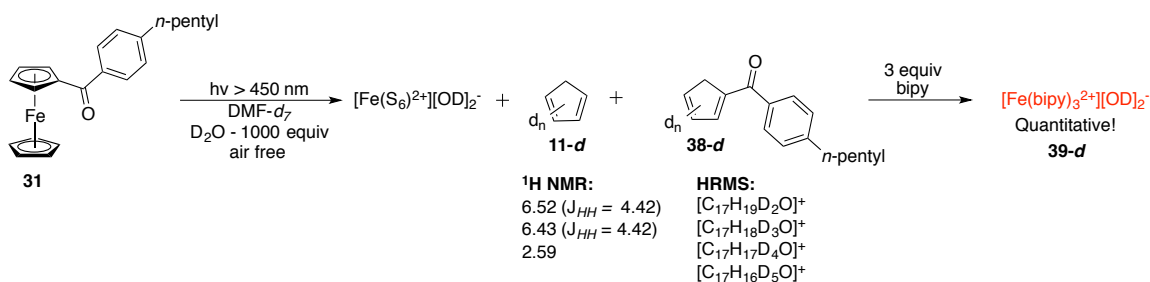
13. ^1H and ^{13}C NMR spectroscopic monitoring of the photochemical decomposition of **31**

Irradiation of **31** in a Teflon-sealed NMR tube (CD_3CN) resulted in a slow color change from red to dark brown with concurrent formation of a fine black

precipitate. ^1H NMR spectroscopy was employed to monitor the reaction, and over the course of several days the singlet resonance of the unsubstituted cyclopentadienyl-ring-hydrogens gradually broadened and disappeared. The exact photoproducts were not identified due to significant line broadening in the ^1H NMR spectrum; however, broad peaks located between δ 6.2 and 6.4 in a 1:1 ratio suggested the formation of cyclopentadiene. To model the aqueous conditions in cells, we next investigated the photodecomposition of **31** in a saturated mixture of $\text{DMF-}d_7$ and D_2O (0.6 mL : 0.1 mL) and followed the reaction progress by ^1H and ^{13}C NMR spectroscopy. When open to the air during the course of photolysis the solution immediately took on a purple hue similar to that described by Ali⁴⁰ and a brown intractable solid formed that was insoluble in DMF, acetone, DMSO and water. A ^1H NMR spectrum of the mother liquor still contained broad and distorted signals even following filtration, suggesting the presence of paramagnetic products. The only identifiable product was cyclopentadiene due to significant line broadening in the ^1H NMR spectrum.

When **31** was rigorously freeze/pumped/thaw degassed and photolyzed (> 450 nm) in a flame sealed NMR tube (0.1 mL D_2O /0.6 mL $\text{DMF-}d_7$, ~1000 equivalents of D_2O) with hexamethyldisiloxane as an internal standard, the orange color slowly faded to clear and a pale grey-green solid formed, consistent with the observations of Tarr and Wiles.²⁰ Monitoring of the reaction by ^1H NMR spectroscopy revealed clean disappearance of the cyclopentadienyl resonances between δ 4.2 - 4.6 ppm within 30 min of light exposure (Figure 2.19); however,

further analysis of this ^1H NMR spectrum was unenlightening due to significant line broadening. After removal of the green solids by filtration under nitrogen, a ^1H NMR spectrum of the sample exhibited resonances for the aryl (δ 7.71 and 7.38, $J_{\text{HH}} = 8.07$) and *n*-pentyl hydrogens (δ 0.5 – 2.65) of **38-d**. Additional signals at δ 6.52 ($J_{\text{HH}} = 4.42$), 6.43 ($J_{\text{HH}} = 4.42$), and 2.59 were assigned to free cyclopentadiene by comparison to a spectrum of the authentic compound in the same solvent system. Resonances for the benzoylcyclopentadiene ring-hydrogens were not present, but minor complex multiplets were observed at $\sim \delta$ 3.5 and between δ 7 and 8 ppm (Figure 2.19). Suspecting that the less basic substituted benzoylcyclopentadienide anion may have been exchanging with the deuterium oxide solvent, we employed high resolution mass spectrometry (HRMS), which detected masses consistent with incorporation of two, three, four, and five deuterium atoms into the substituted cyclopentadiene ring (Scheme 2.9). Due to the solvent exchange over the course of the reaction a ^1H NMR yield was not calculated for the organic fragments. Photolysis of an identically prepared sample, followed by addition of bipy under an atmosphere of nitrogen, resulted in consumption of the pale-green solid and formation of a deep red solution. A ^1H NMR spectrum of this sample exhibited resonances identical to an authentic solution of $[\text{Fe}(\text{bipy})_3]^{2+}[\text{Cl}^-]_2$.⁴¹ The yield of the $\text{Fe}(\text{bipy})_3^{2+}$ from complex **31** was determined to be quantitative relative to the internal standard (hexamethyldisiloxane, Scheme 2.9).



Scheme 2.9. Photoactivity of **31** in DMF- d_7 and D_2O .

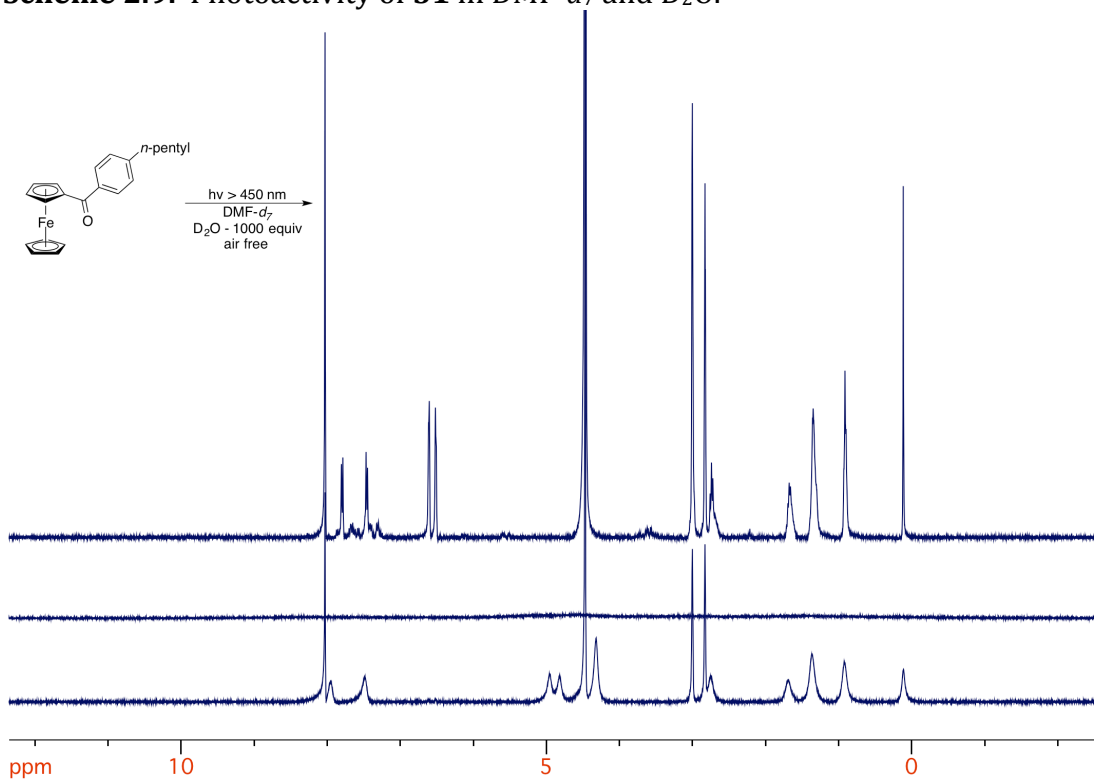
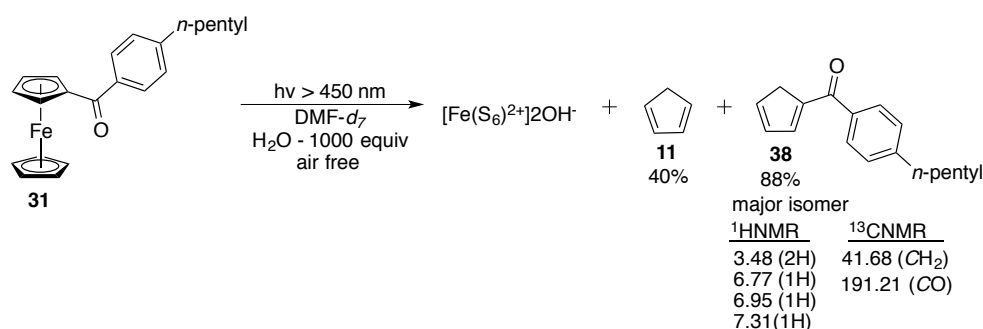


Figure 2.19. 1H NMR spectra of photoreaction for complex **31** in DMF- d_7 and D_2O . Bottom: $t = 0$; Middle: $t = 30$ min; top: following filtration.

Repeating the same reaction using H_2O as a co-solvent rather than D_2O largely obscured the cyclopentadienyl peaks for the starting sandwich complex, but allowed for detection of the hydrogen atoms located on the benzoyl-substituted cyclopentadiene. Following filtration, vinylic peaks for a major isomer were observed at δ 6.77 (d, $J_{HH} = 5.0$ Hz, 1H), 6.95 (d, $J_{HH} = 5.0$ Hz, 1H), and 7.31 (m, 1H).

Additionally, a methylene hydrogen signal was found at δ 3.43 and aryl hydrogen resonances were observed at 7.34 (d, $J_{HH} = 7.9$ Hz, 2H) and 7.68 (d, $J_{HH} = 7.9$ Hz, 2H) (Scheme 2.10). A ^{13}C NMR spectrum (0.6 mL DMF- d_7 , 0.1 mL H $_2$ O) of the photoproducts confirmed the presence of cyclopentadiene; the resonances at δ 133.50, 132.36, and 41.66 were consistent with an authentic sample in the same solvent. Also evident in the ^{13}C NMR spectrum was a single CO resonance at δ 191.03 and a second methylene signal at 41.68. By ^1H NMR spectroscopy, the yield of this benzoylcyclopentadiene isomer was calculated to be 88% relative to the internal standard. The low ^1H NMR yield of cyclopentadiene (40%), is likely due to evaporative loss during filtration. As three regioisomers could be formed upon protonation of the benzoylcyclopentadienide anion, the regiochemistry of the 4-pentylbenzoylcyclopentadiene was assigned using DFT calculations (Figure 2.20, Table 2.11). As would be predicted, isomer **38** is the lowest energy, likely due to the extended conjugation between the cyclopentadiene ring and benzoyl group. Given the zero point energy of **38'** and **38''** are significantly higher than **38**, we tentatively assigned the major benzoylcyclopentadiene photoproduct as isomer **38**.



Scheme 2.10. ^1H NMR and ^{13}C NMR spectral data for the photoreaction of **31** in DMF- d_7 and D $_2$ O.

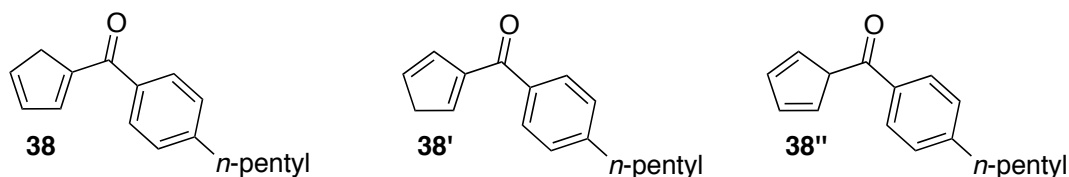


Figure 2.20. Potential isomers formed upon protonation of anion **38**.

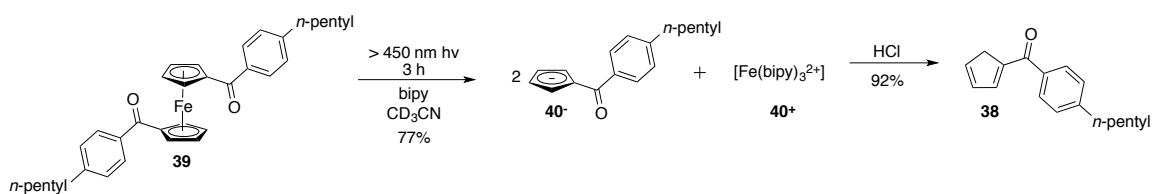
Table 2.11. Relative energies of cyclopentadiene isomers calculated using Density Functional Theory (B3LYP, 6-311++G**).

Isomer:	38	38'	38''
Final Single Point Energy (Eh)	-735.254786	-735.252141	-735.245549
Relative Energy (kcal/mol)	0.00	1.66	5.80

14. Photochemical generation of 4-*n*-pentylbenzoylcyclopentadienide anion (**40**⁻)

To further confirm the identity of the benzoylcyclopentadiene product, **40**⁻ was generated photochemically in CD₃CN from **39** with three equivalents of bipy to trap free Fe(II) as it formed (Scheme 2.11).⁴² Within three hours, the starting ferrocenyl signals at δ 4.61 (t, J_{HH} = 1.8 Hz, 4H) and 4.84 (t, J_{HH} = 1.8 Hz, 4H) had disappeared, and were supplanted by new peaks at 7.34 (m), 8.04 (t, J_{HH} = 6.3 Hz, 6H), 8.47 (d, 6H, J_{HH} = 7.8 Hz). These signals are consistent with an authentic sample of the Fe(bipy)₃²⁺ dication.⁴¹ A broad singlet at δ 5.77 integrating to four hydrogens was assigned to the ring-hydrogens on the cyclopentadienide anion. The ¹H NMR yield of **40**⁻ relative to the internal standard (hexamethyldisiloxane) was 79%. Addition of aqueous HCl to the NMR tube gave a spectrum that was consistent with the photolysis products of **31**, a multiplet at δ 3.45 (4H, 2CH₂), three vinylic

resonances at δ 6.69 (2H), 6.87 (2H), and 7.22 (2H), and aryl peaks at 7.32 (d, J_{HH} = 7.4 Hz, 4H) and 7.69 (d, J_{HH} = 7.4 Hz, 4H). The ^1H NMR yield for conversion of **40** to **38** was 92%. The photolysis of 1,1'-dibenzoylferrocene with 1,10-phenanthroline (phen) to yield benzoylcyclopentadiene, following aqueous work up with HCl, has been previously reported in the literature. The spectrum obtained by the authors for this reaction sequence is similar to what we obtained for **38**.⁴²



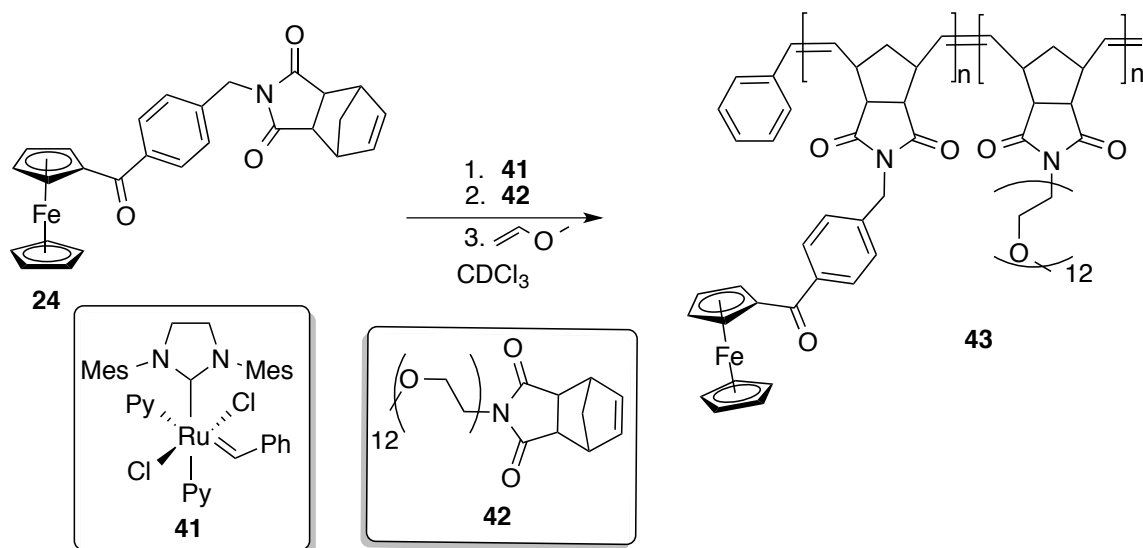
Scheme 2.11. Photochemical synthesis of **40**.

A preparatory-scale reaction was also performed where 1,10-phenanthroline was used as the chelating ligand for iron rather than bipy. Photolysis of **39** (50 mg) with 3 equivalents of phen in acetonitrile for 48 h resulted in complete consumption of the starting sandwich complex. Complex **40(phen)** was isolated in 75% yield following crystallization from acetonitrile, toluene and pentane (1:1:1). The spectrum of this complex was similar to the spectrum obtained from photolysis of **31** with bipy.

15. Nanoparticles

As ROMP monomer **24** had displayed promising phototoxicity, we wished to explore the possibility of delivering the organoferrous prodrug within a nanoparticle.

Monomer **24** was polymerized using a modified Grubbs second-generation catalyst (**41**). Complete polymerization of **24**, immediately following addition of the ruthenium catalyst, was evident by the disappearance of the olefin peaks assigned to complex **24** in the ^1H NMR spectrum (CDCl_3) (Scheme 2.12). A solution of the hydrophilic OEG-monomer (**42**) was then added to the NMR tube and the mixture was left at rt for an additional 30 min. Ethyl vinyl ether quenching and addition of cold diethyl ether led to precipitation and isolation of the polymers. The nanoparticles were then prepared by self-assembly of the block copolymers from a DMF solution in water by dialysis over two days. TEM images of the iron-loaded nanoparticles are shown in Figure 2.21.



Scheme 2.12. Synthesis of benzoylferrocene-containing polymers.

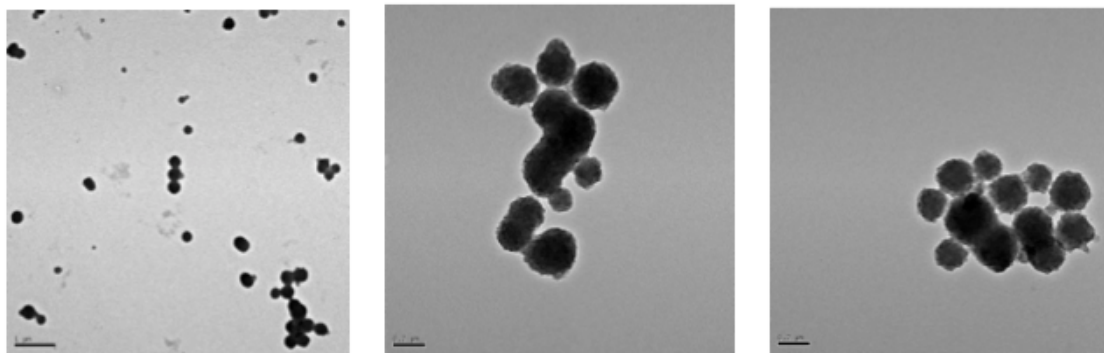
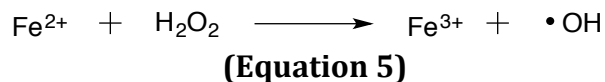


Figure 2.21. TEM of dialyzed micelles.

C. Discussion

A vital characteristic of cell metabolism is the existence of highly evolved mechanisms that sense ferrous and ferric ion levels in the local environment, allowing for precise control of iron homeostasis.⁴³ Many ferrocene-based antitumor compounds are simply mimics of known organic drugs, synthesized and tested with the hopes that modification of the three dimensional shape or lipophilicity by incorporation of the ferrocene moiety will be enough to induce interesting biological activity. An advantage of ferrocene-based antitumor drugs is they have a potential mechanism of action unique to iron-containing drugs; iron(II) can be oxidized *in vitro* to iron(III) by hydrogen peroxide to generate the highly toxic hydroxyl radical via the Fenton Reaction (Equation 5). Once formed, the hydroxyl radical rapidly abstracts hydrogen atoms from the nearest biomolecule, such as the lipid bilayer or DNA, resulting in cell death.^[44,45,46]

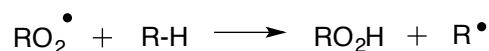
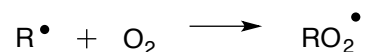
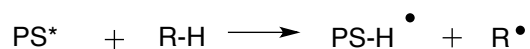
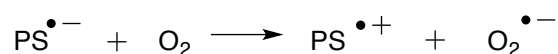
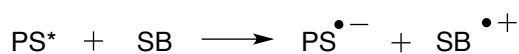


Based on this precedent, we proposed a new class of photoactivated, organoferrous prodrugs that were designed to circumvent the highly sophisticated iron transportation and storage mechanisms in cells. Taking inspiration from Kutal, we set out to prepare a series of substituted benzoylferrocene-based prodrugs where the reactive, cytotoxic iron(II) is masked as the organometallic sandwich complex. We speculated that in the absence of light the organic ligands would stabilize the electron-deficient central iron atom to oxidation. Following cell uptake, exposure to visible light would trigger the release of solvated, cytotoxic iron(II). Rapid reaction with endogenous hydrogen peroxide would then generate the highly toxic hydroxyl radical with high degrees of spatiotemporal control. Alternatively, the photochemically generated iron(II) could react directly with oxygen in an electron-transfer reaction to give iron(III) and superoxide. Once formed, superoxide can dismutate to hydrogen peroxide and molecular oxygen, providing the necessary reagents for the Fenton reaction even in the absence of endogenous hydrogen peroxide.⁴⁶ Based on these precedents, we proposed the resulting disruption to iron homeostasis and vital hydrogen peroxide cell signaling pathways, in addition to high local concentration of hydroxyl radicals, would ultimately lead to cell death.^[47,46]

We believed this approach would be unique as photodynamic therapy (PDT) traditionally involves excitation of a ground state photosensitizer (PS) to generate a

short-lived photoexcited state that undergoes two types of reactions (Figure 2.22). In a type I reaction, the excited state (PS*) undergoes a direct *redox* reaction with the substrate (SB) to give a radical anion that readily reacts with oxygen. The superoxide anion that is formed from this process can then go on to generate hydrogen peroxide and hydroxyl radical. PS* can also abstract a hydrogen atom from a nearby biomolecule to give a radical that can react with oxygen to form a hydroperoxide (RO₂H). Alternatively in a type II reaction, the triplet excited state (³PS) transfers *energy* directly to molecular oxygen (³O₂), generating cytotoxic singlet oxygen (¹O₂) which oxidizes nearby biomolecules by reacting with nearby carbon-carbon double bonds.^[48,49] The half-life of singlet oxygen in the cell is very short (< 0.05 μs) which is reflected in the small radius of action (0.02 μm). In this paradigm continual irradiation is required for generation of the cytotoxic species.^{50,51} In contrast, the organoferrous PDT agents we envisioned are expected to photo-generate ferrous *catalysts* via the Haber-Weiss cycle (Figure 2.3), and significantly, may continue to function in the absence of light.

Type I Reactions



Type II Reactions

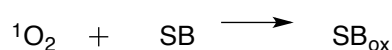
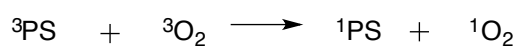


Figure 2.22. Equations for Type I and Type II processes in photodynamic therapy.⁴⁹

The absorbance spectra of the synthesized derivatives (**14**, **15**, **21**, **25-37**) are similar to the benzoylferrocene spectra reported by other groups.^[40,18] All of the complexes are stable indefinitely when stored in the solid state in the absence of light; however, upon photolysis in DMF:H₂O (50:50, air free, > 450 nm) solutions of the benzoylferrocene prodrugs rapidly changed from a deep red color to colorless, concurrent with formation of a pale green precipitate. The only exception to this trend was observed during photolysis of electron-rich derivatives **32** and **33**, which were unreactive under these photoconditions. When monitored by UV-Vis spectroscopy, photolysis of **7**, **15**, **21**, **24**, **30** and **31** resulted in a rapid

disappearance of both MLCT bands in the visible region of the spectrum for each complex, indicating the photodecomposition of the prodrugs was not sensitive to benzoyl ring substitution. The structural similarities of the substituted benzoylferrocene complexes were evident in the solid-state structures of **7**, **15**, **29**, **30**, and **31** (Figure 2.10 – 2.14 and Table 2.1). The C(1)-C(5)-C(6)-O(1) torsion angle, reflective of conjugation between the cyclopentadienyl ring and the neighboring carbonyl, ranges between -12.58° to 13.93° , with complex **29** displaying the smallest angle (2.20°). The substituted cyclopentadienyl ring in all the benzoylferrocene derivatives is essentially planar. Displacements of the O(1) carbonyl oxygen atom from this plane range between 0.028 (**29**) and 0.339 Å (**7**), with derivative **29** displaying the smallest displacement from the mean C(1)-C(5) plane, presumably due to a steric effect of the chlorine substituents on C(8) and C(12). The remarkable similarities displayed by each of the solid-state structures indicate that delocalization between the π -orbitals of the cyclopentadienyl ring and the adjacent carbonyl group is largely unaffected by substitution on the phenyl ring.

With a small library of photoactive benzoylferrocene complexes synthesized and characterized, preliminary cytotoxicity data was obtained for each derivative in a three-concentrations test. The HeLa cells were seeded then incubated with varying concentrations of each complex in the dark for 24 h prior to irradiation with a > 450 nm longpass filter. Cells exposed to similar concentrations of the iron complexes but kept away from light were used as a dark control. Cell viability was

determined by the crystal violet staining assay when the cells reached confluency (48 h post irradiation).

We initially suspected the low solubility of ferrocene in aqueous media would be the major obstacle in finding a cytotoxic, organoferrous photosensitizer. For this reason, much time and effort was expended on synthesizing water-soluble benzoylferrocene derivatives **15** and **21**. Disappointingly, both complexes were found to be inactive in the absence of light and under irradiation conditions up to concentrations of 1 mM. Increasing electron density at the iron center by addition of a pyrrolidine substituent on the cyclopentadienyl ring (**33**, $E_{1/2} = -0.160$ V (Fc/Fc⁺)) led to a drastic lowering of the IC₅₀ value in the dark, but gave no appreciable increase in toxicity upon light exposure. The only other electron-rich complex tested, Cp* derivative **32** ($E_{1/2} = 0.160$ V (Fc/Fc⁺)), induced toxicity at its solubility limit (40 μM), but no increase in activity was noted upon light exposure (Table 2.3).

We were also interested in 1,1'-dibenzoylferrocenes as targets because of their reported higher quantum yields relative to the mono-substituted analogs.¹⁹ We also suspected the higher oxidation potentials (Table 2.9) of these complexes would result in reduced cytotoxicity in the dark, as the more electron-deficient prodrugs would be less likely to participate in detrimental redox chemistry. The tested 1,1'-dibenzoylferrocene complexes **34-37** induced mild toxicity in the dark at their solubility limit (40 μM), but no increase in cytotoxicity was noted following irradiation.

ROMP monomer **24** was the first complex tested that induced a slight increase in cytotoxicity upon exposure to visible light; however, due to the solubility limit of the organometallic complex, we were unable to calculate an IC_{50} in the absence of light and under irradiation conditions. Complexes **7** and **29** were significantly more soluble than their 1,1'-dibenzoylferrocene analogs, and induced cytotoxicity in the initial three-concentrations assay. For each of these complexes, IC_{50} values were determined in both the absence of light and under irradiation conditions. Disappointingly, **7** and **29** were each found to have similar cytotoxicity values in the dark and under irradiation conditions (Table 2.3).

The observation that charged derivatives **15** and **21** displayed no activity, but **7** and **29** were cytotoxic at reasonable concentrations, led us to speculate that increasing the hydrophobicity of the organometallic complex could lead to an increase in biological activity. In a preliminary three-concentrations assay we observed that incorporation of a *para*-cyclohexyl (**30**) or *para*-pentyl (**31**) substituent onto the benzene ring lead to a slight decrease in activity in the dark and a significant increase in cytotoxicity under irradiation conditions.

With lead compounds **30** and **31** in hand, optimal irradiation conditions for the organoferrous prodrugs were determined in both HeLa and A549 cells. The microtiter plates were exposed to varying concentrations of **30** or **31** for 24 h, and irradiated for 1 h, 2 h, 3 h, or 5 h at 37 °C using a solid aluminum block for temperature control. Each experiment was preformed in at least triplicate and an $IC_{50-light}$ was determined for each time period of light exposure. A significant

increase in cytotoxicity was observed for up to three hours of irradiation, the most pronounced increase in cytotoxicity being for complex **30** in HeLa cells (Figure 2.23). Prolonged photolysis (5 h) led to no increase in phototoxicity for any of the derivatives (Table 2.2). All irradiation experiments henceforth were conducted with an irradiation period of 3 h.

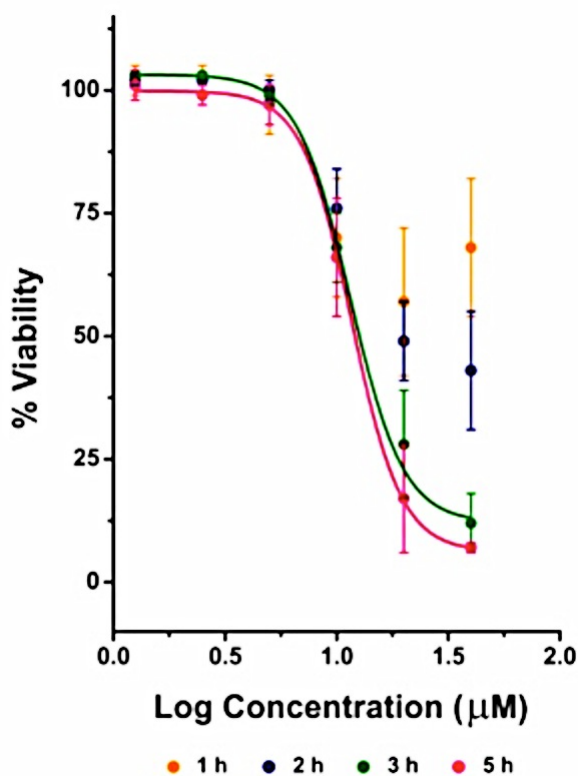


Figure 2.23. Cytotoxicity dose response of **30** in HeLa cells when exposed to > 450 nm light for various amounts of time.

As shown in Table 2.3, photo-experiments with organoferrous agent **31** led to IC₅₀ values of 12.8(1.8) and 9.5(2.7) μM in HeLa and A549 cells respectively. In the absence of light **31** induced significantly weaker cytotoxicity, with IC₅₀ values equal to 57.9(5.0) μM and 49(6.7) μM in HeLa and A549 cells, respectively.

Irradiation of cells incubated with the less water-soluble derivative **30** resulted in $IC_{50-light}$ values of 8.4(2.8) μM and 7.0(2.9) μM for HeLa and A549 cells respectively. No cell death was observed in the dark up to the limit of compound solubility for **30** (40 μM). Even immediately post photolysis, the cytotoxic effect of **30** upon irradiation was easily seen by use of an inverted microscope (Figure 2.24, Appendix 3). The effect was even more pronounced 12 h post-photolysis, visualized by the lack of continued cell growth and the significant change in cell morphology over the time period. Drug-free control wells demonstrated that irradiation alone led to no decrease in cell viability.

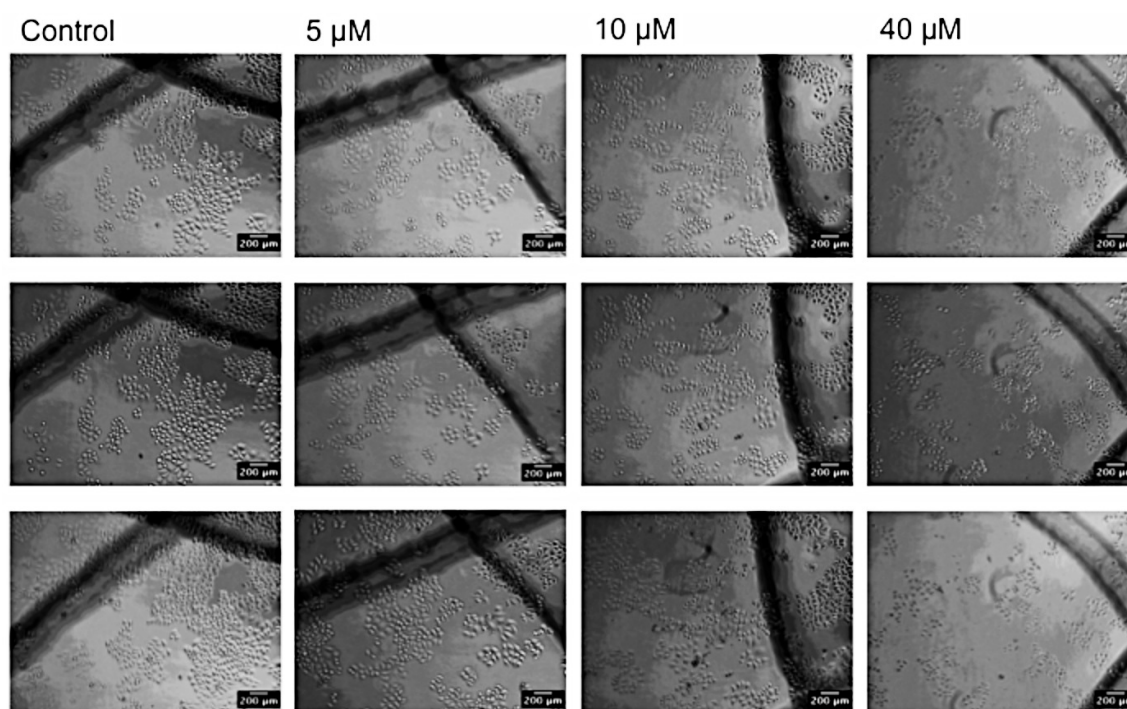


Figure 2.24. HeLa cells before and after being subjected to standard photolysis conditions with complex **30** at 10x magnification. Top row: before photolysis, middle row: immediately following photolysis, bottom row: 12 h post photolysis.

One of the benefits of photodynamic therapy is that it allows for spatiotemporal control; the cytotoxic species are only generated in the cancerous tissues irradiated with light.^[50,51] Given the organoferrous prodrugs could potentially accumulate in healthy cells as well as cancer cells, we established the toxicity of lead complexes **30** and **31** in a series of healthy cell lines, human embryonic kidney 293 cells (HEK-293), mouse subcutaneous connective tissue (L929) and healthy human fibroblast lung cells (MRC-5) (Table 2.5). Under irradiation conditions **30** and **31** induced similar toxicity in both healthy and cancer cell lines. Clinically however, the most relevant comparison is that of the $IC_{50-dark}$ values in healthy cells to the $IC_{50-light}$ values in the cancer cells; once inside the body the organoferrous prodrugs can diffuse into healthy or cancerous tissue, but only the cancerous cells are irradiated (spatiotemporal control). The phototoxicity index (P.I., Table 2.12) is a commonly referenced value that expresses the dark to light IC_{50} ratio for a drug; a P.I. equal to one indicates there is no enhancement of cytotoxicity following light exposure and P.I. greater than one indicates that irradiation of the prodrug results in a decrease of cell viability. While the relatively high $IC_{50-dark}$ for **30** and **31** in HEK-293 cells initially looked promising, control studies in HeLa cells demonstrated that comparison of IC_{50} results obtained by the two different cell viability staining methods gave slightly different results; thus, cross comparisons between crystal violet and cell titer blue assays is not advisable. The $IC_{50-dark}$ in L929 cells for **30** and **31** were comparable to the $IC_{50-dark}$ in HeLa and A549 cells. The most applicable P.I. is that of the healthy lung cells (MRC-5) in the dark and

cancerous lung cells (A549) in the light. Complex **30** was non-toxic up to the solubility limit of the complex (40 μM) in MRC-5 cells in the dark. In the same cell line, the $\text{IC}_{50\text{-dark}}$ for complex **31** is greater than the solubility limit of the complex. Due to this relatively high $\text{IC}_{50\text{-dark}}$ (> 150 μM) and the low $\text{IC}_{50\text{-light}}$ in A549 cells (9.5 (2.7) μM), the phototoxicity index for this complex was the highest obtained in all the cell studies (Figure 2.25 and Table 2.12).

Table 2.12. Photobiological activity of benzoylferrocene complexes.

Complex	Phototoxicity Index				
	HeLa ^a	L929/HeLa ^b	A549 ^c	L929/A549 ^d	MRC-5/A549 ^e
7	1.1	n.d.	0.9	n.d.	n.d.
31	4.5	2.8	5.2	3.8	15.8
30	> 4.6*	> 3.1*	> 5.9*	> 5.9*	> 5.9*
29	1.2	n.d.	1.1	n.d.	n.d.
33	1.6	n.d.	n.d.	n.d.	n.d.

^aHeLa_{dark}/HeLa_{light}; ^bL929_{dark}/HeLa_{light}; ^cA549_{dark}/A549_{light}; ^dL929_{dark}/A549_{light}; ^eMRC-5_{dark}/A549_{light}. *not all IC_{50} values were able to be calculated due to solubility constraints.

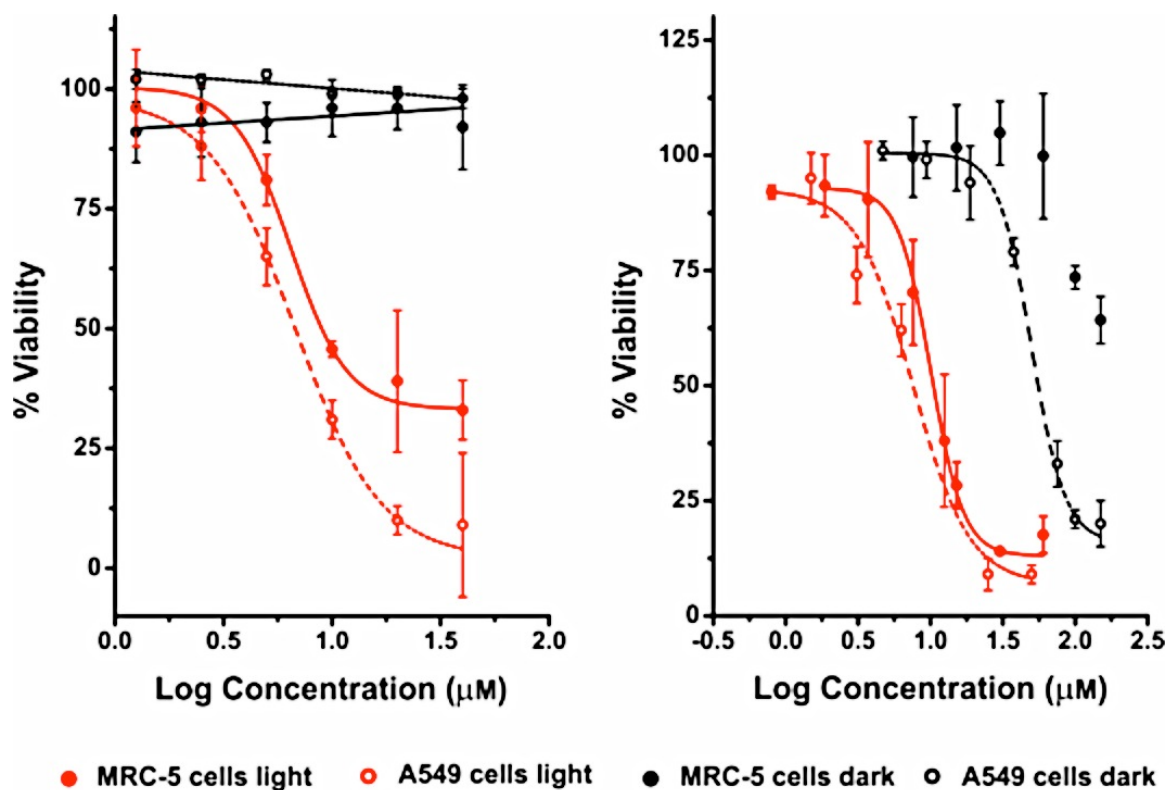


Figure 2.25. Cytotoxicity dose responses for **30** (left panel) and **31** (right panel) in A549 and MRC-5 cells in the dark and under irradiation conditions.

With the photobiological activity of **30** and **31** determined, we wished to demonstrate the organometallic prodrug was accumulating inside the cell prior to photochemical generation of the cytotoxic iron(II), effectively circumventing iron transportation mechanisms. When **30** or **31** were pre-irradiated in media at the same concentrations used to dose the cells for the cell viability studies, biological activity was non-existent for **30**, and the IC_{50} for the photoproducts of **31** was determined to be $>150 \mu\text{M}$ (the solubility limit of **31**). When A549 cells were exposed to **31** for 24 h, washed to remove any extracellular ferrous prodrug, treated with fresh drug free media and then photolyzed, the IC_{50} was same as in the original

cell viability experiment, further indicating the organometallic complex must localize inside the cell prior to irradiation to induce cytotoxicity. Studies with FeSO_4 in HeLa cells demonstrated that treatment with a solvated iron(II) source resulted in no induction of cytotoxicity in the light or the dark up to $1000 \mu\text{M}$. In A549 cells, FeSO_4 was non-toxic in the dark up to the solubility limit of **31** ($150 \mu\text{M}$), but in the light FeSO_4 induced moderate toxicity at $150 \mu\text{M}$ (67.9 (6.2) % viability).

Many biologically active ferrocene complexes are relatively electron-rich in nature and their cytotoxicity is speculatively related to facile oxidation of the iron atom in the organometallic complex.^[10,11,13] We postulated benzoylferrocene derivatives with higher oxidation potentials would be more difficult to oxidize and thus less prone to detrimental redox chemistry; therefore, an attempt was made to correlate oxidation potential to cytotoxicity in the absence of light. For each of the 1-benzoylferrocenes the oxidation potential was nearly identical (Table 2.9) and the cytotoxicity of the pro-drugs in the dark could not be correlated to oxidation potential. 1,1'-Dibenzoylferrocenes, while much more difficult to oxidize, were not significantly cytotoxic at their respective solubility limits in either the light or the dark.

While we were unable to correlate activity in the dark to the oxidation potentials of the benzoylferrocene complexes, we suspected the remarkable cytotoxicity of **30** and **31** under irradiation conditions was related to the enhanced lipophilicity of **30** and **31** relative to the other analogs. Cells are isolated from their outside environment by a continuous phospholipid bilayer, with polar phosphate

groups in contact with the aqueous environment outside and inside of the cell and a non-polar inner core. The ability of small molecules to pass through this lipid bilayer via passive diffusion is closely related to the molecule's lipophilicity, which is one of the most important factors in structure-activity relationships. The octanol-water partition coefficient P , first proposed by Fujita and Haush,⁵² simulates this biological partition by separating potential drug candidates between 1-octanol (representative of solubility inside the lipid bilayer) and water. The logarithm of P has since become one of the most widely used tools to express lipophilicity. Given the enhanced phototoxicity displayed by hydrophobic derivatives **30** and **31**, and the inactivity of the other derivatives tested, we experimentally determined the $\log P$ for each tested benzoylferrocene in an attempt to correlate the biological activity to the lipophilicity of the organoferrous pro-drugs.

While accurate, the traditional shake-flask method^[52,53] to determine $\log P$ is tedious and time consuming.³⁴ In 1978 Veith and co-workers streamlined the process by demonstrating the linear relationship between $\log P$ and the log of the retention factor (k) on a reverse phase HPLC column,³² where k is easily calculated from the retention time (t_R) and dead time (t_0) (Equation 2). Using a set of standards, the observed retention times on a reverse phase HPLC column can be correlated to known $\log P$ values tabulated in the literature and a calibration curve can be constructed by use of a linear regression. The obtained equation can then be used to determine the lipophilicity of potential drug candidates using only the observed HPLC retention times. This method has gained widespread use as it

provides a fast, facile, and reproducible way to determine the log P of new drug candidates based solely on HPLC retention time.³⁴

Using this method, the log P values for all neutral benzoylferrocene complexes were determined by reverse phase HPLC. The experimental values were found to vary widely (between 0.56 and 5.89) and depended on the substitution of both the cyclopentadienyl and phenyl rings. The archetypal metallocene complex, ferrocene, was demonstrated under our experimental conditions to have a log P of 3.72, in good agreement with other values published in the literature.⁵⁴ The relationship between lipophilicity of the organometallic complexes and biological activity is shown in Table 2.13 and Figure 2.26. Complexes that were inactive in both the light and the dark up to 1000 μM , or the solubility limit of the complex, had log P values ≤ 3.28 with the exception of **33**. Benzoylferrocene derivatives with intermediate values of lipophilicity had equal activity in both the light and the dark (complexes **7** and **29**). The lipophilicity of the prodrugs was increased by addition of a *para*-pentyl group (**31**, log P = 5.62) or *para*-cyclohexyl group (**30**, log P = 5.54) onto the benzene ring, or by exchanging the Cp ligand for Cp* (**32**, log P = 5.89). This increase in lipophilicity correlated to both higher IC₅₀ values in the dark and lower IC₅₀ values under irradiation conditions for complexes **30** and **31** (Table 2.13). The most lipophilic derivative tested, **32**, induced no additional toxicity under irradiation conditions but was determined to be photochemically inactive by ¹H NMR spectroscopy when irradiated in a DMF-*d*₇/H₂O.

Table 2.13. Comparison of lipophilicity and PI ratios for active complexes.

Complex	Log <i>P</i>	HeLa ^a	A549 ^b	MRC-5/A549 ^c
7	3.3	1.1	0.9	n.d.
29	3.86	1.2	1.1	n.d.
30	5.54	> 4.6*	> 5.9*	> 5.9*
31	5.62	4.5	5.2	15.8

^aHeLa_{dark}/HeLa_{light}; ^bA549_{dark}/A549_{light}; ^cMRC-5_{dark}/A549_{light}. *IC₅₀ values could not be determined for 26 in the dark due to solubility constraints. PI was calculated using the solubility limit (40 μM) as IC_{50-dark}.

To further demonstrate inhibition of cell growth was correlated to the prodrug's lipophilicity, the log *P* values of the biologically active complexes were plotted against their respective IC₅₀ values in HeLa cells. In the absence of light, the biological activity of the benzoylferrocene complexes decreased as lipophilicity increased, exemplified by a linear coefficient of 0.87 when the low solubility complex **30** was not taken into account (Figure 2.26). Under irradiation conditions the opposite result was obtained; as lipophilicity of the prodrug increased cytotoxicity also increased (R² = 0.78). While the correlation is not strong the trend is clear, increasing the lipophilicity of the organoferrous prodrugs resulted in greater toxicity under photoconditions.

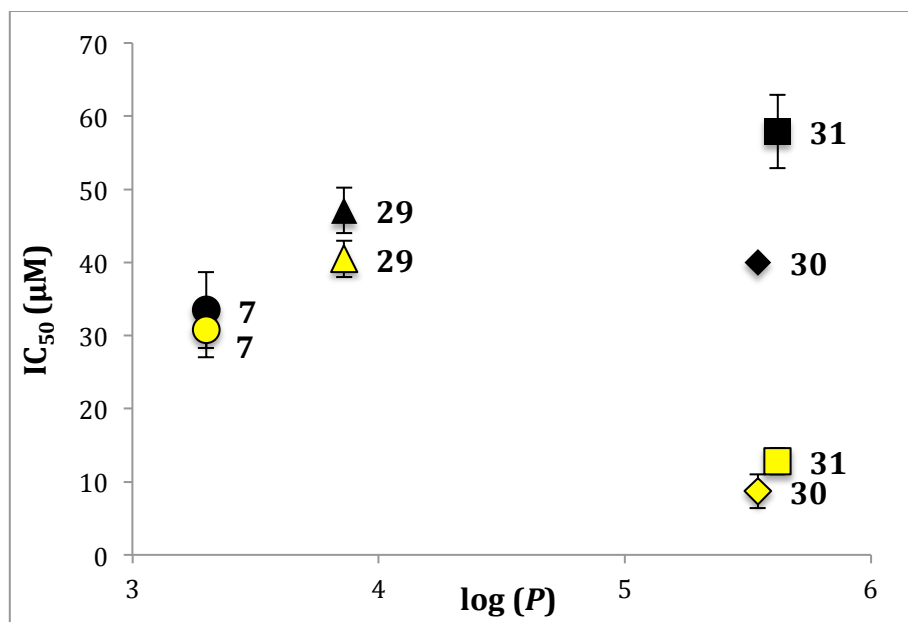


Figure 2.26. Relationship of $\log P$ to IC_{50} of selected benzoylferrocene complexes (black = absence of light; yellow = under irradiation conditions).

Having demonstrated the relationship between phototoxicity and lipophilicity, and recognizing passage through the lipid bilayer is the first step towards a drug possessing favorable antiproliferative effects, we sought to correlate accumulation of the pro-drugs in HeLa cells to biological activity. Since the nature of the aryl substituents greatly influenced both cell viability and lipophilicity, we speculated that cell uptake would likely be influenced by this same factor. Additionally, since the photoproducts of **30** and **31** were non-toxic (Figure 2.15) and removal of extracellular **31** prior to irradiation had no effect on cytotoxicity (Table 2.4), we suspected that the active prodrugs were passing through the lipid bilayer prior to irradiation and were causing cytotoxic effects inside the cell. With these results in mind, we proposed that cell accumulation studies would be a powerful tool to determine if the ferrous pro-drugs were indeed able to enter cells.

To this end, we employed ICP-OES to unambiguously determine the iron concentration in cells treated with 60 μM solutions (the $\text{IC}_{50\text{-dark}}$ of complex **31** and well below the solubility of each complex) of selected organoferrous drugs. To account of differences in biomass between samples, the iron concentration in the cell lysates was then related to protein concentration of each sample.

The protein concentration of the cell lysates was determined by the Bradford method, a common biochemical technique that works by measuring the UV-Vis absorbance of coomassie brilliant blue dye, which upon protein binding forms a deep blue complex that absorbs at 594 nm.³⁶ In this assay, a standard curve is first constructed by adding known quantities of a protein standard to a solution of the dye. The UV-Vis absorption at 594 nm is then measured and plotted against the protein concentration to generate a calibration curve. Despite its popularity, the Bradford Method often exhibits significant deviations from linearity due to spectral overlap; the dye is present in three forms under the assay conditions, resulting in three potential absorbance maxima at 470, 590, and 650 nm. Additional deviations from linearity occur as the concentration of the reagent decreases as more dye is bound to protein in the sample. Zor reported in 1996 the accuracy and sensitivity of the Bradford Assay is improved 10-fold by reducing the background signal caused by the unbound dye/dye-protein equilibrium.⁵⁵ Independent measurement of absorbance at 450 and 590 nm and calculation of the A_{590}/A_{450} ratio results in linearity over a wider concentration range, allowing for detection down to 50 ng of bovine serum albumin.

Using Zor's method, the standard curve was constructed by first adding zero to 50 μL of diluted human serum albumin solution (0.1 mg/mL, 0.001% Triton X-100) to triplicate wells of a 96-well plate. The total volume of each well was raised to 100 μL using the same concentration of Triton X-100. 100 μL of diluted Bradford reagent was then added to each well such that the total volume of each well was 200 μL , except for a blank which contained only 200 μL of 0.001% Triton X-100 solution. The absorbances at 450 and 590 nm were then recorded by use of a microplate reader and the calibration curve was constructed. The calibration curve was prepared independently each day unknown protein concentrations were determined to account for small differences in experimental technique (a typical standard curve is shown in Figure 2.27). With the calibration curve constructed, the protein content of the cells treated with the organoferrous pro-drugs was determined by first adding 5, 10, 15, and 25 μL of cell lysate (0.001% Triton X-100) to triplicate wells. The total volume was then raised to 100 μL using 0.001% Triton X-100 and 100 μL of the Bradford Reagent was added to each well. The absorbances at 450 and 590 were then measured and the ratio of the absorbances was compared to the calibration curve to determine the protein concentration in the cell lysates. Once the protein concentration was determined for each flask, the concentration of iron in the cell lysate was determined by ICP-OES, and the iron concentration was related to the protein concentration in each sample to determine the cell accumulation.

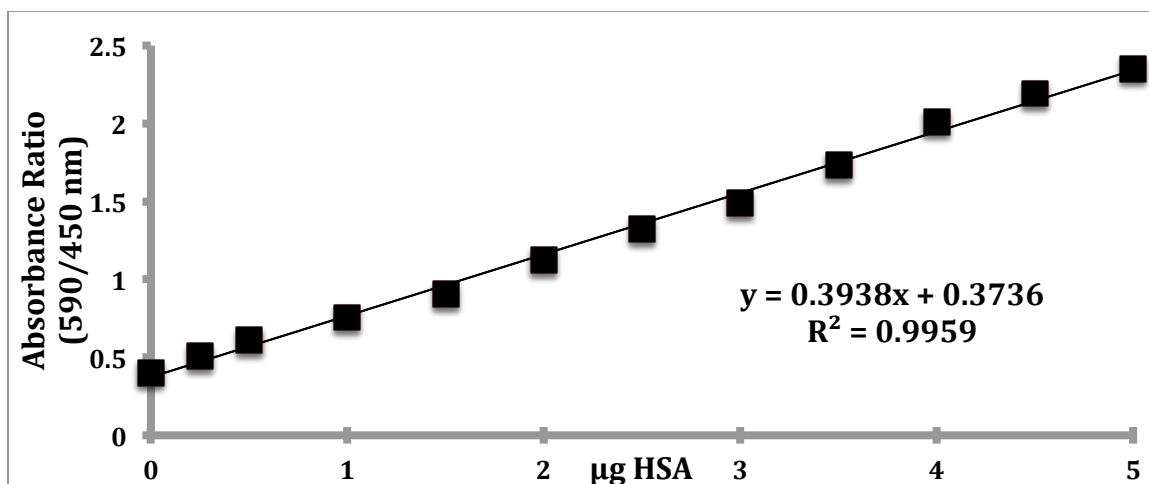


Figure 2.27. Typical Bradford Assay standard curve.

Accumulation data was obtained in HeLa cells for three iron-containing drugs, **7**, **21**, **31**, and ferrous sulfate (Table 2.8). Cells treated with a 60 μM solution of the inactive water-soluble sulfonate complex **21** had iron accumulation values nearly identical to the control (Table 2.14). HeLa cells treated with the parent benzoylferrocene complex (**7**), which had equivalent toxicity in the dark and under irradiation conditions, also had a similar cellular iron accumulation as the control cells. As predicted from the cytotoxicity studies, the iron content of the cells treated with a 60 μM solution of **31** had increased iron accumulation, 18.9 times that of the control cells. While the data is limited, it suggests the observed phototoxicity of the benzoylferrocene derivatives is closely related to accumulation of the organoferrous prodrugs inside the cell, which is in turn related to the lipophilicity of the organometallic complex.

Table 2.14. Concentration of iron in cell lysates following treatment with various iron containing complexes (60 μ M).

Complex	Average Fe*	Standard Deviation	Ratio**
7	415.8	145.4	1.3
21	397.6	123.5	1.2
31	6,157	496.5	18.9
FeSO₄	6,996	651.1	20.2
Control (H₂O)	345.7	82.1	-
Control (DMF)	325.9	89	-

*ng Fe/mg of cellular protein. **[Average Fe in drug-containing cell lysates]/[Average Fe in control cell lysates].

HeLa cells treated with a 60 μ M solution of the labile iron source FeSO₄ also displayed impressive iron accumulation, but treatment with FeSO₄ at even 16 times this concentration did not have a detrimental effect on cell viability in the dark or upon photolysis. While this is an intriguing result, it raises many additional questions. At this time it is not clear if the iron is merely adhered to the negatively charged cell membrane or if it is scavenged by the cell machinery and enters the cell such that the redox chemistry of the solvated Fe(II) is controlled. In **31** the redox-active iron is masked as the organometallic sandwich complex and may be distributed differently than inorganic iron within the cell compartments, possibly accounting the drastic differences in cytotoxicity. The possibility remains, however, that Fe(II) is *not* the cytotoxic species being generated upon photolysis

Cell accumulation studies also demonstrated that uptake is dependent on the concentration of **31** used to dose the HeLa cells (Figure 2.17). Given adequate time, most small molecules will diffuse across the lipid bilayer down their concentration gradient depending on their size and lipophilicity. The relationship of cellular iron accumulation and concentration of **31** used to dose the cells was found to be linear

($R^2 = 0.846$, Figure 2.17). While the observed correlation was not great, one must remember the multiple sources of experimental variation in cell accumulation studies; higher concentrations of organoferrous agents should favor the influx process and result in a greater iron accumulation. However, the same concentration of the organoferrous prodrugs can lead to a drastic decrease in biomass due to increasing cytotoxic effects.

At the outset of this project we proposed that photolysis of benzoylferrocene in cell media would give solvated iron(II) *in situ*. We also predicted this photochemically generated iron(II) would participate in detrimental Fenton chemistry and ultimately induce cell death. While initially inspired by the work of Kutal, the reported identities of the metal-containing and organic benzoylferrocene photoproducts vary widely (see Chapter 1).^[56,40,23,20,19,18] Therefore, with the biological activity of the ferrous prodrugs established, we wished to identify and characterize the photoproducts of lead complex **31**.

Irradiation of **31** in a Teflon sealed NMR tube using photolysis conditions identical to those used for cell viability assays, with a rigorously dried aprotic solvent (CD_3CN or $THF-d_8$), resulted in a slow color change from red to black with concurrent formation of a fine black precipitate. 1H NMR spectroscopy was employed to monitor the reaction, which took several days to reach completion. The photoproducts were unable to be identified under these conditions due to significant line broadening in the 1H NMR spectrum even following filtration. To more closely mimic the conditions in cells, we next photolyzed **31** in $DMF-d_7$ and

1000 equivalents of water. When open to the air during the course of photolysis the solution took on a light purple hue, similar to the observations of Ali,⁵⁶ and a brown solid formed that was insoluble in acetone, DMF, DMSO and water. The only identifiable product from the reaction mixture was cyclopentadiene due to significant line broadening in the ¹H NMR spectrum.

Exclusion of dissolved oxygen by freeze/pump/thaw degassing the NMR tube prior to irradiation gave much better results. Photolysis of **31** (DMF-*d*₇:D₂O 0.6 mL:0.1 mL) followed by treatment with bipy (3 equivalents) under nitrogen resulted in quantitative formation of the tris-bipy complex by ¹H NMR spectroscopy (relative to the internal standard hexamethyldisiloxane, Scheme 2.9). An additional experiment where a sample of **31** (0.5 mM, DMF:H₂O 1 mL:1 mL) was photolyzed with bipy (3 equiv) and monitored by UV-Vis spectroscopy further confirmed the formation of iron(II) by the development of the characteristic Fe(bipy)₃²⁺ λ_{max} peak at 520 nm (Figure 2.18) over the course of photolysis.^[38,39]

While we speculated the cytotoxic species being produced upon photolysis was solvated iron(II), we could not rule out the possibility that the organic ligands were the cytotoxic species. To identify the organic ligands formed upon photolysis, **31** was photolyzed in DMF-*d*₇ and D₂O (0.6 mL:0.1 mL, air free). Following filtration of a pale green solid under nitrogen we observed signals in the ¹H NMR spectrum, consistent with an authentic sample of free cyclopentadiene, at δ 6.52 (*J*_{HH} = 4.42), 6.43 (*J*_{HH} = 4.42), and 2.59. High resolution mass spectrometry of the sample revealed the presence of benzoylcyclopentadiene that had acquired deuterium from

the solvent mixture, explaining the absence of peaks in the vinyl region of the ^1H NMR spectrum (Scheme 2.9). The same experiment with H_2O obscured the cyclopentadienyl signals for **31**, but allowed for detection of the hydrogens located on the substituted cyclopentadiene ring. Signals corresponding to the benzoyl-substituted cyclopentadiene were found at δ 3.48, 6.77, 6.95, 7.31 ppm in a 2:1:1:1 ratio. The ^1H NMR yield of benzoylcyclopentadiene and cyclopentadiene was calculated to be 88% and 40% respectively (relative to the internal standard hexamethyldisiloxane) following photolysis (Scheme 2.10). ^{13}C NMR spectroscopic analysis of the same reaction mixture revealed a single CO signal at δ 191.2, indicative of a ketone, and two cyclopentadiene methylene peak at δ 41.68 and 41.25 (Appendix 1, Figures 2.78 and 2.79). Very low intensity signals in the ^1H NMR, possibly corresponding to a minor regioisomer of benzoylcyclopentadiene, resonated between δ 7 and 8 ppm but were unable to be assigned due to their low concentration under these reaction conditions. Chromatographic separation of these isomers from a preparatory scale reaction was attempted but deemed unfeasible as Diels-Alder adducts of the cyclopentadiene monomers quickly formed upon manipulation. In order to further confirm the organic photoproduct was indeed the neutral cyclopentadiene **38** and not the anion, we independently synthesized **40** photochemically from 1,1'-dibenzoylferrocene analog **39** (Scheme 2.11).⁴² Treatment of the cyclopentadienide anion with aqueous HCl in an NMR tube gave a ^1H NMR spectrum consistent with the benzoylcyclopentadiene photoproduct of **31**.

Since protonation of the benzoylcyclopentadienyl anion by water could potentially lead to the formation of three isomers, the regiochemistry of the benzoylcyclopentadiene product was investigated using Density Functional Theory (DFT) calculations (Figure 2.20 and Table 2.11). As predicted, isomer **38** is the most stable due to the extended conjugation between the cyclopentadiene ring and benzoyl group. **38'** is only cross-conjugated and thus less stable than **38**. Unconjugated isomer **38''** was calculated to be the highest energy of all three isomers. Given the zero point energy of **38'** and **38''** are significantly higher than **38**, we tentatively assigned the major benzoylcyclopentadiene photoproduct as **38**.

With this ^1H NMR, ^{13}C NMR, HRMS, and UV-Vis data in hand, we were able to assign the photoproducts of complex **31**. The change in color from orange to purple noted by both Ali⁴⁰, and Tarr and Wiles²⁰ was only observed when the reaction was not thoroughly degassed prior to irradiation. The quantitative formation of $\text{Fe}(\text{bipy})_3^{2+}$, confirmed by both ^1H NMR and UV-Vis spectroscopy, further conflicts with their reports, which proposed ferrous benzoates as the major iron-containing product. The observed ^1H NMR yield of 4-pentylbenzoylcyclopentadiene is inconsistent with aquation of the carbonyl to form either the benzoate or benzoic acid. In any of our studies under stringent oxygen free conditions neither 4-pentylbenzoic acid or 4-pentylbenzoate were detected by ^1H NMR, ^{13}C NMR, or high resolution mass spectrometry. For these reasons, we propose the photochemical decomposition of **31** is consistent with the mechanism put forth by Kutal (Figure 2.28).¹⁹ While the details for the dissociation of both ligands remains unknown, it is

likely that photochemically initiated, sequential η^5 , η^4 , η^2 ring slippage occurs before the benzoylcyclopentadienyl ligand is liberated from the metal to form **40**.¹⁹ Protonation of the released benzoylcyclopentadienide anion by water is then possible given the estimated pKa of the conjugate acid.⁵⁷ The decomposition mechanism for the CpFe^+L_3 fragment has not been studied to our knowledge, but a likely mechanism involving a thermal series of ring-slipped intermediates to give solvated iron(II) and free cyclopentadiene following protonation is possible. At this time, it is not clear if the cytotoxic species generated *in vitro* is indeed solvated iron(II), one of the protonated cyclopentadiene ligands, or a combination of both.

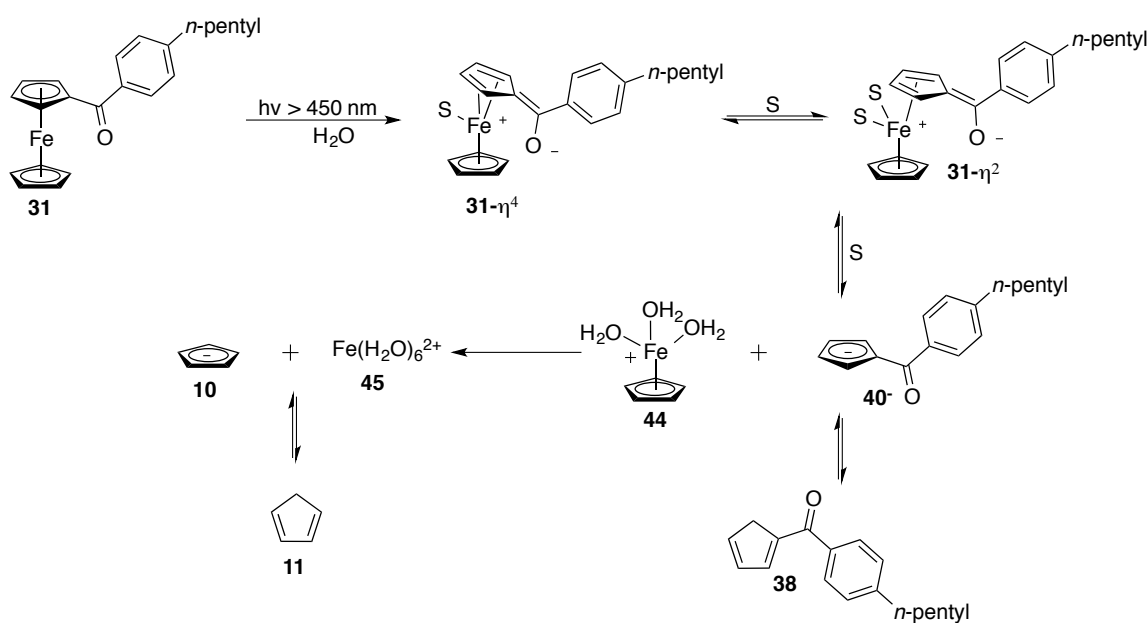


Figure 2.28. Proposed mechanism for photochemical decomposition of **31**.

D. Conclusions

A series of benzoylferrocene complexes were synthesized and fully characterized (^1H NMR, ^{13}C NMR, HRMS, IR, UV-Vis and cyclic voltammetry).

Modifications to both the cyclopentadienyl and phenyl substituents were made to explore the effects of substitution on cytotoxicity. The synthesized compounds were then tested for their toxicity in both the dark and under photoconditions in a series of cancer and healthy cell lines. The photobiological activity of the organometallic prodrugs was dependent on both the lipophilicity and cell accumulation of the complexes, with more lipophilic complexes displaying greater accumulation and enhanced phototoxicity. Spectroscopic and computational studies of lead compound **31** allowed us to confirm the photoproducts upon exposure to visible light as solvated iron(II), cyclopentadiene, and 1-(4-pentylbenzoyl)cyclopentadiene. At this time it has not been determined if the cytotoxic agent is solvated iron(II) or one of the organic photoproducts, however it is clear that the organoferrous prodrug must accumulate inside the cell prior to photolysis to induce phototoxicity. Future studies in our group will involve synthesizing and testing compounds that absorb at longer wavelengths such as ansa-ferrocene derivative **46** (Figure 2.28). Additional projects with the aid of collaborators will involve targeted delivery to cancer cells using silica based nanoparticles, *in vitro* mechanism of action studies on lead complex **31**, and mouse studies on **31** to investigate potential clinical applications.

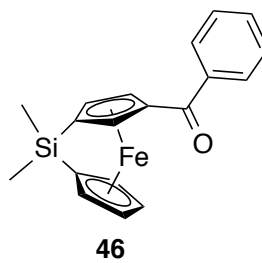


Figure 2.29. Ansa ferrocene derivative **46**.

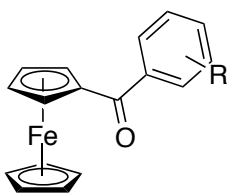
E. Experimental

General Methods

All synthetic reagents were purchased from Aldrich, Fisher Scientific, or Alfa Aesar, and were used without further purification. All solvents for anhydrous reactions were obtained from Fisher scientific and dried on alumina columns prior to use. All reactions were performed under N₂ or argon using standard Schlenk techniques unless otherwise noted. Solvents used for chromatography were ACS technical grade and used without further purification. Water (18.2 μΩ/cm) was filtered through a NANOPure Diamond™ (Barnstead) water purification system before use. All ¹H NMR and ¹³C NMR spectra were recorded on a Varian Mercury Plus 400 MHz NMR spectrometer or a Varian VNMRs NMR spectrometer equipped with a 500MHz XSens Cold Probe. Deuterated solvents were purchased from Cambridge Isotopes. Chemical shifts are reported as δ in units of parts per million (ppm) referenced to the residual solvent peak. Coupling constants are reported as a J value in Hertz (Hz). High-resolution mass spectrometry analysis was performed by the UCSD Chemistry and Biochemistry Molecular Mass Spectrometry Facility on a ThermoFinnigan MAT900XL mass spectrometer with an ESI source. UV-Vis absorption spectra were collected with a Shimadzu UV 3600 and plotted using Excel. Cyclic voltammetry measurements were performed at room temperature in acetonitrile under an argon atmosphere with a CH Instrument potentiostat (CHI620e) with freshly polished Pt disk working electrode, a Ag wire counter electrode, a Ag/Ag⁺ pseudo reference electrode, and [nBu₄N][PF₆] (0.1 M) as

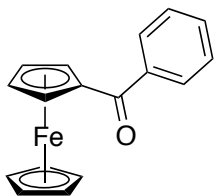
electrolyte. Potentials were then calibrated against the Fc/Fc⁺ couple as an internal standard and plotted in Excel. FTIR spectra were recorded on a Thermo-Nicolet iS10 FTIR spectrometer. Samples were prepared as a thin film using NaCl or BaF₂ windows as noted. Equilibrium geometry ground state calculations were performed by Spartan '14 molecular modeling with Density Functional Theory methods (B3LYP, 6-311++G**) in a vacuum.

Synthesis of 1-Benzoylferrocenes

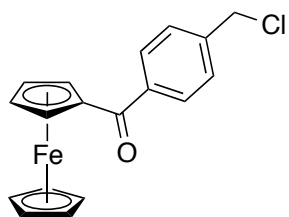


General Procedure A^{30,31}: Ferrocene (5.00 g, 26.9 mmol, 1 equiv) was dissolved in anhydrous dichloromethane (107 mL, 0.25 M) and the corresponding acid chloride (29.6 mmol, 1.1 equiv) was added via syringe. The reaction mixture was cooled to 0 °C by use of an ice bath and anhydrous AlCl₃ (3.75 g, 29.6 mmol, 1.1 equiv, 0.3 M) was added in three portions over a 15 min period. The dark blue solution was allowed to warm to RT slowly while stirring overnight (12 h). The reaction mixture was poured into a flask of ice water, extracted into 100 mL of CH₂Cl₂, then washed successively with 10% NaOH solution, water, and brine. The organic layer was dried over MgSO₄, filtered, and the solvent was removed under reduced pressure.

Chromatography on SiO₂ gel with 90:10 hexanes:ethyl acetate as eluent (unless noted otherwise) led to isolation of the pure 1-benzoylferrocenes.



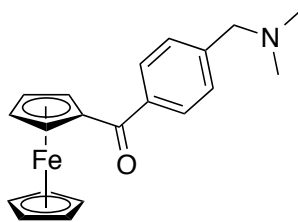
Benzoylferrocene (7)³¹: Previously known complex prepared according to General Procedure A. Yielded a red solid (85%). Analytical data corresponded with that in the literature.³¹ ¹H NMR (500 MHz, CD₂Cl₂) δ 4.20 (s, 5H), 4.59 (t, *J*_{HH} = 1.9 Hz, 2H), 4.86 (t, *J*_{HH} = 1.9 Hz, 2H), 7.47 (t, *J*_{HH} = 7.5 Hz, 2H), 7.55 (t, *J*_{HH} = 7.4 Hz, 1H), 7.87 (d, *J*_{HH} = 7.1 Hz, 2H); ¹³C NMR (500 MHz, CD₂Cl₂) δ 70.51 (Cp), 71.71 (Cp'), 72.92 (Cp'), 78.55 (*ipso*-Cp'), 128.34 (aryl), 128.51 (aryl), 131.70 (aryl), 140.18 (aryl), 198.89 (CO). UV-Vis λ_{max} (50:50 DMF:H₂O, nm) 368, 487. E_{1/2} (V) 0.250.



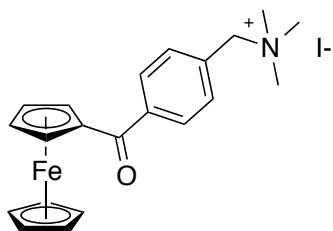
4-(Chloromethylbenzoyl)ferrocene (13): Prepared according to General Procedure A using commercially available 4-(chloromethyl)benzoyl chloride. Yielded 6.09 g of a red solid (67%). ¹H NMR (400 MHz, CD₂Cl₂) δ 4.22 (s, 5H), 4.63 (t, *J*_{HH} = 1.9 Hz, 2H), 4.69 (s, 2H), 4.88 (t, *J*_{HH} = 1.9 Hz, 2H), 7.52 (d, *J*_{HH} = 8.3 Hz, 2H), 7.90 (d, *J*_{HH} = 8.3 Hz, 2H); ¹³C NMR (500 MHz, CD₂Cl₂) δ 46.08 (benzylic-CH₂), 70.55 (Cp), 71.68 (Cp'), 73.05 (Cp'), 78.39 (*ipso*-Cp'), 128.75 (aryl), 128.80 (aryl), 140.05

(aryl), 141.11 (aryl), 198.26 (aryl); IR (NaCl, cm^{-1}) 800, 819, 1285, 1440, 1633.

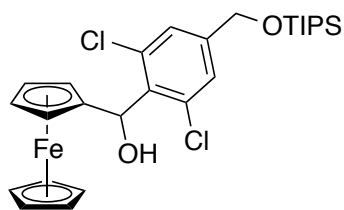
HRMS (ESI-TOFMS) m/z calcd for $[\text{C}_{18}\text{H}_{16}\text{ClFeO}]^+$: 339.0234; found 339.0236.



4-((Dimethylamino)methylbenzoyl)ferrocene (14): Compound **13** (1.00 g, 2.62 mmol, 1.00 equiv) was dissolved in THF (0.25 M, 10 mL) and dimethylamine (5 mL, 40% aqueous solution) was poured in at RT. The red solution was allowed to stir 14 h at RT before extraction into diethyl ether. The free amine was extracted twice into water using 15% citric acid solution, returned to a basic pH with 1M NaOH, then extracted twice into diethyl ether. The combined organic layers were dried with MgSO_4 , and the crude product isolated by rotary evaporation. The amine was purified by SiO_2 chromatography, eluting with 95:5 dichloromethane:MeOH, and if necessary was further purified by recrystallization from ethyl acetate/hexanes. Yielded 0.85 g of an orange solid (94%). ^1H NMR (400 MHz, CDCl_3) δ 2.30 (s, 6H, $\text{RN}(\text{CH}_3)_2$), 3.52 (s, 2H, CH_2), 4.20 (s, 5H, Cp), 4.58 (t, $J_{\text{HH}} = 1.6$ Hz, 2H, Cp'), 4.90 (t, $J_{\text{HH}} = 1.6$ Hz, 2H, Cp'), 7.43 (d, $J_{\text{HH}} = 8.0$ Hz, 2H, aryl), 7.88 (d, $J = 8.0$ Hz, 2H, aryl); ^{13}C NMR (500 MHz, CD_2Cl_2) δ 45.32 ($\text{RN}(\text{CH}_3)_2$), 63.93 (benzylic- CH_2), 70.50 (Cp), 71.70 (Cp'), 72.83 (Cp'), 78.68 (*ipso*-Cp'), 128.45 (aryl), 129.15 (aryl), 139.03 (aryl), 198.54 (CO); IR (NaCl, cm^{-1}) 1026, 1289, 1451, 1564, 1615, 2776, 2928, 3082, 3009. HRMS (ESI-TOFMS): m/z calcd for $[\text{C}_{20}\text{H}_{22}\text{FeNO}]^+$ 348.1046; found 348.1047. UV-Vis λ_{max} (50:50 DMF:H₂O, nm) 364, 488. $E_{1/2}$ (V) 0.254.



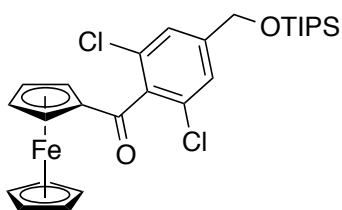
4-N,N,N-trimethylmethanaminiumbenzoylferrocene iodide (15): Benzylic amine **14** (0.85 g, 2.45 mmol, 1 equiv) was dissolved in acetonitrile (0.25 M, 10 mL) and methyl iodide (0.20 mL, 3.06 mmol, 1.25 equiv) was added via syringe. The red solution was brought to a reflux for 2 h. The volatiles were then removed under reduced pressure. At this point the ammonium salt was spectroscopically pure by ^1H NMR, but was crystallized from ethyl acetate if necessary. Yielded 1.04 g of **15** as dark purple crystals (87%). ^1H NMR (400 MHz, CD_2Cl_2) δ 3.40 (s, 9H, $\text{RN}(\text{CH}_3)_3$), 4.22 (s, 5H, Cp), 4.64 (t, $J_{\text{HH}} = 1.9$ Hz, 2H, Cp'), 4.85 (t, $J_{\text{HH}} = 1.9$ Hz, 2H, Cp'), 5.15 (s, 2H, CH_2 -benzylic), 7.83 (d, $J_{\text{HH}} = 7.4$ Hz, 2H, aryl), 7.98 (d, $J_{\text{HH}} = 6.9$ Hz, 2H, aryl); ^{13}C NMR (400 MHz, CD_2Cl_2) δ 68.33 (benzylic- CH_2), 70.56 (Cp), 71.57 (Cp'), 73.37 (Cp'), 77.79 (*ipso*-Cp'), 128.93 (aryl), 130.31 (aryl), 133.39 (aryl), 142.26 (aryl), 198.18 (CO); ^{13}C NMR (500 MHz, CD_3CN) δ 53.44 ($\text{RN}(\text{CH}_3)_3$), 69.22 (benzylic- CH_2), 71.18 (Cp), 72.16 (Cp'), 74.07 (Cp'), 78.71 (*ipso*-Cp'), 129.37 (aryl), 131.47 (aryl), 133.91 (aryl), 142.64 (aryl), 198.98 (CO). IR (NaCl, cm^{-1}) 1281, 1444, 1563, 1621, 2949, 3002, 3082. HRMS (ESI-TOFMS) m/z calcd for $[\text{C}_{21}\text{H}_{24}\text{FeNO}]^+$ 362.1202; found 362.1201. UV-Vis λ_{max} (H_2O , nm) 343, 482. $E_{1/2}$ (V) 0.272.



(2,6-Dichloro-4-(((triisopropylsilyl)oxy)methyl)phenyl)(ferrocenyl)methanol

(18): A 0.1 M solution of ((3,5-dichlorobenzyl)oxy)triisopropylsilane (0.5 g, 1.5 mmol, 1.0 equiv) in THF was cooled to -78 °C in a dry ice acetone bath with magnetic stirring. *n*-BuLi (1.36 mL, 1.20 M in hexanes, 1.64 mmol, 1.1 equiv) was then added dropwise via syringe, causing the clear colorless solution to become pink. The deprotonation was allowed to continue at the same temperature for 45 minutes during which time it slowly faded back to colorless. Ferrocenecarboxaldehyde (0.4 g, 1.875 mmol, 1.25 equiv) was then syringed in as a 0.25 M solution in dry THF. Immediately following addition of the aldehyde the reaction was determined to be complete by TLC. The orange solution was immediately quenched with sat. NH₄Cl at -78 °C, extracted into diethyl ether, dried with MgSO₄, and absorbed onto SiO₂. The product was purified by chromatography on SiO₂ gel eluting with 90:10 hexanes:ethyl acetate. Yielded 0.62 g of an orange oil (76%). ¹H NMR (CD₂Cl₂, 500 MHz) δ 1.08-1.21 (m, 21H, TIPS), 3.06 (d, *J*_{HH} = 9.54 Hz, 1H, OH), 4.03 (dt, *J*_{HH} = 2.42, 1.23 Hz, 1H, Cp-H), 4.08 (td, *J*_{HH} = 2.42, 1.33, 1H, Cp-H), 4.16 (td, *J*_{HH} = 2.42, 1.33, 2H, Cp-H), 4.20 (s, 5H, Cp), 4.59 (dt, *J*_{HH} = 2.42, 1.23, 1H, Cp-H), 4.67 (s, 2H, CH₂), 6.47 (d, *J*_{HH} = 9.54 Hz, 1H, CH), 7.30 (s, 1H, aryl); ¹³C NMR (CD₂Cl₂, 500 MHz) δ 11.90 (TIPS-CH₃), 17.74 (TIPS-CH), 63.40 (benzylic-CH₂), 67.04 (Cp), 67.29 (Cp), 67.41 (Cp), 67.64 (Cp), 68.95 (CH), 70.25 (Cp), 89.98 (Cp-*ipso*),

126.43 (aryl), 133.94 (aryl), 135.89 (aryl), 143.63 (aryl). IR (NaCl, cm^{-1}) 1400, 1455, 1544, 1600, 2861, 3088, 3587.39, 3446.42. HRMS (ESI-TOFMS) m/z calcd for $[\text{C}_{27}\text{H}_{36}\text{Cl}_2\text{FeO}_2\text{Si}]^+$: 546.1212; found 546.1213.

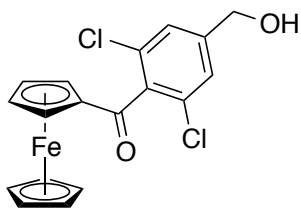


(2,6-Dichloro-4-

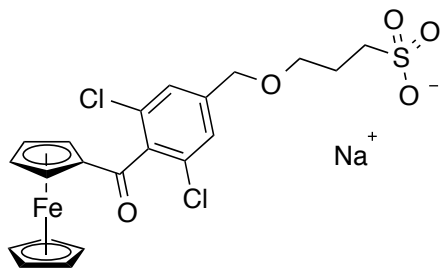
(((triisopropylsilyloxy)methyl)phenyl)(ferrocenyl)methanone(19):

Compound **18** (0.62 g, 1.13 mmol, 1 equiv) was dissolved in CH_2Cl_2 (0.1M) and freshly activated MnO_2 was added in one portion (3.9 g, 56.6 mmol, 40 equiv). The suspension was stirred at RT and was monitored by TLC for progress. Additional MnO_2 (20 equiv) was added if necessary after one hour to consume remaining **18**. Upon completion the crude reaction mixture was poured unto a short plug of SiO_2 and which was washed with CH_2Cl_2 until the eluent ran clear. A bright red oil was isolated following rotary evaporation and was determined to be pure without further manipulation (89%). ^1H NMR (CD_2Cl_2 , 500 MHz) δ 1.10 (d, $J_{\text{HH}} = 6.97$ Hz, 18H, TIPS- CH_3), 1.19 (septet, $J_{\text{HH}} = 6.97$ Hz, 3H, TIPS-CH), 4.31 (s, 5H, C_p), 4.59 (t, $J_{\text{HH}} = 1.89$ Hz, 2H, C_p'), 4.62 (t, $J_{\text{HH}} = 1.89$, 2H, C_p'), 4.82 (s, 2H, benzylic- CH_2), 7.24 (s, 2H, aryl). ^{13}C NMR (CD_2Cl_2 , 500 MHz) δ 12.25 (TIPS- CH_3), 18.09 (TIPS-CH), 63.87 (CH_2 -benzylic), 70.72 (C_p), 70.80 (C_p'), 72.92 (C_p'), 79.98 (*ipso*- C_p'), 125.75 (aryl), 132.01 (aryl), 136.87 (aryl), 145.71 (aryl), 197.47 (CO). IR (NaCl, cm^{-1}) 816, 882, 1116,

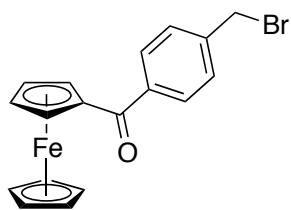
1282, 1454, 1549, 1599, 1660, 2864, 2945. HRMS (ESI-TOFMS) m/z calcd for $[C_{27}H_{34}Cl_2FeO_2SiNa]^+$: 567.0948; found 567.0947.



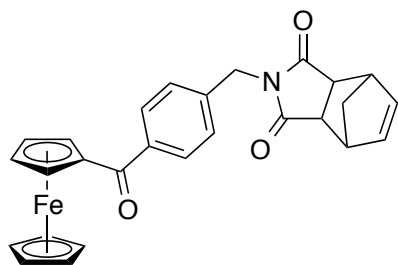
(2,6-Dichloro-4-(hydroxymethyl)phenyl)(ferrocenyl)methanone (20): TIPS protected alcohol (**19**) (0.55 g, 1.0 mmol, 1 equiv) was dissolved in THF with magnetic stirring (15 mL, 0.06M) and was cooled to 0 °C by use of an ice bath. Tetrabutylammoniumfluoride (1.2 mmol, 1.2 equiv, 1.0M solution in THF) was added dropwise via syringe. The reaction was allowed to warm to RT and react for 1 h. The crude reaction mixture was evaporated to dryness under reduced pressure, dissolved in ethyl acetate, and loaded on a SiO₂ column. The pure alcohol was obtained by eluting with 80:20 hexanes:ethyl acetate. Yielded a red solid (67%). ¹H NMR (CD₃CN, 500 MHz) δ 3.40 (t, J_{HH} = 5.96 Hz, 1H, OH), 4.32 (s, 5H, Cp), 4.60 (s, 2H, CH₂OH), 4.61 (t, J_{HH} = 1.90 Hz, 2H, Cp'), 4.64 (t, J_{HH} = 1.90 Hz, 2H, Cp'), 7.41 (s, 2H, aryl); ¹³C NMR (CDCl₃, 500 MHz) δ 63.1 (CH₂) 70.6 (Cp) ,70.8 (Cp'), 73.0 (Cp'), 79.3 (*ipso*-Cp), 126.0 (aryl), 132.0 (aryl), 136.5 (aryl), 145.1 (aryl), 198.7 (CO); ¹³C NMR (CD₃CN, 500 MHz) δ 62.90 (benzylic CH₂), 71.26 (Cp), 73.74 (Cp'), 80.54 (Cp'-*ipso*), 127.13 (aryl), 132.23 (aryl), 137.44 (aryl), 147.22 (aryl), 197.98 (CO). IR (NaCl, cm⁻¹) 3422.46 (OH), 1636.79 (CO). HRMS (ESI-TOFMS) m/z calcd for $[C_{18}H_{14}Cl_2FeO_2Na]^+$: 410.9613; found 410.9614.



3-((4-Benzoyl-3,5-dichlorobenzyl)oxy)propane-1-sulfonate (21): **20** (100 mg, 0.25 mmol, 1 equiv) was dissolved in dry, degassed tetrahydrofuran (0.1 M) and cooled to 0 °C with magnetic spinning. Dry sodium hydride (12 mg, 0.49 mmol, 2 equiv) was then added carefully in one portion. The solution bubbled vigorously initially and formed a suspension while stirring at RT over the course of thirty min. 1,3-propanesultone was then added in one portion to the red solution which was heated to a reflux overnight (12 h). The crude reaction mixture was evaporated onto SiO₂ gel and purified using 90:10 CH₂Cl₂:MeOH as an eluent. Yielded 30 mg of a red oil (23%). ¹H NMR (400 MHz, CD₃OD) δ 2.13 (s, 2H, OCH₂CH₂), 3.00 (s, 2H, OCH₂), 3.68 (s, 2H, CH₂SO₃), 4.34 (s, 5H, Cp), 4.55 (s, 2H, Cp'), 4.63 (s, 2H, Cp'), 4.68 (s, 2H, CH₂-benzylic), 7.44 (s, 2H, aryl); ¹³C NMR (500 MHz, CD₃OD) δ 26.58 (CH₂), 54.83 (CH₂), 70.52 (Cp), 71.60, 71.74, 71.76, 74.2 (Cp'), 80.60 (Cp'), 128.14 (aryl), 132.99 (aryl), 138.18 (aryl), 144.54 (aryl), 199.94 (CO). IR (NaCl, cm⁻¹) 1160, 1440, 1587, 1651, 2498, 2695, 2853, 2928, 2978. HRMS (ESI-TOFMS) *m/z* calcd for [C₂₁H₁₉Cl₂FeO₅S]⁻: 506.9732; found 506.9729. UV-Vis λ_{max} (H₂O, nm) 359, 491. E_{1/2} (V) 0.302.

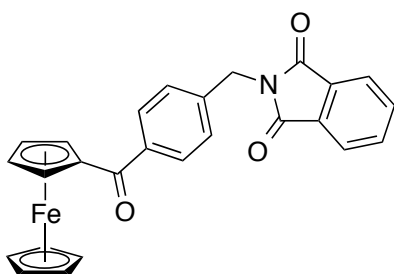


4-(Bromomethylbenzoyl)ferrocene (22): 4-(bromomethyl)benzoic acid (6.36 g, 29.6 mmol, 1.1 equiv) was dissolved in CH_2Cl_2 (0.5 M, 60 mL) and 1 mL of dry DMF. Oxalyl chloride (2.71 mL, 32.3 mmol, 1.2 equiv) was added dropwise at 0 °C and the suspension was allowed to stir while warming to RT during which time it became a pale golden solution. The volatiles were removed by rotary evaporation and the crude acid chloride was subjected immediately to General Procedure A. Yielded a red solid (26%) over two steps (2.32 g). ^1H NMR (500 MHz, CD_2Cl_2) δ 4.21 (s, 5H, Cp), 4.57 (s, 2H, CH_2Br), 4.61 (t, $J = 1.9$ Hz, 2H, Cp'), 4.87 (t, $J = 1.9$ Hz, 2H, Cp'), 7.51 (d, $J = 8.2$ Hz, 2H, aryl), 7.87 (d, $J = 8.2$ Hz, 2H, aryl); ^{13}C NMR (500 MHz, CD_2Cl_2) δ 33.14 (CH_2Br), 70.56 (Cp), 71.68 (Cp'), 73.04 (Cp'), 78.39 (*ipso* -Cp'), 128.87 (aryl), 129.23 (aryl), 139.98 (aryl), 141.52 (aryl), 198.16 (CO). IR (NaCl, cm^{-1}) 822, 1044, 1005, 1443, 1604, 1632, 3095. HRMS (ESI-TOFMS): m/z calcd for $[\text{C}_{18}\text{H}_{15}\text{BrFeONa}]^+$: 404.9550; found 404.9553.



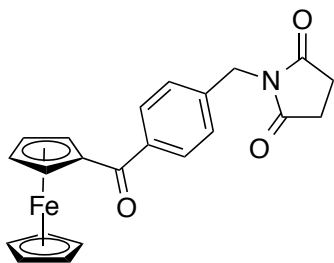
2-(4-Benzoylferrocenyl)-3a,4,7,7a-tetrahydro-1H-4,7-methanoisoindole-1,3(2H)-dione (24): 22 (0.5 g, 1.30 mmol, 1 equiv) was dissolved in a 0.25 M

solution of acetone (5.25 mL) and 3a,4,7,7a-tetrahydro-1H-4,7-methanoisoindole-1,3(2H)-dione (0.24 g, 1.43 mmol, 1.1 equiv) and K_2CO_3 (0.89 g, 6.5 mmol, 5 equiv) were added in one portion. The red solution was heated to a reflux for 5 h. The solvent was removed under reduced pressure and the crude residue was extracted into ethyl acetate and washed with brine. The product was purified by silica gel chromatography, eluting with 90:10 hexanes:ethyl acetate. Any remaining impurities were removed by recrystallization with ethyl acetate/hexanes. Yielded 0.53 g of an orange powder (87%). 1H NMR (400 MHz, CD_2Cl_2) δ 1.12 (d, $J_{HH} = 9.8$ Hz, 1H, CH), 1.44 (d, $J_{HH} = 9.8$ Hz, 1H, CH), 2.71 (s, 2H, CH_2), 3.24 (s, 2H, CH), 4.19 (s, 5H, Cp), 4.59 (s, 2H, Cp'), 4.67 (s, 2H, Cp'), 4.84 (s, 2H, benzylic- CH_2), 6.29 (s, 2H), 7.43 (d, $J = 8.0$ Hz, 2H), 7.83 (d, $J = 8.0$ Hz, 2H); ^{13}C NMR (500 MHz, CD_2Cl_2) δ 42.12, 42.89, 45.60, 48.10, 70.47 (benzylic- CH_2), 71.62 (Cp), 72.93 (Cp'), 78.41 (*ipso*-Cp'), 128.58 (aryl), 128.62 (aryl), 130.14 (aryl), 138.09 (aryl), 139.46 (CH), 139.75 (CH), 177.78 (amide-CO), 198.24 (CO). IR (NaCl) 1635.16, 1701.77, 1771.16, 2873.09, 2948.03, 2986.89. HRMS (ESI-TOFMS) m/z calcd for $[C_{27}H_{23}FeNO_3]^+$: 465.2028; found 465.1030. UV-Vis λ_{max} (MeOH, nm) 359, 483. $E_{1/2}$ (V) 0.250.



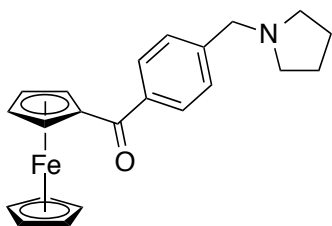
4-((Benzyl)isoindoline-1,3-dione)benzoylferrocene (25): **22** (0.5 g, 1.30 mmol, 1 equiv) was dissolved in a 0.25 M solution of acetone (5.25 mL) and phthalimide

(0.24 g, 1.43 mmol, 1.1 equiv) and K_2CO_3 (0.89 g, 6.5 mmol, 5 equiv) were added in one portion. The red solution was heated to a reflux for 5 h. The volatiles were removed under reduced pressure and the crude residue was extracted into ethyl acetate and washed with brine. The product was purified by silica gel chromatography, eluting with 90:10 hexanes:ethyl acetate. Any remaining impurities were removed by recrystallization with ethyl acetate/hexanes. 1H NMR (500 MHz, CD_2Cl_2) δ 4.18 (s, 5H, Cp), 4.57 (t, $J_{HH} = 2.0$ Hz, 2H, Cp'), 4.83 (t, $J_{HH} = 1.9$ Hz, 2H, Cp'), 4.90 (s, 2H, benzylic- CH_2), 7.48 (d, $J_{HH} = 8.1$ Hz, 2H, aryl), 7.77-7.74 (m, 2H, aryl), 7.87-7.84 (m, 4H, aryl); ^{13}C NMR (500 MHz, $CDCl_3$) δ 41.43 (benzylic- CH_2), 70.37 (Cp), 71.64 (Cp'), 72.75 (Cp'), 78.15 (*ipso*-Cp'), 123.64 (aryl), 128.47 (aryl), 128.72 (aryl), 132.13 (aryl), 134.32 (aryl), 139.35 (aryl), 139.83 (aryl), 168.16 (amide-CO), 198.82 (CO). IR (NaCl, cm^{-1}) 1285, 1390, 1443, 1601, 1629, 1712, 1773. HRMS (ESI-MS) m/z calcd for $[C_{26}H_{20}FeNO_3]^+$: 450.0787; found 450.0784. UV-Vis λ_{max} (50:50 DMF:H₂O, nm) 367, 489. $E_{1/2}$ (V) 0.255.



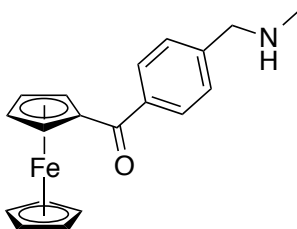
4-((Pyrrolidine-2,5-dione)methylbenzoyl)ferrocene (26): Compound **13** (0.3 g, 0.67 mmol, 1 equiv) was refluxed in acetone in the presence of succinimide (0.13 g, 1.35 mmol, 2 equiv) for 8 h. The volatiles were removed by rotary evaporation and the residue was taken up in Et_2O and washed with water. Pure **26** was obtained by

column chromatography (SiO₂ 80:20 hexanes:ethyl acetate). Yielded an orange powder (72%). ¹H NMR (400 MHz, CD₂Cl₂) δ 2.72 (s, 4H, CH₂-succinimide), 4.19 (s, 5H, Cp), 4.59 (s, 2H, Cp'), 4.70 (s, 2H, CH₂-benzylic), 4.84 (s, 2H, Cp'), 7.43 (d, *J* = 7.9 Hz, 2H, aryl), 7.84 (d, *J* = 7.9 Hz, 2H, aryl); ¹³C NMR (400 MHz, CD₂Cl₂) δ 28.66 (CH₂), 42.26 (CH₂), 70.55 (Cp), 71.72 (Cp'), 72.97 (Cp'), 78.55 (*ipso*-Cp), 128.62 (aryl), 128.75 (aryl), 139.65 (aryl), 139.76 (aryl), 177.22 (CO), 198.34 (CO); IR (NaCl, cm⁻¹) 1171, 1396, 1626, 1701, 1776. HRMS (ESI-TOFMS) *m/z* calcd for [C₂₂H₂₀FeNO₃]⁺: 422.0653; found 422.0650. UV-Vis λ_{max} (50:50 DMF:H₂O, nm) 367, 490. E_{1/2} (V) 0.251.



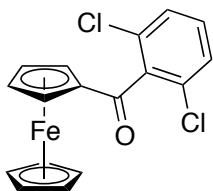
4-(Pyrrolidin-1-ylmethyl)benzoylferrocene (27): Compound **22** (1.00 g, 2.62 mmol, 1.00 equiv) was dissolved in THF (0.25 M, 10 mL) and pyrrolidine (5 equiv, 40% aqueous solution) was poured in at RT. The red solution was allowed to stir 14 h at room temperature before extraction into diethyl ether. The free amine was extracted twice into water using 15% citric acid solution, returned to a basic pH with 1M NaOH, then extracted twice into diethyl ether. The combined organic layers were dried with MgSO₄ and the crude product isolated by rotary evaporation. The amine was purified by SiO₂ chromatography (50:50 hexanes:ethyl acetate). If necessary **27** was recrystallized from ethyl acetate/hexanes. Yielded 0.92 g of an orange solid (95%). ¹H NMR (400 MHz, CD₂Cl₂) δ 1.77 (m, 4H, 2CH₂), 2.50 (m, 4H,

2CH₂), 3.66 (s, 2H, benzylic-CH₂), 4.20 (s, 5H, Cp-5H), 4.58 (t, $J_{HH} = 2.0$ Hz, 2H, Cp'), 4.86 (t, $J_{HH} = 2.0$ Hz, 2H, Cp'), 7.42 (d, $J_{HH} = 8.3$ Hz, 2H, aryl), 7.84 (d, $J_{HH} = 8.3$ Hz, 2H, aryl); ¹³C NMR (500 MHz, CD₂Cl₂) δ 23.87 (CH₂), 54.47 (CH₂), 60.48 (benzylic-CH₂), 70.49 (Cp), 71.71 (Cp'), 72.77 (Cp'), 78.78 (*ipso*-Cp'), 128.41 (aryl), 128.68 (aryl), 138.64 (aryl), 144.21 (aryl), 198.56 (CO). IR (NaCl, cm⁻¹) 1101, 1377, 1443, 1599, 1632, 2785, 2919, 2957, 3082. UV-Vis λ_{max} (50:50 DMF:H₂O, nm) 360, 481. E_{1/2} (V) 0.262.

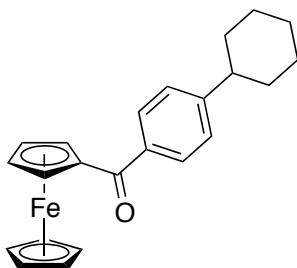


4-((Methylamino)methylbenzoyl)ferrocene (28): Compound **13** (1.00 g, 2.62 mmol, 1.00 equiv) was dissolved in THF (0.25 M, 10 mL) and methylamine (5 mL, 40% aqueous solution) was poured in at room temperature. The red solution was allowed to stir 14 h at RT before extraction into diethyl ether. The free amine was extracted twice into water using 15% citric acid solution, returned to a basic pH with 1M NaOH, then extracted twice into diethyl ether. The combined organic layers were dried with MgSO₄ and the crude product isolated by rotary evaporation. The amine was purified by SiO₂ chromatography (95:5 dichloromethane:MeOH) and if necessary **28** was recrystallized from ethyl acetate:hexanes. Yielded 0.85 g of an orange solid (96%). ¹H NMR (500 MHz, CDCl₃) δ 2.60 (s, 3H, CH₃), 4.17 (s, 2H, CH₂), 4.19 (s, 5H, Cp), 4.60 (s, 2H, Cp'), 4.85 (s, 2H, Cp'), 7.68 (d, $J_{HH} = 7.2$ Hz, 2H, aryl), 7.91 (d, $J_{HH} = 7.2$ Hz, 2H, aryl); ¹³C NMR (500 MHz, CDCl₃) δ 32.05 (Me), 52.14 (CH₂),

70.43 (Cp), 71.59 (Cp'), 73.07 (Cp'), 77.72 (Cp'), 128.94 (aryl), 130.21 (aryl), 133.61 (aryl), 140.90 (aryl), 198.64 (CO). IR (NaCl, cm^{-1}) 1280, 1625, 2480, 2685, 2751, 3092. HRMS (ESI-TOFMS) m/z calcd for $[\text{C}_{19}\text{H}_{20}\text{FeNO}]^+$: 334.0866; found 334.0889.

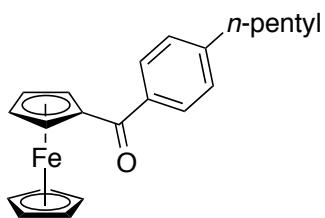


2,6-Dichlorobenzoylferrocene (29): Prepared according to General Procedure A with commercially available 2,6-dichlorobenzoyl chloride. Yielded a deep red solid (82%). ^1H NMR (500 MHz, CD_2Cl_2) δ 4.39 (s, 5H, Cp), 4.67 (t, $J = 1.9$ Hz, 2H, Cp'), 4.69 (t, $J_{\text{HH}} = 1.9$ Hz, 2H, Cp'), 7.45-7.37 (m, 3H, aryl) ^{13}C NMR (500 MHz, CDCl_3) δ 70.60 (Cp), 70.72 (Cp'), 72.76 (Cp'), 79.53 (*ipso*-Cp'), 128.52 (aryl), 130.60 (aryl), 132.28 (aryl), 138.52 (aryl), 197.84 (CO). IR (NaCl, cm^{-1}) 791, 849, 1426, 1451, 1574, 1651. HRMS (ESI-TOFMS) m/z calcd for $[\text{C}_{17}\text{H}_{13}\text{Cl}_2\text{FeO}]^+$: 356.9734; found 356.9731. UV-Vis λ_{max} (50:50 DMF:H₂O, nm) 361, 485 nm. $E_{1/2}$ (V) 0.296.



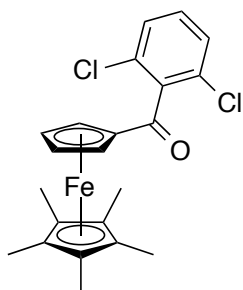
4-Cyclohexylbenzoylferrocene (30): 4-Cyclohexylbenzoic acid (5.42 g, 5.42 mmol) was dissolved in 10 mL of neat thionyl chloride and heated to a reflux for 6 h. The volatiles were removed by rotary evaporation, and the crude acid chloride was used immediately without further purification for reaction with ferrocene according

to General Procedure A. Yielded a red solid (54%) over two steps. ^1H NMR (500 MHz, CD_2Cl_2) δ 1.28 (m, $J_{\text{HH}} = 8.5, 4.0$ Hz, 1H, CH), 1.50-1.37 (m, 4H, CH_2), 1.75 (d, $J_{\text{HH}} = 12.9$ Hz, 1H), 1.90-1.84 (m, 4H, CH_2), 2.58 (ddt, $J_{\text{HH}} = 11.5, 7.8, 3.7$ Hz, 1H), 4.19 (s, 5H, Cp), 4.57 (t, $J_{\text{HH}} = 2.0$ Hz, 2H, Cp'), 4.86 (t, $J_{\text{HH}} = 2.0$ Hz, 2H, Cp'), 7.30 (d, $J_{\text{HH}} = 8.3$ Hz, 2H, aryl), 7.82 (d, $J_{\text{HH}} = 8.3$ Hz, 2H, aryl); ^1H NMR (500 MHz, CDCl_3) δ 1.32-1.20 (m, 1H, cyclohexyl), 1.44 (dq, $J = 24.8, 12.6$ Hz, 4H, cyclohexyl- CH_2), 1.78 (d, $J_{\text{HH}} = 12.6$ Hz, 1H, CH-cyclohexyl), 1.89 (dd, $J_{\text{HH}} = 20.4, 11.6$ Hz, 4H, CH_2 -cyclohexyl), 2.58 (t, $J_{\text{HH}} = 11.6$ Hz, 1H, CH-cyclohexyl), 4.21 (s, 5H, C_5H_5), 4.57 (t, $J_{\text{HH}} = 1.9$ Hz, 2H, Cp'-H), 4.91 (t, $J_{\text{HH}} = 1.9$ Hz, 2H, Cp'-H), 7.30 (d, $J_{\text{HH}} = 8.2$ Hz, 2H, Aryl-H), 7.85 (d, $J_{\text{HH}} = 8.2$ Hz, 2H, Aryl-H); ^{13}C NMR (500 MHz, CD_2Cl_2) δ 26.41, 27.13, 34.55, 44.92, 70.46, 71.72, 72.67, 78.88, 126.98, 128.63, 137.73, 152.40, 198.43; ^{13}C NMR (500 MHz, CDCl_3) δ 26.23 (cyclohexyl), 26.93 (cyclohexyl), 34.35 (cyclohexyl), 44.77 (cyclohexyl), 70.34 (Cp), 71.70 (Cp'), 72.46 (Cp'), 78.60 (*ipso*-Cp'), 126.84 (aryl), 128.54 (aryl), 137.52 (aryl), 152.17 (aryl), 198.93 (CO); IR (BaF_2 , cm^{-1}) 1295, 1368, 1446, 1597, 1620, 2849, 2992. HRMS (ESI-TOFMS) m/z calcd for $[\text{C}_{23}\text{H}_{24}\text{FeO}]^{\pm}$: 373.1255; found 373.1253. UV-Vis λ_{max} (50:50 DMF:H₂O, nm) 350, 460. $E_{1/2}$ (V) 0.251.



4-Pentylbenzoylferrocene (31): Prepared according to the General Procedure A using commercially available 4-pentylbenzoyl chloride. Yielded an orange solid

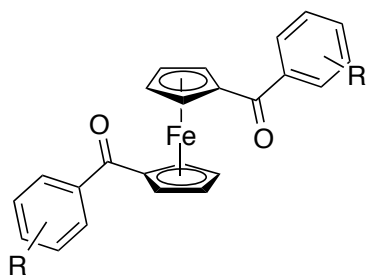
(76%). ^1H NMR (500 MHz, CDCl_3) δ 0.91 (t, $J_{\text{HH}} = 6.7$ Hz, 3H, CH_3), 1.38-1.35 (m, 4H, 2H, $\text{CH}_2\text{CH}_2\text{CH}_2\text{CH}_2\text{CH}_3$), 1.66 (m, 2H, $\text{CH}_2\text{CH}_2\text{CH}_2\text{CH}_2\text{CH}_3$), 2.68 (t, $J_{\text{HH}} = 7.5$ Hz, 2H, $\text{CH}_2\text{CH}_2\text{CH}_2\text{CH}_2\text{CH}_3$), 4.21 (s, 5H, C_5H_5), 4.57 (s, 2H, Cp'-H), 4.91 (s, 2H, Cp'-H), 7.28 (d, $J_{\text{HH}} = 8.0$ Hz, 2H, Aryl-H), 7.84 (d, $J_{\text{HH}} = 8.0$ Hz, 2H, Aryl-H); ^{13}C NMR (500 MHz, CDCl_3) δ 14.20 (pentyl- CH_3), 22.68 (pentyl- CH_2), 31.06 (pentyl- CH_2), 31.63 (pentyl- CH_2), 36.09 (pentyl- CH_2), 70.34 (C_5H_5), 71.70 (Cp'), 72.50 (Cp'), 78.56 (Cp'-*ipso*), 128.39 (Aryl), 137.36 (Aryl), 147.19 (Aryl), 198.98 (CO). IR (BaF_2 , cm^{-1}) 1163, 1291, 1376, 1442, 1558, 1616, 2849, 2992, 2945. HRMS (ESI-TOFMS) m/z calcd for $[\text{C}_{22}\text{H}_{25}\text{FeO}]^+$: 361.1125; found 361.1253. UV-Vis λ_{max} (50:50 DMF:H₂O, nm) 360, 486. $E_{1/2}$ (V) 0.251.



Cp*-(2,6-dichlorobenzoyl)ferrocene (32): Cp*CpFe (5.00 g, 26.9 mmol, 1 equiv) was dissolved in dichloromethane (107 mL, 0.25 M) and 2,6-dichlorobenzoyl chloride (3.75 mL, 29.6 mmol, 1.1 equiv) was added via syringe. The reaction mixture was cooled to 0 °C in an ice bath and anhydrous AlCl_3 (3.75 g, 29.6 mmol, 1.1 equiv) was added in three portions over a 15 minute period. The dark blue solution was allowed to warm to RT while stirring overnight (12 h). The reaction mixture was poured into a flask of ice water, extracted into 100 mL of CH_2Cl_2 , then washed successively with 10% NaOH solution, water, and brine. The organic layer

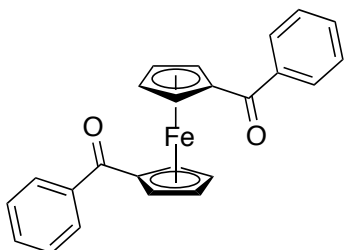
was dried over MgSO_4 , filtered, and the solvent removed under reduced pressure. Chromatography on SiO_2 gel with 90:10 hexanes:ethyl acetate as eluent led to isolation of the pure benzoylferrocene in 72% yield. ^1H NMR (500 MHz, CD_2Cl_2) δ 1.89 (s, 15H, Cp*), 4.14 (m, 4H, Cp), 7.37-7.29 (m, 3H, aryl); ^{13}C NMR (500 MHz, CD_2Cl_2) δ 11.08 (Cp*), 73.52 (Cp), 76.66 (Cp), 82.25 (Cp), 83.01 (Cp), 128.95 (aryl), 130.72 (aryl), 132.47 (aryl), 139.35 (aryl), 196.52 (CO). IR (NaCl, cm^{-1}) 844, 1032, 1449, 1694, 2850, 2914. HRMS (ESI-TOFMS) m/z calcd for $[\text{C}_{22}\text{H}_{23}\text{Cl}_2\text{FeO}]^+$ 429.0471; found 429.0473. UV-Vis λ_{max} (CD_3CN , nm) 382, 509. $E_{1/2}$ (V) 0.010.

Synthesis of 1,1'-Dibenzoylferrocenes

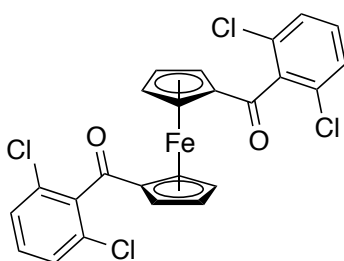


General Procedure B³¹: Ferrocene (5.00 g, 26.9 mmol, 1 equiv) was dissolved in anhydrous dichloromethane (107 mL, 0.25 M) with magnetic stirring and acid chloride (59.2 mmol, 2.2 equiv) was added via syringe. The reaction mixture was cooled to 0 °C in an ice bath and anhydrous AlCl_3 (7.5 g, 59.2 mmol, 2.2 equiv) was added in three portions over a 15 minute period. The dark blue solution was allowed to warm to RT while stirring overnight. The reaction mixture was poured into a flask of ice water, extracted into 100 mL of CH_2Cl_2 , then washed successively with 10% NaOH solution, water, and brine. The organic layer was dried over MgSO_4 ,

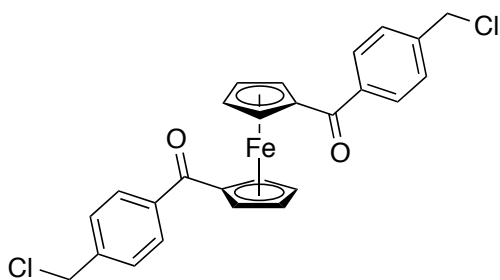
filtered, and the solvent removed under reduced pressure. Chromatography on SiO₂ gel with hexanes:ethyl acetate (80:10) as eluent led to isolation of the pure 1,1'-dibenzoylferrocenes.



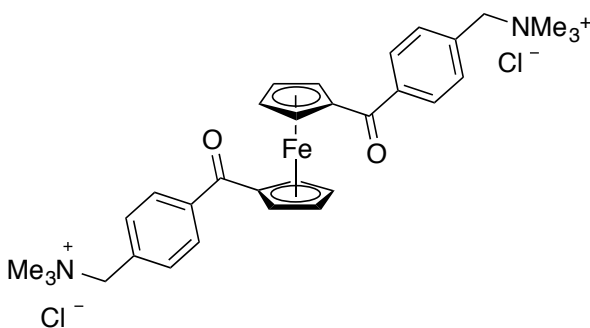
1,1'-Benzoylferrocene (34): Previously known compound prepared according to General Procedure B. Yielded a red solid (89%). Analytical data corresponded to that in the literature.³¹ UV-Vis λ_{max} (50:50 DMF:H₂O, nm) 352, 481. $E_{1/2}$ (V) 0.462.



1,1'-Bis(2,6-dichlorobenzoyl)ferrocene (35): Prepared according to General Procedure B using 2,6-dichlorobenzoyl chloride (76%). ¹H NMR (400 MHz, CD₂Cl₂) δ 4.75 (t, $J_{\text{HH}} = 1.9$ Hz, 4H, Cp), 4.79 (t, $J_{\text{HH}} = 1.9$ Hz, 4H, Cp), 7.37-7.33 (m, 6H, aryl); ¹³C NMR (500 MHz, CD₂Cl₂) δ 72.23 (Cp), 75.37 (Cp), 81.05 (Cp), 128.99 (aryl), 131.27 (aryl), 132.28 (aryl), 138.16 (aryl), 196.37 (CO). IR (NaCl, cm⁻¹) 1279, 1374, 1449, 1559, 1575, 1659. HRMS (ESI-MS) m/z calcd for [C₂₄H₁₅Cl₄FeO₂]⁺: 530.9172; found 530.9165. UV-Vis λ_{max} (50:50 DMF:H₂O, nm) 488. $E_{1/2}$ (V) 0.464.

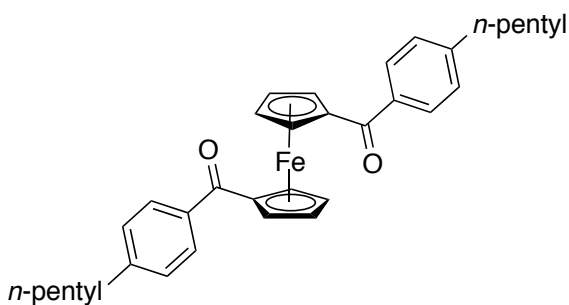


1,1'-Bis(4-chloromethylbenzoyl)ferrocene (36): Prepared according to General Procedure B using 4-chloromethylbenzoyl chloride (79%). ^1H NMR (400 MHz, CD_2Cl_2) δ 4.63-4.62 (m, 4H, Cp'), 4.68 (s, 4H, CH_2Cl), 4.90-4.89 (m, 4H, Cp'), 7.48 (d, J = 8.1 Hz, 4H, Aryl-H), 7.78 (d, J = 8.1 Hz, 4H, Aryl-H); ^{13}C NMR (400 MHz, CD_2Cl_2) δ 45.87 (CH_2), 73.28 (Cp), 74.61 (Cp), 79.78 (*ipso*-Cp), 125.04 (aryl), 128.73 (aryl), 139.21 (aryl), 141.42 (aryl), 196.89 (CO). IR (NaCl, cm^{-1}) 950, 1012, 1165, 1284, 1370, 1410, 1446, 1604, 1636, 2335, 2361. HRMS (ESI-TOFMS) m/z calcd for $[\text{C}_{26}\text{H}_{20}\text{Cl}_2\text{FeO}_2\text{Na}]^+$ 513.0087; found 513.0079. $E_{1/2}$ (V) 0.474.



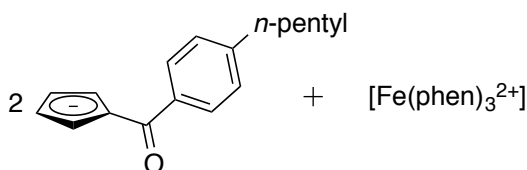
1,1'-Bis(4-N,N,N-trimethylmethanaminiumbenzoyl)ferrocene (37): **36** (1.00 g, 2.62 mmol, 1.00 equiv) was dissolved in THF (0.25 M, 10 mL) and trimethylamine (5 mL, 40% aqueous solution) was poured in at room temperature. The red solution was allowed to stir overnight at RT. Evaporation of the volatiles gave a dark red residue that was purified by SiO_2 chromatography with 95:5

dichloromethane:MeOH as eluent. If necessary, **37** was recrystallized from ethyl acetate and hexanes. Yielded 0.85 g of a red solid (89%). ^1H NMR (400 MHz, D_2O) δ 3.00 (s, 9H, CH_3), 4.45 (s, 4H), 4.74 (s, 4H), 4.86 (s, 4H), 7.52 (d, $J_{\text{HH}} = 7.8$ Hz, 4H, aryl), 7.72 (d, $J_{\text{HH}} = 7.8$ Hz, 4H, aryl); ^1H NMR (500 MHz, CD_3OD) δ 3.20 (s, 18H, RNMe_3), 4.72 (s, 4H, Cp), 4.78 (s, 4H, Cp), 4.95 (s, 4H, benzylic- CH_2), 7.74 (d, $J_{\text{HH}} = 8.1$ Hz, 4H, aryl), 7.92 (d, $J_{\text{HH}} = 8.1$ Hz, 4H, aryl); ^{13}C NMR (500 MHz, CD_3OD) δ 53.41 (CH_3), 69.64 (CH_2), 74.72 (Cp), 76.07 (Cp), 80.49 (Cp), 129.87 (aryl), 132.63 (aryl), 134.29 (aryl), 142.26 (aryl), 198.97 (CO). IR (BaF_2 , cm^{-1}) 1279, 1440, 1640, 2945, 3006. HRMS (ESI-TOFMS) m/z calcd for $[\text{C}_{32}\text{H}_{38}\text{FeN}_2\text{O}_2]^{2+}$: 269.1136; found 269.1140. UV-Vis λ_{max} (H_2O , nm) 333, 478.



1,1'-Bis(4-*n*-pentylbenzoyl)ferrocene (39): Prepared according to General Procedure B using commercially available 4-pentylbenzoylchloride. Yielded a red solid (70%). ^1H NMR (400 MHz, CD_2Cl_2) δ 0.91 (t, $J = 6.7$ Hz, 6H, CH_3), 1.35 (m, 8H, CH_2CH_2), 1.65 (m, 4H, CH_2), 2.67 (t, $J_{\text{HH}} = 7.7$ Hz, 4H, CH_2 -benzylic), 4.56 (s, 4H, Cp), 4.87 (s, 4H, Cp), 7.24 (d, $J_{\text{HH}} = 8.1$ Hz, 4H, aryl), 7.71 (d, $J_{\text{HH}} = 8.1$ Hz, 4H, aryl); ^1H NMR (400 MHz, CD_3CN) δ 0.91 (t, $J_{\text{HH}} = 6.8$ Hz, 6H), 1.38-1.34 (m, 8H), 1.65 (dt, $J_{\text{HH}} = 14.8, 7.6$ Hz, 4H), 2.68 (t, $J_{\text{HH}} = 7.6$ Hz, 4H), 4.61 (t, $J_{\text{HH}} = 1.8$ Hz, 4H), 4.84 (t, $J_{\text{HH}} = 1.8$ Hz, 4H), 7.27 (d, $J = 8.2$ Hz, 4H), 7.71 (d, $J = 8.2$ Hz, 4H); ^{13}C NMR (500 MHz, CD_2Cl_2)

δ 14.15 (pentyl), 22.87 (pentyl), 31.28 (pentyl), 31.85 (pentyl), 36.21 (pentyl), 73.30 (Cp), 74.59 (Cp), 80.22 (Cp), 128.58 (aryl), 128.61 (aryl), 136.98 (aryl), 147.87 (aryl), 197.36 (CO). IR (BaF₂, cm⁻¹) 857, 1277, 1562, 1601, 1624, 2861, 2931. HRMS (ESI-TOFMS) m/z calcd for [C₃₄H₃₉FeO₂]⁺: 535.2295; found 535.2294. UV-Vis λ_{\max} (DMF, nm) 348, 476. E_{1/2} (V) 0.441.



[Bis-4-*n*-pentylbenzoylcyclopentadienylanion]Iron(tris-phenanthroline) (40-

phen): Complex **39** (50 mg, 0.10 mmol, 1 equiv) and 1,10-phenanthroline (51 mg, 0.28 mmol, 3 equiv) were added to a Teflon-sealed NMR tube and dry, degassed acetonitrile was added by distillation on a Schlenk line. The red solution was photolyzed for 12 h (> 450 nm) at RT. The volatiles were removed under reduced pressure and pure **40-phen** was obtained by recrystallization from acetonitrile, toluene, and pentane (1:1:1; 76%, red solid). ¹H NMR (400 MHz, CD₃CN) δ 0.87 (t, J = 7.8 Hz, 6H), 1.32-1.26 (m, 8H), 1.58 (s, 4H), 2.58 (s, 4H), 5.74 (s, 4H), 6.18 (s(br), 4H), 7.09 (s(br), 4H), 7.54 (10H), 7.62 (dd, J = 5.2, 1.2 Hz, 6H), 8.22 (s, 6H), 8.57 (dd, J = 8.2, 1.2 Hz, 6H). IR (NaCl, cm⁻¹) 1346, 1418, 1463, 1521, 1565, 2853, 2917, 3039. HRMS (ESI-TOFMS) m/z calcd for cation [C₃₆H₂₄FeN₆]²⁺: 298.0701; found 298.0698. HRMS (ESI-TOFMS) m/z calcd for anion [C₁₇H₁₉O]⁻: 239.1441; found 239.1438.

General Tissue Culture Methods

Cell Lines and Growth Conditions: All cell lines were purchased from ATCC. HeLa, A549, HEK-293, L929 and MRC-5 cells were cultivated as a monolayer cultures at 37 °C in a humidified atmosphere (95% air, 5% carbon dioxide) in 25 cm² culture flasks using DMEM supplemented with FBS 5% (V/V), non-essential amino acids (1%), sodium pyruvate (1%), GlutaMax (1%), and antibiotics (penicillin/streptomycin, 1%) as growth medium. All cell seeding and manipulations were carried out in a sterile laminar flow hood unless noted otherwise. Passage into a fresh flask was done at 80-90% confluency as needed. At the time of passage, the old medium was removed by pipette and the cells were washed with 5 mL of sterile dPBS. Trypsin solution (1x) was washed gently over the cells and the flask was incubated for 10 min to detach the cells. Following treatment with trypsin, the cells were resuspended in fresh medium and a 0.2 mL aliquot of cell suspension was added to a fresh flask with new medium.

HeLa: Cells were passaged every 3-4 days, and no medium change was necessary.

A549: Cells were passaged every 3-4 days, and no medium change was necessary.

L929: Cells were passaged every 5-6 days, and no medium change was necessary.

MRC-5: Cells were passaged every 6-7 days, and no medium change was necessary.

HEK-293: Cells were passaged every 4-5 days, and no medium change was necessary.

All micro-plate UV-Vis data was collected using a PerkinElmer Health Sciences Inc., EnSpire multimode basic unit plate reader. Images of cells at various

stages of drug exposure were taken using a Axio Vert.A1 inverted microscope equipped with Zen lite 2012 software. For all reverse phase-high pressure liquid chromatography experiments, isocratic solvent systems were used in which Buffer A was 0.1% TFA in water and Buffer B was 0.1% TFA in acetonitrile. Experiments were conducted at 1150 psi with a flow rate of 1 mL/min. Iron quantification was determined using a model 3000DV Perkin Elmer inductively coupled plasma-optical emission spectrometer (ICP-OES) in the laboratory of Dr. Paterno Castillo at the Scripps Institution of Oceanography.

***In-Vitro* Cell Viability Assays**

The cytotoxicity of the ferrocene complexes and their photoproducts were determined by the effect on growth rate as quantified by crystal violet staining at the end of drug exposure. Cells were seeded in 100 μ L of media in 96-well plates at a density specific to the cell line: HeLa (3.5×10^4 cells/well), A549 (3.5×10^4 cells/well), L929 (3.5×10^4 cells/well), HEK-293 (3.0×10^4 cells/well), and MRC-5 (5.0×10^4 cells/well). After incubation for 24 h at 37°C the cells were exposed to various concentrations of drug containing media for 24 h. At this time, the dark plate was left in the incubator and an identically prepared plate was illuminated with a Richee 2014-SLT-CW/WW 50W Flood Light (0.031 W) for 3 hours with a 455 nm long pass filter (Pol filter 152x100x3mm GG455) resting on top of the 96 well plate. Temperature during photolysis was kept constant at 37°C using a Denville Incubloc solid aluminum block. 48 h after photolysis, the cell cultures were fixed with 4%

paraformaldehyde, washed three times with DPBS, and stained with crystal violet. The absorbance at 595 nm was measured for each well using a microplate reader scanning spectrophotometer. Cytotoxicity was then determined using equation 1. In assays using the weakly adherent HEK-293 cells, toxicity was determined by use of CellTiter-Blue (Promega). Each experiment was performed in at least triplicate.

$$\frac{(\text{Absorbance}_{\text{drug containing wells}} - \text{Absorbance}_{\text{control wells}})}{\text{Absorbance}_{\text{control wells}}}$$

(Equation 1)

Cell Imaging: HeLa cells treated with **30** were imaged at various stages of light exposure in parallel with cells allowed to remain under exclusion of light.

Cytotoxicity of 30 and 31 Photoproducts in HeLa and A549 cells: HeLa and A549 cells were seeded in 100 μL of media in 96-well plates. After incubation for 48 h the cells were exposed to serial concentrations of photoproduct containing media. The DMEM solutions of the photoproducts were prepared using photolysis conditions identical to those used in the cell viability studies and were added to the 96-well plates immediately post-photolysis. 48 hours after addition, the cell viability was determined using the crystal violet staining assay described above. Each experiment was performed in at least triplicate.

Cytotoxicity Experiment Using Washed A549 Cells: A549 cells were seeded in 100 μL of media in 96-well plates. 24 h later the cells were exposed to varying concentrations of **31**. After exposure to the organoferrous pro-drug for 24 h, the media containing extracellular **31** was removed by use of a multichannel pipette. Each well was then washed three times with 100 μL warm dPBS to remove any

residual **31** and 200 μL of fresh DMEM media was added to each well. The 96-well plates were then immediately irradiated using the same conditions used for the cell viability assays. Cell viability was determined 48 h post photolysis using the crystal violet staining assay. The experiment was performed in triplicate.

Illumination Time Experiments: 96-well plates containing HeLa cells were seeded as previously described. 24 h later the cells were then exposed to serial concentrations of **30** containing media. 24 h post pro-drug exposure, the cells were photolyzed for 1 h, 2 h, 3 h or 5 h. Cell viability was determined 48 h post photolysis by the crystal violet staining assay. Each experiment was performed in at least triplicate.

Lipophilicity Determinations

Linear Correlation of Retention Time and log(P): Nine compounds for which the $\log(P)$ is known³⁴ were used to correlate reverse phase HPLC retention time to $\log(P)$ as described by Veith and coworkers.³² Each small molecule was injected separately, chromatographed isocratically (MeCN:water 55:45), and the observed retention time (t_R) and dead time (t_0) were used to calculate $\log(k)$ using Equation 2.

$$k = (t_r - t_0)/t_0$$

(Equation 2)

The data was then plotted using the experimental $\log(k)$ and literature $\log(P)$ ³⁴ values and the data was fit using a linear regression (Equation 3).

$$y = 2.9257x + 1.5648$$
$$R^2 = 0.96116$$

(Equation 3)

Unknown Lipophilicity Determinations: Benzoylferrocene complexes were prepared as solutions in MeCN and chromatographed individually under conditions identical to that of the standards. Their $\log(P)$ values were obtained using the observed retention time, column dead time, and Equation 3. Results are reported as the mean of three independent experiments.

Iron Accumulation Studies

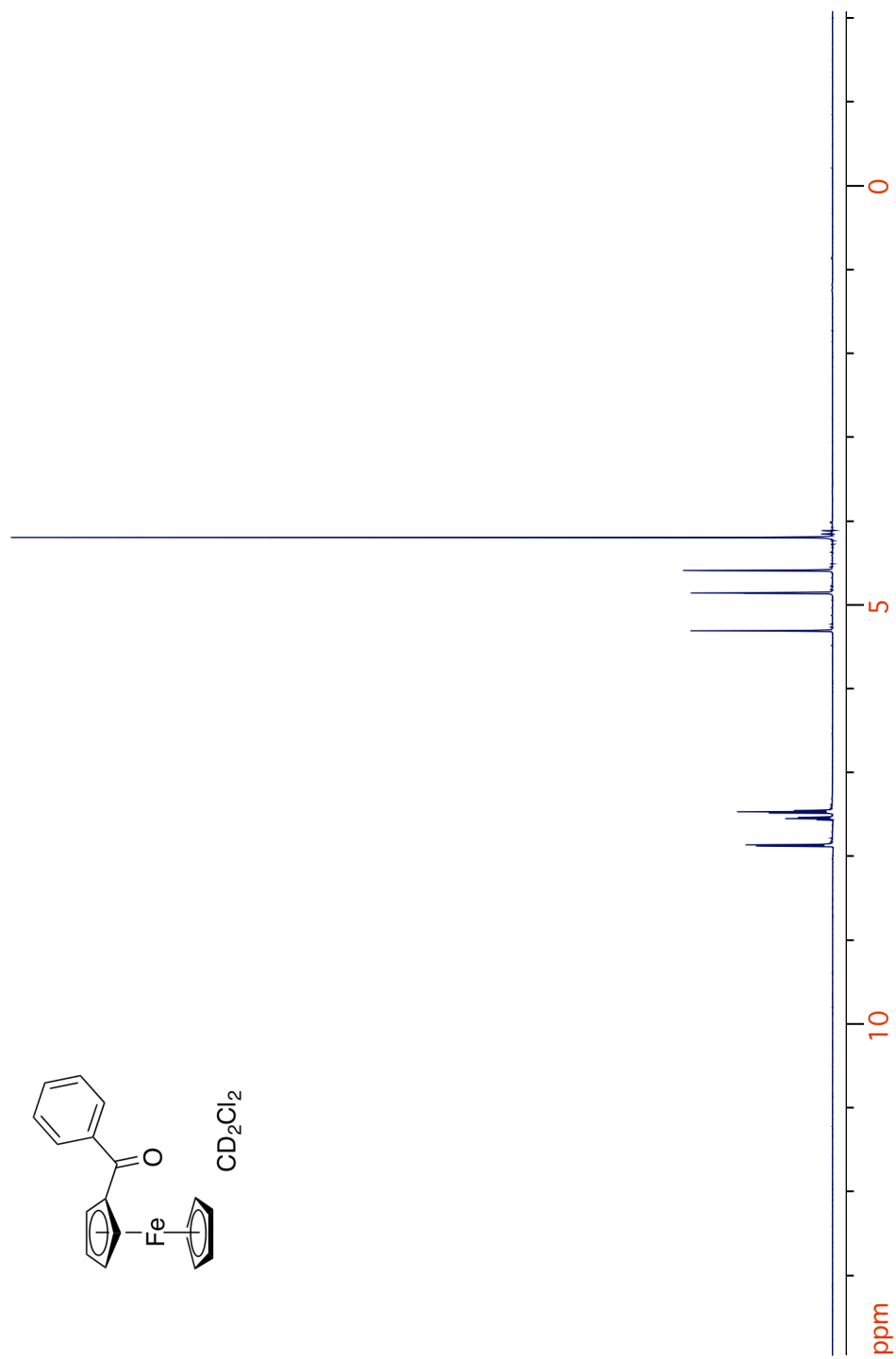
Cell Cultivation, Addition of Complexes, and Cell Harvesting: HeLa cells were cultivated as a monolayer in 75 cm² flasks under conditions previously described. For each drug containing flask a separate control flask was also prepared. The substances were diluted in DMF (**7**, **31**) or water (FeSO₄ and **21**) then added to FBS-free cell growth medium. The HeLa cells were exposed to the drug containing media for a period of two hours then the media was removed by pipette and the cell monolayer was washed gently three times with 10 mL of warm dPBS. The cells were then treated with 3 mL of 1x trypsin for ten minutes and resuspended in 10 mL of fresh FBS-free media. The cell suspension was subsequently centrifuged at 1200 rpm (4 °C) for 5 min, and the pellets were washed twice with 10 mL of dPBS between additional centrifugation cycles. The pellets were drained 10 minutes then stored at -18 °C until analysis.

Determination of Protein Concentration: The cell pellets were homogenized in 5

mL of 0.001% Triton X-100 solution by vortexing followed by sonication (5 x 5 s). 1 mL was removed for protein quantification and the remaining 4 mL were lyophilized in preparation for iron quantification. Protein concentration was determined by the Bradford method³⁶ using the commercially available Bio-Rad Protein Assay Dye Reagent Concentrate #500-0006 prepared per the manufacturer's instructions. Protein standards were prepared using human serum albumin (HSA) in 0.001% Triton X-100 solution. As Triton X-100 is a known interfering substance, additional dilutions of the protein standards were done using an identical concentration of the detergent. A calibration curve was constructed by calculating the 590/450 nm absorbance ratio using a micro-plate reader. The protein concentration of the cell lysates were determined as described by Zor and Selinger (see discussion section).⁵⁵

Determination of Iron Concentration: The lyophilized samples were dissolved in 115 μ L of concentrated nitric acid and heated at 65°C for 6 h. The samples were then diluted to a total volume of 4 mL using 0.1% Triton X-100 and the iron concentration (ng/g) was determined by ICP-OES. The iron concentration was then related to the protein concentration to account for differences in biomass between separate flasks. Results are expressed as an average of three independent experiments.

F. Appendix 1

Figure 2.30. ^1H NMR spectrum of 7.

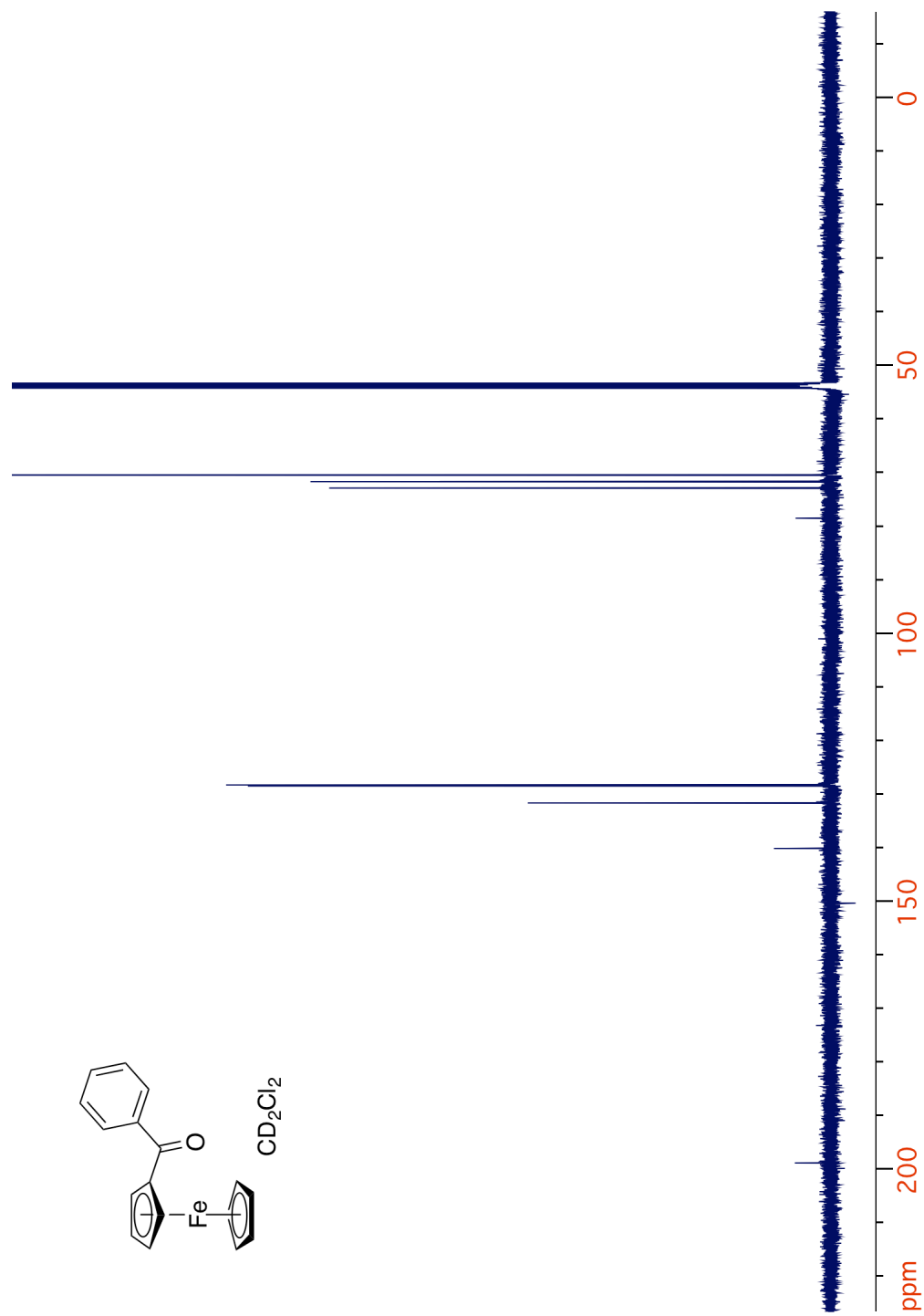


Figure 2.31. ^{13}C NMR spectrum of 7.

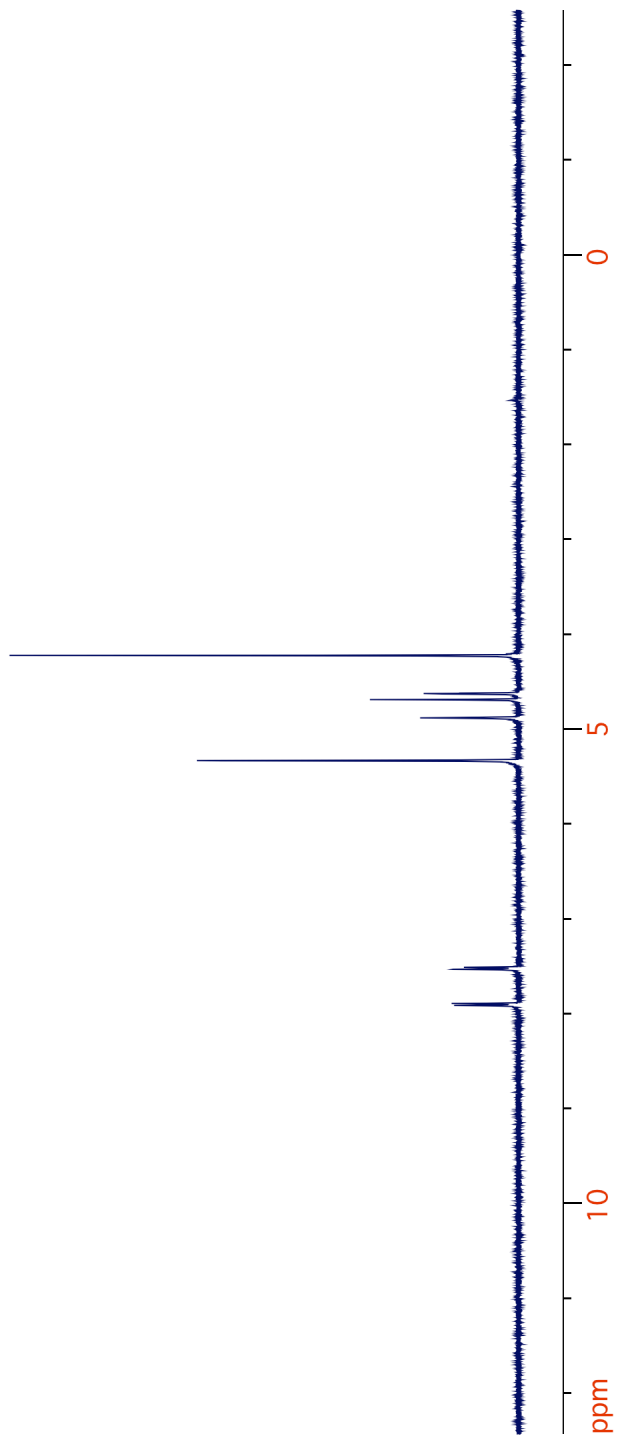
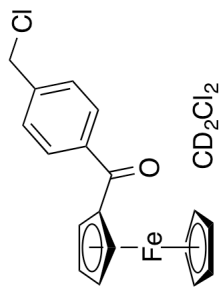
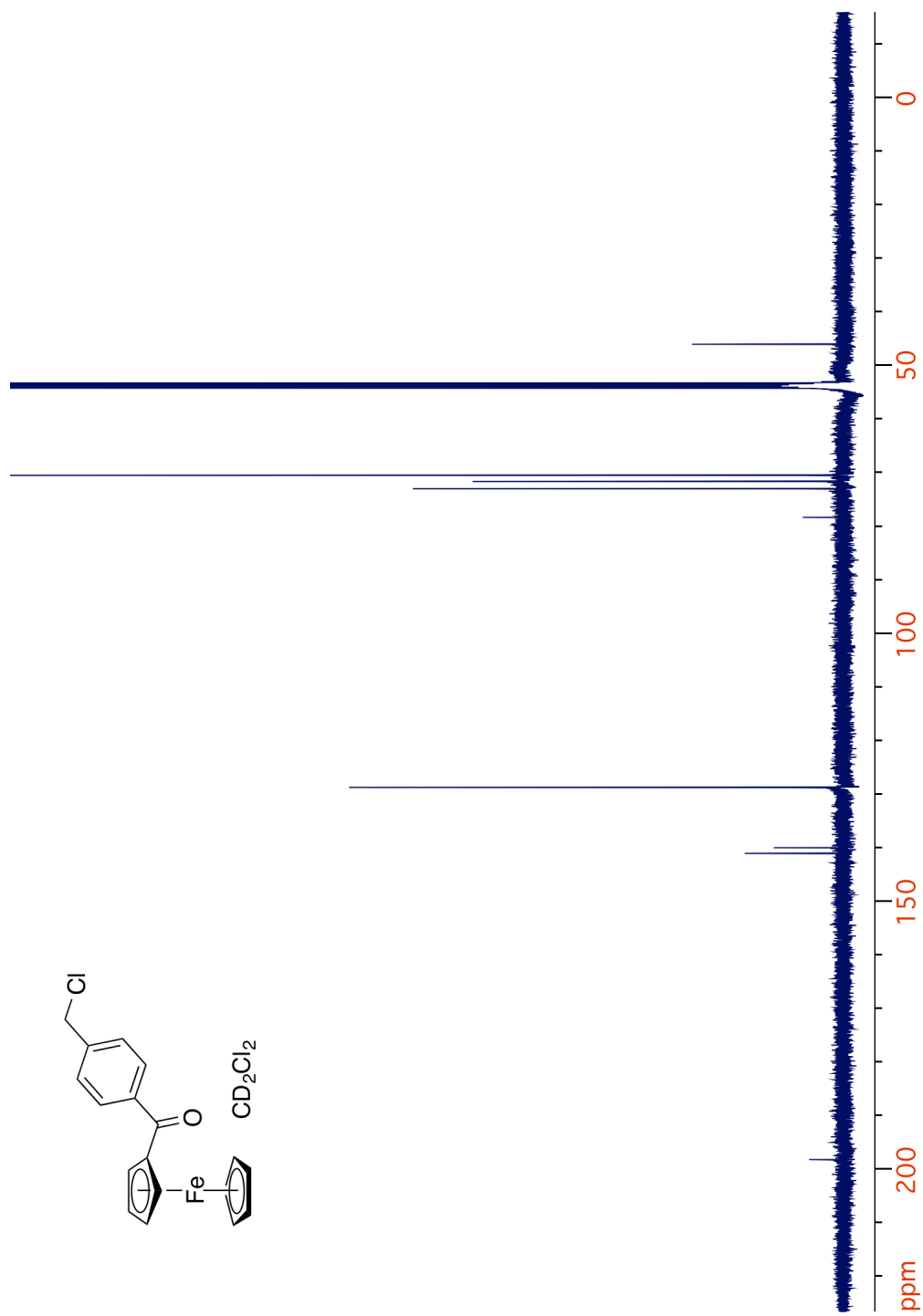


Figure 2.32. ¹H NMR spectrum of 13.

Figure 2.33. ^{13}C NMR spectrum of 13.

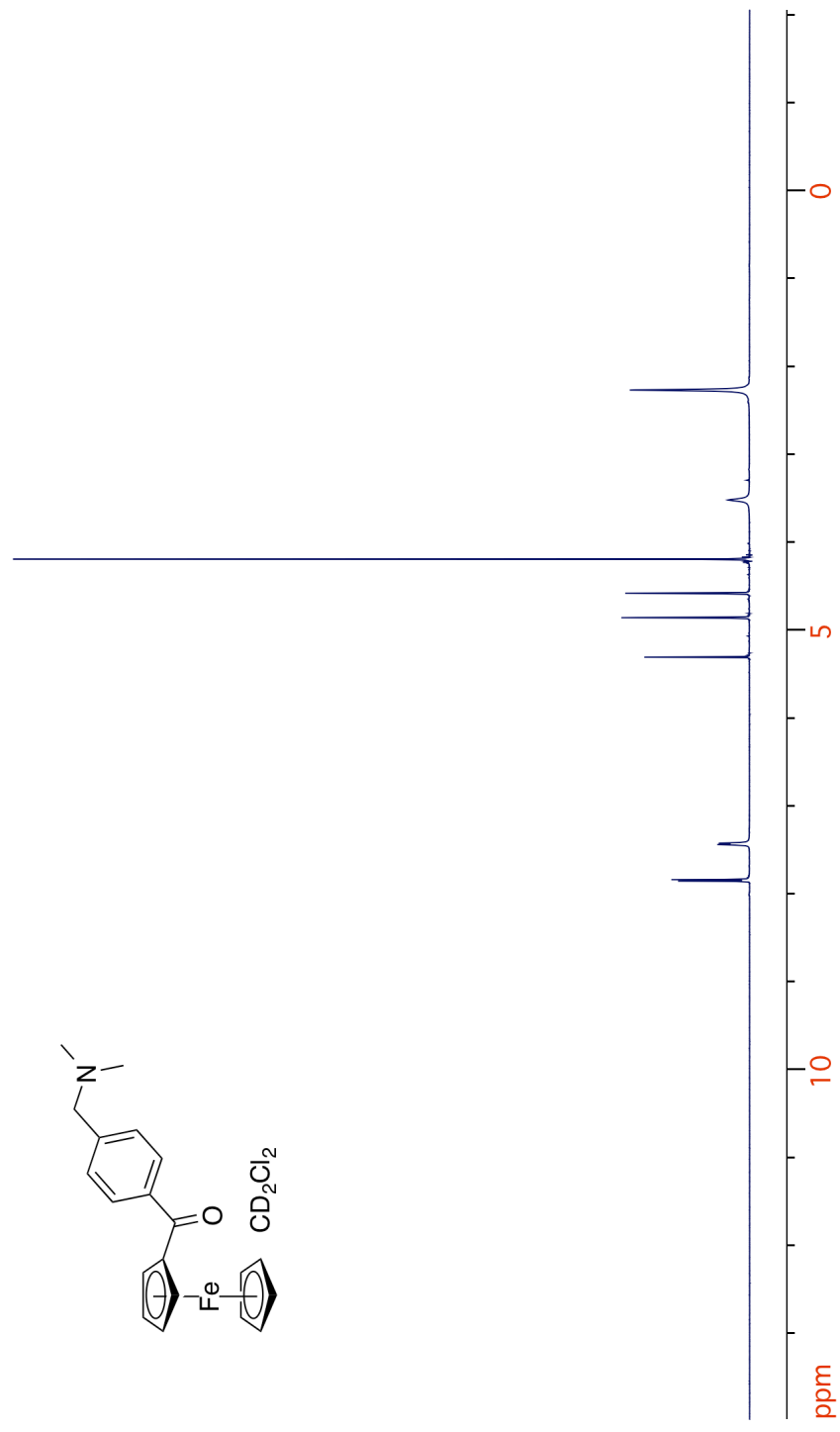
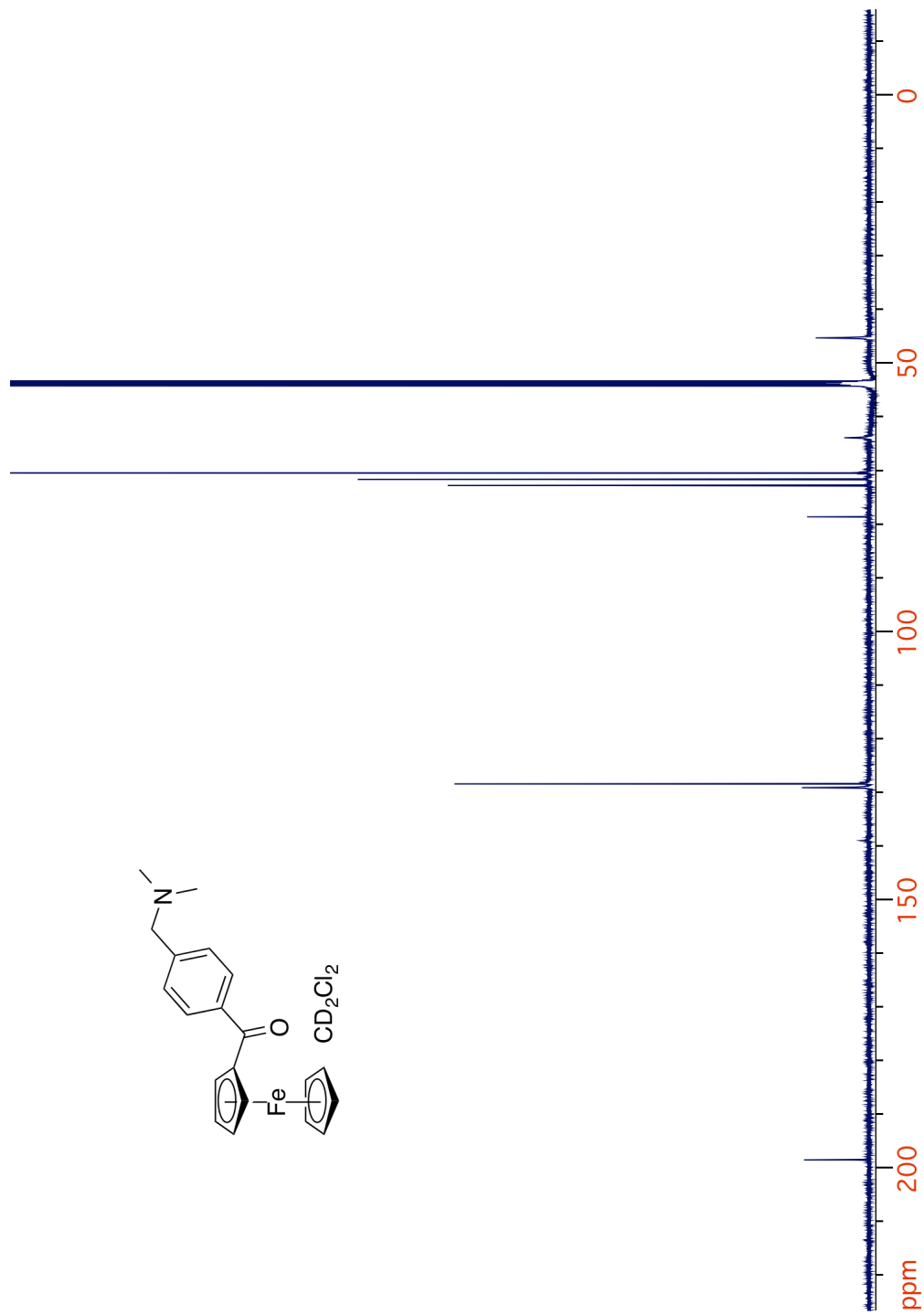


Figure 2.34. ¹H NMR spectrum of 14.

Figure 2.35. ^{13}C NMR spectrum of **14**.

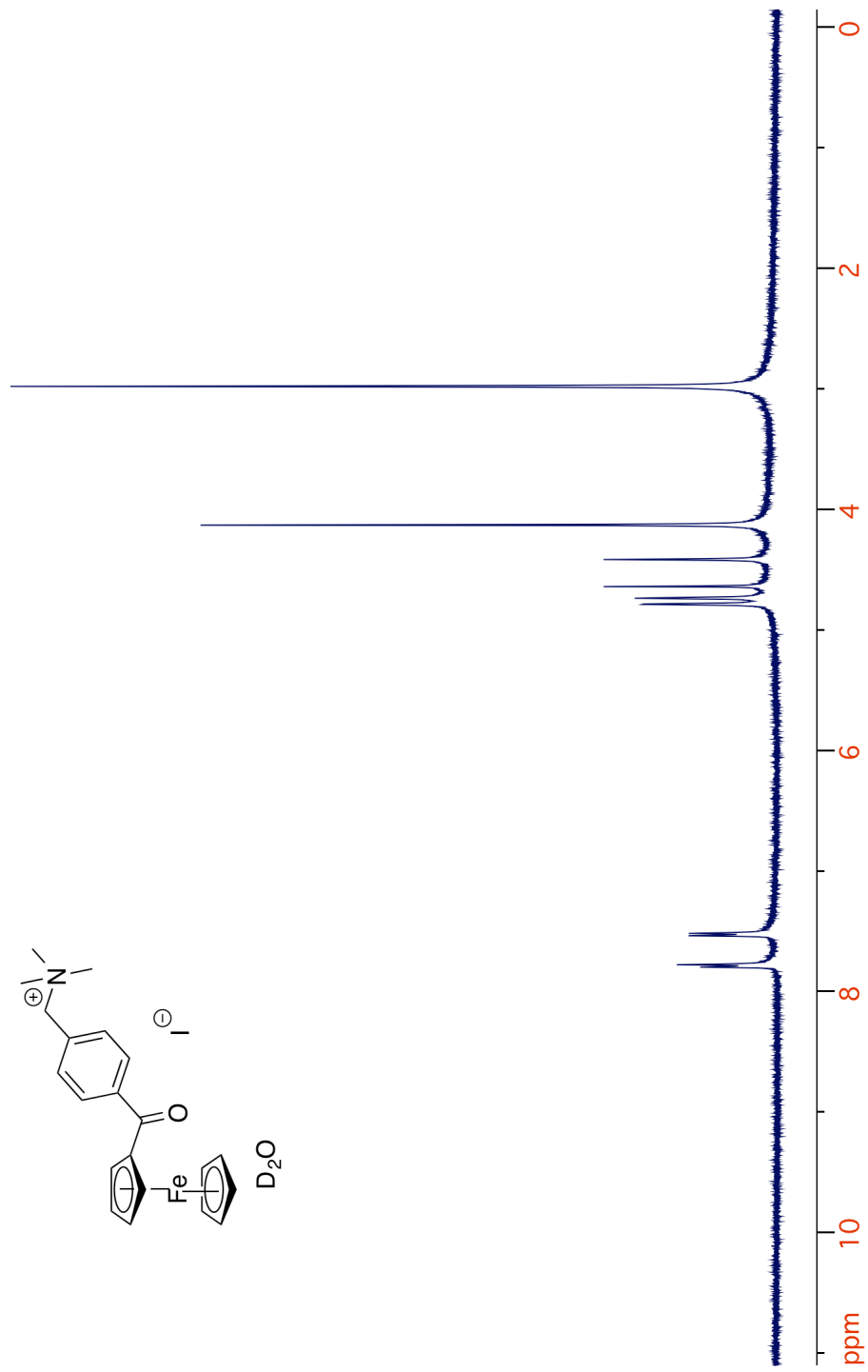
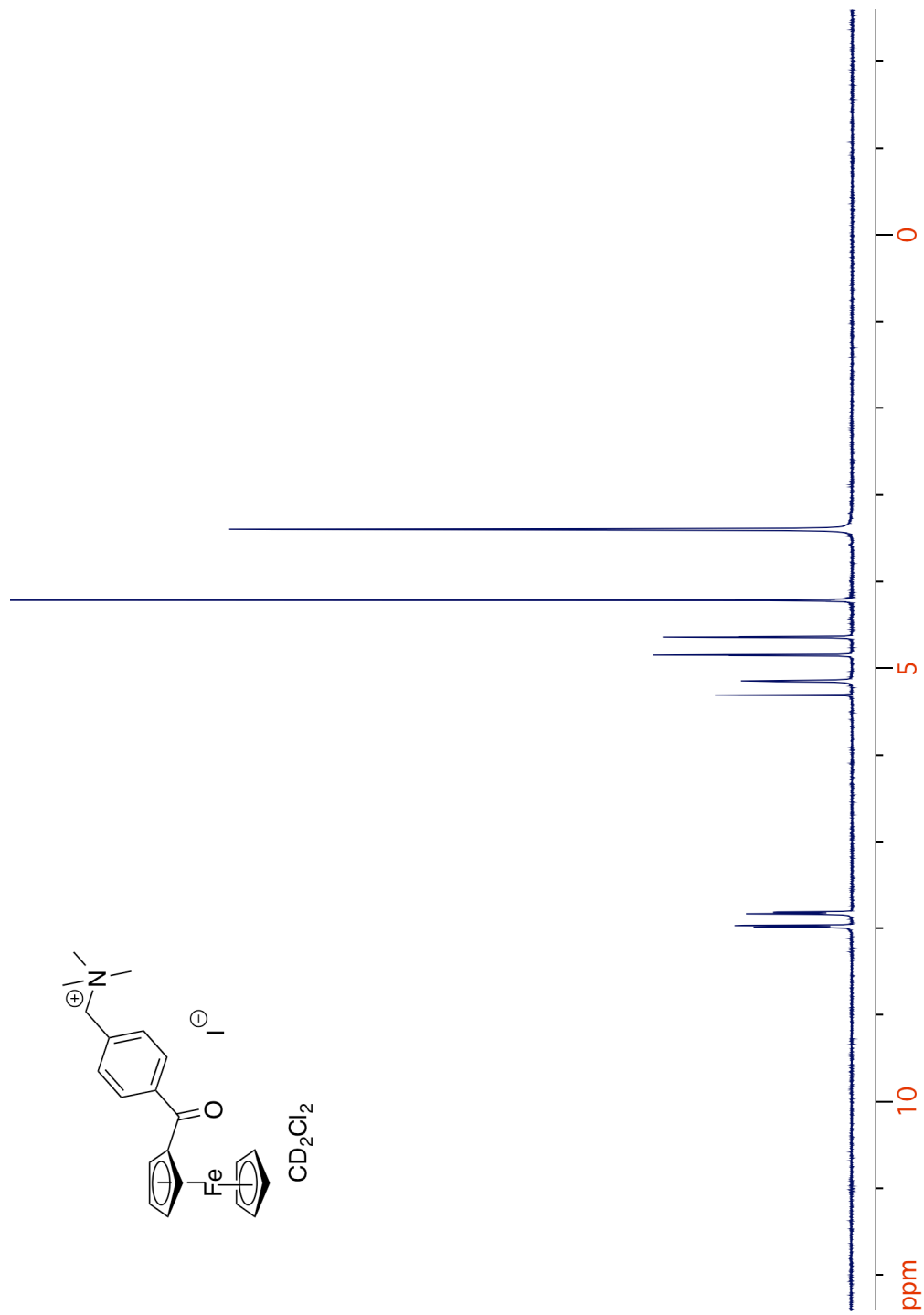
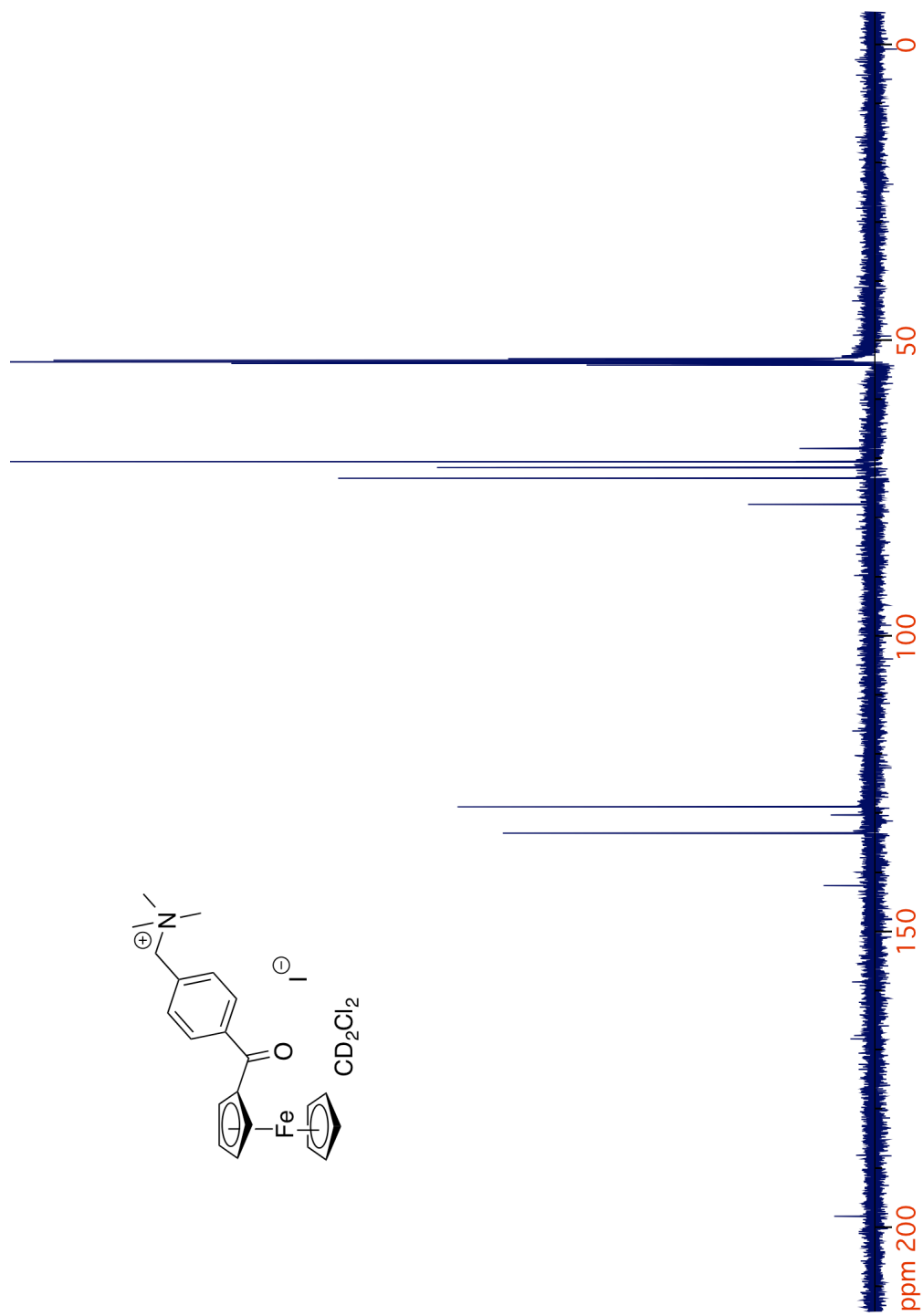
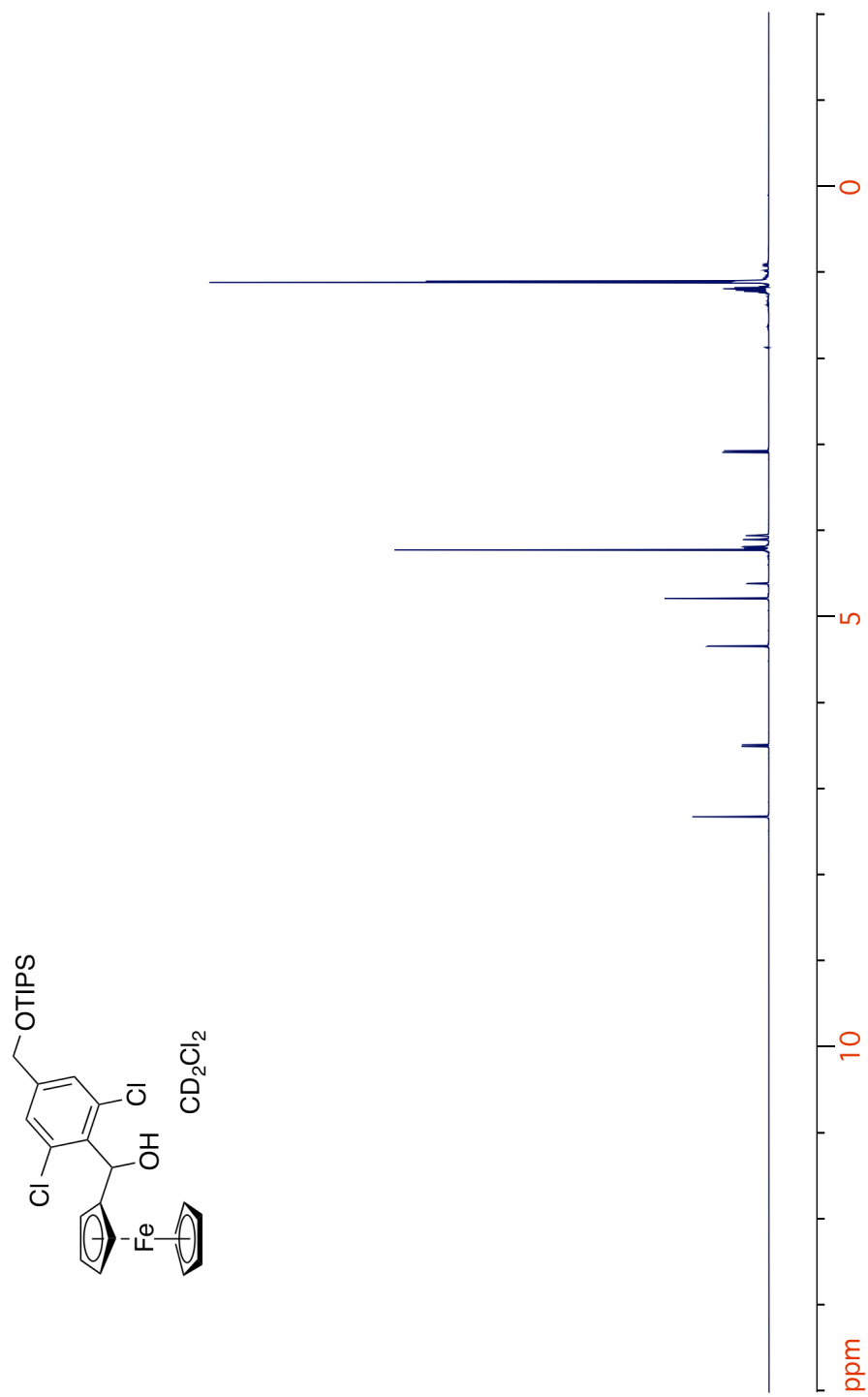


Figure 2.36. 1H NMR spectrum of 15.

Figure 2.37. ^1H NMR spectrum of **15**.

Figure 2.38. ^{13}C NMR spectrum of 15.

Figure 2.39. ^1H NMR spectrum of **18**.

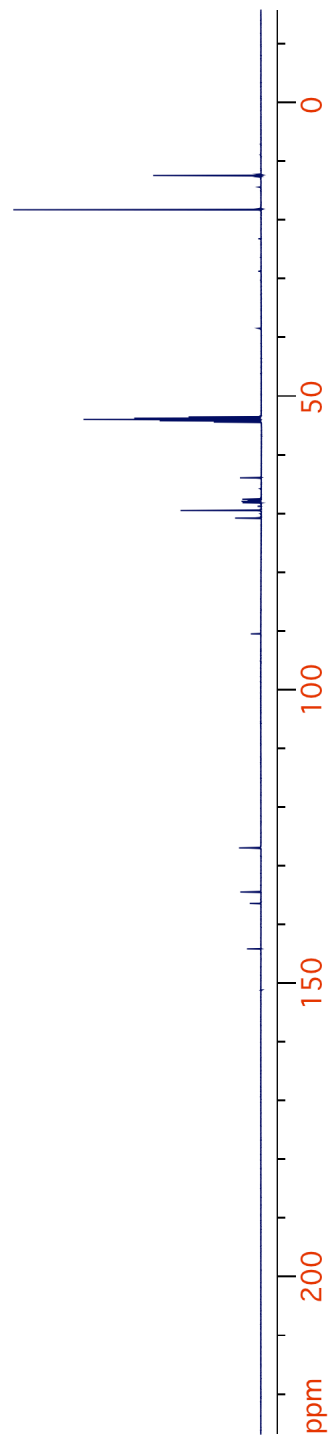
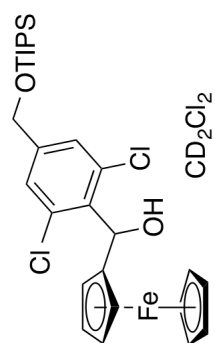


Figure 2.40. ¹³C NMR spectrum of 18.

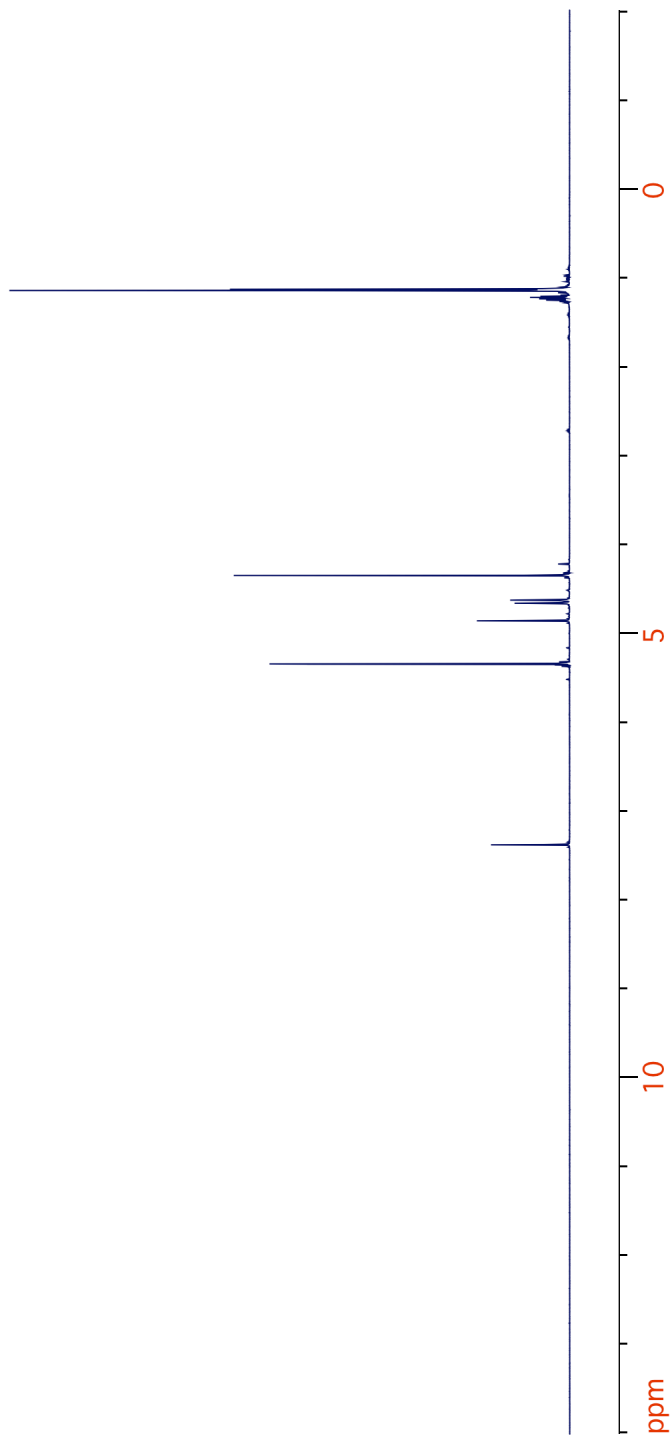
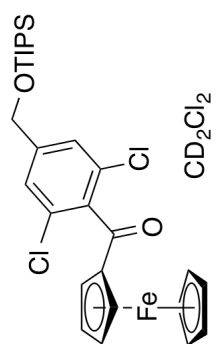


Figure 2.41. ¹H NMR spectrum of 19.

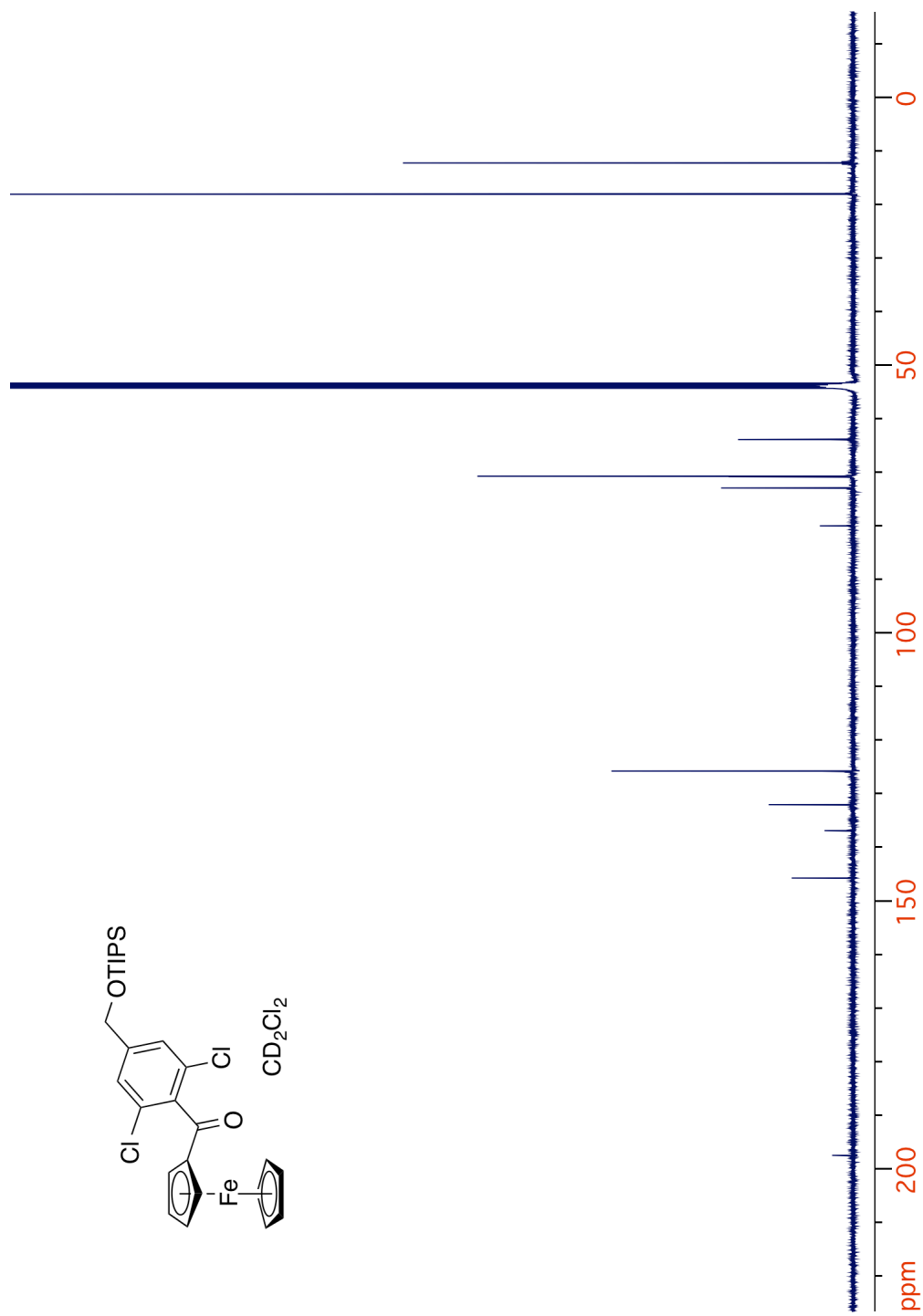


Figure 2.42. ^{13}C NMR spectrum of **19**.

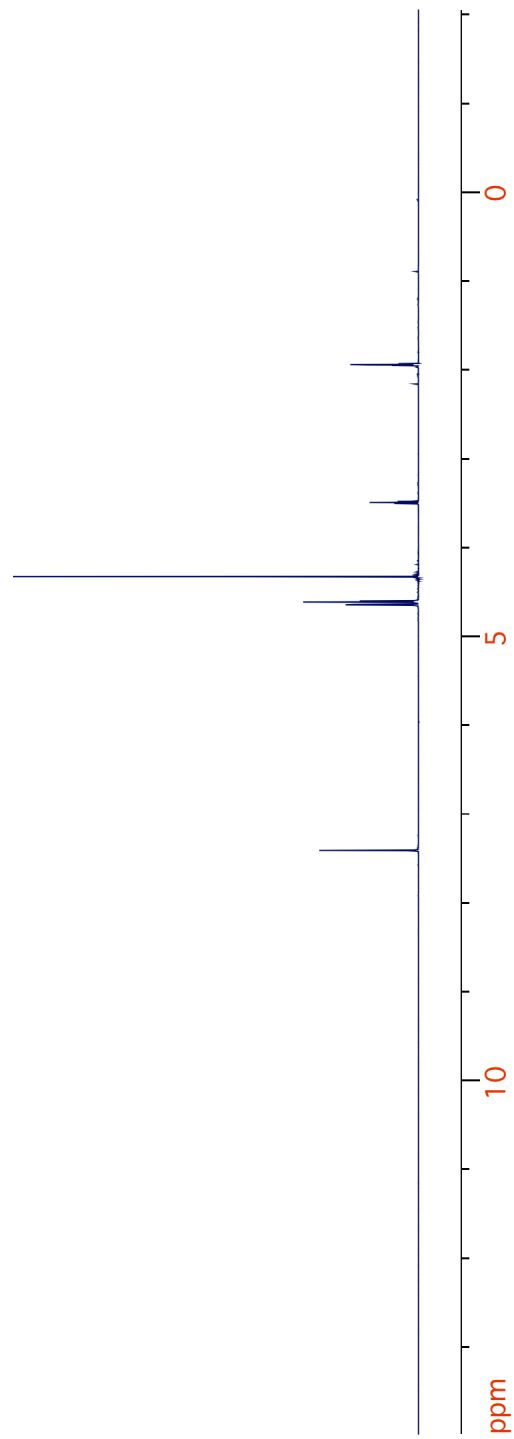
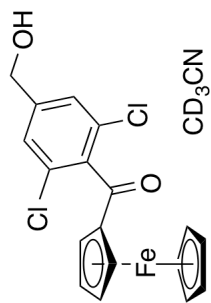


Figure 2.43. ¹H NMR spectrum of 20.

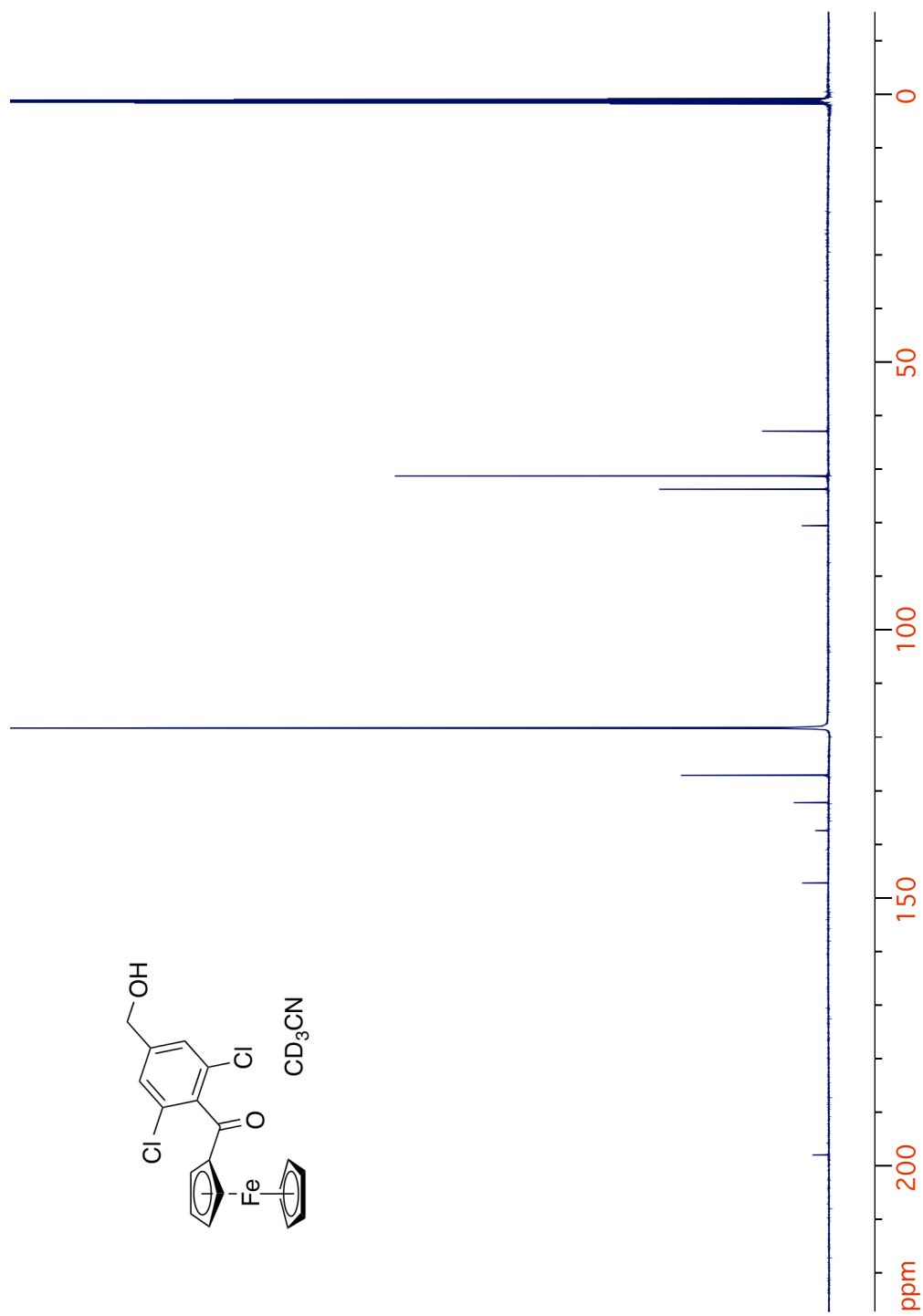


Figure 2.44. ^{13}C NMR spectrum of **20**.

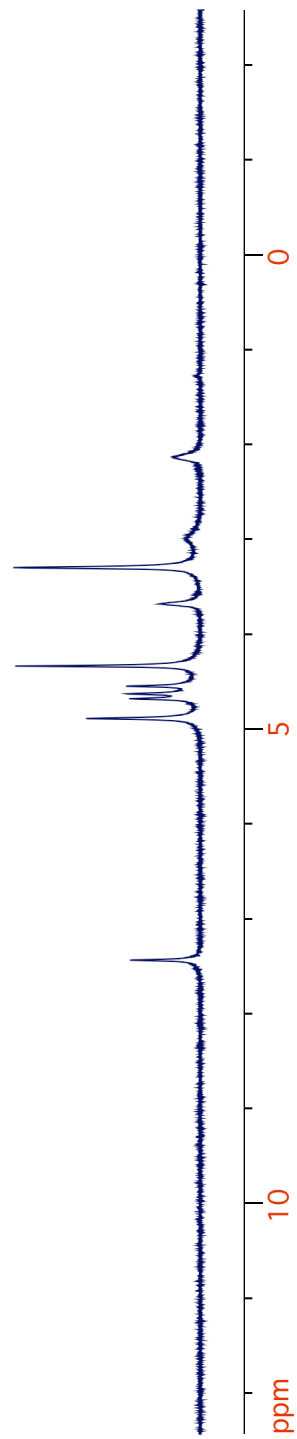
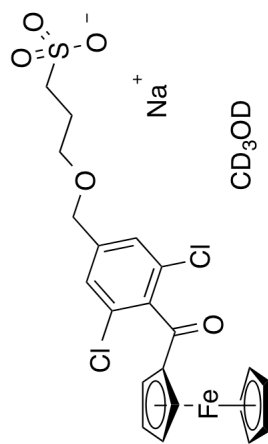
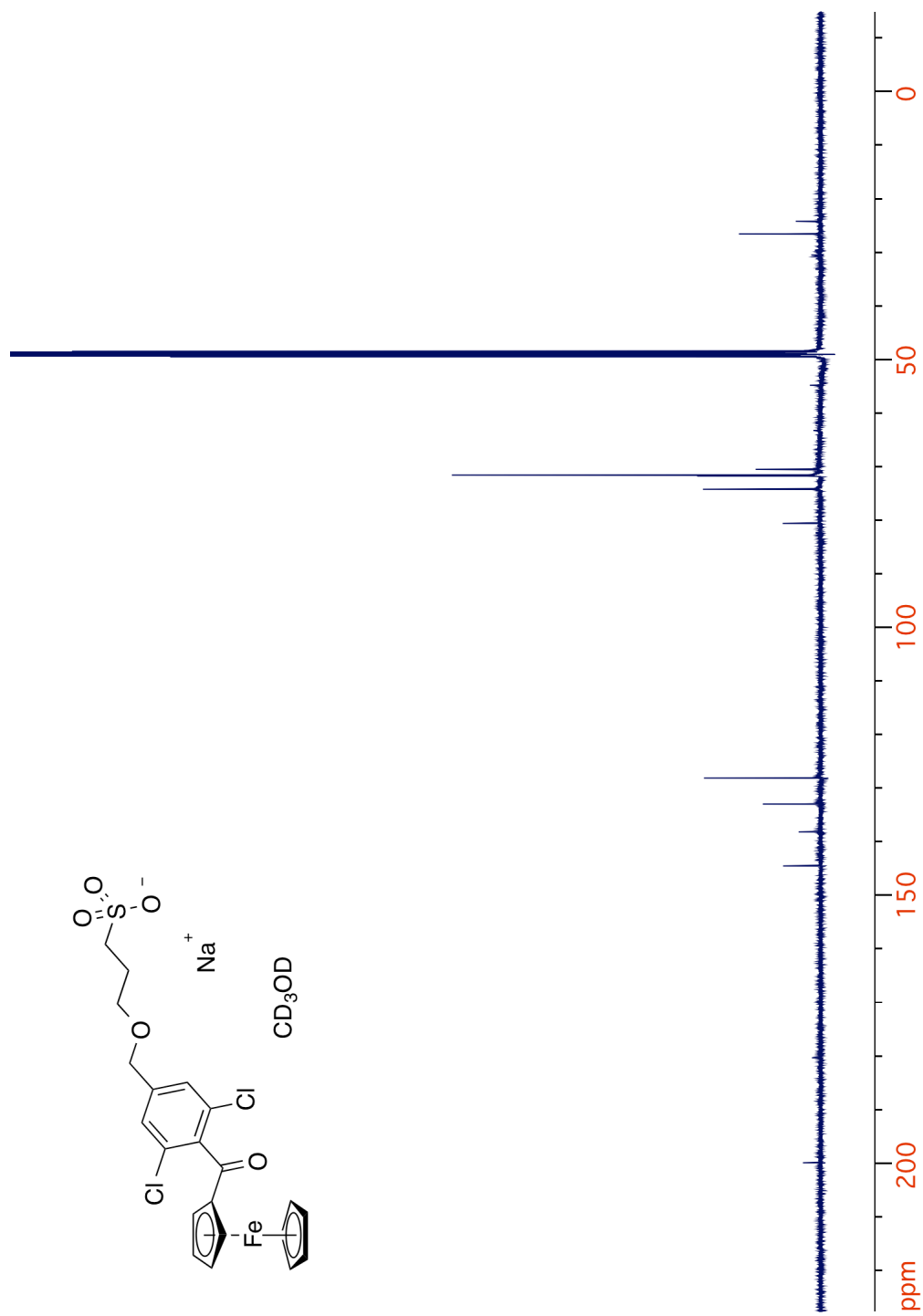


Figure 2.45. ¹H NMR spectrum of 21.

Figure 2.46. ^{13}C NMR spectrum of 21.

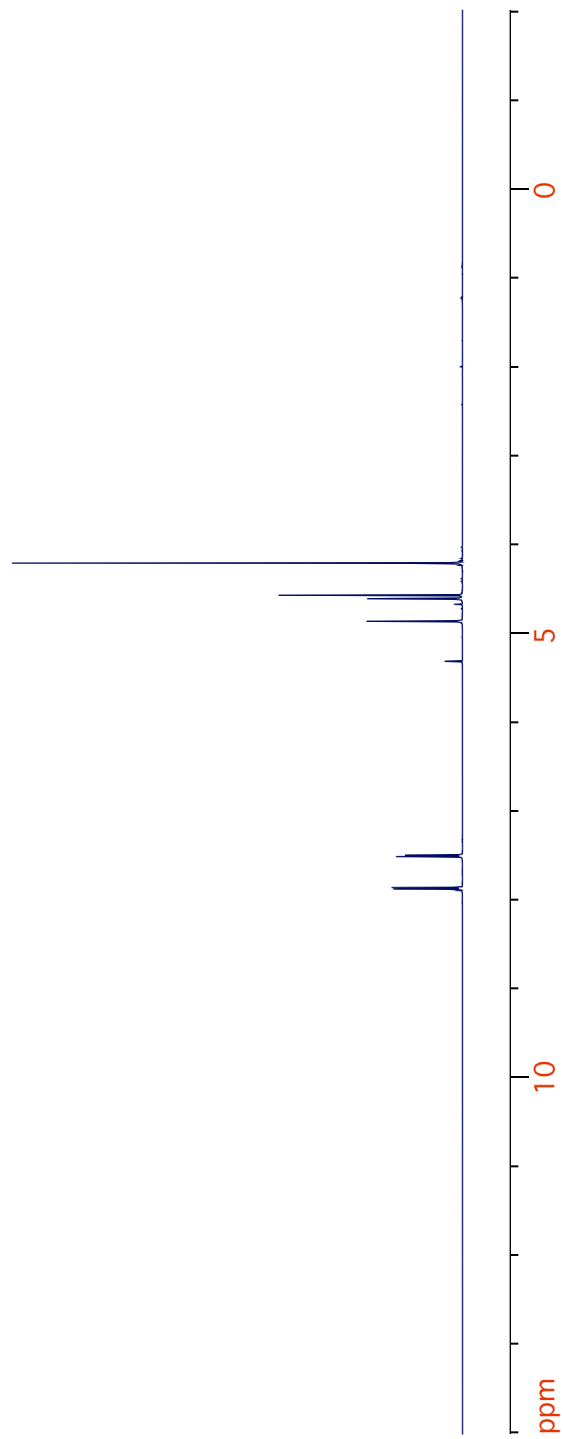
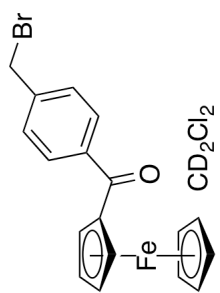


Figure 2.47. ¹H NMR spectrum of **22**.

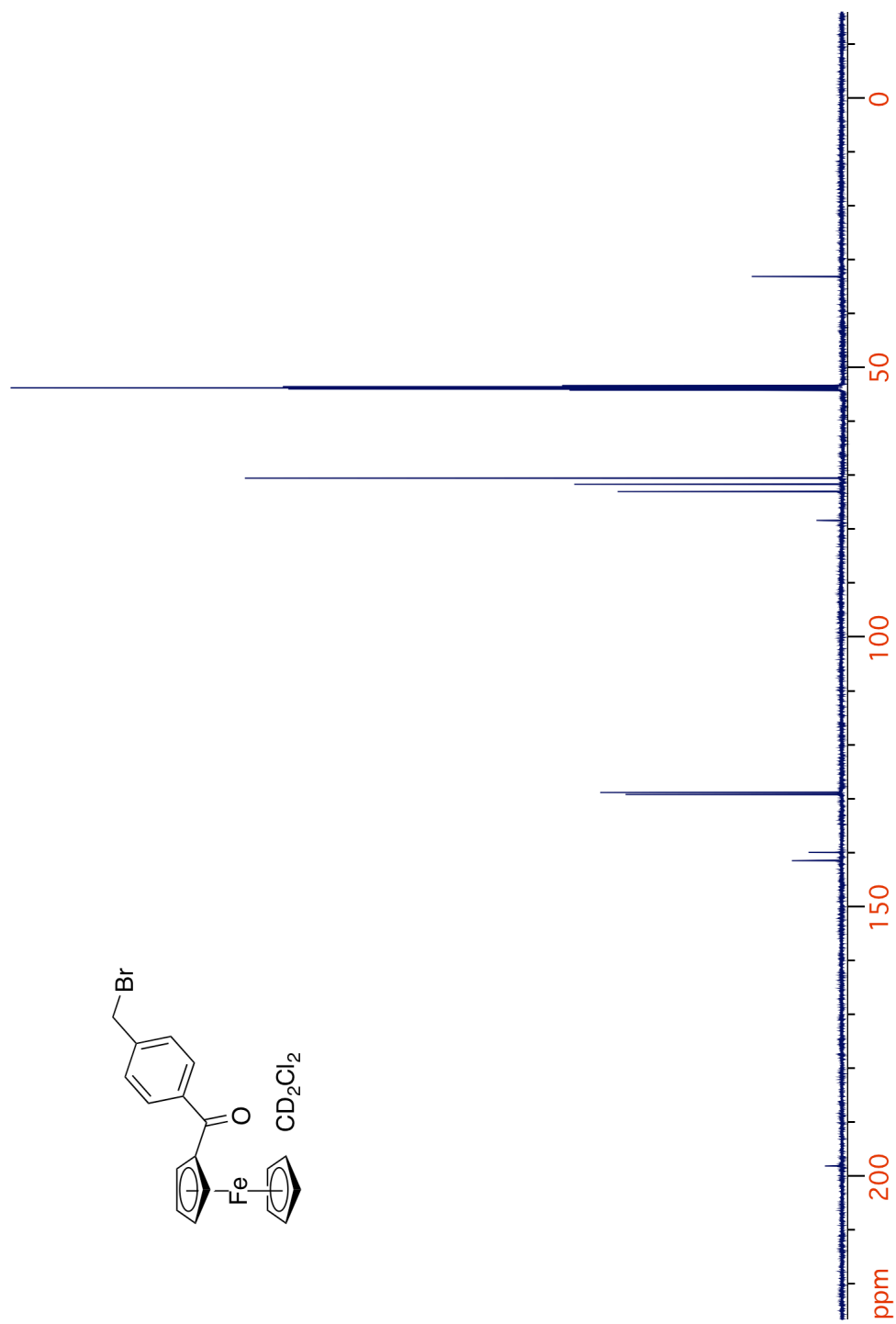
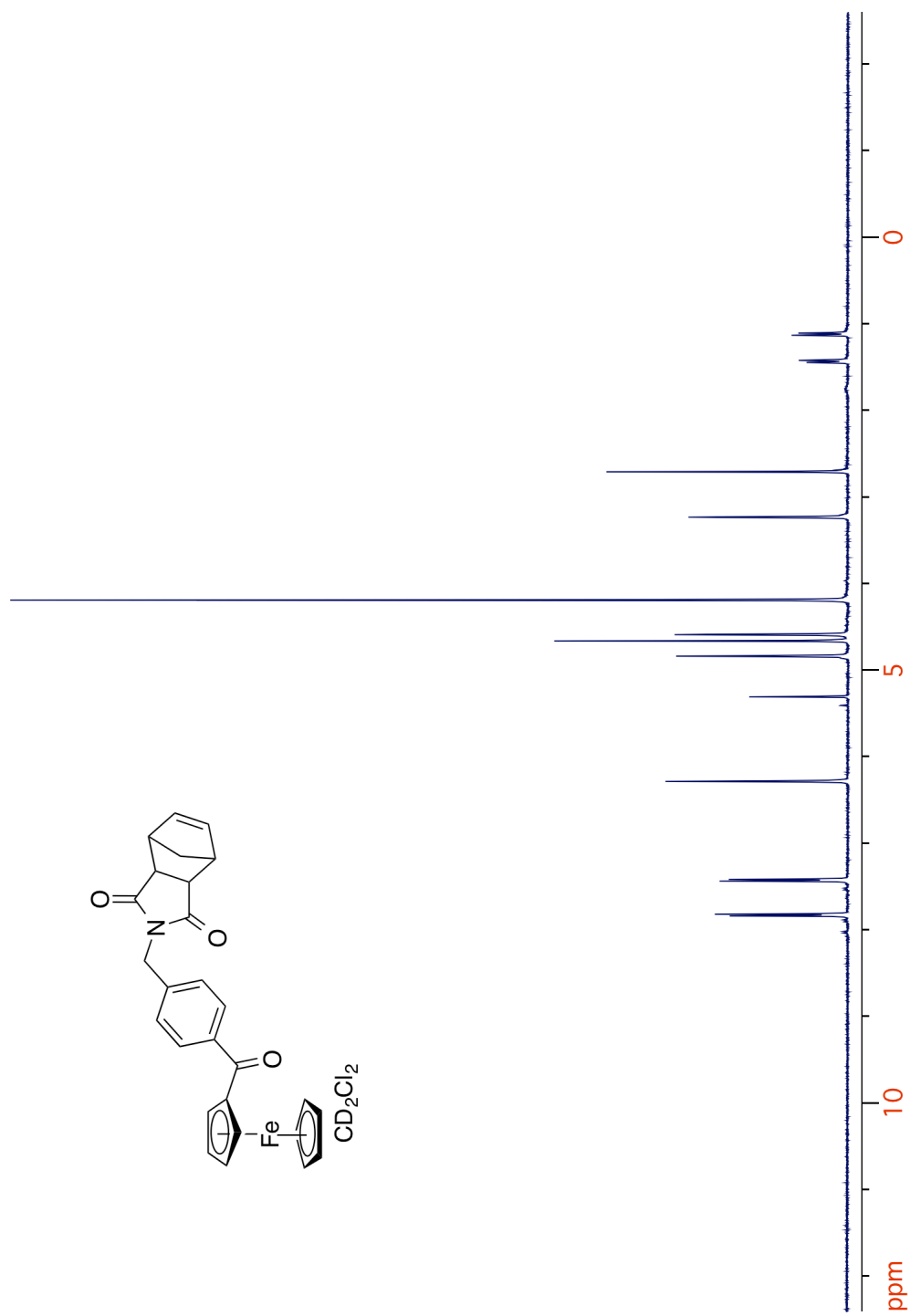
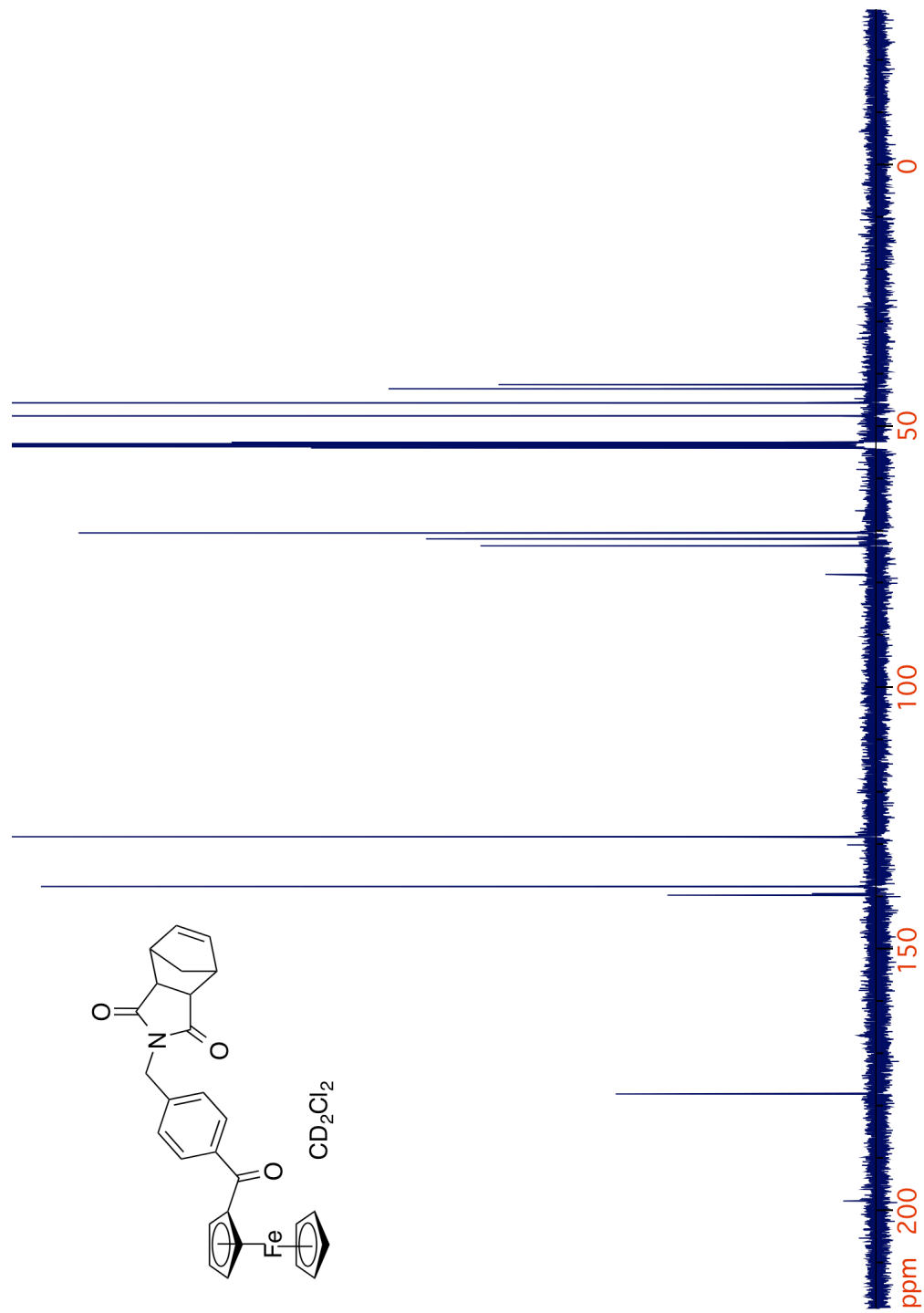
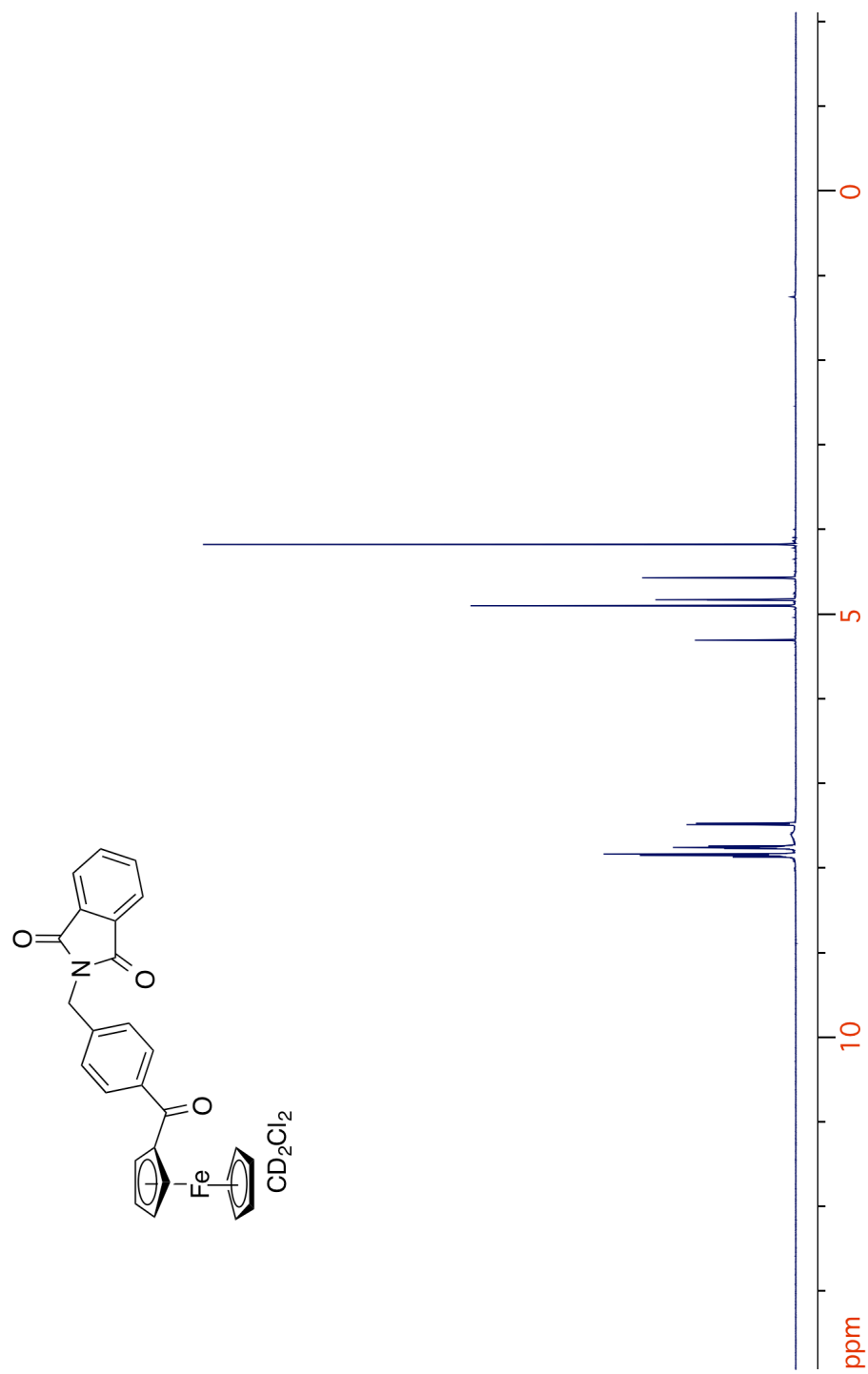
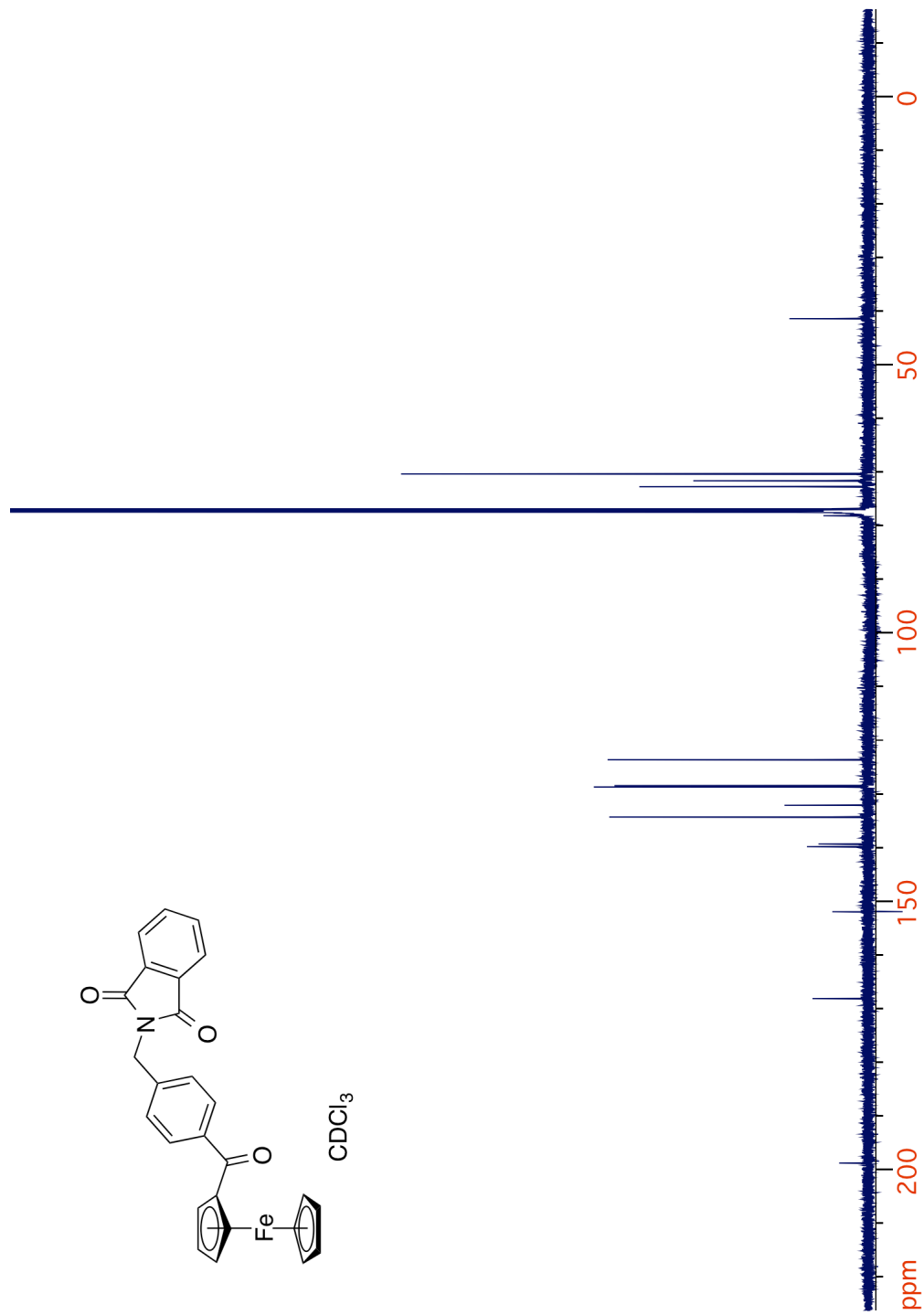


Figure 2.48. ^{13}C NMR spectrum of **22**.

Figure 2.49. ^1H NMR spectrum of **24**.

Figure 2.50. ¹³C NMR spectrum of 24.

Figure 2.51. ^1H NMR spectrum of **25**.

Figure 2.52. ^{13}C NMR spectrum of 25.

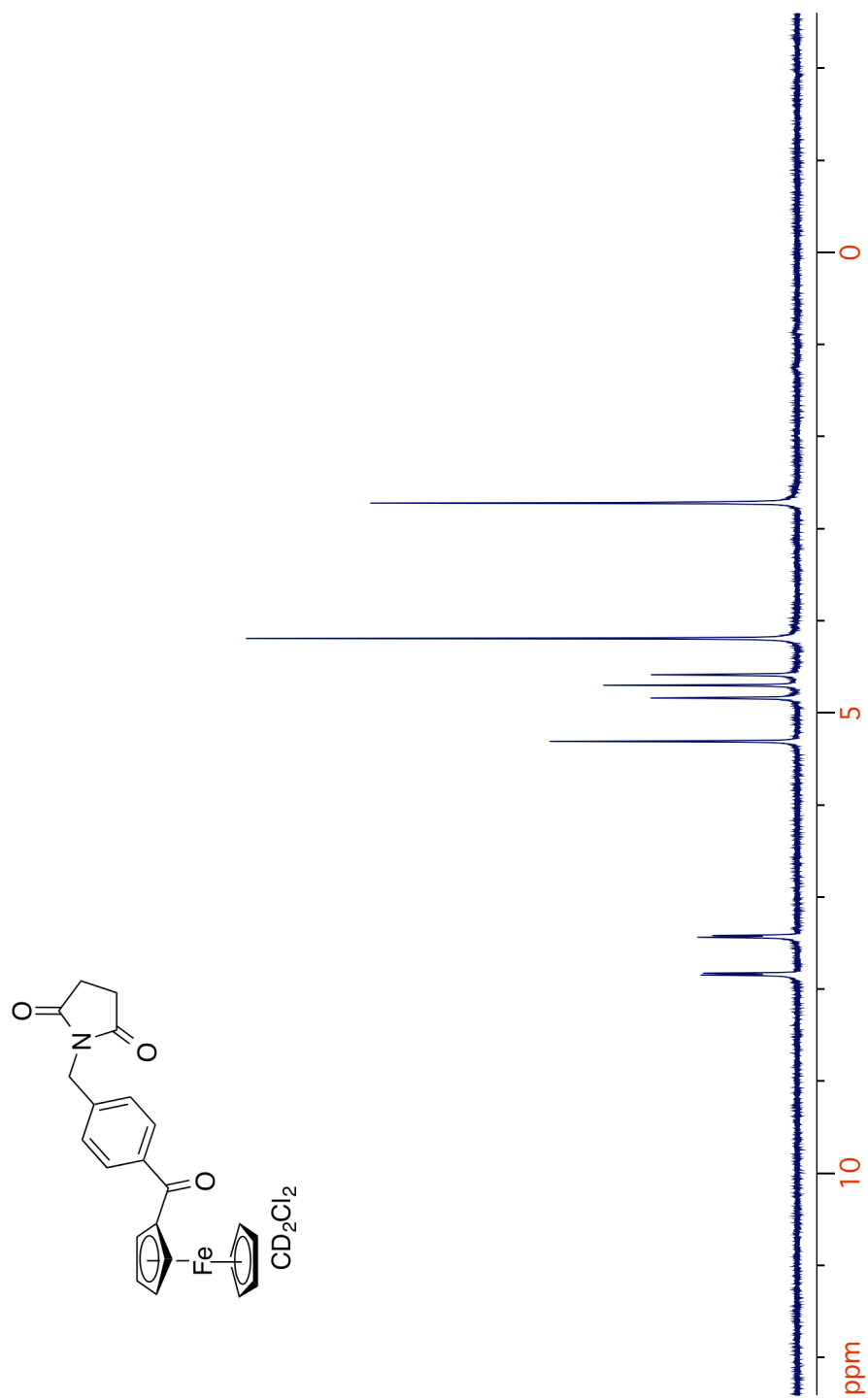


Figure 2.53. ^1H NMR spectrum of **26**.

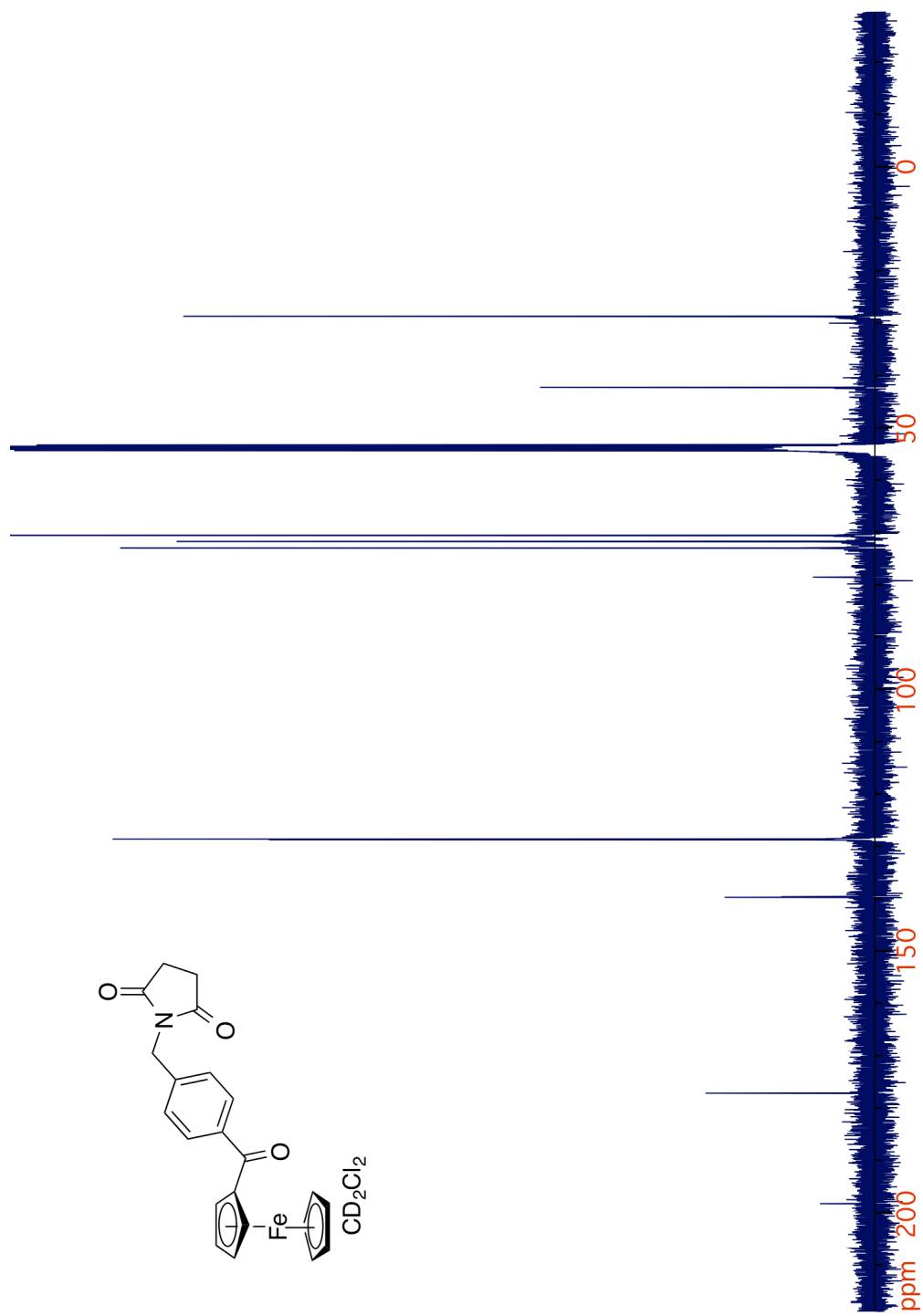


Figure 2.54. ^{13}C NMR spectrum of **26**.

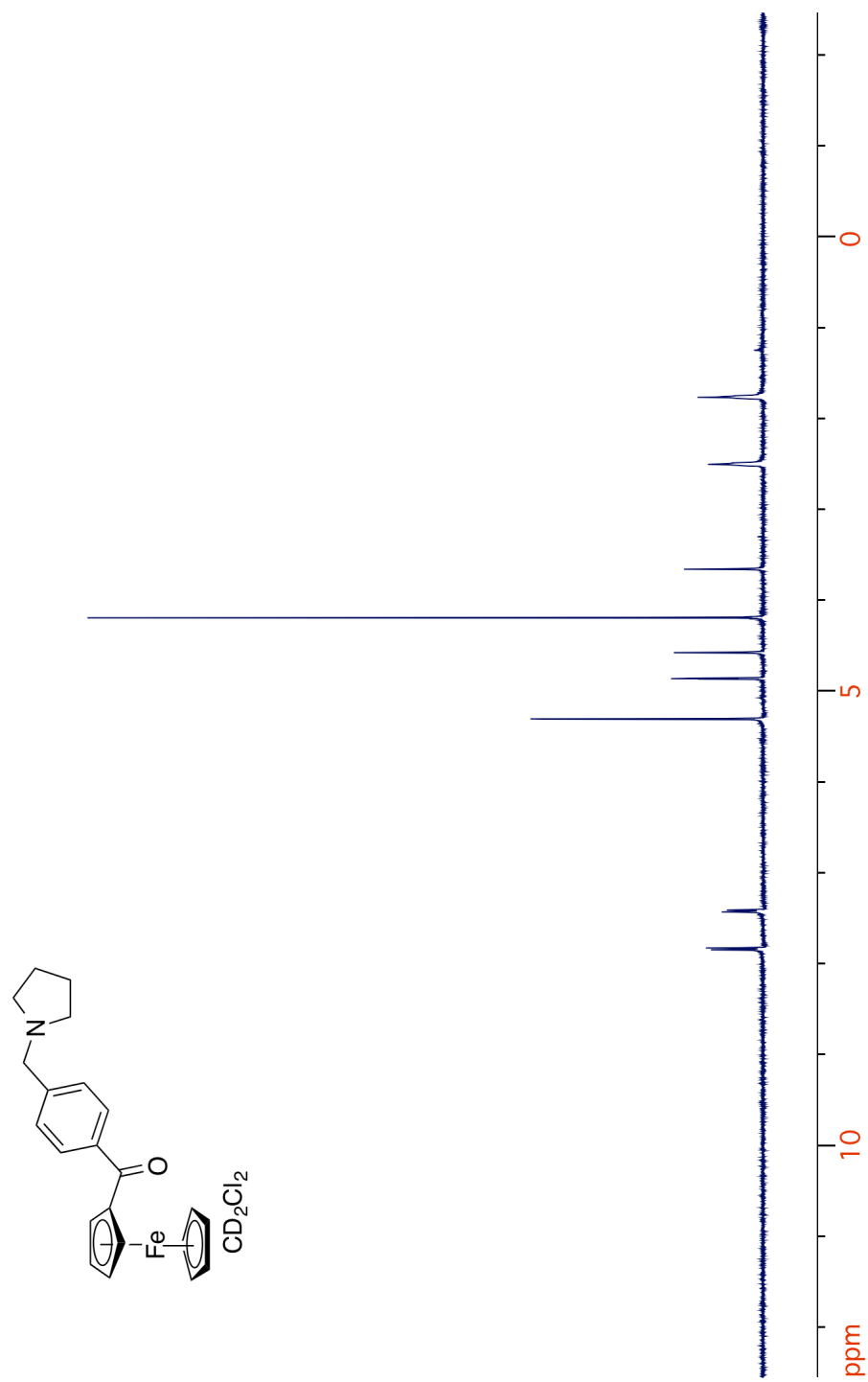
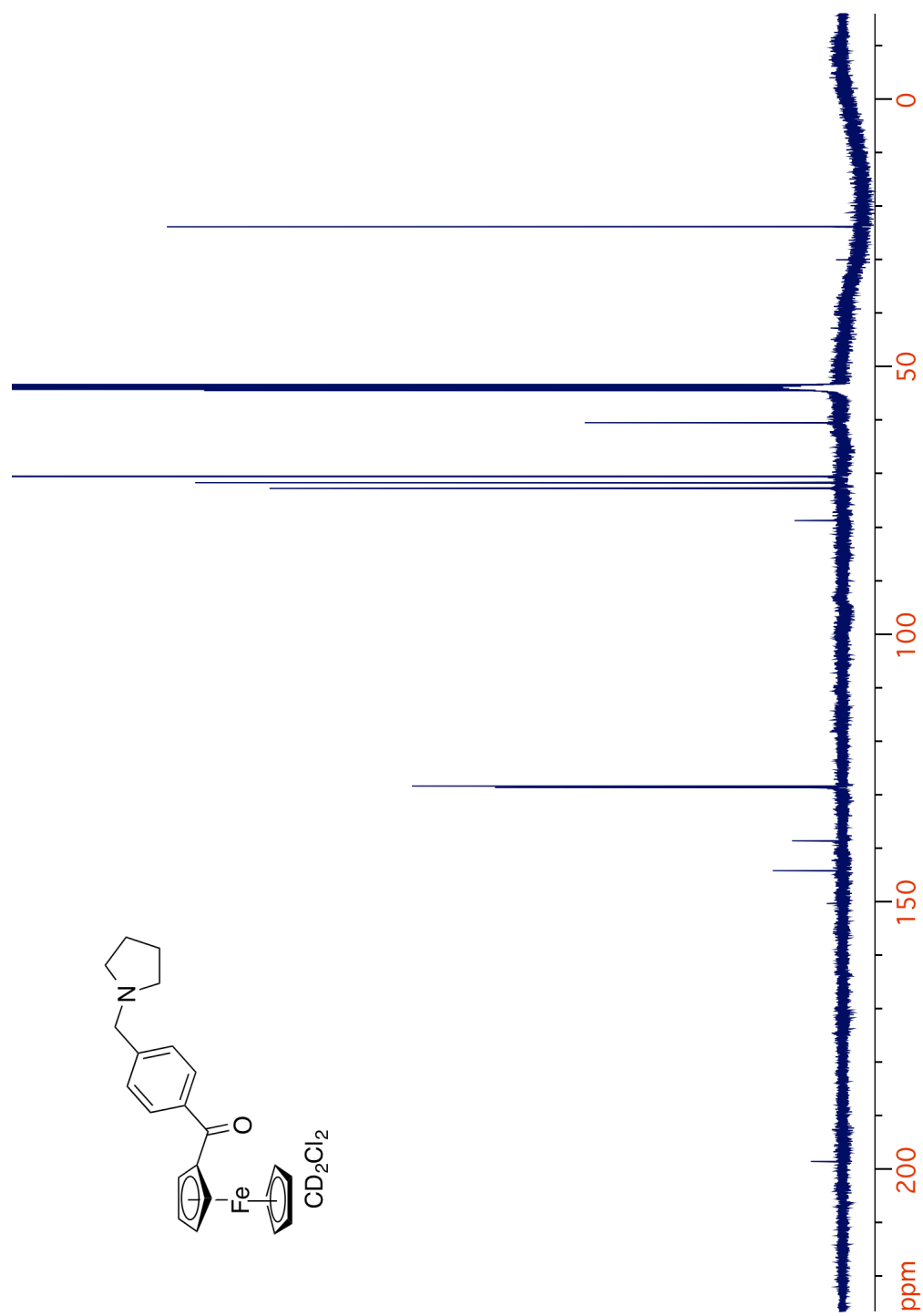


Figure 2.55. ^1H NMR spectrum of **27**.

Figure 2.56. ^{13}C NMR spectrum of **27**.

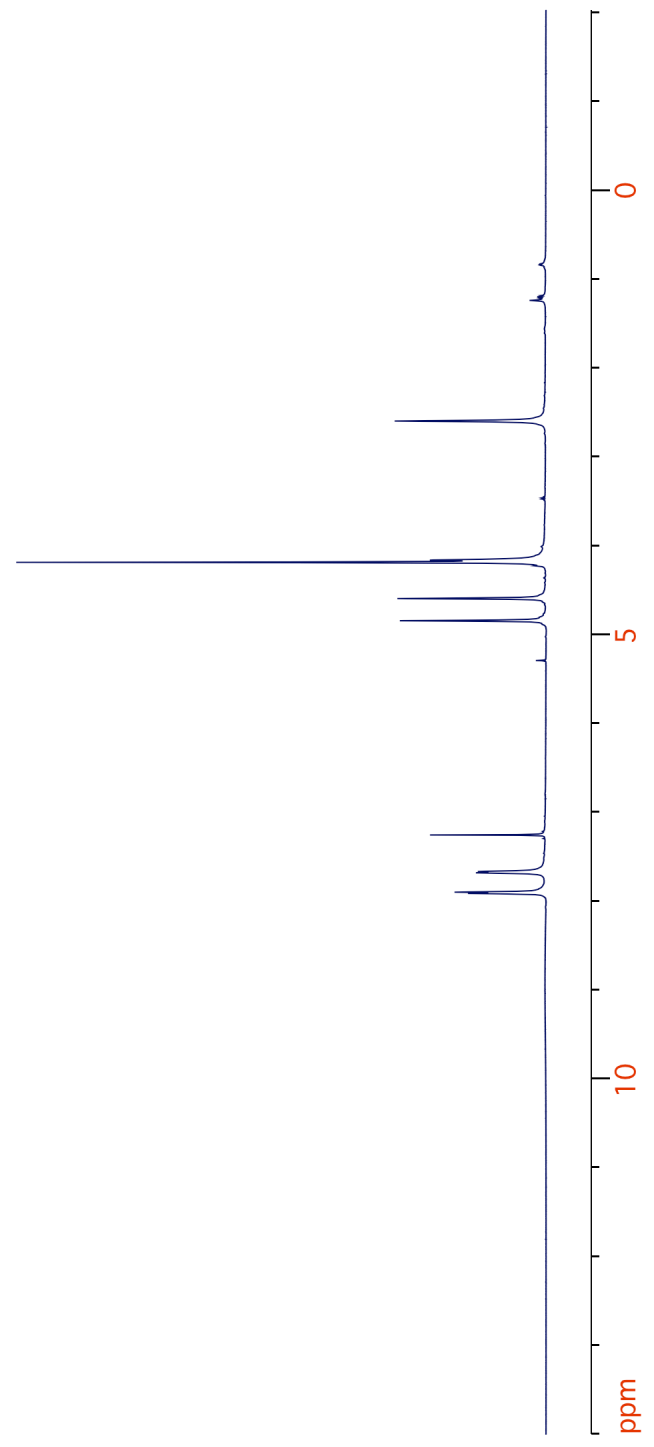
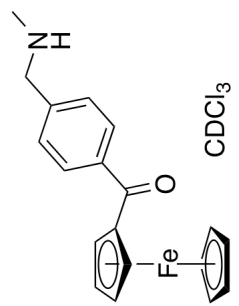


Figure 2.57. ¹H NMR spectrum of 28.

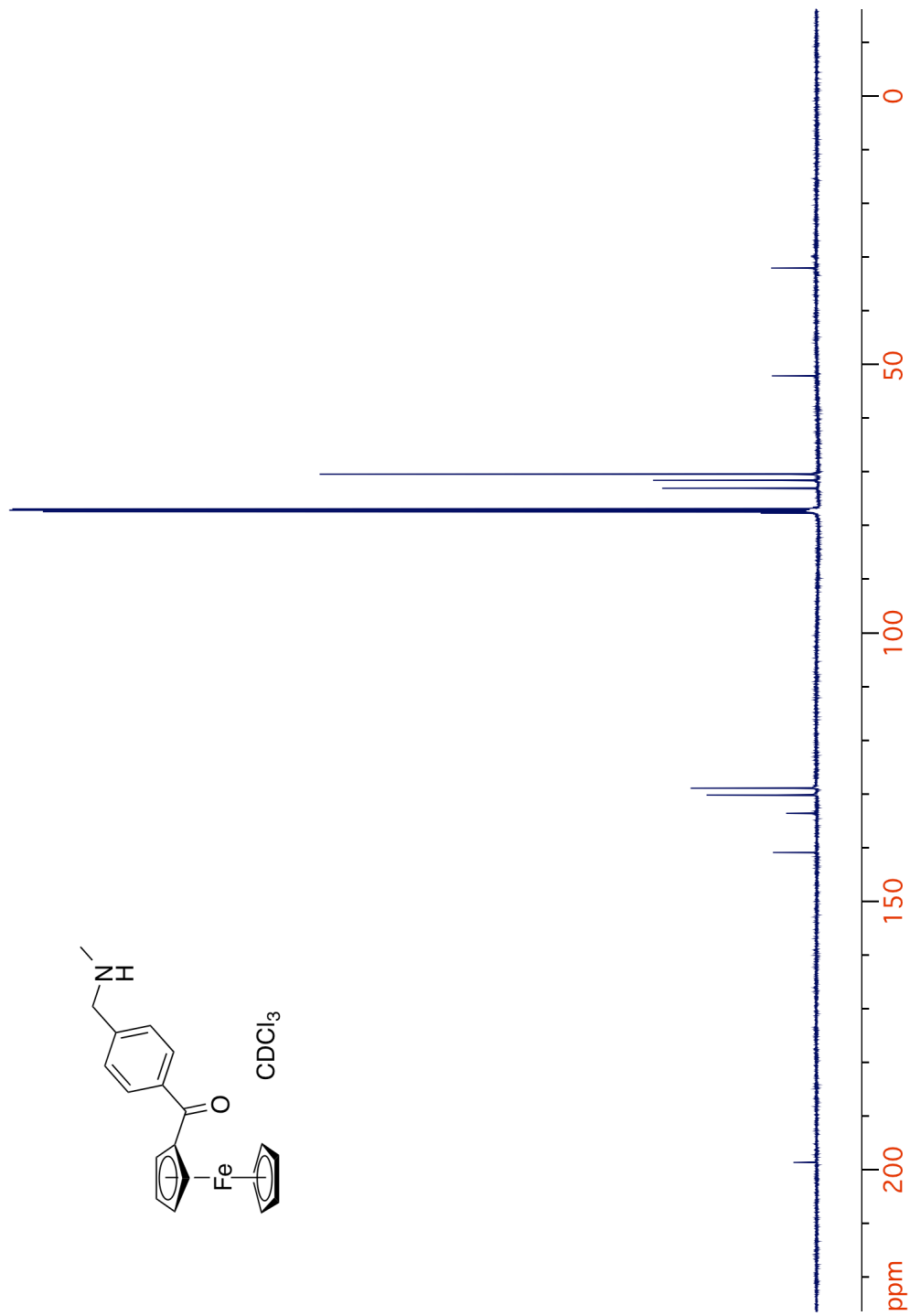


Figure 2.58. ^{13}C NMR spectrum of 28.

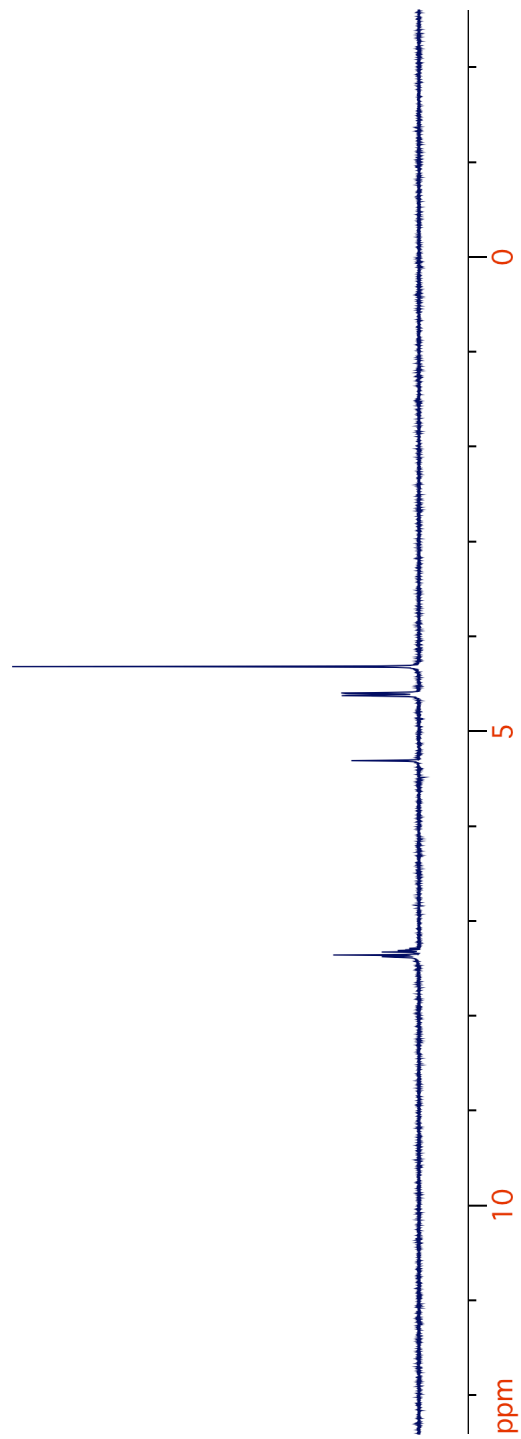
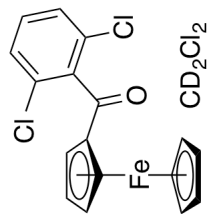


Figure 2.59. ¹H NMR spectrum of 29.

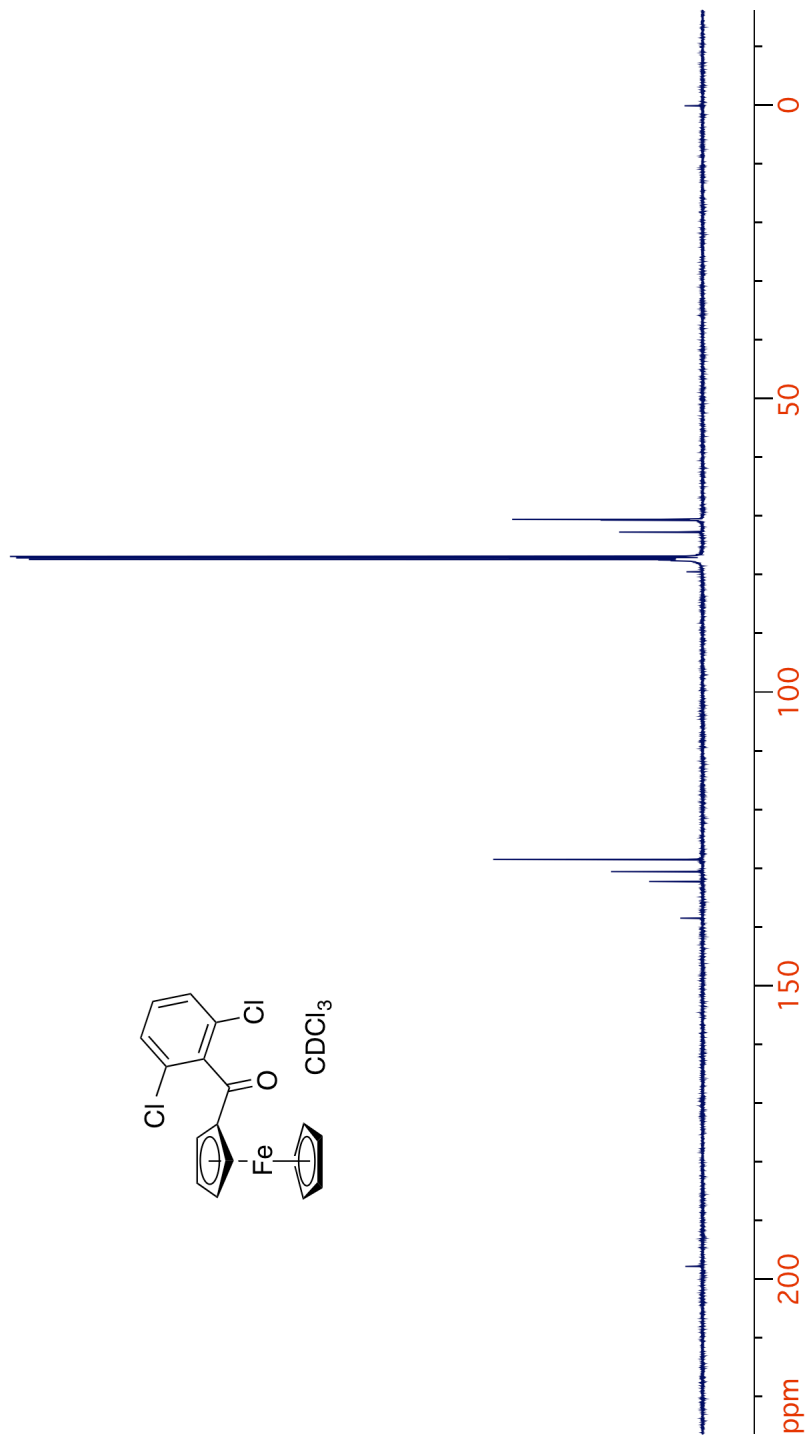


Figure 2.60. ^{13}C NMR spectrum of **29**.

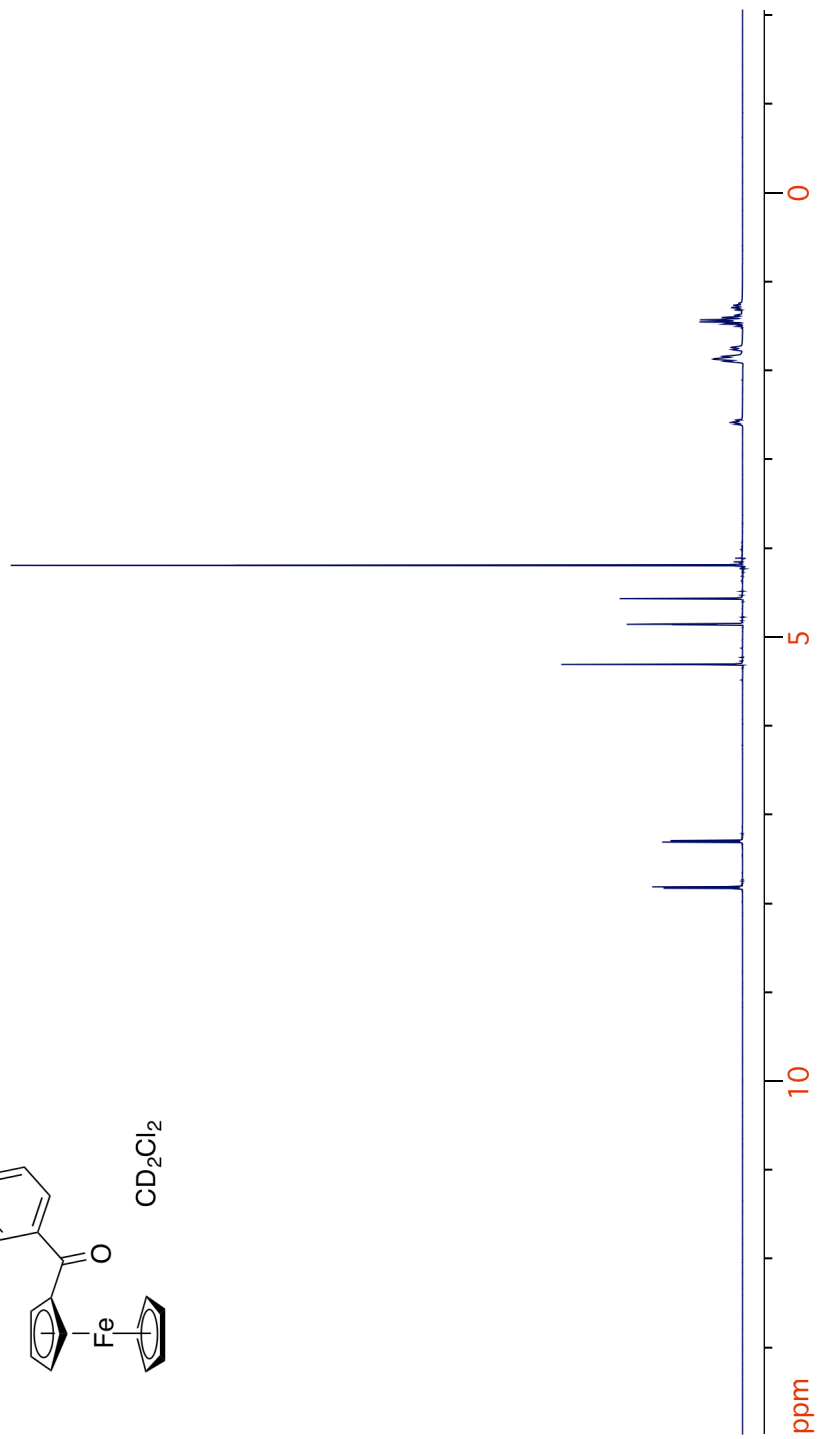
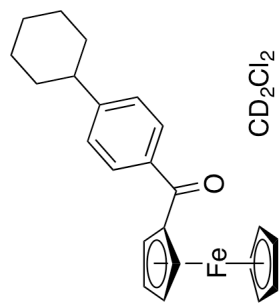


Figure 2.61. ¹H NMR spectrum of 30.

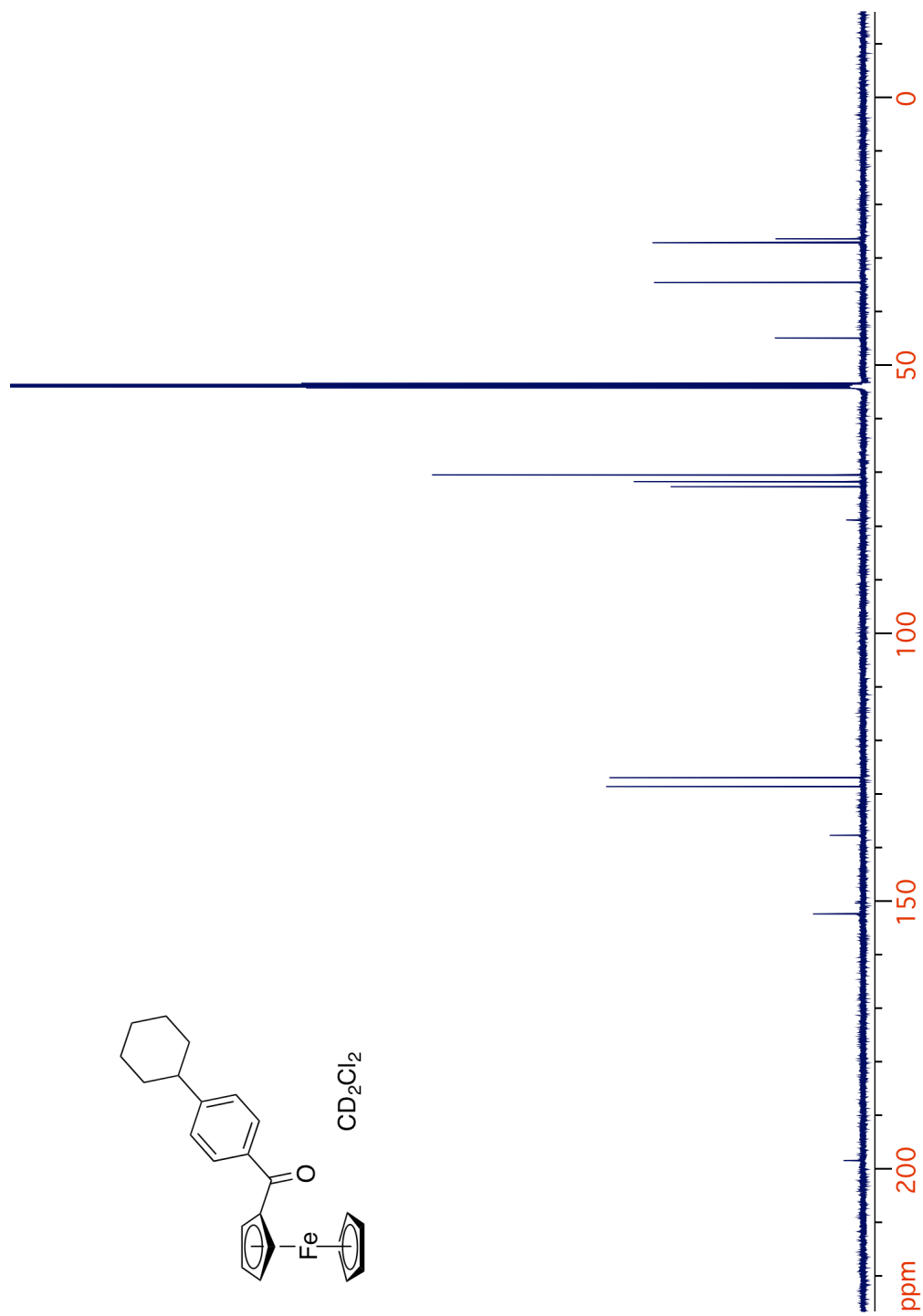


Figure 2.62. ^{13}C NMR spectrum of **30**.

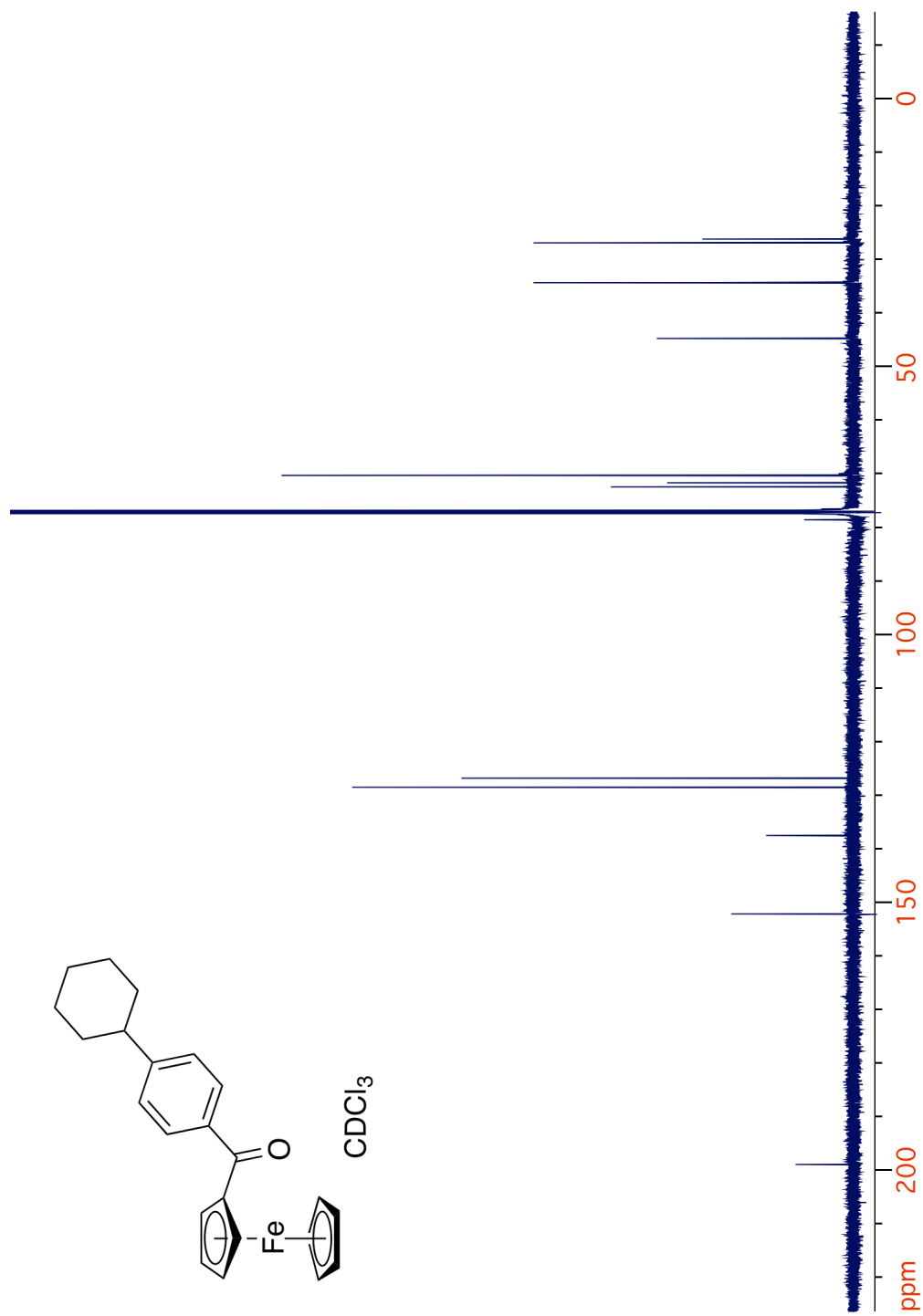


Figure 2.63. ^{13}C NMR spectrum of 30.

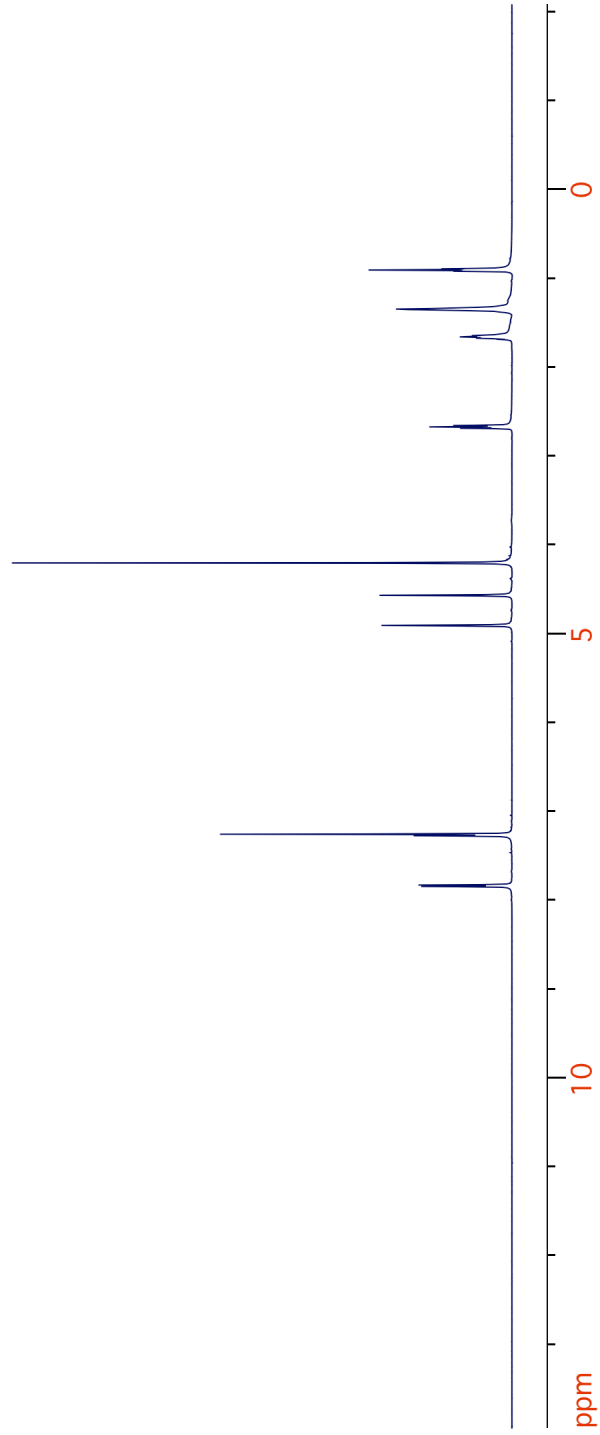
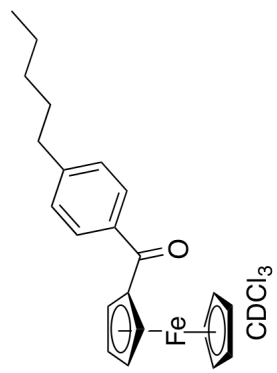
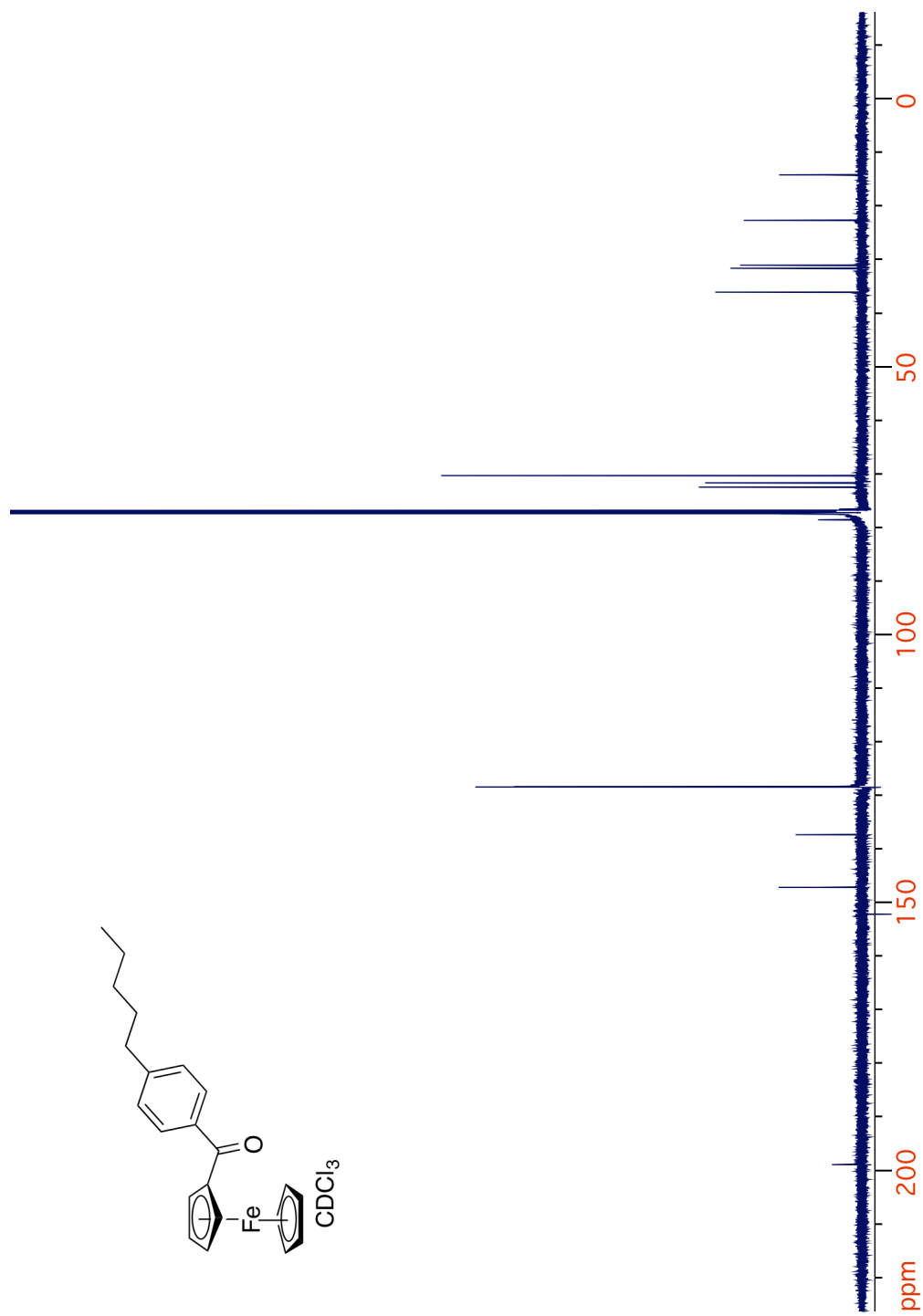


Figure 2.64. ¹H NMR spectrum of 31.

Figure 2.65. ^{13}C NMR spectrum of 31.

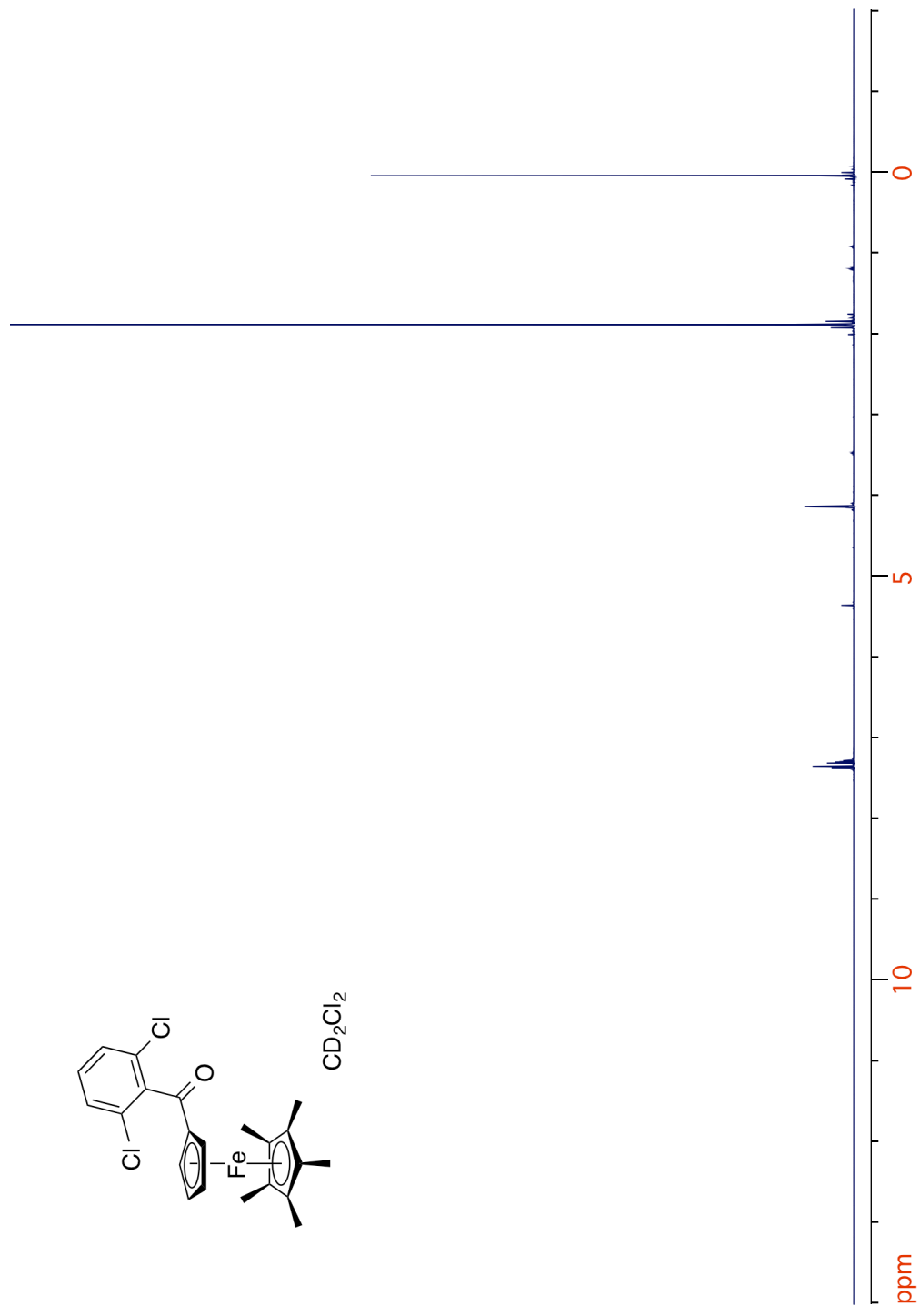


Figure 2.66. ^1H NMR spectrum of 32.

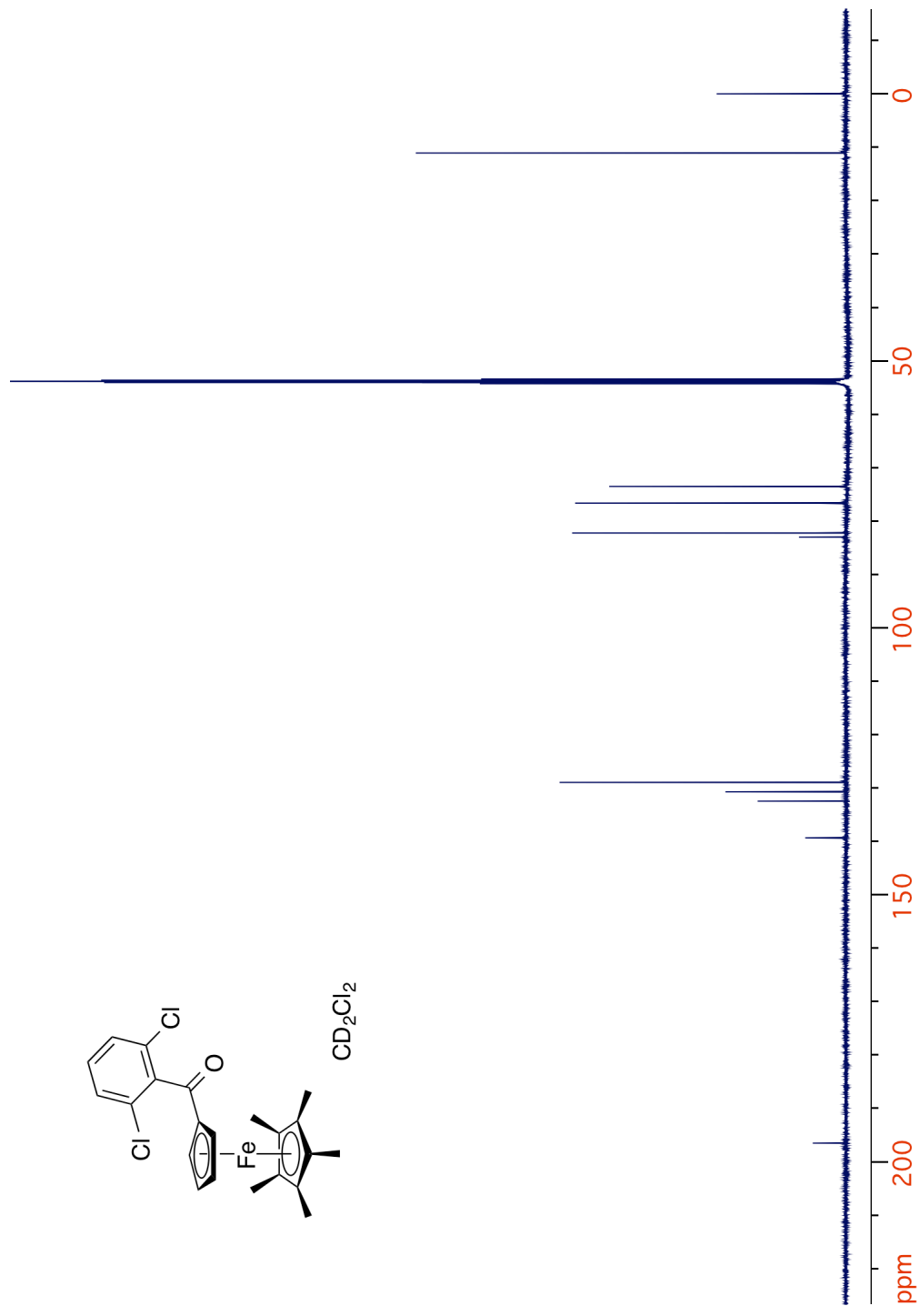
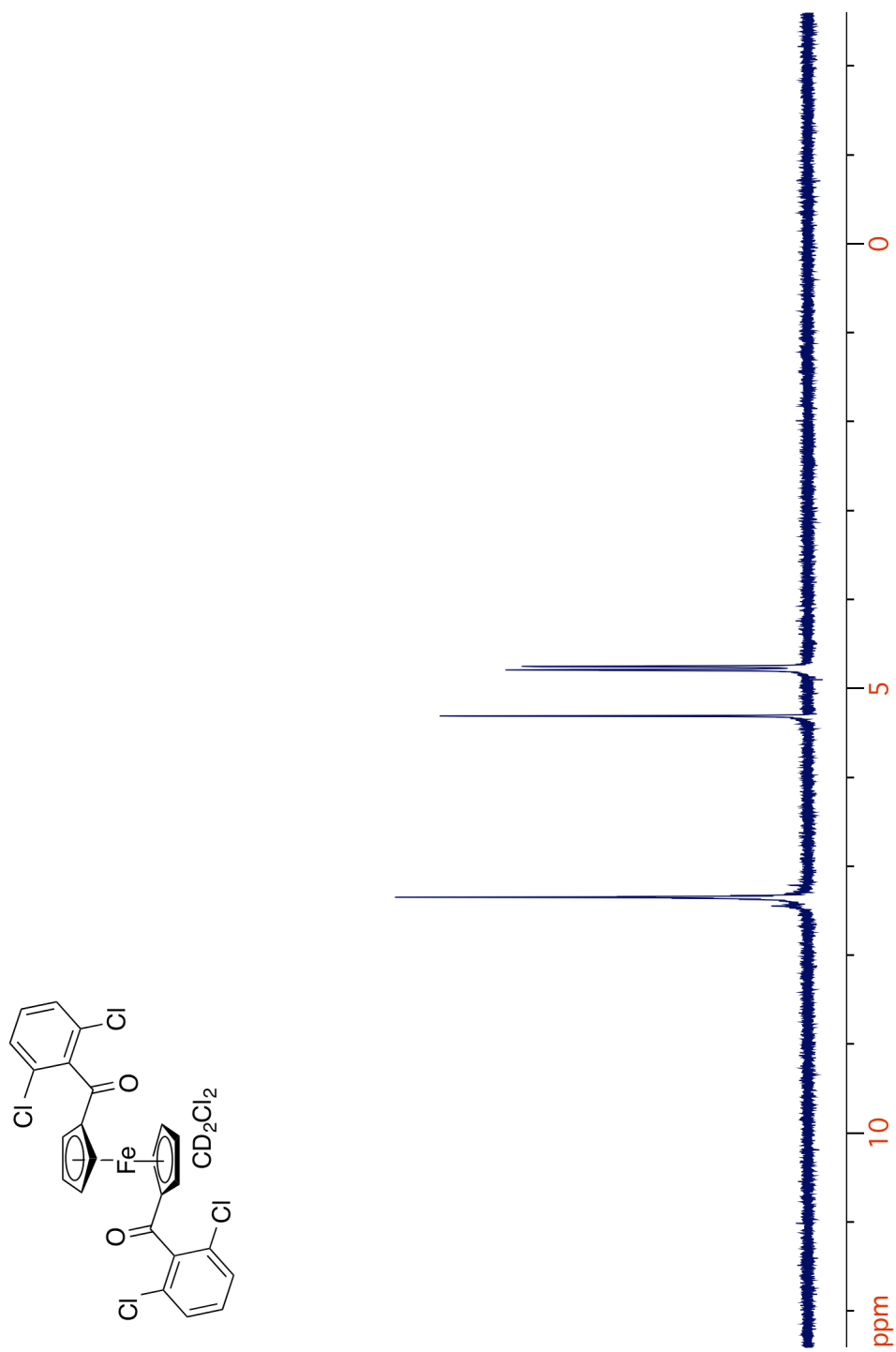
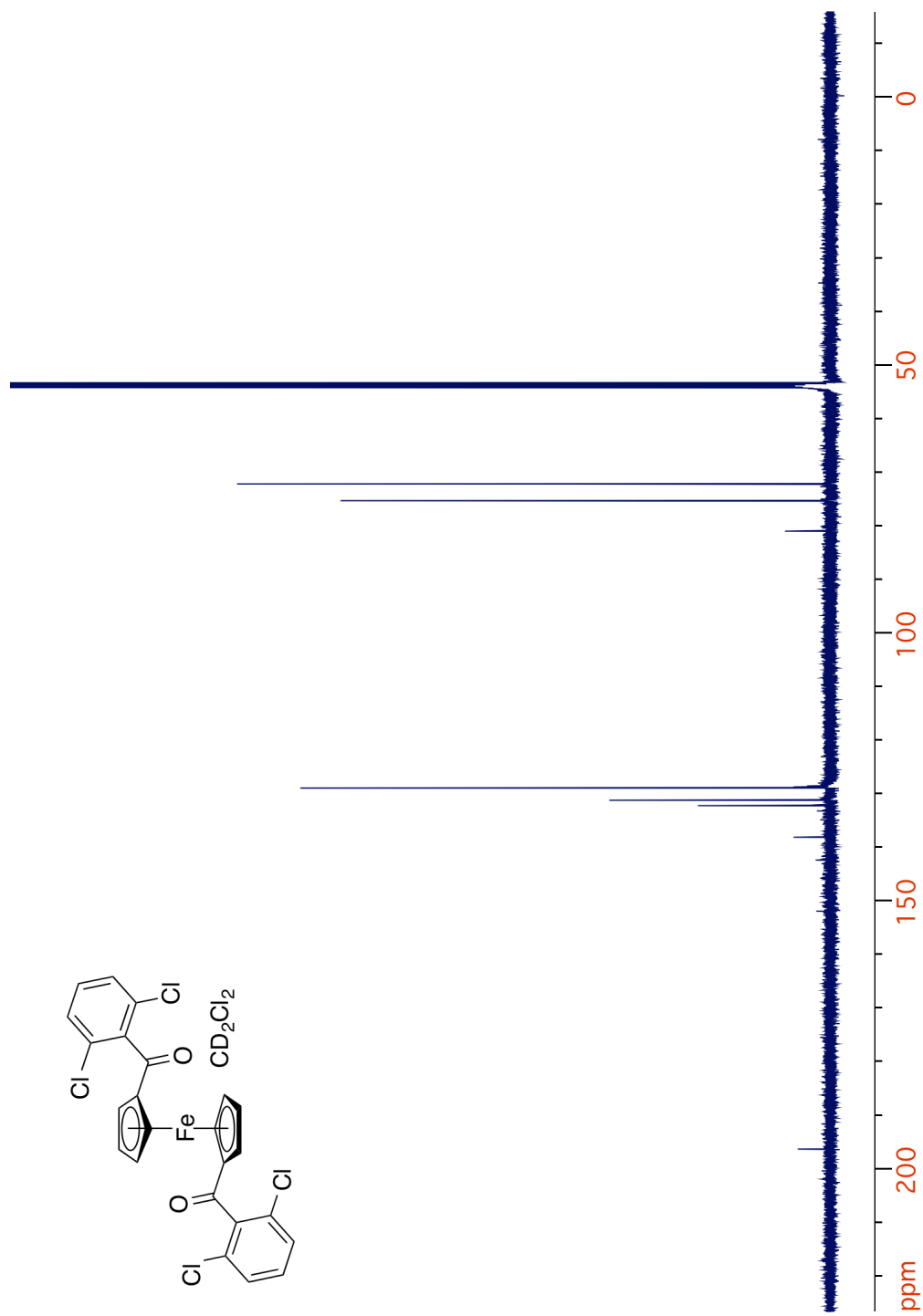


Figure 2.67. ^{13}C NMR spectrum of 32.

Figure 2.68. ^1H NMR spectrum of 35.

Figure 2.69. ^{13}C NMR spectrum of 35.

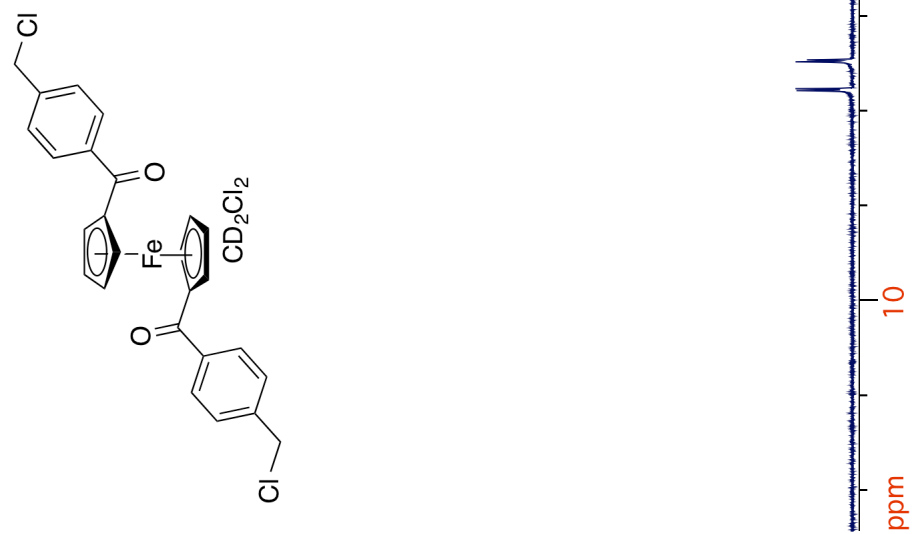


Figure 2.70. ^1H NMR spectrum of 36.

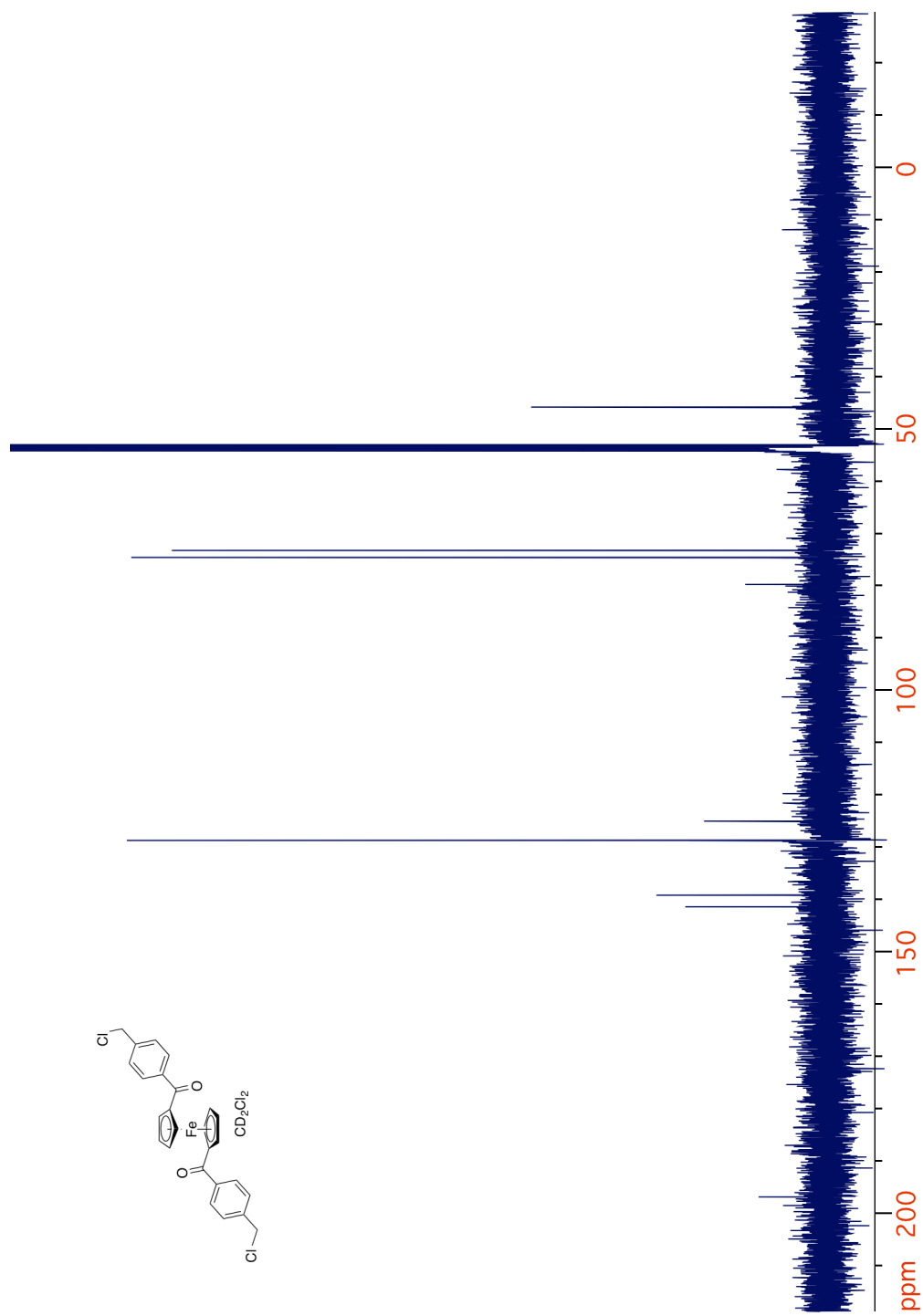
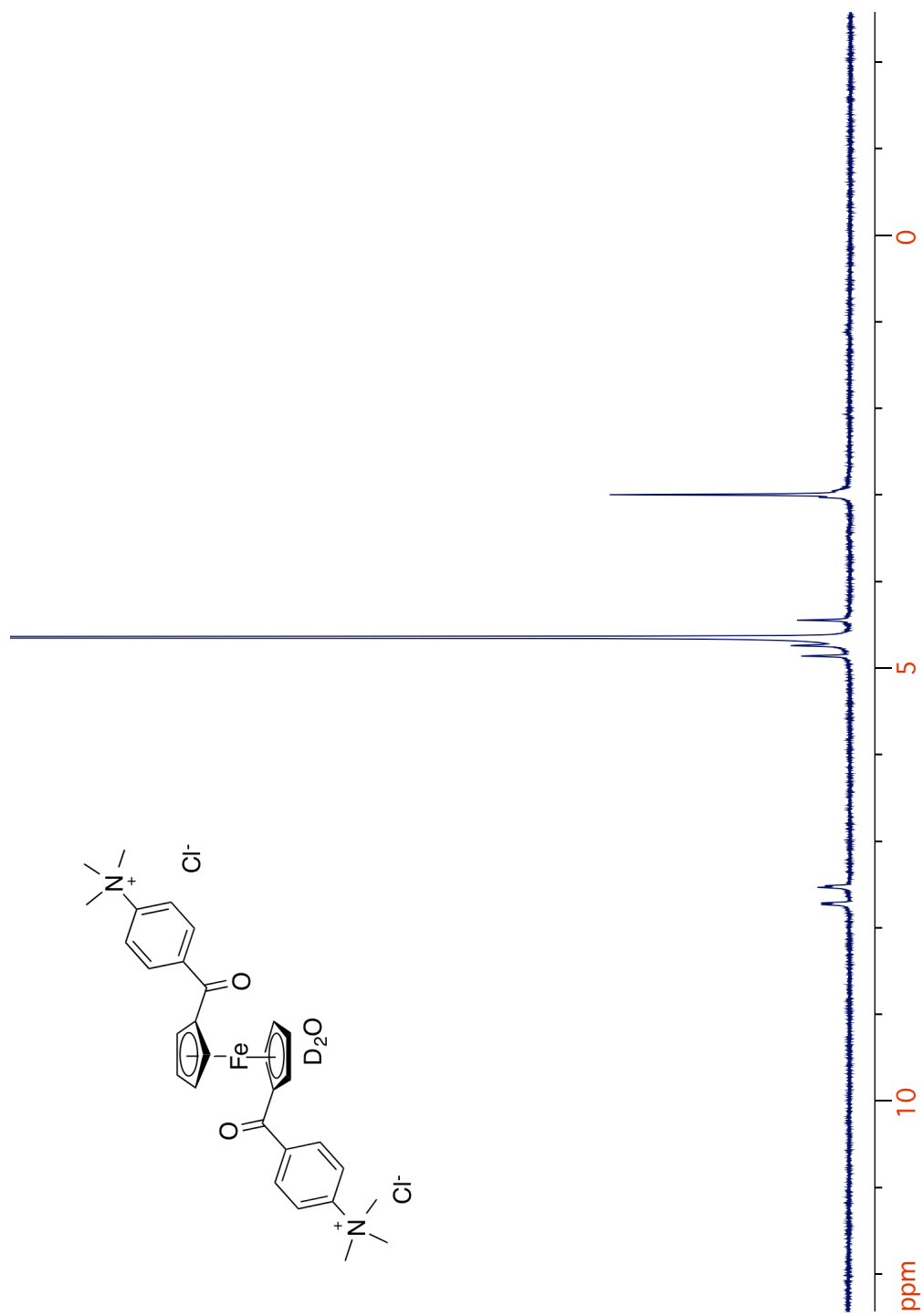
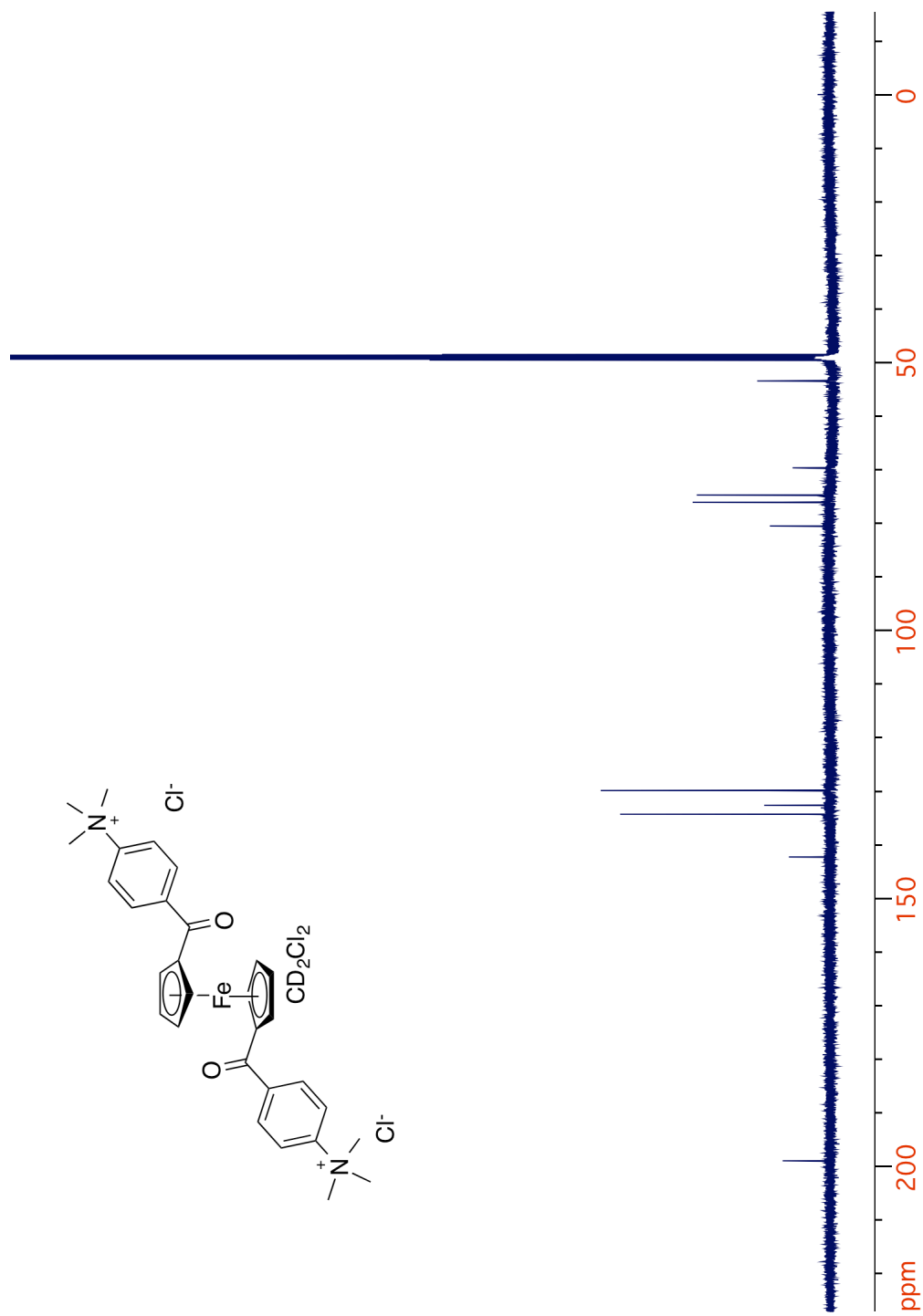


Figure 2.71. ^{13}C NMR spectrum of 36.

Figure 2.72. ^1H NMR spectrum of 37.

**Figure 2.73.** ^{13}C NMR spectrum of 37.

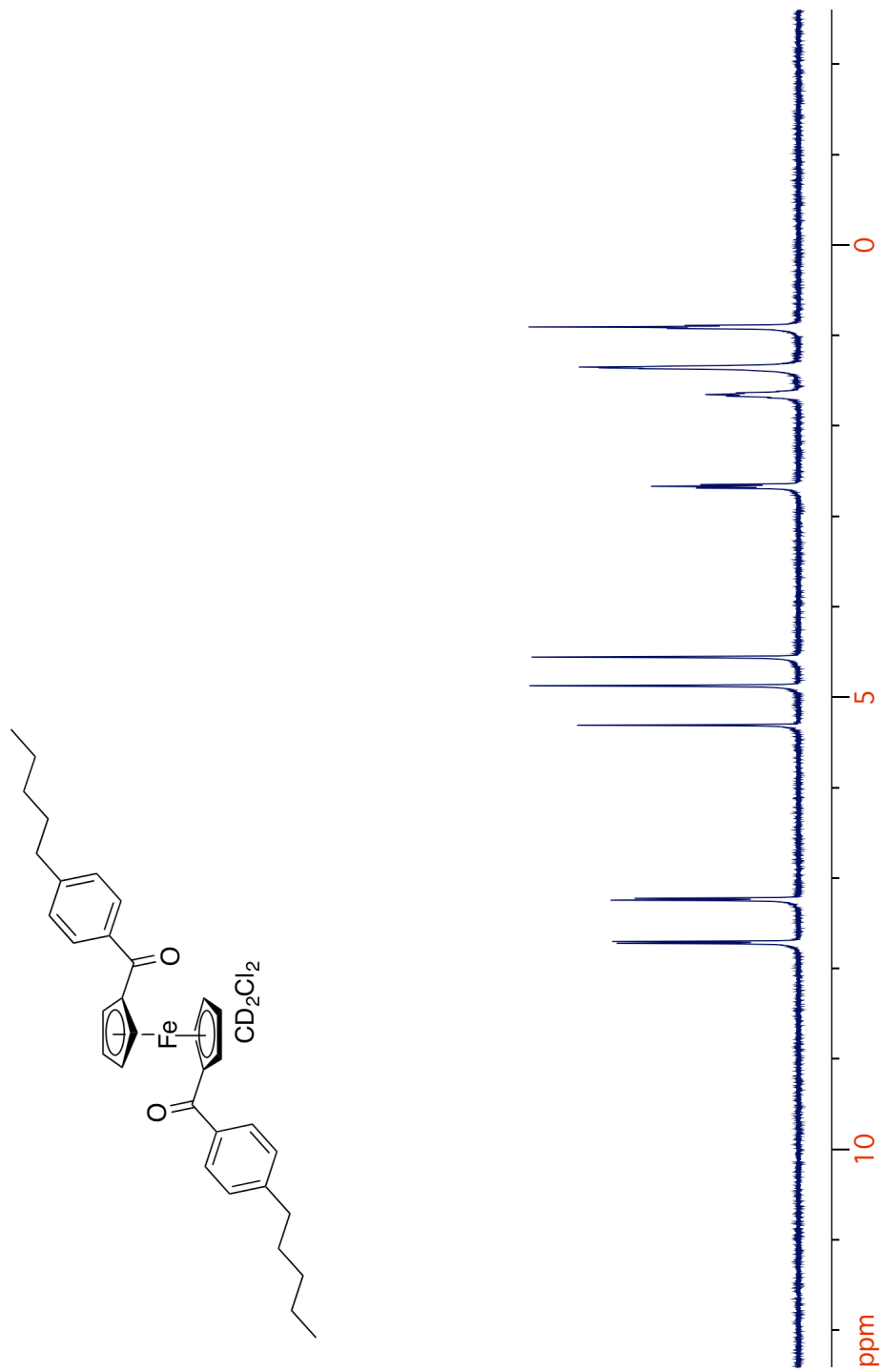
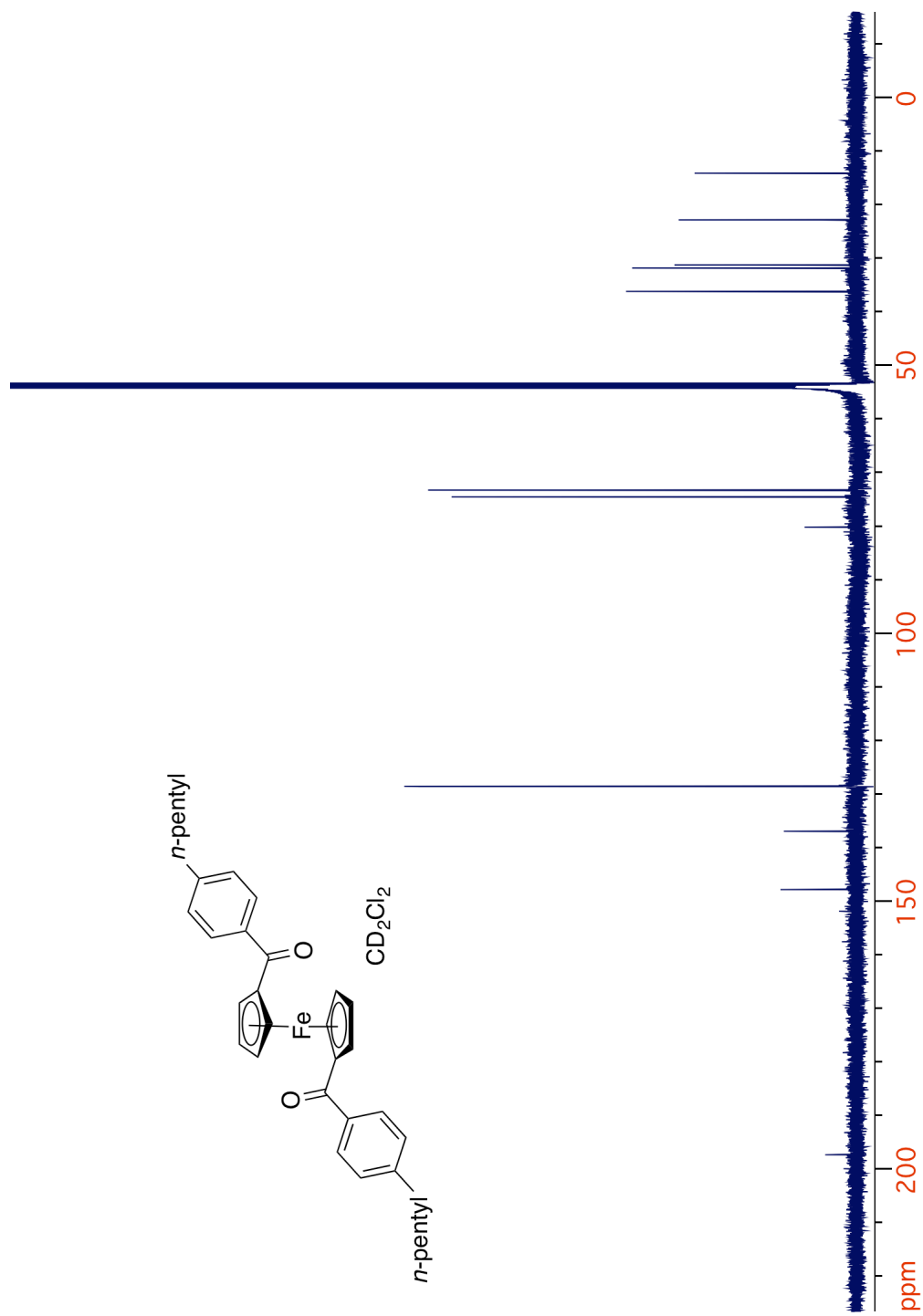


Figure 2.74. ^1H NMR spectrum of 39.

Figure 2.75. ^{13}C NMR spectrum of **39**.

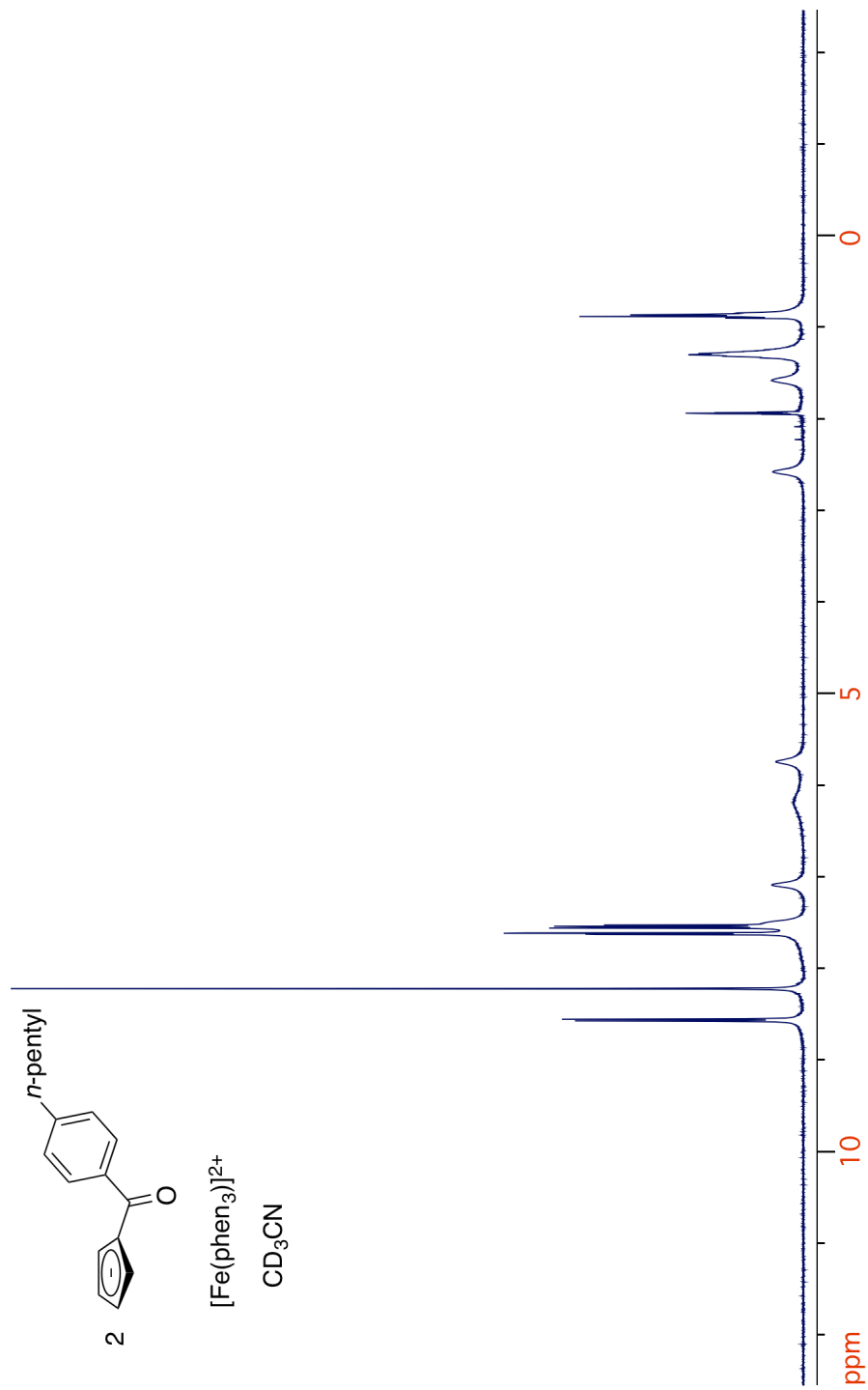
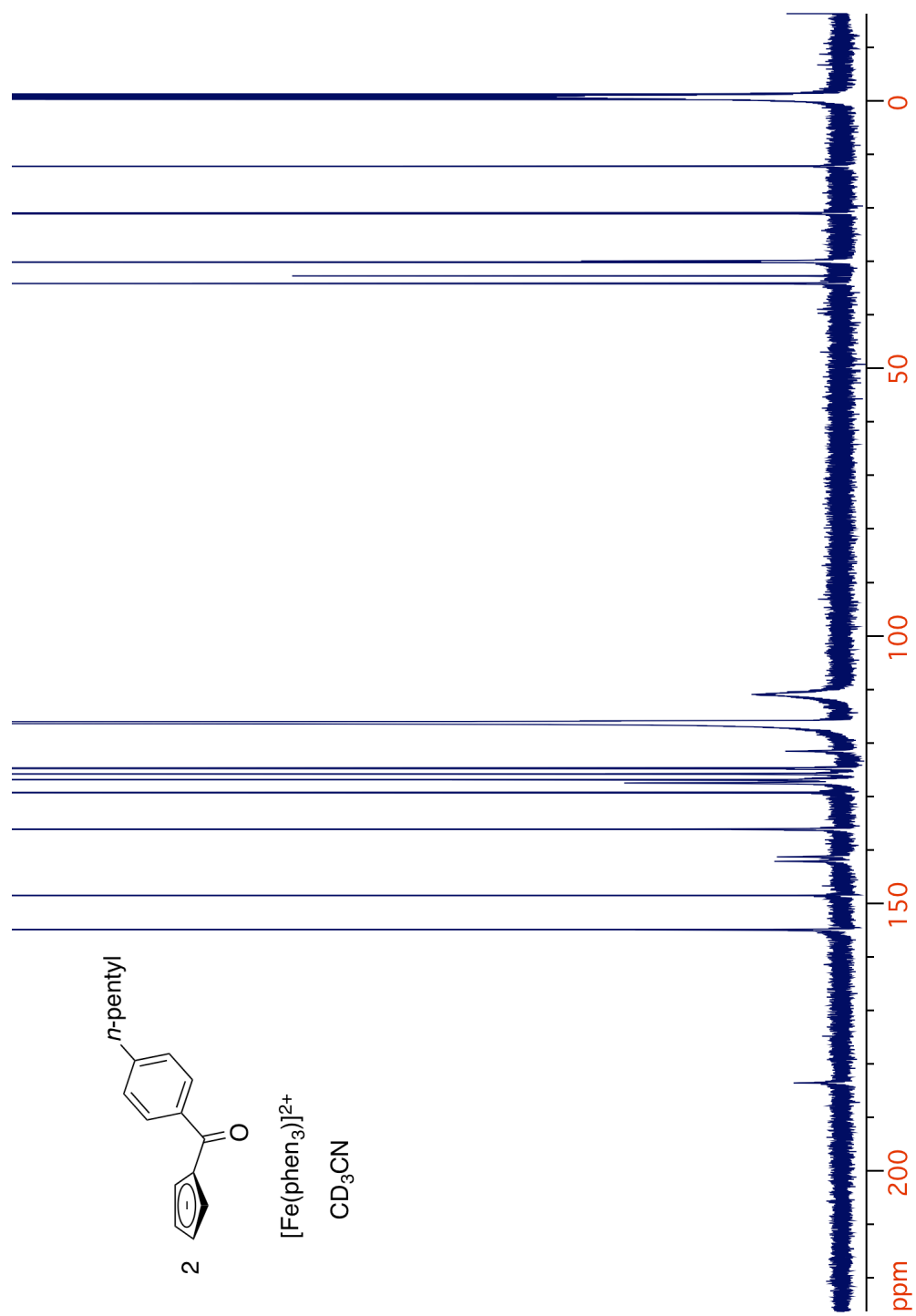


Figure 2.76. ^1H NMR spectrum of **40(phen)**.

Figure 2.77. ^{13}C NMR spectrum of 40(phen).

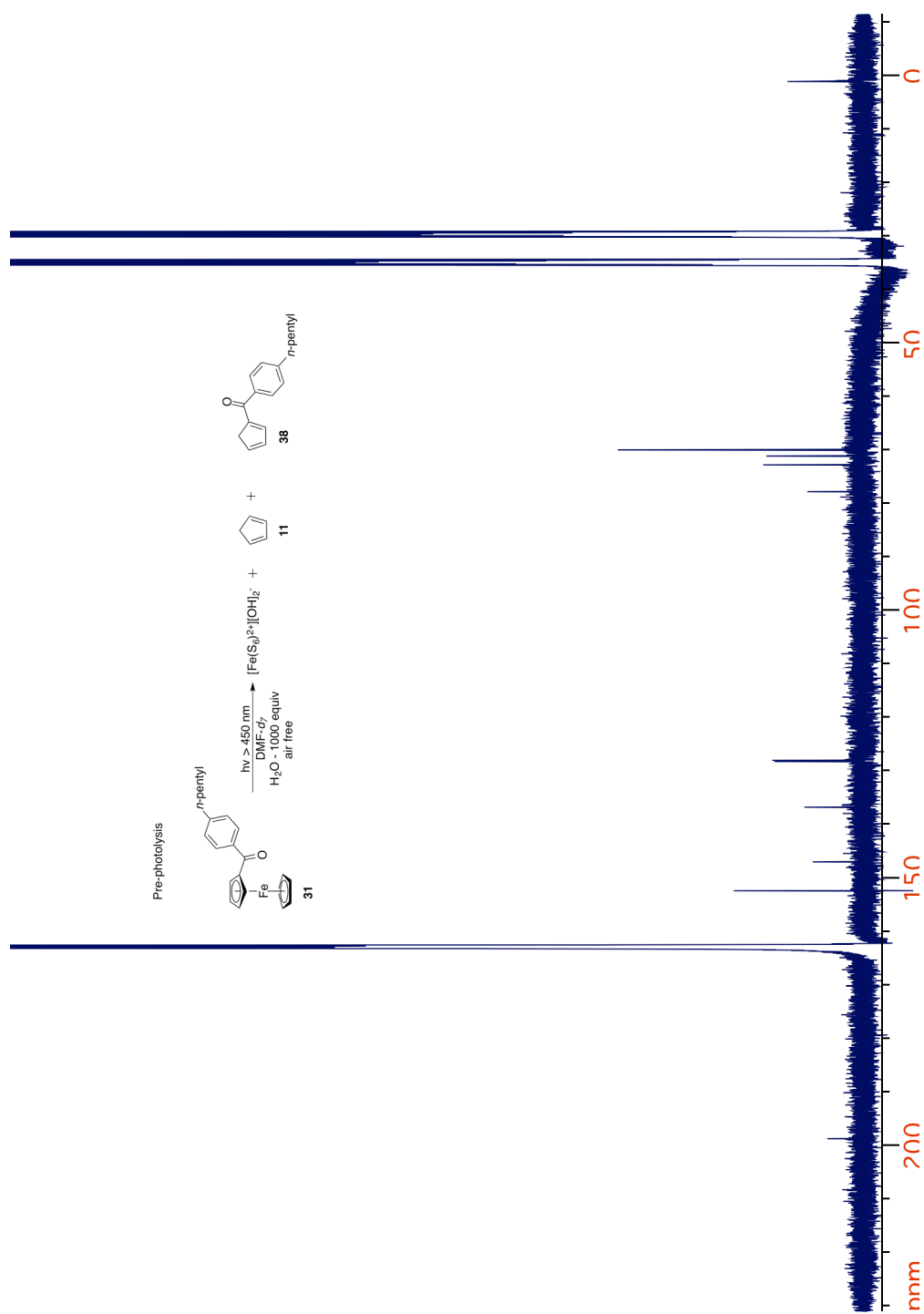


Figure 2.78. ¹³C NMR spectrum of **31** in DMF-*d*₇, H₂O (0.6 mL, 0.1 mL).

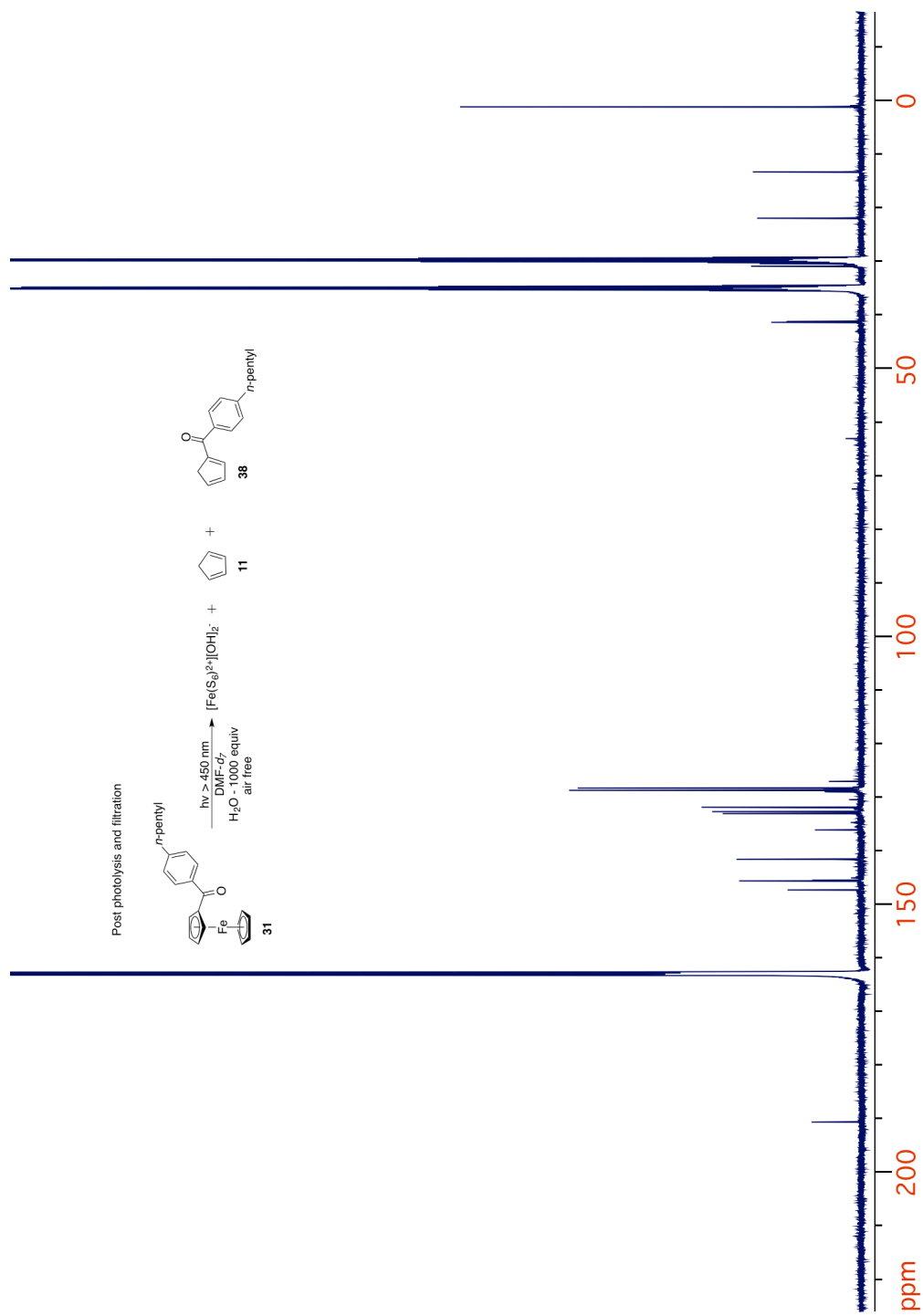


Figure 2.79. ^{13}C NMR spectrum of **31** photoproducts in $\text{DMF-}d_7$, H_2O (0.6 mL, 0.1 mL).

G. Appendix 2

Table 2.15. Crystal data and structure refinement for **7**

Identification code	MA-VI-83	
Empirical formula	C ₁₇ H ₁₄ Fe O	
Formula weight	290.13	
Temperature	100(2) K	
Wavelength	0.71073 Å	
Crystal system	Monoclinic	
Space group	P2(1)/n	
Unit cell dimensions	a = 6.1396(4) Å	a = 90°.
	b = 15.1266(11) Å	b = 99.3430(10)°.
	c = 13.7343(10) Å	g = 90°.
Volume	1258.60(15) Å ³	
Z	4	
Density (calculated)	1.531 Mg/m ³	
Absorption coefficient	1.184 mm ⁻¹	
F(000)	600	
Crystal size	0.28 x 0.11 x 0.05 mm ³	
Crystal color, habit	Red-Orange Block	
Theta range for data collection	2.02 to 28.48°.	
Index ranges	-8<=h<=8, -20<=k<=18, -18<=l<=18	
Reflections collected	8298	
Independent reflections	2924 [R(int) = 0.0330]	
Completeness to theta = 25.00°	99.8 %	
Absorption correction	Semi-empirical from equivalents	
Max. and min. transmission	0.9432 and 0.7327	
Refinement method	Full-matrix least-squares on F ²	
Data / restraints / parameters	2924 / 0 / 172	
Goodness-of-fit on F ²	1.036	
Final R indices [I>2sigma(I)]	R1 = 0.0336, wR2 = 0.0795	
R indices (all data)	R1 = 0.0428, wR2 = 0.0869	
Extinction coefficient	not measured	
Largest diff. peak and hole	0.439 and -0.302 e.Å ⁻³	

Table 2.16. Crystal data and structure refinement for **15**.

Identification code	ocon_ma2014	
Empirical formula	C ₂₁ H ₂₄ D ₂ Fe I N O ₂	
Molecular formula	C ₂₁ H ₂₄ Fe N O, I, D ₂ O	
Formula weight	509.19	
Temperature	100(2) K	
Wavelength	0.71073 Å	
Crystal system	Triclinic	
Space group	P-1	
Unit cell dimensions	a = 9.3958(3) Å	a = 91.515(2)°.
	b = 10.1973(3) Å	b = 92.675(2)°.
	c = 10.5931(3) Å	g = 93.217(2)°.
Volume	1011.81(5) Å ³	
Z	2	
Density (calculated)	1.671 Mg/m ³	
Absorption coefficient	2.285 mm ⁻¹	
F(000)	508	
Crystal size	0.22 x 0.15 x 0.10 mm ³	
Crystal color, habit	BLOCK / orange-red	
Theta range for data collection	2.17 to 26.54°.	
Index ranges	-11<=h<=11, -12<=k<=12, -13<=l<=13	
Reflections collected	23654	
Independent reflections	4195 [R(int) = 0.0424]	
Completeness to theta = 25.00°	99.9 %	
Absorption correction	multi-scan / sadabs	
Max. and min. transmission	0.8037 and 0.6333	
Refinement method	Full-matrix least-squares on F ²	
Data / restraints / parameters	4195 / 3 / 244	
Goodness-of-fit on F ²	1.043	
Final R indices [I>2sigma(I)]	R1 = 0.0313, wR2 = 0.0636	
R indices (all data)	R1 = 0.0406, wR2 = 0.0682	
Largest diff. peak and hole	1.752 and -1.283 e.Å ⁻³	

Table 2.17. Crystal data and structure refinement for **29**.

Identification code	ocon122	
Empirical formula	C17 H12 Cl2 Fe O	
Formula weight	359.02	
Temperature	100(2) K	
Wavelength	0.71073 Å	
Crystal system	Orthorhombic	
Space group	Pna2(1)	
Unit cell dimensions	a = 17.9196(7) Å	$\alpha = 90^\circ$
	b = 7.3294(3) Å	$\beta = 90^\circ$
	c = 11.0768(4) Å	$\gamma = 90^\circ$
Volume	1454.83(10) Å ³	
Z	4	
Density (calculated)	1.639 g/cm ³	
Absorption coefficient	1.397 mm ⁻¹	
F(000)	728	
Crystal size	0.36 x 0.35 x 0.30 mm ³	
Theta range for data collection	3.33 to 28.28°	
Index ranges	-23 ≤ h ≤ 23, -9 ≤ k ≤ 9, -14 ≤ l ≤ 9	
Reflections collected	12354	
Independent reflections	3100 [R(int) = 0.0285]	
Completeness to theta = 25.00°	99.8 %	
Absorption correction	Multi-scan	
Max. and min. transmission	0.6793 and 0.6332	
Refinement method	Full-matrix least-squares on F ²	
Data / restraints / parameters	3100 / 1 / 190	
Goodness-of-fit on F ²	1.034	
Final R indices [I > 2σ(I)]	R1 = 0.0196, wR2 = 0.0471	
R indices (all data)	R1 = 0.0209, wR2 = 0.0478	
Absolute structure parameter	0.003(10)	
Largest diff. peak and hole	0.285 and -0.222 e Å ⁻³	

Table 2.18. Crystal data and structure refinement for **30**.

Identification code	ocon132	
Empirical formula	C ₂₃ H ₂₄ Fe O	
Formula weight	372.27	
Temperature	100(2) K	
Wavelength	0.71073 Å	
Crystal system	Triclinic	
Space group	P -1	
Unit cell dimensions	a = 6.1662(7) Å	á= 102.493(6)°.
	b = 11.2169(12) Å	â= 100.587(6)°.
	c = 13.2843(15) Å	ã = 95.063(6)°.
Volume	873.91(17) Å ³	
Z	2	
Density (calculated)	1.415 Mg/m ³	
Absorption coefficient	0.870 mm ⁻¹	
F(000)	392	
Crystal size	0.300 x 0.100 x 0.050 mm ³	
Theta range for data collection	1.876 to 25.452°.	
Index ranges	-7<=h<=7, -13<=k<=13, -15<=l<=16	
Reflections collected	16890	
Independent reflections	3223 [R(int) = 0.0418]	
Completeness to theta = 25.000°	99.9 %	
Absorption correction	Multi-scan	
Refinement method	Full-matrix least-squares on F ²	
Data / restraints / parameters	3223 / 0 / 226	
Goodness-of-fit on F ²	1.013	
Final R indices [I>2sigma(I)]	R1 = 0.0579, wR2 = 0.1324	
R indices (all data)	R1 = 0.0761, wR2 = 0.1461	
Extinction coefficient	n/a	
Largest diff. peak and hole	1.167 and -1.173 e.Å ⁻³	

Table 2.19. Crystal data and structure refinement for **31**.

Identification code	rlh3142_0m_a	
Empirical formula	C ₂₂ H ₂₄ Fe O	
Formula weight	360.26	
Temperature	100.0 K	
Wavelength	0.71073 Å	
Crystal system	Triclinic	
Space group	P-1	
Unit cell dimensions	a = 11.2753(4) Å b = 12.3811(4) Å c = 13.2168(5) Å	a = 86.253(2)°. b = 69.899(2)°. g = 83.810(2)°.
Volume	1721.79(11) Å ³	
Z	4	
Density (calculated)	1.367 Mg/m ³	
Absorption coefficient	0.879 mm ⁻¹	
F(000)	760	
Crystal size	0.16 x 0.04 x 0.04 mm ³	
Theta range for data collection	1.641 to 25.421°.	
Index ranges	-13<=h<=13, -14<=k<=14, -15<=l<=15	
Reflections collected	28459	
Independent reflections	6319 [R(int) = 0.0287]	
Completeness to theta = 25.421°	99.6 %	
Absorption correction	Semi-empirical from equivalents	
Max. and min. transmission	0.7452 and 0.6304	
Refinement method	Full-matrix least-squares on F ²	
Data / restraints / parameters	6319 / 0 / 435	
Goodness-of-fit on F ²	1.063	
Final R indices [I>2sigma(I)]	R1 = 0.0301, wR2 = 0.0811	
R indices (all data)	R1 = 0.0385, wR2 = 0.0873	
Extinction coefficient	n/a	
Largest diff. peak and hole	0.409 and -0.641 e.Å ⁻³	

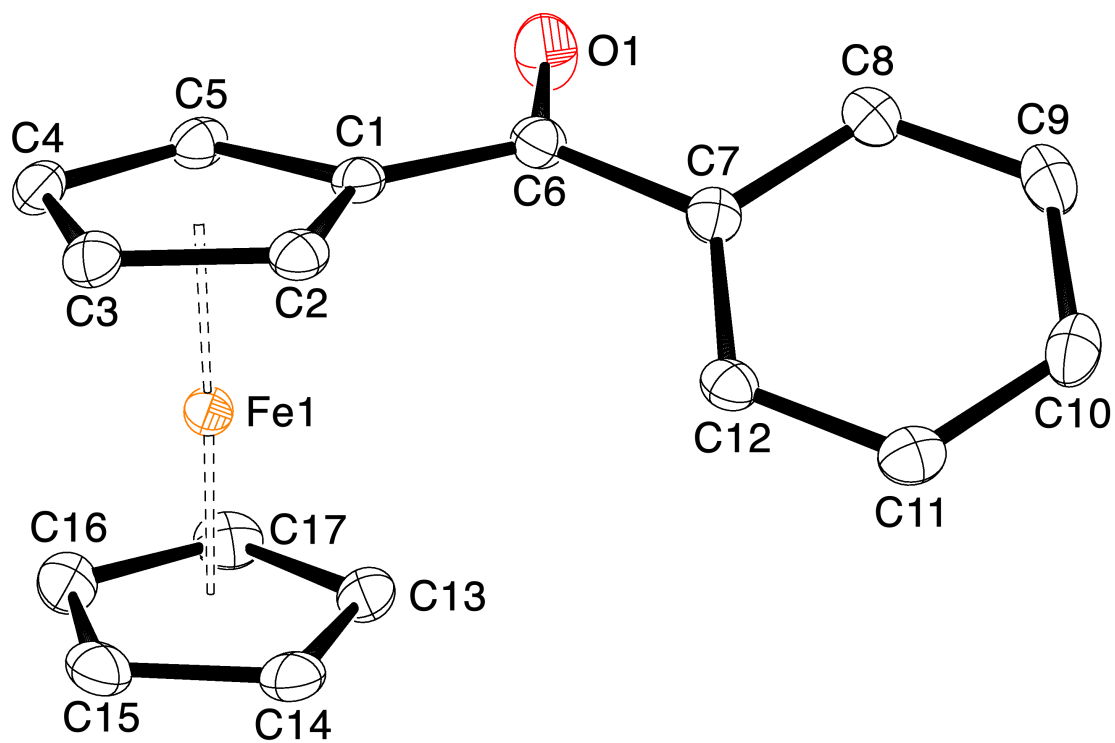


Figure 2.80. Numbered ORTEP of 7.

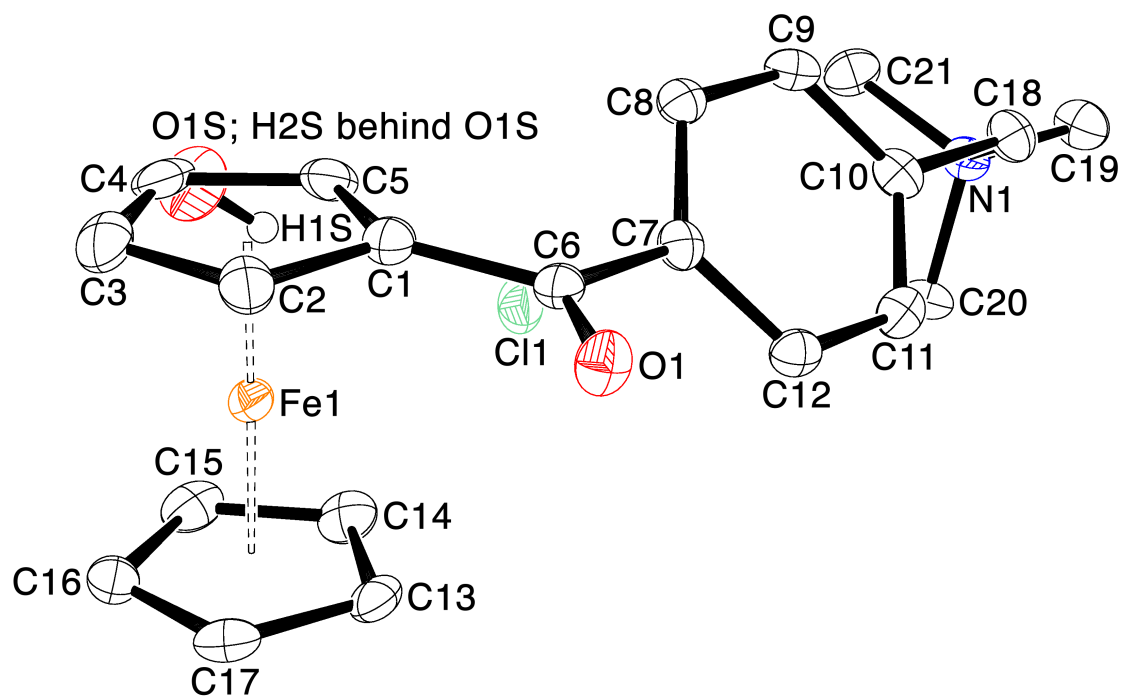


Figure 2.81. Numbered ORTEP of 15.

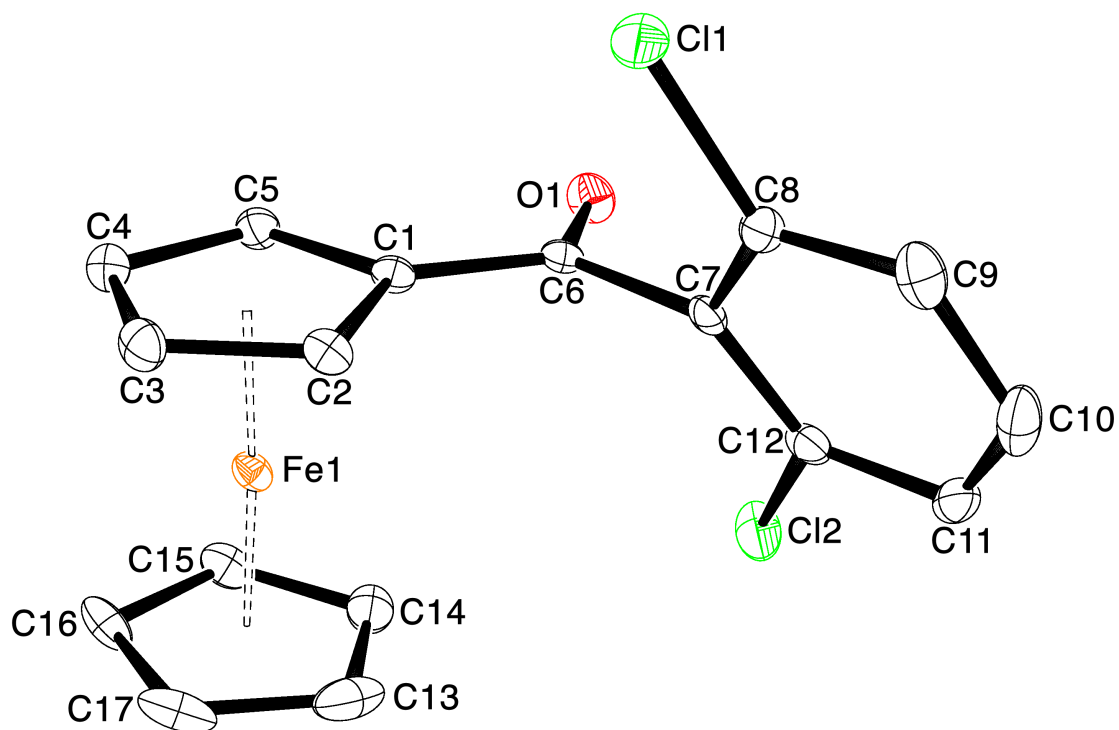


Figure 2.82. Numbered ORTEP of 29.

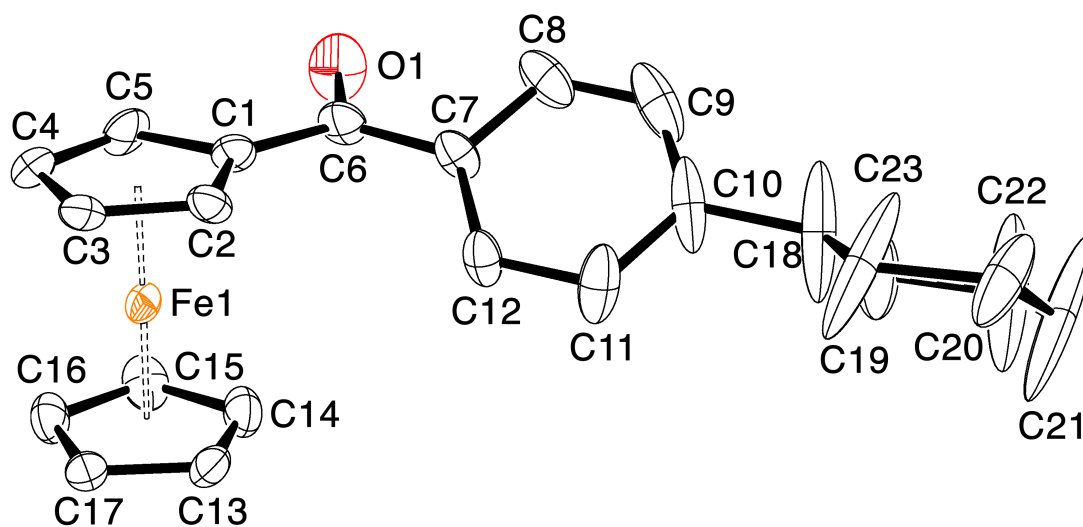


Figure 2.83. Numbered ORTEP of 30.

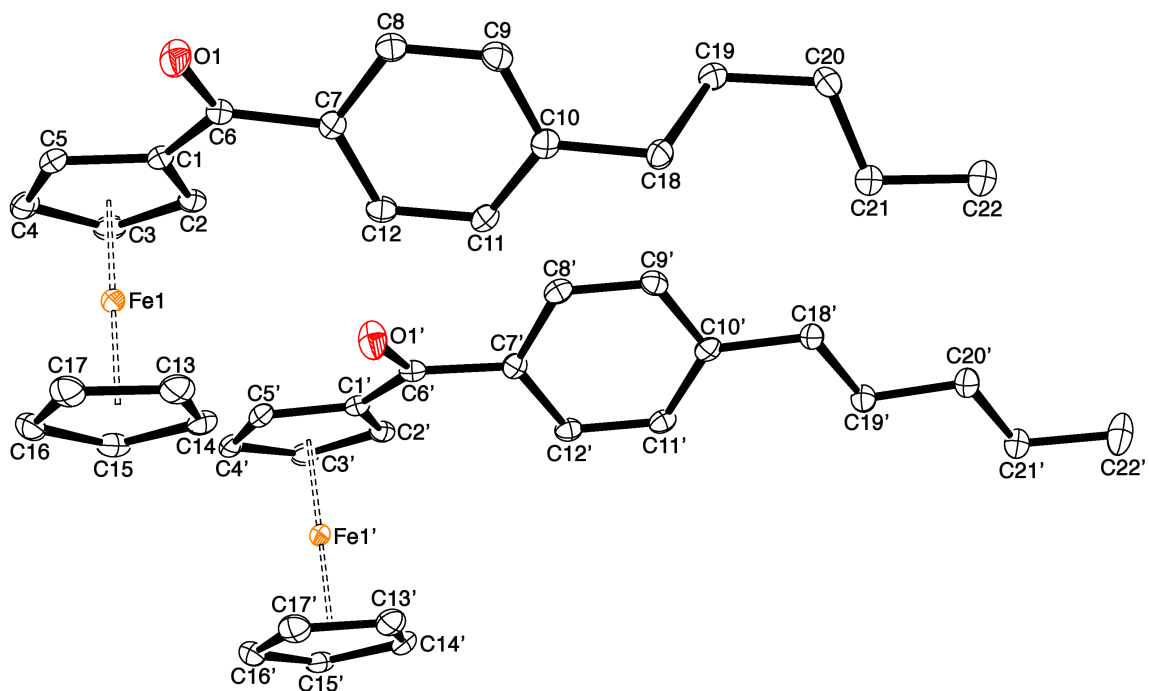


Figure 2.84. Numbered ORTEP of 31.

H. Appendix 3

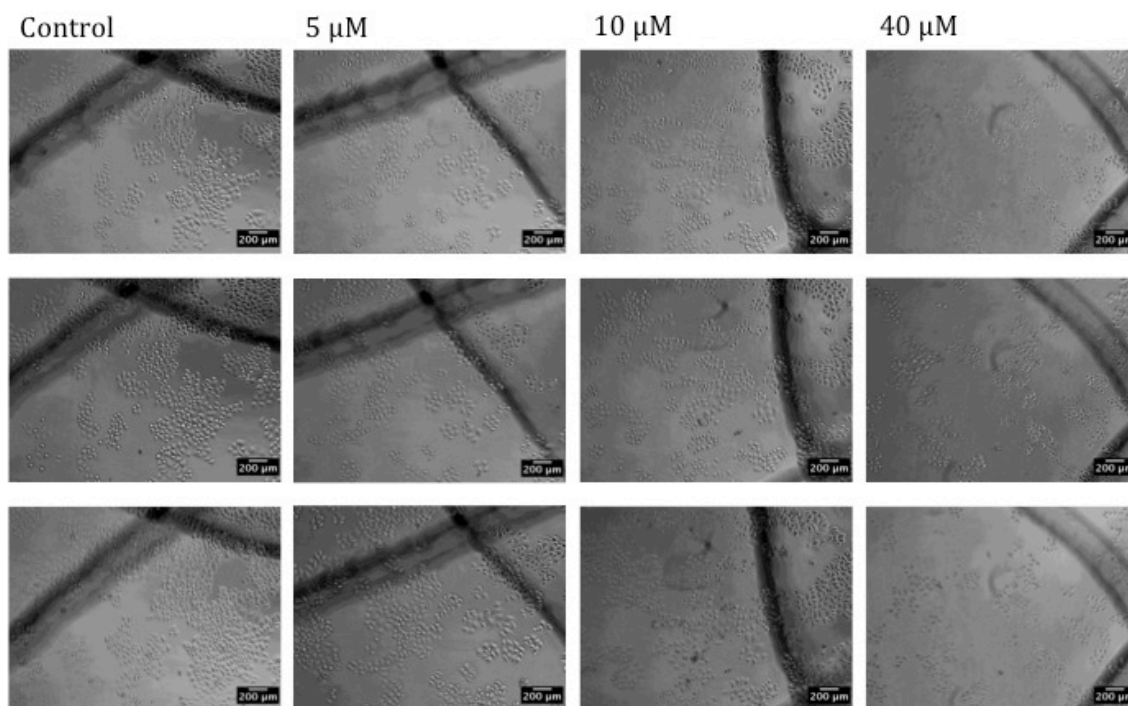


Figure 2.85. HeLa cells before and after being subjected to standard photolysis conditions with complex **30** at 10x magnification. Top row: before photolysis, middle row: immediately following photolysis, bottom row: 12 h post photolysis.

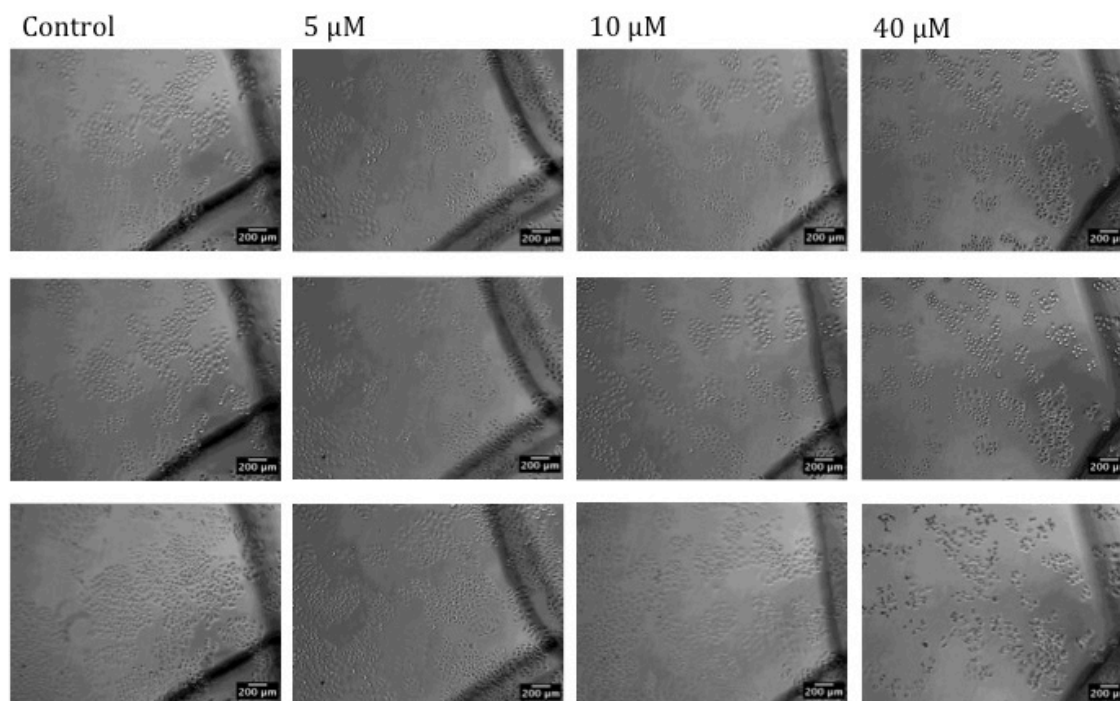


Figure 2.86. HeLa cells before and after being treated with complex **30** in the dark at 10x magnification. Images taken in parallel with corresponding photolyzed samples. Top row: before photolysis, middle row: immediately following photolysis, bottom row: 12 h post photolysis.

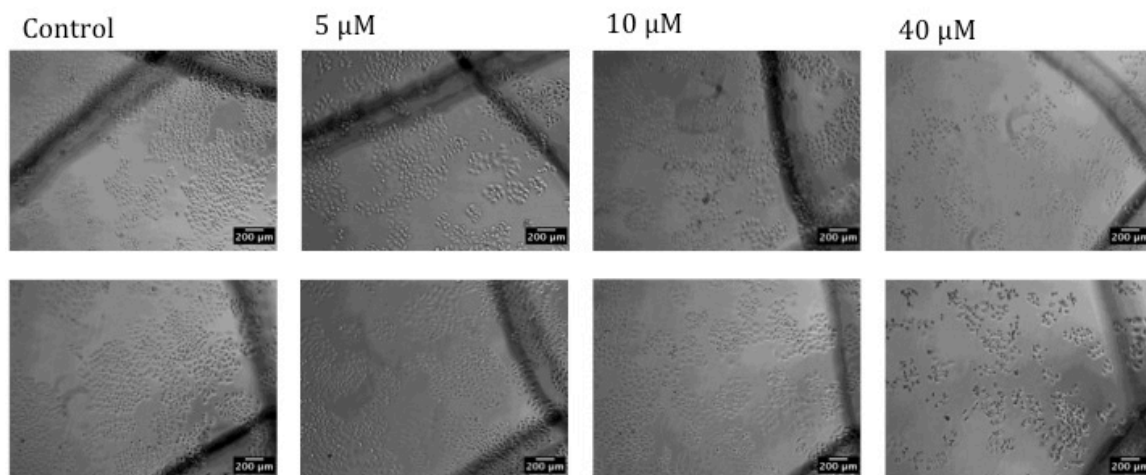


Figure 2.87. Cells after being subjected to **30** and standard photolysis conditions (top row) or ferrocene complex without irradiation in the dark (bottom row) at 10x magnification (images of both plates taken in parallel).

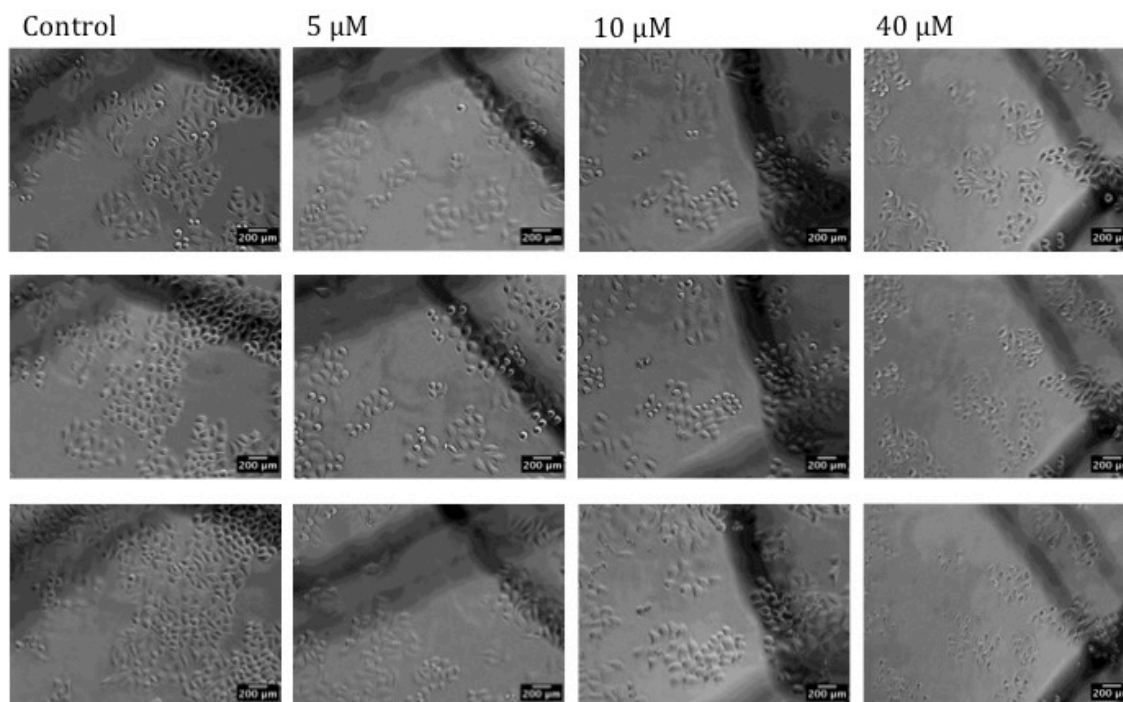


Figure 2.88. HeLa cells before and after being subjected to standard photolysis conditions at 20x magnification with **30**. Top Row: Before photolysis, middle row: immediately following photolysis, bottom row: 12 h post photolysis.

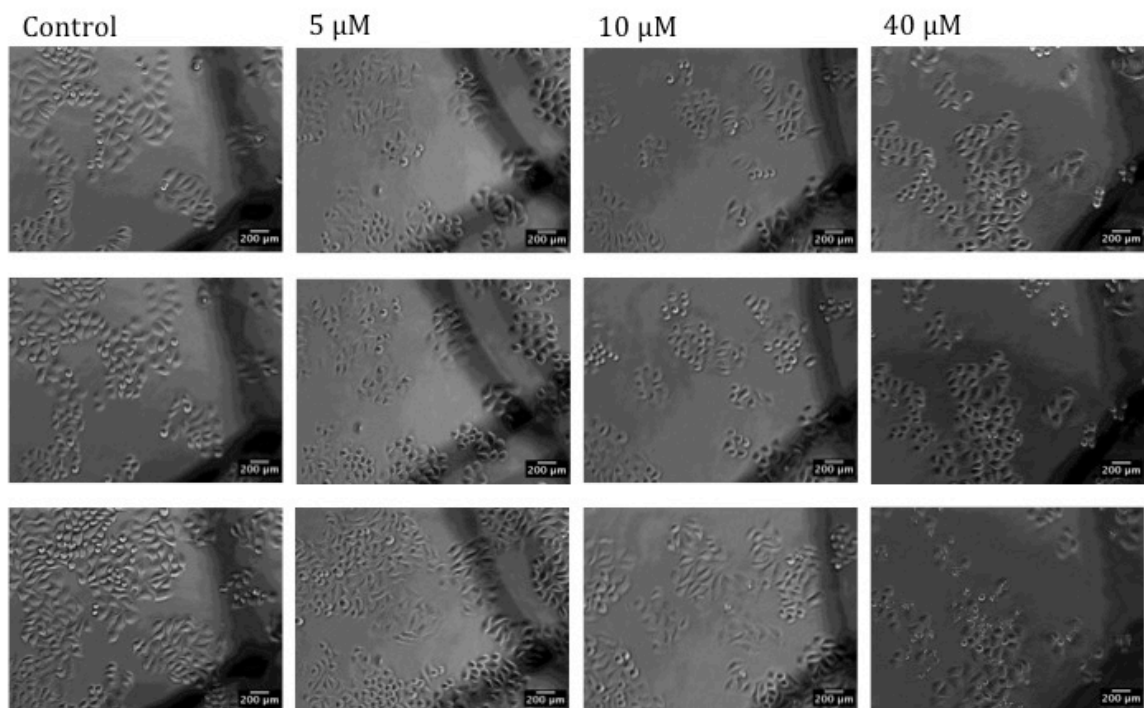


Figure 2.89. HeLa cells before after being treated with ferrocene complex **30** in the dark at 20x magnification. Images taken in parallel with corresponding photolyzed samples. Top row: before photolysis, middle row: immediately following photolysis, bottom row: 12 h post photolysis.

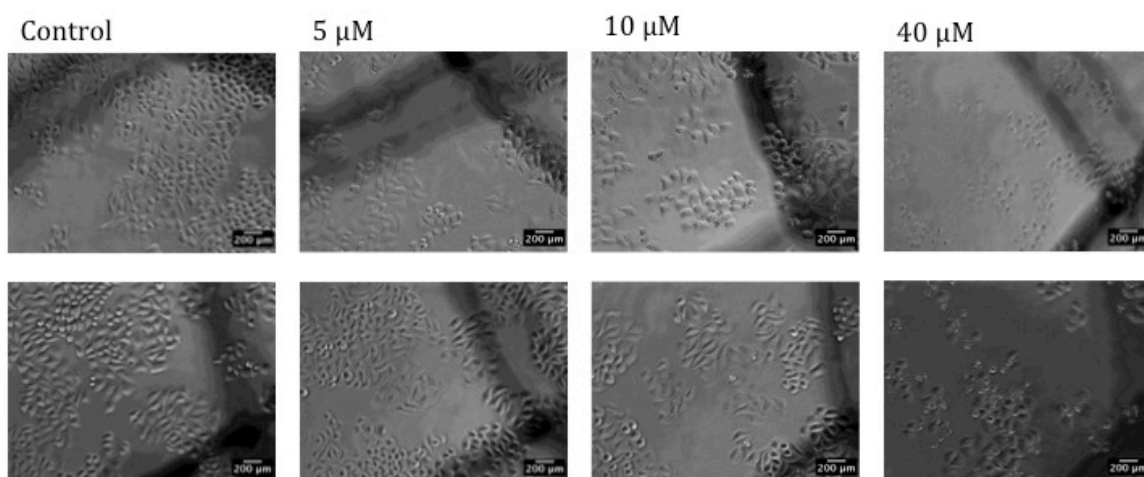


Figure 2.90. HeLa Cells before after being subjected to ferrocene complex **30** and standard photolysis conditions (top row) or ferrocene complex in the dark (bottom row) at 20x magnification (images of both plates taken in parallel).

I. References

- (1) Köpf-Maier, P.; Köpf, H. *Chem. Rev.* **1987**, *87*, 1137.
- (2) Schatzschneider, U.; Metzler-Nolte, N. *Angew. Chem. Int. Ed.* **2006**, *45*, 1504.
- (3) Simonneaux, G. *Bioorganometallic Chemistry*; Springer: Heidelberg Germany, 2006.
- (4) Jaouen, G. *Bioorganometallics*; Jaouen, G., Ed.; Wiley-VCH Verlag GmbH & Co: Weinheim, 2006.
- (5) Salmain, M.; Metzler-Nolte, N. In *Ferrocenes*; Stepnicka, P., Ed.; John Wiley & Sons, Ltd: West Sussex England, 2008; pp. 499–641.
- (6) Jaouen, G.; Metzler-Nolte, N. In *Topics in Organometallic Chemistry*; 2010.
- (7) Gasser, G.; Ott, I.; Metzler-Nolte, N. *J. Med. Chem.* **2011**, *54*, 3.
- (8) Gasser, G.; Metzler-Nolte, N. *Curr. Opin. Chem. Biol.* **2012**, *16*, 84.
- (9) Köpf-Maier, P.; Köpf, H.; Neuse, E. W. *J. Cancer Res. Clin. Oncol.* **1984**, *108*, 336.
- (10) Tamura, H.; Miwa, M. *Chem. Lett.* **1997**, 1177.
- (11) Osella, D.; Ferrali, M.; Zanello, P.; Laschi, F.; Fontani, M.; Nervi, C.; Cavigliolo, G. *Inorganica Chim. Acta* **2000**, *306*, 42.
- (12) Hillard, E.; Vessières, A.; Thouin, L.; Jaouen, G.; Amatore, C. *Angew. Chemie - Int. Ed.* **2005**, *45*, 285.
- (13) Vessières, A.; Corbet, C.; Heldt, J. M.; Lories, N.; Jouy, N.; Laïos, I.; Leclercq, G.; Jaouen, G.; Toillon, R. A. *J. Inorg. Biochem.* **2010**, *104*, 503.
- (14) Braga, S. S.; Silva, A. M. S. *Organometallics* **2013**, *32*, 5626.
- (15) Ornelas, C. *New J. Chem.* **2011**, *35*, 1973.
- (16) Pohl, H. R.; Wheeler, J. S.; Murray, H. E. *Interrelations between Essential Metal Ions and Human Diseases*; 2013; Vol. 13.
- (17) Yamaguchi, Y.; Kutal, C. *Inorg. Chem.* **1999**, *38*, 4861.

- (18) Yamaguchi, Y.; Ding, W.; Sanderson, C. T.; Borden, M. L.; Morgan, M. J.; Kotal, C. *Coord. Chem. Rev.* **2007**, *251*, 515.
- (19) Ding, W.; Sanderson, C.T.; Conover, R.C.; Johnson, M.K.; Amster, I.J.; Kotal, C. *Inorg. Chem.* **2003**, *42*, 1532.
- (20) Tarr, A. M.; Wiles, D. M. *Can. J. Chem.* **1968**, *46*, 2725.
- (21) Bozak, R.E.; Javaheripour, H. *Chem. Ind.* **1973**, 696.
- (22) Ali, L.H.; Cox, A.; Kemp, T. J. *J.C.S. Dalt.* **1973**, 1468.
- (23) Heaney, E.D.; Logan, R.; Powell, J. A. *J. Chem. Soc., Faraday Trans. 1.* **1977**, *73*, 699.
- (24) Goldman, I. M. *J. Org. Chem.* **1969**, *34*, 1979.
- (25) Nielsen, J.; Givskov, M. Compounds and Methods for Controlling Bacterial Virulence. International Publication Number WO 03/106445 A1, December 24, 2015.
- (26) Weber, C. D.; Bradley, C.; Lonergan, M. C. *J. Mater. Chem.* **2014**, *2*, 303.
- (27) *UV-Vis spectra were obtained in the laboratory of Cliff Kubiak at UC-San Diego.*
- (28) Saotome, K.; Morita, H.; Umeda, M. *Toxicol. In Vitro* **1989**, *3*, 317.
- (29) Chiba, K.; Kawakami, K.; Tohyama, K. *Toxicol. Vitro.* **1998**, *12*, 251.
- (30) García-Barrantes, P. M.; Lamoureux, G. V.; Pérez, A. L.; García-Sánchez, R. N.; Martínez, A. R.; San Feliciano, A. *Eur. J. Med. Chem.* **2013**, *70*, 548.
- (31) Carroll, M. a.; White, A. J. P.; Widdowson, D. a.; Williams, D. J. *J. Chem. Soc. Perkin Trans. 1* **2000**, 1551.
- (32) Veith, G. D.; Austin, N. M.; Morris, R. T. *Water Res.* **1979**, *13*, 43.
- (33) Lambert, W. J. *J. Chromatogr. A* **1993**, *656*, 469.
- (34) Sangster, J. *J. Phys. Chem. Ref. Data* **1989**, *18*, 1111.
- (35) *ICP-OES experinemnts were conducted in the lab of Dr. Paterno Castillo at the Scripps Institution of Oceanography with Chris MacIsaac.*

- (36) Bradford, M. M. *Anal. Biochem.* **1976**, *72*, 248.
- (37) Connelly, N. G.; Geiger, W. E. *Chem. Rev.* **1996**, *96*, 887.
- (38) Khattak, R.; Imam Naqvi, I.; Akhyar Farrukh, M. *J. Iran. Chem. Soc.* **2008**, *5*, 631.
- (39) Bellér, G.; Bátki, G.; Lente, G.; Fábián, I. *J. Coord. Chem.* **2010**, *63*, 2586.
- (40) Ali, L. H.; Cox, a.; Kemp, T. J. *J. Chem. Soc. Chem. Commun.* **1972**, 265.
- (41) Pazderski, L.; Pawlak, T.; Sitkowski, J.; Kozerski, L.; Edward Szłyk. *Magn. Reson. Chem.* **2010**, *48*, 450.
- (42) Che, D.-J.; Li, G.; Du, B.-S.; Zhang, Z.; Li, Y. H. *Inorganica Chim. Acta* **1997**, *261*, 121.
- (43) Crichton, R. *Iron Metabolism*; 3rd ed.; Wiley: West Sussex U.K., 2009.
- (44) Halliwell, B.; Gutteridge, J. M. *Biochem. J.* **1984**, *219*, 1.
- (45) Pierre, J. L.; Fontecave, M. *BioMetals* **1999**, *12*, 195.
- (46) Halliwell, B.; Gutteridge, J. M. *Free Radicals in Biology and Medicine*; 4th ed.; Oxford University Press: Oxford, 2007.
- (47) Irie, M. *Photochem. Photobiol. Sci.* **2010**, *9*, 1535.
- (48) Moan, J.; Peng, Q. In *Photodynamic Therapy*; Patrice, T., Ed.; 2003; pp. 1–18.
- (49) Stacey, O. J.; Pope, S. J. a. *RSC Adv.* **2013**, *3*, 25550.
- (50) Dolmans, D.; Fukumura, D; Jain, R. *Nat. Rev. Cancer* **2003**, *3*, 380.
- (51) Juarranz, Á.; Jaén, P.; Sanz-Rodríguez, F.; Cuevas, J.; González, S. *Clin. Transl. Oncol.* **2008**, *10*, 148.
- (52) Fujita, T.; Iwasa, J.; Hansch, C. *J. Am. Chem. Soc.* **1964**, *86*, 5175.
- (53) Lipinski, C. a; Lombardo, F.; Dominy, B. W.; Feeney, P. J. *Adv. Drug Deliv. Rev.* **2001**, *46*, 3.
- (54) Jaouen, G.; Top, S. . V. In *Organometallics Target to Specific Biological Sites: the development of New Therapies*; Jaouen, G., Ed.; Weinheim, 2006; p. 76.

- (55) Zor, T.; Selinger, Z. *Anal. Biochem.* **1996**, 236, 302.
- (56) Ali, L.H.; Cox, A.; Kemp, T. J. *J.C.S. Dalt.* **1973**, 1468.
- (57) Lowry, T.H.; Richardson, K. S. *Mechanism and Theory in Organic Chemistry*; Harper and Row: New York, 1976.

J. Acknowledgments

The material in Chapter II, in part, will be included in the submission for publication. Aubrey, Marissa; Proetto, María; Hoong, Christina; Melaimi, Mohand; O'Connor, Joseph. "Photoactivated Organoferrous Antitumor Agents". The dissertation author was the primary investigator and author of this material.

Chapter III.

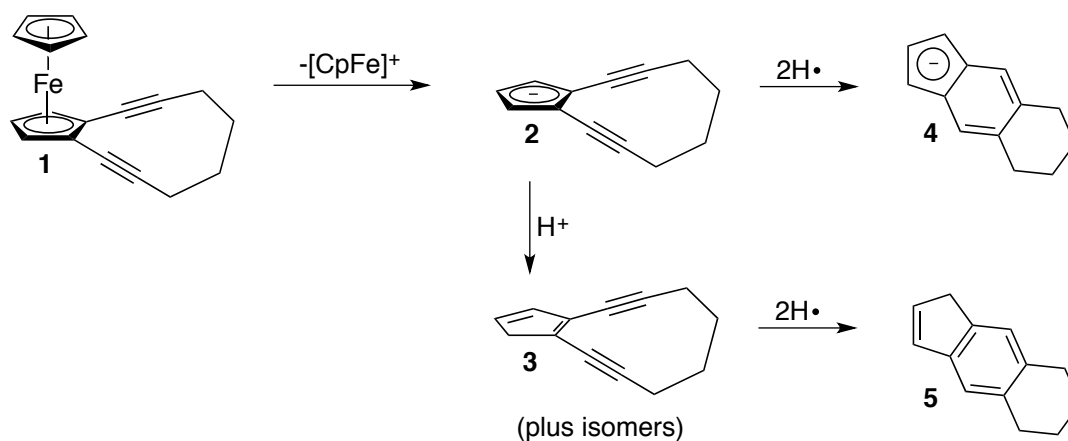
Photosensitive Ferrocene-Based Eneidyne

A. Introduction

Since the discovery of the naturally occurring enediyne antibiotics, chemists have been bewitched by both the unique reactivity and remarkable biological activity of the novel class of molecules.^[1,2,3,4,5] Nature accomplishes the cyclization of these structures in seemingly simple and elegant fashions by converting a stable precursor to a highly reactive enediyne warhead which cleaves DNA once the target is reached; however chemists have struggled to control the highly cytotoxic *para*-benzyne diradical in the lab and *in vitro*.^[6,7,8,9] Traditionally, the cycloaromatization of enediynes has been accomplished by (1) heating the substrate until the energy to rearrange to the biradical is reached, or (2) by introduction of ring strain into the enediyne framework. For any biological application however, the drug candidate cannot require excessive heat to form the diradical, nor should it cyclize too quickly and in an unselective fashion. With these constraints in mind, triggering mechanisms that allow for controlled generation of the highly reactive *para*-benzyne diradical at biologically temperatures are currently of great interest to medicinal chemists.

One method to affect the cycloaromatization of enediyne substrates using transition metals is by coordination to either heteroatoms on the enediyne termini⁶ or the enediyne π -system. Specifically, previous students in the O'Connor Lab demonstrated the facile metal-assisted cyclization of otherwise unreactive enediynes using $[\text{Cp}^*\text{ML}_3]^+$ complexes ($M = \text{Ru}$ or Fe). These novel metal triggers were found to easily form the arene products at room temperature in the presence

of a hydrogen atom donor (THF or 1,4-cyclohexadiene).^[10,11,12] A second method to perturb the enediyne cycloaromatization parameters involves transition metal coordination to the *ene* of a reactive, aromatic, strained enediyne. Compound **1**, where the *ene* of the highly strained enediyne is incorporated into the cyclopentadienyl ligand, was synthesized in our group and shown to be stable to cycloaromatization up to temperatures of 150 °C in THF-*d*₈ (Scheme 3.1). The cyclopentadienide anion (**2**), or cyclopentadiene (**3**), formed upon oxidative release from the central iron, were predicted to undergo cyclization to form compounds **4** or **5** (respectively); however, chemical oxidation to induce ligand dissociation via the ferrocenium analogue¹³ failed to give products that could be characterized by NMR spectroscopy. For ferrocene-based enediynes to be successful candidates for studies in biological systems, derivatives would need to be synthesized that readily give the organic enediyne upon triggering using a method other than oxidation.



Scheme 3.1. Proposed dissociation and aromatization of ferrocenyl-enediynes.

A fundamental precedent for our current proposal is work by Kutal, who

described the remarkable photoactivity of 1-benzoylferrocene and 1,1-dibenzoylferrocene upon exposure to visible light (490 nm).^[14,15,16] Kutal proposed that conjugation between π orbitals of the cyclopentadienyl ring and neighboring carbonyl group results in charge delocalization over several atoms (Figure 3.1). This delocalization stabilizes the low energy excited states and lowers transition energies. As a result, the electron-deficient iron atom in the excited state (**6***) is prone to ring-slippage and under photo conditions, dissociates one or both cyclopentadienyl ligands. With this precedent in mind, we speculated that incorporation of a benzoyl functional group unto a ferrocenyl-enediyne could introduce a photochemical triggering device to control cycloaromatization for biological applications. Based on previous results in the O'Connor lab with complex **1**, and taking inspiration from the work of Kutal, we proposed a series of benzoylferrocene-based enediynes that would be activated by visible light triggered cyclopentadienyl ligand dissociation (**7-10**). The activated complexes would cycloaromatize by either metal coordination (**8**) or by simple release of the *ene* fragment from the metal (**9** and **10**) to generate the highly cytotoxic *para*-benzyne diradical (Figure 3.2).

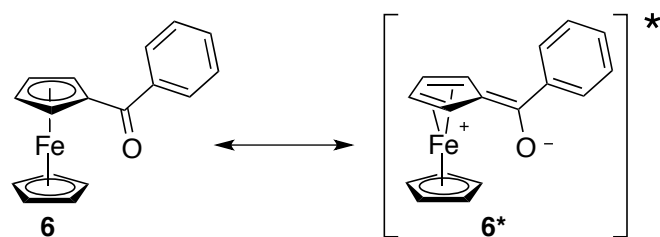


Figure 3.1. Resonance structure representative of the MLCT character in the low-energy excited state of **6**.

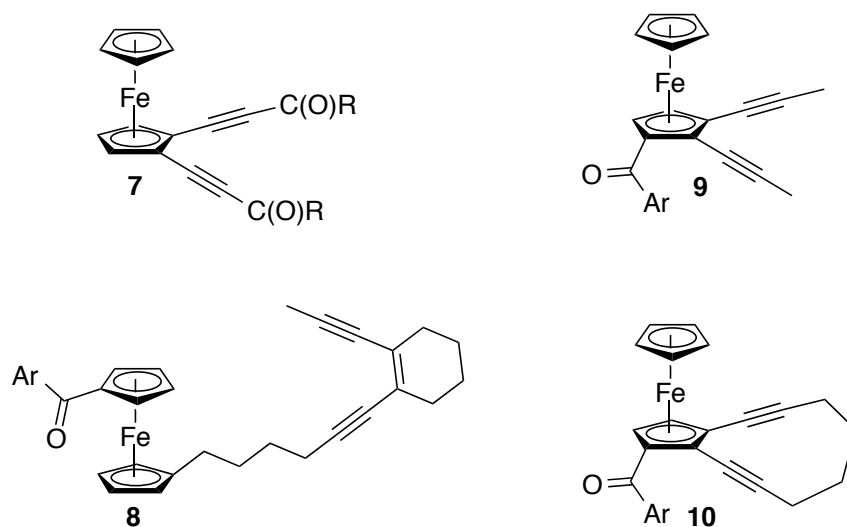
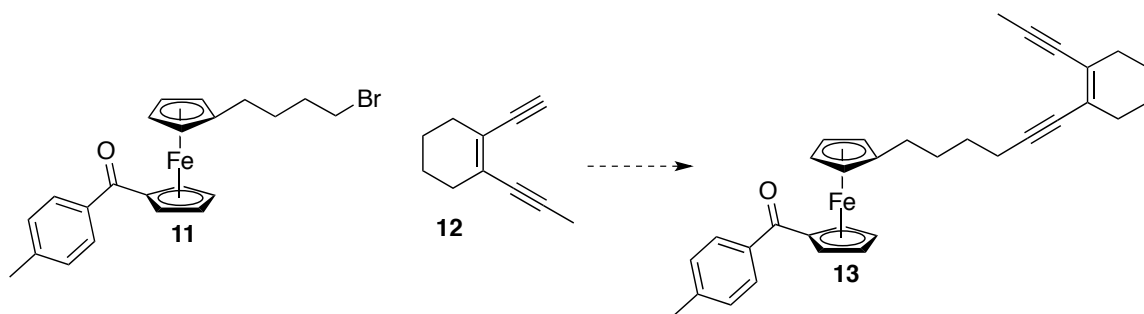


Figure 3.2. Proposed ferrocenyl-enediynes.

B. Results

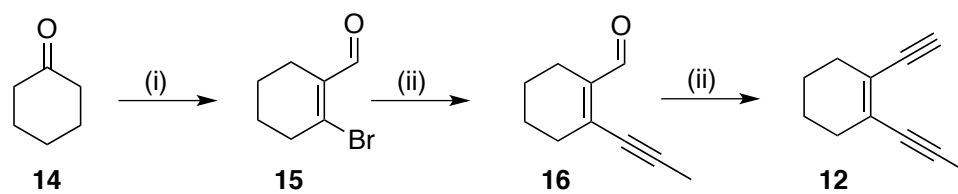
1. Synthesis of enediyne **13**.

To synthesize tethered enediyne **13** we proposed a convergent synthetic plan where primary alkyl halide **11** would participate in an S_N2 reaction with the anion of terminal enediyne **12** to generate cycloaromatization precursor **13** (Scheme 3.2).



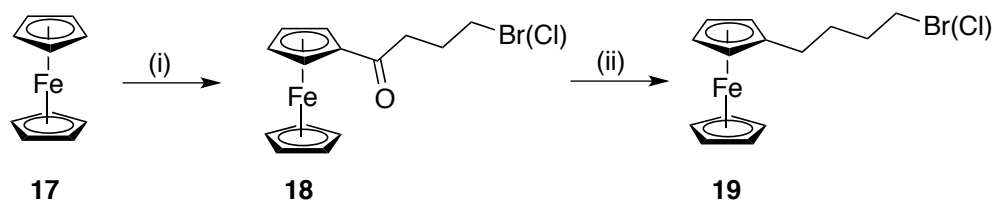
Scheme 3.2. Proposed synthesis of tethered enediyne **13**.

The preparation of 1-ethynyl-2-(prop-1-yn-1-yl)cyclohex-1-ene (**12**) was reported by previous members of the O'Connor Lab. To briefly summarize, 2-bromocyclohex-1-ene-1-carbaldehyde was synthesized from cyclohexanone (**14**), dimethylformamide, and PBr₃ (Scheme 3.3). Installation of the first alkyne was achieved by Sonogashira coupling of vinyl bromide **15** with propyne using palladium(0) and cuprous iodide. Deprotonation of (trimethylsilyl)dizaomethane with *n*-BuLi followed by addition of aldehyde **16** at -78 °C gave enediyne **12** via a Peterson homologation in good yield. Using this methodology we were able to synthesize enediyne **12** in 35% overall yield.



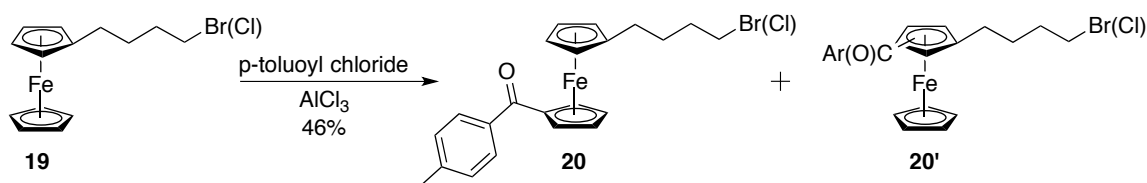
Scheme 3.3. Synthesis of enediyne **12**. (i) DMF, PBr₃, CH₂Cl₂; (ii) propyne, Pd(PPh₃)₄, CuI, benzene; (iii) TMSCHN₂, *n*-BuLi, THF.

Synthesis of the organometallic precursor **11** was more challenging. Using a literature procedure^[17,18] we were able to prepare primary halide **19** from ferrocene by a two step synthesis. Reaction of ferrocene with 4-bromobutanoyl chloride and aluminum chloride gave ketone **18**. Subsequent reduction of ketone **18** with sodium borohydride in the presence of AlCl₃ allowed for isolation of (4-bromobutyl)ferrocene (**19**) in good yield.



Scheme 3.4. Synthesis of primary alkyl halide **19**. (i) (4-bromobutanoyl) chloride, AlCl_3 , CH_2Cl_2 ; (ii) NaBH_4 , AlCl_3 , CH_2Cl_2 .

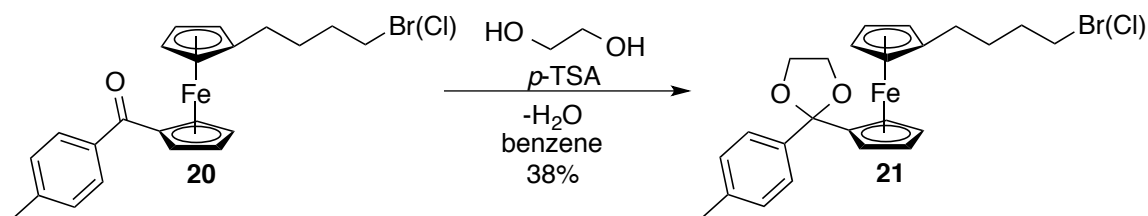
Friedel-Crafts acylation of **19** with *para*-toluoyl chloride gave a mixture of regioisomeric benzoylferrocenes including the desired 1,1'-substituted isomer, which was isolated by column chromatography. The regiochemistry of the product was confirmed by resonances in the ^1H NMR spectrum (CDCl_3) at δ 4.05, 4.09, 4.52, and 4.84 in a 2:2:2:2 ratio, and by resonances attributed to the *ipso*-carbons of the two cyclopentadienyl rings at δ 78.76 and 90.46 in the ^{13}C NMR spectrum (CDCl_3).



Scheme 3.5. Friedel-Crafts acylation to generate benzoylferrocene **20**.

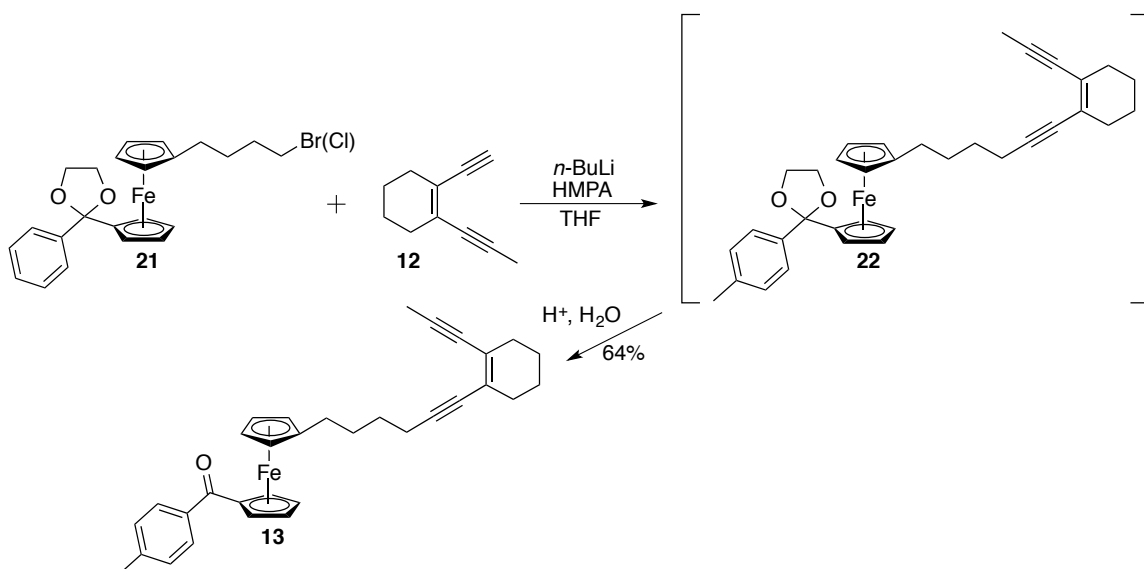
We first attempted to synthesize **13** by deprotonation of enediyne **12** with *n*-butyllithium, or lithium bis(trimethylsilyl)amide (LiHMDS), and reaction with ketone **20**; however we were unable to detect the desired product in the reaction mixture. Suspecting the alkynyl anion of **12** was attacking the ketone rather than the primary carbon bearing the halide, the carbonyl was protected as an acetal (Scheme 3.6). Formation of the acetal required forcing conditions; **21** was only able

to be isolated in 38% yield following reflux for two days in benzene with azeotropic removal of water by use of a Dean-Stark trap. Installation of the acetal was confirmed by the upfield chemical shifts (^1H NMR, CD_2Cl_2) of the cyclopentadienyl hydrogens on the ring bearing the phenyl group, which appeared as a complex multiplet between δ 4.04-4.18.



Scheme 3.6. Synthesis of acetal **21** by azeotropic removal of water.

$\text{S}_{\text{N}}2$ reaction to generate tethered enediyne **13** from precursor **21** failed with sodium hydride (NaH) and 18-crown-6, LiHMDS, and n -BuLi. Success was eventually achieved by deprotonation of **12** with n -butyllithium followed by treatment with four equivalents of hexamethylphosphoramide (HMPA) and dropwise addition of the primary alkylhalide **21** at -78 °C. Deprotection of the ketone by workup with aqueous p -TSA gave final product **13**.



Scheme 3.7. Synthesis of tethered enediyne **13** from **21**.

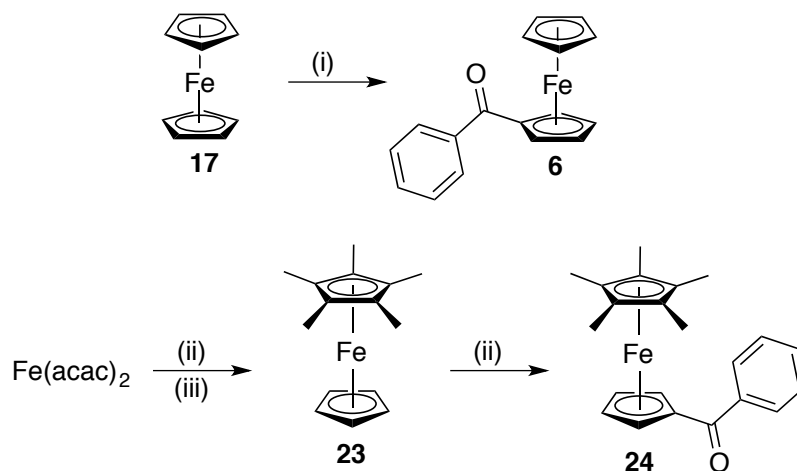
2. Cyclization attempts with ferrocenyl-enediyne **13**.

We expected that photochemical liberation of the benzoylcyclopentadienyl ligand from **13** would generate a reactive CpFeL_3^+ equivalent *in situ*. Once formed, the CpFeL_3^+ fragment would cycloaromatize the tethered enediyne and generate the arene product in the presence of a hydrogen-atom donor. However, photolysis of complex **13** in CD_3CN with the hydrogen-atom donor 1,4-cyclohexadiene (1,4-CHD) failed to give the expected arene product. Suspecting the strongly coordinating acetonitrile solvent was precluding enediyne binding, we next photolyzed **13** in acetone- d_6 with 5 equivalents of acetonitrile to stabilize the CpFe^+ fragment as it was generated photochemically. Under these conditions we observed only a black precipitate that adhered to the walls of the J. Young tube and was insoluble in acetonitrile, tetrahydrofuran, dichloromethane, and chloroform. Prolonged

photolysis (72 h) led to extreme peak broadening in the ^1H NMR spectrum that persisted even following filtration under nitrogen, suggestive of paramagnetic iron decomposition products.

3. Attempted cycloaromatization of **25** with **6** and **24**.

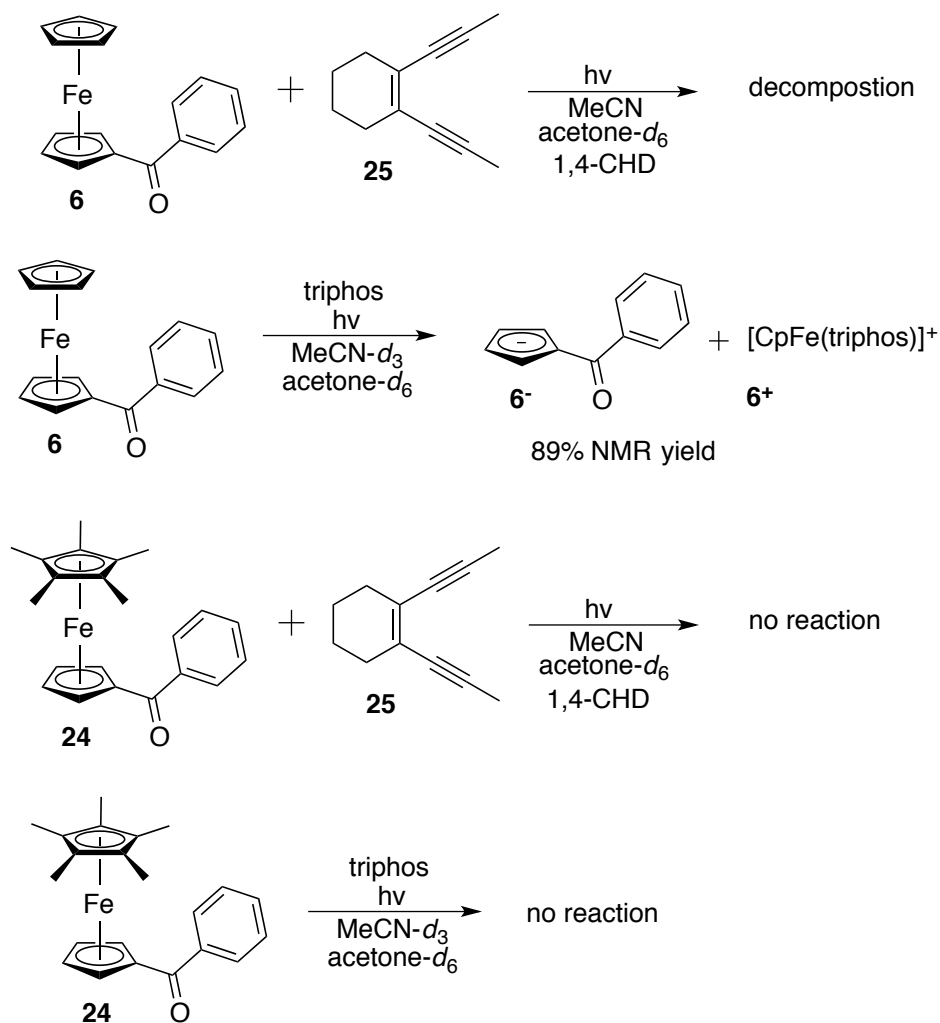
Previously in the O'Connor lab we demonstrated the ability of pentamethylcyclopentadienylirontris(acetonitrile), $[\text{Cp}^*\text{Fe}(\text{NCMe}_3)^+]$, to cyclize acyclic enediynes. Suspecting the relatively electron-deficient Cp ligand in the CpFeL_3^+ fragment was causing the cycloaromatization reaction to fail, we prepared benzoylferrocene and the Cp^* analog **24** (Scheme 3.8) to test their ability as cyclization pre-catalysts.¹⁹



Scheme 3.8. Synthesis of **6** and **24**. (i) benzoylchloride, AlCl_3 , CH_2Cl_2 ; (ii) pentamethylcyclopentadiene, $n\text{-BuLi}$, THF; (iii) NaCp ; (iv) benzoylchloride, AlCl_3 , CH_2Cl_2 .

Photolysis of benzoylferrocene **6** and enediyne **25** using sunlight or a Hanovia lamp resulted in only extreme peak broadening and slow disappearance of

the starting sandwich complex peaks in the ^1H NMR spectrum (Scheme 3.9). Following filtration no cycloaromatized products were observed by ^1H NMR spectroscopy or mass spectrometry. Photolysis (sunlight or Hanovia lamp) with the strong chelating ligand 1,1,1-tris(diphenylphosphinomethyl)ethane (triphos) in acetone- d_6 and MeCN- d_3 (3:1) resulted in a gradual disappearance of the starting metallocene peaks at δ 4.83 (2H), 4.61 (2H) and 4.20 (5H) in the ^1H NMR spectrum. During the course of the experiment, new resonances appeared at δ 5.77 (broad, 4H) and 4.97 (s, 5H) which were assigned to the benzoylcyclopentadienide anion and $[\text{CpFe}(\text{triphos})]^+$, respectively. By ^1H NMR spectroscopy, conversion to the photoproducts was complete after 12 h with a calculated ^1H NMR yield of 89% relative to an internal standard (hexamethyldisiloxane). A control reaction in the absence of light gave no reaction even after several days. Photolysis of **24** and **25** in the same solvent system also resulted in no formation of cycloaromatized product. Similarly, when **24** was photolyzed in the presence of triphos, no benzoylcyclopentadienide anion or half sandwich complex was observed by ^1H NMR spectroscopy. Even when photolyzed exhaustively (96 h, Hanovia lamp), all that was observed in the ^1H NMR spectrum was analytically pure **24** and **25**.

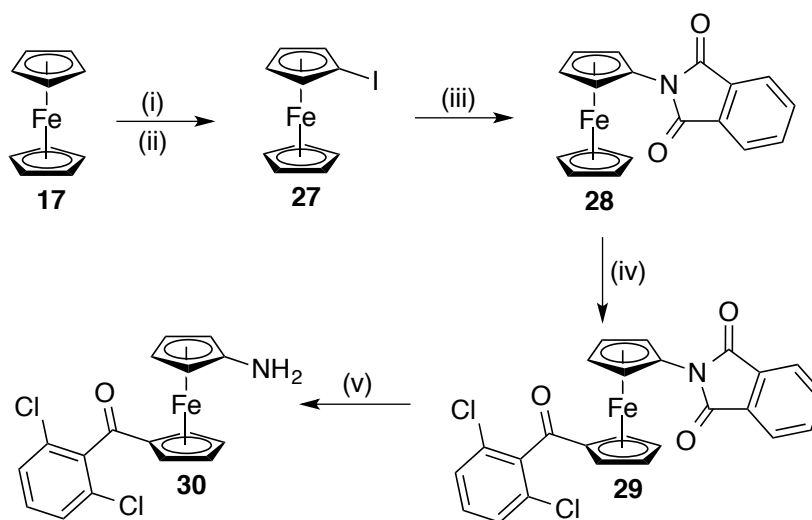


Scheme 3.9. Photolysis of benzoylferrocenes **6** and **24** with **25** or triphos.

4. Studies on electron-rich benzoylferrocene **26**.

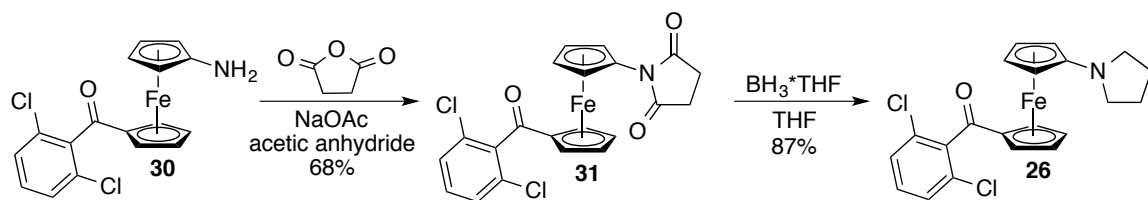
Suspecting **24** was failing to photodissociate the benzoylcyclopentadienyl ligand due to the electron-rich and sterically demanding Cp* ligand, we synthesized a pyrrolidine-substituted cyclopentadienyl derivative we predicted to be electron-rich like Cp* but less sterically encumbering (**26**). Reaction of ferrocene with *t*-butyllithium and iodine gave iodoferrocene,²⁰ which was refluxed in pyridine for

two days with phthalimide and Cu_2O to generate 2-ferrocenylisoindole-1,3-dione (Scheme 3.10).²¹ Treatment of **28** with 2,6-dichlorobenzoyl chloride under Friedel-Crafts acylation conditions gave **29**, which was then reduced to amine **30** by reaction with hydrazine²².



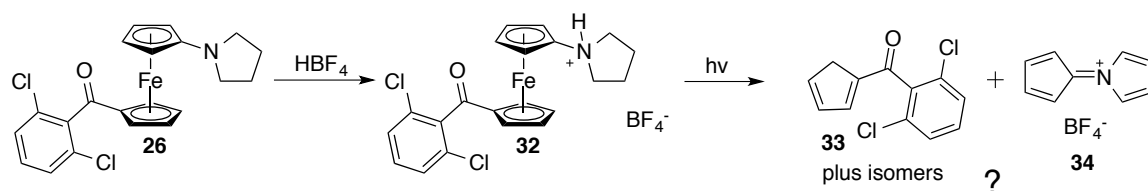
Scheme 3.10. Synthesis of complex **30**. (i) *t*-BuLi, THF, (ii) I_2 ; (iii) phthalimide, Cu_2O , pyridine, reflux 48 h; (iv) 2,6-dichlorobenzoyl chloride, AlCl_3 , CH_2Cl_2 ; (v) hydrazine.

Concerned the primary amine in **30** could easily coordinate to a photochemically generated CpFeL_n^+ fragment, we next prepared tertiary amine **26**. Complex **31**²³ was synthesized by reacting **30** with succinic anhydride and sodium acetate (Scheme 3.11). Product formation was confirmed by a new methylene peak at δ 2.74 in the ^1H NMR spectrum (CD_2Cl_2) and by a new signal corresponding to the amide carbonyl carbon at 175.92 in the ^{13}C NMR spectrum (CD_2Cl_2). Refluxing this complex with borane ($\text{BH}_3 \cdot \text{THF}$) at room temperature gave the desired tertiary amine **26** in 87% yield.



Scheme 3.11. Synthesis of pyrrolidine **26**.

Photolysis (Hanovia lamp) of **26** in the presence of enediyne **25** (acetone- d_6 , 10 equiv 1,4-CHD, 5 equiv MeCN) failed to give cycloaromatized product. Prolonged photolysis (96 h) in the presence of triphos failed to give the half-sandwich complex, reminiscent of experiments with Cp* derivative **24**. When treated with one equivalent of HBF₄, the conjugate acid of **26** was formed, evidenced by downfield chemical shifts for the pyrrolidine methylene hydrogens in **32** (δ CD₃CN; 3.90, 2.10) relative to **26** (δ CD₂Cl₂; 2.94, 1.92) (Scheme 3.12). Exposure of **32** to sunlight in the presence of enediyne **25** or triphos led to an immediate color change from red to yellow, formation of a clear precipitate, and severe peak broadening in the ¹H NMR spectrum. Following filtration under nitrogen, gas-chromatography-mass spectrometry only detected benzoylcyclopentadiene **33** and iminium ion **34**. At this time, the exact identity of the organic photoproducts and fate of the iron remain unknown. Control reactions in the absence of light demonstrated both **26** and **32** are stable in the absence of light.



Scheme 3.12. Synthesis and photochemical activity of **32**.

5. X-ray crystallographic analysis of **24**, **26** and **32**.

Deep red X-ray quality crystals of **24** were grown by slow evaporation of ethyl acetate and dark purple crystals of both **26** and **32** were grown from slow diffusion of pentane into acetonitrile. Full refinement data can be found in Appendix 2. Key bond metrics are summarized in Tables 3.1-3.5. The ORTEP for **6** was previously presented in Chapter 2.

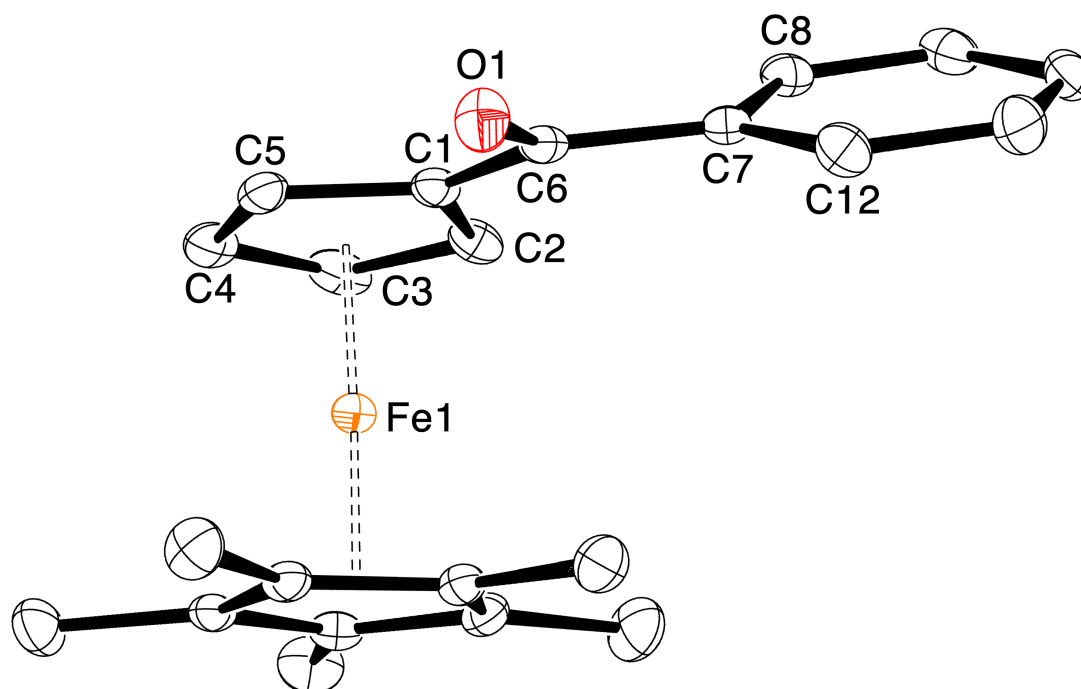


Figure 3.3. ORTEP drawing for **24**.

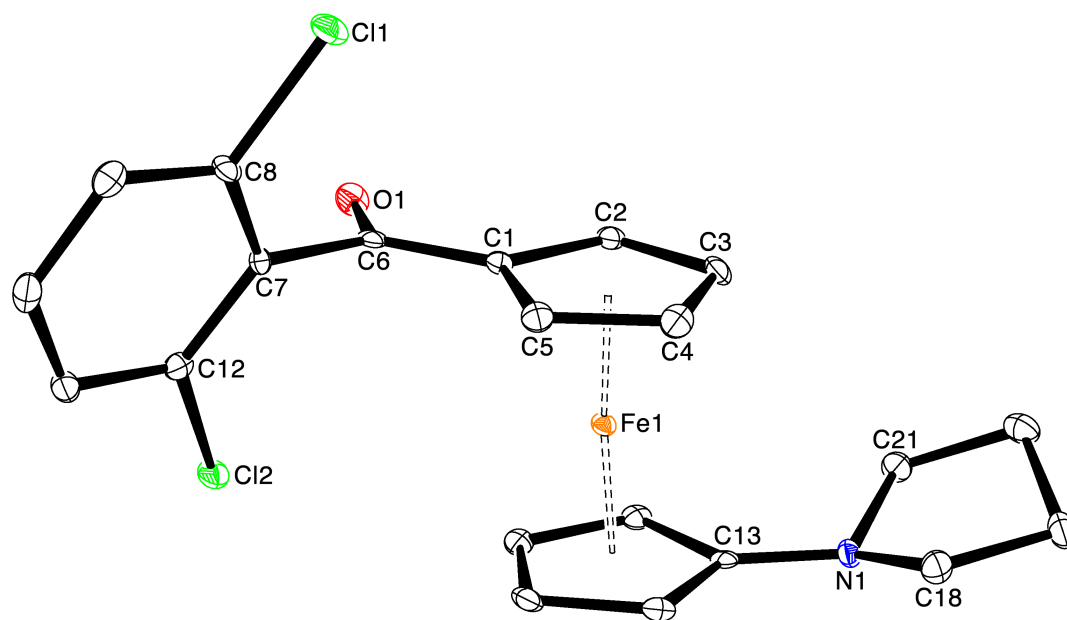


Figure 3.4. ORTEP drawing for **26**.

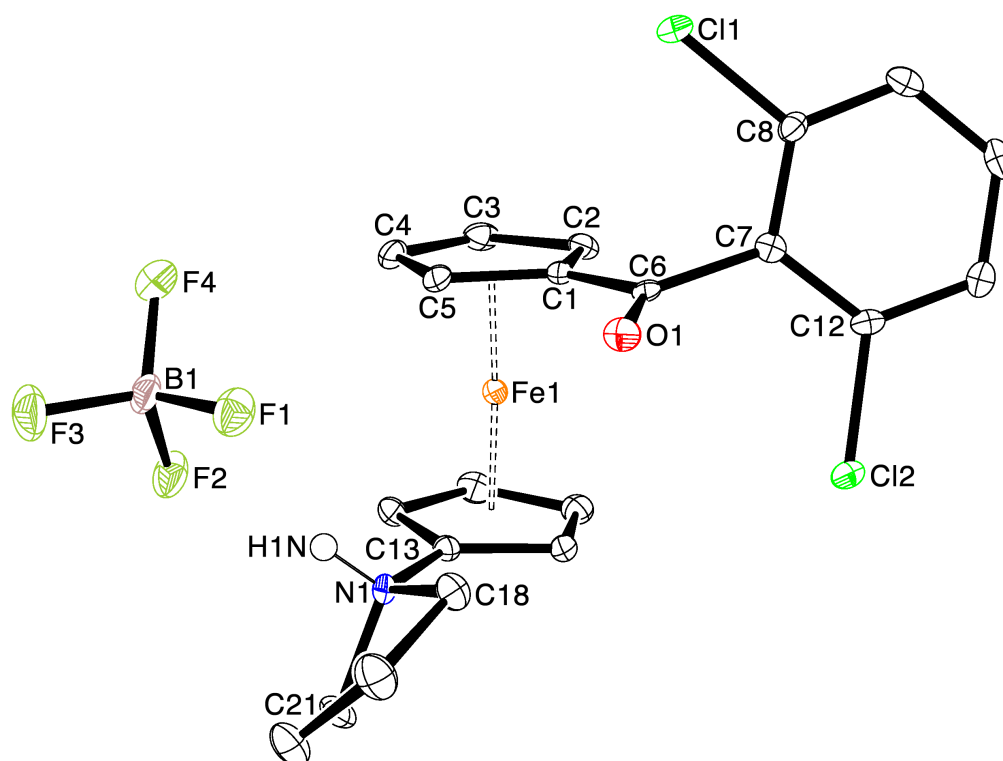


Figure 3.5. ORTEP drawing for **32**.

Table 3.1. Key angles for complexes **6**, **24**, **26** and **32**.

Complex	C(1)-C(6) [Å]	C(6)-O(1) [Å]	C(6)-C(7) [Å]
6	1.472(3)	1.224(2)	1.505(3)
24	1.479(1)	1.233(2)	1.494(2)
26	1.457(3)	1.221(2)	1.517(3)
32	1.464(3)	1.226(3)	1.513(3)

Table 3.2. Iron Cp-carbon bond distances for complexes **6**, **24**, **26** and **32**.

Complex	Fe-C(1) [°]	Fe-C(2) [°]	Fe-C(3) [°]	Fe-C(4) [°]	Fe-C(5) [°]
6	2.042(2)	2.049(2)	2.057(2)	2.049(2)	2.041(2)
24	2.045(1)	2.039(1)	2.053(2)	2.054(1)	2.033(1)
26	2.058(2)	2.046(2)	2.048(2)	2.051(3)	2.044(2)
32	2.040(2)	2.045(2)	2.060(2)	2.058(3)	2.052(2)

Table 3.3. Key bond distances and angles for complexes **6**, **24**, **26** and **32**.

Complex	C(1)-C(5)- C(6)-O(1) Torsion Angle [°]	O(1)-C(1- 5) plane [Å]*	Fe(1)- C(1- 5) plane [Å]**	C(1)-C(6)- O(1) [°]	C(7)-C(6)- O(1) [°]
6	14.0(3)	0.339	1.648(2)	119.4(2)	118.9(2)
24	-4.8(2)	0.274	2.045(2)	120.1(1)	118.6(1)
26	2.5(4)	0.026	1.652(2)	123.4(2)	119.3(2)
32	12.72(3)	0.187	1.653(2)	123.1(1)	118.7(2)

*O(1)-C(1-5) is the distance O(1) lies from the C(1)-C(2)-C(3)-C(4)-C(5) plane.
**Fe(1)-C(1-5) is the distance of the iron atom from the C(1)-C(2)-C(3)-C(4)-C(5) plane.

Table 3.4. Key bond distances for complexes **26** and **32**.

Complex	C(13)-N(1) [Å]	N(1)-C(18) [Å]	N(1)-C(21) [Å]	Fe(1)-C(13-17) plane [Å]
26	1.369(3)	1.472(3)	1.464(3)	1.670
32	1.465(3)	1.509(3)	1.509(3)	1.652

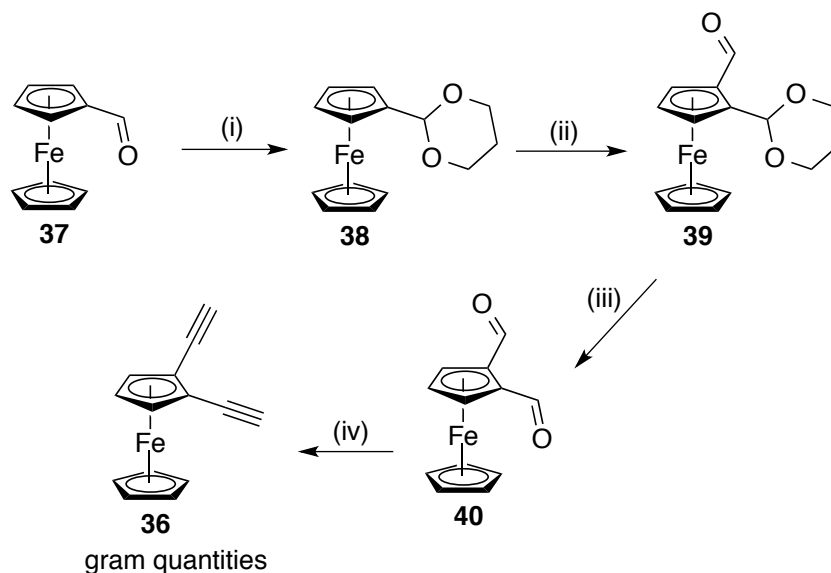
Table 3.5. Key bond angles for complexes **26** and **32**.

Complex	C(13)-N(1)-C(18) [°]	C(13)-N(1)-C(21) [°]	C(21)-N(1)-C(18) [°]
26	119.3(2)	110.7(2)	119.5(2)
32	116.2	116.2(2)	103.9(2)

6. Synthesis of 1,2-di(methylethynoate)ferrocene (**35**)

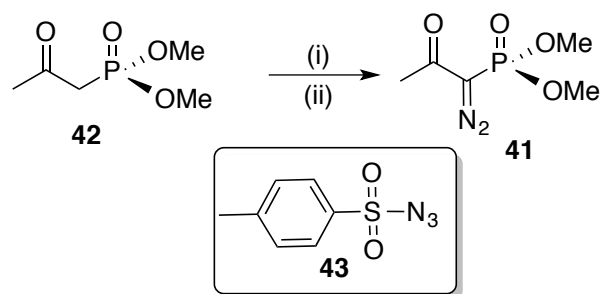
To synthesize **35** we proposed to first synthesize 1,2-diethynylferrocene (**36**), then deprotonation and reaction with methyl chloroformate would yield the target ferrocenyl-enediyne. Attempts to generate **36** by Sonogashira coupling of diiodoferrocene and trimethylsilyl acetylene failed under several reaction conditions, and **36** was ultimately synthesized using an alternative literature procedure published by Bunz.²⁴ Following this protocol we were able to synthesize

36 on a multi-gram scale.



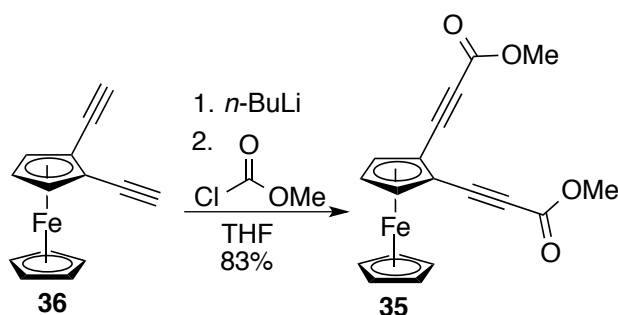
Scheme 3.13. Literature procedure for synthesis of diethynylferrocene. (i) 1,3-propanediol, *p*-TSA, benzene, reflux; (ii) *sec*-BuLi, NFP; (iii) *p*-TSA, THF, H₂O; (iv) **41**, K₂CO₃, MeOH.²⁴

The only challenging feature of this synthesis was conversion of the light sensitive dialdehyde **40** to diethynyl ferrocene using Ohira-Taber reagent **41** (Scheme 3.14). The yields for this conversion were found to vary drastically (40-90%) depending on the purity of the synthesized dimethyl-(1-diazo-2-oxopropyl) phosphonate. While **42** can be synthesized from chloroacetone and trimethylphosphite, in our hands yields of the alkynylated product were significantly improved by use of commercial **42**.²⁵



Scheme 3.14. Synthesis of Ohira-Taber reagent **41**. (i) NaH, THF, toluene; (ii) **43**, toluene.

With diethynylferrocene in hand, ester **35** was readily synthesized by deprotonation with *n*-butyllithium in tetrahydrofuran (THF) and subsequent addition of methylchloroformate (Scheme 3.15).

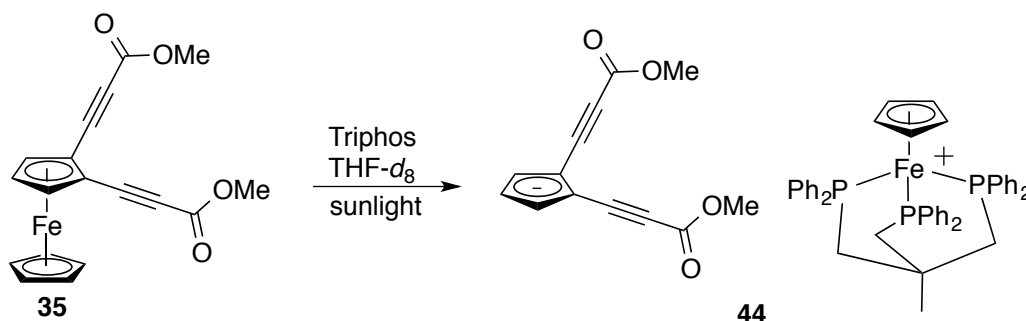


Scheme 3.15. Synthesis of ferrous enediyne **35**.

7. Photolysis of 1,2-di(methylethynoate)ferrocene (**35**).

Due to the extended conjugation in **35**, we believed the ferrous enediyne would display enhanced photoactivity relative to benzoylferrocene. When a solution of **35** in dry degassed THF-*d*₈ was exposed to sunlight, a brown precipitate quickly formed and the ¹H NMR spectrum exhibited only broad and distorted signals. A control experiment where an identically prepared sample was left in the

dark showed no change over the course of 96 h. Suspecting that the highly unstable CpFeL_3^+ fragment, formed following liberation of the cyclopentadienide anion, was decomposing and precipitating from solution, we employed triphos as a chelating agent to stabilize the cationic iron fragment. Photolysis of **35** with one equivalent of triphos in THF- d_8 gave clean photodissociation to form the cyclopentadienide anion and the $[\text{CpFe}(\text{triphos})]^+$ cation (Scheme 3.16). When the reaction was monitored by ^1H NMR spectroscopy (THF- d_8) the resonances for the protons on the substituted cyclopentadienide anion in **44** (δ 5.87 and 6.45) gradually replaced the corresponding upfield signals of **35** (δ 4.48, 4.73). Additionally, a new singlet at δ 4.84, integrating to five hydrogens, grew in over the course of photolysis, indicating formation of the $[\text{CpFe}(\text{triphos})]^+$ cation. Following photolysis, spectroscopically pure crystals of **44** were obtained by slow diffusion of hexanes into the NMR tube.

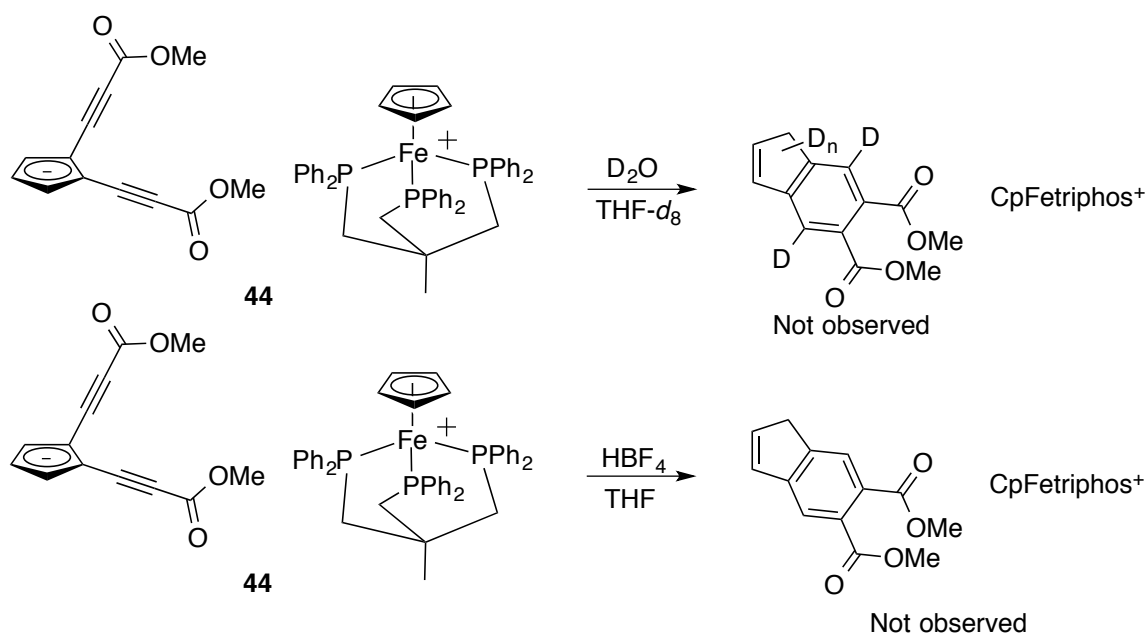


Scheme 3.16. Photolysis of **35** to generate **44**.

8. Attempted protonation and cycloaromatization of anion **44**.

With the cyclopentadienidoenediyne **44** in hand, we made several attempts at inducing cycloaromatization (Scheme 3.17). Addition of D_2O to a NMR tube

containing **44** (THF- d_8) led to gradual disappearance of the cyclopentadienide anion signals at δ 5.87 and 6.45 ppm, indicating deuterium was incorporating into the cyclopentadienide ring; however, no cycloaromatized product was observed by ^1H NMR spectroscopy or gas chromatography-mass spectrometry. A preparatory scale reaction with a stronger acid, HBF_4 , resulted in only decomposition of **44**; neither the conjugate acid of **44** or the cycloaromatized product were detected by ^1H NMR spectroscopy or gas chromatography-mass spectrometry.

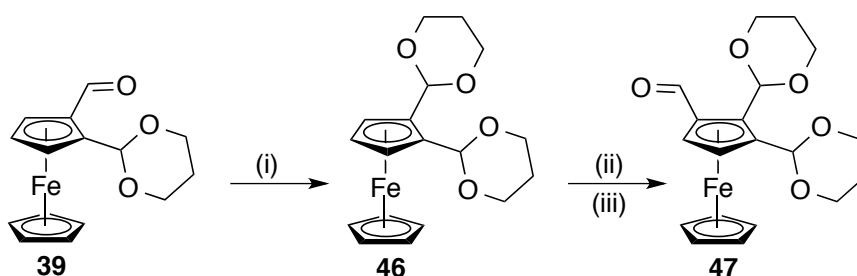


Scheme 3.17. Attempted cycloaromatization reactions of **44**.

4. Synthesis of Benzoyl-2,3-di(1-propynyl)ferrocene (**45**).

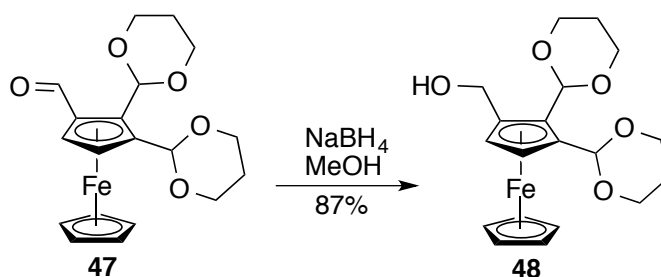
Having established precedent that photochemical liberation of a cyclopentadienide enediyne anion from a ferrocene precursor was possible, we wished to synthesize, characterize, and conduct biological testing on a series of 1-

benzoyl-2,3-ferrocenyl-enediynes. The synthesis of the tri-substituted ferrocenyl-enediynes began with preparation of compound **39** from ferrocene carboxaldehyde using a literature procedure (Schemes 3.13 and 3.18).²⁴ The methodology was amenable to large scale reactions; up to 100 g of ferrocene carboxaldehyde could be used and carried through the subsequent steps without significantly lowering the yield of **47**, which was isolated in 38% yield over four steps.



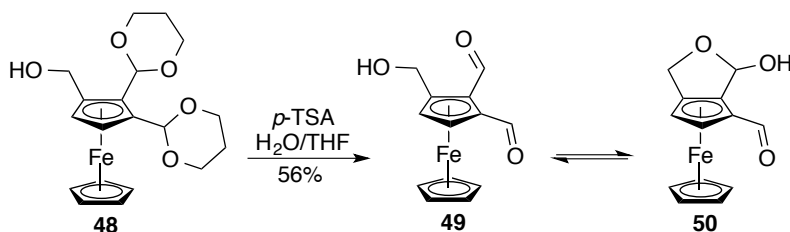
Scheme 3.18. Synthesis of **47**. (i) 1,3-propanediol, p-TSA, benzene, reflux; (ii) *sec*-butyllithium, THF; (iii) N-formylpiperidine.²⁴

Aldehyde **47** was easily reduced to the primary alcohol by sodium borohydride in methanol at 0 °C (Scheme 3.19). Evidence of product formation included the disappearance of the aldehyde proton signal and appearance of a new resonance for the methylene hydrogens at δ 4.61 in the ¹H NMR spectrum (CD₂Cl₂).



Scheme 3.19. Sodium borohydride reduction of **47** to yield **48**.

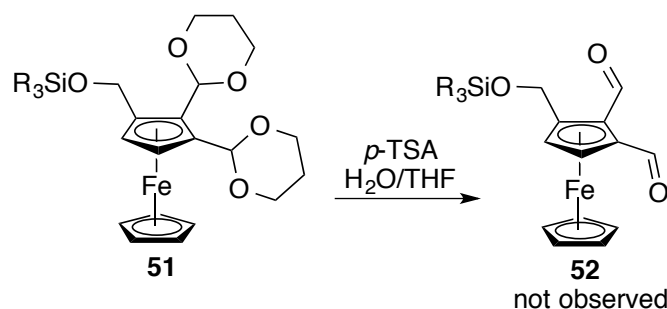
In order to obtain the 1,2-dialdehyde, removal of the acetal protecting groups was then necessary. Clean formation of alcohol **49** from precursor **48** was unmanageable, presumably due to reversible, intramolecular cyclization of the alcohol and neighboring aldehyde to form hemiacetal **50** (Scheme 3.20). The extraneous peaks observed in the ^1H NMR spectrum between δ 5.5 and 5.6 following workup and chromatography are typical for hemiacetal chemical shifts and are inconsistent with the ^1H NMR spectrum of diacetal **48**. Dialdehyde **49** is also extremely unstable and must be used immediately following deprotection. Not only is **49** light sensitive, it also completely decomposes thermally to black iron salts within hours at $-20\text{ }^\circ\text{C}$, presumably due to the electron-deficient nature of the substituted cyclopentadienyl ligand.



Scheme 3.20. Deprotection of acetal **48**.

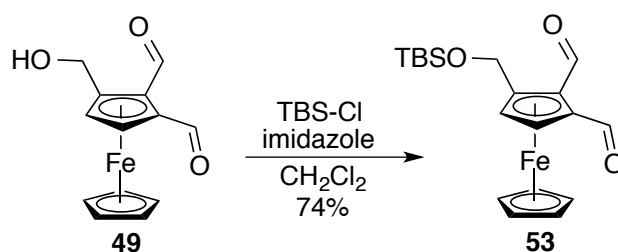
Reaction of **49** with the Ohira-Taber reagent was initially the preferred method for installation of the alkynes; however, yields of the enediyne obtained under these reaction conditions were drastically lower than for generation of **36** from **40**. We next explored a protecting group strategy for alcohol **48** to avoid intramolecular hemiacetal formation and increase the yield of the subsequent alkylation step (Scheme 3.21). While reaction of **48** with trimethylsilyl chloride

(TMSCl) or *tert*-butyldimethylsilyl chloride (TBSCl) in the presence of imidazole in CH_2Cl_2 led to clean formation of the protected alcohol (**51**), subsequent exposure to *p*-TSA resulted in deprotection of the acetals and the primary alcohol.



Scheme 3.21. Attempted acetal deprotection to synthesize **52**.

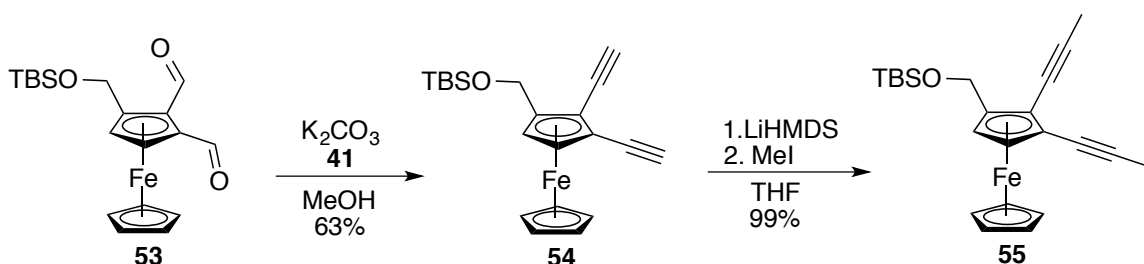
In the end, the best strategy was acid-catalyzed removal of the acetals to give dialdehyde **49** and immediate treatment with TBSCl and imidazole to form **53** (Scheme 3.22). The structure of TBS-protected dialdehyde **53** was confirmed by aldehyde resonances at δ 10.28 and 10.55 in the ^1H NMR spectrum (CDCl_3) and by new carbonyl signals at δ 193.8 and 194.0 in the ^{13}C NMR spectrum (CDCl_3).



Scheme 3.22. Protection of alcohol **49** to form **53**.

Alkynylation of **53** was performed using the Ohira-Taber reagent in the presence of potassium carbonate in methanol at 0°C (Scheme 3.23). The identity of

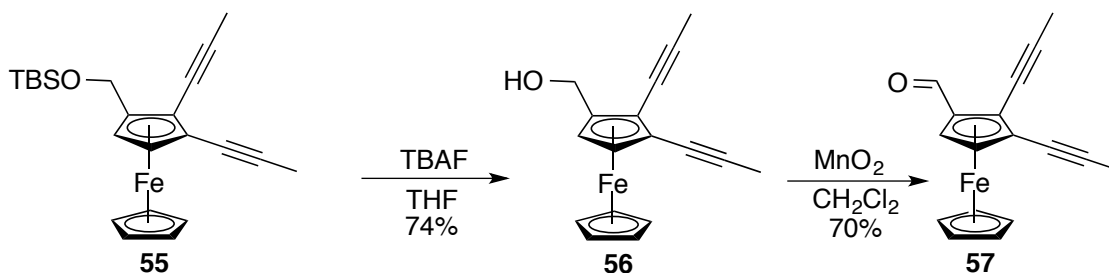
54 was confirmed by terminal alkyne resonances δ 2.94 and 3.06 in the ^1H NMR spectrum (CD_2Cl_2). Formation of the ferrocenyl-enediynes under these conditions generally went smoothly with typical yields ranging from 40 - 80%. Treatment of terminal enediynes **54** with two equivalents of LiHMDS at 0 °C and subsequent addition of excess methyl iodide gave complex **55** in quantitative yield. The formation of **55** was confirmed by ^1H NMR spectroscopy (CDCl_3), with the terminal alkyne resonances having been replaced by two singlets at δ 2.00 and 2.03 integrating to three hydrogens each.



Scheme 3.23. Alkynylation of protected dialdehyde **53** with **41** and subsequent methylation to give enediyne **55**.

With ferrous enediyne **55** in hand, all that remained to synthesize the target molecule was installation of the benzoyl chromophore. Removal of the silyl protecting group was easily accomplished by treatment of **55** with one equivalent of tetrabutylammonium fluoride. The primary alcohol was identified in the ^1H NMR spectrum by a lack of hydrogen resonances corresponding to the silyl protecting group at δ 0.06, 0.11, and 0.91 (CD_2Cl_2) (Scheme 3.24). Oxidation of alcohol **56** to aldehyde **57** with PCC was unsuccessful and led only to recovery of the starting material. Manganese dioxide (MnO_2) at first appeared to give a mediocre yield of

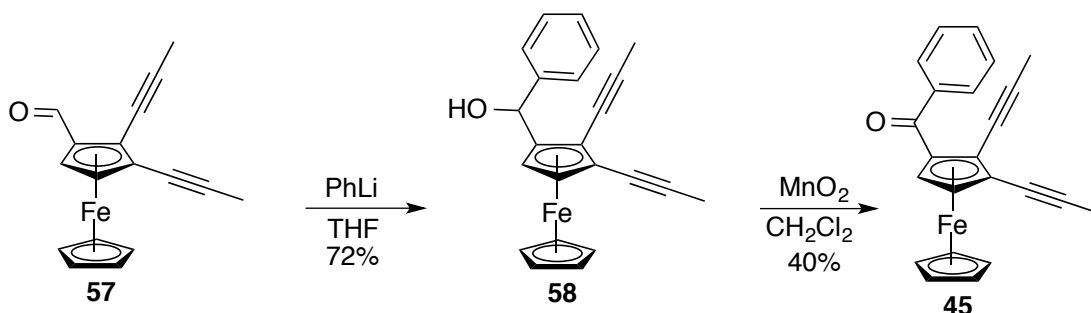
57, but treatment with freshly activated MnO_2 that had been stored overnight at 130 °C resulted in clean conversion of the primary alcohol to the aldehyde within thirty minutes.²⁶ Product formation was confirmed by signals consistent with an aldehyde in the ^1H NMR spectrum at δ 10.16 and in the ^{13}C NMR spectrum at 193.1, as well as a carbonyl stretching frequency (1676 cm^{-1}) in the infrared spectrum (thin film).



Scheme 3.24. Deprotection of **55** and oxidation of **56** to form aldehyde **57**.

Treatment of aldehyde **57** with one equivalent of phenyllithium (2.0 M solution in dibutyl ether) in anhydrous THF at -78 °C led to an immediate color change from deep-red to yellow (Scheme 3.25). Upon warming to room temperature and quenching with ammonium chloride, secondary alcohol **58** was isolated as a yellow oil in 72% yield. The identity of this complex was confirmed by new aryl resonances at δ 7.21, 7.28, and 7.38, and a new resonance at 5.65, assigned to the benzylic hydrogen, in the ^1H NMR spectrum (CD_2Cl_2). Finally, 1-benzoyl-2,3-diethynylferrocene was isolated following a second manganese dioxide oxidation in diethyl ether. Oxidation of the secondary alcohol was much more sluggish than oxidation of **56**; the oxidant failed to completely consume the starting material even with 40 equivalents of MnO_2 . The pure benzoyl ferrocenyl-enediynes **45** was finally

obtained by either slow chromatography to separate the alcohol from the ketone, or by repeated treatments of the crude reaction mixture with manganese dioxide. The formation of enediyne **45** was confirmed by the absence of the benzylic hydrogen signal in the ^1H NMR spectrum (CD_2Cl_2), and by the significant downfield chemical shifts (CD_2Cl_2) for the cyclopentadienyl hydrogens on the substituted ring from δ 4.21 and 4.31 in **58** to 4.67 (2H) in **45**. The yield of **45** was 1.5% over 13 steps.

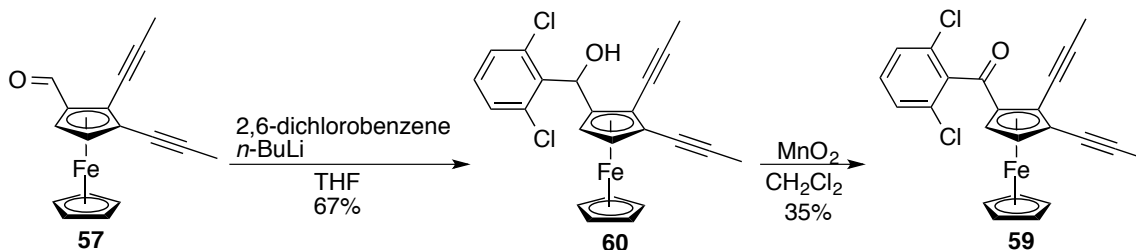


Scheme 3.25. Two step conversion of aldehyde **57** to benzoyl ketone **45**.

6. Synthesis of 2,6-dichlorobenzoyl-2,3-di(1-propynyl)ferrocene (**59**).

Starting from complex **57**, **60** was synthesized by treatment with *in situ* generated 2,6-dichloro-phenyllithium, prepared from 2,6-dichlorobenzene and *n*-BuLi in anhydrous THF at $-78\text{ }^\circ\text{C}$ (Scheme 3.26). Key to the success of this reaction was slow addition of the aldehyde at $-78\text{ }^\circ\text{C}$ followed by slow warming to $-40\text{ }^\circ\text{C}$ and immediate quenching with 5% HCl. Confirmation that **60** was formed was evident in the ^1H NMR spectrum (CD_2Cl_2), which displayed the characteristic resonance for the benzylic hydrogen at δ 6.70 and signals for the aryl ring at δ 7.15 and 7.28. Oxidation of this alcohol to ketone **59** was even more difficult than for **45**, likely due to increased steric demand caused by the chlorine substituents on the aryl ring.

Ultimately benzoyl enediyne **59** was isolated in 1.2% overall yield.



Scheme 3.26. Synthesis of enediyne **59**.

6. Solid state structure of **59**.

X-ray quality crystals of compound **59** were grown by slow evaporation of ethyl acetate. Full refinement data can be found in the Appendix section. Key bond metrics are presented here in Tables 3.6-3.8.

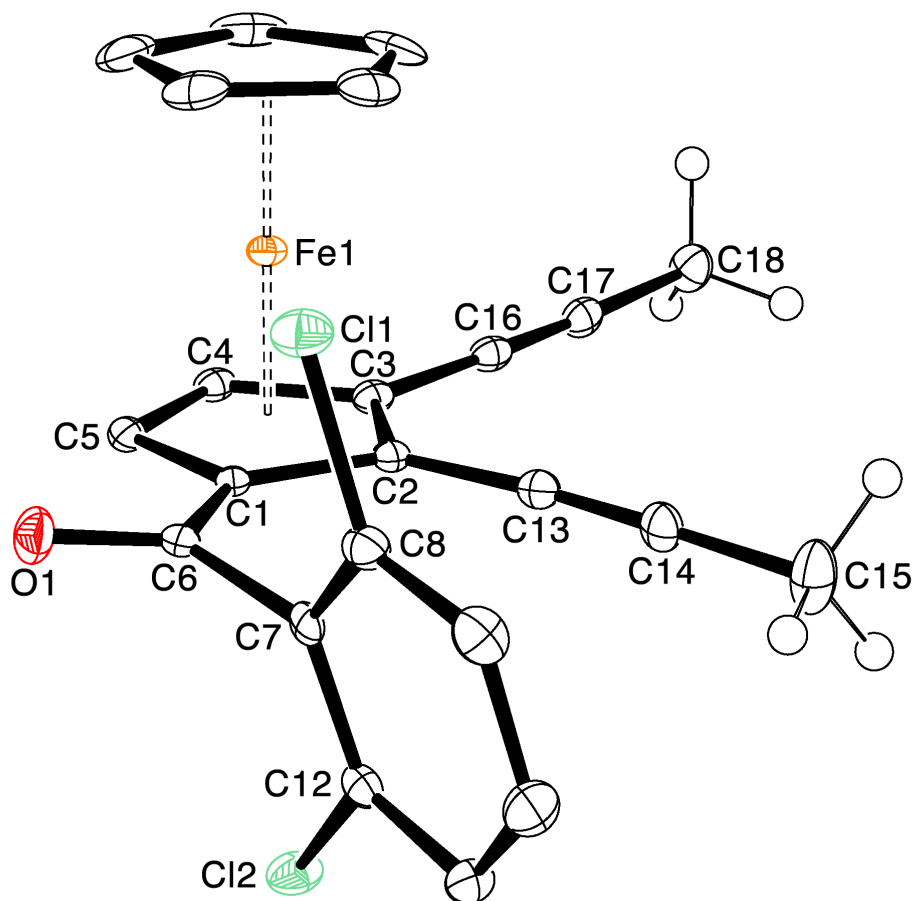


Figure 3.6. ORTEP Drawing of **59**.

Table 3.6. Key bond lengths and angles for complex **59**.

Complex	C(1)-C(6) [Å]	C(6)-O(1) [Å]	C(6)-C(7) [Å]	C(1)-C(6)-O(1) [°]
59	1.457(2)	1.223(2)	1.515(2)	122.1(1)

Table 3.7. Iron Cp-carbon bond distances for complex **59**.

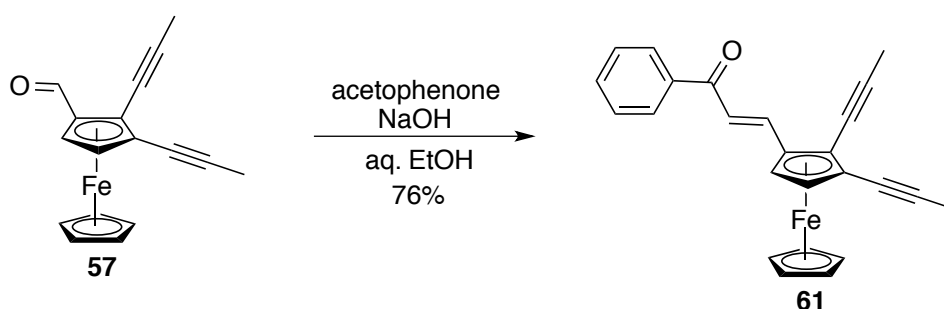
Complex	Fe-C(1) [Å]	Fe-C(2) [Å]	Fe-C(3) [Å]	Fe-C(4) [Å]	Fe-C(5) [Å]
59	2.039(2)	2.042(2)	2.046(2)	2.047(2)	2.043(2)

Table 3.8. Key bond lengths and angles for complex **59**.

Complex	C(1)-C(5)- C(6)-O(1) Torsion Angle [°]	O(1) distance from C(1-5) plane [Å]	Fe distance from C(1-5) plane [Å]	cd distance [Å]
59	-8.3(2)	0.231	1.639	4.636(2)

7. Synthesis of (*E*)-3-(2,3-di(propynyl)ferrocene)-1-phenylprop-2-en-1-one (**61**).

While the photodecomposition of ferrous α,β -unsaturated benzoyl ketones has been less studied than benzoylferrocenes,²⁷ we wished to synthesize and study the photochemistry of enediyne **61** containing an extended π -conjugation system. To synthesize **61**, aldehyde **57** was dissolved in absolute ethanol with one equivalent of acetophenone in the absence of light. Addition of aqueous sodium hydroxide to the reaction mixture gave ketone **61** following reaction at room temperature for 12 h (Scheme 3.27). Complex **61** was isolated in moderate yield and was easily identified by the new vinylic and aryl hydrogen resonances in the ¹H NMR spectrum (CDCl₃) at δ 7.52-7.48 (m, 3H), 7.58 (t, J = 7.1 Hz, 1H, aryl), 7.89 (d, J = 15.5 Hz, 1H, vinyl), and 8.00 (d, J = 7.3 Hz, 2H, aryl).

**Scheme 3.27.** Adol Condensation to form ketone **61**.

8. Cell Studies on 45, 59, and 61

Complexes **45**, **59**, and **61** were each tested for their biological activity in both the absence of light and upon irradiation using the conditions discussed at length in Chapter II. Briefly, for all half-maximal inhibitory concentration assays, cells were seeded at a density specific to the cell line, incubated with varying concentrations of complexes in the dark for 24 h, then irradiated with a Richee 2014-SLT-CW/WW 50W Flood Light (0.031 W) with a 455 nm longpass filter (Pol filter 152x100x3mm GG455) resting on top of the 96-well plate. Forty-eight hours post photolysis when the cells reached confluency, the efficacy of the complexes in both the light and the dark was determined by the crystal violet staining method and toxicity was calculated using Equation 1. Each test was performed independently in at least triplicate.

$$\frac{(\text{Absorbance}_{\text{drug containing wells}} - \text{Absorbance}_{\text{control wells}})}{\text{Absorbance}_{\text{control wells}}}$$

(Equation 1)

To study the effect of irradiation time on cell viability, we tested the cytotoxicity of **59** in the dark and under photo-conditions using irradiation times of 45 minutes, 1.5 h, and 3 h in cervical cancer (HeLa) cells. While the cytotoxicity of **59** did appear to increase with longer irradiation time, IC₅₀ values could not be calculated due to the low solubility of the ferrocene complex in cell media (Table 3.9). Compound **59** proved to be slightly more toxic in human carcinoma lung cancer (A549) cells, but no increase in toxicity was observed upon exposure to visible light (3 h).

Table 3.9. IC₅₀ values (μM) for ferrous enediyne complexes.

Complex	HeLa		A549	
	IC _{50-dark}	IC _{50-light}	IC _{50-dark}	IC _{50-light}
45	n.d.	n.d.	8.3 (1.1)	11.0 (1.3)
59	> 40*	> 20*	> 20*	20.5 (6.6)
61	n.d.	n.d.	> 40*	11.7 (5.7)

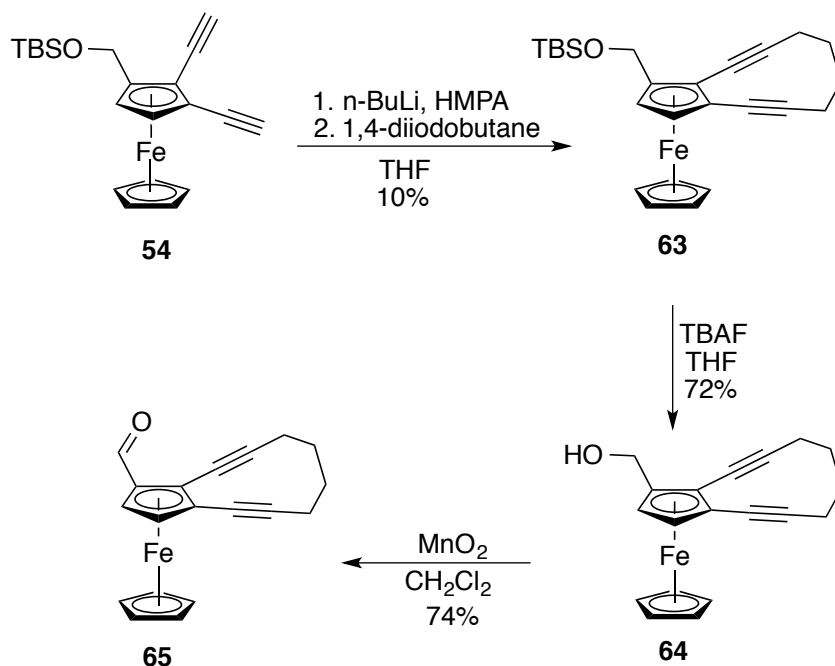
*some IC₅₀ values were not able to be calculated due to solubility limits of the parent ferrocene complex in cell media. Irradiation time = 3 h.

Benzoyl enediyne **45** was more water-soluble than its chlorine-substituted analog, but exposure to visible light resulted in no increase of cytotoxicity. The most promising complex tested was α,β -unsaturated ketone **61**; while no IC_{50-dark} value was able to be calculated due to low solubility of the complex, under photoconditions the IC₅₀ dropped to 11.7 μM .

7. Synthesis of 2,3-ferrocenyl-cyclodec-2-ene-1,5-diyne chalcone (**62**).

With the synthesis and photobiological activity of 1-benzoyl-2,3-ferrocenylenediyne established we wished to synthesize and conduct biological testing on an analog containing a strained-ring, which we predicted had a better chance of cyclizing to *para*-benzyne following photochemical liberation from the metal. Synthesis of the 10-membered ring enediyne **63** from **54** and 1,4-diodobutane failed with LiHMDS, sodium hydride, and *n*-butyllithium. Installation of the four-carbon tether was achieved by deprotonation with *n*-BuLi followed by treatment with HMPA for 20 minutes then slow addition of 1,4-diodobutane as a solution in THF over 3 h (Scheme 3.28). Slow chromatography to separate **63** from the undesired side products gave typical isolated yields ranging from 10-15%. The

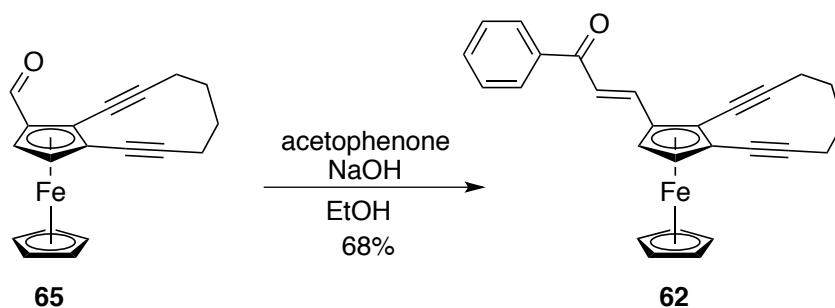
identity of **63** was confirmed in the ^1H NMR spectrum (CDCl_3) by replacement of the singlets assigned to the terminal alkyne hydrogens in **54** at δ 2.94 and 3.06 with two multiplets at δ 1.94 and 2.33, assigned to the methylene hydrogens in the four-carbon tether. Removal of the silyl protecting group went smoothly in anhydrous THF with tetrabutylammonium fluoride. The identify of alcohol **64** was confirmed by the presence of two doublet of doublets in the ^1H NMR spectrum (CDCl_3) at δ 4.40 (dd, $J_{HH} = 12.28, 6.13$ Hz) and 4.48 (dd, $J_{HH} = 12.3, 6.13$ Hz) that were assigned to the diastereotopic hydrogens of the CH_2OH group, and an O-H stretching frequency in the infrared spectrum at 3383 cm^{-1} (thin film). Addition of freshly activated manganese dioxide to a solution of primary alcohol **64** in dichloromethane caused an immediate color change from yellow to red. The conversion of **64** to **65** was complete by TLC within two hours. The structure of the product was confirmed by a new resonance at δ 10.02 in the ^1H NMR spectrum (CD_2Cl_2), and by the ^{13}C NMR spectrum (CD_2Cl_2), which displayed a new CO carbon signal at δ 191.8.



Scheme 3.28. Synthesis of 10-membered ring ferrocenyl-enediynes **65**.

Given the low yield of **63** from **54**, and the greater phototoxicity of **61** relative to both **45** and **59**, we chose at this juncture to focus our efforts on synthesizing a strained-ring derivative incorporating the α,β -unsaturated chromophore. To achieve the long-sought **62**, a solution of **65** and acetophenone was prepared in absolute ethanol, and aqueous sodium hydroxide was added dropwise. Stirring overnight (12 h) gave the strained-ring enediynes **62** in 68% yield following purification (Scheme 3.29). The final product was characterized by new vinyl and aryl signals in the ¹H NMR spectrum (CD₂Cl₂) at δ 7.50 (t, J = 7.5 Hz, 2H), 7.60-7.56 (m, 1H), 7.65 (d, J = 15.4 Hz, 1H), 7.69 (d, J = 15.4 Hz, 1H), 7.99-7.98 (m, 2H), and by a new CO carbon resonance at 189.62 in the ¹³C NMR spectrum (CD₂Cl₂).

The yield of **62** over 12 steps was 0.4%.



Scheme 3.29. Synthesis of α,β -unsaturated ferrocene enediyne **62**.

8. Photobiological activity of **62**.

Complex **62** was tested for biological activity in both the absence of light and under the irradiation conditions discussed at length in Chapter II. The techniques employed were identical to the testing conditions used for compounds **45**, **59** and **61**. The results of the ferrous chalcone enediyne phototoxicity studies are summarized in Table 3.10.

Table 3.10. IC₅₀ values (μM) for ferrous enediyne complexes.

Complex	HeLa		A549	
	IC _{50-dark}	IC _{50-light}	IC _{50-dark}	IC _{50-light}
61	n.d.	n.d.	> 40	11.7 (5.7)
62	> 80	19.7 (3.5)	> 80	19.2 (4.2)

*some IC₅₀ values were not able to be calculated due to solubility limits of the parent ferrocene complex in cell media.

9. Lipophilicity studies

The procedures and methods to determine lipophilicity using reverse phase HPLC were discussed at length in Chapter II.²⁸ To briefly summarize here, a series of standards were injected onto a reverse phase HPLC column and the retention times were related to the known $\log P$ values tabulated in the literature. A linear regression was then used to generate a calibration curve. The ferrous enediynes were then injected and their retention times and the calibration curve were used to calculate $\log P$ (Table 3.11). Each experiment was performed in at least triplicate.

Table 3.11. $\log P$ values for synthesized ferrocenyl-enediynes.

Complex	Retention Time (min)	$\log P$
45	10.6	4.1
59	16.1	4.7
61	17.3	4.7
62	31.4	5.2

10. Photolysis studies on 61.

Photolysis of **61** in a J. Young tube (DMF-*d*₇:D₂O, 0.60 mL:0.10 mL) led to a rapid color change from red to black and formation of black precipitate that adhered to the walls of the NMR tube. ¹H NMR spectroscopic analysis of this mixture suggested presence of cyclopentadiene by broad and distorted signals centered at δ 6.5. Even following filtration of the precipitate under nitrogen, the distortions persisted and a usable spectrum could not be obtained. The presumed weaker basicity of the benzoylcyclopentadienoidenediyne relative to the

benzoylcyclopentadienide anion may account for the difference in photoactivity between **61** and the 1-benzoylferrocenes discussed in Chapter II. At the time of writing, the exact identities of the photolysis products of **61** remains unknown.

C. Discussion

Given the remarkable and elegant methods by which nature accomplishes the Bergman cycloaromatization,^[4,5,1,29] it is no surprise chemists are continually seeking novel ways to mimic and control the reactivity of enediyne structures.^[9,7,8] Since the discovery of the enediyne antibiotics, extensive work has been done by the organometallic chemistry community to determine how transition metals affect cycloaromatization. In some instances, metals have been demonstrated to lower the barrier to cyclization, typically by reducing the distance between the alkyne termini upon coordination to heteroatoms in the enediyne framework.⁶ Similarly, coordination of a transition metal to the π -backbone of an enediyne has been shown to alter the geometry and electronics of the polyunsaturated system, allowing for more favorable cyclization conditions.^[11,12,30] The opposite effect is observed upon metal binding when the *ene* portion is incorporated into an aromatic ring; while 3,4-benzo-cyclodec-3-ene-1,5-diyne cyclizes at 84 °C with a half life of 24 hours, we previously demonstrated in the O'Connor Lab that ferrous enediyne **1** is stable to cyclization up to temperatures of 150 °C.

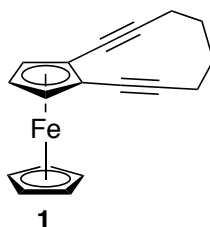


Figure 3.7. Ferrocenyl-enediyne **1**.

Given the intriguing reactivity of enediyne framework and the potent cytotoxicity of the enediyne antibiotics, the O'Connor lab became interested in synthesizing enediyne derivatives where formation of the highly cytotoxic *para*-benzyne could be controlled by transition metal coordination. As previous work in our lab had demonstrated that **1** is unreactive up to temperature of 150 °C,¹³ we proposed incorporation of a cycloaromatization 'trigger' unto the ferrocene framework could potentially give a selective Bergman Cycloaromatization *in vitro*.

A key precedent for this proposal was a report by Kutal¹⁴ who noted the remarkable photoactivity of 1-benzoylferrocene and 1,1'-dibenzoylferrocene relative to ferrocene. Exposure of either benzoyl-substituted sandwich complex to visible light results in rapid cyclopentadienyl ring-slippage due to the metal-to-ligand charge transfer character mixed into the low energy excited states of **6** (represented by resonance structure **6***, Figure 3.8). We speculated that the photosensitivity of these complexes could provide a unique method to deliver toxic enediynes selectively to cancer cells. Photodynamic therapy is already in use clinically,³¹ and traditionally uses photosensitizers that upon visible light excitation become cytotoxic by either hydrogen-atom transfer to form free radicals or by

direct energy transfer to molecular oxygen and generation of cytotoxic singlet oxygen.^[32,33,34] The spatiotemporal control gained by the extra requirement of irradiation results in a more targeted, selective drug for the treatment of cancer, and for this reason, several therapeutic agents are already approved for the treatment of esophageal and lung cancer.^[32,34] With these precedents in mind, we proposed two classes of benzoylferrocene-based enediyne prodrugs, one where an *unreactive* enediyne would be triggered to cyclize upon coordination to iron, and a second where iron would serve to stabilize a *reactive* enediyne until triggered. Upon reaching the target tumor cell we proposed visible light irradiation would ‘activate’ the organometallic complexes to cycloaromatization, and the resultant *para*-benzyne diradical would induce cytotoxicity.

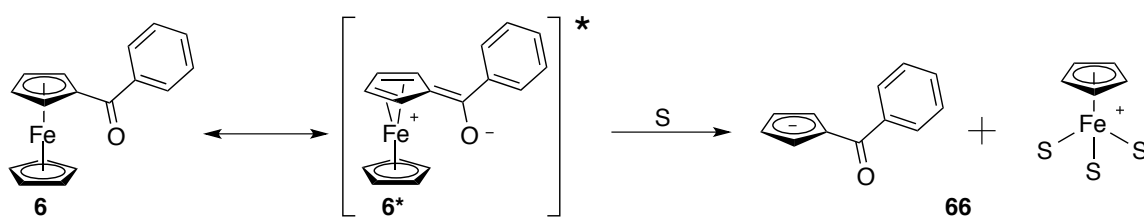


Figure 3.8. Excitation and conversion of **6** to **66**.

Previously in the O'Connor lab, we demonstrated that the iron complex $[\text{Cp}^*\text{Fe}(\text{NCMe})_3]\text{PF}_6$ (**67**, $\text{Cp}^* = \eta^5\text{-C}_5\text{Me}_5$) functions as a cycloaromatization catalyst (Figure 3.9). In acetone- d_6 and in the presence of a hydrogen-atom donor (γ -terpinene), **67** undergoes rapid reaction with **69** or **72** to give cycloaromatized products in high yield at room temperature. We speculated that since the $\text{Cp}^*\text{Fe}(\text{NCMe})_3^+$ cation easily cycloaromatizes enediynes that do not cyclize

thermally at biological temperature, the methodology would be ideal for biological applications.¹¹ Based on this precedent for metal-assisted cycloaromatization, and with Katal's photochemical studies of benzoylferrocene in mind, we proposed **13** would photochemically liberate the benzoylcyclopentadienide anion upon exposure to light and give the cycloaromatization catalyst **75** *in situ* (Scheme 3.30). Intramolecular, iron-mediated Bergman cycloaromatization of the tethered enediyne could then give the highly reactive *para*-benzyne diradical **76**, which in a tumor cell could abstract hydrogen-atoms from nearby biomolecules and induce cell death.

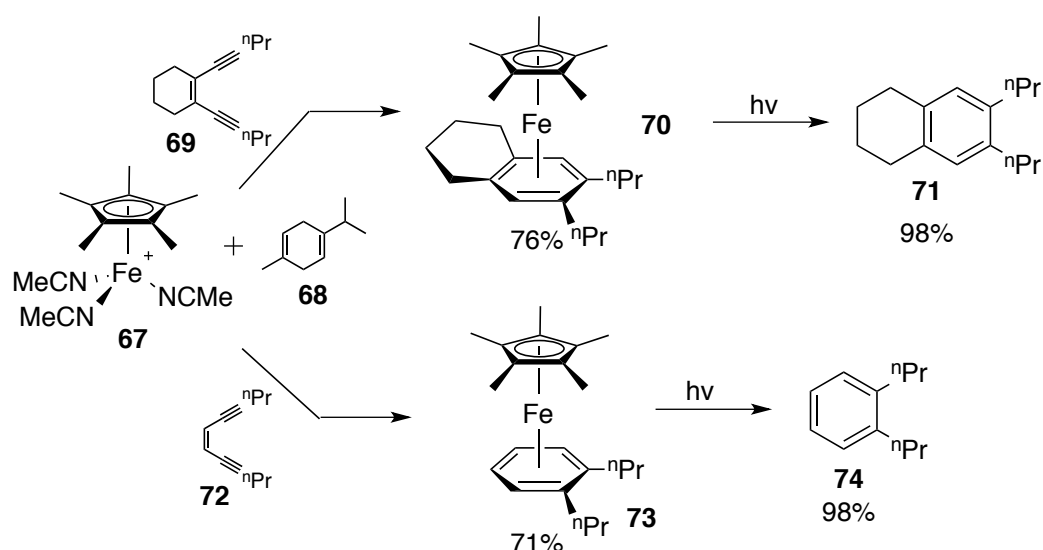
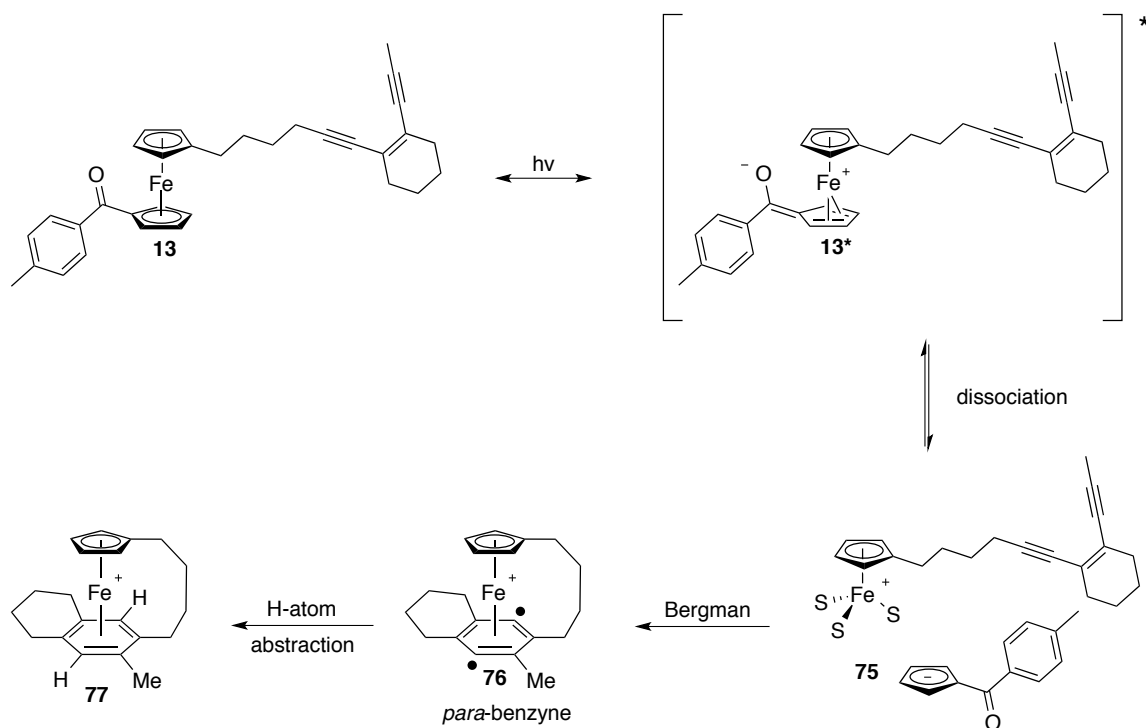


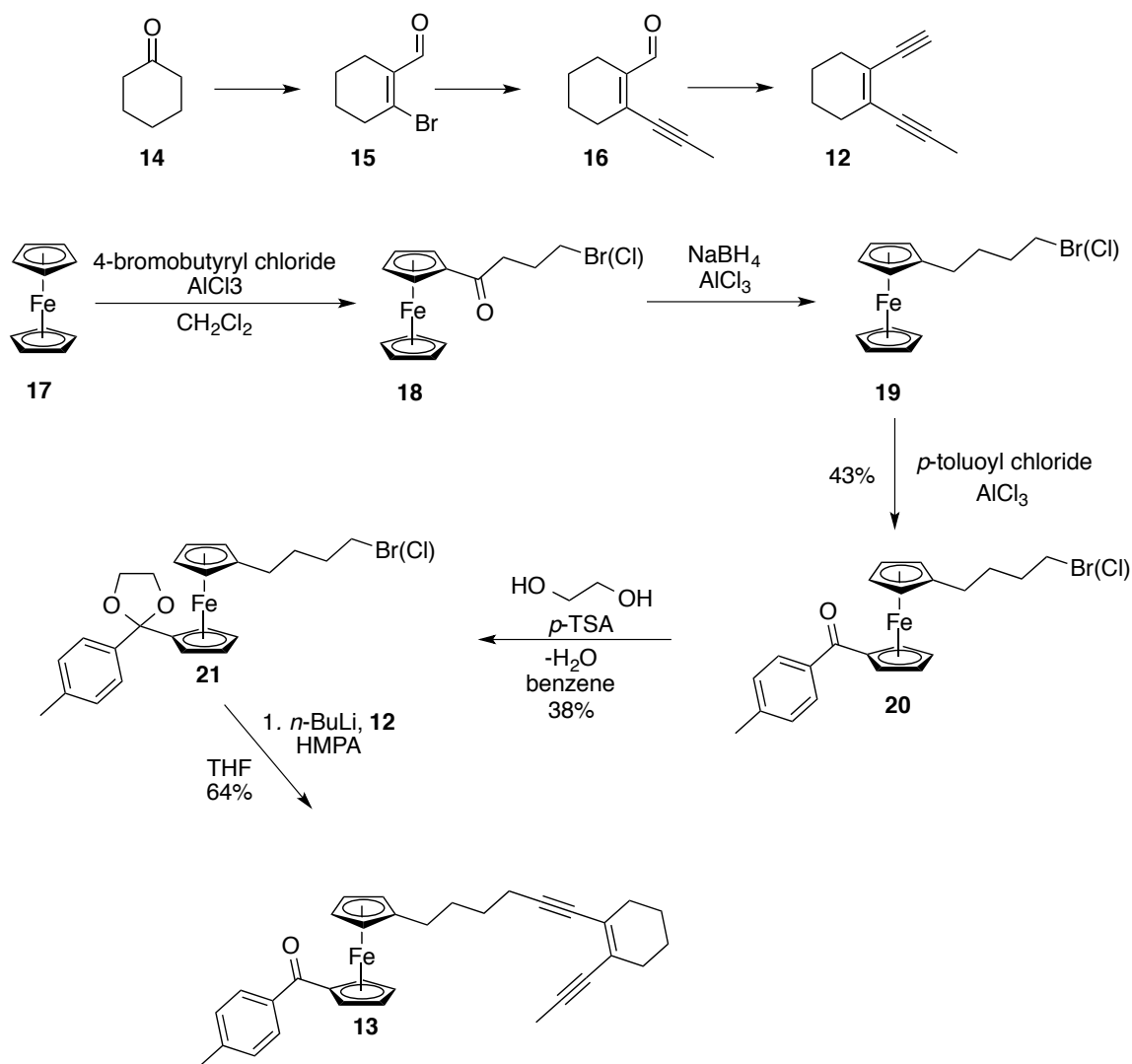
Figure 3.9. Previous work on metal-assisted cyclization reactions.



Scheme 3.30. Proposed mechanism for metal-assisted enediyne cyclization of **13**.

The synthesis of **13** began with preparation of acyclic enediyne **12** using a procedure developed in our lab (Scheme 3.31). Starting with cyclohexanone, bromo-aldehyde **15** was synthesized using a modified Baylis-Hillman procedure. Sonogashira coupling of **15** with propyne converted the vinyl bromide to internal alkyne **16**. Trimethylsilyldiazomethane was then used in the presence of base to generate enediyne **12**. The preparation of the organometallic portion of the molecule began with Friedel-Crafts acylation to generate ketone **18** and reduction to obtain **19**. The benzoyl functionality was incorporated by a Friedel-Crafts acylation of the unsubstituted cyclopentadienyl ring. Ketone **20** was then converted to acetal

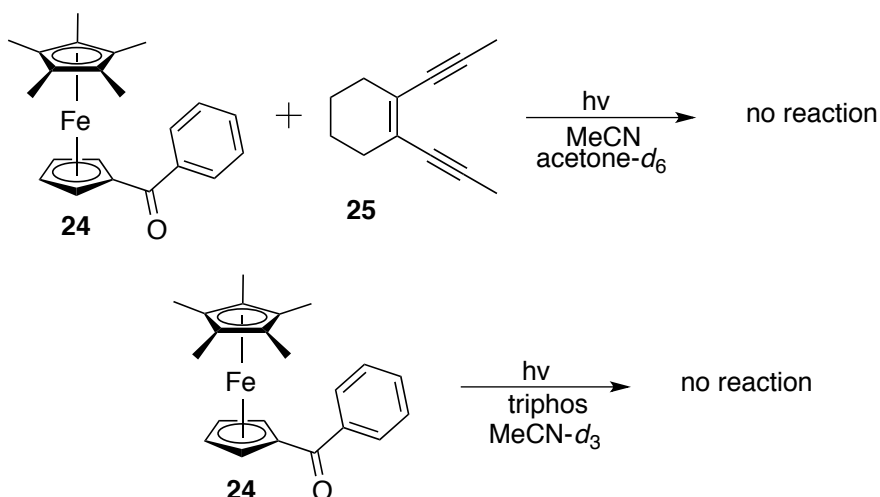
21 by azeotropic water removal, and S_N2 reaction with the anion of terminal enediene **12** gave tethered enediene **13** following aqueous workup with *p*-TSA.



Scheme 3.31. Synthesis of **13**.

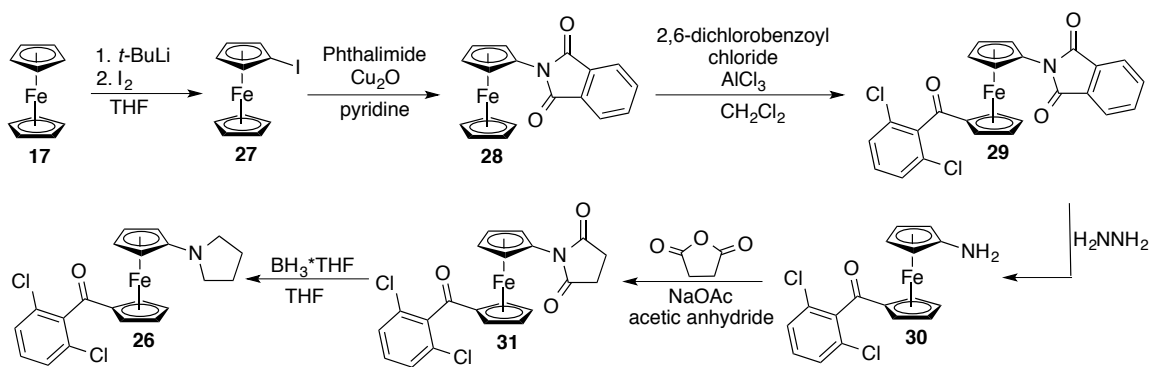
We predicted from previous work in our group that photochemical dissociation of the benzoylcyclopentadienide anion from **13** in the presence of acetonitrile would generate the reactive $CpFe(NCMe)_3^+$ cation, which would mediate

cyclization of the tethered enediyne *in situ* (Scheme 3.30). Photolysis of **13** in acetone-*d*₆ (5 equiv MeCN, 10 equiv 1,4-CHD) resulted in formation of a black precipitate that adhered to the walls NMR tube and a slow color change from red to dark brown. Even following filtration under nitrogen, no cycloaromatized product was detected by ¹H NMR spectroscopy or gas chromatography-mass spectrometry. The instability of CpFe(MeCN)₃⁺ relative to the Cp*Fe(MeCN)₃⁺ has been documented in the literature; photolysis of [Cp*Fe(CO)₃]⁺PF₆⁻ readily gives the tris(acetonitrile) complex, but the cyclopentadienyl analog under identical reaction conditions generates half an equivalent of both ferrocene and inorganic Fe(II) rather than the half sandwich complex.³⁵ Suspecting the electron-deficient nature of the Cp ligand relative to Cp* or steric protection of the iron center afforded by the permethylated Cp ligand were potential reasons **13** was unable to affect cycloaromatization, we prepared pre-catalyst **24** to test if intermolecular cyclization of **25** was feasible. In stark contrast to the highly photoactive benzoylferrocene **6**, when **24** was exposed the light for several days (sunlight or Hanovia lamp) in the presence of **25** or triphos, no benzoylcyclopentadienide anion was released from the metal to form the respective half sandwich complexes.



Scheme 3.32. Attempted photochemical reactions of **24**.

To further investigate the effect of cyclopentadienyl ring substitution on the photoliberation of the benzoylcyclopentadienide anion, we prepared electron-rich pyrrolidine derivative **26** from ferrocene (Scheme 3.33). Primary amine **30** was synthesized using published literature procedures.^[20,22] Reaction of **30** with succinic anhydride readily gave compound **31** which was easily reduced with borane in THF to tertiary amine **26**.²³ The photoactivity of the pyrrolidine complex was similar to that observed for **24**; even when irradiated for several days in acetone-*d*₆ with 5 equivalents of MeCN, 10 equivalents of 1,4 CHD, and enediyne **25**, no cycloaromatized product was detected by ¹H NMR spectroscopy or gas chromatography-mass spectrometry. Protonation of **26** with HBF₄ to obtain a more electron-deficient ligand resulted in photodecomposition upon exposure to visible light; however exposure to either **25** (10 equiv 1,4 CHD) or triphos during the course of photolysis led to no formation of the respective half-sandwich complexes.



Scheme 3.33. Synthesis of pyrrolidine **26**.

The solid-state structures of **6**, **24**, **26** and **32** are somewhat instructive with regards to the observed photochemical activity. O(1) of the photochemically active 1-benzoylferrocene lies 0.339 Å out of the plane of the Cp [C(1-5)] π -system while the photochemically inactive Cp* derivative **24** shows significantly less distortion (0.274 Å). The C(1)-C(5)-C(6)-O(1) torsion angle for benzoylferrocene is also significantly larger than for **24** (14.0(3) vs -4.8(2) respectively). These bond metrics indicate the observed photostability of **24** is not due to a lack of π -overlap between the pentamethylcyclopentadienyl ring and neighboring carbonyl. The Fe(1) distance from the C(1-5) plane is nearly identical for benzoylferrocene, **26** and **32** (1.648(2), 1.652(2), and 1.653(2) Å) even though the photoactivity of **26** and **32** are drastically different. For **24** the iron distance from the C(1-5) plane (2.045(2) Å) is significantly longer than any of the other derivatives, presumably a steric effect of the permethylated cyclopentadienyl ring. In the pyrrolidine substituted derivatives, the N(1)-C(13) distance in **32** is significantly lengthened compared to **26** (1.465(3) and 1.369(3) Å respectively), indicative of a loss of conjugation between the

cyclopentadienyl ring and the lone pair on nitrogen upon protonation.

Based on the photochemical studies of **6**, **24**, **26**, and **32** it is clear that photochemical liberation of the benzoylcyclopentadienide anion from the organometallic precursor is affected by the steric and electronic properties of the starting sandwich complex. The solid-state structures indicate that the π -overlap between the cyclopentadienyl ligand and neighboring CO group necessary for photoactivity is preserved across the series. The UV-Vis spectra for **24**, **26**, and **32** all display absorbances at ~ 360 and 500 nm, consistent with the metal-to-ligand charge transfer bands Katal observed in **6**. The observation that electron-rich derivatives **24** and **26** fail to react under photoconditions, while relatively electron-poor analogs (**6** and **32**) are photochemically active, suggests that the electronics of the cyclopentadienyl ligand have a strong effect on reactivity. At this time, the effect of cyclopentadienyl ligand sterics on photochemical activity is not clear. Given the longer Fe-Cp bond distance in **24** relative to the other derivatives, it seems reasonable to suspect the permethylated Cp-ring imparts some steric protection to the iron center, potentially accounting for the greater stability of $\text{Cp}^*\text{Fe}(\text{MeCN})_3^+$ relative to $\text{CpFe}(\text{MeCN})_3^+$. The failure of **13** to cycloaromatize may be due to electronic or steric effects of the cyclopentadienyl ligand following photodissociation of the benzoylcyclopentadienyl ligand (**75**). Additionally, the tether length between the Cp ligand and enediyne moiety may be non-optimal, making it difficult for the iron center to bind to the enediyne framework and induce cyclization.

Given the complex steric and electronic variables involved in the intramolecular metal-mediated cyclization of tethered enediyne **13**, we turned our attention to our second strategy. Based on previous work in the O'Connor lab with **1**, we proposed incorporation of a reactive enediyne unto the benzoylferrocene moiety would impart stability to the enediyne at biological temperature. We predicted photochemically-triggered cyclopentadienyl ligand dissociation would then generate the reactive enediyne, which would readily cyclize to *para*-benzyne and induce in cell death (Figure 3.10).

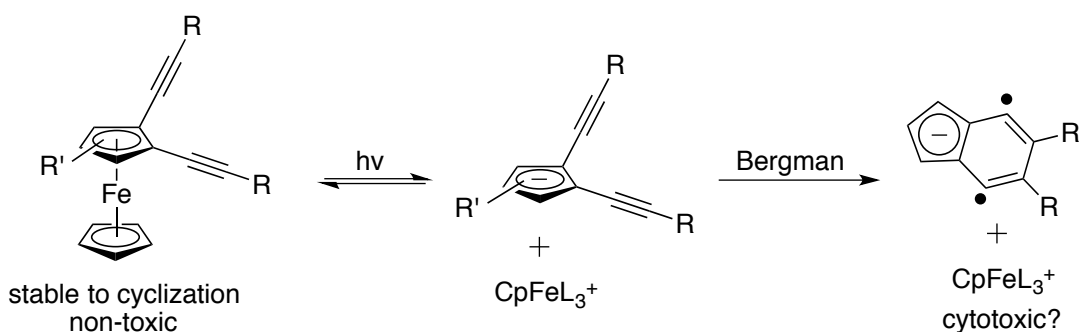


Figure 3.10. Proposed method to generate reactive enediynes from ferrocene.

While we suspected iron coordination to the *ene* in the proposed ferrocenyl-enediynes would ensure thermodynamic stability of the enediyne to very high temperatures, the thermal reactivity of the proposed enediyne cyclopentadienide anions was unknown. The propensity of organic enediynes to cyclize is complex and depends on several factors, primarily: the aromatic nature of the *ene* portion of the π -system, the distance between the alkyne termini, and the energy of the enediyne ground state relative to the transition state for cycloaromatization (Figure 3.11 and

3.12). With regards to the first point, while the barrier to cyclization for benzannulated enediynes is lower than for their non-aromatic counterparts, enediynes where the alkene is incorporated into the aromatic ring have higher cyclization enthalpies than non-aromatic alkenes. This difference in enthalpy has been attributed to the smaller amount of resonance energy released upon formation of the second aromatic ring compared to formation of benzene.^[36,9] The stabilizing effect of *ene* incorporation into an aromatic ring has also been demonstrated experimentally by the lower temperatures and shorter half-lives required for cyclization for *enes* (*Z*)-hexa-3-en-1,5-diyne (**78**) and cyclodeca-1,5-diyne-3-ene (**79**) compared to their corresponding benzannulated analogs (**80** and **81**, Figure 3.11).^[9,37]

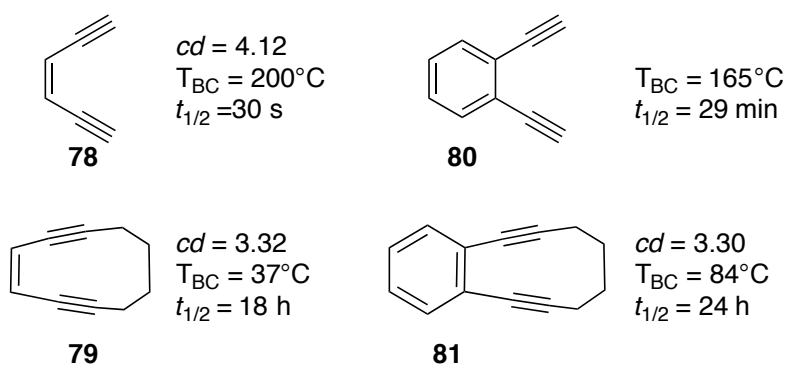


Figure 3.11. Thermal parameters for some characterized enediynes.

A second factor known to impact an enediyne's ease of cycloaromatization is the distance between the two alkyne termini, termed the *cd* distance.³⁸ The *cd* distances and half-lives for cyclization for a series of enediynes are shown in Figure 3.11; generally for acyclic enediynes, the wider the span of the distal alkynes the

greater the barrier to cyclization (**78** and **80**). Incorporation of a carbon tether between the alkyne termini adds a third layer of complexity to the enediyne framework, often drastically lowering the barrier to cyclization. While the presence of a tether does result in shorter *cd* distances (**79** and **81**), the major driving force for cyclization of these types of substrates are strain effects that raise the ground state energy of the enediyne relative to the transition state for cycloaromatization, lowering the barrier to cyclization (Figure 3.12). The effect of ring strain on enediyne cyclization has been demonstrated experimentally by the drastically lowered cyclization temperature for cyclodec-3-ene-1,5-diyne relative to (*Z*)-hexa-3-en-1,5-diyne (**78** and **79**) and by their respective benzannulated analogs (**80** and **81**) (Figure 3.11). While ferrous enediynes **1**, **82**, and **83** do not cyclize under thermal conditions, calculations and solid-state structures of the ferrous enediynes demonstrate that incorporation of the enediyne moiety into a strained-ring reduces the *cd* distance and induces severe angle strain in the alkynes; the average angle about the sp-carbon atoms bonded to the Cp-ring in **1** and **83** are 163° and 168° degrees (respectively).³⁹ The significant angle strain and shorter *cd* distances in **1** and **83** indicate that the organic fragment should cyclize following liberation from the metal. While the proposed photochemically generated cyclopentadienide anions incorporate the *ene* into an aromatic ring, cyclopentadienide has been calculated to be more aromatic than benzene⁴⁰ and additionally bears a formal negative charge. The temperature and rate of the Bergman Cyclization on this type of substrate is unknown. Additional potential complications arise *in vitro* as the pH of cellular

compartments can vary. Thus the photo-liberated enediyne may persist as the anion, or a mixture of cyclopentadiene isomers upon photolysis in the cell media.

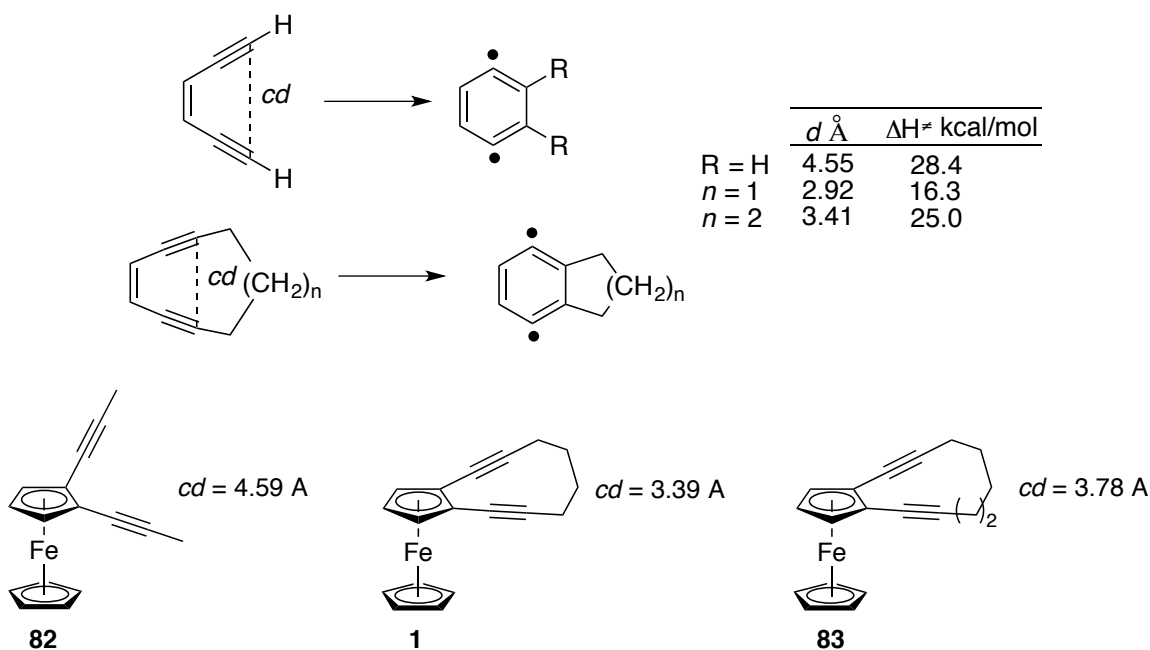
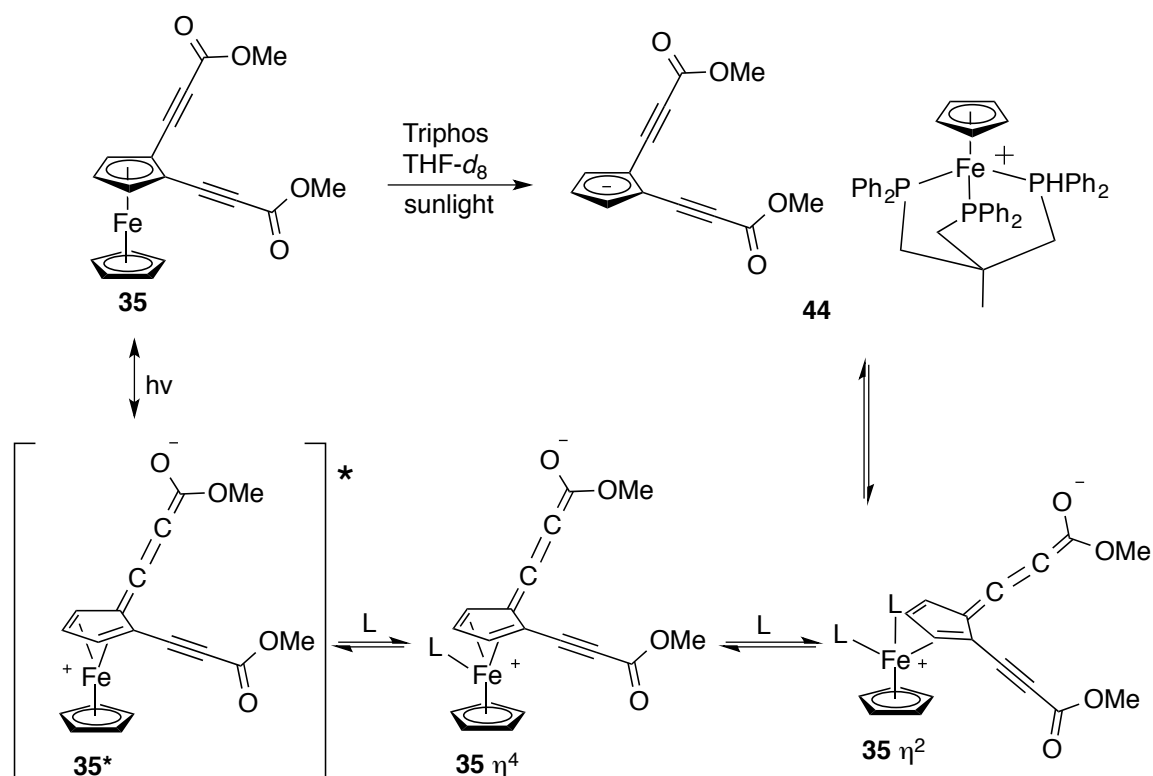


Figure 3.12. Ring strain effects in organic and ferrocene-based enediynes.

Our first attempt to demonstrate enediynes could be photo-liberated from the ferrous metallocene focused on complex **35**. First, 1,2-diethynylferrocene was synthesized using a literature procedure by Bunz (Scheme 3.13).²⁴ Deprotonation with *n*-BuLi and reaction with methyl chloroformate gave enediyne **35** in good yield (Scheme 3.15). While **35** was found to be stable indefinitely in the solid phase and in solution in the absence of light, upon exposure to sunlight in a coordinating solvent (THF-*d*₈) **35** quickly decomposed to iron precipitates that prevented product identification. Addition of a chelating ligand, triphos, to the photolysis reaction resulted in clean liberation of the anionic enediyne from the metal (Scheme

3.16).⁴¹ While the exact mechanism for the photochemical transformation remains unknown, we propose photochemical excitation to a low energy excited state generates electron deficient iron center **35*** (Scheme 3.34). Sequential solvent-assisted ring-slippage generates the observed salt **44**. Pleased we were able to form anionic enediyne **44** from **35** photochemically, we made several attempts at thermal cyclization; however, treatment of **44** with D₂O or HBF₄ in THF failed to give cycloaromatized product.



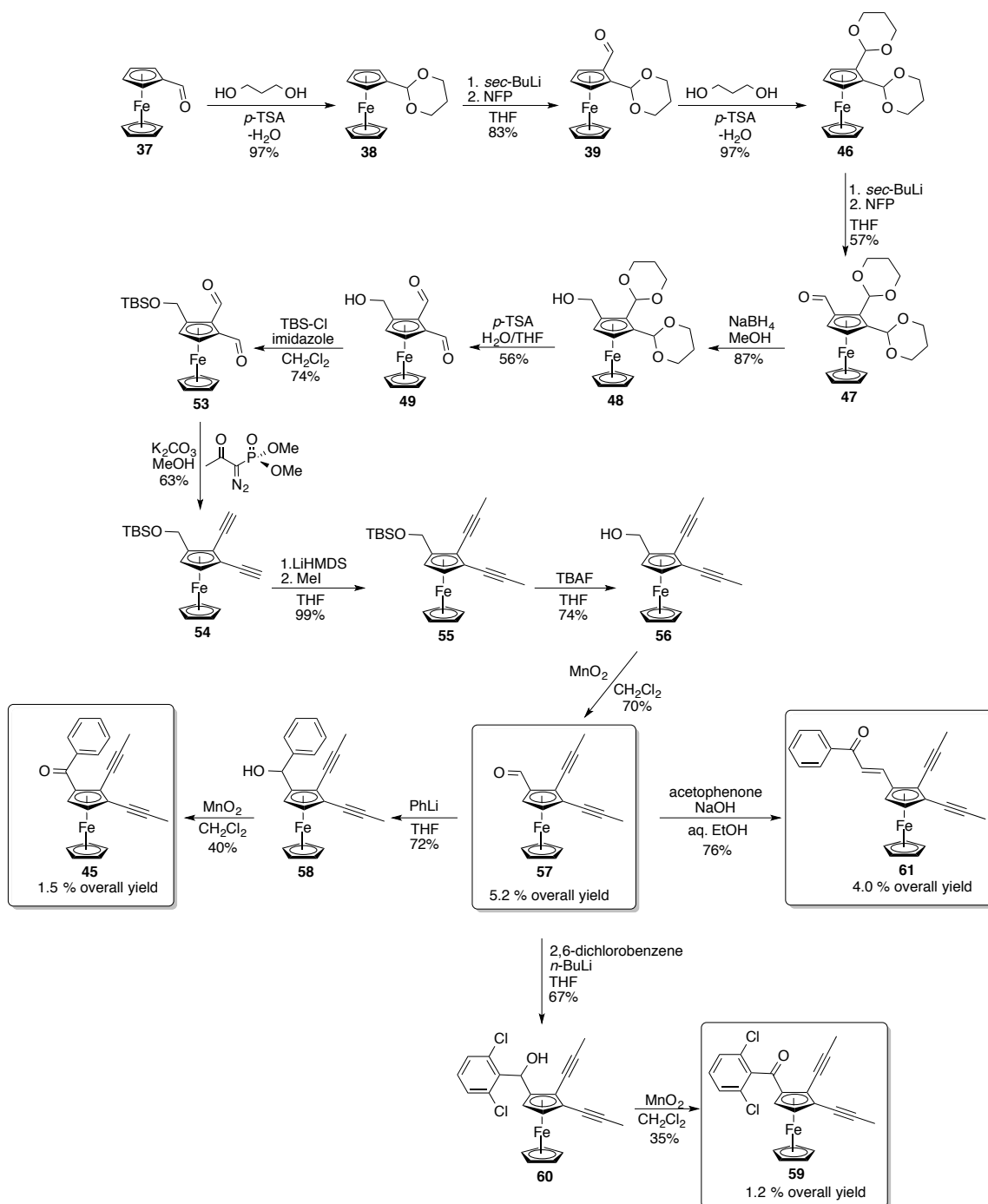
Scheme 3.34. Possible mechanism for photochemical decomposition of **35**.

Having established photochemical liberation of an enediyne from a ferrocene precursor was possible, we set out to synthesize and conduct biological testing on the much more difficult to obtain 1-benzoyl-2,3-ferrocenylenediynes (Scheme 3.35).

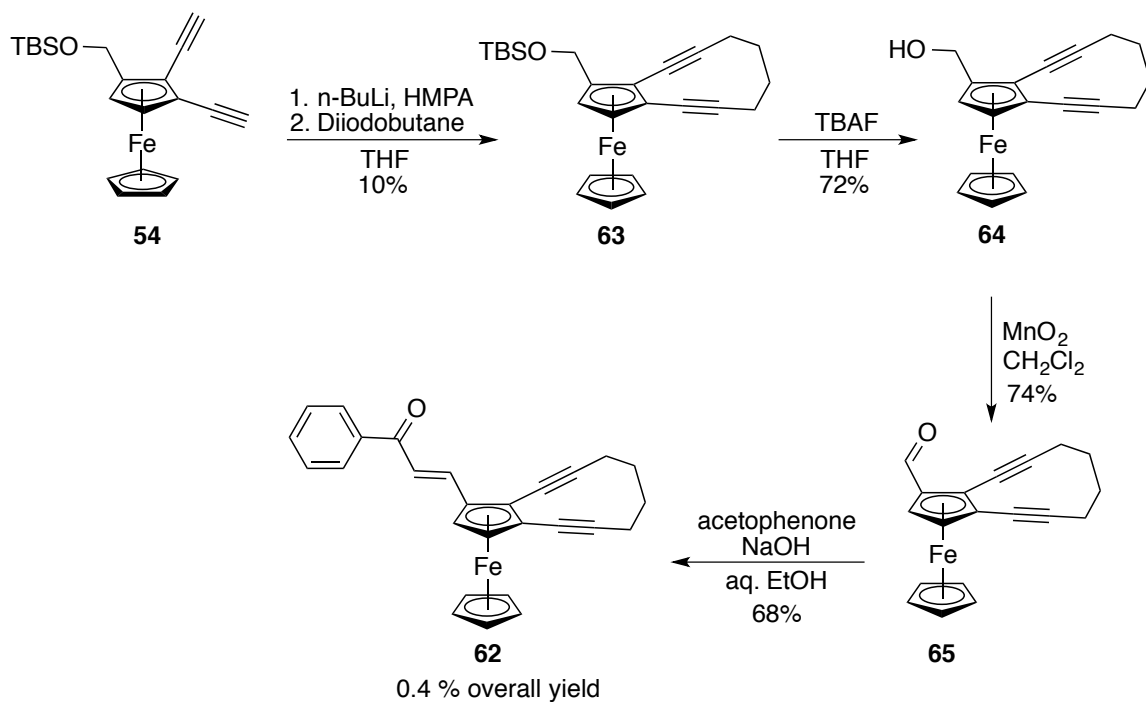
To briefly summarize, compound **47** was synthesized using a published procedure by Bunz in an overall yield of 44%.²⁴ Reduction of aldehyde **47** to primary alcohol **48** went smoothly with sodium borohydride in methanol. Removal of the acetal protecting groups with *para*-toluenesulfonic acid gave dialdehyde **49**. The alcohol was then protected using *tert*-butyldimethylsilyl chloride and imidazole in dichloromethane. Exposure of the light sensitive dialdehyde to Ohira-Taber conditions gave terminal alkyne **54**. Deprotonation of the terminal acetylenes with lithium bis(trimethylsilyl)amide and quenching with methyl iodide yielded complex **55**. Removal of the silyl protecting group with tetrabutylammonium fluoride and subsequent oxidation with manganese dioxide gave aldehyde **57** in an overall yield of 5.2%. From here, intermediate **57** was used to synthesize a small library of light-sensitive ferrocenyl-enediynes. Treatment with phenyllithium, or 2,6-dichlorophenyllithium, gave alcohols **58** and **60**. Following oxidation with manganese dioxide, **45** and **59** were obtained in overall yields of 1.5 and 1.2% (respectively). To synthesize **61** all that was required from aldehyde **57** was a simple Aldol Condensation to generate the α,β -unsaturated ketone (4.0% overall yield).

With the details of the enediyne synthesis in hand, the significantly more challenging synthesis of strained-ring enediyne **62** was performed (Scheme 3.36). Terminal alkyne **54** was deprotonated with *n*-BuLi, then treated with hexamethylphosphoramide and diiodobutane to obtain 10-membered ring **63**. Deprotection with tetrabutylammonium fluoride and oxidation with manganese

dioxide gave aldehyde **65**. From **65**, an Aldol Condensation with acetophenone gave the long-sought ferrocenyl-enediynes **62** in an overall yield of 0.4%.



Scheme 3.35. Synthesis of key intermediate **57** and enediynes **45**, **59**, and **61**.



Scheme 3.36. Synthesis of strained-ring enediyne **62**.

With photosensitive enediyne **45**, **59**, **61**, and **62** in hand we predicted that photochemically initiated ring-slippage would generate cyclopentadienide anions **84-87** *in vitro* which, depending on the pH of the cellular compartment, may persist as the anions or be in equilibrium with one or more of the protonated cyclopentadiene isomers (Figure 3.13).

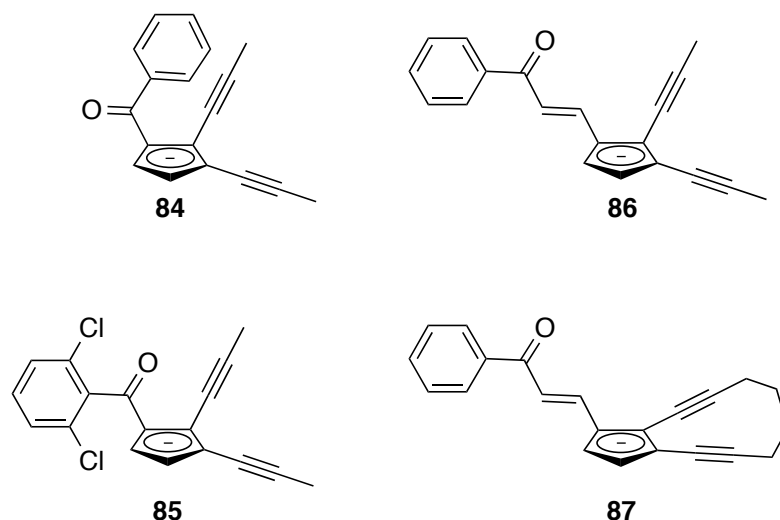
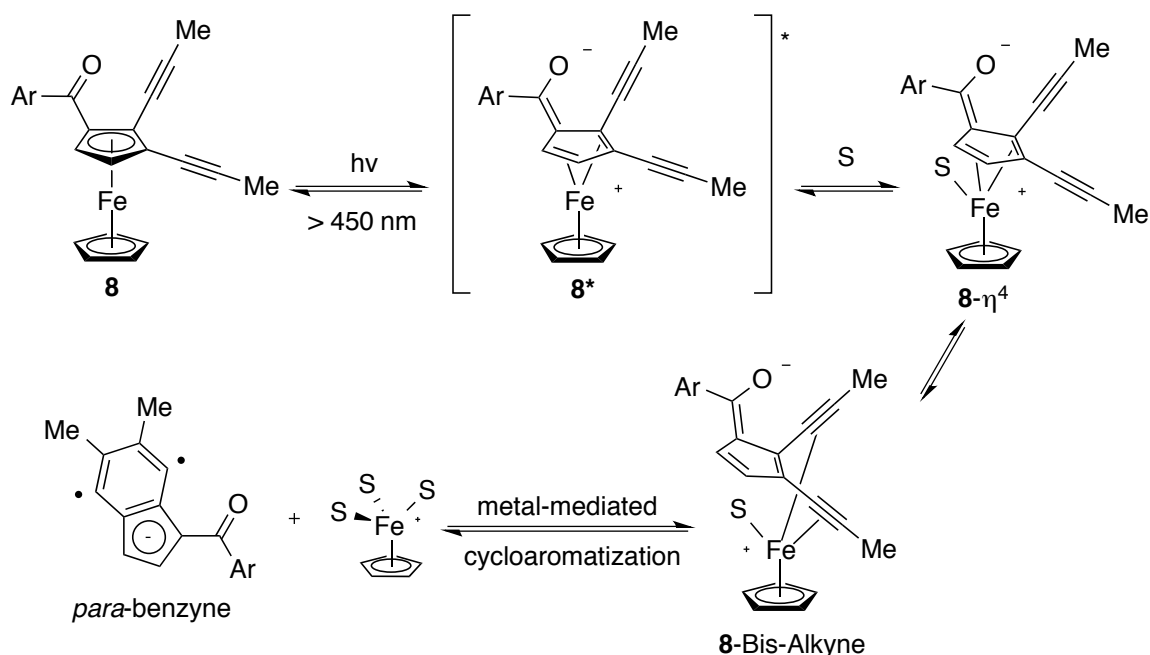


Figure 3.13. Proposed organic photoproducts of **45**, **59**, **61**, and **62**.

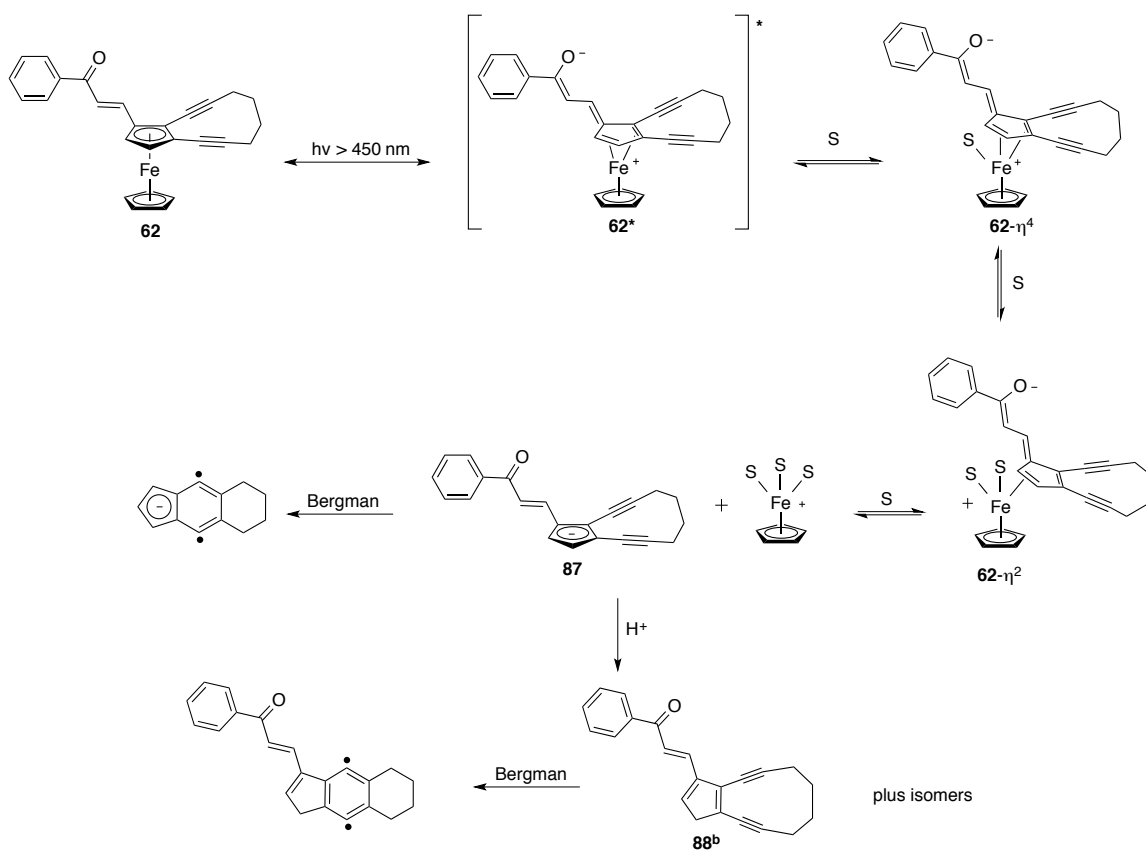
The X-ray crystal structure of **59** suggests dimethyl enediynes **84**, **85**, and **86** (or one of the cyclopentadiene analogs) are unlikely to cyclize thermally due to the large *cd* distance (4.636(2) Å) and lack of angle strain in the Cp-alkyne carbon bonds (175.6(2)° and 178.5(2)°) in the organometallic precursor. While the thermal cyclization parameters for enediynes where the *ene* is part of a cyclopentadienide ring or cyclopentadiene are unknown, based on thermal data for **78** and **80** it seems unlikely at biological temperatures. While a pure thermal cycloaromatization pathway for enediynes **84**, **85**, and **86** *in vitro* seemed increasingly unlikely, we could not rule out the possibility of a metal-mediated mechanism (Scheme 3.37). We postulated that following excitation to **8*** and solvent substitution to form ring-slipped intermediate **8-η⁴**, the iron atom could slide over to form the bis-alkyne complex and cyclize the cyclopentadienyl ligand by a metal assisted pathway.



Scheme 3.37. Photochemical metal-mediated cycloaromatization of enediynes **45**, **59**, and **61**.

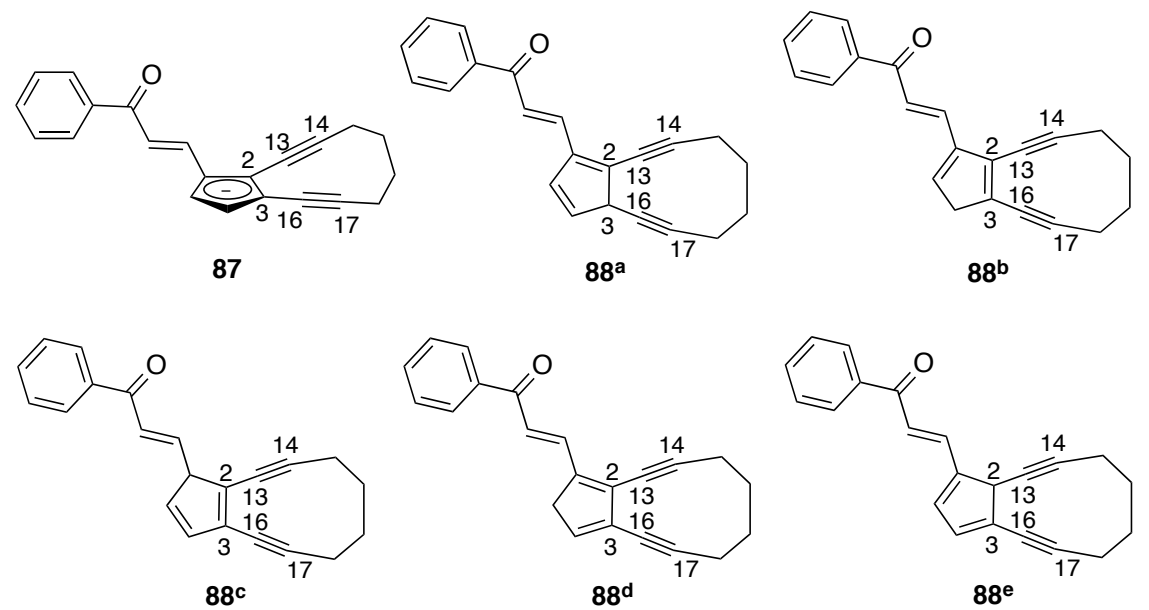
Following photolysis of **62**, we predicted thermal cycloaromatization of 10-membered ring **87**, or one of its protonated analogs **88^{a-e}**, would be much more favorable *in vitro* than **84-86** given the significant angle strain displayed by ferrous enediyne **1** and the thermal parameters for cyclization of enediyne **79** (Figure 3.11, 3.12 and Scheme 3.38). As no X-ray data was available for **62**, we calculated the equilibrium geometries and zero point energies for the cyclopentadiene anion **87** and each of the conjugate acids (Table 3.12). For the cyclopentadiene isomers, only **88^b** and **88^c** have the correct regiochemistry to undergo a Bergman cyclization and fortuitously, **88^b** was calculated to be the lowest in energy. Given the decrease in *cd* distance upon incorporation of the four-carbon tether (Figure 3.12) and significant angle strain in the alkyne framework (Table 3.12), we predicted **87** and **88^b** would

both have a reasonable chance of cycloaromatization at biological temperature. The formed *para*-benzyne diradical from either precursor *in vitro* could then readily abstract hydrogen-atoms from DNA or other important biomolecules, inducing cell death.



Scheme 3.38. Photolysis of **62** and proposed cycloaromatization of **87** and **88^b**.

Table 3.12. Calculated Bond lengths (Å), angles, and energies for free enediynes **88a-88e** using DFT BLYP++G** (vacuum).



Molecule	<i>cd</i> distance	C(2)-C(13)- (C14) bond angle (°)	C(3)-C(16)- (C17) bond angle (°)	Zero Point Energy (Hartrees)	Relative Energy (kcal/mol)
87	3.53	165.52	165.40	-	-
88^a	3.41	162.61	163.10	-924.089779	246
88^b	3.40	163.04	163.54	-924.481792	0.00
88^c	3.41	163.16	163.14	-924.473145	5.43
88^d	3.40	164.34	164.41	-924.477080	2.96
88^e	3.39	162.97	162.36	-924.092582	244

The cytotoxicity of ferrous enediynes **45**, **59**, **61**, and **62** was determined in both the dark and under photoconditions in HeLa and A549 cells (Table 3.13). The benzoylated ferrous enediynes **45** and **59** displayed no enhancement of toxicity upon exposure to visible light; however, incorporation of a α,β -unsaturated ketone (**61**) moiety gave a modest increase in phototoxicity. Since **61** was our most successful enediyne candidate to date and obtaining significant amounts of the 10-membered ring analogs was extremely difficult, we focused our attention of the

toxicity of α,β -unsaturated ketone **62**. While **62** does display the greatest phototoxicity index, and is predicted to be the most likely to cycloaromatize thermally, at this time it is not known if the enhanced cytotoxicity is due to photo-triggered cycloaromatization to *para*-benzyne, or simply higher lipophilicity relative to **45**, **59**, and **61** and thus greater cellular uptake, resulting in higher concentrations of reactive oxygen species generated via the Fenton reaction (Table 3.13).

Table 3.13. IC₅₀ (μ M), phototoxicity index (P.I.) and log *P* for tested ferrocene enediynes.

Complex	Cell Line	IC _{50-dark}	IC _{50-light}	P.I.	Log <i>P</i>
45	A549	11.0 (1.3)	8.3 (1.1)	1.3	4.1
59	HeLa	> 40*	> 20*	2*	4.7
59	A549	> 20*	20.5 (6.6)	1*	4.7
61	A549	> 40	11.7 (5.7)	3.4	4.8
62	HeLa	> 80	19.7 (3.5)	4.1	5.2
62	A549	> 80	19.2 (4.2)	4.2	5.2

*not all IC₅₀ values could be determined due to solubility limits of the parent metallocene. P.I. = IC_{50-dark}/IC_{50-light}

D. Conclusions

A series of ferrocenyl-enediynes were synthesized with a benzoyl chromophore incorporated unto the ferrocene moiety, providing a photochemical triggering mechanism for cycloaromatization to *para*-benzyne. Two methods to selectively generate the highly cytotoxic *para*-benzyne diradical *in vitro* were investigated: (1) photochemical, metal-assisted cyclization of unreactive acyclic enediynes by metal coordination to the π -backbone (**13**) and (2) enediyne

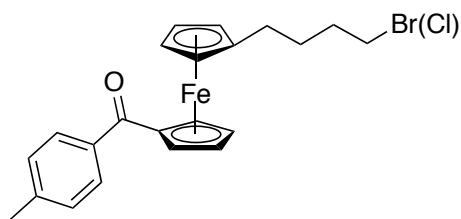
stabilization by *ene*-metal coordination followed by photochemical *ene*-release and cycloaromatization (**45**, **59**, **61**, and **62**). Eneidyne **13** failed to cycloaromatize, likely a steric or electronic effect of CpFeL₃⁺ fragment and/or a non-optimal tether length. While α,β -unsaturated ketones **61** and **62** displayed mild photocytotoxicity in both HeLa and A549 cells, at this time the mechanism of action is not clear. Future studies will focus on the photochemical aqueous reactivity of enediynes of **62** and on *in vitro* mechanistic studies to determine if the observed cytotoxicity is due to the generation of reactive oxygen species and/or formation of *para*-benzyne.

E. Experimental

General Methods

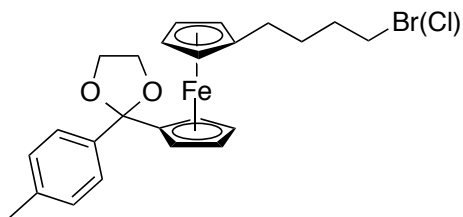
All synthetic reagents were purchased from Aldrich, Fisher Scientific, or Alfa Aesar, and were used without further purification. All solvents for anhydrous reactions were obtained from Fisher scientific and dried on alumina columns prior to use. All reactions were performed under N₂ or argon using standard Schlenk techniques unless otherwise noted. Solvents used for chromatography were ACS technical grade and used without further purification. Water (18.2 μΩ/cm) was filtered through a NANOPure Diamond™ (Barnstead) water purification system before use. All ¹H NMR and ¹³C NMR spectra were recorded on a Varian Mercury Plus 400 MHz NMR spectrometer or a Varian VNMRs NMR spectrometer equipped with a 500MHz XSens Cold Probe. Deuterated solvents were purchased from Cambridge Isotopes. Chemical shifts are reported as δ in units of parts per million (ppm) referenced to the residual solvent peak. Coupling constants are reported as a J value in Hertz (Hz). High-resolution mass spectrometry analysis was performed by the UCSD Chemistry and Biochemistry Molecular Mass Spectrometry Facility on a ThermoFinnigan MAT900XL mass spectrometer with an ESI source. UV-Vis absorption spectra were collected with a Shimadzu UV 3600 and plotted using Excel. FTIR spectra were recorded on a Thermo-Nicolet iS10 FTIR spectrometer. Samples were prepared as a thin film using NaCl or BaF₂ windows as noted. Equilibrium geometry ground state calculations were performed by Spartan '14 molecular

modeling with Density Functional Theory methods (B3LYP, 6-311++G**) in a vacuum.

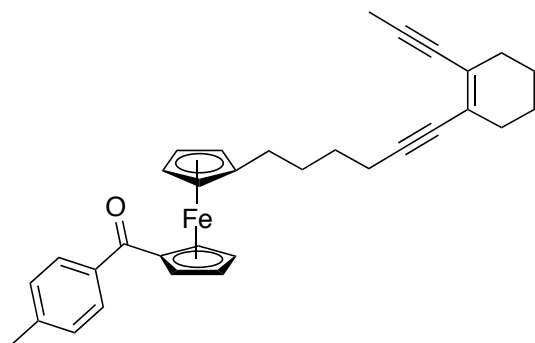


1-(*para*-Toyl)-1'-bromobutylferrocene (20): Complex **19** (5.00 g, 15.6 mmol, 1 equiv) was dissolved in anhydrous dichloromethane (100 mL, 0.15 M) and *para*-toluoyl chloride (2.34 mL, 17.6 mmol, 1.1 equiv) was added via syringe. The reaction mixture was cooled to 0 °C by use of an ice bath and anhydrous AlCl₃ (2.34 g, 17.6 mmol, 1.1 equiv) was added in three portions over a 15 minute period. The dark blue solution was allowed to warm to RT slowly while stirring overnight (12 h). The reaction mixture was poured into a flask of ice water, extracted into 100 mL of CH₂Cl₂, then washed successively with 10% NaOH solution, water, and brine. The organic layer was dried over MgSO₄, filtered, and the solvent was removed under reduced pressure. Chromatography on SiO₂ gel with 90:10 hexanes:ethyl acetate as eluent led to isolation of the pure 1,1'-ferrocene. ¹H NMR (500 MHz, CDCl₃) δ 1.55 (t, *J*_{HH} = 6.9 Hz, 2H), 1.93-1.71 (m, 2H), 2.22 (t, *J*_{HH} = 6.9 Hz, 2H), 2.44 (s, 3H), 3.35 (t, *J*_{HH} = 5.9 Hz, 2H), 4.05 (s, 2H), 4.09 (s, 2H), 4.52 (s, 2H), 4.84 (s, 2H), 7.27 (d, *J*_{HH} = 6.8 Hz, 3H), 7.80 (d, *J*_{HH} = 6.8 Hz, 2H); ¹³C NMR (500 MHz, CDCl₃) δ 21.74 (CH₃), 27.81 (CH₂), 29.51 (CH₂), 32.47 (CH₂), 33.75 (CH₂), 69.67 (s, 1C), 70.30 (s, 1C), 72.18 (s, 1C), 73.20 (s, 1C), 78.76 (*ipso*-Cp), 90.46 (*ipso*-Cp), 128.41 (aryl), 129.00 (aryl), 137.26 (aryl), 142.20 (aryl), 198.65 (CO). IR (NaCl, cm⁻¹) 1287, 1442, 1632, 2857,

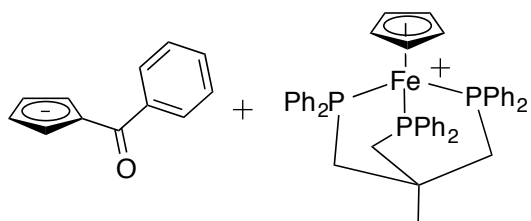
2921. HRMS (ESI-TOFMS) m/z calcd for $[C_{22}H_{23}BrFeONa]^+$: 461.0176; found 461.0179.



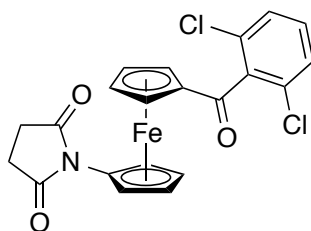
1-[(*para*-Toyl)-1,3-dioxolane]-1'-bromobutylferrocene (21): Ethylene glycol (10 mL) and benzene (100 mL) were refluxed 12 h with a Dean-Stark trap, then **20** (5.9 g, 13.5 mmol) and *p*-TSA (0.64 g, 3.38 mmol, 0.25 equiv) were added as a solution in 10 mL of benzene at room temperature. The solution was allowed to return to a reflux for 14 h with a Dean Stark trap. The reaction was quenched with saturated Na_2CO_3 , washed with water, and the organic layer was dried with anhydrous $MgSO_4$. The crude product was isolated under reduced pressure and purified by silica gel chromatography (98:2 hexanes:ethyl acetate). Yielded 1.95 g of a yellow solid (38%). 1H NMR (500 MHz, CD_2Cl_2) δ 1.64-1.59 (m, 2H), 1.88 (m, 2H), 2.26 (t, $J = 7.8$ Hz, 2H), 2.43 (s, 2H), 3.47 (t, $J = 6.9$ Hz, 2H), 3.87-3.84 (m, 2H), 4.18-4.04 (m, 10H), 7.25 (d, $J = 8.1$ Hz, 2H), 7.53 (d, $J = 8.1$ Hz, 2H); ^{13}C NMR (500 MHz, CD_2Cl_2) δ 21.20 (CH_3), 28.55 (CH_2), 29.81 (CH_2), 32.96 (CH_2), 34.35 (CH_2), 65.15 (OCH_2CH_2O), 68.02 (Cp), 68.61 (Cp), 69.00 (Cp), 69.45 (Cp), 89.40 (*ipso*-Cp), 91.66 (*ipso*-Cp), 109.51 (ketal), 126.41 (aryl), 128.65 (aryl), 137.83 (aryl), 139.69 (aryl). IR (NaCl, cm^{-1}) 958, 1457, 2881, 2934, 3086. HRMS (ESI-TOFMS) m/z calcd for $[C_{24}H_{28}BrFeO_2]^+$: 483.0618; found 483.0617.



1-*para*-Tolyl-1'-[1-(hexynyl)-2-(propynyl)cyclohex-1-ene] (13): **12** (95 mg, 0.66 mmol, 1.25 equiv) was dissolved in THF (5 mL), cooled to $-78\text{ }^{\circ}\text{C}$ by use of a dry ice/acetone bath, and *n*-BuLi (0.58 mL, 0.72 mmol, 1.25 equiv, 1.25 M solution in hexanes) was added dropwise. The reaction was allowed to warm to $0\text{ }^{\circ}\text{C}$ for 45 min before cooling to $-78\text{ }^{\circ}\text{C}$. HMPA (0.13 mL, 0.72 mmol, 1.35 equiv) was then added via syringe and the solution was stirred an additional 15 min. Complex **21** (0.25 g, 0.53 mmol, 1 equiv) was then syringed into the reaction as a solution in 1 mL of THF. The reaction was warmed to RT and stirred for 14 h. The solution was then quenched with 10% *p*-TSA solution, extracted twice into diethyl ether, and the organic layers were dried with anhydrous MgSO_4 . The crude product was purified by silica gel chromatography (95:5 hexanes:ethyl acetate). Yielded 0.17 g of a yellow oil (64%). $^1\text{H NMR}$ (400 MHz, CDCl_3) δ 1.54 (m, 8H, 4 CH_2), 1.96 (s, 3H, enediyne- CH_3), 2.16 (m, 4H, 2 CH_2), 2.21 (t, $J = 7.1\text{ Hz}$, 2H, CH_2), 2.34 (t, $J = 6.4\text{ Hz}$, 2H, CH_2), 2.43 (s, 3H, benzoyl- CH_3), 4.06 (m, 4H, Cp), 4.50 (t, $J = 1.7\text{ Hz}$, 2H, Cp), 4.83 (t, $J = 1.7\text{ Hz}$, 2H, Cp), 7.27 (d, 2H, aryl), 7.80 (d, $J_{\text{HH}} = 8.1\text{ Hz}$, 2H, aryl). MS (ESI) m/z calcd for $[\text{C}_{33}\text{H}_{35}\text{FeO}]^+$: 503.20; found 503.14.

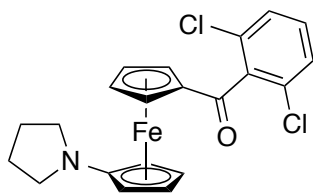


[CpFe{MeC(CH₂PPh₂)₃][C₅H₄C(O)Ph] (6⁻/6⁺): A Pyrex reaction tube containing a acetonitrile (2 mL) solution of benzoylferrocene (50 mg, 0.17 mmol, 1 equiv) and 1,1,1-tri(diphenylphosphino-methyl)ethane (108 mg, 0.17 mmol, 1 equiv) was irradiated with a flood light for 12 h. The volatiles were removed *in vacuo* and the residue was washed with toluene to yield a golden solid (89% NMR yield). ¹H NMR (400 MHz, CD₃CN) δ 1.58-1.46 (s, 3H, CH₃), 2.41-2.22 (s, 6H, 3CH₂), 4.93 (s, 5H, Cp), 5.94-5.73 (s (br), 4H, Cp⁻), 7.17-7.00 (m, 24h, triphos), 7.41-7.19 (m, 6H, triphos), 7.62 (t, *J*_{HH} = 2.9 Hz, 2H, benzoyl); ¹³C NMR (500MHz, CD₃CN) δ 34.99 (triphos-CH₃), 35.79 (triphos-CH₂), 36.24 (triphos-C), 80.72 (Cp), 104.99 (Cp[']), 122.53 (Cp[']), 126.98 (aryl), 127.50 (aryl), 128.25 (aryl), 128.53 (aryl), 128.62 (aryl), 129.40 (aryl), 132.02 (aryl), 132.84 (aryl), 184.63 (CO).



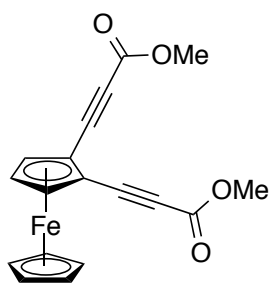
1-N-Succinimide-1' (2,6-dichlorobenzoyl)ferrocene (31): **30** was dissolved in 20 mL of diethyl ether. A solution of succinic anhydride in 10 mL of THF (0.13 g, 1.34 mmol, 1.00 equiv) was added and the mixture was allowed to stir for a period of two hours at RT. The volatiles were removed under reduced pressure and a

solution of sodium acetate (0.10 g, 1.34 mmol, 1.00 equiv) in acetic anhydride (10 mL) was added in one portion. The suspension was then heated for 1 h at 80 °C before cooling to RT. The reaction contents were poured into an ice cold solution of NaHCO₃, extracted twice with ethyl acetate, then washed successively with water and brine. The organic layers were dried with MgSO₄ and the volatiles were removed under reduced pressure. The product was purified on a short SiO₂ plug by elution with 40:60 hexanes:ethyl acetate. Yielded a dark red solid (68 % yield). ¹H NMR (500 MHz, CD₂Cl₂) δ 2.74 (m, 4H, CH₂CON), 4.36 (t, *J*_{HH} = 2.0 Hz, 2H, Cp), 4.61 (t, *J*_{HH} = 1.9 Hz, 2H, Cp), 4.66 (t, *J*_{HH} = 1.9 Hz, 2H, Cp), 5.02 (t, *J*_{HH} = 2.0 Hz, 2H, Cp), 7.37-7.29 (m, 3H, aryl); ¹³C NMR (500 MHz, CD₂Cl₂) δ 28.62 (CH₂), 65.24 (Cp), 68.37 (Cp), 71.96 (Cp), 74.66 (Cp), 80.66 (Cp-*ipso* benzoyl), 90.32 (Cp-*ipso*), 128.78 (aryl), 131.01 (aryl), 132.11 (aryl), 138.73 (aryl), 175.92 (NCO), 196.97 (CO). IR (NaCl, cm⁻¹) 1154, 1352, 1574, 1651, 1710, 2850, 2920. HRMS (ESI-TOFMS) *m/z* calcd for [C₂₁H₁₆Cl₂FeNO₃]⁺: 453.9898; found 453.9895.



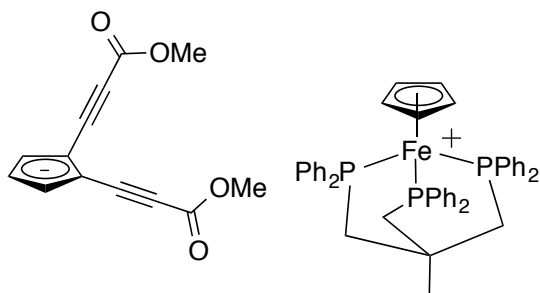
1-N-Pyrrolidine-1'-(2,6-dichlorobenzoyl)ferrocene (26): BH₃•THF (4.4 mL, 2.20 mmol, 4 equiv, 0.5 M solution) was added slowly to a solution of (31) (0.25 g, 0.55 mmol) at room temperature in THF (50 mL) with fast stirring. Once the vigorous bubbling ceased the red solution was heated to a reflux for 2 h. The reaction was cooled to RT and the crude product was extracted into diethyl ether, washed

successively with 10% NaOH, water, and brine, then dried with MgSO₄. Filtration through celite yielded the pure pyrrolidine was dark purple crystals (87%). ¹H NMR (400 MHz, CD₂Cl₂) δ 1.90 (m, 4H, CH₂), 2.93-2.89 (m, 4H, CH₂N), 3.77 (t, *J*_{HH} = 1.9 Hz, 2H, Cp), 4.14 (t, *J*_{HH} = 1.9 Hz, 2H, Cp), 4.62 (t, *J*_{HH} = 1.9 Hz, 2H, Cp), 4.67 (t, *J*_{HH} = 1.9 Hz, 2H, Cp), 7.37-7.27 (m, 3H, aryl); ¹³C NMR (500 MHz, CD₂Cl₂) δ 25.25 (CH₂), 50.60 (CH₂), 56.75 (Cp), 66.50 (Cp), 69.85 (Cp), 72.20 (Cp), 78.99 (Cp), 116.10 (Cp), 128.75 (aryl), 130.70 (aryl), 132.31 (aryl), 139.05 (aryl), 197.32 (CO). IR (NaCl, cm⁻¹) 675, 787, 1442, 1651, 2953. HRMS (ESI-TOFMS) *m/z* calcd for [C₂₁H₂₀Cl₂FeNO]⁺: 428.0267; found 428.0267. UV-Vis λ_{max} (CH₃CN, nm) 362, 498.



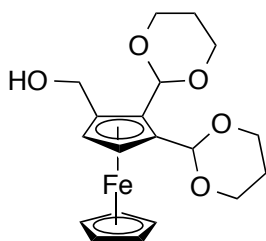
(Cp)Fe[η⁵-C₅H₃-1,2-(CCCO₂Me)₂] (35): A cyclohexane solution of *n*-BuLi (6.67 mmol, 2.7 mL of a 2.5 M solution) was added dropwise to a -78 °C THF solution of 1,2-diethynylferrocene (0.710 g, 3.05 mmol). The reaction mixture was warmed to 0 °C for 10 min, re-cooled to -78 °C, and methyl chloroformate (0.5 mL, 6.65 mmol) was added dropwise. The solution was stirred for 15 h at RT, quenched with saturated NH₄Cl (aq.), and extracted into diethyl ether. The organic extracts were dried over MgSO₄ and the volatiles removed in vacuo. SiO₂ column chromatography (80:20 hexanes:ethyl acetate) of the residue gave **43** as bright red microcrystals (710 mg, 67% yield). ¹H NMR (CDCl₃, 500 MHz) δ 3.81 (s, 6H, OCH₃), 4.33 (s, 5H, C₅H₅),

4.48 (t, $J_{HH} = 2.5$ Hz, 1H, Cp'), 4.73 (d, $J_{HH} = 2.5$ Hz, 2H, Cp'); ^{13}C NMR (CDCl_3 , 400 MHz) δ 52.8 (COCH_3), 64.5 (Cp'), 71.6 (Cp'), 72.7 (Cp), 74.6 (Cp'), 80.4 (CC), 85.0 (CC), 154.0 (COCH_3). IR (NaCl, cm^{-1}) 1430, 1457, 1701, 2215, 2956, 3033, 3097, 3384. HRMS (FAB) m/z calcd for $[\text{C}_{18}\text{H}_{14}\text{O}_4\text{Fe}]^+$: 348.0282; found 348.0285.



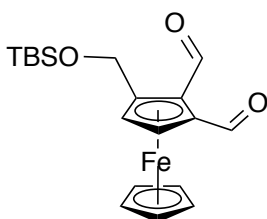
[(Cp)Fe{MeC(CH₂PPh₂)₃}] [C₅H₃-1,2-(CCCO₂Me)₂] (44**):** A Pyrex reaction tube containing a THF (3 mL) solution of **35** (100 mg, 0.29 mmol) and 1,1,1-tris(diphenylphosphino- methyl)ethane (196 mg, 0.31 mmol) was irradiated with a broad-spectrum 400 W Hanovia lamp for 72 h. The volatiles were removed *in vacuo* and the residue was recrystallized from CH_2Cl_2 /hexanes to yield **44** as dark red-brown, almost black crystals that were air-stable for weeks (150 mg, 0.15 mmol, 53% yield). ^1H NMR (CDCl_3 , 400 MHz) δ 1.54 (s, 3H, Triphos- CH_3), 2.27 (s, 6H, Triphos- CH_2), 3.76 (s, 6H, COCH_3), 4.84 (s, 5H, Cp), 5.86 (t, $J_{HH} = 3.44$ Hz, 1H, Cp'), 6.44 (d, $J_{HH} = 3.44$ Hz, 2H, Cp'), 6.86 (m, 18H, Triphos-Ph), 7.04 (m, 12H, Triphos-Ph). ^1H NMR ($\text{THF-}d_8$, 400 MHz) δ 1.58 (s, 3H, Triphos- CH_3), 2.41 (s, 6H, Triphos- CH_2), 3.62 (s, 6H, COCH_3), 5.01 (s, 5H, Cp), 5.63 (t, $J_{HH} = 3.51$ Hz, 1H, Cp'), 6.19 (d, $J_{HH} = 3.51$ Hz, 2H, Cp'), 7.05 (m, 12H, Triphos-Ph), 7.23 (m, 12H, Triphos-Ph), 7.30 (m, 6H, Triphos-Ph); ^1H NMR (CD_3CN , 400 MHz) δ 1.54 (s, 3H, Triphos- CH_3), 2.36 (s, 6H,

Triphos-CH₂), 3.69 (s, 6H, COCH₃), 4.94 (s, 5H, Cp), 5.78 (t, $J_{HH} = 3.51$ Hz, 1H, Cp'), 6.29 (d, $J_{HH} = 3.51$ Hz, 2H, Cp'), 7.06 (m, 24H, Triphos-Ph), 7.25 (m, 6H, Triphos-Ph); ¹³C NMR (CDCl₃, 500 MHz) δ 25.8 (s, 3H, Triphos-CH₃), 38.1 (s, 3H, Triphos-CH₂), 53.1 (Triphos-CCH₃), 68.2 (COCH₃), 80.9 (Cp), 83.5 (C \equiv C), 99.2 (C \equiv C), 102.7 (Cp'), 112.8 (Cp'), 122.4 (Cp'), 128.8 (Triphos-Ph), 129.9 (Triphos-Ph), 132.2 (Triphos-Ph), 139.0 (Triphos-Ph), 157.4 (COCH₃). IR (NaCl, cm⁻¹) 1671.04, 2124.43, 2155.44. UV-Vis λ_{\max} 248, 370, 448. HRMS(FAB) m/z calcd for anion [C₁₃H₁₀O₄]⁻: 230.0574; found 230.0576.



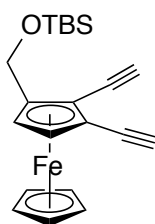
1,2-Bis-[1,3]dioxin-3-(hydroxymethyl)ferrocene (48): Aldehyde **47** (20 g, 49 mmol, 1 equiv) was dissolved in MeOH (250 mL, 0.2 M) and cooled to 0 °C in an ice/salt bath. Sodium borohydride (7.40 g, 195 mmol, 4 equiv) was added in four portions during which time the red solution bubbled vigorously. After 30 min of stirring at RT the solution turned yellow and bubbling ceased. Approximately 90% of the methanol was removed under reduced pressure and the residue was taken up in THF/H₂O. The solution was extracted once with diethyl ether, washed with brine, and dried with anhydrous MgSO₄. The compound was found to be pure by NMR upon evaporation of the organic solvents (17.4 g, 87%). ¹H NMR (500 MHz, CD₂Cl₂) δ 5.53 (s, 1H, acetal-CH), 5.39 (s, 1H, acetal-CH), 4.61 (dd, $J_{HH} = 11.9, 3.9$ Hz, 2H, CH₂OH), 4.33-4.21 (m, 3H, acetal-CH₂CH₂CH₂ and Cp'), 4.16 (s, 5H, Cp), 4.13-4.06 (m,

3H, acetal-CH₂CH₂CH₂ and Cp'), 3.98-3.84 (m, 4H, acetal-CH₂CH₂CH₂), 3.00 (dd, $J_{HH} = 9.0, 4.0$ Hz, OH), 2.14-2.03 (m, 2H, acetal-CH₂CH₂CH₂), 1.38 (t, $J = 13.1$ Hz, 2H, acetal-CH₂CH₂CH₂); ¹³C NMR (500 MHz, CD₂Cl₂) δ 26.15 (acetal), 26.21 (acetal), 59.98 (CH₂OH), 65.73 (Cp'), 67.57 (acetal), 67.62 (acetal), 67.95 (acetal), 68.02 (acetal), 68.97 (Cp'), 70.44 (Cp), 83.17 (Cp'), 85.62 (Cp'), 87.51 (Cp'), 100.08 (acetal), 100.67 (acetal). HRMS (ESI-TOFMS) m/z calcd for [C₁₉H₂₄FeO₅Na]⁺: 411.0867; found 411.0866.



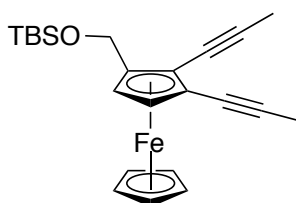
tert-Butyldimethylsilyl methyl ether-2,3-diformylferrocene (53): **48** (10.0 g, 24.3 mmol, 1.0 equiv) was dissolved in THF (250 mL) and H₂O (25 mL) and a catalytic amount of *para*-toluenesulfonic acid (0.46 g, 24.3 mmol, 10%) was added. The solution was stirred in the dark for 45 min at RT then dried rigorously with MgSO₄. The volatiles were then removed under reduced pressure. The resulting red oil was run through a short plug of silica with 50:50 hexanes:ethyl acetate to obtain **49**. Alcohol **49** (10.8 g, 39.2 mmol, 1.0 equiv), in equilibrium with its hemiacetal isomer **50**, was dissolved in 100 mL of CH₂Cl₂ then TBSCl (7.1 g, 47.6 mmol, 1.2 equiv) and imidazole (6.30 g, 94.0 mmol, 2.4 equiv) were added together in one portion. The red suspension was allowed to stir for 2 h at RT. The reaction was extracted with CH₂Cl₂, washed with brine, dried with anhydrous MgSO₄, and isolated under reduced pressure. Column chromatography (SiO₂, 90:5:5 hexanes:ethyl

acetate:NEt₃) yielded **53** as a red solid (4.07 g, 41% over two steps). ¹H NMR (400 MHz, CDCl₃) δ 0.14 (s, 6H, Si(CH₃)), 0.96 (s, 9H, SiC(CH₃)₃), 4.36 (s, 5H, Cp), 4.85-4.71 (m, 2H, CH₂OH), 5.09 (d, *J*_{HH} = 2.7 Hz, 1H, Cp'-H), 5.11 (d, *J*_{HH} = 2.7 Hz, 1H, Cp'), 10.28 (s, 1H, COH), 10.55 (s, 1H, COH); ¹³C NMR (400 MHz, CDCl₃) δ -5.16 (Si-CH₃), -5.09 (Si-CH₃), 18.45 (Si-CH₃), 26.11 (Si-C), 60.05 (CH₂), 72.21 (Cp), 74.22 (Cp'), 75.43 (Cp'), 81.18 (*ipso*-Cp'), 92.61 (*ipso*-Cp'), 98.19 (*ipso*-Cp'), 193.80 (CO), 194.73 (CO). IR (NaCl, cm⁻¹) 860, 1105, 1254, 1357, 1426, 1471, 1668, 1682, 2853, 2923, 2956. HRMS (ESI-TOFMS) *m/z* calcd for [C₁₉H₂₆FeO₃SiNa]⁺: 409.0893; found 409.0894.



tert-Butyldimethylsilyl ether-2,3-diethynylferrocene (54): A round bottom flask containing compound **53** (0.83 g, 2.15 mmol, 1 equiv) was filled with methanol (22 mL, 0.1 M), degassed with argon for 10 minutes, and cooled to 0 °C by use of an ice bath. (1-Diazo-2-oxopropyl)-phosphonic acid dimethyl ester (1.44 g, 7.52 mmol, 3.5 equiv) was added via pipette and K₂CO₃ (2.07 g, 15.1 mmol, 7 equiv) was added in one portion. The reaction was allowed to continue while warming to RT slowly overnight (14 h). The volatiles were removed under reduced pressure and the residue was partitioned between CH₂Cl₂ and brine. The organic layers were dried over anhydrous MgSO₄ and purified by column chromatography (SiO₂, 99:1, hexanes:NEt₃). Yielded the dialkyne as an orange oil in 63% yield. ¹H-NMR (500 MHz, CD₂Cl₂) δ 0.08 (s, 3H), 0.10 (s, 3H), 0.91 (s, 9H), 2.94 (s, 1H), 3.06 (s, 1H), 4.19

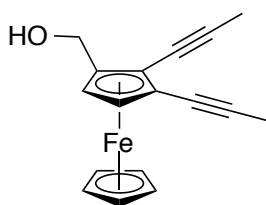
(s, 5H), 4.37 (d, $J_{HH} = 2.6$ Hz, 1H), 4.47 (d, $J_H = 2.6$ Hz, 1H), 4.54 (q, $J_{HH} = 13.4$ Hz, 2H); ^{13}C NMR (500 MHz, CD_2Cl_2) δ -5.20 (SiCH₃), 18.55 (SiC(CH₃)), 25.99 (SiC), 60.12 (CH₂), 67.42 (CCH), 67.53 (CCH), 69.38 (Cp'), 71.65 (Cp'), 72.83 (Cp), 76.27 (CCH), 78.50 (CCH), 79.87 (Cp'), 80.90 (Cp'), 90.97 (Cp'). IR (NaCl, cm^{-1}) 1105, 1668, 2853, 2923, 2956. HRMS (ESI-TOFMS) m/z calcd for $[\text{C}_{21}\text{H}_{27}\text{FeOSi}]^+$: 379.1175; found 379.1171.



tert-Butyldimethylsilyl methyl ether-2,3-di(1-propynyl)ferrocene (55):

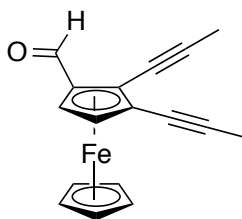
Compound **54** (0.52 g, 1.37 mmol, 1 equiv) was dissolved in THF (14 mL), degassed for 10 minutes with argon, and cooled to 0 °C by use of an ice bath. Lithium bis(trimethylsilyl)amide (3.44 mL, 3.44 mmol, 2.5 equiv, 1 M solution in THF/ethylbenzene) was added via syringe and the solution was allowed to stir for 15 min before addition of methyl iodide (0.23 mL, 3.76 mmol, 2.75 equiv) in one portion via syringe. The reaction mixture was warmed to RT and stirred overnight (12 h). The solution was washed with brine, extracted into diethylether, dried with anhydrous MgSO_4 , and isolated by rotary evaporation. Column chromatography (SiO_2 , 90:10 hexanes: NEt_3) yielded **54** as an orange oil (0.55 g, 99%). ^1H NMR (400 MHz, CDCl_3) δ 0.06 (s, 3H, CH₃), 0.11 (s, 3H, CH₃), 0.91 (s, 9H, 3CH₃), 2.00 (s, 3H, CH₃), 2.03 (s, 3H, CH₃), 4.16 (s, 5H, Cp), 4.26 (d, $J_{HH} = 2.6$ Hz, 1H, Cp'), 4.31 (d, $J_{HH} = 2.6$ Hz, 1H, Cp'), 4.53 (q, $J_{HH} = 10.1$ Hz, 2H, CH₂); ^1H NMR (500 MHz, CD_2Cl_2) δ 0.07

(s, 2H, CH₂), 0.10 (s, 3H, CH₃), 0.91 (s, 9H, 3 CH₃), 1.98 (s, 3H, CH₃), 2.01 (s, 3H, CH₃), 4.13 (s, 5H, Cp), 4.24 (d, $J_{HH} = 2.4$ Hz, 1H, Cp'), 4.29 (d, $J_{HH} = 2.4$ Hz, 1H, Cp'), 4.57-4.46 (m, 2H, CH₂); ¹³C NMR (400 MHz, CDCl₃) δ -5.03 (CH₃), -4.99 (CH₃), 5.01 (CH₃), 5.14 (C), 18.49 (C), 26.09 (C), 60.36, 67.91, 69.16, 69.35, 70.18, 71.89, 75.21, 76.25, 84.21 (*ipso*-Cp'), 86.39 (*ipso*-Cp'), 89.22 (*ipso*-Cp'); ¹³C NMR (500 MHz, CD₂Cl₂) δ -5.44 (CH₃), 4.42(CH₃), 4.56(CH₃), 18.33 (C), 25.75 (C), 60.25, 68.12, 69.13, 69.43, 70.2, 71.80, 74.96, 75.99, 84.03 (*ipso*-Cp'), 86.30(*ipso*-Cp'), 89.08(*ipso*-Cp'). IR (NaCl, cm⁻¹) 769, 835, 1007, 1068, 1107, 1249, 1454, 1471, 2853, 2923, 2953. HRMS (ESI-TOFMS) m/z calcd for [C₂₃H₃₀FeOSi]⁺: 406.1410; found 406.1406.

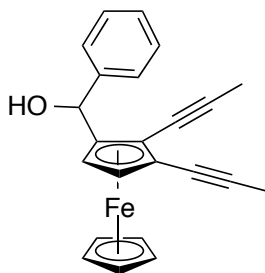


(1,2-Di(1-propynyl)-3(hydroxymethyl)ferrocene (56): Compound **55** (0.55 g, 1.35 mmol, 1 equiv) was dissolved in 14 mL of THF (0.1 M) and cooled to 0 °C in a ice bath. Tetra-*n*-butylammonium fluoride (1.60 mL, 1.69 mmol, 1.25 equiv, 1.0M solution in THF) was added and the solution was allowed to warm to RT. The solution was stirred overnight at RT (12 h) then extracted into diethylether, washed with brine, and dried with MgSO₄. The organic layers were concentrated under reduced pressure. Column chromatography (SiO₂, 90:10 hexanes:ethyl acetate) yielded **55** as an orange oil (0.30 g, 74%). ¹H NMR (500 MHz, CD₂Cl₂) δ 1.71 (t, $J_{HH} = 6.2$ Hz, 1H, OH), 1.99 (s, 3H, CH₃), 2.02 (s, 3H, CH₃), 4.16 (s, 5H, Cp), 4.23 (d, $J_{HH} = 2.6$ Hz, 1H, Cp'), 4.32 (d, $J_{HH} = 2.6$ Hz, 1H, Cp'), 4.35 (dd, $J_{HH} = 12.2, 6.2$ Hz, 1H, CH₂), 4.49

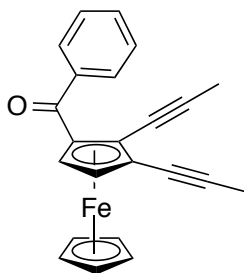
(dd, $J_{HH} = 12.2, 6.2$ Hz, 1H, CH₂); ¹³C NMR (500 MHz, CD₂Cl₂) δ 4.71 (CH₃), 4.84 (CH₃), 60.04, 68.17, 69.76, 69.92, 70.69, 72.09, 74.75, 75.99, 84.68 (*ipso*-Cp'), 86.98 (*ipso*-Cp'), 89.43 (*ipso*-Cp'). IR (NaCl, cm⁻¹) 1001, 1443, 2231, 2847, 2911, 2947, 3092, 3386. HRMS (ESI-TOFMS) m/z calcd for [C₁₇H₁₆FeO]⁺: 292.0545; found 292.0544.



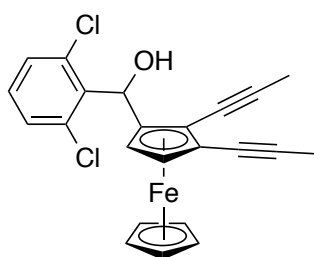
1,2-di(1-propynyl)-3-formylferrocene (57): Alcohol **56** (0.58 g, 1.99 mmol, 1 equiv) was dissolved in CH₂Cl₂ (6 mL, 0.1 M) and MnO₂ (1.73 g, 19.9 mmol, 10 equiv) was added in one portion at room temperature. The reaction was determined to be complete by TLC within 30 minutes. The black suspension was filtered through a pad of celite and the volatiles were removed under reduced pressure. Yielded 0.41 g of spectroscopically pure **57** (70%). ¹H NMR (400 MHz, CDCl₃) δ 2.03 (s, 3H), 2.08 (s, 3H), 4.31 (s, 5H), 4.76 (d, $J_{HH} = 2.8$ Hz, 1H), 4.83 (d, $J_{HH} = 2.8$ Hz, 1H), 10.16 (s, 2H); ¹H NMR (500 MHz, CD₂Cl₂) δ 2.04 (s, 4H), 2.09 (s, 3H), 4.32 (s, 5H), 4.77 (d, $J_{HH} = 2.8$ Hz, 1H), 4.81 (d, $J_{HH} = 2.8$ Hz, 1H), 10.15 (s, 1H); ¹³C NMR (500 MHz, CD₂Cl₂) δ 4.68 (CH₃), 4.86 (CH₃), 67.39, 73.29, 73.64, 73.70, 74.63, 74.72, 75.1, 79.22 (*ipso*-Cp'), 86.40 (*ipso*-Cp'), 89.12 (*ipso*-Cp'), 193.08 (CO). IR (NaCl, cm⁻¹) 1299, 1430, 1676, 2845, 2915. HRMS (ESI-TOFMS) m/z calcd for [C₁₇H₁₅FeO]⁺: 291.0467; found 291.0466.



1,2-Di(1-propynyl-3-(1-hydroxyl-1-phenyl)methylferrocene (58): Compound **57** (85 mg, 0.29 mmol, 1 equiv) was dissolved in 3 mL of THF (0.1 M) and cooled to -78 °C by use of a dry-ice acetone bath. Phenyllithium (0.18 mL, 0.35 mmol, 1.2 equiv, 1.9 M solution in dibutylether) was added dropwise and the reaction was allowed to stir for 15 minutes before being warmed to RT. After 1 h the yellow solution was quenched with 10% hydrochloric acid and extracted twice into dichloromethane. The organic layers were dried with MgSO₄ and the volatiles removed under reduced pressure. The benzylic alcohol was purified by silica gel column chromatography by elution with 97:7 hexanes:ethyl acetate. Yielded 76 mg **58** as a yellow oil (72%). ¹H NMR (500 MHz, CD₂Cl₂) δ 1.98 (s, 3H, CH₃), 2.05 (s, 3H, CH₃), 2.45 (d, 1H, OH), 4.21 (d, *J*_{HH} = 2.5 Hz, 1H, Cp'), 4.29 (s, 5H, Cp), 4.31 (d, *J*_{HH} = 2.5 Hz, 1H, Cp'), 5.65 (s, 1H, CH), 7.21 (t, *J*_{HH} = 7.3 Hz, 1H, aryl), 7.28 (t, *J*_{HH} = 7.6 Hz, 2H, aryl), 7.38 (d, *J*_{HH} = 7.6 Hz, 2H, aryl); ¹³C NMR (500 MHz, CD₂Cl₂) δ 4.72 (CH₃), 4.87, (CH₃), 64.82, 69.00, 69.75, 70.38, 70.84, 72.27, 74.92, 75.74, 84.95 (*ipso*-Cp'), 87.80 (*ipso*-Cp'), 96.32 (*ipso*-Cp'), 126.25 (aryl), 127.73 (aryl), 128.50 (aryl), 143.58 (aryl). IR (NaCl, cm⁻¹) 993, 1451, 2848, 2914, 3436, 3555. HRMS (ESI-TOFMS) *m/z* calcd for [C₂₃H₂₀FeO]⁺: 368.0858; found 368.0861.

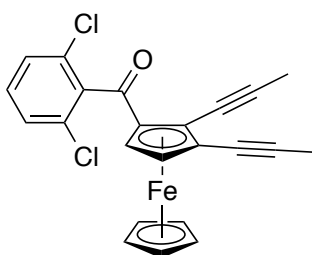


Benzoyl-2,3-di(1-propynyl)ferrocene (45): Complex **58** (60 mg, 0.16 mmol, 1 equiv) was dissolved in 2 mL of Et₂O (0.1 M) and freshly activated MnO₂ (0.29 g, 3.26 mmol, 20 equiv) was added in one portion. The black suspension was stirred for 2 h during which time the solution changed color from yellow to deep red. The slurry was then filtered through a pad of celite. Purification by silica gel chromatography with 95:5 hexanes:ethyl acetate gave 24 mg of **45** as a red solid (40%). ¹H NMR (400 MHz, CD₂Cl₂) δ 1.94 (s, 3H, CH₃), 2.02 (s, 3H, CH₃), 4.23 (s, 5H, Cp), 4.67 (s, 2H, Cp'), 7.45 (d, *J*_{HH} = 6.6 Hz, 2H), 7.53 (t, *J*_{HH} = 5.1 Hz, 1H), 7.81 (d, *J*_{HH} = 7.4 Hz, 2H); ¹³C NMR (500 MHz, CD₂Cl₂) δ 4.72 (CH₃), 4.89 (CH₃), 71.80, 72.39, 73.69, 73.83 (Cp), 74.40, 75.16, 75.56, 86.22 (*ispo*-Cp'), 88.48 (*ispo*-Cp'), 128.23 (aryl), 128.82 (aryl), 131.94 (aryl), 139.62 (aryl), 198.07 (CO). IR (NaCl, cm⁻¹) 1407, 1430, 1651, 2325, 2356. HRMS (ESI-TOFMS) *m/z* calcd for [C₂₃H₁₉FeO]⁺: 367.0780; found 367.0774.



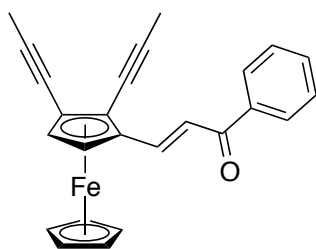
1,2-Di(1-propynyl-3-(1-hydroxyl-1-(2,6-dichlorophenyl)))methylferrocene

(60): 2,6-dichlorobenzene (0.20 mL, 1.76 mmol, 1.25 equiv) was dissolved in 7 mL of THF, cooled to -78 °C, and *n*-BuLi (1.52 mL, 1.83 mmol, 1.3 equiv) was added dropwise. The white suspension was stirred for 1.5 h then compound **57** (0.41 g, 1.41 mmol, 1 equiv) dissolved in 7 mL of THF was added dropwise. The solution was stirred an additional hour at -78 °C, quenched with saturated ammonium chloride solution, extracted twice with diethyl ether, and dried with anhydrous MgSO₄. Column chromatography (SiO₂, 90:10 hexanes:ethyl acetate) then recrystallization from CH₂Cl₂ and hexanes yielded **59** as a yellow solid (0.41 g, 67%). ¹H NMR (400 MHz, CD₂Cl₂) δ 1.78 (s, 3H, CH₃), 1.95 (s, 3H, CH₃), 2.90 (d, *J* = 9.1 Hz, 1H, OH), 4.24 (s, 5H, Cp), 4.31 (d, *J*_{HH} = 2.5 Hz, 1H, Cp'), 4.66 (d, *J*_{HH} = 2.5 Hz, 1H, Cp'), 6.70 (d, *J*_{HH} = 9.1 Hz, 1H, CH), 7.15 (t, *J*_{HH} = 7.9 Hz, 1H, aryl), 7.28 (d, *J*_{HH} = 7.9 Hz, 2H, aryl); ¹³C NMR (400 MHz, CD₂Cl₂) δ 4.69 (CH₃), 4.90 (CH₃), 68.04, 68.35, 69.23, 69.78, 70.15, 72.78, 74.39, 75.95, 84.81 (*ipso*-Cp'), 87.90 (*ipso*-Cp'), 92.05 (*ipso*-Cp'), 129.41 (aryl), 129.72 (aryl), 135.49 (aryl), 137.03 (aryl). IR (NaCl, cm⁻¹) 990, 1177, 1483, 1652, 2912, 3441. HRMS (ESI-TOFMS) *m/z* calcd for [C₂₃H₁₈Cl₂FeO]⁺: 436.0085; found 436.0087.



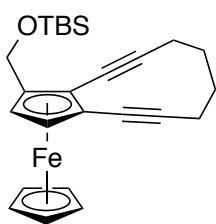
2,6-Dichlorobenzoyl-2,3-di(1-propynyl)ferrocene (59): Compound **60** (8.5 mg, 0.019 mmol, 1 equiv) was dissolved in 0.5 mL of Et₂O under an atmosphere of argon.

Freshly activated MnO_2 (68 mg, 0.77 mmol, 40 equiv) was added in one portion and the slurry was stirred for 18 h. The mixture was filtered through a plug of celite and rinsed thoroughly with Et_2O . Pure **59** was obtained by SiO_2 preparatory TLC by development with 95:5 hexanes:ethyl acetate. Yielded 3 mg of an orange solid (35%). ^1H NMR (400 MHz, CDCl_3) δ 1.69 (s, 3H, CH_3), 2.01 (s, 3H, CH_3), 4.37 (s, 5H, Cp), 4.77 (s, 1H, Cp'), 4.94 (s, 1H, Cp'), 7.26 (m, 3H, aryl); ^1H NMR (400 MHz, CD_2Cl_2) δ 1.70 (s, 3H, CH_3), 2.01 (s, 3H, CH_3), 4.36 (s, 5H, Cp), 4.78 (d, $J_{\text{HH}} = 2.7$ Hz, 1H, Cp'), 4.90 (d, $J_{\text{HH}} = 2.7$ Hz, 1H, Cp'), 7.39-7.28 (m, 3H, aryl); ^{13}C NMR (500 MHz, CDCl_3) δ 4.85 (CH_3), 5.08 (CH_3), 71.03, 73.56, 73.87 (Cp), 74.12, 74.91, 78.98, 86.01 (*ipso*-Cp'), 88.90 (*ipso*-Cp'), 127.98 (aryl), 130.41 (aryl), 138.56 (aryl), 197.37 (CO). HRMS (ESI-TOFMS) m/z calcd for $[\text{C}_{23}\text{H}_{17}\text{Cl}_2\text{FeO}]^+$: 435.0001; found 435.0087.



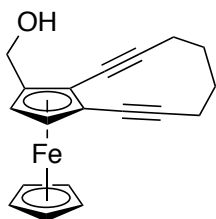
1,2-Di(1-propynyl)ferrocenylchalcone (61): Complex **57** (25 mg, 0.074 mmol, 1 equiv) and acetophenone (10 μL , 0.09 mmol, 1.2 equiv) were dissolved in 1 mL of absolute ethanol (0.1 M). An aqueous solution of sodium hydroxide (3 mg, 0.074 mmol, 1 equiv, in 1 mL of H_2O) was then added dropwise at RT and the reaction was allowed to stir at RT for a period of 24 h. The crude reaction mixture was partitioned between diethyl ether and brine, the organic layer was dried over anhydrous MgSO_4 , and the crude product was isolated under reduced pressure. Purification by SiO_2 column chromatography with 95:5 hexanes:ethyl acetate as

eluent yielded 19 mg of **61** (68%). $^1\text{H-NMR}$ (400 MHz, CDCl_3) δ 2.03 (s, 3H), 2.11 (s, 3H), 4.21 (s, 5H), 4.61 (d, $J_{\text{HH}} = 2.5$ Hz, 1H), 4.65 (d, $J_{\text{HH}} = 2.5$ Hz, 1H), 7.52-7.48 (m, 3H), 7.58 (t, $J_{\text{HH}} = 7.1$ Hz, 1H), 7.89 (d, $J_{\text{HH}} = 15.5$ Hz, 1H), 8.00 (d, $J_{\text{HH}} = 7.3$ Hz, 2H); $^{13}\text{C NMR}$ (500 MHz, CDCl_3) δ 4.99 (CH_3), 5.23 (CH_3), 67.34 (Cp), 71.64 (Cp), 72.17, 72.73, 73.18 (Cp), 73.27, 73.65, 74.85, 75.48, 79.93 (*ipso*-Cp), 85.73 (*ipso*-Cp), 88.75 (*ipso*-Cp), 120.23 (CH), 128.53 (aryl), 128.68 (aryl), 132.63, 138.74, 144.90, 189.86 (CO). IR (NaCl, cm^{-1}) 1263, 1571, 1582, 1601, 2845, 2917. HRMS (ESI-TOFMS) m/z calcd for $[\text{C}_{25}\text{H}_{21}\text{FeO}]^+$: 393.0937; found 393.0937. λ_{max} (50:50 DMF: H_2O , nm) 339, 499.

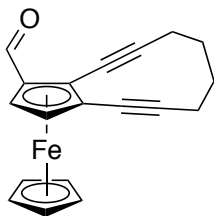


tert-Butyldimethylsilyl methyl ether-2,3-(ferrocenyl-cyclodec-2-ene-1,5-diyne) (63): To a -78 °C solution of **54** (0.5 g, 1.32 mmol, 1 equiv) in dry THF (130 mL, 0.01 M) was added a 1.6 M solution of *n*-BuLi (1.73 mL, 2.77 mmol, 2.1 equiv). The reaction was allowed to proceed at this temperature for 45 min, then a solution of 1,4-diodobutane (0.17 mL, 1.32 mmol, 1 equiv) in 10 mL of anhydrous THF was added over a period of 3 h by use of a syringe pump. The reaction mixture was allowed to warm to RT and was stirred an additional 72 h. The solution was then quenched with saturated ammonium chloride solution and extracted with twice with diethyl ether. The organic layers were washed with brine, dried over MgSO_4 , and the volatiles were removed under reduced pressure. Slow SiO_2

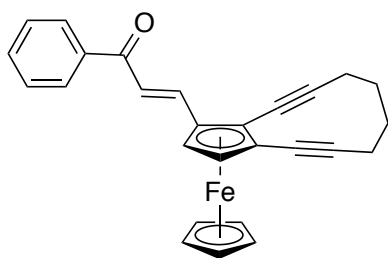
chromatography with hexanes provided 60 mg of **63** as an orange oil (10%). ^1H NMR (400 MHz, CDCl_3) δ 0.07 (s, 3H, CH_3), 0.12 (s, 3H, CH_3), 0.92 (s, 9H, 3CH_3), 1.94 (m, 4H, 2CH_2), 2.33 (m, 4H, 2CH_2), 4.13 (s, 5H, Cp), 4.21 (m, 2H, Cp'), 4.51 (s, 2H, CH_2). IR (NaCl, cm^{-1}) 860, 1105, 1668, 2854, 2923, 2956, 3095. HRMS (ESI-TOFMS) m/z calcd for $[\text{C}_{25}\text{H}_{32}\text{FeOSiNa}]^+$: 455.1464; found 455.1463.



1-(hydroxymethyl)-2,3-(ferrocenyl-cyclodec-2-ene-1,5-diyne) (64): Compound **63** (60 mg, 0.13 mmol, 1 equiv) was dissolved in 1.5 mL of THF (0.1 M) and cooled to 0 °C in a ice bath. Tetra-*n*-butylammonium fluoride (0.16 mL, 0.16 mmol, 1.25 equiv, 1.0M solution in THF) was added and the solution was warmed to RT. The solution was stirred overnight at RT (12 h), extracted into diethylether, washed with brine, and dried with MgSO_4 . The organic layers were concentrated under reduced pressure. Column chromatography (SiO_2 , 90:10 hexanes:ethyl acetate) yielded 30 mg of **64** as an orange oil (72%). ^1H NMR (400 MHz, CDCl_3) δ 1.95 (m, 4H, 2CH_2), 2.34 (m, 4H, 2CH_2), 4.17 (d, $J = 2.2$ Hz, 1H, Cp'), 4.18 (s, 5H, Cp), 4.29 (d, $J = 2.2$ Hz, 1H, Cp'), 4.40 (dd, $J = 12.3, 6.1$ Hz, 1H, CH_2), 4.48 (dd, $J = 12.3, 6.1$ Hz, 1H, CH_2); ^{13}C NMR (500 MHz, C_6D_6) δ 21.87 (CH_2), 21.98 (CH_2), 29.08 (CH_2), 59.99, 66.91, 67.18, 72.19 (Cp), 74.76, 74.85, 79.73, 80.66, 87.14 (*ipso*-Cp'), 96.33 (*ipso*-Cp'), 98.47(*ipso*-Cp'). IR (NaCl, cm^{-1}) 822, 996, 1101, 1450, 2911, 3383. HRMS (ESI-TOFMS) m/z calcd for $[\text{C}_{19}\text{H}_{18}\text{FeO}]^+$: 318.0702; found 318.0704.



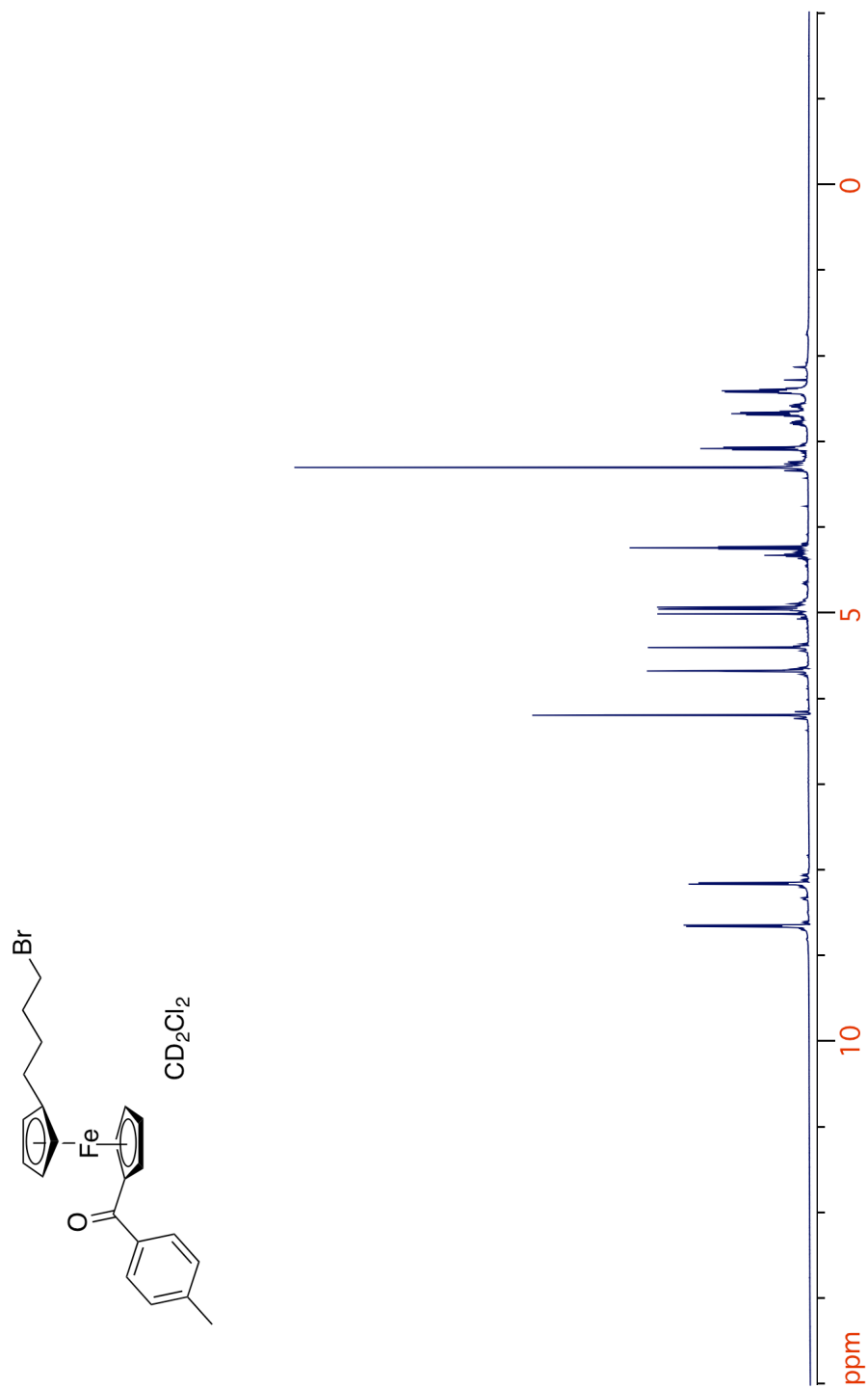
1-Formyl-2,3-(ferrocenyl-cyclodec-2-ene-1,5-diyne) (65): Alcohol **64** (30 mg, 0.1 mmol, 1 equiv) was dissolved in 1 mL of CH₂Cl₂ (0.1 M) and MnO₂ (81 mg, 1 mmol, 10 equiv) was added in one portion at RT. The reaction was determined to be complete by TLC within 30 minutes. The black suspension was filtered through a pad of celite and the volatiles were removed under reduced pressure. Yielded 23 mg of a red solid (74%). ¹H NMR (500 MHz, CD₂Cl₂) δ 1.95 (dd, *J*_{HH} = 5.2, 2.3 Hz, 1H), 2.38 (ddq, *J*_{HH} = 20.3, 8.6, 4.3 Hz, 1H), 4.27 (s, 1H), 4.68 (d, *J*_{HH} = 2.8 Hz, 1H), 4.70 (d, *J*_{HH} = 2.8 Hz, 1H), 10.02 (s, 1H); ¹³C NMR (500 MHz, CD₂Cl₂) δ 21.53 (CH₂), 21.79 (CH₂), 28.66 (CH₂), 67.51, 71.17, 73.09, 76.45, 76.52, 77.57, 78.10, 79.19 (*ipso*-Cp'), 98.51 (*ipso*-Cp'), 100.36 (*ipso*-Cp'), 191.81 (CO). IR (NaCl, cm⁻¹) 825, 1412, 1669, 2724, 2924. HRMS (ESI-TOFMS) *m/z* calcd for [C₁₉H₁₇FeO]⁺: 317.0623; found 317.0625.



2,3-Ferrocenyl-cyclodec-2-ene-1,5-diyne chalcone (62): Complex **65** (23 mg, 0.074 mmol, 1 equiv) and acetophenone (10 μL, 0.09 mmol, 1.2 equiv) were dissolved in 1 mL of absolute ethanol. An aqueous solution of sodium hydroxide (3

mg, 0.074 mmol, 1 equiv, in 1 mL of H₂O) was then added dropwise at RT and the reaction was allowed to stir at RT for a period of 24 h. The crude reaction mixture was partitioned between diethyl ether and brine, the organic layer was dried with anhydrous MgSO₄, and the crude product was isolated under reduced pressure. Purification by SiO₂ column chromatography with 95:5 hexanes:ethyl acetate as eluent yielded 21 mg of **65** (68%). ¹H NMR (500 MHz, CD₂Cl₂) δ 1.96 (s, 4H, 2CH₂), 2.44-2.32 (m, 4H, 2CH₂), 4.17 (s, 5H, Cp), 4.51 (d, *J*_{HH} = 2.7 Hz, 1H), 4.56 (d, *J*_{HH} = 2.7 Hz, 1H), 7.50 (t, *J* = 7.5 Hz, 2H), 7.60-7.56 (m, 1H), 7.65 (d, *J* = 15.4 Hz, 1H), 7.69 (d, *J* = 15.4 Hz, 1H), 7.99-7.98 (m, 2H); ¹³C NMR (500 MHz, CD₂Cl₂) δ 21.93 (CH₂), 22.19 (CH₂), 29.14 (CH₂), 68.85, 69.76, 73.59, 75.04, 77.24, 77.55, 79.17, 79.32 (*ipso*-Cp'), 97.89 (*ipso*-Cp'), 100.62 (*ipso*-Cp'), 120.72, 128.62, 128.86, 132.73, 138.83, 144.43, 189.62 (CO). HRMS (ESI-TOFMS) *m/z* calcd for [C₂₇H₂₃FeO]⁺: 419.1093; found 419.1096.

F. Appendix 1

Figure 3.14. ^1H NMR spectrum of **20**.

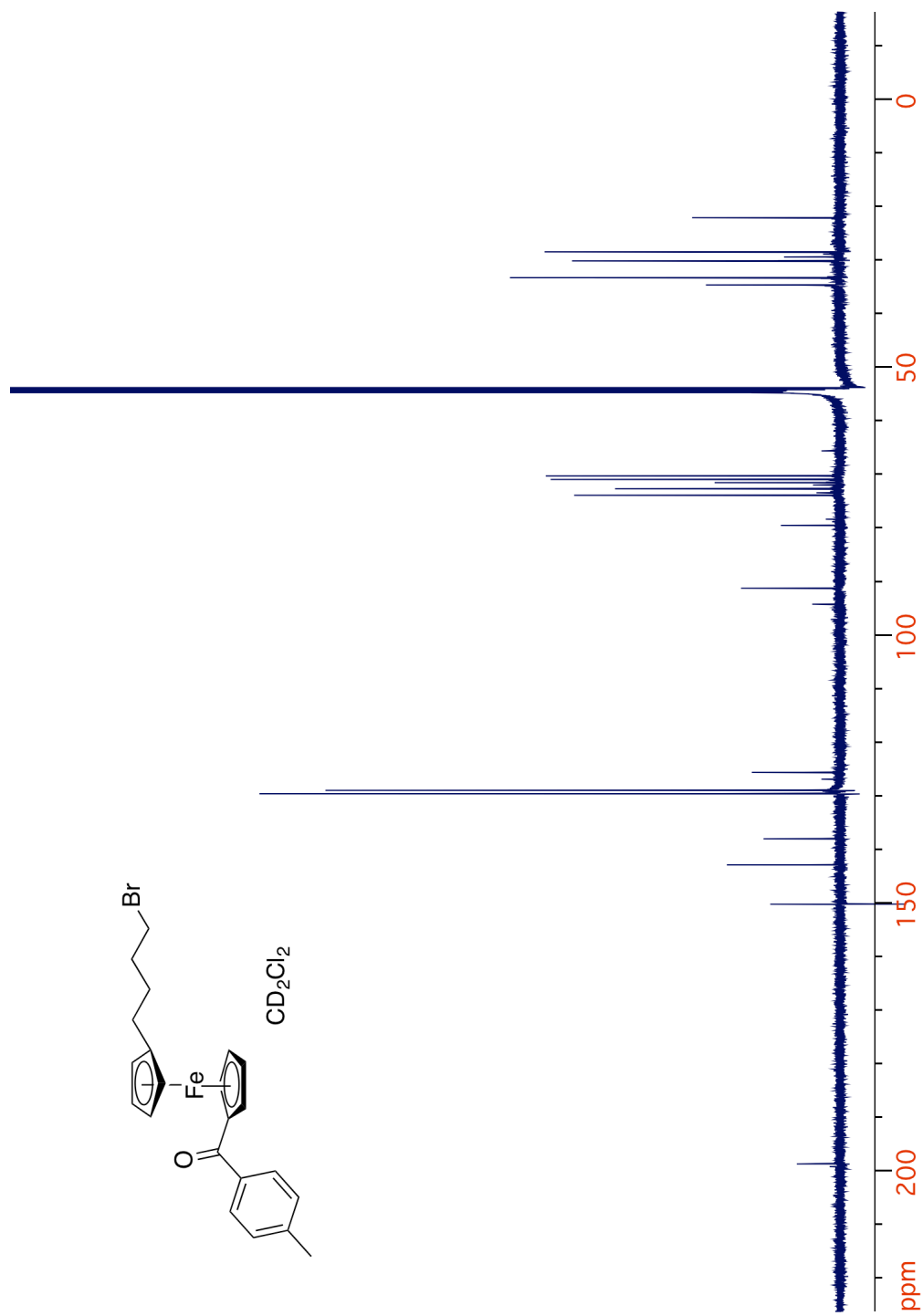


Figure 3.15. ^{13}C NMR spectrum of **20**.

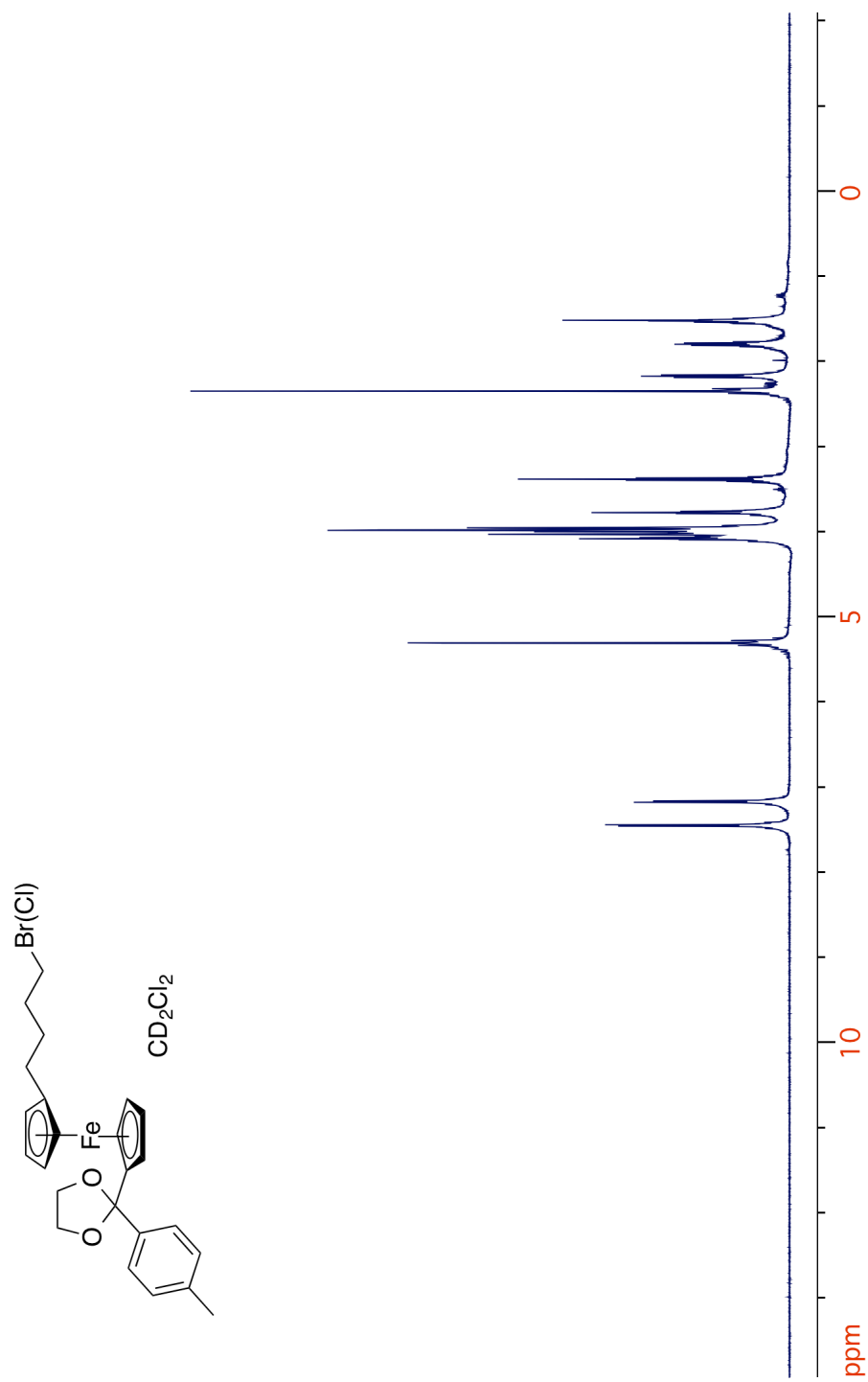


Figure 3.16. ^1H NMR spectrum of **21**.

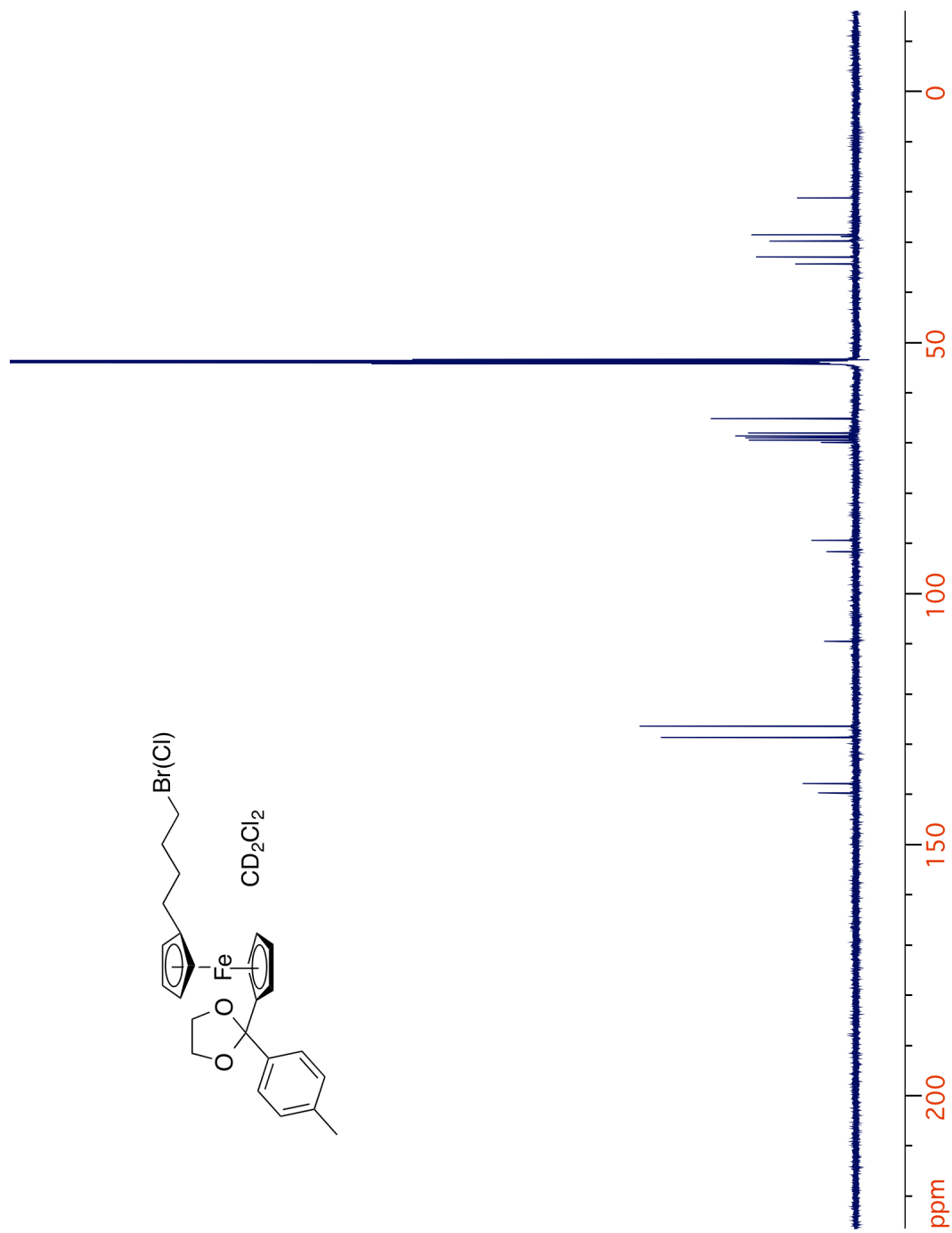


Figure 3.17. ^{13}C NMR spectrum of 21.

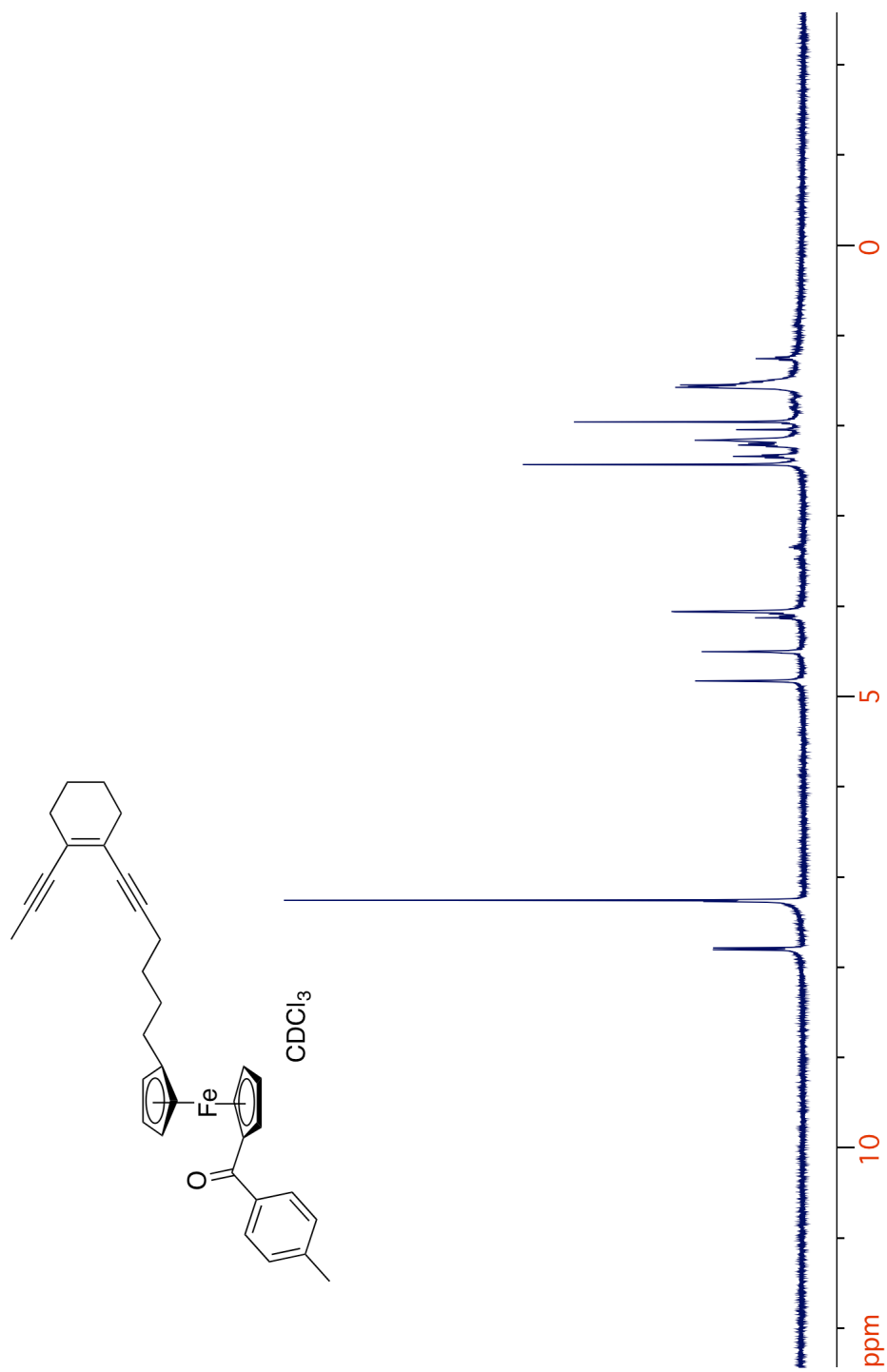


Figure 3.18. ^1H NMR spectrum of 13.

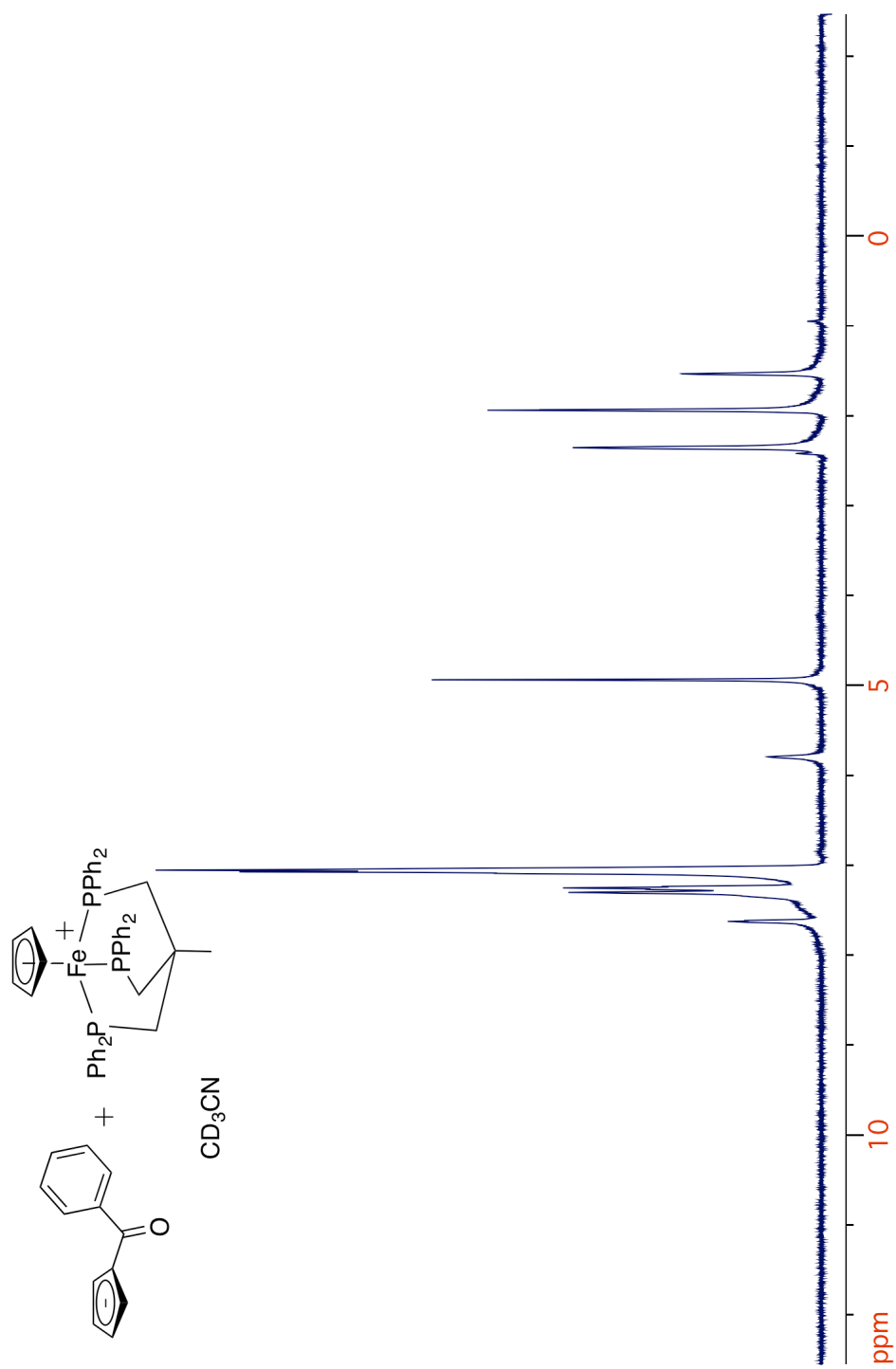


Figure 3.19. ^1H NMR spectrum of **6/6⁺**.

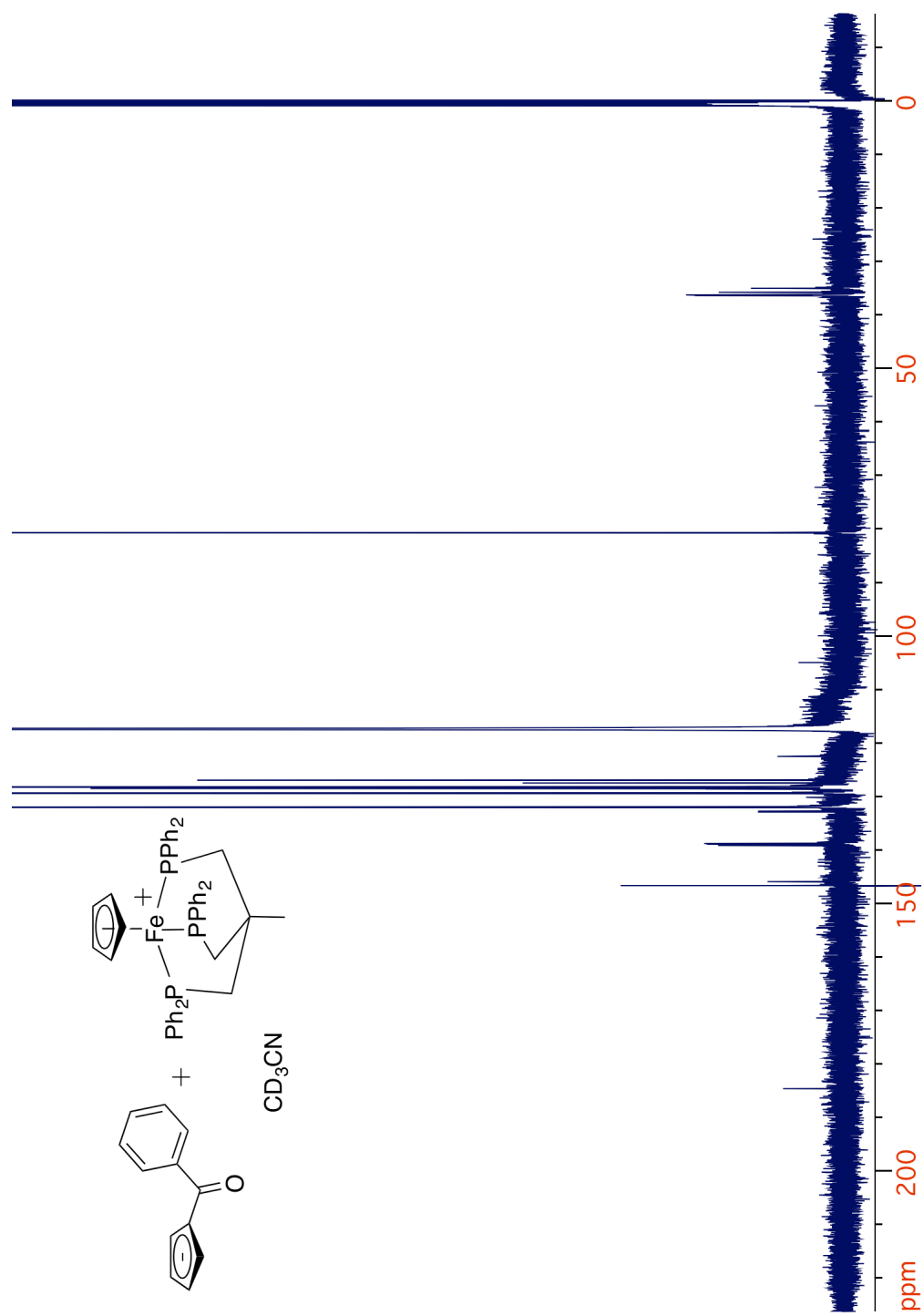


Figure 3.20. ^{13}C NMR spectrum of **6/6⁺**.

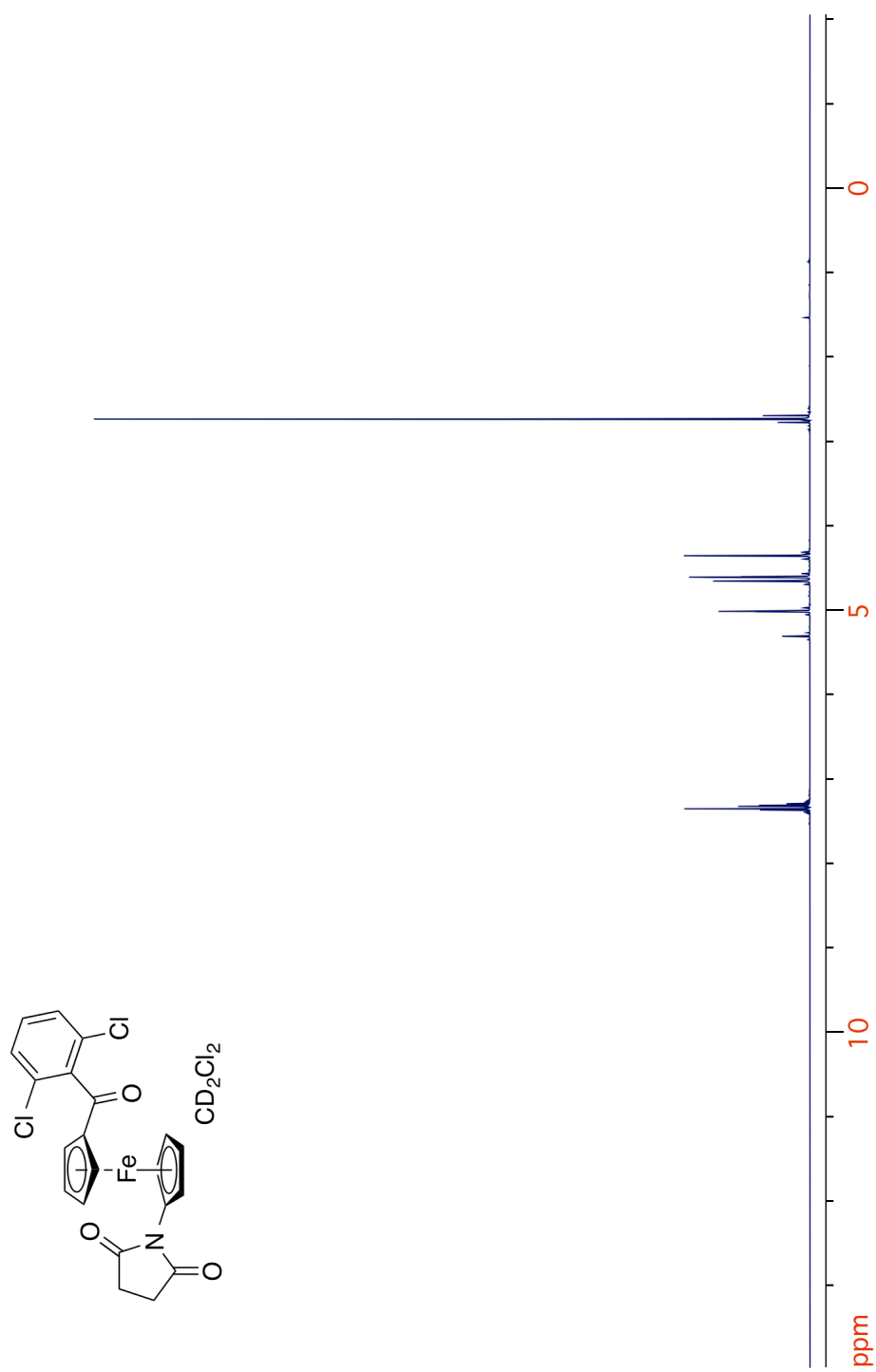


Figure 3.2.1. ^1H NMR spectrum of **31**.

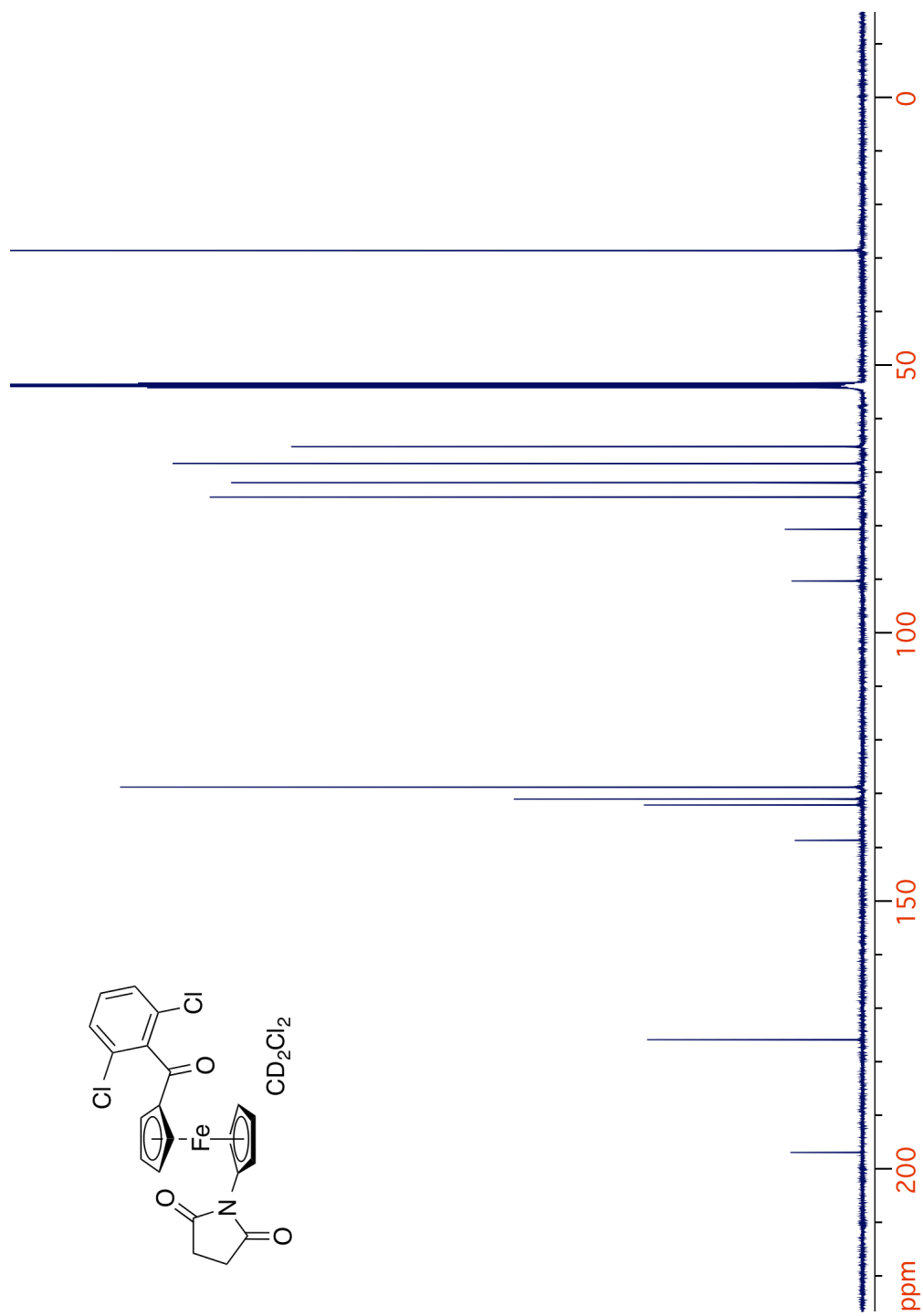


Figure 3.22. ^{13}C NMR spectrum of 31.

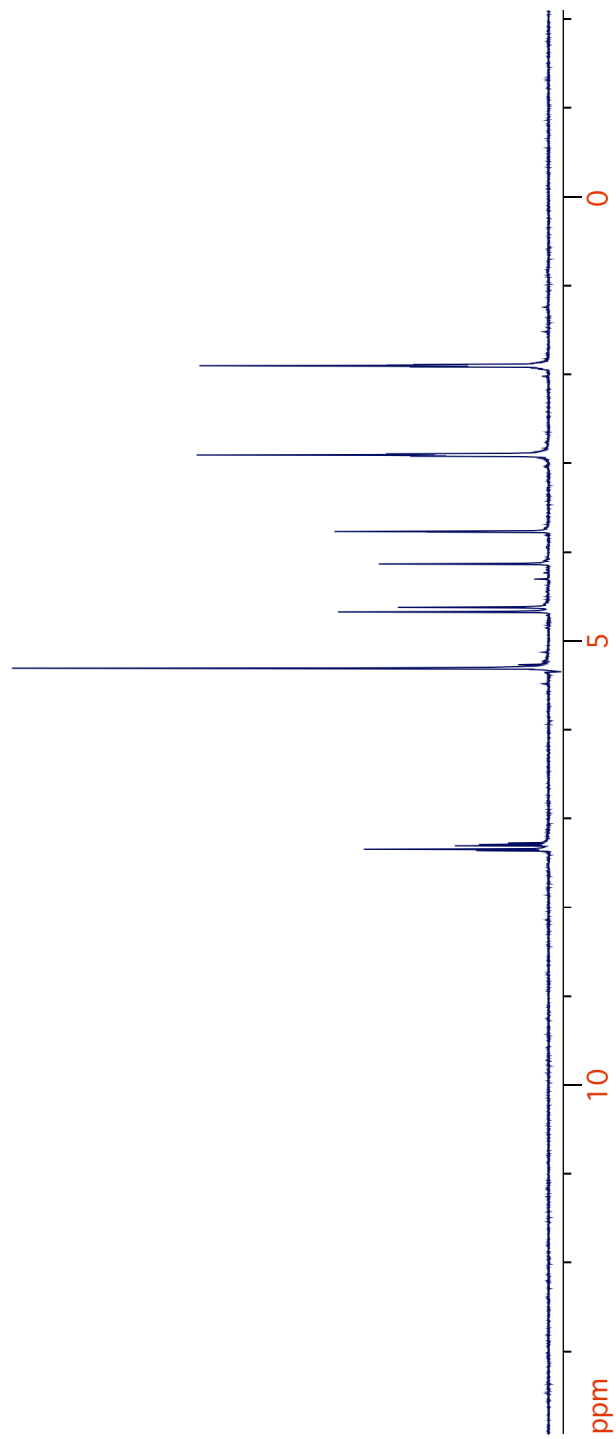
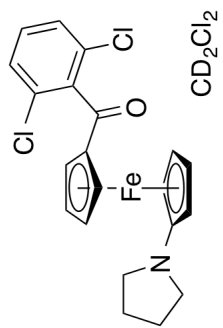
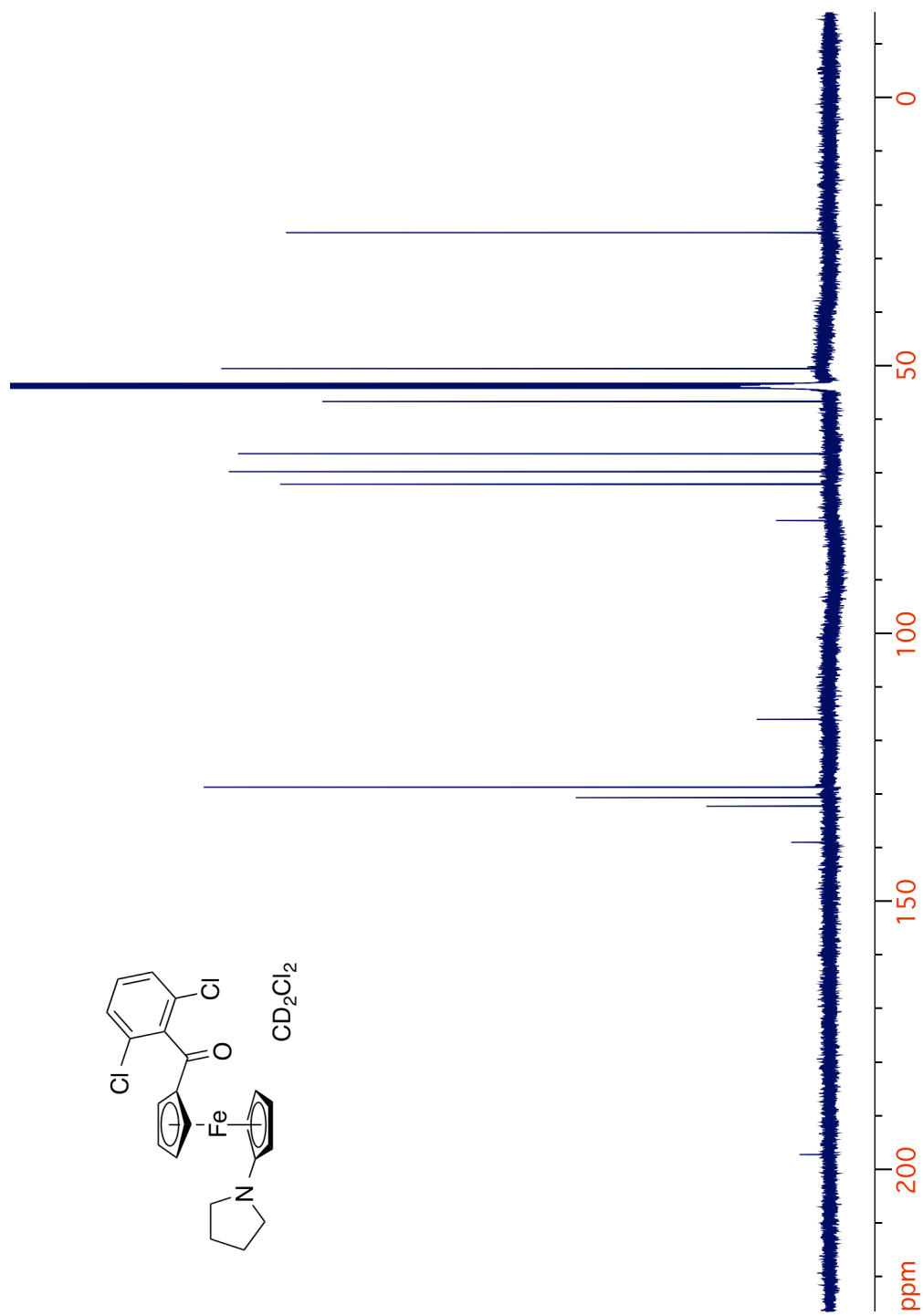


Figure 3.23. 1H NMR spectrum of 26.

Figure 3.24. ^{13}C NMR spectrum of **26**.

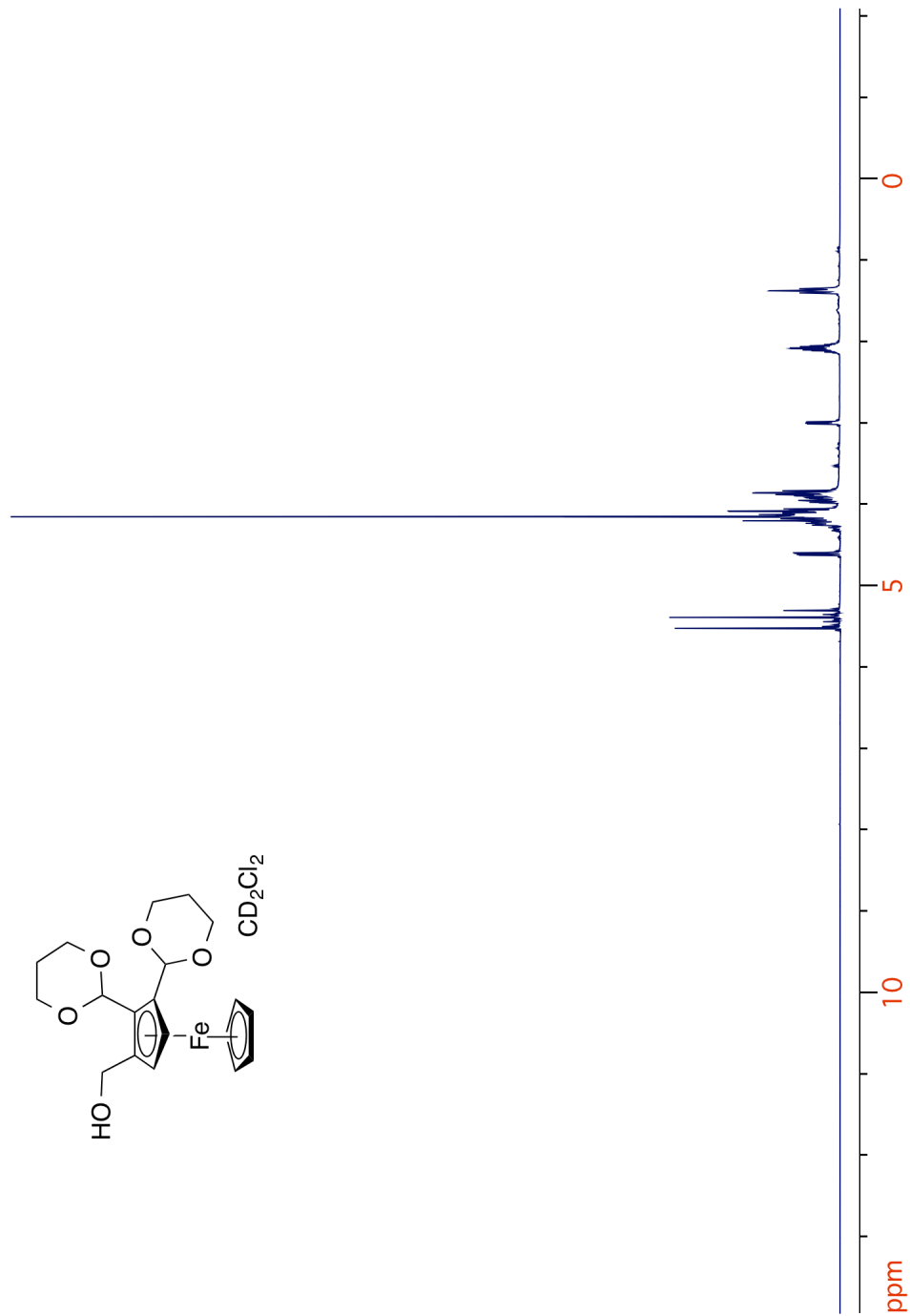


Figure 3.25. ¹H NMR spectrum of **48**.

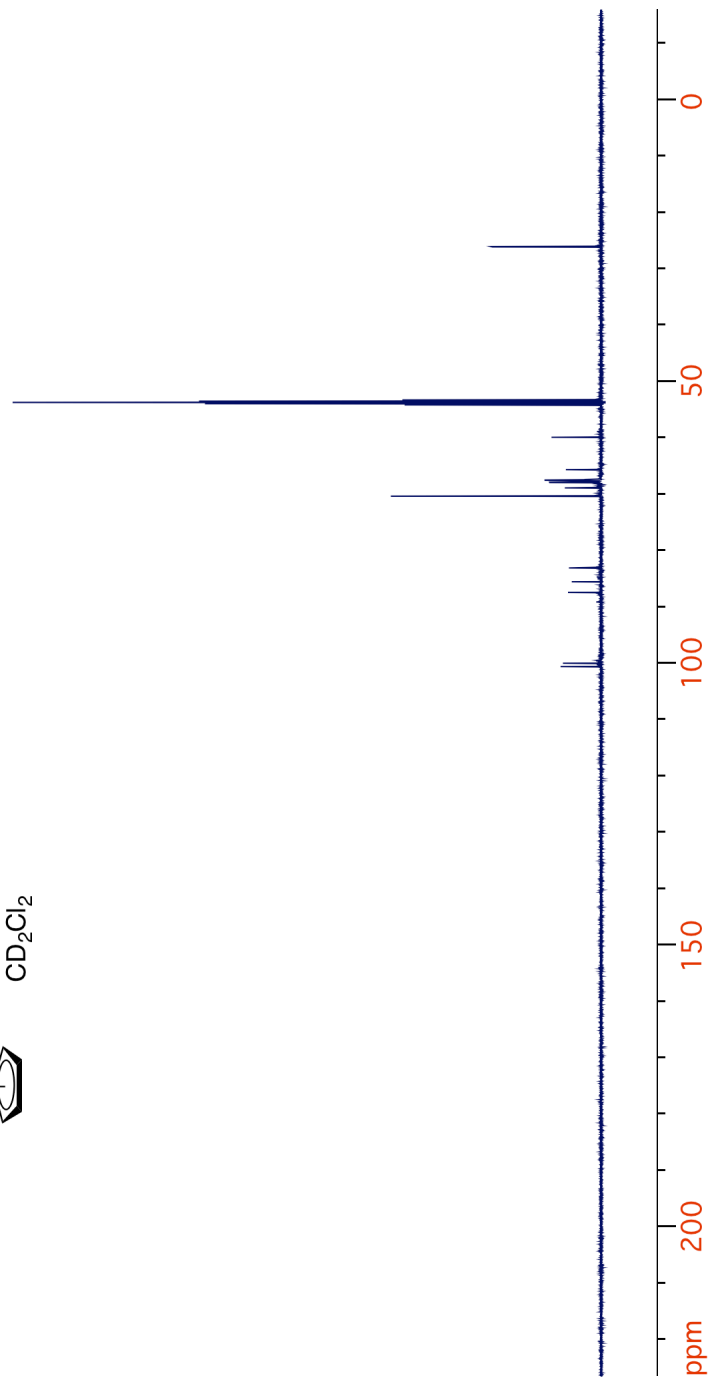
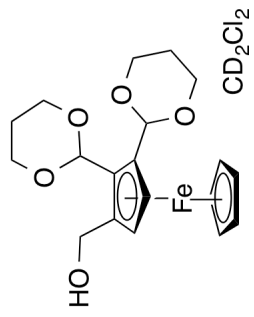


Figure 3.26. ¹³C NMR spectrum of 48.

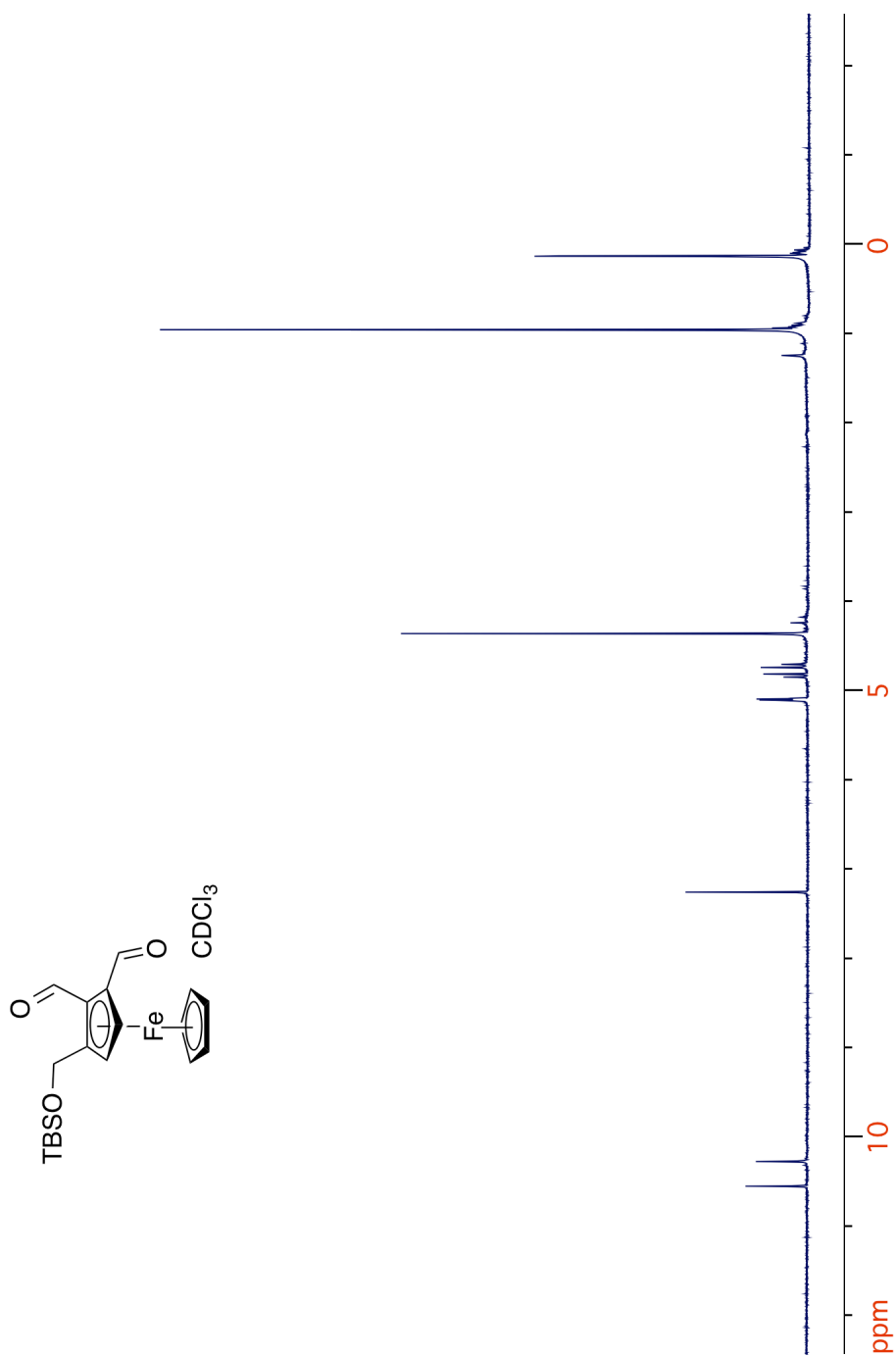


Figure 3.27. ^1H NMR spectrum of 53.

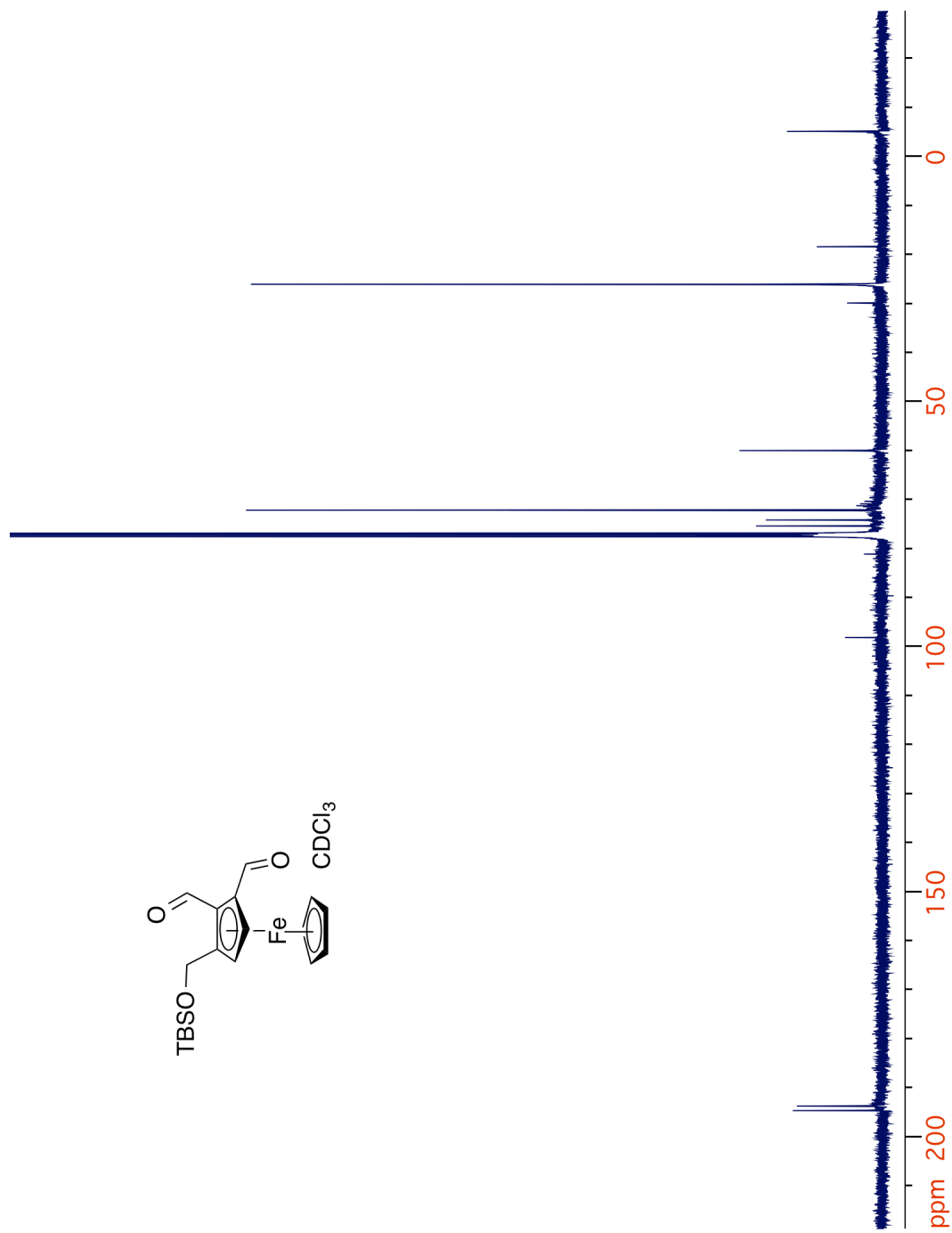


Figure 3.28. ^{13}C NMR spectrum of 53.

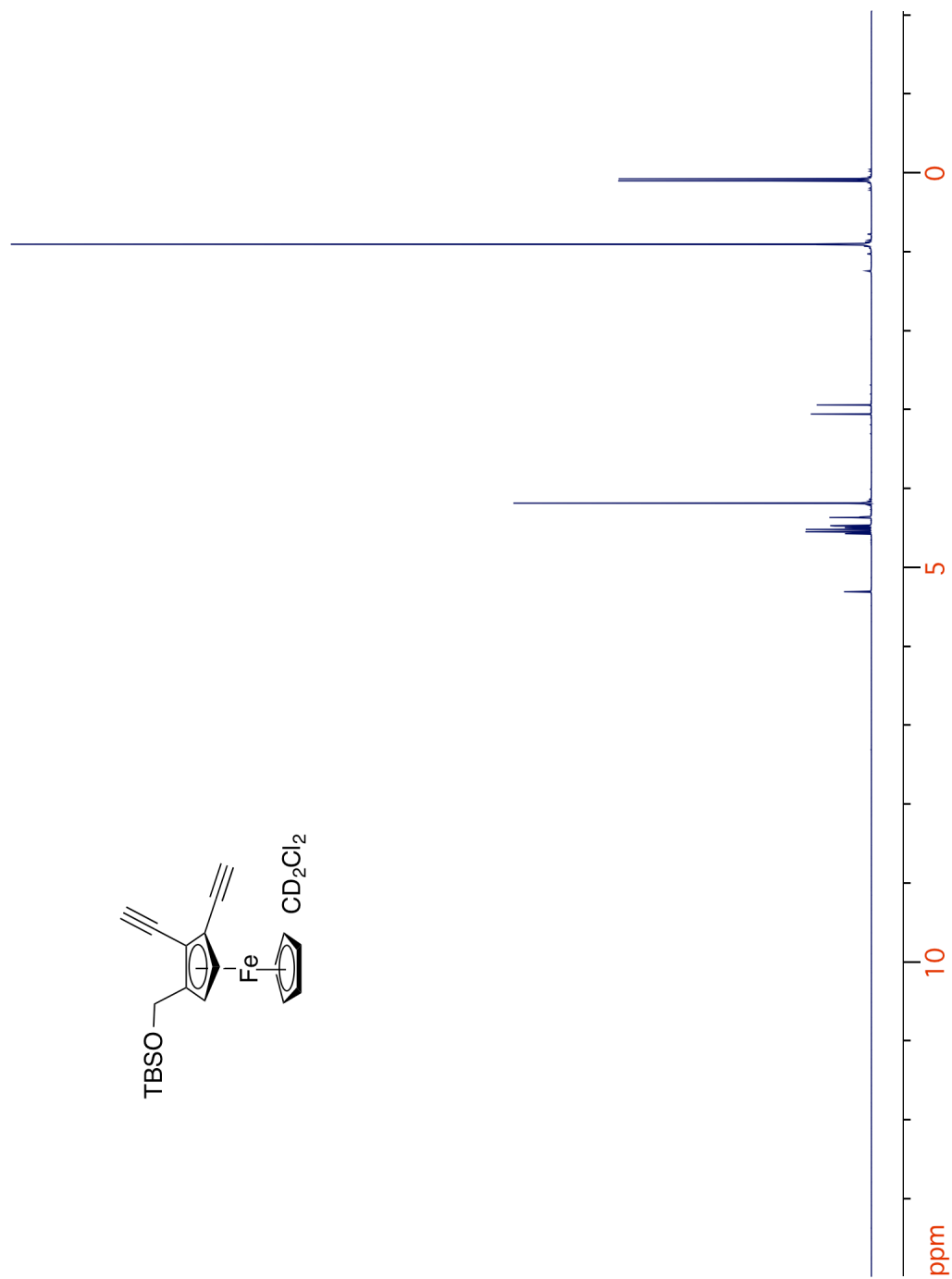


Figure 3.29. ^1H NMR spectrum of 54.

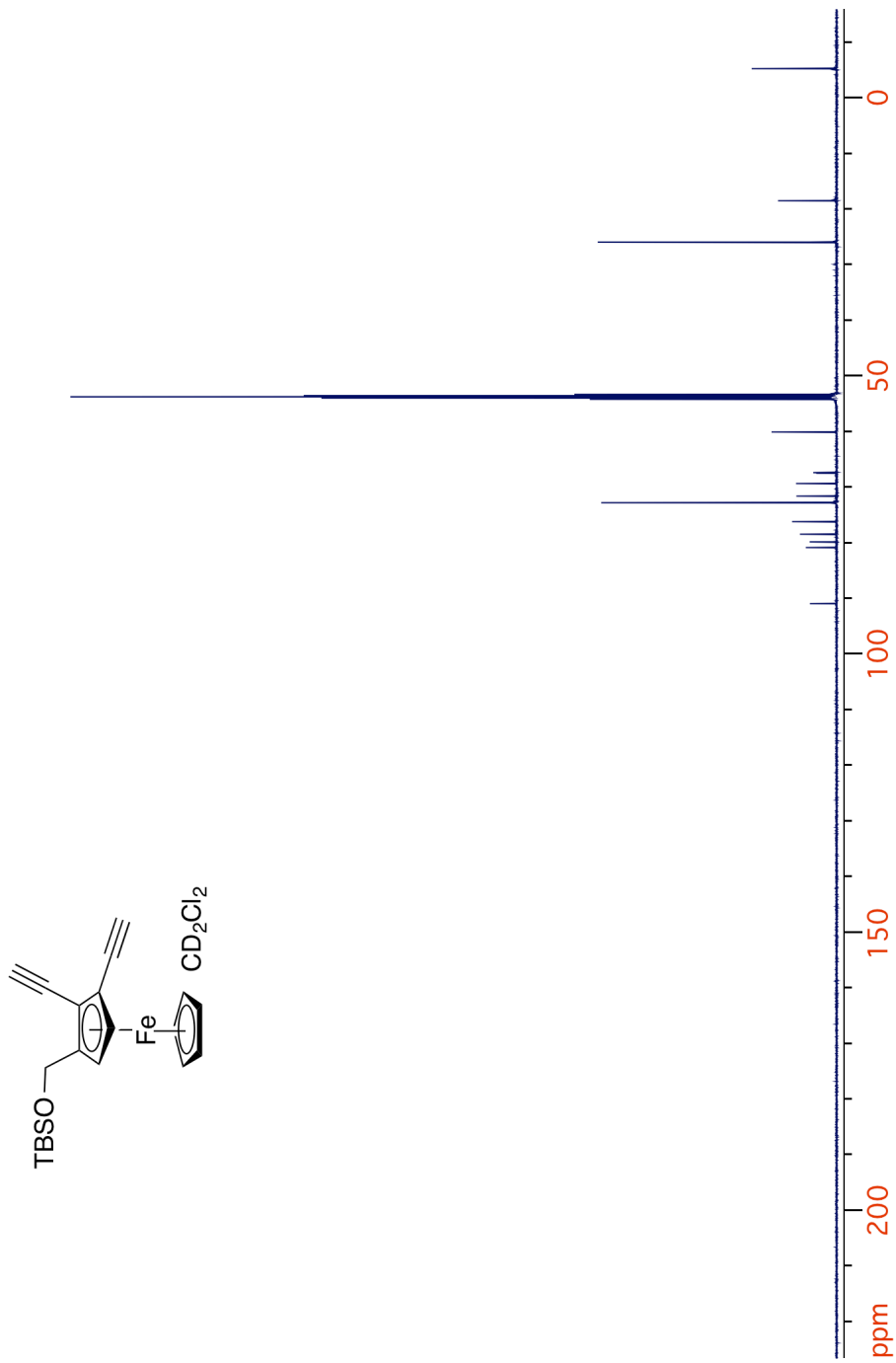


Figure 3.30. ^{13}C NMR spectrum of 54.

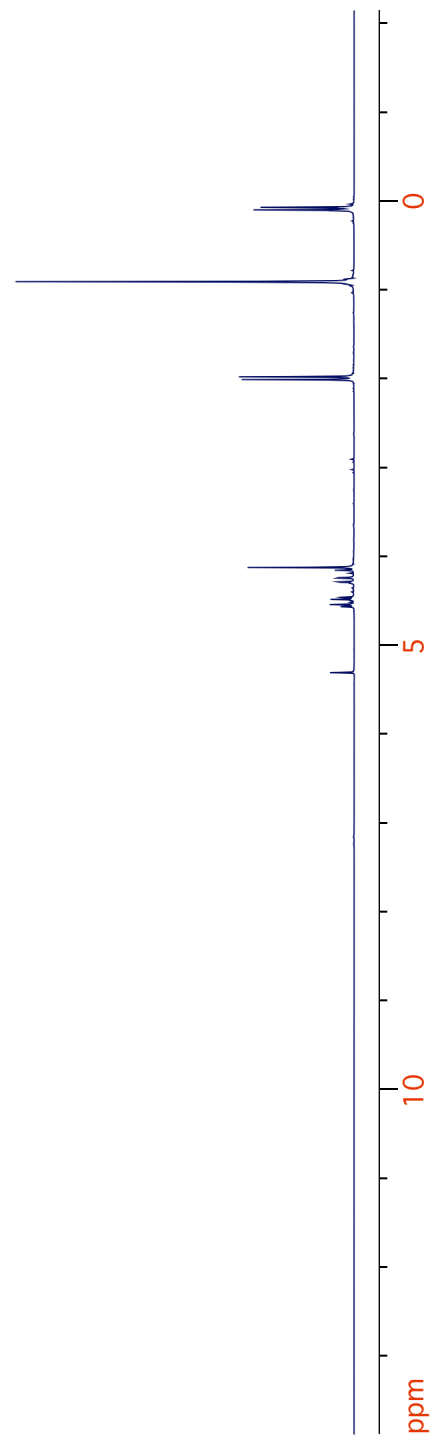
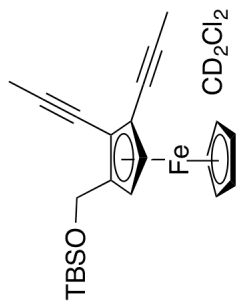


Figure 3.31. ^1H NMR spectrum of 55.

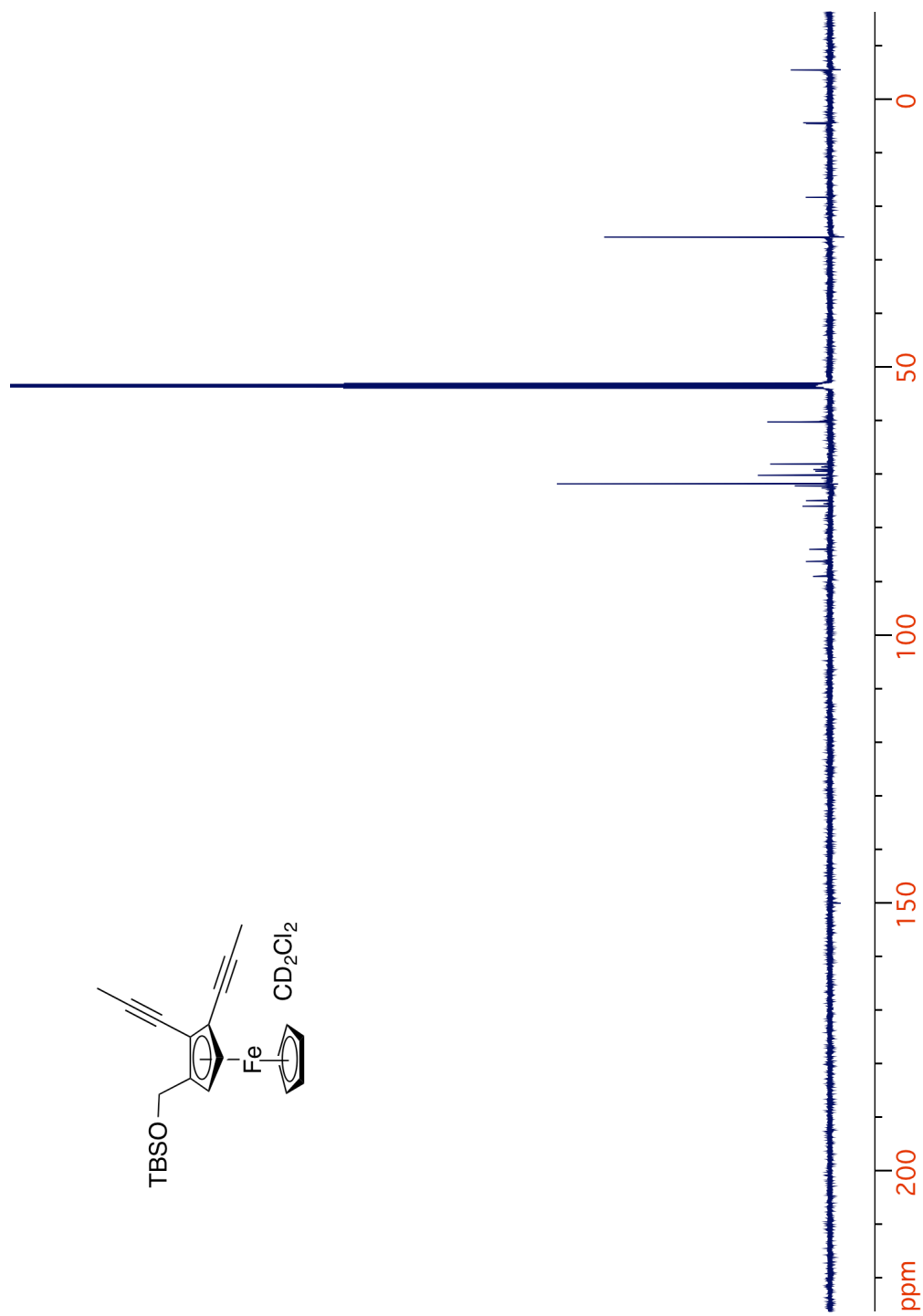


Figure 3.32. ^{13}C NMR spectrum of 55.

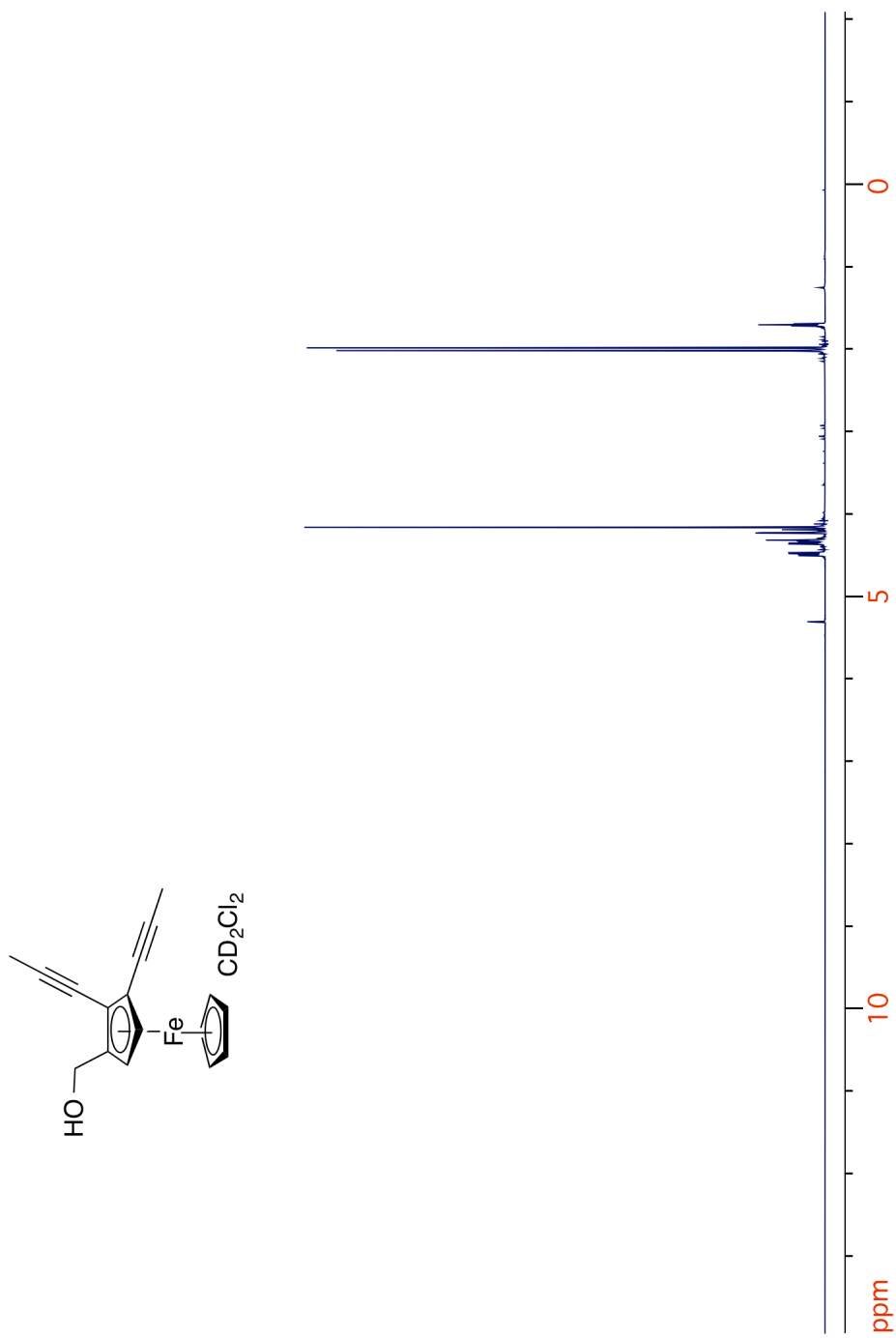


Figure 3.33. ^1H NMR spectrum of **56**.

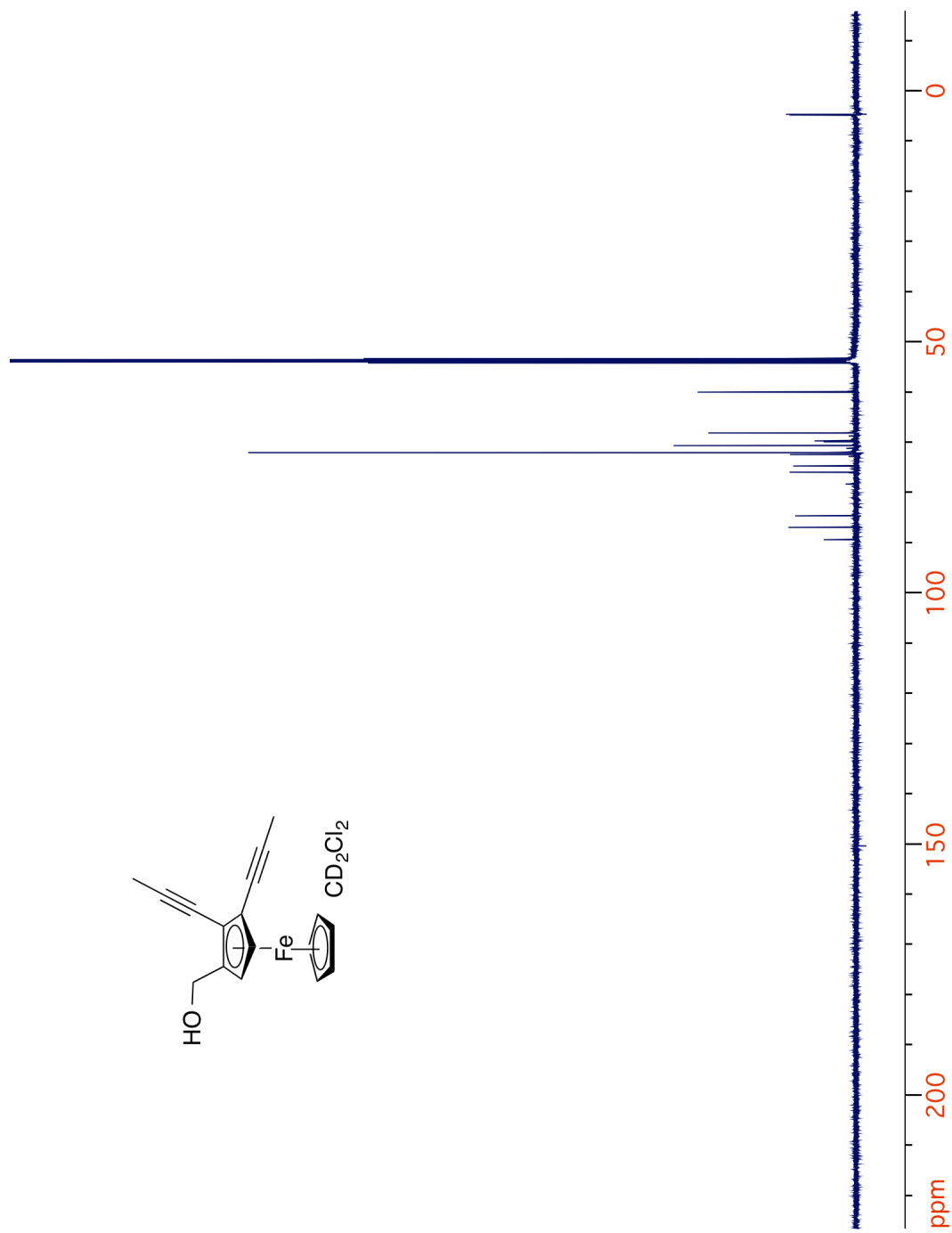
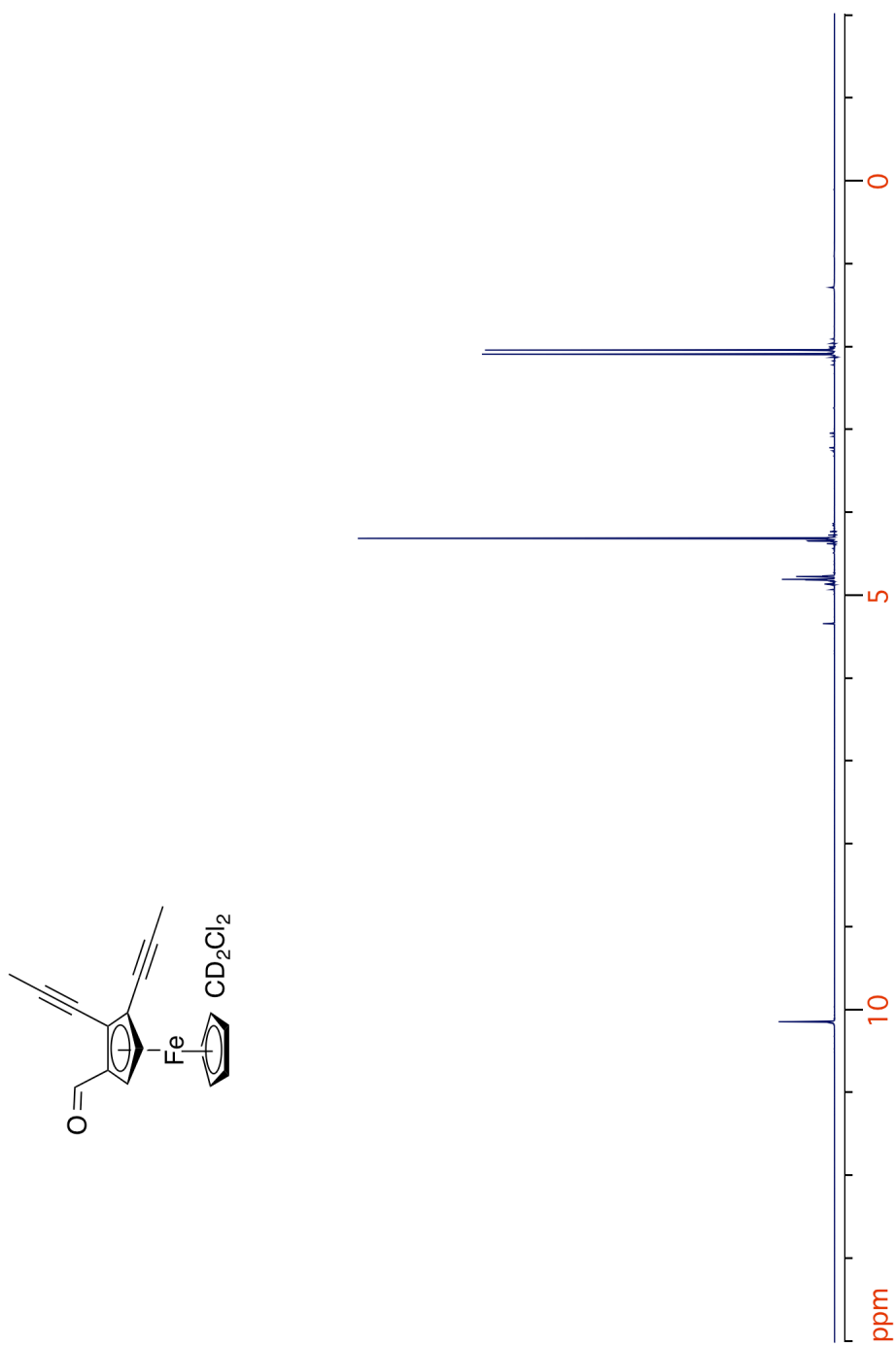


Figure 3.34. ^{13}C NMR spectrum of **56**.

Figure 3.35. ^1H NMR spectrum of 57.

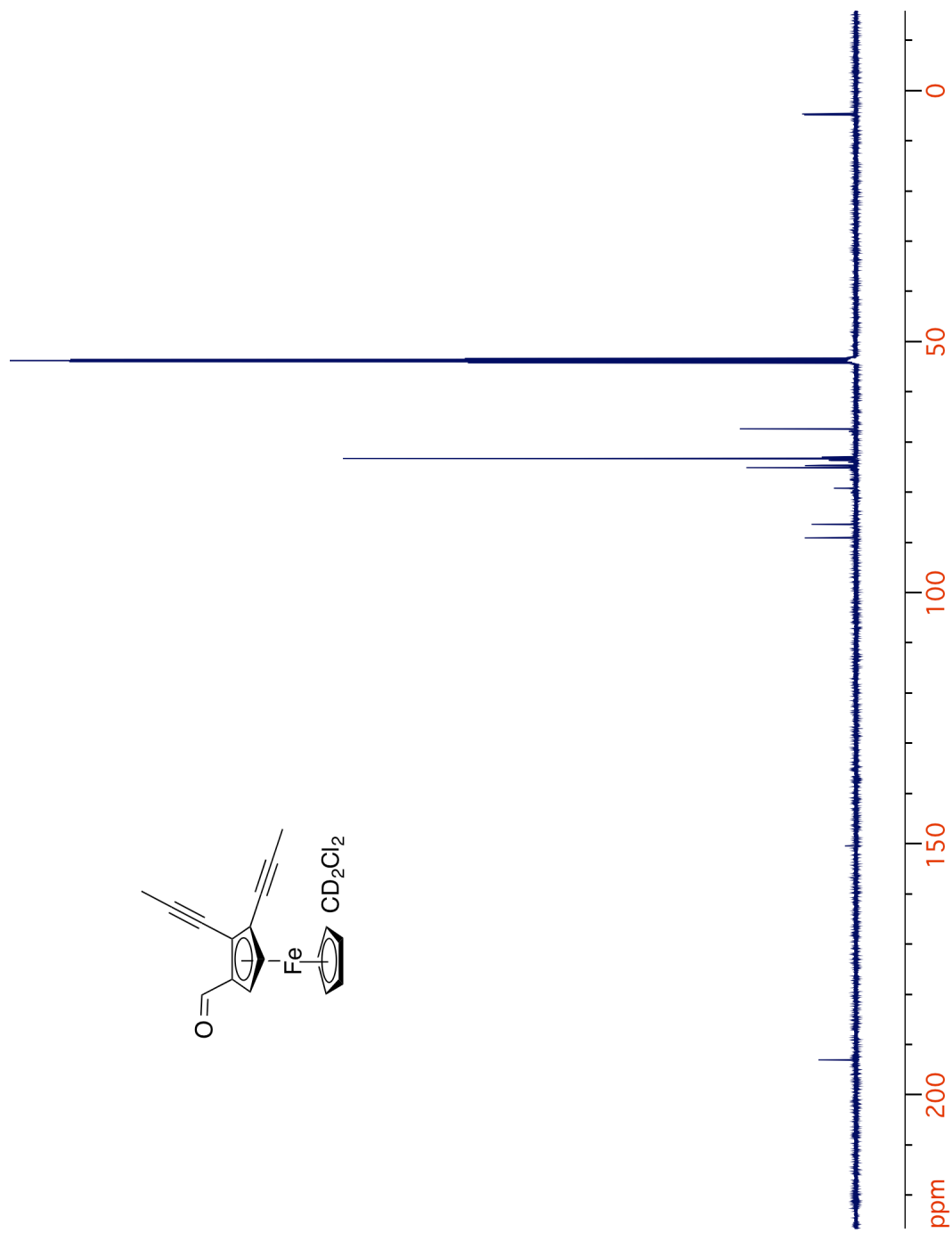
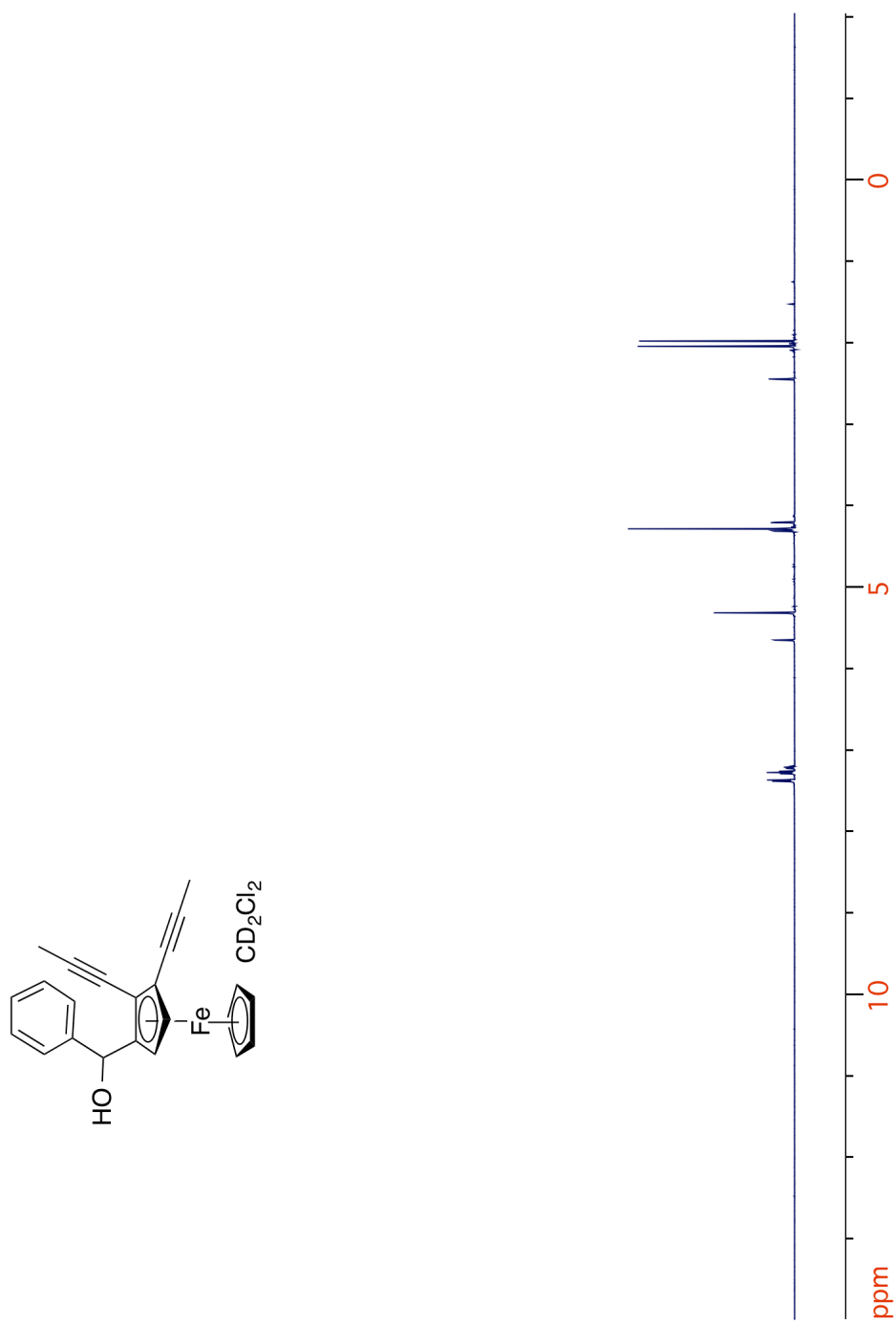


Figure 3.36. ^{13}C NMR spectrum of 57.

Figure 3.37. ^1H NMR spectrum of 58.

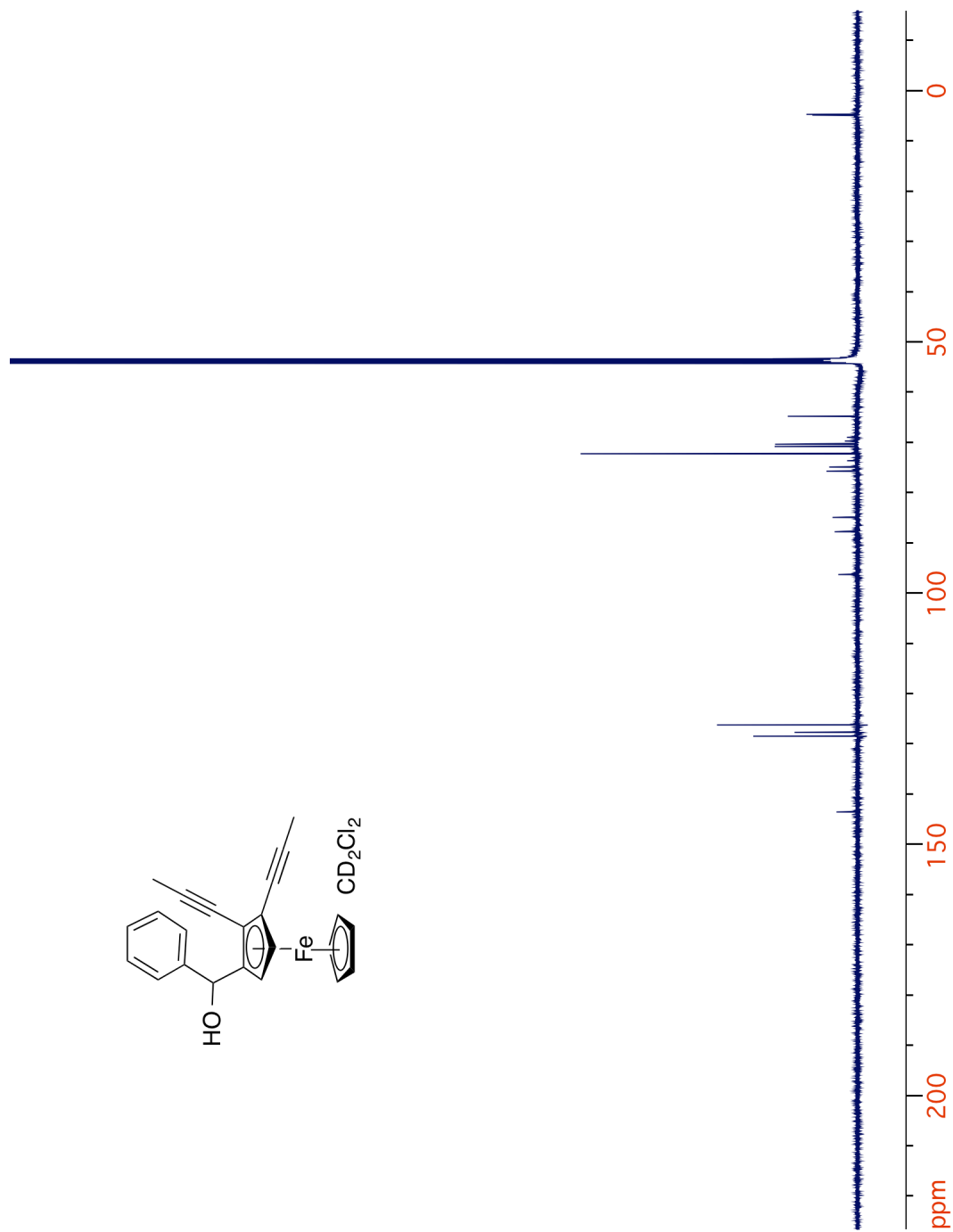
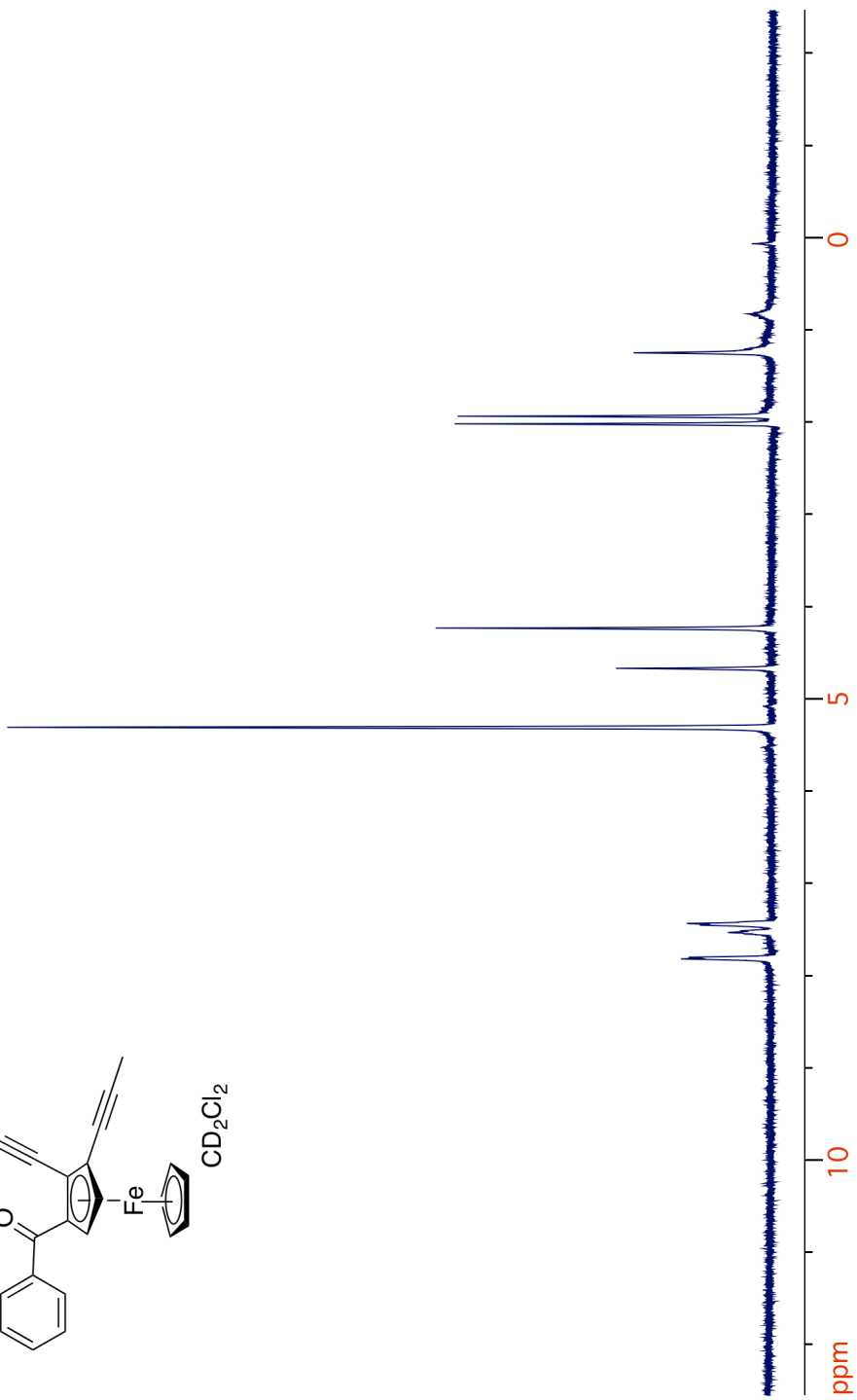
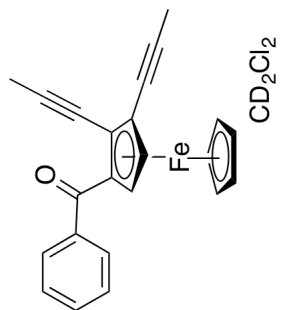


Figure 3.38. ^{13}C NMR spectrum of 58.

Figure 3.39. ^1H NMR spectrum of 45.

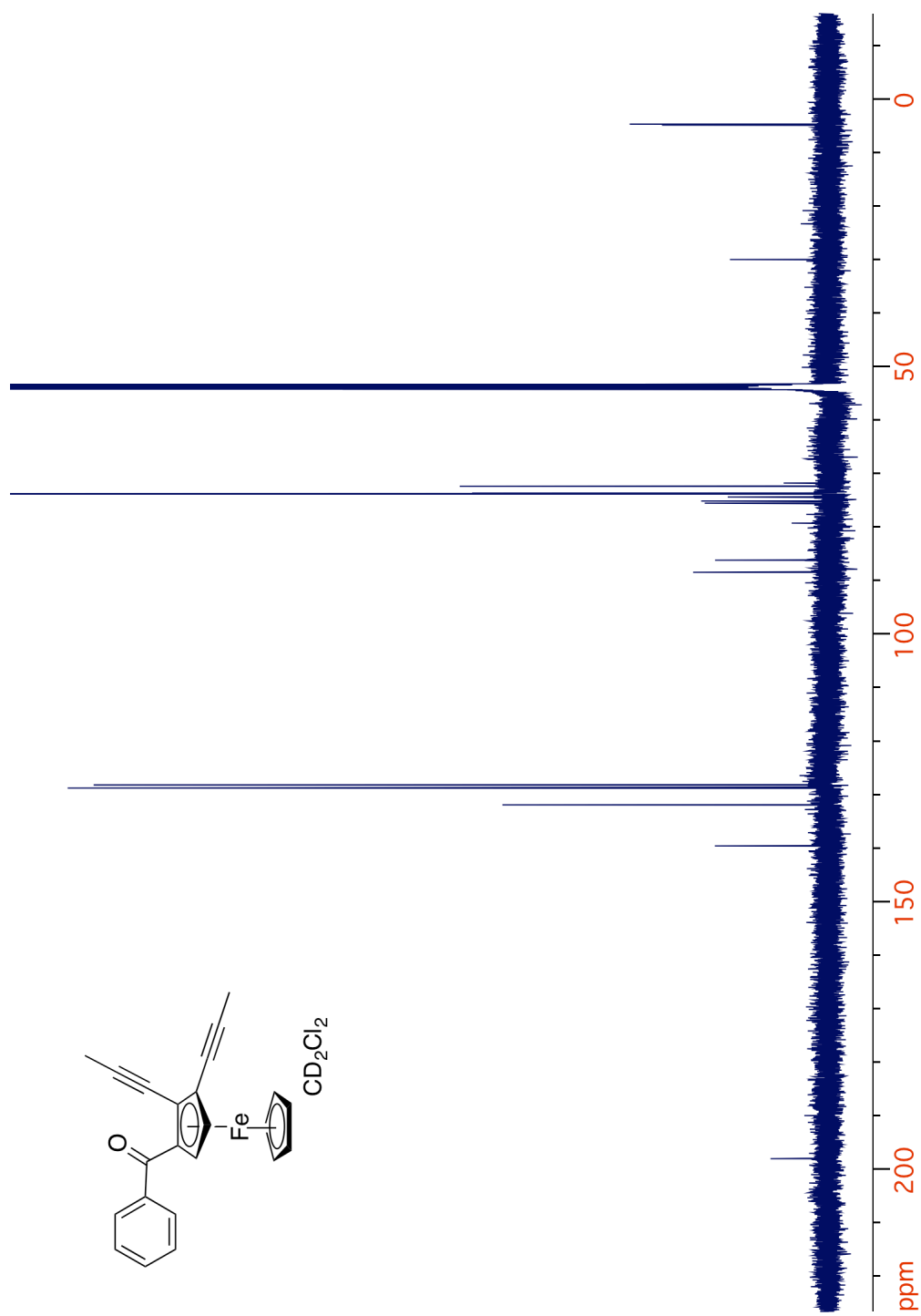


Figure 3.40. ^{13}C NMR spectrum of 45.

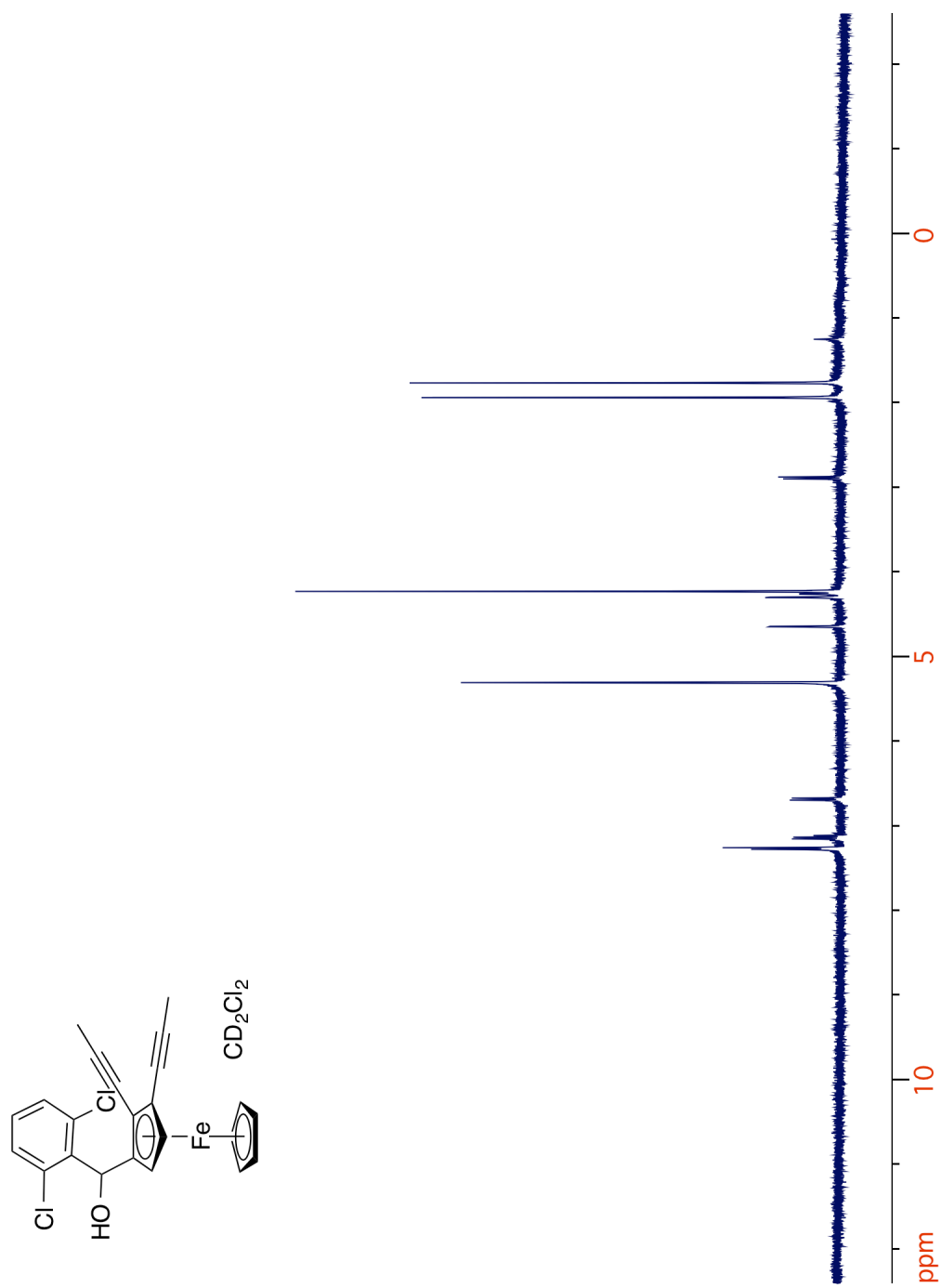


Figure 3.4.1. ^1H NMR spectrum of **60**.

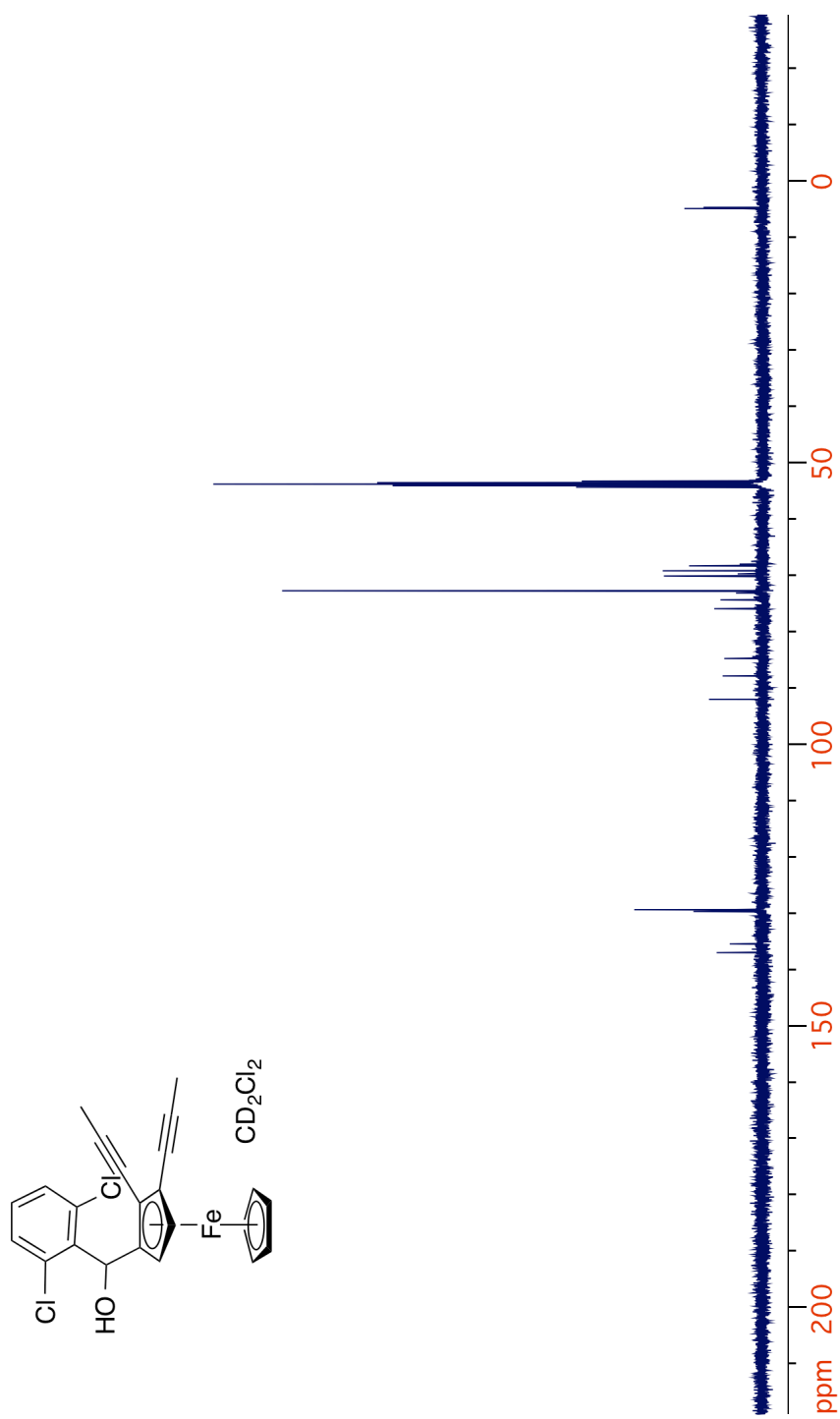
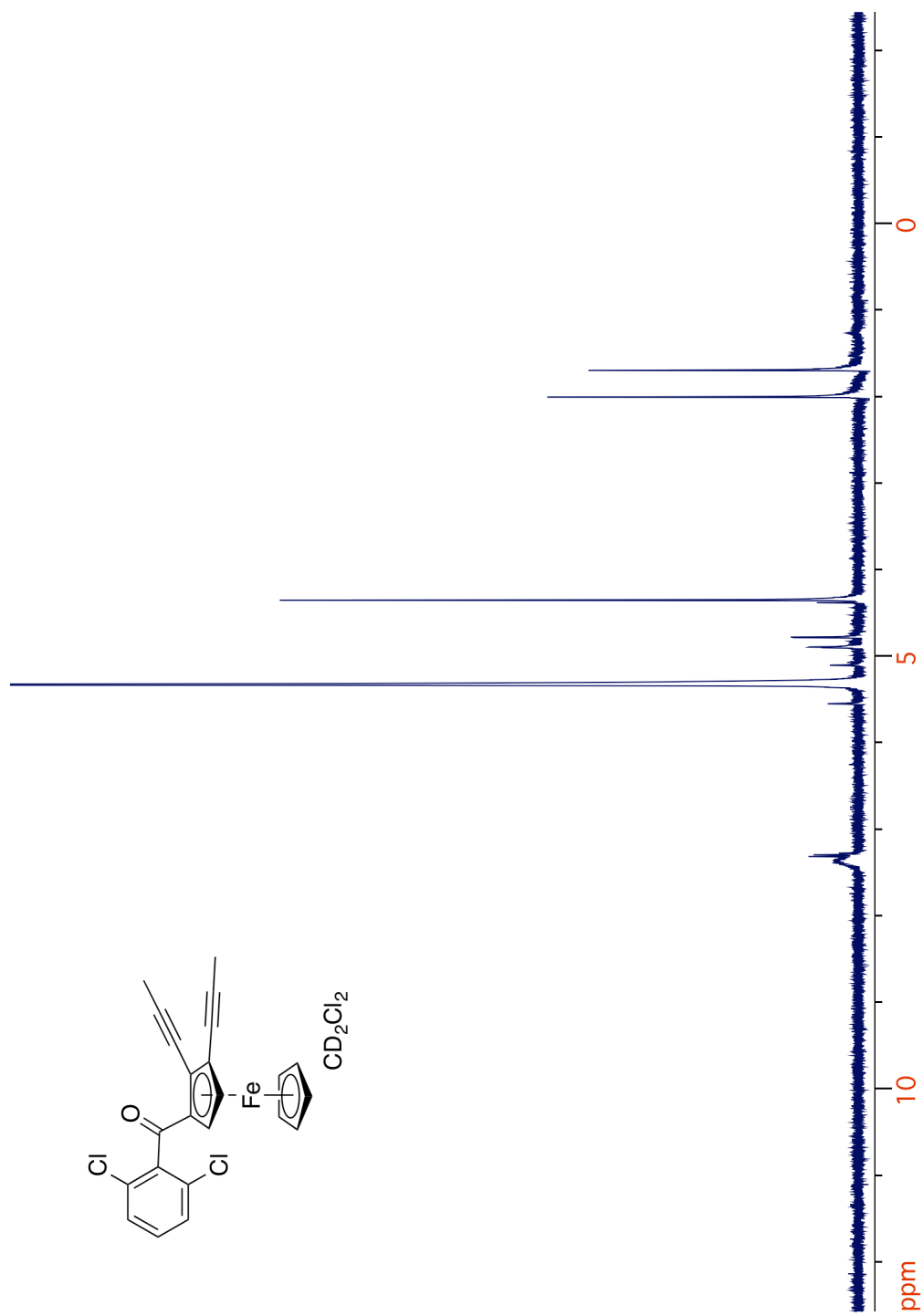


Figure 3.42. ^{13}C NMR spectrum of **60**.

Figure 3.43. ^1H NMR spectrum of 59.

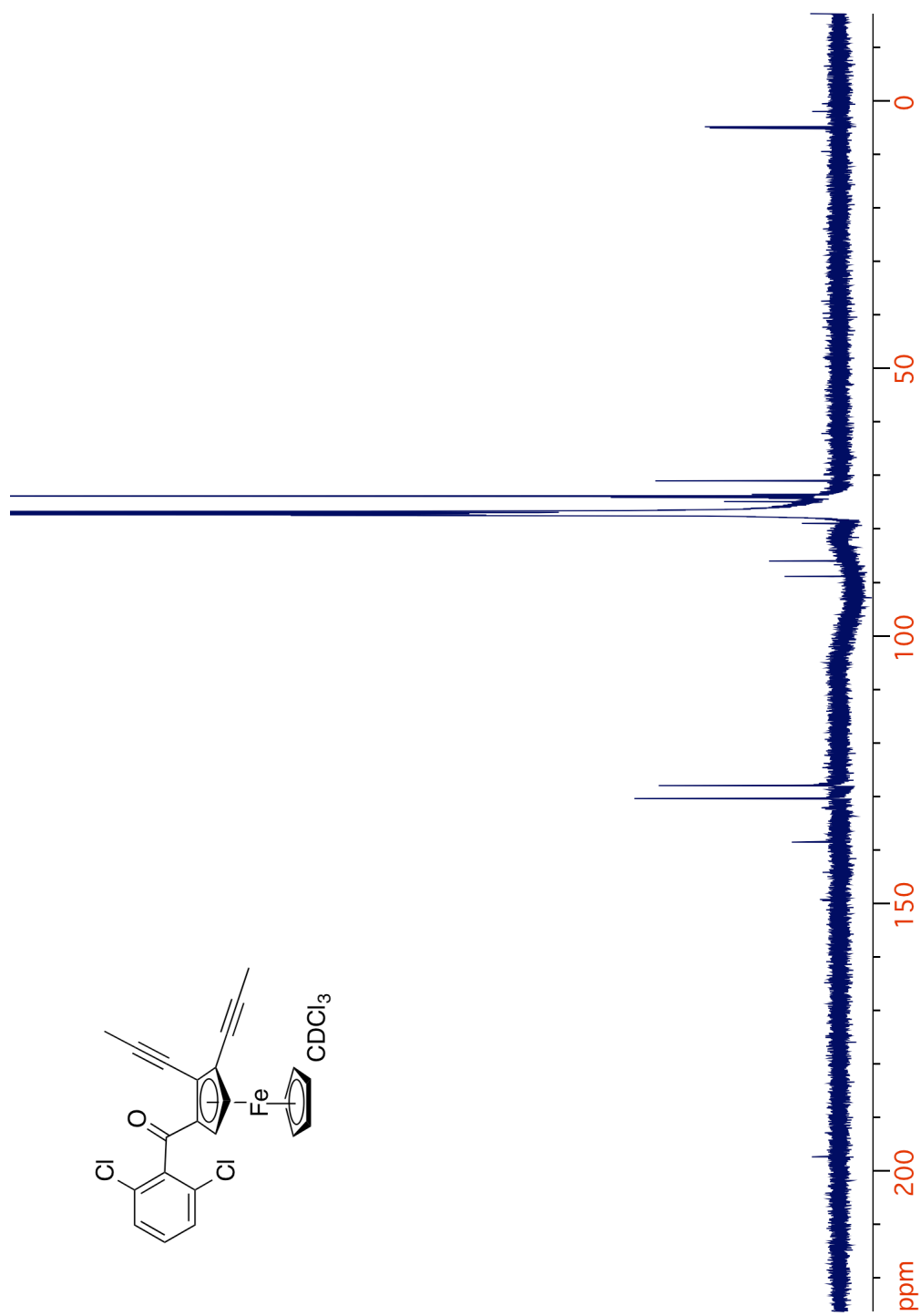


Figure 3.44. ^{13}C NMR spectrum of 59.

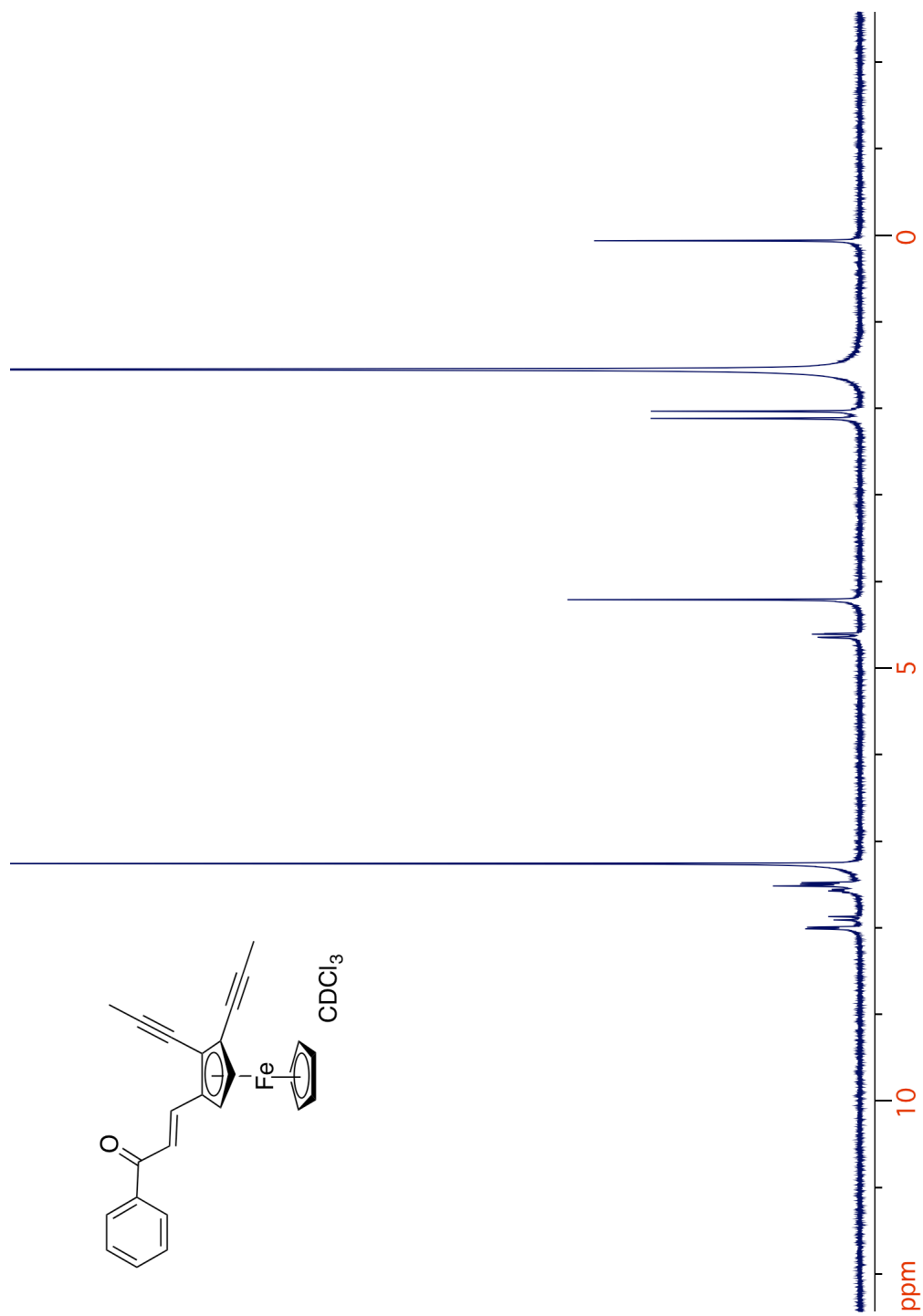


Figure 3.45. ^1H NMR spectrum of **61**.

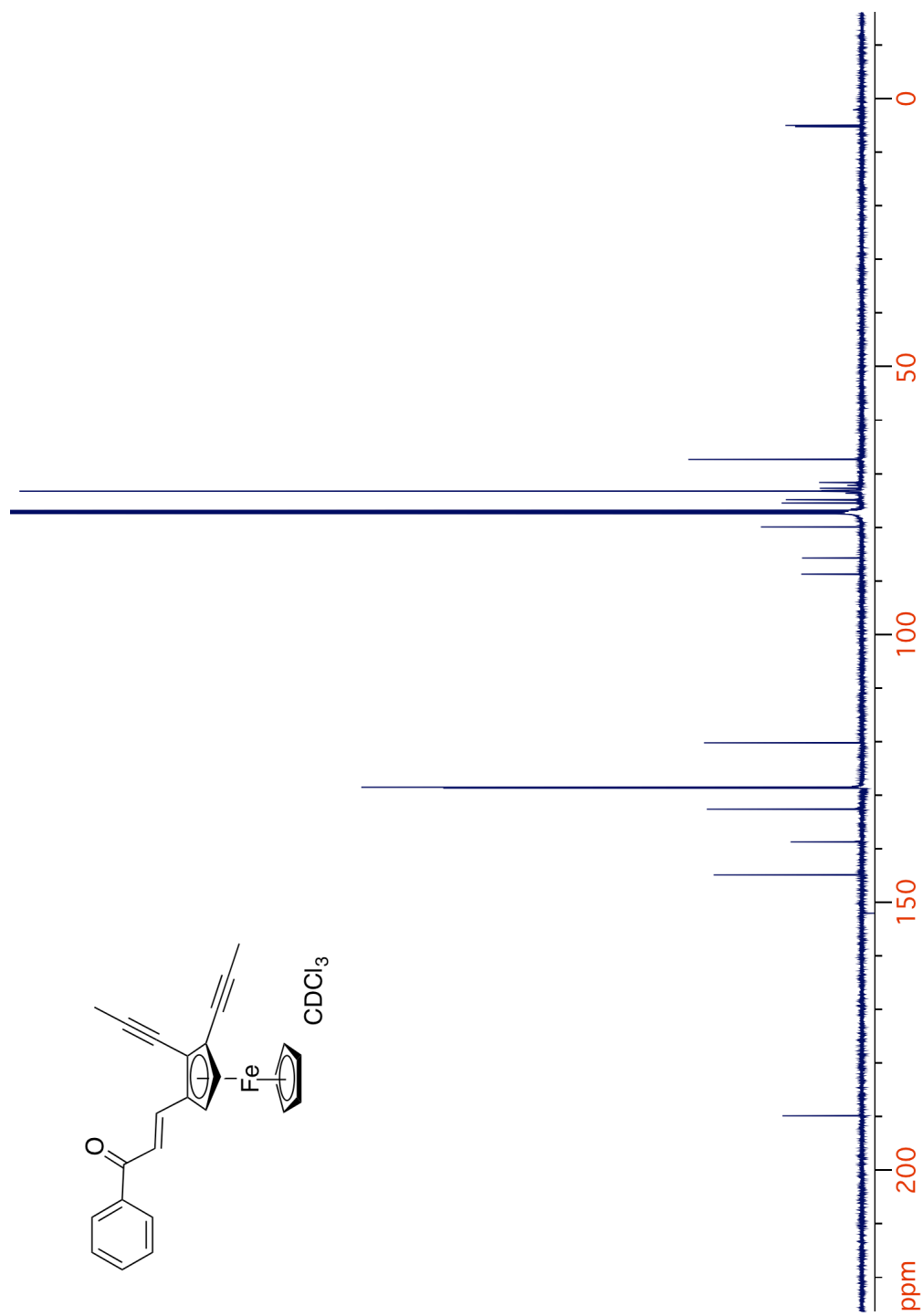


Figure 3.46. ^{13}C NMR spectrum of **61**.

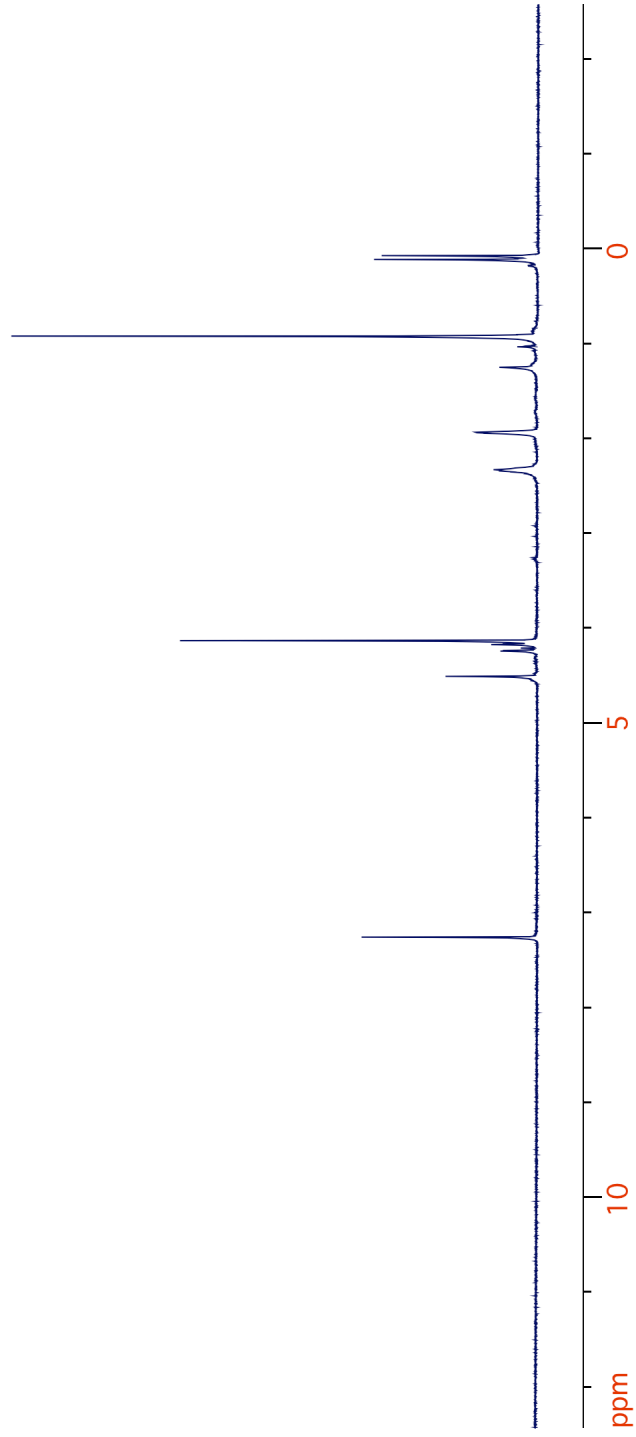
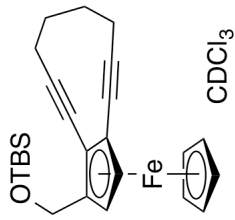


Figure 3.47. ¹H NMR spectrum of **63**.

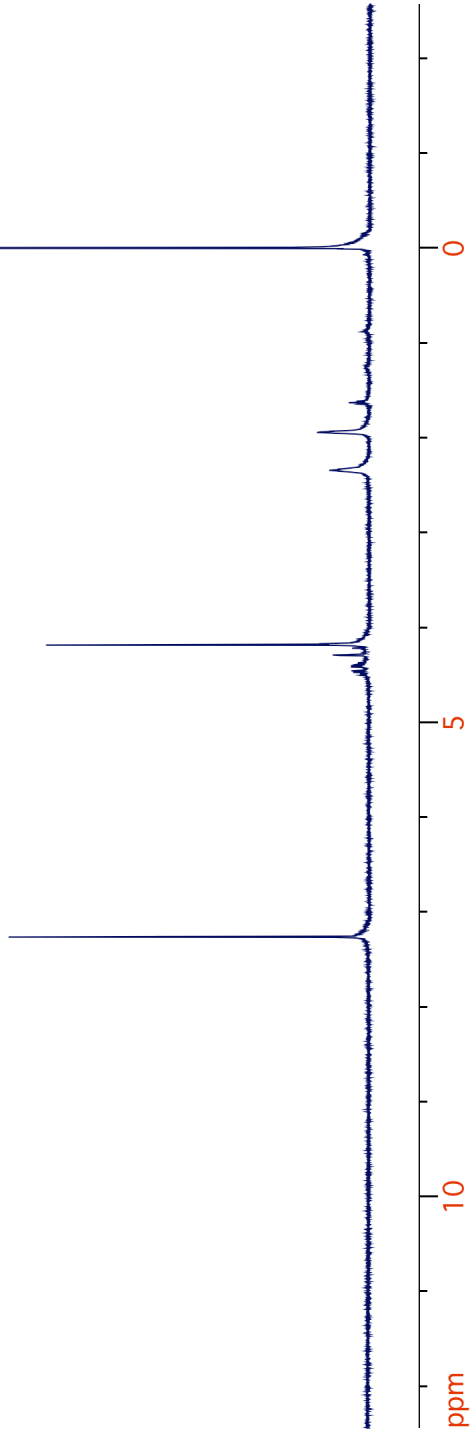
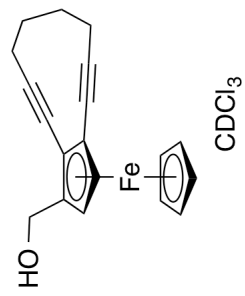


Figure 3.48. ¹H NMR spectrum of **64**.

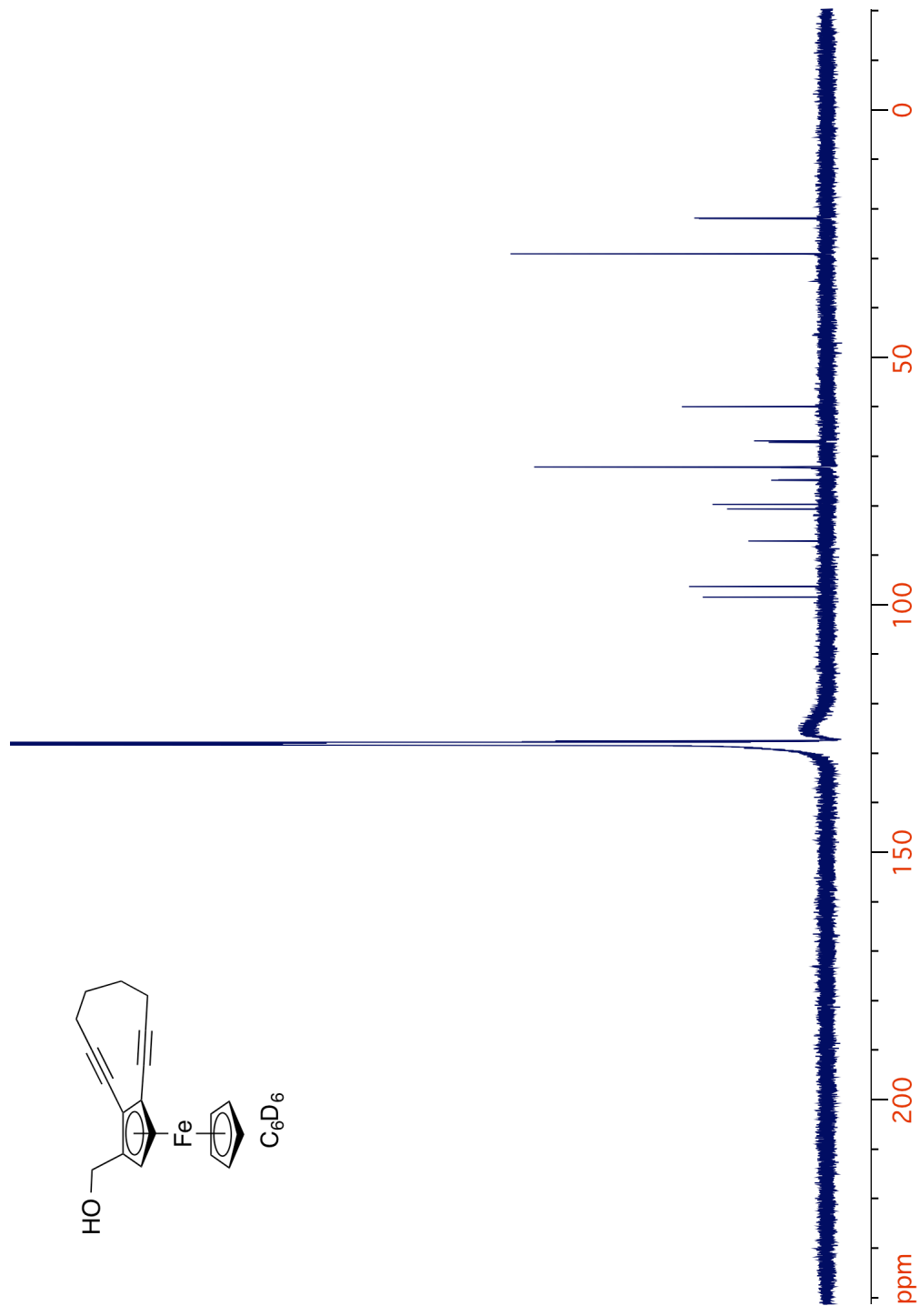


Figure 3.49. ^{13}C NMR spectrum of **64**.

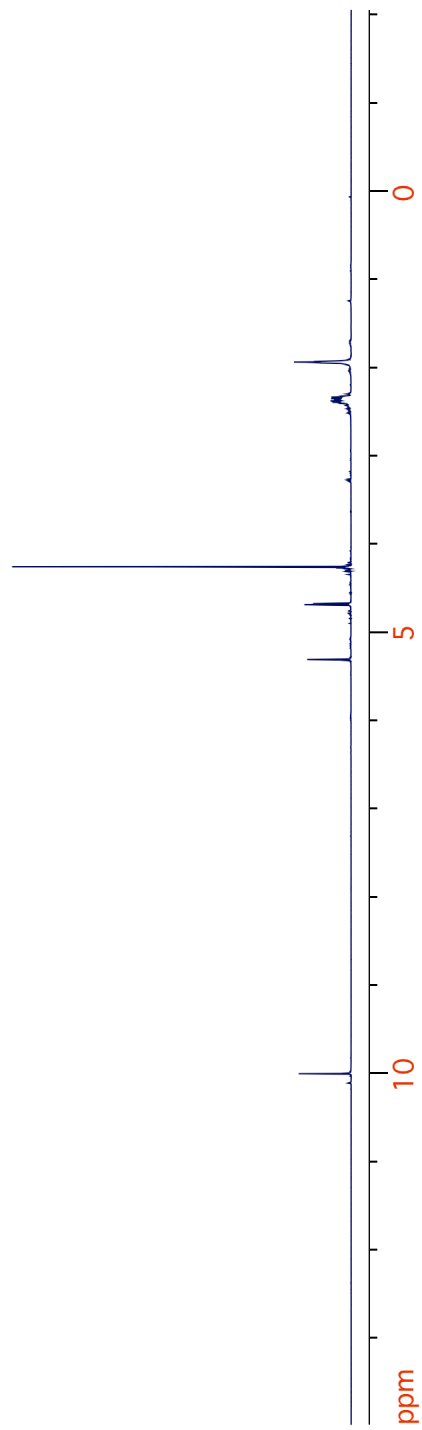
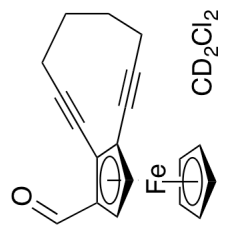


Figure 3.50. ¹H NMR spectrum of **65**.

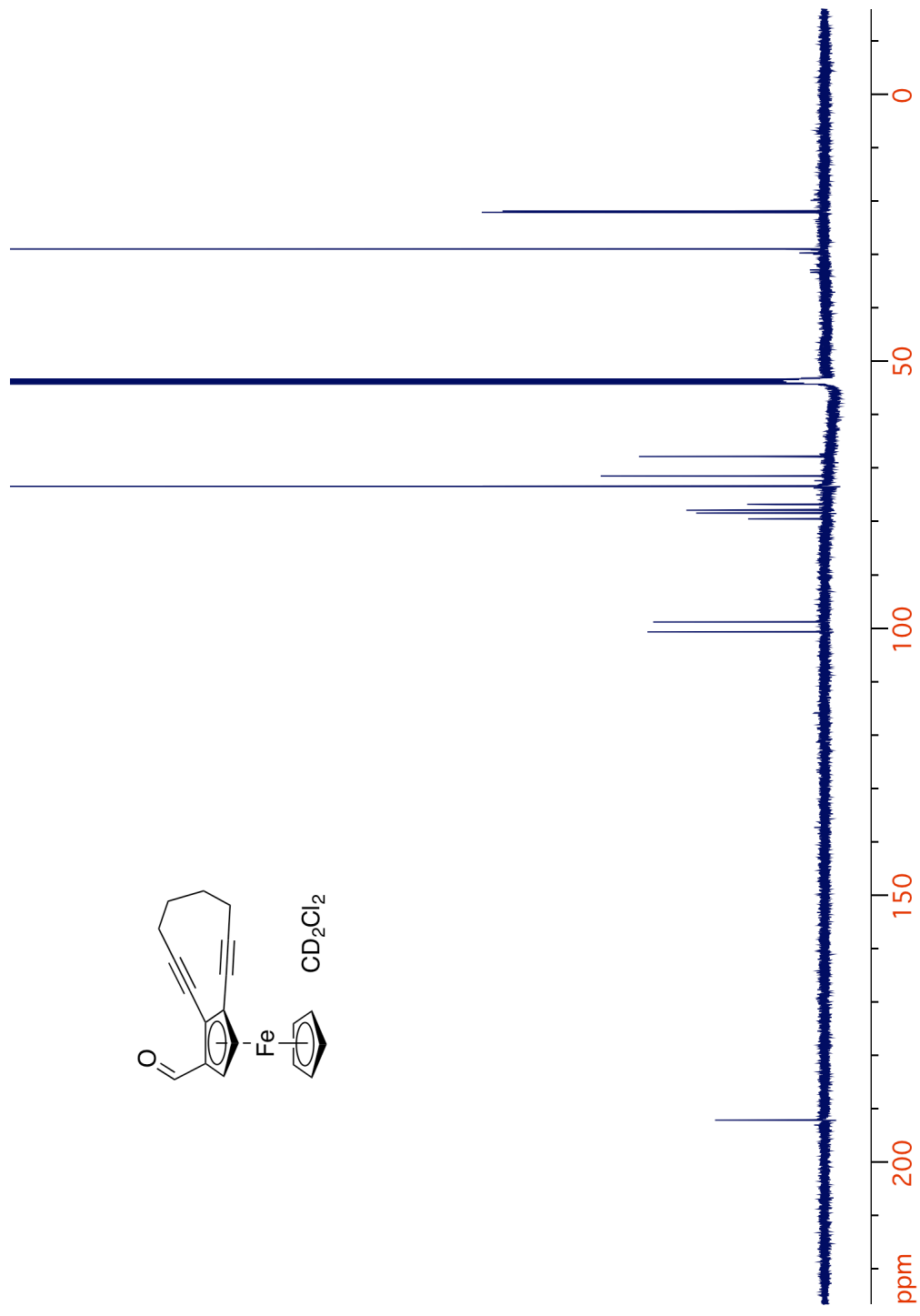


Figure 3.51. ^{13}C NMR spectrum of 65.

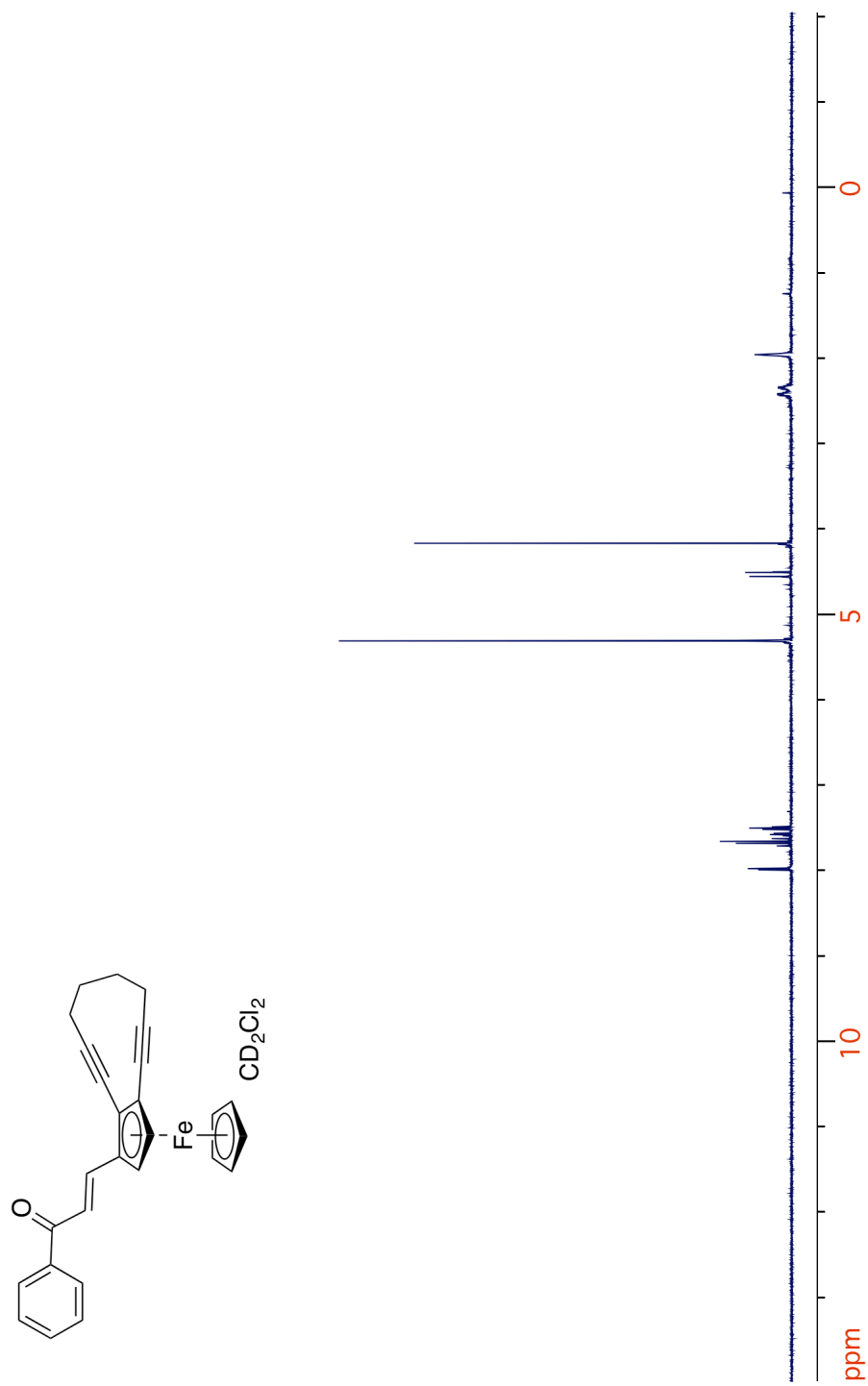


Figure 3.52. ^1H NMR spectrum of **62**.

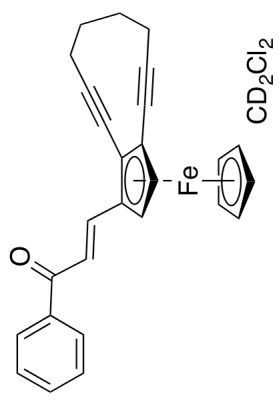
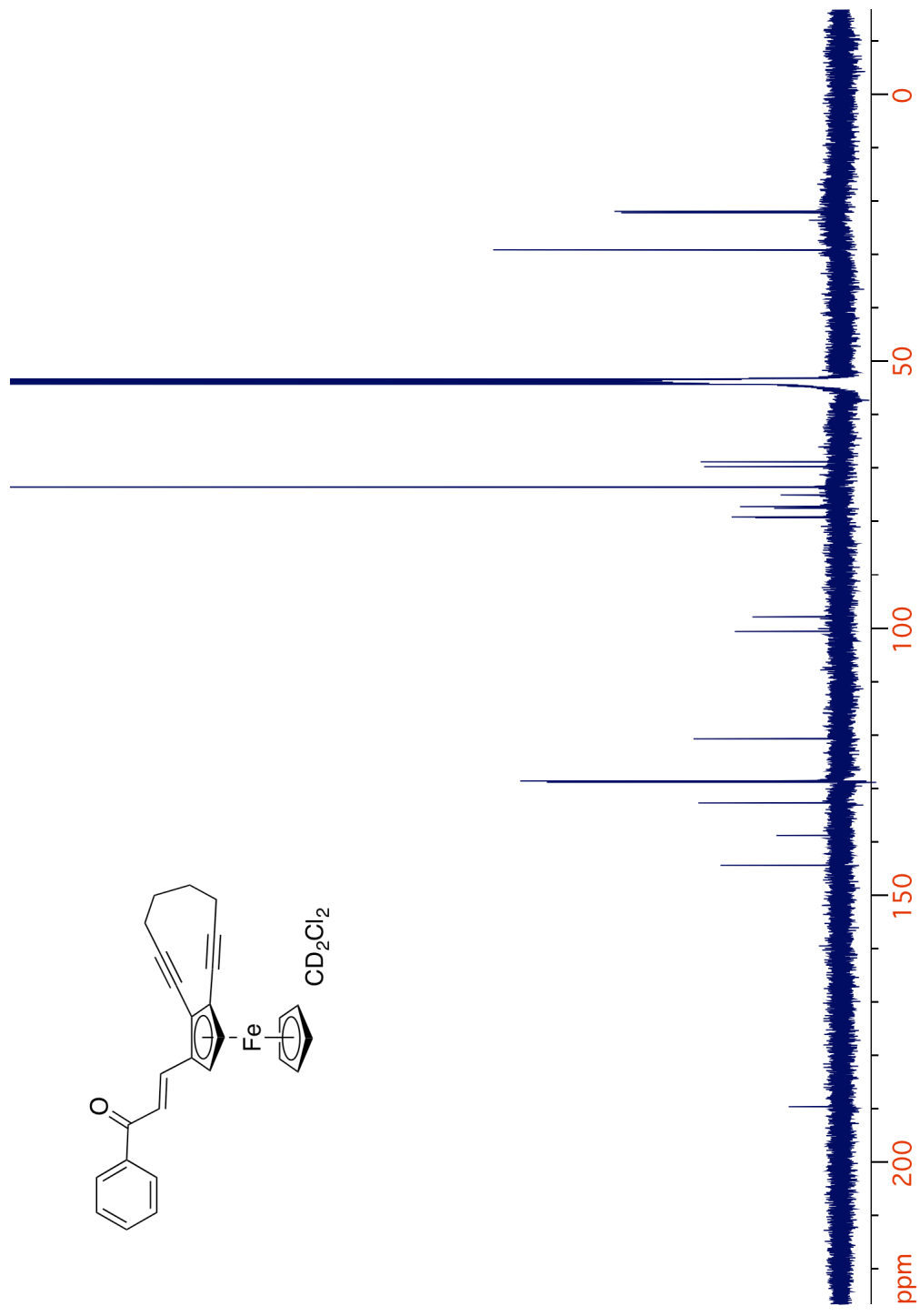


Figure 3.53. ¹³C NMR spectrum of 62.

G. Appendix 2**Table 3.14.** Crystal data and structure refinement for **24**.

Identification code	ocon118	
Empirical formula	C ₂₂ H ₂₄ Fe O	
Formula weight	360.26	
Temperature	100(2) K	
Wavelength	0.71073 Å	
Crystal system	Orthorhombic	
Space group	Pbca	
Unit cell dimensions	a = 14.8682(9) Å	α = 90°
	b = 15.6038(9) Å	β = 90°
	c = 15.6040(9) Å	γ = 90°
Volume	3620.1(3) Å ³	
Z	8	
Density (calculated)	1.322 g/cm ³	
Absorption coefficient	0.838 mm ⁻¹	
F(000)	1520	
Crystal size	0.33 x 0.30 x 0.24 mm ³	
Crystal color, habit	Dark red block	
Theta range for data collection	2.30 to 26.44°	
Index ranges	-17 ≤ h ≤ 18, -19 ≤ k ≤ 19, -18 ≤ l ≤ 14	
Reflections collected	12679	
Independent reflections	3605 [R(int) = 0.0257]	
Completeness to theta = 25.00°	98.0 %	
Absorption correction	Multi-scan	
Max. and min. transmission	0.8243 and 0.7696	
Refinement method	Full-matrix least-squares on F ²	
Data / restraints / parameters	3605 / 0 / 222	
Goodness-of-fit on F ²	1.051	

Final R indices [$I > 2\sigma(I)$]	R1 = 0.0253, wR2 = 0.0658
R indices (all data)	R1 = 0.0306, wR2 = 0.0673
Largest diff. peak and hole	0.278 and -0.265 e \AA^{-3}

Table 3.15. Crystal data and structure refinement for **26**.

Identification code	ocon121	
Empirical formula	C21 H19 Cl2 Fe N O	
Formula weight	428.12	
Temperature	100(2) K	
Wavelength	0.71073 \AA	
Crystal system	Monoclinic	
Space group	P2(1)/c	
Unit cell dimensions	a = 7.4094(3) \AA	$\alpha = 90^\circ$
	b = 22.6604(10) \AA	$\beta = 106.364(2)^\circ$
	c = 10.9863(5) \AA	$\gamma = 90^\circ$
Volume	1769.88(13) \AA^3	
Z	4	
Density (calculated)	1.607 g/cm ³	
Absorption coefficient	1.164 mm ⁻¹	
F(000)	880	
Crystal size	0.35 x 0.35 x 0.10 mm ³	
Theta range for data collection	3.00 to 28.38°	
Index ranges	-9 ≤ h ≤ 8, -30 ≤ k ≤ 30, -14 ≤ l ≤ 12	
Reflections collected	24080	
Independent reflections	4248 [R(int) = 0.0434]	
Completeness to theta = 25.00°	98.3 %	
Absorption correction	Multi-scan	
Max. and min. transmission	0.8925 and 0.6861	

Refinement method	Full-matrix least-squares on F ²
Data / restraints / parameters	4248 / 0 / 235
Goodness-of-fit on F ²	1.082
Final R indices [I > 2σ(I)]	R1 = 0.0388, wR2 = 0.0781
R indices (all data)	R1 = 0.0532, wR2 = 0.0822
Largest diff. peak and hole	0.530 and -0.443 e Å ⁻³

Table 3.16. Crystal data and structure refinement for **32**.

Identification code	ocon120	
Empirical formula	C ₂₁ H ₂₀ B Cl ₂ F ₄ Fe N O	
Formula weight	515.94	
Temperature	100(2) K	
Wavelength	0.71073 Å	
Crystal system	Monoclinic	
Space group	C2/c	
Unit cell dimensions	a = 42.561(3) Å	α = 90°
	b = 7.9923(5) Å	β = 107.854(4)°
	c = 13.0591(7) Å	γ = 90°
Volume	4228.2(4) Å ³	
Z	8	
Density (calculated)	1.621 g/cm ³	
Absorption coefficient	1.015 mm ⁻¹	
F(000)	2096	
Crystal size	0.33 x 0.33 x 0.10 mm ³	
Theta range for data collection	3.12 to 28.10°	
Index ranges	-56 ≤ h ≤ 56, -10 ≤ k ≤ 9, -17 ≤ l ≤ 14	
Reflections collected	24055	
Independent reflections	5166 [R(int) = 0.0526]	
Completeness to theta = 25.00°	99.8 %	
Absorption correction	Multi-scan	
Max. and min. transmission	0.9053 and 0.7306	
Refinement method	Full-matrix least-squares on F ²	

Data / restraints / parameters	5166 / 0 / 284
Goodness-of-fit on F^2	1.024
Final R indices [$I > 2\sigma(I)$]	R1 = 0.0362, wR2 = 0.0846
R indices (all data)	R1 = 0.0545, wR2 = 0.0928
Largest diff. peak and hole	0.430 and -0.422 e \AA^{-3}

Table 3.17. Crystal data and structure refinement for **59**.

Identification code	ocon119	
Empirical formula	C23 H16 Cl2 Fe O	
Formula weight	435.11	
Temperature	100(2) K	
Wavelength	0.71073 \AA	
Crystal system	Orthorhombic	
Space group	Pna2(1)	
Unit cell dimensions	a = 21.9685(7) \AA	$\hat{a} = 90^\circ$
	b = 7.3135(3) \AA	$\hat{b} = 90^\circ$
	c = 11.7060(4) \AA	$\hat{c} = 90^\circ$
Volume	1880.76(12) \AA^3	
Z	4	
Density (calculated)	1.537 g/cm ³	
Absorption coefficient	1.096 mm ⁻¹	
F(000)	888	
Crystal size	0.32 x 0.27 x 0.20 mm ³	
Theta range for data collection	3.41 to 26.42°	
Index ranges	-17 ≤ h ≤ 27, -9 ≤ k ≤ 8, -14 ≤ l ≤ 14	
Reflections collected	15754	
Independent reflections	3805 [R(int) = 0.0270]	
Completeness to theta = 25.00°	99.7 %	
Absorption correction	Multi-scan	
Max. and min. transmission	0.8106 and 0.7206	
Refinement method	Full-matrix least-squares on F^2	
Data / restraints / parameters	3805 / 1 / 246	
Goodness-of-fit on F^2	1.039	

Final R indices [$I > 2\sigma(I)$]	R1 = 0.0189, wR2 = 0.0480
R indices (all data)	R1 = 0.0196, wR2 = 0.0484
Absolute structure parameter	-0.001(9)
Largest diff. peak and hole	0.278 and -0.198 e \AA^{-3}

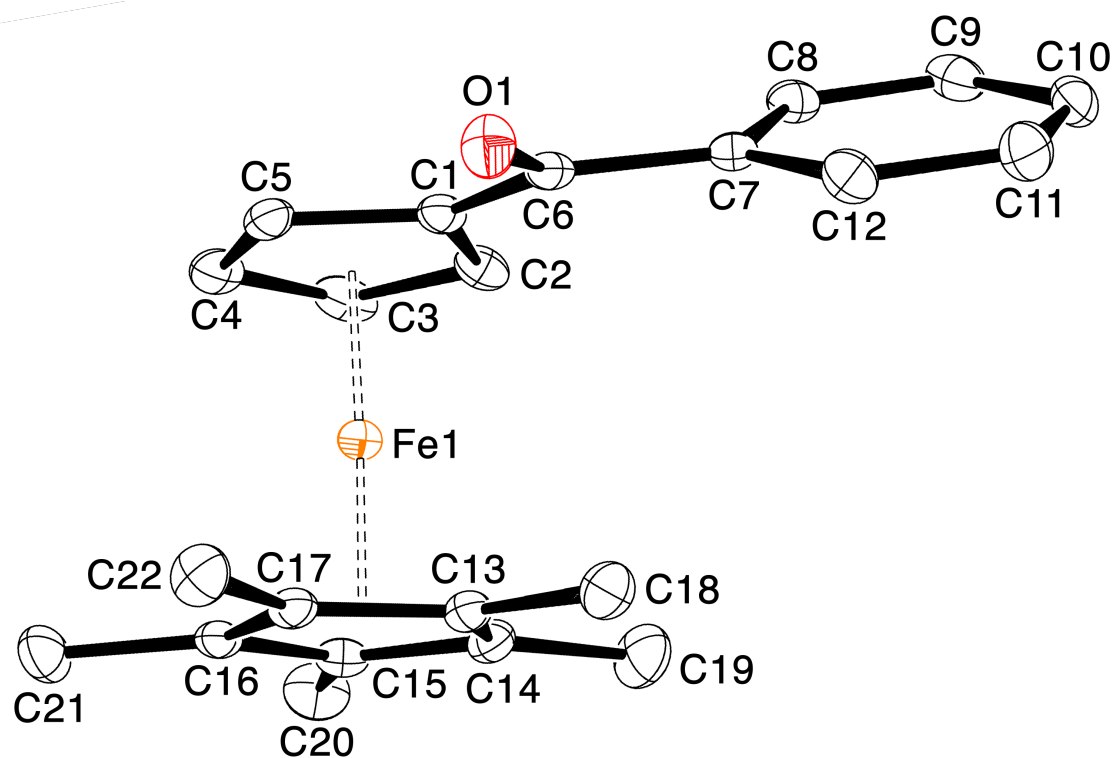


Figure 3.54. Numbered ORTEP of 24.

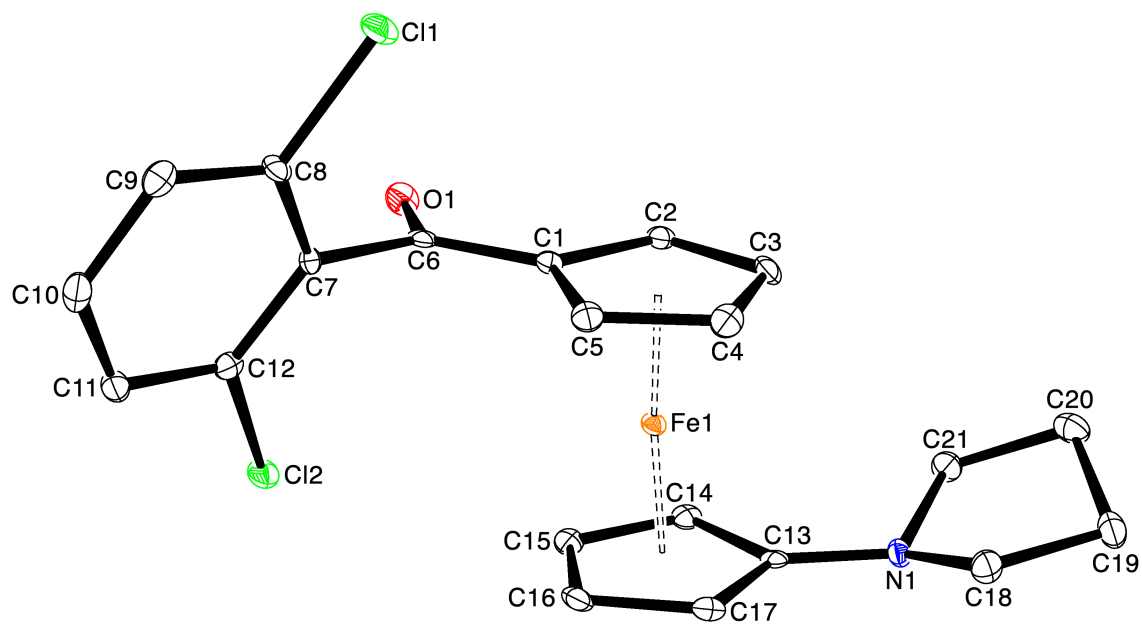


Figure 3.55. Numbered ORTEP of 26.

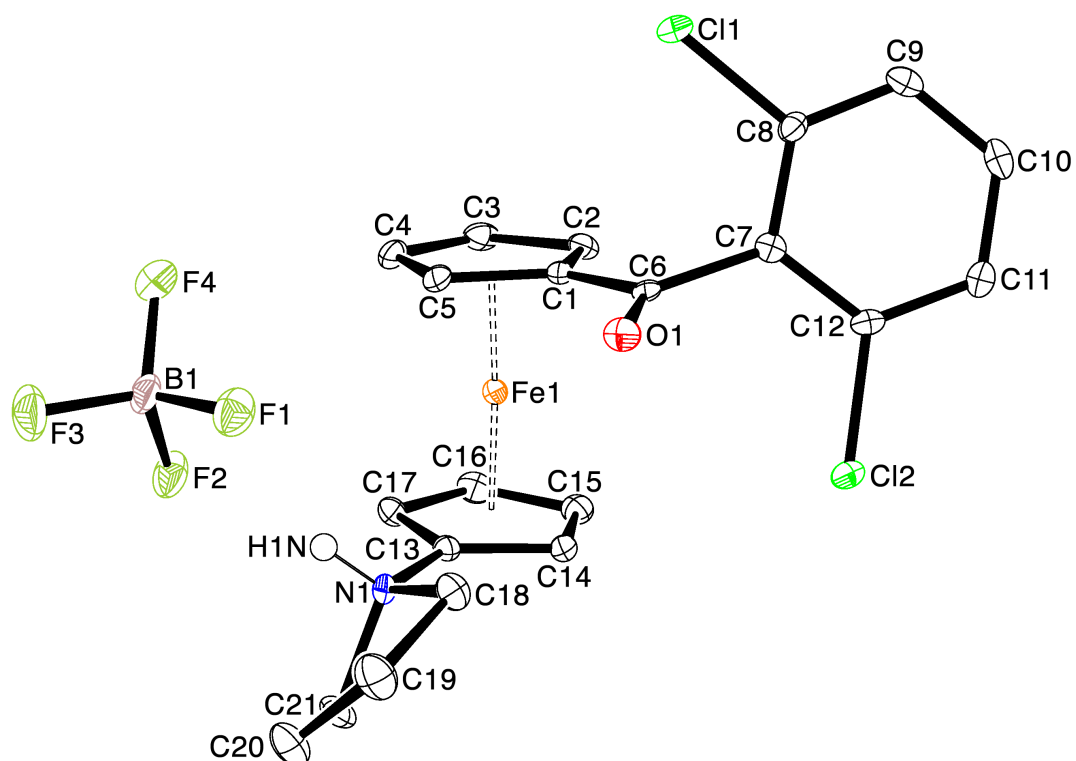


Figure 3.56. Numbered ORTEP of **32**.

H. References

- (1) Golik, J.; Dubaj, G.; Groenewold, G.; Kawaguchi, H.; Konishi, M.; Krishan, B.; Ohkuma, H.; Saitoh, K.; Doyle, T. W. *J. Am. Chem. Soc.* **1987**, *109*, 3462.
- (2) Golik, J.; Clardy, J.; Dubay, G.; Groenewold, G.; Kawaguchi, H.; Konishi, M.; Krishan, B.; Ohkuma, H.; Saitoh, K.; Doyle, T. W. *J. Am. Chem. Soc.* **1987**, *109*, 3461.
- (3) Lee, M.D.; Dunne, T.S.; Chang, C.C.; Allestad, G.A.; Siegel, M.M; Morton, G.O.; McGahren, W.J.; Borders, D. B. *J. Am. Chem. Soc.* **1987**, *109*, 3466.
- (4) Nicalaou, K.C.; Dai, W. *Angew. Chem. Int. Ed.* **1991**, *30*, 1387.

- (5) Galm, U.; Hager, M. H.; Van Lanen, S. G.; Ju, J.; Thorson, J. S.; Shen, B. *Chem. Rev.* **2005**, *105*, 739.
- (6) Basak, A.; Mandal, S.; Bag, S. S. *Chem. Rev.* **2003**, *103*, 4077.
- (7) Nicolaou, K. C.; Ogawa, Y.; Zuccarello, G.; Kataoka, H. *J. Am. Chem. Soc.* **1988**, *110*, 7247.
- (8) Mohamed, R. K.; Peterson, P. W.; Alabugin, I. V. *Chem. Rev.* **2013**, *113*, 7089.
- (9) Wenk, H. H.; Winkler, M.; Sander, W. *Angew. Chemie - Int. Ed.* **2003**, *42*, 502.
- (10) O'Connor, J. M.; Friese, S. J.; Tichenor, M. *J. Am. Chem. Soc.* **2002**, *124*, 3506.
- (11) O'Connor, J. M.; Friese, S. J.; Rodgers, B. L. *J. Am. Chem. Soc.* **2005**, *127*, 16342.
- (12) O'Connor, J.M.; Friese, S.J.; Rodgers, B.L.; Rheingold, A.L; Zakharov, L. *J. Am. Chem. Soc.* **2005**, *127*, 9346.
- (13) Prins, R.; Korswagen, a. R.; Kortbeek, a. G. T. G. *J. Organomet. Chem.* **1972**, *39*, 335.
- (14) Yamaguchi, Y.; Ding, W.; Sanderson, C. T.; Borden, M. L.; Morgan, M. J.; Kutal, C. *Coord. Chem. Rev.* **2007**, *251*, 515.
- (15) Yamaguchi, Y.; Kutal, C. *Inorg. Chem.* **1999**, *38*, 4861.
- (16) Ding, W.; Sanderson, C.T.; Conover, R.C.; Johnson, M.K.; Amster, I.J.; Kutal, C. *Inorg. Chem.* **2003**, *42*, 1532.
- (17) Wang, X.; Li, D.; Deuther-Conard, W.; Lu, J.; Xie, Y.; Jia, B.; Cui, M.; Steinbach, J.; Brust, P.; Liu, B.; Jia, H. *J. Med. Chem* **2014**, *57*, 7113.
- (18) Safa, K.D.; Abbasi, H.; Teimuri-Mofrad, R.; Charandabi, F. Z. *Aust. J. Chem* **2014**, *67*, 784.
- (19) Sevier, E.; Malleier, R. *J. Organomet. Chem.* **1997**, *540*, 127.
- (20) Goeltz, J. C.; Kubiak, C. P. *Organometallics* **2011**, *30*, 3908.
- (21) Bildstein, B.; Malaun, M.; Kopacka, H.; Wurst, K.; Mitterböck, M.; Ongania, K.; Opromolla, G.; Zanello, P. *Organometallics* **1999**, *18*, 4325.
- (22) Heinze, K.; Beckmann, M. *J. Organomet. Chem.* **2006**, *691*, 5576.

- (23) Metallinos, C.; Zaifman, J.; Dudding, T.; Van Belle, L.; Taban, K. *Adv. Synth. Catal.* **2010**, *352*, 1967.
- (24) Steffen, W.; Laskoski, M.; Collins, G.; Bunz, U. H. . *J. Organomet. Chem.* **2001**, *630*, 132.
- (25) Pietruszka, J.; Witt, A. *Synthesis (Stuttg)*. **2006**, *24*, 4266.
- (26) Goldman, I. M. *J. Org. Chem.* **1969**, *34*, 1979.
- (27) Tarr, a. M.; Wiles, D. M. *Can. J. Chem.* **1968**, *46*, 2725.
- (28) Veith, G. D.; Austin, N. M.; Morris, R. T. *Water Res.* **1979**, *13*, 43.
- (29) Danishefsky, S. J.; Shair, M. D. *J. Org. Chem.* **1996**, *61*, 16.
- (30) Ylijoki, K. E. O.; Lavy, S.; Fretzen, A.; Kündig, E. P.; Berclaz, T.; Bernardinelli, G.; Besnard, C. *Organometallics* **2012**, *31*, 5396.
- (31) Schuitemaker, J.J.; Baas, P.; van Leengoed, H.L.L.M.; van der Meulen, F.W.; Star, W.M.; van Zandwijk, N. *J. Photochem. Photobiol. B.* **1996**, *34*, 3.
- (32) Dolmans, D.; Fukumura, D; Jain, R. *Nat. Rev. Cancer* **2003**, *3*, 380.
- (33) Juarranz, Á.; Jaén, P.; Sanz-Rodríguez, F.; Cuevas, J.; González, S. *Clin. Transl. Oncol.* **2008**, *10*, 148.
- (34) Yano, S.; Hirohara, S.; Obata, M.; Hagiya, Y.; Ogura, S. I.; Ikeda, A.; Kataoka, H.; Tanaka, M.; Joh, T. *J. Photochem. Photobiol. C Photochem. Rev.* **2011**, *12*, 46.
- (35) Catheline, D.; Astruc, D. *J. Organomet. Chem* **1983**, *248*, C9.
- (36) Roth, W. R.; Hopf, H.; Horn, C. *Chem. Ber.* **1994**, *127*, 1765.
- (37) Semmelhack, M.F.; Neu, T.; Foubelo, F. *J. Org. Chem* **1994**, *59*, 5038.
- (38) Nicolaou, K. C.; Zuccarello, G.; Riemer, C.; Estevez, V. a.; Dai, W. M. *J. Am. Chem. Soc.* **1992**, *114*, 7360.
- (39) Baldrige, K. K.; Donovan-Merkert, B. T.; O'Connor, J. M.; Lee, L. I.; Closson, A.; Fandrick, D.; Tran, T.; Bunker, K. D.; Fouzi, M.; Gantzel, P. *Org. Biomol. Chem.* **2003**, *1*, 763.

- (40) Jiao, H.; Von Ragué Schleyer, P.; Mo, Y.; McAllister, M. a.; Tidwell, T. T. *J. Am. Chem. Soc.* **1997**, *119*, 7075.
- (41) O'Connor, J. M.; Baldrige, K. K.; Rodgers, B. L.; Aubrey, M.; Holland, R. L.; Kassel, W. S.; Rheingold, A. L. *J. Am. Chem. Soc.* **2010**, *132*, 11030.